

AES 2016 Malaga - Spain

The 4th Advanced Electromagnetics Symposium

Proceedings

ISSN 2491-2417

mysymposia.org





CONSEJO SUPERIOR DE INVESTIGACIONES CIENTÍFICAS



A LETTERS JOURNAL EXPLORING THE FRONTIERS OF PHYSICS



AES 2016 Malaga - Spain

The 4th Advanced Electromagnetics Symposium

Please share your comments, photos & videos !

facebook

www.facebook.com/aes.symposium

twitter

[@aes_contact](#) ; [#aes16malaga](#)

Edited by

Said Zouhdi | Paris-Sud University, France
Eva Rajo-Iglesias | University Carlos III of Madrid, Spain
Enrique Marquez Segura | University of Malaga, Spain

CONTENTS

AES 2016 ORGANIZATION	1
SPONSORS AND SUPPORTERS	3
PLENARY SPEAKERS	5
AES 2016 VENUE	6
GUIDELINES FOR PRESENTERS	8
TECHNICAL PROGRAM	9

AES 2016 ORGANIZATION



Said Zouhdi
General Chair
Paris–Sud University, France



Eva Rajo-Iglesias
General Co-Chair
University Carlos III, Spain



Enrique Marquez Segura
General Co-Chair
University of Malaga, Spain

ORGANIZING COMMITTEE



Laurent Santandrea, Chair
GeePs-CNRS, France

Laurent Daniel, CentraleSupélec, France

INTERNATIONAL ADVISORY COMMITTEE

Yahia Antar, Canada
Jean Chazelas, France
Wen-Shan Chen, Taiwan
Christos Christopoulos, UK
Apostolos Georgiadis, Spain
Dave V. Giri, USA
Xun Gong, USA
Lixin Guo, China

Yang Hao, United Kingdom
Nathan Ida, USA
Koichi Ito, Japan
Andrzej Karwowski, Poland
Kwai Man Luk, Hong Kong
Peter de Maagt, Netherlands
Adel Razek, France
Alain Sibille, France

Ari Sihvola, Finland
Paul Smith, Australia
C-K Clive Tzuang, China
J(Yiannis) C. Vardaxoglou, UK
Junhong Wang, China
Jian Wu, China
Yong-Jun Xie, China
Yu Zhang, China

TECHNICAL PROGRAM COMMITTEE

Xavier Begaud, France
Silvio Ernesto Barbin, Brazil
Muhammad Bawa'aneh, Jordan
Elisenda Bou-Balust, Spain
Qin Chen, China
Christophe Craeye, Belgium
Tie Jun Cui, China
Inigo Cuinas Gomez, Spain
Laurent Daniel, France
Salvador G. Garcia, Spain

Brahim Guizal, France
Tian Sen Jason Horng, Taiwan
Ruey-Bing Hwang, Taiwan
Zhirun Hu, UK
Tommaso Isernia, Italy
Ali Khenchaf, France
Ahmed Kishk, Canada
Ken-ichi Kitayama, Japan
Maciej Krawczyk, Poland
Hamza Kurt, Turkey

Mustafa Kuzuoglu, Turkey
Sebastien Lallechere, France
Jean-Claude Levy, France
Jean-Marc Lopez, France
Erik S. Lotfi, Qatar
Andrea Massa, Italy
Ozlem Ozgun, Turkey
Cheng-Wei Qiu, Singapore
Oscar Quevedo-Teruel, Sweden
Adroaldo Raizer, Brazil

Blaise Ravelo, France
Josaphat T. S. Sumantyo, Japan
Goran Stojanovic, Serbia

Nian X. Sun, USA
Van Yem Vu, Viet Nam
Amir I. Zaghloul, USA

Qi-Jun Zhang, Canada
Tao Zhou, China
Arkady Zhukov, Spain

SPECIAL SESSIONS ORGANIZERS

Hulusi Acikgoz, Turkey
Mohamed Boutchich, France
Kofi Edee, France
Bruno Gallas, France
Sebastien Lallechere, France
Erik S. Loffi, Qatar
Hichame Maanane, France

Salah Obayya, Egypt
Rocco Pierri, Italy
Khalid Z. Rajab, UK
Jerome Rossignol, France
Harald Schwefel, New Zealand
Raffaele Solimene, Italy
Mohamed Swillam, Egypt

Farid Temcamani, France
Wenjie Wan, China
Wei Wu, USA
Ying Wu, Saudi Arabia
Linjie Zhou, China

SPONSORS AND SUPPORTERS

AES 2016 gratefully acknowledges the support of these institutions and companies for their contribution to the success of this conference :

SUPPORTERS



UNIVERSIDAD
DE MÁLAGA



Universidad
Carlos III de Madrid



CentraleSupélec



Génie électrique et électronique de Paris

GOLD SPONSORS



epl A LETTERS JOURNAL
EXPLORING THE
FRONTIERS OF PHYSICS

EPL
www.epljournal.org



NT-MDT

NT-MDT Co.
www.ntmdt.com



STS
ELIONIX

STS-Elionix
www.sts-elionix.com



ACS
Photonics

ACS Photonics
pubs.acs.org/photronics



CST
www.cst.com



Smart Force Technologies
www.smartforcetechnologies.com

SILVER SPONSORS



WITec
www.witec.de



Neaspec
www.neaspec.com



Photon Design
www.photond.com

PLENARY SPEAKERS



Ismo V. Lindell

Aalto University, Finland

Coordinate-Free Classifications of Electromagnetic Media

Ismo V. Lindell is a Professor Emeritus in the Department of Radio Science and Engineering, in the School of Electrical Engineering at the Aalto University, Finland. He has authored or coauthored more than 270 refereed scientific papers and 11 books, for example, *Multiforms, Dyadics and Electromagnetic Media* (Wiley, 2015), *Methods for Electromagnetic Field Analysis* (IEEE Press, 2002), *Electromagnetic Waves in Chiral and Bi-Isotropic Media* (Artech House, 1994), *Differential Forms in Electromagnetics* (IEEE Press, 2004). Dr. Lindell received the IEEE S.A. Schelkunoff price (1987),

the IEE Maxwell Premium (1997 and 1998) and the URSI van der Pol gold medal (2005).



Koji Yamada

National Institute of Advanced Industrial Science and Technology (AIST), Japan

Back-end Si photonics for high-performance photonic systems

Koji Yamada received his B.E., M.E. and Ph.D. degrees in nuclear engineering from Kyushu University, Japan, in 1986, 1988 and 2003, respectively. Currently, he is a group leader of Silicon Photonics Group in National Institute of Advanced Industrial Science and Technology (AIST), Japan. From 1988 to 2015, in NTT laboratories, he was engaged in studies on accelerator physics/engineering for synchrotron light sources and studies on silicon-

based photonic platform. Since joining AIST in 2015, he continues studying silicon-based photonic platform. He is a member of IEEE, the Institute of Electronics, Information and Communication Engineers (IEICE), the Japan Society of Applied Physics, the Atomic Energy Society of Japan and the Particle Accelerator Society of Japan.

AES 2016 VENUE

AES 2016 will be held at the **Palacio de Congresos y Exposiciones de la Costa del Sol** (Torremolinos Congress Center), 3 Calle Mexico, 29620 Torremolinos, Spain, from **25 to 28 July 2016**.



GETTING TO VENUE

Address

Palacio de Congresos y Exposiciones de la Costa del Sol, 3 Calle Mexico, 29620 Torremolinos, Spain.

Getting to Torremolinos from Malaga Airport

Torremolinos is around 8km away from Malaga international airport. You can go from the airport to the city center by taxi, by train or by bus.

By Taxi

The airport has a well-signposted taxi rank outside the arrivals area of Terminal T3. Make sure that the taxi driver has started the taximeter at the beginning of the journey (minimum fare). We recommend requesting a receipt for any complaint or claim. The cost of a taxi from the airport into Torremolinos City Centre will cost between €15-20 depending on your time of travel.

By Train

The new suburban train station in the new Terminal T3 building links the airport with Torremolinos city centre and other cities like Benalmadena and Fuengirola in one direction, and it links Malaga city center in the other direction.

The new train station is situated underground and accessed via escalators. It is well signposted and can be reached via the square outside arrivals or outside departures. Before the station entry barriers you will see several self-service tickets machines on your right where you can buy your tickets.

The first train to Torremolinos leaves the airport at 05 :32, leaving every 20-30 minutes until the last train at 23.42. Line : C1. Estimated travel time : 10 minutes. The single fare for this journey is €1.80.

By Bus

You will find the bus stop straight in front of you outside the arrivals area of Terminal T3 on the side of the road where there are a couple of shelters with seats.

You will also see a ticket office in the left hand corner of the arrivals forecourt where you should purchase your tickets for the journey. Line : Torremolinos-Benalmadena-Airport. Estimated travel time : 30

minutes. The single fare for this journey is €3.80.

Getting to Torremolinos from Malaga train station

There are two train stations in the centre of Malaga : Maria Zambrano and Centro Alameda. Maria Zambrano station provides high-speed (AVE) and long-distance links to many Spanish cities like Barcelona, Cordoba, Madrid, Santiago de Compostela, Seville..., as well as local and regional routes.

You can take Line C1 from any of the two stations to reach Torremolinos. Estimated travel time : 20 minutes. The single fare for this journey is €1.80. You can check the timetables on the website of the national rail company RENFE (<http://www.renfe.com/viajeros/cercanias/malaga/>).

Getting to Torremolinos from Malaga bus station

Malaga bus station is located at the street "Paseo de los Tilos" very near Maria Zambrano train station. So it will be very easy to take a bus or a train from this station. You can take bus line Malaga-Torremolinos. Estimated travel time : 20 minutes. The single fare for this journey is €1.42.

GUIDELINES FOR PRESENTERS

ORAL PRESENTATIONS

Each session room is equipped with a stationary computer connected to a LCD projector. Presenters must load their presentation files in advance onto the session computer. Technician personnel will be available to assist you.

Scheduled time slots for presentation are 15 mn for regular, 20 mn for invited presentations, 30 mn for keynote talks and 40 mn plenary talks, including questions and discussions. Presenters are required to report to their session room and to their session Chair at least 15 minutes prior to the start of their session.

The session chair must be present in the session room at least 15 minutes before the start of the session and must strictly observe the starting time and time limit of each paper.

POSTER PRESENTATIONS

Presenters are requested to stand by their posters during their session. One panel, A0 size (118.9 x 84.1 cm), in vertical orientation, will be available for each poster (there are no specific templates for posters). Pins or thumbtacks are provided to mount your posters on the board. All presenters are required to mount their papers one hour before the session and remove them at the end of their sessions.

GENERAL INFORMATION

Venue

Palacio de Congresos y Exposiciones de la Costa del Sol (Torremolinos Congress Center)
3 Calle Mexico, 29620 Torremolinos, Spain

Registration Desk

Monday 25 July (16 :30 – 18 :30) : Reception of the Congress Center
26 July – 28 July (08 :00 – 17 :00) : Reception of the Congress Center

Banquet

Date : Wednesday, 27 July
Time : 19 :30 – 23 :00
Venue : Malaga

Best Poster Award Ceremony

Date : Wednesday, 27 July (to be announced at the Symposium Banquet)
Time : 19 :30 – 23 :00
Venue : Malaga

TABLE OF CONTENTS

Plenary Presentation

Coordinate-Free Classifications of Electromagnetic Media (pp. 24)

Ismo V. Lindell,

Back-end Si photonics for high-performance photonic systems (pp. 26)

Koji Yamada,

Smart Materials and Systems

Frequency and magnetic field dependence of the skin depth in Co-rich soft magnetic microwires (pp. 29)

Arkady Zhukov, Ahmed Talaat, Mihail Ipatov, Alexandr Granovsky, Valentina Zhukova,

Inverse Scattering and Imaging

Precision analysis based on Cramer-Rao bound for 2D inverse scattering (pp. 33)

L. Diong, A. Roueff, Ph. Lasaygues, Amelie Litman,

Sensitivity study of homogenised parameters in the framework of the subsoil water content imaging using microwave datas. (pp. 34)

Herve Tortel, Christelle Eyraud, Anabela Da Silva, Amelie Litman,

Inverse Scattering, Reciprocal Structures and Superresolution (pp. 35)

Michael A. Fiddy,

Enhancement of multi-frequency microwave breast images using a tissue-dependent mapping technique with discontinuous Galerkin contrast source inversion (pp. 37)

Cameron Kaye, Ian Jeffrey, Joe Lovetri,

Two-stage reconstruction of complex dielectric permittivity and magnetic permeability for biomedical microwave imaging employing magnetic contrast agents (pp. 40)

Cameron Kaye, Ian Jeffrey, Joe Lovetri,

Inverse Scattering in a Multipath Environment (pp. 43)

Antonio Cuccaro, Raffaele Solimene,

Metric entropy in linear inverse scattering (pp. 50)

Maria Antonia Maisto, Raffaele Solimene, Rocco Pierri,

Comparison between different decorrelation techniques in vital sign detection (pp. 57)

Angela Dell'Aversano, Andrea Natale, Raffaele Solimene,

Performance Evaluation of Linear Sampling Method for Mixed Boundary Objects in the Half-Space Scenario (pp. 63)

Mallikarjun Erramshetty, Amitabha Bhattacharya,

Recent Advances in Reconfigurable and Multiband Antenna Technology

Non-Foster Matched Reconfigurable Antenna in UHF band (pp. 68)

Deepak S. Nagarkoti, Yang Hao, Khalid Z. Rajab,

Applications of Nanoimprint in photonics and metamaterials

Sidewall relief gratings imprinted on optical fiber sidewall for sensing applications (pp. 72)

Zhouyang Zhu, Wen-Di Li,

High contrast gratings fabricated using Nanoimprint lithography for color reflective display (pp. 74)

He Liu, Yuanrui Li, Yuhan Yao, Yifei Wang, Wei Wu,

Sub-10-nm Three-Dimensional Plasmonic Probes and sensors (pp. 76)

G. Calafiore, A. Koshelev, T. Darlington, N. J. Borys, J. Schuck, A. Weber-Bargioni, S. Babin, K. Munechika, S. Cabrini,

Nanoimprint-Assisted Shear Exfoliation + Transfer Printing (NASE+TP) for Producing Emerging Transition Metal Dichalcogenide Heterostructures (pp. 77)

Xiaogan Liang, Da Li, Sungjin Wi,

Absorption and emission of electromagnetic radiation in 2D layered materials

Coherent absorption of N00N states (pp. 81)

Thomas Roger, S. Restuccia, A. Lyons, D. Giovannini, J. Romero, J. Jeffers, M. Padgett, D. Faccio,

Nanoscale Terahertz Sensing and Imaging with Graphene and Arrayed Carbon Nanotubes (pp. 83)

Yukio Kawano,

Growth and applications of 2D materials in electron emitters and renewable energy (pp. 85)

Daniel H. C. Chua,

Strongly Coupled Graphene-Metamaterial Hybrids (pp. 86)

Isaac Luxmoore, Peter Liu, Sergey Mikhailov, Nadya Savostyanova, Federico Valmorra, Penglei Li, Jerome Faist, Geoff Nash,

Spatio-temporal observation of photogenerated electron dynamics in twisted graphene (pp. 88)

Keiki Fukumoto, M. Boutchich, H. Arezki, K. Sakurai, K. Onda, S. Koshihara,

Generation and detection of light in 2D materials and heterostructures (pp. 90)

Thomas Mueller,

Homogenization and effective medium theories

High-frequency homogenization for layered hyperbolic metamaterials (pp. 92)

Arkadii Krokhin, Jesus Arriaga, Lyudmila N. Gumen, Vladimir P. Drachev,

Nonlocal effective medium theory for photonic crystals and metamaterials (pp. 94)

Jie Luo, Yun Lai,

Boundary optical stress in metamaterial and effective-medium systems (pp. 96)

Shubo Wang, C. T. Chan,

A scheme to homogenize anisotropic metamaterials with elliptical inclusions (pp. 98)

Xiujuan Zhang, Ying Wu,

Homogenization scheme for metamaterials in scalar waves (pp. 100)

Min Yang, Guancong Ma, Ying Wu, Zhiyu Yang, Ping Sheng,

Dynamic Homogenization of Metamaterials: Nonlocal Effects and Additional Constitutive Parameters (pp. 102)

Marie-Fraïse Ponge, Olivier Poncelet, Daniel Torrent,

Higher order terms and origin dependence in metamaterial homogenization (pp. 103)

Christopher Dirdal, Hans Olaf Hagenvik, Johannes Skaar,

Superluminal propagation of Dirac-cone modes in photonic crystal slabs (pp. 105)

Kazuaki Sakoda,

An integral equation method for the homogenization of periodic inhomogeneous media with complex microstructure (pp. 106)

William James Parnell, Duncan Joyce, Raphael Assier, I. David Abrahams,

Bounds on Eddy Current Losses Estimate for Soft Magnetic Composites (pp. 108)

Xiaotao Ren, Romain Corcolle, Laurent Daniel,

Effective-medium theory for coated particles and magnetic metamaterials (pp. 110)

Shiyang Liu, Jialin Zhou, Xinning Yu, Huajin Chen, Zhifang Lin,

Photonics, Optics and Laser Technology

Novel platform for Optical Modulation Using Silicon Photonics (pp. 116)

Mohamed Swillam,

Plasma technology for industrial wastewater treatment and hydrogen production (pp. 117)

Erik S. Lotfi,

Recent progresses for EMC applications: numerical and experimental tools

Optimization of EMC shielding procedures by means of statistical re-sampling: from mean trends to reliability assessments (pp. 119)

Sebastien Lallechere, Chaouki Kasmi, Jose Lopes-Esteves, Sebastien Girard, Pierre Bonnet, Françoise Paladian,

Microwave microscopy: Effect of material deposition on the distributions of E/H-fields in the vicinity of electronic circuits (pp. 121)

Jerome Rossignol, Didier Stuerger, Guillaume Bailly, Valentin Colin, Jordan Dufresne, Sebastien Lallechere, Sebastien Girard,

Kapton-based 1x2 passive antenna array physical parameters sensitivity analysis (pp. 123)

Y. G. Rabobason, Blaise Ravelo, N. Benjelloun,

Silicon photonic devices and integration

Demonstration of integrated optical matrix-vector multiplier based on two-dimensional silicon microring resonator array (pp. 128)

Lei Zhang, Hao Jia, Jianfeng Ding, Lin Yang,

Fano resonance photonic crystal Si membrane photonics (pp. 129)

Weidong Zhou, Deyin Zhao, Hongjun Yang, Zhenqiang Ma, Mattias Hammar,

Novel Application and Design for Silicon Photonic Devices (pp. 130)

Xiaoping Liu, Minghui Lu, Yanfeng Chen,

Chirp-free silicon ring optical modulator with a dual-ring push-pull coupler (pp. 132)

Xiaomeng Sun, Linjie Zhou, Lars Zimmermann, Klaus Petermann,

Low-voltage monolithic silicon optical modulators for high-capacity optical-fiber communications (pp. 134)

Kensuke Ogawa,

Diffraction Grating theories as applied to nanophotonics, plasmonics and metamaterials

Full-wave approach for modeling cylindrical microresonators with aperiodic Fourier modal method (pp. 137)

Haitao Liu, Ying Li, Hongwei Jia, Fang Bo, Guoquan Zhang, Jingjun Xu,

Efficient Fourier representation of complex crossed grating corrugations within the Generalized Source Method (pp. 139)

Alexey Alexandrovich Shcherbakov, Alexandre Valentinovich Tishchenko,

On the stability of modal methods when dealing with lamellar structures with extreme filling ratios (pp. 141)

Brahim Guizal, Maha Ben Rhouma, Kofi Edee,

Graphene surface plasmons excited through diffraction gratings (pp. 142)

Maha Ben Rhouma, Meherzi Oueslati, Brahim Guizal,

Hypersingularity of transverse electric field at sharp edges: a case study of the simplest lamellar grating problem (pp. 143)

Lifeng Li,

Derivation of the radiation pattern of a spheroidal particle with the Aperiodic Fourier Modal Method (pp. 145)

Mira Abboud, Hassan Saleh, Julien Charon, Kofi Edee, Jean-Michel Geffrin, Jean-Francois Cornet, Jeremi Dauchet, Gerard Granet,

Modal analysis of V-groove plasmonic waveguides (pp. 147)

Gerard Granet,

Optical investigations of the quality and optical processes of photonic and plasmonic nanostructures (pp. 148)

Roman Antos, Martin Veis, Lukas Beran, Karel Palka, Jan Mistrík, Petr Janíček, Miroslav Vlček,

Leaky Modes and Plasmonics - The Impact of Layered Structures (pp. 149)

Steven Brueck, Seung Chang Lee,

Casimir Interaction between a sphere and a grating (pp. 151)

Mauro Antezza, Riccardo Messina, Paulo Maia Neto, Brahim Guizal,

Wide angle boundary models for periodic structures with subwavelength periods (pp. 152)

Ya Yan Lu,

Efficient statistical analysis of plasmonic devices response with a stochastic collocation method (pp. 154)

Kofi Edee, Pierre Bonnet,

Rigorous and extremely fast electromagnetic methods for diffraction problems (pp. 155)

Wolfgang Alexander Iff, Thomas Kampfe, Yves Jourlin, Alexandre V. Tishchenko,

Reliability and failures in electronic devices

GaN heterostructures for next generation of highly robust RF power electronics: from growth design to devices (pp. 159)

E. Dogmus, A. Linge, M. Zegaoui, Farid Medjdoub,

Measuring and Improving Reliability in Today's Consumer Electronics Industry (pp. 161)

Martin Shaw,

Thermal Management of GaN Electronics (pp. 162)

James Pomeroy, Martin Kuball,

Reliability study of mechatronic power components using spectral photon emission microscopy (pp. 164)

Niemat Moulitif, Eric Joubert, Olivier Latry,

Reliability and Failure Analysis of UHF-RFID Tags for Harsh Environments Applications (pp. 169)

Sanae Taoufik, Ahmed El Oualkadi, Pascal Dherbecourt, Farid Temcamani, Bruno Delacressonniere,

Overview on Zener diode pulsed EOS characterization (pp. 171)

Feiyi Zhu, Francois Fouquet, Blaise Ravelo, Bernadette Domenges, Moncef Kadi,

Biomedical Applications of Electromagnetics

Microwave Antennas for Cancer Ablation Therapy: Backward Heating Problem. (pp. 175)

Hulusi Acikgoz,

Magnetic Particle Imaging for Probing Viscosity (pp. 176)

Emine Ulku Saritas,

Wideband Electromagnetic Nearfield Imaging Using Compressed Sensing (pp. 178)

Ibrahim Elshafiey, Md. Anowar Hossain,

Computational Techniques for Plasmonics, metamaterial and Graphene

Pseudospectral modal method for analyzing bent waveguides (pp. 184)

Dawei Song, Ya Yan Lu,

Sensitivity analysis for photonic crystal microcavities (pp. 186)

Zhen Hu, Ya Yan Lu,

Time Domain Modelling of Parity-Time Symmetric Structure with Dispersive Gain/Loss (pp. 188)

Sendy Phang, Ana Vukovic, Stephen Creagh, Gabriele Gradoni, Phillip Sewell, Trevor Mark Benson,

A Surface Integral Equation Solver for Transient Analysis of Graphene Devices (pp. 189)

Yifei Shi, Ping Li, Ismail Enes Uysal, Huseyin Arda Ulku, Hakan Bagci,

Novel Design of High Directivity Hybrid Yagi-Uda Antenna (pp. 191)

AbdelRahman Ghanim, Mohamed Hussein, Mohamed Farhat, O. Hameed, Ashraf Yahia, Salah Obayya,

Efficient Wideband Adjoint Sensitivity Analysis of Dispersive Structures using FDTD (pp. 193)

Mohamed Bakr, Yu Zhang, Osman Ahmed,

Novel Wide Band Smoothed Finite Element Time Domain Analysis of Resonant modes in Photonic Bandgap Cavities (pp. 194)

Khaled S. R. Atia, A. M. Heikal, S. S. Obayya,

Recent Advances in Optical Micro-cavities

Phase matched SHG in an on-chip crystalline microresonator (pp. 197)

Jintian Lin, Yingxin Xu, Zhiwei Fang, Min Wang, Wei Fang, Y. Cheng,

Electro-optical modulator with 0.1 percent quantum efficiency (pp. 198)

Alfredo R. Rueda Sanchez, Florian Sedlmeir, Harald G. L. Schwefel,

Electrically tunable silicon dual-ring assisted Mach-Zehnder interferometer switches (pp. 200)

Linjie Zhou, Liangjun Lu, Shuoyi Zhao, Jianping Chen,

High-Q Micro/Nanoresonators for Nonlinear/Quantum Photonics and Sensing (pp. 202)

Qiang Lin,

Electromagnetic Theory

Electromagnetic Nuclear Physics. (pp. 204)

Bernard Schaeffer,

Electromagnetic Field Visualization with Jefimenko's Equations (pp. 210)

Brandon Gore, Peng Ye, Paul Huray,

Analyzing the properties of quantized electromagnetic waves in time-varying media (pp. 212)

Jeong Ryeol Choi,

Electromagnetic and material contributions to stress, energy, and momentum in metamaterials (pp. 214)

Brandon A. Kemp, Cheyenne J. Sheppard,

Applying the Retarded Solutions of Electromagnetic Fields to Transmission Line RLGC Modeling (pp. 223)

Peng Ye, Brandon Gore, Paul Huray,

Antenna and Propagation

New Ultra Wide Band antenna design with innovative materials. (pp. 231)

Houda Nadir, R. Negrier, N. Essaidi, E. Martinod, N. Feix, V. Bertrand, S. Rossignol, M. Lalande,

Low-Cost Transmit and Receive Reflectarray Antenna for Satellite Communications in Ka-Band (pp. 233)

Eduardo Martinez-de-Rioja, Jose A. Encinar, Rafael Florencio, Rafael R. Boix,

Study of the Complementary Strip-Slot with Circular Geometry (pp. 235)

Yordanis Alonso-Roque, Elena Abdo-Sanchez, Carlos Camacho-Penalosa,

Simple Design Procedure for 2D SWAs with Specified Sidelobe Levels and Inclined Coupling Slots (pp. 237)

Hilal M. El Misilmani, Mohammed Al-Husseini, Karim Y. Kabalan,

Simple Design Method for Dielectric-Filled Low-Sidelobe Slotted Waveguide Antennas (pp. 239)

Mohammed Al-Husseini, Hilal M. El-Misilmani, Karim Y. Kabalan, Ali El-Hajj, Elias Nassar,

Interesting Combinations of Phase and Group Velocities in the Transmission Line Negative Delay Metamaterials Explained by the Forward-Transmission-Matrix (FTM) Method (pp. 241)

Omar Siddiqui,

Performance Enhancement of Proximity Coupled Patch Antenna Using Fishnet Metamaterial (pp. 243)

A. Yilmaz, C. Sabah,

Performance Evaluation of Conventional and Planar Feeds in Resonant Cavity Antennas (pp. 244)

Arslan Kiyani, Raheel Hashmi, Karu Esselle,

Diffraction by a lossless dielectric wedge on a ground plane: time domain formulas (pp. 247)

Marcello Frongillo, Gianluca Gennarelli, Giovanni Riccio,

The Complementary Dumbbell-Shaped Strip-Slot Radiating Element (pp. 251)

Rocio Rodriguez Cano, Elena Abdo Sanchez, Teresa M. Martin Guerrero, Carlos Camacho Penalosa,

Microwave and Millimeter Circuits and Systems

A generalized approach to analyze broadband arrow-shaped loaded-stub phase shifters (pp. 258)

Badar Muneer, An Sensong, Abdul Waheed Umrani, Faisal Karim Shaikh, Umair Ahmed Korai,

Broadband TE₁₀ to TE₂₀ Mode Transformer for X Band (pp. 261)

Davide Passi, Alberto Leggieri, Rocco Citroni, Franco Di Paolo,

New Six-Way Waveguide to Microstrip Transition applied in X Band Spatial Power Combiner (pp. 264)

Davide Passi, Alberto Leggieri, Rocco Citroni, Franco Di Paolo,

Theoretical analysis of MSSW propagation in ferrimagnetic bilayer structures for band-stop zones in microwaves spectrum (pp. 267)

Jose Roberto Fragoso, Daniel Matatagui, Oleg Kolokoltsev,

Electromagnetic Compatibility

Simulation of Upset of Electronic Systems from Intentional Electromagnetic Interference (pp. 271)

Robert L. Gardner,

Investigation on EM radiations from Interconnects in Integrated Circuits (pp. 273)

L. Belhimer, A. Benfdila, A. Lakhlef,

Computational Electromagnetics

Accuracy of Norton Approximation Formulas for the Radiation of an Electric Current Element over a Homogeneous Ground (pp. 275)

Julien Vincent, Pierre Borderies, Vincent Gobin, Martin Lelong, Jean-Rene Poirier,

Analysis of Optical Properties of Nanowires Using Surface Integral Equations and the Multilevel Fast Multipole Algorithm (pp. 277)

Akif Yilmaz, Bariscan Karaosmanoglu, Ozgur Ergul,

Coupled Field Problems

Modeling and analysis of loaded multilayered magnetoelastic structures composite materials: Applications (pp. 283)

Mounia Ajdour, A. Bakkali, L. Azrar, A. El Omri,

RF and Wireless Communication

Exploiting Large-Scale Cooperative MIMO Approach in Relay-Assisted Next-Generation Cellular Systems (pp. 286)

Mostafa Hefnawi,

Optics and Photonics

Optical Attenuators with Translational Risley Prisms (pp. 291)

Virgil-Florin Duma,

Family of paraxial Laguerre-Gaussian beams with complex shift in Cartesian coordinates (pp. 293)

Alexey Andreevich Kovalev, Victor Victorovich Kotlyar, Alexey Petrovich Porfirev, Daria Sergeevna Kalinkina,

Emergence of classicality from initial quantum world for dissipative optical waves (pp. 295)

Jeong Ryeol Choi,

Remote Sensing, Inverse Problems, Imaging Radar

Polarization effects on 3D imaging from scattering measurements (pp. 298)

Christelle Eyraud, Jean-Michel Geffrin, Amelie Litman, Herve Tortel,

Identification of the electromagnetic scattering by dynamic sea surfaces with a stochastic differential equation model (pp. 299)

Arnaud Coatanhay, Alexandre Baussard,

EM and Nanophotonic Materials (metamaterials, plasmonics, etc)

Properties of isofrequency surfaces of 3D periodic dielectric composites with finite periods (pp. 302)

Andrey Alexandrovich Ushkov, Alexandre Valentinovich Tishchenko, Alexey Alexandrovich Shcherbakov,

Competition between the antiferromagnetic phase and the superconducting state in undoped BaFe₂-xNixAs₂ (RF measurements) (pp. 304)

Abdellatif Abbassi, M. Saint-Paul, C. Guttin, M. R. Britel, Rachid Dkiouak, Zhao-Sheng Wan, Huinqian Luo, Xingye Lu, Cong Ren, Hai-Hu Wen,

Electroactive and Magnetoactive Materials

Engineering of giant magnetoimpedance effect of amorphous and nanocrystalline microwires (pp. 309)

Valentina Zhukova, Ahmed Talaat, Mihail Ipatov, Alexandr Granovsky, Arkady Zhukov,

Bioeffects of EM fields, Biological Media, Medical electromagnetics

Bio-inspired inversion method for the retrieval of the frequency-dependent permittivities of natural multilayer materials (pp. 315)

Demetrio Macias, Diana C. Skigin, Marina E. Inchaussandague, Alexandre Vial,

Measurement Techniques

In situ permittivity measurements using stand-alone end effect probe (pp. 318)

Francois Demontoux, Gilles Ruffie, Fabrice Bonnaudin,

Comparison of Software and Hardware Time Gating Techniques on the Measurements of Low RCS Targets in a Bistatic Configuration. (pp. 320)

Hassan Saleh, Jean-Michel Geffrin, Herve Tortel,

Physico-Chemical study of the Electrically Degraded Silicone (pp. 322)

Nacera Rouha, Djenkel Kaissa, Kettir Khallil,

Microwave Interferometry Based Open-ended Coaxial Technique for High Sensitivity Liquid Sensing (pp. 326)

Hind Bakli, Kamel Haddadi, Tuami Lasri,

General Papers

Sintering temperature and iso-valent dopant effects on microstructural and dielectric properties of lead-free ceramic $\text{La}_{0.01}(\text{Ba}_{1-x}\text{Ca}_x)_{0.99}\text{Ti}_{0.9975}\text{O}_3$ (pp. 332)

Lhousain Kadira, Abdelilah Elmesbahi, Salaheddine Sayouri,

Exploring the Temporal Aspect of Energy-Tunneling in a Wire-Loaded Microstrip Cavity (pp. 334)

Muhammad Arif Shah, Rashad Ramzan, Omar Farooq Siddiqui,

Analysis of Electromagnetic Scattering at a Radially Inhomogeneous Dielectric Sphere Using the Hybrid Projection Method (pp. 336)

Alina R. Gabdullina, Olga N. Smolnikova, Sergei P. Skobelev,

Automatic finite element Tool for the Error Estimation of the Probe trajectory in Eddy Current NDT of Steam Generator Tubes (pp. 338)

Laurent Santandrea,

Toxic Effects of X-Rays and Frequency Heterodyning (pp. 339)

Sara Liyuba Vesely, Sibilla Renata Dolci,

Plenary Presentation

Coordinate-Free Classifications of Electromagnetic Media.

I. V. Lindell¹

¹Aalto University, Finland
ismo.lindell@aalto.fi

Abstract— Different natural (coordinate independent) possibilities to classify electromagnetic media are considered in terms of compact four-dimensional differential-form and dyadic formalism. Various classifications based on Hehl-Obukhov decomposition, on representation of medium bidyadic in terms of a dyadic of lower dimension, on medium bidyadic being a solution of algebraic equation of certain order, and on certain properties of fields in the medium, are reviewed.

Applying four-dimensional differential-form formalism [1], the Maxwell equations obtain a compact form in which the electromagnetic fields are represented by two two-forms Φ and Ψ , each of which has six components. Their expansions in a given temporal coordinate t is

$$\Phi = \mathbf{B} + \mathbf{E} \wedge \varepsilon_4, \quad \Psi = \mathbf{D} - \mathbf{H} \wedge \varepsilon_4, \quad (1)$$

where $\varepsilon_4 = \mathbf{d}(ct)$ denotes the temporal one-form. The mapping between the field two-forms in a linear medium can be expressed in terms of a medium bidyadic $\overline{\overline{\mathbf{M}}}$ as [2]

$$\Psi = \overline{\overline{\mathbf{M}}} \Phi, \quad (2)$$

which in the general case involves 36 scalar parameters. Handling the most general medium appears quite troublesome. This makes it necessary to define special classes of media definable by a smaller number of parameters which have application in various situations. In the present paper a few possible definitions are considered and some properties of the medium classes are discussed. The medium classes defined can be called "natural" in the sense that they are independent of any choice of basis.

1. The most obvious classification is based on decomposing the medium bidyadic $\overline{\overline{\mathbf{M}}}$ (36 parameters) in three components,

$$\overline{\overline{\mathbf{M}}} = \overline{\overline{\mathbf{M}}}_1 + \overline{\overline{\mathbf{M}}}_2 + \overline{\overline{\mathbf{M}}}_3 \quad (3)$$

in a manner independent of any basis system, called the Hehl-Obukhov decomposition [3]. The general medium bidyadic is split in principal, skewon and axion parts each of which defines a certain class of media, respectively involving 20, 15 and 1 medium parameters. The decomposition is analogous to decomposing a 6x6 matrix in its trace-free symmetric, antisymmetric and trace parts. For example for the four-parameter class of bi-isotropic media, defined in terms of Gibbsian 3D formalism, the axion part corresponds to the Tellegen parameter, the skewon part to the chirality parameter and the principal part to the permittivity and permeability parameters.

2. Classes of media can also be defined by requiring that the medium bidyadic (6x6 matrix) can be expressed as the double-wedge square of a dyadic (4x4 matrix) involving 16 parameters. The definition can be made in two basic ways which defines two classes labeled as P and Q media. For example, the P media are defined by medium bidyadics of the form

$$\overline{\overline{\mathbf{M}}} = \overline{\overline{\mathbf{P}}}^{(2)} = \frac{1}{2} \overline{\overline{\mathbf{P}}} \wedge \overline{\overline{\mathbf{P}}}. \quad (4)$$

3. The general medium bidyadic satisfies an algebraic equation of the sixth order, the Cayley-Hamilton equation. Bidyadics satisfying lower-order equations define certain classes of media. For example medium bidyadics satisfying the second-order equation (SD media)

$$\overline{\overline{\mathbf{M}}}^2 + A \overline{\overline{\mathbf{M}}} + B \mathbb{1} = 0 \quad (5)$$

can be shown to define self-dual media, media invariant in certain duality transformations.

4. Finally, media can be classified by certain properties of fields existing in such media. For example, considering plane-waves whose wave vector \mathbf{k} is restricted by a dispersion equation $D(\mathbf{k}) = 0$ in the general case, we can define a class of media in which the dispersion equation is an identity, $D(\mathbf{k}) = 0$ for any vector \mathbf{k} . Such a class is called that of NDE (no dispersion equation) media. P media or skewon-axion media mentioned above are examples of NDE media. Another classification can be made in terms of the polarization of the plane wave. A well-known example is the uniaxially anisotropic medium in which any field can be decomposed in to independent fields with TE and TM polarizations. More generally, the class of decomposable media is defined by requiring that any field two-forms can be decomposed in two parts satisfying orthogonality conditions in terms of two bivectors.

To conclude, various possibilities to define natural classes of electromagnetic media, independent of any basis system, are considered in this paper. The definitions are invariant in any affine transformation, e.g., independent of the motion of the observer [2]. Working with medium classes with reduced number of parameters, whenever applicable, helps in mathematical analysis of media when compared to the full medium bidyadic involving 36 parameters.

REFERENCES

1. Deschamps, G. A, "Electromagnetics and differential forms," *Proc. IEEE*, Vol. 69, No. 6, 676–696, 1981.
2. Lindell, I. V., *Multiforms, Dyadics, and Electromagnetic Media*, Wiley and IEEE Press, Hoboken, N.J., 2015.
3. Hehl, F. W. and Yu. N. Obukhov, *Foundations on Classical Electrodynamics*, Birkhäuser, Boston, 2003.

Back-end Si photonics for high-performance photonic systems.

K. Yamada^{1*}

¹National Institute of Advanced Industrial Science and Technology, Japan

*corresponding author: yamada.koji@aist.go.jp

Abstract- Advanced functionality integration using back-end-on-line (BEOL) silicon process technologies is reviewed for high-performance silicon-based photonic platform. The functionalities can be realized by add-on waveguide systems made of silicon-rich silica, silicon oxynitride, silicon nitride and amorphous silicon, which can be constructed on silicon waveguide system by using BEOL technologies.

Silicon (Si) photonics is an emerging technology for high-density photonic-electronic integration, which could lead to compact, cost-effective and energy-efficient data-communications/telecommunications equipment for sustainable information-trading systems. Despite technological improvements in a wide area of applications, hurdles to practical applications are still high for advanced applications, such as medium/long range data transmissions, for which high-performance photonic devices with a large dynamic range are required. One of the most significant hurdles is the fabrication error of photonic devices. Since the effective index of silicon waveguides is extremely sensitive to geometrical errors in waveguide cores, allowable fabrication error for high-performance passive devices, such as low cross-talk, high-resolution, polarization-independent wavelength filters, must be on an angstrom order[1]. Such a severe fabrication tolerance cannot be achieved even if state-of-art fabrication technologies are applied. The large optical nonlinearity of Si, which causes various impairments in transmission performance, is another hurdle to practical applications.

To overcome these hurdles, add-on waveguide systems, which can be constructed on a Si photonic platform using low-temperature back-end-on-line (BEOL) process, have recently been proposed. The cores of the add-on waveguides are typically made of medium-index materials, such as Si-rich silica (SiOx)[2] or Si oxynitride/nitride (SiON/SiN)[2,3]. Thanks to the moderate refractive index contrast between the core and cladding, allowable fabrication error can be significantly relaxed while keeping reasonable integration density, as shown in Fig. 1. Using these waveguides, high-performance arrayed waveguide grating (AWG) wavelength filters integrated with high-speed Si/Ge-based active devices has been demonstrated for DWDM applications[4,5]. Moreover, thanks to the low optical nonlinearities in these materials, various impairments caused by four-wave-mixing and two-photon-absorption effects can be reduced significantly. Furthermore, since the propagation characteristics of add-on waveguides are

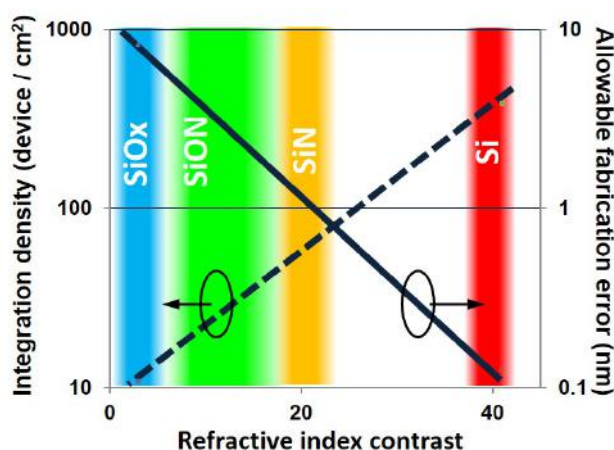


Fig. 1. Integration density vs. fabrication tolerance in AWG-type wavelength filters. Calculation conditions: 1.6 nm x 16 wavelength channels with a crosstalk of less than -20 dB.

different from those of Si waveguides, combining them would introduce a new degree of freedom for attaining novel functionalities, such as polarization/higher-order mode manipulation [6,7] and temperature dependence compensation [8]. The layer separation of active and passive/guiding functions is also an important feature of add-on waveguides. If we can construct active layers directly on bulk Si wafer and connect them with add-on waveguides, we might not have to use SOI wafers[9]. As well as SiO_x and SiON/SiN, amorphous silicon is also a promising material for add-on waveguide system with active functions, such as optical modulation and detection[10,11].

This talk reviews recent progress in these advanced functionality integration using BEOL silicon process technologies for high-performance photonic systems.

Acknowledgements, The author thanks Taturou Hiraki, Kota Okazaki, Tsuyoshi Yamamoto of NTT Device Technology Laboratories, and Yoichi Sakakibara of the National Institute of Advanced Science and Technology for fruitful discussions on their excellent work.

REFERENCES

1. Okamoto, K., *Laser & Photonics Review* Vol. 6, 14–23, 2012.
2. Tsuchizawa, T., “Guided Light in Silicon-based Materials,” *Handbook of Silicon Photonics* (CRC Press, 2013).
3. Okazaki, K. et al., *the 62nd JSAP Spring Meeting, 2015*, 11p-A16-2 (in japanese).
4. Hiraki, T. et al., *IEEE Photonics Journal* Vol. 5, 4500407, 2013.
5. Nishi, H. et al., *Applied Physics Express* Vol. 3, 102203, 2010.
6. Hiraki, T. et al., *Optical Fiber Communication Conference 2015, Los Angeles, 22-26 March*, W1A.2.
7. Fukuda, H. et al., *Optics Express* Vol. 16, 4872-4880, 2008.
8. Hiraki, T. et al., *Frontiers in Materials* Vol. 2, Article 26, 2015.
9. Okazaki, K. et al., *the 12th International conf. on Group IV Photonics (GFP 2015), 26-28 August, Vancouver*, WP43.
10. Takei, R. et al, *Optics Express* Vol. 22, 4779-4778, 2014.
11. Furuya, K. et al., *Applied Physics Letters* Vol. 100, 251108, 2012.

Smart Materials and Systems

Frequency and magnetic field dependence of the skin depth in Co-rich soft magnetic microwires

Arcady Zhukov^{1,2,3}, Ahmed Talaat^{1,2}, Mihail Ipatov^{1,2}, Alexandr Granovsky⁴ and Valentina Zhukova^{1,2}

¹School of Energy and Power Engineering, Heat Transfer University, Xi'an, China

¹Dpto. de Fís. Mater., UPV/EHU San Sebastián 20009, Spain

²Dpto. de Física Aplicada, EUPDS, UPV/EHU, 20018, San Sebastian, Spain

³IKERBASQUE, Basque Foundation for Science, 48011 Bilbao, Spain

⁴Moscow State “Lomonosov” University, Moscow, Russia

*corresponding author, E-mail: arkadi.joukov@ehu.es

Abstract

Tuneable metamaterials consisting of thin ferromagnetic wires exhibiting magnetoimpedance effect present tuneability of the effective permittivity by a weak magnetic field or a mechanical stress. Magnetoimpedance effect is related to magnetic field dependence of the skin depth of magnetic conductor. We studied giant magnetoimpedance (GMI) effect in magnetically soft amorphous Co-rich microwires in the extended frequency range. From obtained experimentally dependences of GMI ratio on magnetic field and different frequencies we estimated the penetration depth and its dependence on applied magnetic field and frequency.

1. Introduction

Studies of tuneable metamaterials utilising thin ferromagnetic wires exhibiting magnetoimpedance effect (MI) attracted considerable attention along the last few years [1,2]. These metamaterials contain arrays of metallic wires and present strong dispersion of the dielectric function in the GHz frequency range.

Magnetic wires presenting MI effect is a key for design of these tuneable metamaterials. Studies of magnetic wires have attracted considerable attention of researchers and engineers along many years [3,4]. Perfectly cylindrical symmetry is quite favorable for achievement of high MI effect [3,4]. Consequently giant magneto-impedance (GMI) effect has been discovered [3] and later intensively studied [4- 7] in different families of soft magnetic wires.

The origin of the aforementioned GMI effect is satisfactory explained considering the change in the penetration depth of the alternating current flowing through the magnetically soft conductor caused by the applied static magnetic field. Recently we modified the experimental facility that allowed us to extend the frequency range and measure GMI effect at GHz frequencies [5].

In soft magnetic amorphous wires subjected to an external magnetic field the GMI is in the range of 100% even at frequencies of few GHz [4-6].

Recently we reported on high MI effect in Co and Fe-rich microwires [5-7]. As it is well-known, the penetration depth, δ , depends on the current frequency. For observation of high MI effect the penetration depth must be smaller than the magnetic wires diameter.

Consequently we present our recent studies on the penetration depth of the alternating current flowing through the magnetically soft conductor caused by the applied static magnetic field in thin amorphous wires.

2. Experimental details

We studied various Co-rich ($\text{Co}_{67}\text{Fe}_{3.85}\text{Ni}_{1.45}\text{B}_{11.5}\text{Si}_{14.5}\text{Mo}_{1.7}$ and $\text{Co}_{67.71}\text{Fe}_{4.28}\text{Ni}_{1.57}\text{Si}_{11.24}\text{B}_{12.4}\text{Mo}_{1.25}\text{C}_{1.55}$) with different metallic nucleus diameter, d , and total microwire diameter, D , produced by the modified Taylor-Ulitovsky method described elsewhere.

We have measured the magnetic field dependence of impedance, Z , and GMI ratio, $\Delta Z/Z$, for as-prepared samples and after heat treatments [5,6].

We used a specially designed micro-strip sample holder described elsewhere [5]. The sample holder was placed inside a sufficiently long solenoid that creates a homogeneous magnetic field, H . The sample impedance, Z , was measured using a vector network analyzer from reflection coefficient S_{11} .

The magneto impedance ratio, $\Delta Z/Z$, has been defined as:

$$\Delta Z/Z = [Z(H) - Z(H_{\max})] \cdot 100 / Z(H_{\max}), \quad (1)$$

An axial DC-field with a maximum value H_{\max} up to 8 kA/m was supplied by magnetizing coils.

The frequency range for the diagonal impedance component has been measured from 1 MHz up to 7 GHz.

3. Experimental results and discussion

As described above the diameter reduction must be associated with the increasing of the optimal MI frequency range: a tradeoff between dimension and frequency is required in order to obtain a maximum MI effect [5,8]. Consequently we measured GMI effect at different frequencies.

Co-rich microwires present linear hysteresis loops and high GMI effect in as-prepared state (Fig 1a) and a maximum on frequency dependence of $\Delta Z/Z_{max}$ on be observed (Fig. 1b).

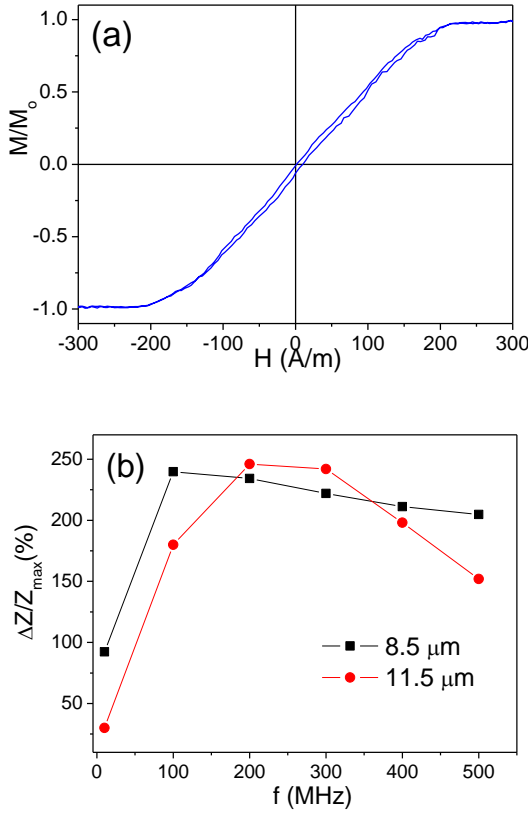


Fig. 1. Hysteresis loop(a) and frequency dependence of $\Delta Z/Z_{max}$ (b) measured in $\text{Co}_{67}\text{Fe}_{3.85}\text{Ni}_{1.45}\text{B}_{11.5}\text{Si}_{14.5}\text{Mo}_{1.7}$ microwires with different d.

For $\text{Co}_{67}\text{Fe}_{3.85}\text{Ni}_{1.45}\text{B}_{11.5}\text{Si}_{14.5}\text{Mo}_{1.7}$ microwire with $d=8.5 \mu\text{m}$ the optimum frequency, $f_o \approx 100\text{MHz}$, while for $\text{Co}_{67}\text{Fe}_{3.85}\text{Ni}_{1.45}\text{B}_{11.5}\text{Si}_{14.5}\text{Mo}_{1.7}$ microwire with $d=11.5 \mu\text{m}$, $f_o \approx 200\text{MHz}$.

From $\Delta Z/Z(H)$ dependences it is possible to estimate the penetration depth at different frequencies using the model previously described in ref. (9) considering that

that the changes in the real component of the impedance are related to changes in the effective area where the AC-current flows as a consequence of the skin-effect. In this model the penetration depth, δ , as a function of the ratio R_{DC}/R_{AC} (R_{DC} is the DC-resistance of the wire, and R_{AC} is the real component of the impedance), can be expressed as:

$$\delta = r[1 - (1 - R_{DC}/R_{AC})^{1/2}], \quad (2)$$

where r is the wire radius.

Consequently we measured $\Delta Z/Z(H)$ dependences for various Co-rich microwires and tried to estimate the $\delta(H)$ dependences.

Obtained $\delta(H)$ dependences demonstrate that at high frequencies the minimum penetration depth of

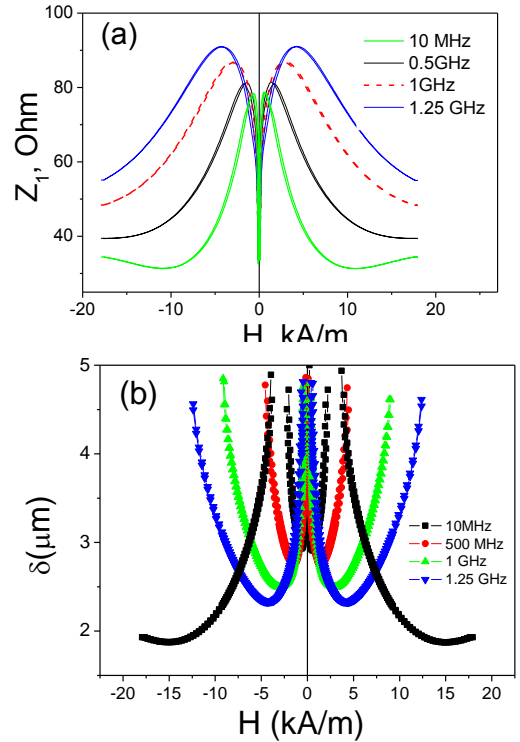


Fig.2. $Z(H)$ dependence (a) and calculated $\delta(H)$ dependences (b) of $\text{Co}_{67}\text{Fe}_{3.85}\text{Ni}_{1.45}\text{B}_{11.5}\text{Si}_{14.5}\text{Mo}_{1.7}$ microwires estimated for different frequencies.

$\text{Fe}_{70.8}\text{Cu}_1\text{Nb}_{3.1}\text{Si}_{14.5}\text{B}_{10.6}$ microwire is about $1.5 \mu\text{m}$ (Fig.2).

Similarly for $\text{Co}_{67.71}\text{Fe}_{4.28}\text{Ni}_{1.57}\text{Si}_{11.24}\text{B}_{12.4}\text{Mo}_{1.25}\text{C}_{1.55}$ microwire ($d \approx 10 \mu\text{m}$) GMI effect is observed even at GHz frequencies (Fig. 3a). For the case of $\text{Co}_{67.71}\text{Fe}_{4.28}\text{Ni}_{1.57}\text{Si}_{11.24}\text{B}_{12.4}\text{Mo}_{1.25}\text{C}_{1.55}$ microwire the minimum calculated penetration depth is below $0.5 \mu\text{m}$ for high frequencies (Fig.3b). From obtained $\delta(H)$ dependences we evaluated δ -values and dependence of minimum δ -values on frequency (see Fig.3c). As can be appreciated from Fig.3c minimum δ -values, δ_{min} , decrease with increasing the frequency and at 2 GHz $\delta_{min} \approx 0.33 \mu\text{m}$ (Fig.3c)

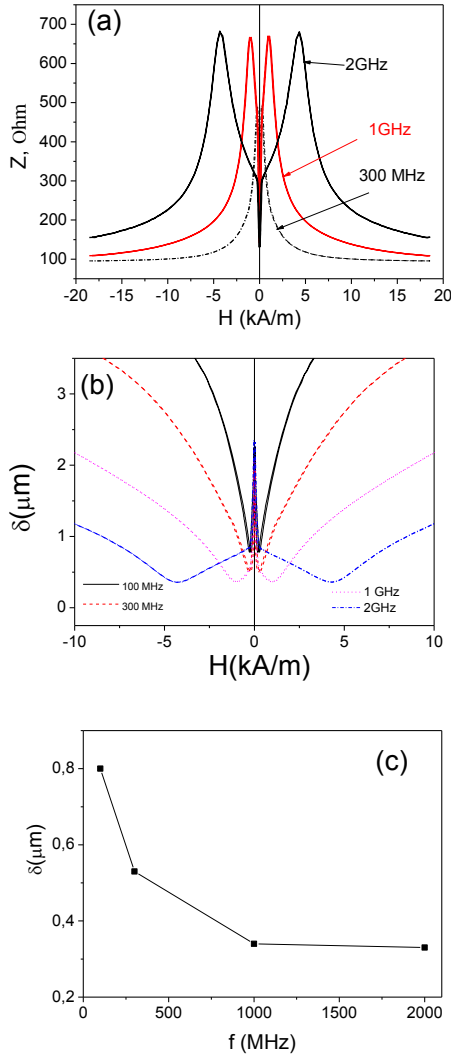


Fig.3. $Z(H)$ dependence (a), calculated $\delta(H)$ dependences (b) and $\delta_{\min}(f)$ of $\text{Co}_{67.71}\text{Fe}_{4.28}\text{Ni}_{1.57}\text{Si}_{11.24}\text{B}_{12.4}\text{Mo}_{0.125}\text{C}_{1.55}$ microwires ($d=10\ \mu\text{m}$, $D=13.8\ \mu\text{m}$) at different frequencies.

Consequently obtained minimum penetration depth for studied Co-rich microwires is few times smaller than the microwires diameter..

4. Conclusions

We measured the GMI effect in Co-rich magnetic wires. From obtained experimentally dependences of GMI ratio on magnetic field and different frequencies we estimated the skin depth and its dependence on applied magnetic field and frequency.

Acknowledgements

This work was supported by Spanish MINECO under MAT2013-47231-C2-1-P and the Russian Science Foundation under the 16-19-10490 grant. Technical and

human support provided by SGIker (UPV/EHU, MICINN, GV/EJ, ERDF and ESF) is gratefully acknowledged.

References

- [1] D.P. Makhnovskiy, L.V. Panina, C. Garcia, A.P. Zhukov, and J. Gonzalez, Experimental demonstration of tunable scattering spectra at microwave frequencies in composite media containing CoFeCrSiB glass-coated amorphous ferromagnetic wires and comparison with theory, *Phys. Rev. B*, Vol. 74 No. 6: 2006.
- [2] M. Ipatov, V. Zhukova, A. Zhukov and L. V. Panina, Microwave Metamaterials Containing Magnetically Soft Microwires, *Advances in Science and Technology*, 75: 224-229, 2010.
- [3] L.V. Panina and K. Mohri, Magneto-impedance effect in amorphous wires, *Appl. Phys. Lett.*, 65: 1189-1191, 1994.
- [4] J. M. Blanco, A. Zhukov and J. Gonzalez, Effect of tensile and torsion on GMI effect in amorphous wire, *J. Magn. Magn. Mat.* 196-197: 377-379, 1999.
- [5] A. Zhukov, A. Talaat, M. Ipatov and V. Zhukova, Tailoring the high-frequency giant magnetoimpedance effect of amorphous Co-rich microwires, *IEEE Magn. Lett.*, 6: 2500104, 2015.
- [6] A. Zhukov, M. Ipatov and V. Zhukova, Advances in Giant Magnetoimpedance of Materials, *Handbook of Magnetic Materials*, ed. K.H.J. Buschow, 24: chapter 2, 139-236, 2015
- [7] D.C. Jiles, Recent advances and future directions in magnetic materials. *Acta Mater.* 51: 5907-5939, 2003
- [8] D. Ménard, M. Britel, P. Ciureanu and A. Yelon, Giant magnetoimpedance in a cylindrical conductor, *J. Appl. Phys.* 84: 2805–2814, 1998.
- [9] H. Lachowicz, K.L. García, M. Kuzminski, A. Zhukov and M. Vázquez, Skin effect and circumferential permeability in micro-wires utilized in GMI-sensors, *Sensors and Actuators A*, 119: 384-389, 2005.

Inverse Scattering and Imaging

Precision analysis based on Cramer-Rao bound for 2D inverse scattering

L. Diong^{1,2}, A. Roueff¹, Ph. Lasaygues² and A. Litman¹

¹Aix-Marseille Université, CNRS, Centrale Marseille, Institut Fresnel (UMR 7249), France

²CNRS, Aix-Marseille Université, Centrale Marseille, LMA (UPR 7051), France
antoine.roueff@fresnel.fr

Abstract— The aim of the present study is to quantitatively predict the expected precision of the reconstructions obtained in inverse scattering configurations for a single object. To conduct such a study, we analyze the precision of the contrast estimators with the Cramer-Rao bound (CRB) assuming an additive complex circular gaussian noise at the receivers. An unified framework is derived to handle both acoustic and electromagnetic imaging configurations. Firstly, we have exploited the CRB to derive some design guidelines when selecting the parameters of the “optimal” experimental configuration. Secondly, we have try to appraise the effect of the error model when a classical linear approximation, such as the Born approximation, is selected or not.

When a characterization instrument is being conceived, one of the key questions is to come up with a design which will provide quantitative results with a given precision. Naturally, one always searches for the best precision, while keeping the instrument as simple as possible. It is thus of interest to be able to predict beforehand the precision of a given apparatus before effectively constructing it.

In the framework of estimation theory, the system performance can be analyzed based on the measurement model and the available a priori knowledge. When the noise model corresponds to a complex circular gaussian noise on the receivers with covariance matrix Σ , the Maximum Likelihood (ML) estimator is given by

$$\hat{\beta}_{\text{ML}} = \arg \min[\mathbf{u}_{\text{meas}}^{\text{sc}} - \mathbf{u}^{\text{sc}}(\beta)]^{\text{H}} \Sigma^{-1} [\mathbf{u}_{\text{meas}}^{\text{sc}} - \mathbf{u}^{\text{sc}}(\beta)]$$

where β corresponds to the contrast parameter and \mathbf{u}^{sc} (resp. $\mathbf{u}_{\text{meas}}^{\text{sc}}$) corresponds to the simulated (resp. measured) scattered field. To assess the performance of the ML estimator, we use the Mean Square Error (MSE)

$$\text{MSE}(\hat{\beta}_{\text{ML}}) = |\mathbb{E}(\hat{\beta}_{\text{ML}}) - \beta_{\text{true}}|^2 + \text{var}(\hat{\beta}_{\text{ML}})$$

where the first term correspond to the bias of the estimate, and the second term its variance. When the forward problem is linear, the MSE evaluation is straight-forward. In non-linear cases, various solutions can be followed to obtain it. One of them is to use Monte Carlo simulations. This solution has several drawbacks: high computational costs, convergence and robustness issues. Another way of computing the MSE is to exploit the Cramer-Rao bound. Indeed, it is known to be a lower bound for the variance of unbiased estimators, i.e.,

$$\text{var}(\hat{\beta}_{\text{ML}}) \geq \text{CRB}(\beta_{\text{true}}) \quad \text{and} \quad \text{MSE}(\hat{\beta}_{\text{ML}}) = \text{CRB}(\beta_{\text{true}}) \text{ in the asymptotic regime.}$$

Therefore, it can be used as a reference measurement to appraise the amount of information available within the experimental data. Moreover, this analysis can be done prior to any inversion algorithm development. Two types of analysis exploiting the CRB will be presented.

In the first one [1], we have studied how the imaging system performance can be improved by adjusting several controllable experimental conditions such as the number of sensors, their spatial positions or the frequency bands. In the second one [2], we have compared two MSE: the error obtained with the Born approximation and the error obtained without it. This enable us to quantify the impact of the Born approximation on the estimation error, while taking into account the noise measurement features.

REFERENCES

1. L. Diong, A. Roueff, Ph. Lasaygues, Ph., and A. Litman, “Precision analysis based on Cramer-Rao bound for 2D acoustics and electromagnetic inverse scattering”, *Inverse Problems*, Vol. 31, 075003, 2015.
2. L. Diong, A. Roueff, Ph. Lasaygues, Ph., and A. Litman, “Impact of the Born approximation on the estimation error in 2D inverse scattering,” *Inverse Problems*, submitted.

Sensitivity study of homogenised parameters in the framework of the subsoil water content imaging using microwave datas.

H. Tortel, C. Eyraud, A. Da Silva, A. Litman

Aix Marseille Université, CNRS, Centrale Marseille, Institut Fresnel UMR 7249, 13397, Marseille, France
herve.tortel@fresnel.fr

Abstract— Developing robust and efficient imaging systems aimed at imaging the near subsurface water content profile is a very challenging task. Indeed in this configuration we are facing many problems (aspect limited data, roughness of the soil, heterogeneities ...) In this work we present a numerical study investigating the influence of different parameters (working frequency, type of soil, water content in the soil, size of the heterogeneities ...) on the value of the effective media found. Proposals for an optimal characterisation system will be also discussed.

Characterising complex media thanks to electromagnetic waves is now widely used in many different applications and domains as biology, medicine or environment. Generally speaking in numerical imaging process the scene under study is illuminated by an electromagnetic wave and the scattered field or physical quantity related to it is measured. These measurements are then used as input datas in numerical algorithms that aim at building maps of quantity related to the physical process involved in the numerical procedure. For example if the numerical model involves Maxwell equations than the recovered quantity is the relative permittivity of the medium [1,2], on the other if we are dealing with the diffusion equation spatial absorption and diffusion maps will be recovered.

Our study is focused on the availability of using microwaves in order to spatially characterize the water content in the subsoil. Until now we have used Maxwell equations in our models and heterogeneities in the soil are generating clutter which must be minimized or removed. On the other hand this multi scattering process can be seen as an homogenisation process of the background (the soil and the heterogeneities) and it is of interest to study the influence of the water content in the permittivity of the background in the final value of the equivalent media in order to develop future experiments which are able to recover this sort of value.

In this work we present a study investigating the influence of different parameters (working frequency, type of soil, water content in the soil, size of the heterogeneities ...) on the value of the effective media found. Proposals for an optimal characterisation system will be also discussed.

REFERENCES

1. Nounouh, S. and Eyraud, C. and Litman, A. and Tortel, H., "Near Surface Geophysics", Vol. 13, 2015.
2. Nounouh, S. and Eyraud, C. and Litman, A. and Tortel, H., "Microwave Optical and Technology Letters", Vol. 56, No. 11, 2014.

Inverse Scattering, Reciprocal Structures and Superresolution

M. A. Fiddy

Optoelectronics Center, University of North Carolina at Charlotte
Charlotte, NC 28223, US
mafiddy@uncc.edu

Abstract- Using a nonlinear inverse scattering algorithm we have observed subwavelength scale features in the reconstructed image; strong or multiple scattering is responsible. We describe the use of reciprocal subwavelength-featured scattering structures that can encode and decode evanescent waves from an object thereby transferring the information to the far field. This approach can remove the need to apply an inverse scattering algorithm or alternatively, the measured encoded far field can be propagated numerically through the decoding structure.

Imaging from scattered fields is a challenging problem unless weak or single scattering approximations (first Born or Rytov) can be made. A nonlinear or iterative procedure is required for strongly scattering media [1]. Image reconstruction fidelity depends on the number of incident and scattered field measurements [2]. A finite number of measurement results in infinite ambiguity which has led to innovative computational methods for selecting an optimal image. Such procedures can also incorporate prior knowledge about the object, trading degrees of freedom for improvements to the information sought, especially improvements in resolution [3]. There are many ways to capture high resolution information, one of which is directly in the near field. It has long been observed that superresolution can result from multiple scattering in the object [3] and we have confirmed this [5].

The creation of high spatial frequencies as a result of strong/multiple scattering from sub-wavelength sized scatterers typically results in evanescent waves which can be coupled back into propagating waves as a result of further scattering. Their modification of the far field suggests a means for obtaining high resolution images assuming a reliable inverse scattering algorithm can be applied. Several interesting super-resolution experiments conducted by Fink's group (e.g. [6]) support this, in which far field data were measured from a strongly scattering volume, time reversed and returned to the scattering volume from which they came.

We have exploited the generalized reciprocity theorem to design complementary scattering structures that achieve this without the need for detection, phase conjugation and rebroadcast of the field back into the same multiply scattering structure. Reciprocity in wave propagation refers to the symmetry of the propagation under the interchange of the source and the observer, where the dielectric tensors of the medium must satisfy certain symmetry. There is a formal equivalence between phase conjugation and time reversal, and time reversed waves undergo time reversed scattering. Materials with reciprocal constitutive parameters can be made in principle for high resolution imaging. We note that S matrix methods show reciprocity with or without evanescent waves and this is equivalent to time reversal invariance if there are no losses. Reciprocity with losses is possible, but is then not invariant under time reversal [7,8]. Phase conjugation is the frequency domain equivalent of time reversal, and the sign reversal of the propagation vector in a negative refractive index medium is its equivalent. There is thus a close connection between the properties of a negative index medium used for super-resolution and phase conjugation was realized by Pendry [9].

We assume the conversion of high spatial frequency (evanescent) waves into propagating waves by a complex scattering structure originally conceived as a metamaterial. The scattering structure serves as an

encoder of the near field information. A metamaterial designed to have complementary scattering characteristics can then be made to serve as a “decoder”. The design of subwavelength-scale features in a scattering object can be used to define effective material properties. Exploiting the connection between time reversal and negative index, we extend this idea to consider generalized reciprocity principles for the design of complementary scattering structures that permit far field superresolution directly, i.e. without the need for intermediate detection, time reversal or further computation.

The complex scattering phenomena occurring in the encoding metamaterial can be conveniently represented in terms of three major components as illustrated in equation (1).

$$\Psi_{scatt} = k^2 \int_D V(\mathbf{r}') e^{-ik\hat{\mathbf{r}} \cdot \mathbf{r}'} \Psi(\mathbf{r}', \hat{\mathbf{r}}_{inc}) d\mathbf{r}' = \Psi_{WSC} + \Psi_{refraction} + \Psi_{disp/diff} \quad (1)$$

where the scattered field, expressed in the far field as the integral of the scattering function (e.g. $V(\mathbf{r})$ the relative permittivity or refractive index distribution) over the total field within the medium's volume, D . Scattered field components can include the scattering from each meta-atom Ψ_{WSC} , all of which will be a little different in practice due to fabrication tolerances, a field from an effective medium approximation within the metamaterial, giving rise to the negative index refraction $\Psi_{refraction}$, and a term which includes dispersive and diffraction phenomena arising from the implicit periodicity in the medium, $\Psi_{disp/diff}$. Periodicities in a metamaterial are generally considered significant when the period $d \sim \lambda$ but when $d < \lambda$, still possess a periodicity at λ .

We present high resolution images obtained using this methodology using a designed metamaterial as the encoding scatterer. We also discuss resolution limits and the advantages and disadvantages of replacing the reciprocal decoding negative index metamaterial by a purely computation step.

Acknowledgements: MAF gratefully acknowledges the support of NSF IUCRC Center for Metamaterials, award number 1068050 and ARO W911NF-14-1-0299.

REFERENCES

1. Fiddy, M. A. and Ritter, R. S., Introduction to Imaging from Scattered Fields, CRC Press, November 2014, ISBN 9781466569584
2. Ritter, R. S. and Fiddy, M. A., “Imaging from scattered fields: limited data and degrees of freedom,” Proc. Imaging Reconstruction from Incomplete Data VII, Proc. SPIE 8500-07, 1-7 (2012).
3. Testorf, M. E. and Fiddy, M. A., “Superresolution Imaging: Revisited,” Advances in Imaging and Electron Physics, Ed. P. W. Hawkes, ed. Vol. 163, Academic Press, 166-218 (2010).
4. Chen, F. C. and Chew, W. C., “Experimental verification of superresolution in nonlinear inverse scattering,” App. Phys. Lett., 72, 23, 3080 (1998).
5. Ritter, R. S. and Fiddy, M. A., “Superresolution imaging from nonlinear inverse scattering,” Image Reconstruction from Incomplete Data VIII, SPIE Optical Engineering + Applications, 9600-12 (2015).
6. Lerosey, G., de Rosney, J., Tourin, A. and Fink, M., “Focusing beyond the diffraction limit with far-field time reversal,” Science, 315, 1120 (2007).
7. Carminati, R., Nieto-Vesperinas, M. and Greffet, J. J., “Reciprocity of evanescent electromagnetic waves,” JOSAA 15, 706-712 (1998).
8. Carminati, R., Sáenz, J. J., Greffet, J.J. and Nieto-Vesperinas, M., “Reciprocity, unitarity, and time-reversal symmetry of the S matrix of fields containing evanescent components,” Phys. Rev. A 62, 012712 (2000).
9. Pendry, J. B., “Time reversal and negative refraction,” Science 322, 71–73 (2008).

Enhancement of multi-frequency microwave breast images using a tissue-dependent mapping technique with discontinuous Galerkin contrast source inversion

Cameron Kaye*, Ian Jeffrey, and Joe LoVetri

Department of Electrical and Computer Engineering, University of Manitoba, Winnipeg, Manitoba, Canada

*corresponding author, E-mail: umkayecj@myumanitoba.ca

Abstract

A previously described discontinuous Galerkin formulation of the Contrast Source Inversion algorithm (DGM-CSI) has been employed to produce 2D images of the dielectric properties of synthetic breast models using a well-established frequency-hopping technique. Reconstructions from low-frequency data are used as initial guesses for higher-frequency inversions to stabilize the otherwise non-physical solutions obtained with high-frequency data alone. A remarkable improvement in overall image quality has been observed when the imaginary part of the reconstructed low-frequency image is modified to reflect the identical tissue geometry as its real part. The imaginary part of the image is intelligently mapped from the real part based on probable tissue types before being passed back to the algorithm as the initial guess between successive frequencies, and held constant during the subsequent reconstructions. A comparison of breast imaging results obtained using traditional frequency hopping versus the new technique is provided.

1. Introduction

One of the remaining hurdles that has thus far prevented widespread clinical application of microwave imaging (MWI) for breast cancer detection has been its relatively low spatial resolution, especially in comparison to competing modalities like computed tomography (CT), magnetic resonance imaging (MRI) and x-ray mammography. The high attenuation of gigahertz-range frequencies in breast tissues, errors inherent to inversion model mismatch, and the ill-posed nature of the underlying inverse scattering problem itself unfortunately all have deleterious effects on the overall quality of reconstructions, limiting the distinguishable anatomic detail of breast images and more importantly, the reliability of small tumour detection. However, some measure of improvement has been achieved through ongoing research in the use of radar-acquired prior information [1], contrast enhancement [2], and further algorithmic sophistication (such as full 3D imaging) [3]. In particular, multi-frequency imaging employing “frequency hopping” aims to improve target reconstruction by first converging to a solution based on low-frequency data and feeding that solution, as an “initial guess”, into a more difficult high-frequency inversion. For modified conjugate gradient-type algorithms like contrast source inversion (CSI), this

initial guess serves as a much better starting point for imaging higher-frequency data than an empty background, placing the search space of the CSI cost functional closer to the true solution and consequently suppressing some non-physical artifacts that tend to emerge in unstable high-frequency reconstructions, particularly at tissue boundaries. It logically follows that the better the initial guess, the closer the algorithm will be able to converge to the true solution. This principle served as motivation to develop a mapping technique described herein that improves the intermediate initial guess solutions of a frequency-hopping formulation of CSI.

The relative permittivity (ϵ_r) of biological tissue is a frequency-dependent complex quantity, with the real part representing the dielectric constant of the tissue and the imaginary part being related to its conductivity (or dielectric loss). While both values vary with tissue type and can be useful distinguishing features in the resulting images, it has been observed that in published MWI results, the fidelity of the reconstructed real part of the complex permittivity is generally superior to that of the imaginary component. Consequently, in these imaging studies, the quality of the distributions of dielectric constant is often emphasized while the less impressive conductivity profiles are glossed over or omitted entirely. The reason behind this apparent disparity in reconstruction quality is open to speculation, but as observed in the breast phantom used herein, the *geometry* of tissues’ permittivity profiles *should* be qualitatively identical in the real and imaginary parts, as both components are correlated based on the expected tissue type. Therefore, it was surmised that if the imaginary part of each intermediate solution used as the initial guess for a successive frequency inversion were replaced with an appropriately mapped copy of its reconstructed real part and “anchored” in place (allowing the algorithm to converge using the real part only), the final image would correspondingly improve.

2. Methods

2.1. DGM-CSI algorithm

All 2D breast images presented here have been reconstructed with an implementation of CSI that uses a high-order frequency-domain formulation of Maxwell’s curl

equations, employing the discontinuous Galerkin method (DGM) as a forward solver. In the resulting DGM-CSI algorithm, unknown field and contrast quantities are represented by nodal coefficients in high-order polynomial expansions. Further details can be found in [4, 5].

2.2. Description of mapping procedure

Taking advantage of the dielectric measurements of different breast tissues and fitted Cole-Cole models available in the literature [6], a mapping procedure that matched the well-reconstructed dielectric constant of a tissue at a given frequency to the expected value of its imaginary component was formulated. The imaging procedure is as follows:

1. An initial DGM-CSI inversion utilizing the first set of data collected from a breast model seeded with dielectric properties corresponding to the lowest frequency (e.g. 1.0 GHz) is allowed to converge (both real and imaginary parts).
2. The imaginary part of the reconstructed ϵ_r is discarded, and a point-by-point search through the real part of each nodal basis coefficient in the DGM-CSI mesh classifies the type of breast tissue. This classification is based solely on the range of expected values of dielectric constant at that frequency, and the node's proximity to the imaging domain boundary (for skin).
3. The real parts of ϵ_r at the mesh nodal points, now categorized by tissue type, are mapped using a simple linear interpolation of the appropriate Cole-Cole model to an imaginary part corresponding to the tissue's expected range of values at the next frequency (e.g. 2.0 GHz) used in the frequency hop succession.
4. The unmodified real part and newly-mapped imaginary part are fed into the algorithm as the initial guess for the next set of data, collected from the breast model seeded with dielectric properties corresponding to the next frequency (e.g. 2.0 GHz). Only the real part is updated to converge to a new solution; the imaginary part is kept constant.
5. If more than two frequencies are used in the frequency hop, steps 2–4 are repeated as necessary.

2.3. Synthetic breast models

Synthetic transverse magnetic (TM) data was collected from a Class 3 (heterogeneously dense) 2D breast model supplied by the University of Calgary, derived from an MRI slice of a cancer patient with a breast tumour visible at the “3 o'clock” position; the model is depicted at three different frequencies (1.0 GHz, 2.0 GHz, and 3.0 GHz) in Fig. 1. The values of the tissue-dependent complex permittivity were calculated for every frequency using an appropriate single-pole Debye model, then subjected to random perturbations of $\pm 10\%$ [7]. Data was collected in a background of $\epsilon_r = 23 - 1.13i$ with 24 transmitters and 24

receivers evenly distributed at a radius of 10 cm, employing a finite-element method (FEM) forward solver with a finely-discretized mesh independent from that used for the DGM-CSI inversion. The E_z scattered electric field data was corrupted by uniformly-distributed noise at 5% of the maximum field magnitude. The only prior information used during inversions was the outer boundary of the skin, which served as the problem's imaging domain. The skin thickness and inner skin boundary both remained unknown.

3. Results and discussion

The imaging results of a frequency-hopping simulation beginning with a DGM-CSI inversion of the 1.0 GHz data, and proceeding through the 2.0 GHz and 3.0 GHz data sequentially, without any modification of the intermediate results, are shown in Fig. 2. Reconstructions of the same data but employing the imaginary-component mapping technique described in Section 2.2 for the intermediate solutions following the 1.0 GHz and 2.0 GHz inversions are shown in Fig. 3. Note that the 1.0 GHz reconstructions are identical in both cases. Although the DGM-CSI algorithm performs reasonably well in recovering the real component of the breast model, especially the skin layer, it has difficulty producing an accurate distribution of the imaginary part, most notably at 2.0 GHz and 3.0 GHz in Fig. 2. It is clear that the mapping technique and “anchoring” of the imaginary component at each subsequent frequency stage in Fig. 3 imparts a benefit to the quality of the real part of the reconstructions following the same number of iterations. Areas of finer anatomic detail in the original model emerge from the 3.0 GHz data inversion in the real part of Fig. 3 that are not present in Fig. 2.

4. Conclusion

A new technique to enhance the reconstruction quality of frequency-hopping microwave breast imaging has been described and demonstrated, consisting of a systematic modification to the initial guess used by the underlying optimization-based imaging algorithm. The mapping technique requires knowledge of the dielectric properties of expected tissues and their frequency dependence. This information is readily available for most human tissues, and the procedure could be improved and tailored to cover imaging of anatomical regions other than the breast. Moreover, subsequent trials on synthetic data have suggested that the improvement in image quality is less dependent on the quantitative accuracy of the mapped value of the imaginary component than the simple act of matching the tissue geometry of the real and imaginary parts. Regardless, it is clear that the imaginary component of the initial guess has a significant effect on high-frequency inversions, and this insight could lead to further improvement of the cost functional minimizations at the core of optimization-based imaging algorithms. This technique has only been tested with 2D synthetic data thus far, but there is a strong motivation to apply it to experimental 3D data in the near future.

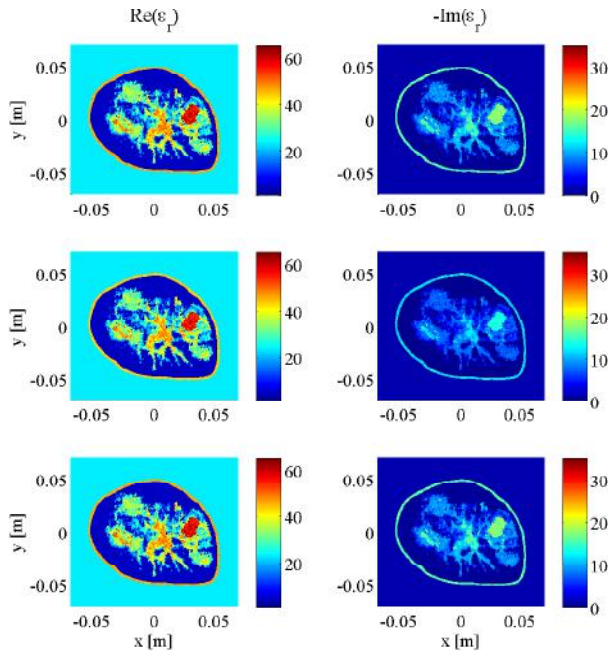


Figure 1: Complex dielectric properties of University of Calgary 2D synthetic breast model at 1.0 GHz (top), 2.0 GHz (middle) and 3.0 GHz (bottom).

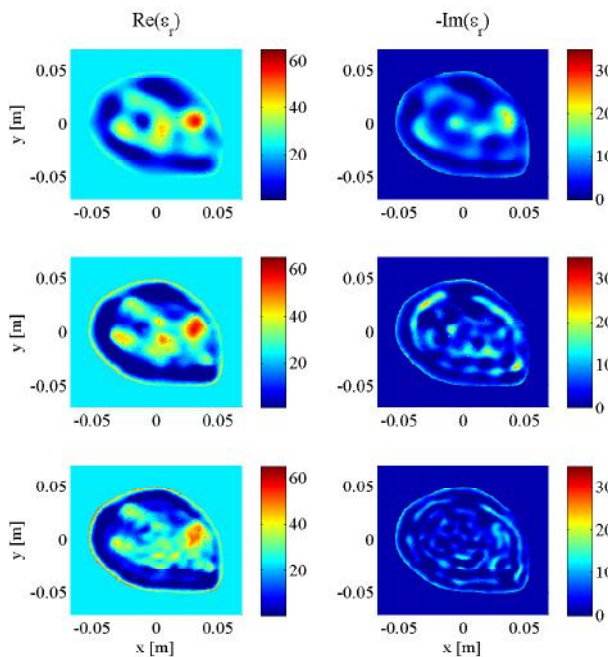


Figure 2: DGM-CSI frequency-hopping reconstructions of complex dielectric properties of synthetic breast model at 1.0 GHz (top), 2.0 GHz (middle) and 3.0 GHz (bottom), without modifying intermediate solutions.

References

[1] A. Baran, *et al.*, Breast Imaging Using Microwave Tomography with Radar-Based Tissue-Regions Estimation, *Progress in Electromagnetics Research* 149: 161–171, 2014.

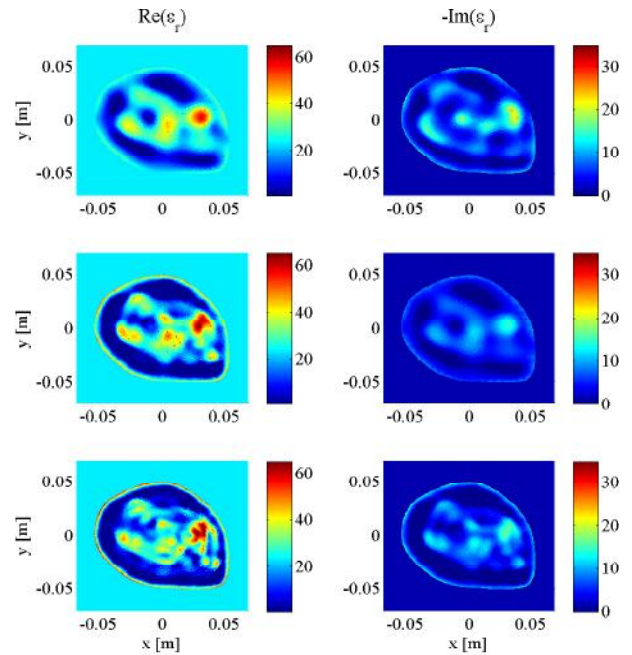


Figure 3: DGM-CSI frequency-hopping reconstructions of complex dielectric properties of synthetic breast model at 1.0 GHz (top), 2.0 GHz (middle) and 3.0 GHz (bottom) using tissue-dependent mapping technique.

[2] J.D. Shea, *et al.*, Contrast-enhanced microwave imaging of breast tumors: a computational study using 3D realistic numerical phantoms, *Inverse Problems* 26(7): 074009, 2010.

[3] A. Zakaria, *et al.*, Full-Vectorial Parallel Finite-Element Contrast Source Inversion Method, *Progress In Electromagnetics Research* 142: 463–483, 2013.

[4] I. Jeffrey, *et al.*, “Microwave Imaging by Mixed-Order Discontinuous Galerkin Contrast Source Inversion,” in *General Assembly and Scientific Symposium (URSI GASS), 2014 XXXIth URSI*, pp.1–4, 16–23 Aug. 2014.

[5] I. Jeffrey, *et al.*, The Time-Harmonic Discontinuous Galerkin Method as a Robust Forward Solver for Microwave Imaging Applications, *Progress in Electromagnetics Research* 154: 1–21, 2015.

[6] M. Lazebnik, *et al.*, A large-scale study of the ultra-wideband microwave dielectric properties of normal, benign and malignant breast tissues obtained from cancer surgeries, *Physics in Medicine and Biology* 52(20): 6093–6115, 2007.

[7] D.J. Kurrant, E.C. Fear, Regional estimation of the dielectric properties of inhomogeneous objects using near-field reflection data, *Inverse Problems* 28(7): 075001, 2012.

Two-stage reconstruction of complex dielectric permittivity and magnetic permeability for biomedical microwave imaging employing magnetic contrast agents

Cameron Kaye*, Ian Jeffrey, and Joe LoVetri

Department of Electrical and Computer Engineering, University of Manitoba, Winnipeg, Manitoba, Canada

*corresponding author, E-mail: umkayecj@myumanitoba.ca

Abstract

An implementation of the Contrast Source Inversion algorithm employing the discontinuous Galerkin method (DGM-CSI) has been modified to produce quantitative 2D images of both the dielectric permittivity and magnetic permeability of synthetic contrast-enhanced breast models. These numerical models contain breast tumours embedded with accumulations of magnetic nanoparticles (MNP), with simulated magnetic properties appropriate for physiologically achievable concentrations. A reconstruction of the breast model's permittivity profile is obtained first and used as an inhomogeneous background for a second-stage reconstruction of the magnetic permeability only, based on differential data obtained through the use of a static magnetic field. A brief description of this two-stage methodology for contrast-enhanced microwave imaging along with an example reconstruction of synthetic data is provided.

1. Introduction

Microwave imaging (MWI) has seen steady advancement towards specialized biomedical applications for several years, particularly in the field of diagnostic breast imaging. To that end, there has been interest in applying contrast enhancement to the modality to bolster its cancer detection and monitoring capabilities, leading to a number of studies of biocompatible substances that alter the gigahertz-range complex electrical permittivity of a tissue of interest, when properly targeted [1, 2]. Magnetic contrast media have been recently explored as an alternative to permittivity-modifying agents, as these materials augment the complex magnetic permeability of the bodily tissues in which they accumulate, a property that has conventionally been ignored in MWI. In particular, suspensions of iron oxide magnetic nanoparticles (MNP), already approved and employed in magnetic resonance imaging (MRI), have encouraging potential as microwave contrast agents due to their strong ferromagnetic resonance properties at gigahertz frequencies [3, 4]. Another attractive quality of MNPs at nanometer diameters is their response to a static polarizing magnetic field (PMF), which modulates their aforementioned ferromagnetic resonance response such that the magnetic permeability boost afforded to the target tissue can effectively be turned on and off [5]. In a clin-

ical setting, this characteristic provides an ideal mechanism to obtain reliable differential measurements through swift application and withdrawal of a weak PMF during signal acquisition. This process would minimize troublesome delays otherwise associated with contrast-enhanced imaging during pre-contrast, post-contrast and wash-out periods that could yield images beset by artifacts related to patient motion. Moreover, the PMF-induced physical separation of tissues' electrical and magnetic responses validated the development of a two-stage reconstruction methodology described here; a discontinuous Galerkin formulation of the Contrast Source Inversion algorithm (DGM-CSI) has consequently been employed to produce quantitative images of both the complex dielectric permittivity and magnetic permeability of a 2D breast model.

2. Methods

2.1. DGM-CSI algorithm

All 2D breast images presented here have been reconstructed with a CSI algorithm that uses a high-order frequency-domain formulation of Maxwell's curl equations, employing the discontinuous Galerkin method (DGM-CSI) as a forward solver to support distinct high-order expansions for the fields, contrasts and contrast sources. Further details on DGM-CSI can be found in [6, 7].

2.2. Two-stage inversion procedure

The DGM-CSI formulation theoretically allows simultaneous recovery of both relative dielectric permittivity (ϵ_r) and magnetic permeability (μ_r) from electric and magnetic field data, but in practice, the coupling between the fields produced by both electric and magnetic targets makes it difficult to recover accurate images for both properties concurrently. Moreover, a small concentration of MNPs in a specific volume of target tissue represents a very weak magnetic scatterer within a highly lossy biological environment, and the useful scattering signal from the MNP inclusion, being several orders of magnitude smaller than the strong electrical responses, is easily drowned out during simultaneous inversion of ϵ_r and μ_r . To overcome this difficulty, a two-stage reconstruction strategy was implemented that hinges on the fact that separate measurement data is avail-

able for two sets of targets within an otherwise identical imaging configuration (i.e. the dielectric and magnetic responses are separable during data collection via the application of a weak PMF). While the foundation of this differential measurement technique was proposed in [3], the important distinction for our reconstruction method lies in the use of inhomogeneous backgrounds in DGM-CSI to offer full quantitative inversion of both ε_r and μ_r .

To illustrate the procedure, suppose the existence of a target characterized by two complex relative permittivity and permeability profiles denoted by ε_1 and μ_1 , and ε_2 and μ_2 . To reflect the physics of applying a PMF, the target representing the scenario where the PMF is ‘on’ has μ_1 equal to some small residual constant above the permeability of free space [5] (for simplicity’s sake, $\mu_1 = 1.0$ is assumed). When the PMF is ‘off’, the target has identical dielectric properties ($\varepsilon_2 = \varepsilon_1$) while μ_2 is now some inhomogeneous magnetic profile, typical of an MNP contrast enhancement. The following two-stage reconstruction is thus proposed:

1. Total fields E_1^{tot} are measured at all receivers for the target defined by the profiles ε_1 and μ_1 . The incident field here, E_1^{inc} , is determined for the imaging system background medium ε_b and μ_b within the imaging domain, and its measured values at the receivers are used to covert total field measurements to scattered field data $E_1^{sct} = E_1^{tot} - E_1^{inc}$.
2. The DGM-CSI algorithm is applied to the scattered field data E_1^{sct} to reconstruct the contrast functions $(\varepsilon_1 - \varepsilon_b)/\varepsilon_b$ and $(\mu_1 - \mu_b)/\mu_b$. As aforementioned, $\mu_1 = \mu_b$ can be assumed for simplicity, such that only ε_1 need be recovered.
3. Total fields E_2^{tot} are measured at all receivers for the target defined by the profiles ε_2 and μ_2 . A new scattered field dataset is taken to be $E_2^{tot} - E_1^{tot}$. The profiles ε_1 and μ_1 recovered in step 2 are used as a numerical inhomogeneous background ε_N and μ_N for this reconstruction [8], and its corresponding “incident” fields within the imaging domain are calculated as required for evaluation of the CSI domain error cost functional.
4. DGM-CSI is now applied to the scattered field data $E_2^{tot} - E_1^{tot}$ to reconstruct $(\varepsilon_2 - \varepsilon_N)/\varepsilon_N$ and $(\mu_2 - \mu_N)/\mu_N$, from which ε_2 and μ_2 can be recovered. As any difference between E_2^{tot} and E_1^{tot} is assumed to be solely due to PMF-induced variations in magnetic permeability, the dielectric contrast is assumed to be zero, and at this stage the algorithm is constrained to recover only μ_2 .

2.3. Synthetic breast model

Synthetic data was generated from a two-dimensional MRI-derived breast model supplied by the University of Wisconsin’s public database (ID: 070604PA2) with tissue-dependent complex permittivity values calculated for a

frequency of 1.0 GHz from fitted 4-pole Cole-Cole models [9]. A simple circular inclusion, 1 cm in diameter, was embedded in a region of fibroglandular tissue at $(x, y) = (-0.01, -0.012)$ [m] and also given a frequency-appropriate permittivity for breast cancer. Additionally, this tumour was seeded with a weak magnetic permeability appropriate for a 10 mg/mL concentration of 10 nm-diameter magnetite MNPs at 1.0 GHz ($\mu_r = \mu_2 = 1.006 - 0.015i$) [4]. The complete model is depicted in Fig. 1.

For this 2D transverse magnetic (TM) model, electric field data (E_z) was generated in a low-loss background of $\varepsilon_b = 23 - 1.13i$ and $\mu_b = 1.0$ with 24 transmitters and 48 receivers evenly distributed at a radius of 10 cm, through the use of a finite-element method (FEM) forward solver with a finely-discretized mesh independent from that used for the DGM-CSI inversion. Doubling the number of receivers per transmitter was found to be helpful in the quantitative recovery of the magnetic inclusion, which produces a very weak scattering signal. Three sets of data (i.e. the fields that would be measured in practice) were separately corrupted by additive Gaussian white noise at an SNR of 80dB: incident field E_1^{inc} , and total fields E_1^{tot} and E_2^{tot} . The outer skin boundary was the only prior information employed during inversions; it was used as the problem’s imaging domain. The inner skin boundary was not provided as prior data to the algorithm.

3. Results and discussion

The imaging results of a 1.0 GHz two-stage DGM-CSI inversion of synthetic data are shown in Fig. 2. This low reconstruction frequency illustrates the usefulness of the two-stage inversion technique for improving the cancer detection potential of contrast-enhanced MWI. The relatively poor spatial resolution achievable at 1.0 GHz has blurred the area of interest around the tumour’s location in $\text{Re}(\varepsilon_r)$ and yielded a poor recovery of $\text{Im}(\varepsilon_r)$, limiting the diagnostic utility of the complex dielectric permittivity reconstruction by itself. However, the inversion of the magnetic permeability, despite some minor noise-related artifacts, has correctly localized the MNP inclusion. This is especially evident when μ_r is rescaled to remove values below 40% of the expected maximums for the real and imaginary parts (see bottom plots of Fig. 2). The real part of μ_r is somewhat less accurate than the imaginary component, as the “hot spot” has been subjected to an erroneous narrowing and a slight medial shift, likely due to noise distortion. Given its minute permeability value above that of free space ($\text{Re}(\mu_r) = 1.006$), difficulties in its reliable reconstruction from noisy data are not surprising. Regardless, given the nebulous region of high permittivity around the “7 o’clock” position in $\text{Re}(\varepsilon_r)$ where the tumour is located, in a hypothetical clinical scenario it is clear that a combination of both ε_r and μ_r would provide a more useful assessment of possible breast pathology than the reconstruction of dielectric permittivity alone.

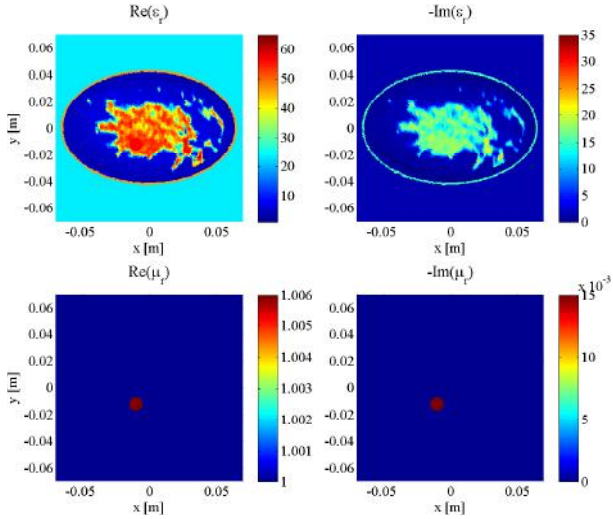


Figure 1: Complex electromagnetic properties of University of Wisconsin 2D synthetic breast model at 1.0 GHz (ID: 070604PA2): ε_r (top) and μ_r (bottom).

4. Conclusion

A two-stage contrast-enhanced MWI reconstruction methodology for the recovery of complex electrical permittivity and magnetic permeability in strongly electrical and weakly magnetic biological targets has been successfully tested using the DGM-CSI algorithm on 2D synthetic data. Follow-up studies with a CSI formulation capable of full 3D quantitative inversion of ε_r and μ_r are ongoing, employing synthetic data acquired from 3D breast models and experimental data from the University of Manitoba Electromagnetic Imaging Lab's latest imaging system.

References

- [1] A. Mashal, J.H. Booske, and S.C. Hagness, Toward contrast-enhanced microwave-induced thermoacoustic imaging of breast cancer: An experimental study of the effects of microbubbles on simple thermoacoustic targets, *Physics in Medicine and Biology* 54(3): 641–650, 2009.
- [2] A. Mashal, *et al.*, Toward carbon-nanotube-based theranostic agents for microwave detection and treatment of breast cancer: Enhanced dielectric and heating response of tissue-mimicking materials, *IEEE Transactions on Biomedical Engineering Letters* 57(8): 1831–1834, 2010.
- [3] G. Bellizzi, O.M. Bucci, I. Catapano, Microwave Cancer Imaging Exploiting Magnetic Nanoparticles as Contrast Agent, *IEEE Transactions on Biomedical Engineering* 58(9): 2528–2536, 2011.
- [4] G. Bellizzi, O.M. Bucci, I. Catapano, L. Crocco, and R. Scapaticci, “Magnetic Nanoparticles Enhanced Microwave Imaging: A Feasibility Assessment,” in *Proc. 6th Eur. Conf. Antennas Propag.*, pp.177–180, 26–30 Mar. 2012.

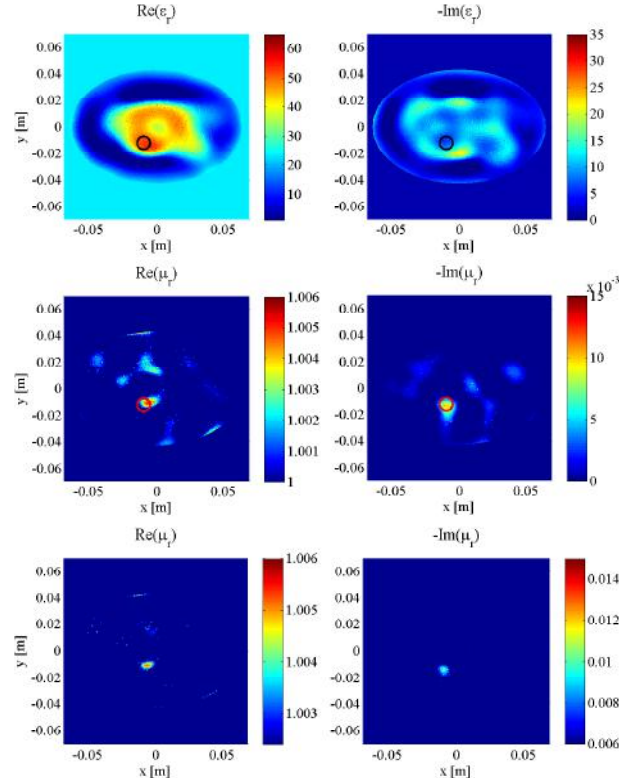


Figure 2: DGM-CSI reconstructions of complex ε_r (top) and μ_r (middle) from synthetic data (SNR = 80dB) at 1.0 GHz, where the tumour's true location has been highlighted by black and red circles. The bottom plots display values above 40% of the expected maximum of μ_r .

- [5] G. Bellizzi and O.M. Bucci, A Novel Measurement Technique for the Broadband Characterization of Diluted Water Ferrofluids for Biomedical Applications, *IEEE Transactions on Magnetics* 49(6): 2903–2912, 2013.
- [6] I. Jeffrey, *et al.*, “Microwave Imaging by Mixed-Order Discontinuous Galerkin Contrast Source Inversion,” in *General Assembly and Scientific Symposium (URSI GASS), 2014 XXXIth URSI*, pp.1–4, 16–23 Aug. 2014.
- [7] I. Jeffrey, *et al.*, The Time-Harmonic Discontinuous Galerkin Method as a Robust Forward Solver for Microwave Imaging Applications, *Progress in Electromagnetics Research* 154: 1–21, 2015.
- [8] A. Zakaria, C. Gilmore, and J. LoVetri, Finite-element Contrast Source Inversion Method for Microwave Imaging, *Inverse Problems* 26(11): 115010, 2010.
- [9] M. Lazebnik, *et al.*, A large-scale study of the ultra-wideband microwave dielectric properties of normal, benign and malignant breast tissues obtained from cancer surgeries, *Physics in Medicine and Biology* 52(20): 6093–6115, 2007.

Inverse Scattering in a Multipath Environment

Antonio Cuccaro and Raffaele Solimene

Dipartimento di Ingegneria Industriale e dell'Informazione
Seconda Università degli Studi di Napoli, via Roma 29, Aversa 81031, Italy
*antonio.cuccaro@unina2.it

Abstract

In this contribution an inverse scattering problem is addressed in a multipath environment. In particular, multipath is created by known "extra" point-like scatterers (passive elements) expressly deployed between the scene under investigation and the source/measurement domains. Through a back-projection imaging scheme, the role of the passive elements on the achievable performance is shown and compared to the free-space case.

1. Introduction

The problem of detecting and localising targets can be tackled by adopting a number of different methods [1]. Back-projection, migration algorithms and time reversal are among the most used in literature due to their simplicity of implementation and easiness of understanding [2].

For these methods, it is known that the achievable performance in the reconstructions is basically related to measurement configuration, i.e., the adopted frequency band and the size of the measurement aperture. However, the presence of known in-homogeneities in the background medium can change the things leading to performance enhancement due to the intervening multipath.

Multipath can be a source of artefacts that can corrupt the reconstructions. However, if the in-homogeneous background is somehow characterised (for example, because it is artificially created) it can be positively exploited in order to improve the spatial resolution. From a physical point of view, the reason is that in-homogeneities re-radiate the field impinging on them and hence act as a further source of illumination/scattering which *virtually* enlarges the actual measurement aperture.

A number of papers support previous claim. The effect of a single point-like in-homogeneity located between the sensors and the scene to be diagnosed is studied in [3], whereas the role of a reflecting plane in [4], for inverse source problem, and in [5], for inverse scattering under linearised scattering operators. Under the same assumption, the impact of a reflecting plane located at the bottom of the scattering scene is addressed in the framework of single and multi-frequency case in [6] and [7], respectively. A dielectric periodic structure located in front of the investigation domain is instead considered in [8].

In this contribution, we address a problem similar to the one considered in [14] and perform the reconstruction

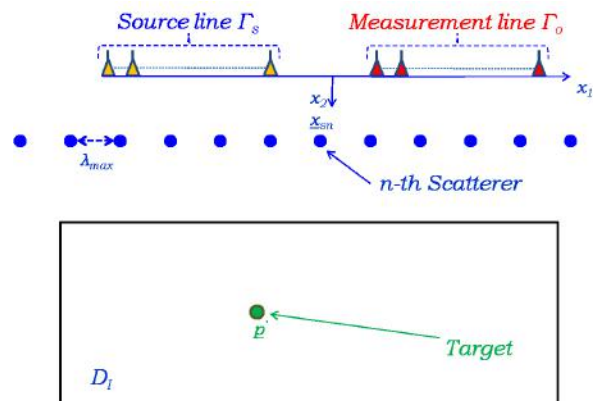


Figure 1: Geometry of interest. The target to be reconstructed is assumed to reside within the investigation domain D_I . A grid of point-like scatterers (blue circles) is expressly located between the source (Γ_s) and observation (Γ_o) lines and the target in order to create multipath. The scattered field is collected over the measurement line for all the frequencies within the band Ω_k .

via the same inversion back-projection scheme. The goal is to extend the results obtained for inverse source to inverse scattering problems.

It is shown that when a sufficient number of point-like scatterers are deployed in the scene, artefacts they introduce actually superimpose so as to return a focalised contribution. As a consequence, an improvement in the achievable spatial resolution is obtained as compared to the free-space (i.e., when no passive scatterers are present) case.

2. Mathematical model

The geometry of interest is depicted in Fig.1 where invariance is assumed along x_3 . The sources are located at $\underline{y}_s \in \Gamma_s$. They are assumed radiating the signal $S(\omega)$ linearly polarised along the x_3 -axis so that the problem is 2D and scalar. The scattered field is collected over $\underline{y}_o \in \Gamma_o$. The target to be reconstructed instead resides within the investigation domain D_I . The scenario also includes an ensemble of N known point-like scatterers located between the source/receiving domains and D_I . The point-like objects have known spatial positions $\eta_p = \{x_1, x_2, \dots, x_N\}$ and "strength" $\eta_m = \{\mu_1, \mu_2, \dots, \mu_N\}$.

Under the Born approximation the scattered field due to

an object inside the investigation domain D_I can be written as

$$E_s(k, \underline{y}_s, \underline{y}_o) = k^2 S(k) \times \int_{D_I} G_N(k, \underline{y}_o, \underline{p}) \chi(\underline{p}) G_N(k, \underline{p}, \underline{y}_s) d\underline{p} \quad (1)$$

where $\chi(\underline{p})$ is the contrast function representing the scattering object within the investigation region D_I , $k = \omega/c$ is the free-space wavenumber. $G_N(\cdot)$ is the Green function pertinent to background medium including the point scatterers.

As the point-like scatterers are by definition much smaller than the employed wavelength, their scattered field can be considered being proportional to the Green function, $G_b(\cdot)$, of the homogeneous medium (free-space). Accordingly, through the Foldy-Lax [9] equations and by further assuming the point scatterers being *well-separated* (this way multiple scattering between them can be neglected), we can write

$$G_N(k, \underline{p}, \underline{y}_s) \approx G_b(k, \underline{p}, \underline{y}_s) \times \left(1 + \sum_{n=1}^N G_b(k, \underline{p}, \underline{x}_n) \mu_n G_b(k, \underline{x}_n, \underline{y}_s) \right) = \sum_{n=0}^N G_n(k, \underline{p}, \underline{y}_s) \quad (2)$$

with $G_0(k, \underline{p}, \underline{y}_s) = G_b(k, \underline{p}, \underline{y}_s)$ and $G_n(k, \underline{p}, \underline{y}_s) = G_b(k, \underline{p}, \underline{x}_n) \mu_n G_b(k, \underline{x}_n, \underline{y}_s)$.

The latter equation represents our background Green function which obviously incorporates the passive elements' scattering.

The object $\chi(\cdot)$ is generally frequency dependent. Such a dependence is neglected in our analysis and therefore in operator notation eq. (1) can be written as

$$\mathcal{G} : \chi(\underline{p}) \in L^2(D_I) \rightarrow E(k, \underline{y}_s, \underline{y}_o) \in L^2(\Omega_k \times \Gamma_s \times \Gamma_o) \quad (3)$$

which is a linear integral operator that links 2D functions. In equation (3) no a priori information related to the source and the field is exploited but the functional spaces they belong to are equipped with usual L^2 Hilbert structure. Ω_k is the wavenumber frequency band.

3. Inversion Scheme

The operator (3) represents the mathematical model to be inverted in order to reconstruct the unknown scatterer. Now, note that through the background Green function (2) the multipath directly influences the scattering operator kernel. Therefore, this phenomenon must effect the reconstruction somehow. The main goal here is to foresee this effect, that is to estimate how extra scatterers act on the achievable performance and to link the latter to the configuration parameters.

In order to invert the model (3) a back-projection scheme is used. This approach actually means processing the scattered field data by the adjoint operator \mathcal{G}^\dagger

$$\mathcal{G}^\dagger : E_s(k, \underline{y}_s, \underline{y}_o) \in L^2(\Omega_k \times \Gamma_s \times \Gamma_o) \rightarrow \tilde{\chi}(\underline{p}) \in L^2(D_I) \quad (4)$$

of the scatterer operator \mathcal{G} . Back-projection algorithms are linear inversion strategy used to achieve the imaging in many areas of applied science, as through-wall imaging (TWI), subsurface imaging (GPR) or in SAR context [2], and in the last two decade even in biomedical applications [10]. Often in literature such methods are addressed in different ways as for example migration [11], time-reversing [12], or back-propagation [13], depending of the scientific contexts. A unified overview of many of those algorithms has been reported in [2]. Actually, performing the inversion through (4) is justified because under certain conditions it is shown that $\mathcal{G}^\dagger \mathcal{G}$ can be cast as a pseudo-differential operator [3]. This entails that back-projection allows retrieving the singularities of the unknown (though filtered) in the right location and with the right orientation.

By adopting the expansion (2) in (3), the scattering operator can be rewritten as

$$\begin{aligned} (\mathcal{G}\chi)(k, \underline{y}_s, \underline{y}_o) &= \sum_{n,m=0}^N (\mathcal{G}_{nm})(k, \underline{y}_s, \underline{y}_o) \times \\ &= k^2 S(k) \sum_{n,m=0}^N \int_{D_I} G_n(k, \underline{y}_o, \underline{p}) G_m(k, \underline{p}, \underline{y}_s) \chi(\underline{p}) d\underline{p} \end{aligned} \quad (5)$$

where with $\mathcal{G}_{00} = G_0(k, \underline{y}_o, \underline{p}) G_0(k, \underline{p}, \underline{y}_s)$ denotes the free-space path that can be divided in two part: the first one from the source point to the scatterer and the second one from the scatterer to the measurement point. The remaining terms instead account for the paths through the point-like scatterers. A similar expansion can be used for the adjoint operator

$$\begin{aligned} (\mathcal{G}^\dagger E_s)(\underline{p}) &= \sum_{l,h=0}^N (\mathcal{G}_{lh}^\dagger)(k, \underline{y}_s, \underline{y}_o) = \\ &= \sum_{l,h=0}^N \int_{\Omega_k \times \Gamma_s \times \Gamma_o} k^2 S^*(k) \times \\ &G_l^*(k, \underline{y}_o, \underline{p}) G_h^*(k, \underline{p}, \underline{y}_s) E_s(k, \underline{y}_s, \underline{y}_o) dk d\underline{y}_s d\underline{y}_o \end{aligned} \quad (6)$$

where $*$ represents the conjugate operator. Hence, the reconstruction computed after the adjoint back-projection procedure can be written as

$$\mathcal{R}\chi(\underline{p}) = \int_{D_I} \mathcal{K}(\underline{p}, \underline{p}') \chi(\underline{p}') d\underline{p}' \quad (7)$$

where, obviously, $\mathcal{K}(\cdot)$ is the kernel of the operator $\mathcal{G}^\dagger \mathcal{G}$. Actually, $\mathcal{K}(\cdot)$ is the point spread function (PSF) of back-projection inversion scheme. Therefore, it is sufficient to study this term in order to evaluate the affect of the point scatterers on the imaging procedure. By employing (5) and (6), the kernel can be recast as

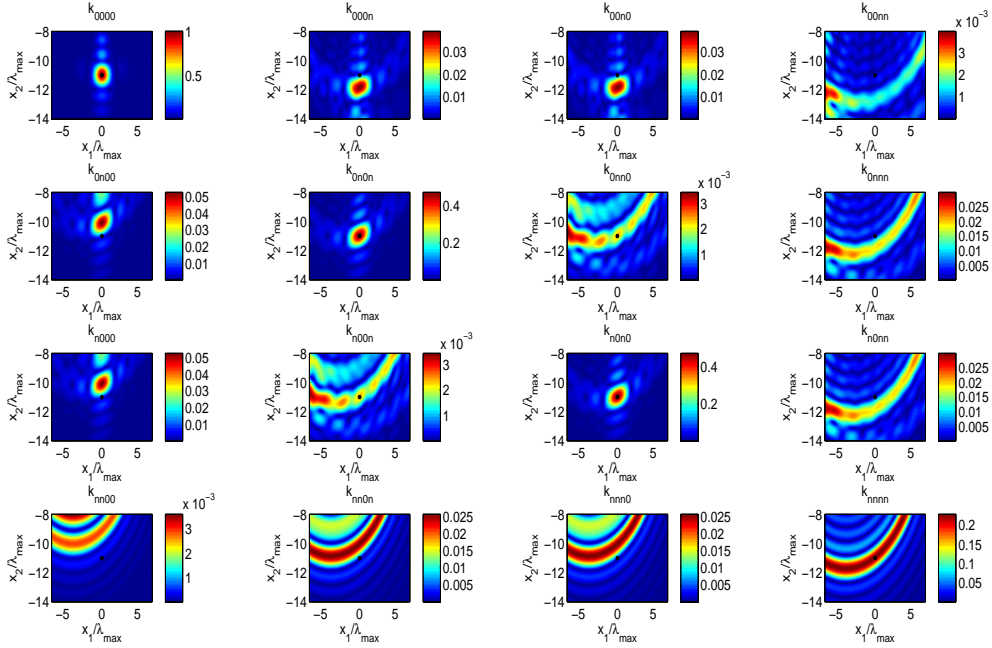


Figure 2: In the panel each single terms is reported when a single scattering point is present. All terms are normalized to $1/\max|\mathcal{K}_{0000}|$. The point scatterer has $\eta_1 = 6$ it is located at $(x_1 = -4\lambda_{max}, x_2 = -\lambda_{max})$. The source and measurement line are both uniformly arranged between $[-2\lambda, 2\lambda]$ along x_1 and located at $x_2 = 0$. The target point is denoted by a black bullet.

$$\mathcal{K}(\underline{p}, \underline{p}') = \sum_{n,m,l,h=0}^N \int_{\Omega_k \times \Gamma_s \times \Gamma_o} G_n^*(k, \underline{y}_o, \underline{p}) G_m^*(k, \underline{p}, \underline{y}_s) \times G_l(k, \underline{y}_o, \underline{p}') G_h(k, \underline{p}', \underline{y}_s) dk d\underline{y}_s d\underline{y}_o \quad (8)$$

where for the sake of simplicity it is assumed $|S(k)|^2 = 1$ and k^4 has been considered included in the Green functions.

Each single term can be more conveniently rewritten as

$$\mathcal{K}_{nmhl}(\underline{p}, \underline{p}') = \int_{\Omega_k \times \Gamma_s \times \Gamma_o} A_{nmhl}(k, \underline{y}_o, \underline{y}_s, \underline{p}, \underline{p}') \times \exp[j\Phi_{nmhl}(k, \underline{y}_o, \underline{y}_s, \underline{p}, \underline{p}')] dk d\underline{y}_o d\underline{y}_s \quad (9)$$

where the large argument expansion of the Hankel function of second kind and zero order (i.e., the Green function pertinent to a homogeneous medium) is used. The terms $A_{nmhl}(\cdot)$ take into account the point scatterers strengths, the amplitude cylindrical spreading due to the propagation and in general the source spectrum. The propagation paths instead is embodied in the phase terms $\Phi_{nmhl}(\cdot)$.

Note that the back-projection procedure is implemented without the amplitude correction step proposed in [3]. This is because we are mainly interested in studying how the ensemble of point scatterers contribute in artefact formation and how they can possibly enlarge the spatial retrievable

spectrum about the unknown. To this end, phase information is generally enough. The stationary phase method can be employed as in [3] so to approximate each contribution $\mathcal{K}_{nmhl}(\cdot)$ by its asymptotic leading order term. These contributions can be evaluated by solving the following equations

$$\nabla_{k, \underline{y}_o, \underline{y}_s} \Phi_{nmhl} = 0 \quad \forall n, m, l, h \quad (10)$$

If equation (10) admit solution only for $\underline{p} = \underline{p}'$ then the PSF will be properly focused, otherwise artefacts are expected to appear in the reconstruction.

4. Imaging

The reconstruction (7) consists of the summation of $(N + 1)^4$ terms.

First, we start by considering the case of a single point scatterer so that only 16 terms are relevant. This corresponds to study the subsets of \mathcal{K}_{nmhl} which only involve the subscript 0 and $n \forall n \in (1, 2, \dots, N)$. For those terms, the results shown in [3] can be applied. Here, we omit analytical details and limits to briefly describe such results.

Two types of contribution arise. The first one includes the *dominant* ones (i.e., the ones coming from the terms \mathcal{K}_{0000} , \mathcal{K}_{0n0n} and \mathcal{K}_{n0n0}) which have stationary points for all $(\underline{y}_o, \underline{y}_s)$ and that correctly focalise in the investigation domain. The second one encompasses the *non dominant*

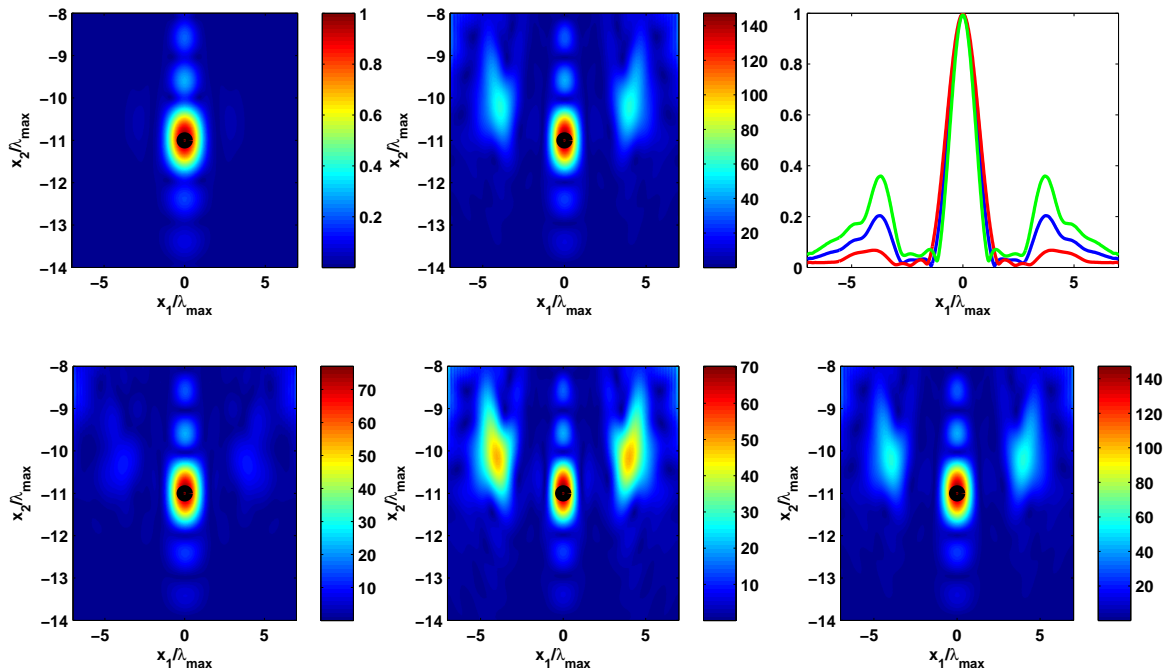


Figure 3: The left and the middle top panels report for comparison purposes $|\mathcal{K}_{0000}|$ and $|\mathcal{K}|$. The right bottom panel displays the total $|PSF| = |PSF_0 + PSF_1 + PSF_2 + PSF_3 + PSF_4|$. Instead, the left and middle bottom panels show the $|PSF| \approx |PSF_0 + PSF_1 + PSF_2|$ and $|PSF| \approx |PSF_3|$, respectively. All reconstructions has been normalized to $|\mathcal{K}_{0000}|$. The right top panel shows the normalised (by their own maxima) cut views passing through the target point (denoted by a black bullet) of $|\mathcal{K}|$ (blue line), $|PSF_0 + PSF_1 + PSF_2|$ (red line) and $|PSF_3|$ (green lines). $N = 5$ scattering points are uniformly arranged between $[-2\lambda, 2\lambda]$ along x_1 and located at $x_2 = -\lambda_{max}$. The target point is denoted by a black bullet.

terms (i.e., coming from $\mathcal{K}_{000n}, \mathcal{K}_{0n00}, \mathcal{K}_{00n0}$ and \mathcal{K}_{n000}) that have stationary points only when some particular aligning conditions are satisfied. Those second terms provide again a contribution that focalise correctly. However, since these happen only for a single (y_o, y_s) , their contribution is lower than the dominant ones. The remaining terms cause potential artefacts when stationary points exist. Fig. 2 shows the reconstructions associated to all the mentioned terms. For example, the terms \mathcal{K}_{nnnn} give rise to circular artefacts. For this reason, the terms \mathcal{K}_{nnnn} have been omitted during the image formation in [3]. Nonetheless, here, we focus right on this kind of terms which, as we are going to show, are mainly responsible of resolution improvement. However, before proceeding further along this path, the terms \mathcal{K}_{nmth} not covered by previous discussion must be addressed. To this end, since the point-like scatterers have been assumed not interacting, it is sufficient to consider the kernel terms corresponding to the case of only two point-like scatterers present in the scene. Say n and m their indexes. Now, 3^4 terms are relevant. However, only terms which involve both the n and m subscripts have to be studied as the other ones (i.e., those ones corresponding to the round-trip propagation paths that involve one single point scatterer) have been already covered by previous discussion. By paralleling the same approach as in [3] and

in [14], it can be shown that these terms tend to have no stationary points. This is surely true for the point scatterers arrangement (i.e., along a line) that we are considering herein. However, it is worth noting that in general this can depend on the configuration setting (i.e., relative positions between point scatterers and Γ_o, Γ_s). As in the previous case, the dominant contribution turns to come from the terms \mathcal{K}_{nmnm} and \mathcal{K}_{mnmn} .

Eventually, as a result of previous discussions the point spread function (8) can be approximated as the sum of five terms

$$\begin{aligned}
 PSF(\underline{p}, \underline{p}') &\approx \mathcal{K}_{0000}(\underline{p}, \underline{p}') + \sum_{n=1}^N \mathcal{K}_{n0n0}(\underline{p}, \underline{p}') + \\
 &+ \sum_{n=1}^N \mathcal{K}_{0n0n}(\underline{p}, \underline{p}') + \sum_{n=1}^N \mathcal{K}_{nnnn}(\underline{p}, \underline{p}') + \sum_{n=1}^{N-1} \mathcal{K}_{nmnm}(\underline{p}, \underline{p}') = \\
 &= PSF_0(\underline{p}, \underline{p}') + PSF_1(\underline{p}, \underline{p}') + \\
 &+ PSF_2(\underline{p}, \underline{p}') + PSF_3(\underline{p}, \underline{p}') + PSF_4(\underline{p}, \underline{p}') \quad (11)
 \end{aligned}$$

In the latter equation, PSF_0 represents the usual term expected from back-projection in free-space which of course focuses on the target. The terms PSF_1 and PSF_2

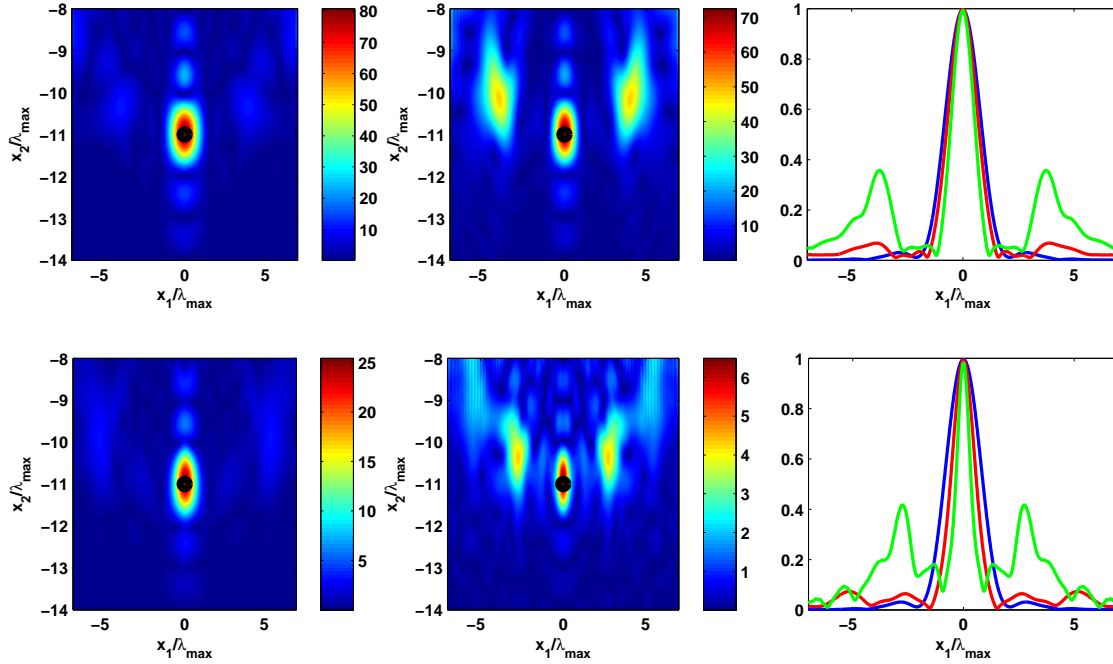


Figure 4: The role of scattering layout: varying the transversal arrangement. The top and the bottom panels refer to $N = 11$ scattering points uniformly arranged between $[-5\lambda, 5\lambda]$ along x_1 and located at $x_2 = -\lambda_{max}$ and $x_2 = -4\lambda_{max}$, respectively. The left and middle panels display $|PSF_0 + PSF_1 + PSF_2| / \max |\mathcal{K}_{0000}|$ and $|PSF_3| / \max |\mathcal{K}_{0000}|$, respectively. The right top and low panel show the normalised (by their own maxima) cut views passing through the target point (denoted by a black bullet) of previous reconstructions reported in red and green lines. In blue the cut views of $|\mathcal{K}_{0000}|$.

are those ones already accounted in [3]. PSF_3 and PSF_4 are the terms that we suggest to retain in the reconstruction procedure. Indeed, as mentioned above, each single term in PSF_3 and PSF_4 is an artefact that passes through the actual scattering position. Therefore, when they are combined together they give rise to a further focalised contribution. More in detail, by paralleling the same approach as in [14], we got

$$PSF_3(\underline{p}, \underline{p}') = \sum_{n=1}^N b_3(\underline{p}', \underline{x}_n, \Omega_k, \Gamma_o, \Gamma_s) \times \hat{\delta}(|\underline{p} - \underline{x}_n| - |\underline{p}' - \underline{x}_n|) \quad (12)$$

$$PSF_4(\underline{p}, \underline{p}') = \sum_{n=1}^{N-1} b_4(\underline{p}', \underline{x}_n, \underline{x}_m, \Omega_k, \Gamma_o, \Gamma_s) \times \hat{\delta}(|\underline{p} - \underline{x}_n| + |\underline{p} - \underline{x}_m| - |\underline{p}' - \underline{x}_n| - |\underline{p}' - \underline{x}_m|) \quad (13)$$

where the $b_i(\cdot)$, with $i = 3, 4$, are amplitude coefficients whereas $\hat{\delta}(\cdot)$ is a smoothed version of a delta function due to the filtering introduced by the measurement configuration through the back-projection scheme. Expressions (12) and (13) actually resemble the *ruler and compass* migration

scheme proposed by Hagedoorn [15]. In particular, these terms can be seen as the outcomes of multimono-static and multistatic (excluding the mono-static data) backprojection schemes, when data are collected at the *virtual* array (that is not at the actual sources and measurements positions) located at points η_p (i.e., the point scatterers). This suggests that by suitably arranging the point scatterers in order to have a virtual aperture larger than the actual one, resolution can be improved.

5. Numerical example

In this numerical analysis the measurement and transmission lines coincide, i.e., $\Gamma_o = \Gamma_s = \Gamma$. In particular, they are segments $[-2\lambda_{max}, 2\lambda_{max}]$ along the x_1 axis, and both are located at $x_2 = 0$. The investigation domain is $D_I = [-7\lambda_{max}, 7\lambda_{max}] \times [-8\lambda_{max}, -14\lambda_{max}]$ and $\Omega_k = [4\pi, 6\pi]m^{-1}$. In order to study how the achievable performance is affected by the point scattering object layout, the parameters of the configuration are kept fixed in all the following examples while the scattering points set up is changed. For all the following examples the point scatterers are deployed over a line parallel to Γ with a λ_{max} spatial step between two consecutive point scatterers. The latter, in turn, are considered of equal strength $\eta_m = 6$.

We start the numerical analysis by showing the compar-

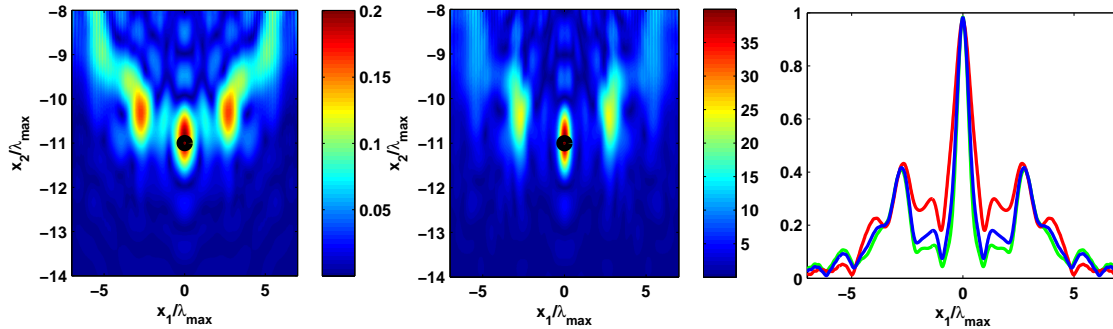


Figure 5: The role of scattering layout: varying the strength of point scatterers. $N = 11$ scattering points are uniformly arranged between $[-5\lambda, 5\lambda]$ along x_1 and located at $x_2 = -4\lambda_{max}$. Left and middle panels display $|PSF_3|/\max|\mathcal{K}_{0000}|$ when $\eta_m = 2$ and $\eta_m = 10$, respectively. The right panel shows the normalised (by their own maxima) cut views passing through the target point (denoted by a black bullet) of previous reconstructions reported in red and green lines. In blue the cut views of $|PSF_3|/\mathcal{K}_{0000}$ corresponding to Fig.4 (middle bottom panel).

ison between the total point spread function \mathcal{K} and \mathcal{K}_{0000} , which would be obtained without scattering points. The ensemble of point scatterers is located at $x_2 = -\lambda_{max}$ and arranged over a segment of length $[-2\lambda_{max}, 2\lambda_{max}]$ (i.e., $N = 5$ point scatterers are in the scene). By looking at the results reported in Fig. 3, it can be concluded that when the scattering grid is close to Γ no significant resolution improvement is observed. This can be explained because for this case the grid and Γ have roughly the same "scene view", that is they practically subtend the same observation cone. This means that the spatial wavenumber band is unchanged by the grid presence and therefore the transverse resolution does not increase. In order to appreciate the goodness of the point spread function approximation in the same figure is depicted the reconstruction obtained by using equation (11) (the same result is obtained if term PSF_4 is omitted). As can be seen, it is very similar to \mathcal{K} (Fig. 3, middle top panel). Accordingly, we conclude that by using the approximated imaging procedure not only it is reduced the computational load (faster computationally) than the traditional back-projection, but it provides similar results to the latter. In the same figure is shown the reconstruction (left bottom panel) obtained when in the inversion back-projection strategy only the first three terms are employed. It is similar (except for some artefact) to result depicted in the middle bottom panel, where instead the imaging procedure is carried out by means only PSF_3 term. This observation suggests to adopt in the inversion scheme only the latter term since it allows to further reduce the computational burden. Hereafter the inversion back-projection scheme is achieved through or only the first three contribute PSF_0, PSF_1, PSF_2 or just the last PSF_3 .

The second example is shown in Fig. 4. Here, the passive grid is arranged over the segment $[-5\lambda_{max}, 5\lambda_{max}]$ (i.e., $N = 11$) and it is first located at $x_2 = -\lambda_{max}$ (Fig. 4, top panels) and then moved at $x_2 = -7\lambda_{max}$ (Fig. 4, bottom panels). As can be seen, when the imaging procedure

is implemented by adopting the first three terms of equation (11), the transverse resolution is improved slightly in both scenarios. However, this improvement becomes more pronounced when the back-projection is carried through only the term PSF_3 , particularly when the grid is closer to D_I (Fig. 4, middle bottom panel). These results are consistent with previous discussion. Indeed, in both the previous case the grid subtend a larger observation cone (with respect to the actual measurement aperture) which means a larger spatial wavenumber band and hence a better transverse resolution. However, this improvement is less marked when the grid is close to Γ . It can be shown that this is due to the coefficient $b_i(\cdot)$ which suffer from of a sort of *tapering* (magnitude decays towards the edges of the grid) which reduce the virtually aperture relevant in the reconstructions. Moreover, it is worth noting that in many applications, the resolution of the imaging algorithm is defined at -3dB with respect to the maximum amplitude of the reconstruction (i.e., only within this interval the amplitude of the reconstruction is preserved). Therefore, although some artefact appears in the reconstruction (Fig. 4, middle top and bottom panels), it can be said that an improvement in resolution occurs. This can be appreciated by cut views through the target position reported in the same figure. Finally, it is noted the reconstruction amplitude of Fig.4 (left and middle top panels) slightly increases (as compared to the case of Fig. 3, left and middle bottom panel). This is because the number of grid elements is increases as well.

The last example shown in Fig. 5 concerns the case where the strength of scatterers is changed. In particular, by choosing the same configuration as in Fig. 4 (middle bottom panel), the strength of scatterers is chosen first equal to $\eta_m = 2$ and then increased at $\eta_m = 10$. By looking at the figures, it can be appreciated the different reconstruction amplitudes, which obviously is a consequence of the adopted different strengths. As far as resolution is concerned, it can be seen that with weak point scatterers the

resolution improvement achieved when $\eta_m = 6$ (Fig. 4, middle panel) disappears. Otherwise, beyond a threshold value of η it is preserved and keep unchanged. Therefore, further increasing η entails only an increase of maximum amplitude of the reconstruction. The cut views depicted in Fig. 5 (right panel) shown clearly this aspect.

6. Conclusions

In this paper an inverse scattering problem in a multipath environment caused by an ensemble of scattering points has been dealt with for a 2D scalar setting through a back-projection inversion method. By approximating the PSF thanks to the stationary phase method, the contribution to the reconstruction due to the scattering grid has been evidenced. In particular, it has been shown that the grid can allow to obtain a finer resolution (compared to free-space) and that the mainly responsible of this resolution improvement is the term PSF_3 . It remember that the latter is considered as artefact in [3] and therefore it is discarded in image formation procedure proposed there.

Finally, it is highlighted that with our proposed procedure (back-projection through only PSF_3) two important aspect are combined: an improvement of the resolution achievable thanks to extra point scatterers and a faster imaging procedure compared to the traditional one.

As future developments, we plan to extend to study to the inverse scattering problem to a 3D dyadic case.

Acknowledgement

This work was supported by the Italian Ministry of University and Research through the FIRB initiative under the project MICENEA (RBFR12A7CD).

References

- [1] I. Catapano, A. Randazzo, E. Slob and R. Solimene, GPR imaging via qualitative and quantitative approaches, in *Civil Engineering Applications of Ground Penetrating Radar*, Springer International Publishing, pp. 239–280, 2015.
- [2] R. Solimene, I. Catapano, G. Gennarelli, A. Cuccaro, A. Dell’Aversano and F. Soldovieri, SAR imaging algorithms and some unconventional applications: a unified mathematical overview, *IEEE Sign. Process. Magaz.* 31: 90–98, 2014.
- [3] M. Cheney and R.J. Bonneau, Imaging that exploits multipath scattering from point scatterers, *Inverse Probl.* 20: 1691–1711, 2004.
- [4] R. Solimene, M.A. Maisto, R. Pierri, Inverse source in the presence of a reflecting plane for the strip case, *J. Opt. Soc. Am. A* 31: 2814–2820, 2014.
- [5] R. Solimene, M.A. Maisto, R.-Pierri, Inverse scattering in presence of a reflecting plane, *J. Opt.* 18: 025603, 2016.
- [6] A.J. Devaney and M. Dennison, Inverse scattering in inhomogeneous background media, *Inverse Probl.* 19: 855–870, 2003.
- [7] M.L. Dennison and A.J. Devaney, Inverse scattering in inhomogeneous background media: II. Multi-frequency case and SVD, *Inverse Probl.* 20: 1307–1324, 2004.
- [8] P.C. Chang, R.J. Burkholder, and J.L. Volakis, Model-Corrected Microwave Imaging through Periodic Wall Structures, *Int. J. Antenn. Prop.* ID 948365, 2012.
- [9] L.L. Foldy, The multiple scattering of waves, *Phys. Rev.* 67: 107–119, 1945.
- [10] H. Lim, N. Nhung, E. Li, and N. Thang, Confocal microwave imaging for breast cancer detection: delaymultiply- and-sum image reconstruction algorithm, *IEEE Trans. Biomed. Eng.* 6: 1697–1704, 2008.
- [11] G. Gilmore, I. Jeffry, and J.Lo Vetri, Derivation and comparison of SAR and frequency-wavenumber migration within a common inverse scalar wave problem formulation, *IEEE Trans. Geosci. Remote Sensing* 44: 1454–1461, 2006.
- [12] D. Cassereau and M. Fink, Time-reversal of ultrasonic fields part III: Theory of the closed time-reversal cavity, *IEEE Trans. Ultrason. Ferroelectr, Freq. Control* 39: 579–592, 1992.
- [13] C. Esmeroy and D. Miller, Backprojection versus backpropagation in multidimensional linearized inversion, *Geophysics* 54: 921–926, 1989.
- [14] R. Solimene, A. Cuccarao and R. Pierri, Back-Projection Source Reconstruction in Presence of Point Scatterers, *J. Opt.* 18: 065606, 2016.
- [15] J.G. Hagedoorn, “A process of seismic reflection interpretation,” *Geophys. Prosp.* 2: 85–127, 1954.

Metric entropy in linear inverse scattering

Maria Antonia Maisto, Raffaele Solimene, Rocco Pierri,

Dipartimento di Ingegneria Industriale e dell'Informazione,
Seconda Università degli studi di Napoli, Aversa (Ce), Italy

*corresponding author, E-mail: mariaantonia.maisto@unina2.it

Abstract

The role of multiple views and/or multiple frequencies on the achievable performance in linear inverse scattering problems is addressed. To this end, the impact of views and frequencies on the Kolmogorov entropy measure is studied. This way the metric information that can be conveyed back from data to the unknown can be estimated. For the sake of simplicity, the study deals with strip scatterers and the cases of discrete angles of incidence and/or frequencies.

1. Introduction

Linear inverse electromagnetic scattering problems amount to inverting an integral equation of the first kind for an object function which is related to the scatterer's features like the shape, the support, the dielectric contrast, etc.. [1]. As is well known, this problem is ill-posed in the sense of Hadamard [2]. Indeed, since the kernel function is a square integrable function, the integral operator is of Hilbert-Schmidt class and hence compact [3]. This entails that the inverse operator is not continuous and in order to obtain meaningful solutions some regularisation method must be employed [4]. Therefore, while in principle an object can be perfectly reconstructed when the operator is injective, actually due to the noise and uncertainties one must content of approximate solutions resulting from a trade-off between accuracy and stability imposed by the adopted regularisation scheme [5].

As known, the achievable performance in the reconstruction can be improved by probing the scattering scene at different angles of incidence (multi-view configuration) or at different frequencies (multi-frequency configuration). When only view or frequency diversity is exploited the corresponding operators are denoted as \mathcal{A}_v and \mathcal{A}_f .

In order to work out the impact of the diversities on the related scattering/inverse scattering problems, the mathematical features of the relevant scattering operator should be analysed. To accomplish such a task the singular value decomposition (SVD) of the involved operator is a natural and fundamental tool. Indeed, determining/estimating the singular value behaviour allows to foresee the number of *significant* singular values (i.e., the so-called number of degrees of freedom, NDF [7], or the *essential dimension* [8]) and hence to estimate the dimension of the space within which the unknown will be stably reconstructed [6]. Also, knowing the singular values permits to estimate the infor-

mation that can be conveyed back from data to the unknown [9].

Of course, a criterion for identifying the *significant* singular values must be given. It is clear that this question belongs to the more general realm of regularisation theory. Here, we implicitly adopt a regularisation method that is based on a spectral cut-off strategy [10]. However, unless the singular values exhibit a step-like behaviour (and this is not the case herein) the choice of the cut-off (truncation) threshold is not so obvious. Indeed, some a priori information is usually required. Here, we follow the same philosophy as in [11], therefore it is assumed that bounds about the norm of the noise as well as of the solution are known. Accordingly, we have that

$$\|\mathcal{A}_i \chi - \tilde{E}_S\| \leq \epsilon, \|\chi\| \leq E \quad (1)$$

where $i \in (v, f)$ and \tilde{E}_S is in general the noisy scattered field. Of course, it is furthermore assumed that the set of object functions χ for which both constraints hold true is not empty. By recalling that \mathcal{A}_i are compact operators the choice of the truncation threshold can be pursued within the framework of the *topological information theory* in terms of the ϵ -entropy \mathcal{H}_ϵ and the maximum number of ϵ -distinguishable messages \mathcal{M}_ϵ that can be conveyed back on the unknown space. In particular, the ensemble composed by the maximum number of distinguishable messages that can be sent back to recover an approximation of the unknown solution, constitutes the backward information flow. In [11], it has been shown that the cut-off threshold must be chosen as $N_\epsilon = \max\{n > 0 : \sigma_n(\mathcal{A}_i) \geq \epsilon/E\}$, $\sigma_n(\mathcal{A}_i)$ being the singular values. By further assuming $E = 1$, the following estimates have been derived

$$\mathcal{H}_{i\epsilon} \geq \sum_{n=0}^{N_\epsilon} \log_2 \sigma_n(\mathcal{A}_i)/\epsilon \quad \text{and} \quad \mathcal{M}_{i\epsilon} \geq 2^{\mathcal{H}_{i\epsilon}} \quad (2)$$

Equation (2) makes it evident that not only the number of singular values but also their magnitudes are important. In [12], the focus was addressed on how the diversities change both these attributes of the singular value behaviour. In particular, mathematical arguments that allow to analytically estimate the singular values were developed. Here, the aim is to exploit the results obtained there in order to derive an analytical expression of the right side of equation (2) in terms of the parameters of the configurations. That

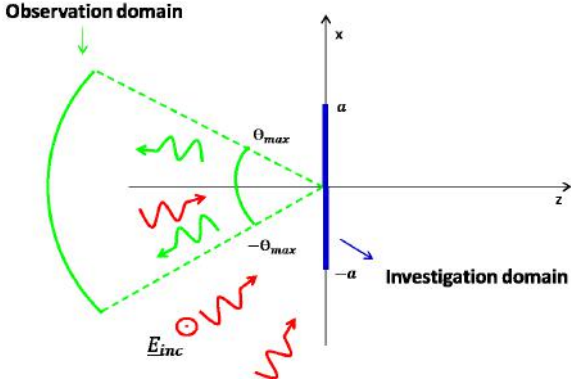


Figure 1: A pictorial view of the scattering configuration considered in this paper is sketched.

is, how the ϵ -entropy changes by varying of the scattering parameters is addressed.

In order to tackle the problem under the simplest conditions, a canonical configuration is considered. In more detail, the scattering domain is assumed to be a strip illuminated by plane waves whereas the scattered field is assumed to be collected in the far zone. Invariance is assumed along the plane wave polarisation direction which in turn is orthogonal to the strip. Accordingly, the study is developed for the two-dimensional scalar configuration sketched in Figure 1.

2. View diversity

Consider the geometry sketched in figure 1. Let $I = [-a; a]$ be the scattering domain which is assumed to lay along the x -axis and $\Omega_o = [-u_{max}; u_{max}]$ the observation angular corner with $u_o = \sin \theta_o \in \Omega_o$. Moreover, thanks to view diversity the scattered field is collected for different incidence directions $u_v = \sin \theta_v \in \Omega_v$ with $\Omega_v \subseteq \Omega_o$. Let us assume that Ω_v be a discrete subset of Ω_o . In particular, say M the number of views which are taken by uniformly sampling Ω_o .

The pertinent scattering operator then writes as

$$\mathcal{A}_v : \chi(x) \in \mathcal{L}_I^2 \longrightarrow E_S(u_o, u_v) = \mathcal{A}_v \chi \in \mathcal{L}_{(\Omega_o \times \Omega_v)}^2 \quad (3)$$

with

$$\mathcal{A}_v \chi = \int_{-a}^a \exp[jk_0(u_o - u_v)x] \chi(x) dx$$

k_0 being the wavenumber at single frequency adopted in the scattering experiment.

In order to estimate the singular system of equation (3), it is convenient to study the eigenspectrum of the associated operator $\mathcal{A}_v^\dagger \mathcal{A}_v$, with \mathcal{A}_v^\dagger being the adjoint operator of \mathcal{A}_v .

In this case it results that

$$\mathcal{A}_v^\dagger \mathcal{A}_v = \sum_{m=1}^M \frac{2\pi}{k_0} \mathcal{P}_I \mathcal{B}_{\Omega_m} \mathcal{P}_I \quad (4)$$

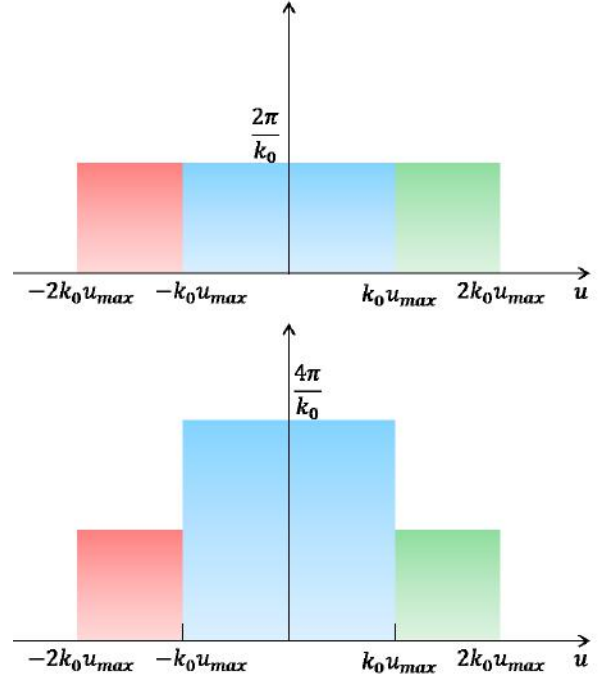


Figure 2: The case of three angles of incidence $\Omega_i = \{-u_{max}, 0, u_{max}\}$. The top panel gives a pictorial view of the frequency bands which now overlap. The bottom panel shows how the spectrum of the kernel can be still given in terms of disjoint bands.

where \mathcal{P}_I and \mathcal{B}_Ω denote the spatial limiting and the band limiting projectors over the spatial I and frequency Ω_m intervals, respectively and $\Omega_m = [-k_0 u_{max} + k_0 u_{im}, k_0 u_{max} + k_0 u_{im}]$. The operator $\mathcal{A}_v^\dagger \mathcal{A}_v$ can be conveniently rearranged as (see Figure 2 for a graphical explanation)

$$\mathcal{A}_v^\dagger \mathcal{A}_v = \sum_{m=1}^{M-1} \frac{2\pi(M-m)}{k_0} [\mathcal{P}_I \mathcal{B}_{\tilde{\Omega}_m} \mathcal{P}_I + \mathcal{P}_I \mathcal{B}_{\hat{\Omega}_m} \mathcal{P}_I] \quad (5)$$

where $\tilde{\Omega}_m = [(m-1)\Delta, m\Delta]$ and $\hat{\Omega}_m = [-m\Delta, -(m-1)\Delta]$, with $\Delta = \frac{2k_0 u_{max}}{M-1}$. In this way, $\tilde{\Omega}_m$ and $\hat{\Omega}_m$ for each $m \in \{1, \dots, M-1\}$ are disjoint bands.

Let be $\lambda_n[\mathcal{A}_v^\dagger \mathcal{A}_v]$ the eigenvalues of $\mathcal{A}_v^\dagger \mathcal{A}_v$. They are not known in closed form. However, as shown in [13], if the spatial-bandwidth products of each single operator in equation (5) ($c_M = a\Delta/2$) are greater than 4, the eigenvalues of $\mathcal{A}_v^\dagger \mathcal{A}_v$ can be very well approximated by the union of those associated to each single operator, the latter being extensively studied in literature [14]-[15]. Therefore, the eigenvalues of $\lambda_n[\mathcal{A}_v^\dagger \mathcal{A}_v]$ can be given in terms of those associated to the prolate spheroidal wave-functions ($\lambda_l(c_M)$) as

$$\{\lambda_n[\mathcal{A}_v^\dagger \mathcal{A}_v]\}_{n=0}^\infty \simeq \bigcup_{m=1}^{M-1} \frac{2\pi(M-m)}{k_0} \{ \{\lambda_l(c_M)\}_{l=0}^\infty \cup \{\lambda_h(c_M)\}_{h=0}^\infty \} \quad (6)$$

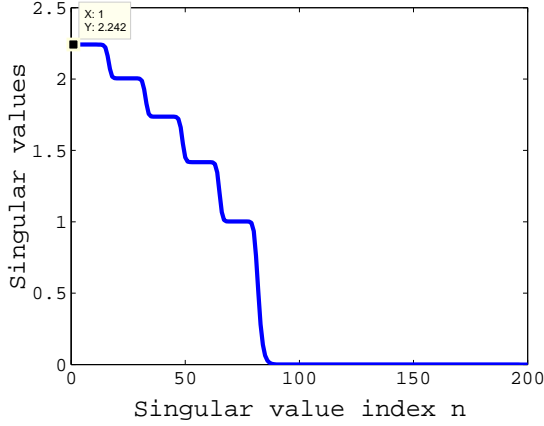


Figure 3: Singular value behavior for six angles of incidence, $\Omega_o = [-1, 1]$ and $a = 20\pi/k_0$. As can be seen, the foreseen five steps are well evident.

The same holds also true for the singular values of the scattering operator, denoted by $\sigma_n[\mathcal{A}_v]$, that are the square root of such eigenvalues. In particular, as the behaviour of $[\{\lambda_l(c_M)\}_{l=0}^\infty \cup \{\lambda_h(c_M)\}_{h=0}^\infty]$ is a step-like one with the knee at the index $[4c_M/\pi]$, the singular values of \mathcal{A}_v exhibit $M - 1$ steps where the first knee occurs at $N_1 = [4c_M/\pi]$. The successive m -th step is comprised between the indexes $N_m = N_1 + \sum_{l=0}^{m-2} [4c_M/\pi]$ and $N_m + [4c_M/\pi]$, for $m \in \{2, 3, \dots, M - 1\}$. Moreover, on each step the singular values are equal to $\sqrt{(M - m)2\pi/k_0}$ with $m \in \{1, 2, \dots, M - 1\}$. An example confirming this result is reported in figure 3.

By exploiting the results obtained for the singular values of \mathcal{A}_v , an upper bound of the ϵ -entropy in equation (2) can be analytically obtained. Assume that the bound about the norm of the noise ϵ is known. Hence, the cut-off threshold must be chosen as $N_\epsilon = \max\{n > 0 : \sigma_n(\mathcal{A}_v) \geq \epsilon\}$. As the $\sigma_n(\mathcal{A}_v)$ exhibit a $M - 1$ steps behaviour, estimating N_ϵ entails evaluating how many steps are above ϵ . Accordingly let $\tilde{m}_\epsilon = \max\{m : (M - m)2\pi/k_0 \geq \epsilon^2\}$ be the number of steps above ϵ , then

$$\mathcal{H}_{v\epsilon} \geq \frac{4c_M}{\pi} \sum_{m=1}^{\tilde{m}_\epsilon} \log_2 \frac{\sqrt{(M - m)(2\pi/k_0)}}{\epsilon} \quad M \geq 2 \quad (7)$$

By substituting $c_M = ak_0 u_{max}/(M - 1)$, it can be obtained an estimate of the ϵ -entropy in terms of the parameter of scattering

$$\mathcal{H}_{v\epsilon} \geq \frac{4ak_0 u_{max}}{(M - 1)\pi} \sum_{m=1}^{\tilde{m}_\epsilon} \log_2 \frac{\sqrt{(M - m)(2\pi/k_0)}}{\epsilon} \quad M \geq 2 \quad (8)$$

In figure 4, a comparison between the metric entropy evaluated from the exact singular values and the one estimated by the equation (8). In particular, it can be appreciated how the estimation given by the equation (8) works very well. Let \mathcal{H}_ϵ be the ϵ -entropy for the single view /single frequency

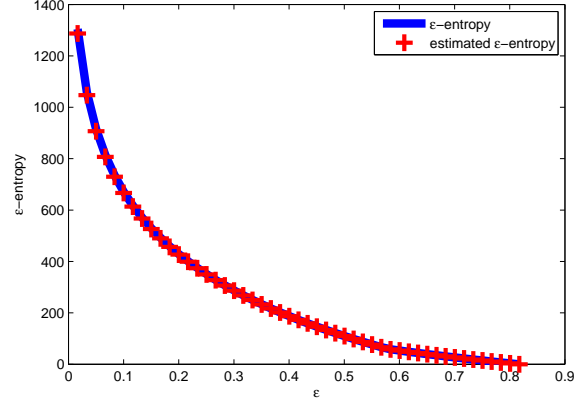


Figure 4: A comparison between the metric entropy evaluated from the exact singular values and the one estimated by the equations (8) for the view diversity when $I = [-10, 10]$ m, $\Omega_o = [-1, 1]$ and $M = 3$.

configuration. Its expression in terms of the parameter of the configuration is

$$\mathcal{H}_\epsilon \geq \frac{2ak_0 u_{max}}{\pi} \log_2 \frac{\sqrt{2\pi/k_0}}{\epsilon} \quad (9)$$

As expected, to collect the field for different angles of illumination entails an increasing on "the information" that can be conveyed back from data to the unknown with respect to the single view case and this improvement, if $\epsilon^2 < 2\pi/k_0$, can be quantified as

$$\mathcal{H}_{v\epsilon}/\mathcal{H}_\epsilon \geq \begin{cases} 2 & M = 2 \\ 2[1 + \frac{1}{(M-1)} \frac{\log_2 \sqrt{(M-1)!}}{\log_2 \frac{\sqrt{2\pi/k_0}}{\epsilon}}] & M > 2 \end{cases} \quad (10)$$

In [12], it has been shown that in order to obtain the maximum number of measures 'linearly independent' two *extremal* views (i.e., having angles corresponding to the edges of Ω_o) are sufficient. Accordingly, multiple views can be considered redundant. From the equation (10), it can be concluded that also the redundant views yield an increasing on "the information" that can be conveyed back from data to the unknown. In fact, the redundancies "amplify" some spectral components of the data against the noise. This suggests that the optimal strategy of data collection would be to illuminate the object by two *extremal* views and probing the scene more times for each view. In this way a maximisation of the NDF and of the ϵ -entropy is obtained, contemporaneously. When $\epsilon^2 > 2\pi/k_0$, \mathcal{H}_ϵ is zero and only collecting the data for $M > 2$ views allows to reconstruct the unknown.

3. Frequency diversity

In this section, the role of frequency diversity is studied. Therefore, let us assume to probe the field by varying the

frequency of the incident waves within the discrete interval $\Omega_k = \{k_{min}, k_{max}\}$. In this case the scattering operator particularises as

$$\mathcal{A}_f : \chi(x) \in \mathcal{L}_I^2 \longrightarrow E_S(u_o, k) \in \mathcal{L}_{(\Omega_o \times \Omega_k)}^2 \quad (11)$$

$$\mathcal{A}_f \chi = \int_{-a}^a \exp(jk u_o x) \chi(x) dx$$

where now $u_o = \sin \theta_o$ and u_i has been assumed equal to zero (normal incidence).

Let Ω_k consists of M frequencies k_m taken uniformly between $[k_{min}, k_{max}]$ at a step of $\Delta k = (k_{max} - k_{min}) / (M - 1)$. Accordingly, it results that

$$\mathcal{A}_f^\dagger \mathcal{A}_f = \sum_{m=1}^M \frac{2\pi}{k_m} \mathcal{P}_I \mathcal{B}_{\Omega_m} \mathcal{P}_I \quad (12)$$

where now $\Omega_m = [-k_m u_{max}, k_m u_{max}]$. For the sake of simplicity, from now on, we assume that $u_{max} = 1$ so that $\Omega_m = [-k_m, k_m]$.

The operator $\mathcal{A}_f^\dagger \mathcal{A}_f$ can be conveniently rearranged as (see figure 5 for a graphical explanation)

$$\begin{aligned} \mathcal{A}_f^\dagger \mathcal{A}_f &= \sum_{m=1}^M \frac{2\pi}{k_m} \mathcal{P}_I \mathcal{B}_{\Omega_1} \mathcal{P}_I + \\ &+ \sum_{m=2}^M \sum_{l=m}^M \frac{2\pi}{k_l} \left(\mathcal{P}_I \mathcal{B}_{\tilde{\Omega}_m} \mathcal{P}_I + \mathcal{P}_I \mathcal{B}_{\hat{\Omega}_m} \mathcal{P}_I \right) \end{aligned} \quad (13)$$

where $\tilde{\Omega}_m = [k_{min} + (m-1)\Delta k, k_{min} + m\Delta k]$ and $\hat{\Omega}_m = [-k_{min} - m\Delta k, -k_{min} - (m-1)\Delta k]$.

Now, $\mathcal{A}_f^\dagger \mathcal{A}_f$ is in a suitable form to apply the results reported in [12]. Hence, it has been shown that as long as $c_M = a\Delta k/2 \gg 1$ and $ak_{min} \gg 1$ the $\lambda_n[\mathcal{A}_f^\dagger \mathcal{A}_f]$ exhibit M steps with knees occurring at $N_m = [2k_{min}a/\pi] + (m-1)[2a\Delta k/\pi]$. Moreover, on the m -th step the numerical value is $\sum_{l=m}^M 2\pi/k_l$, with k_l represents the l th frequency in Ω_k . An example confirming this result is reported in figure 6.

The following analytical estimation for the ϵ -entropy $\mathcal{H}_{f\epsilon}$ follows

$$\begin{aligned} \mathcal{H}_{f\epsilon} &\geq \frac{2k_{min}a}{\pi} \log_2 \frac{\sqrt{\sum_{l=1}^M (2\pi/k_l)}}{\epsilon} + \\ &+ \frac{2(k_{max} - k_{min})a}{\pi(M-1)} \sum_{m=2}^{\hat{m}_\epsilon} \log_2 \frac{\sqrt{\sum_{l=m}^M (2\pi/k_l)}}{\epsilon} \end{aligned} \quad (14)$$

where $\hat{m}_\epsilon = \max\{m : \sum_{l=m}^M (2\pi/k_l) \geq \epsilon^2\}$. Also here, this estimation works very well (see figure 7).

As expected, collecting data for different frequencies below k_{max} entails an increasing of the information as compared to the single frequency $k_0 = k_{max}$ case. This improvement, if $\epsilon^2 < 2\pi/k_{max}$, is estimated as

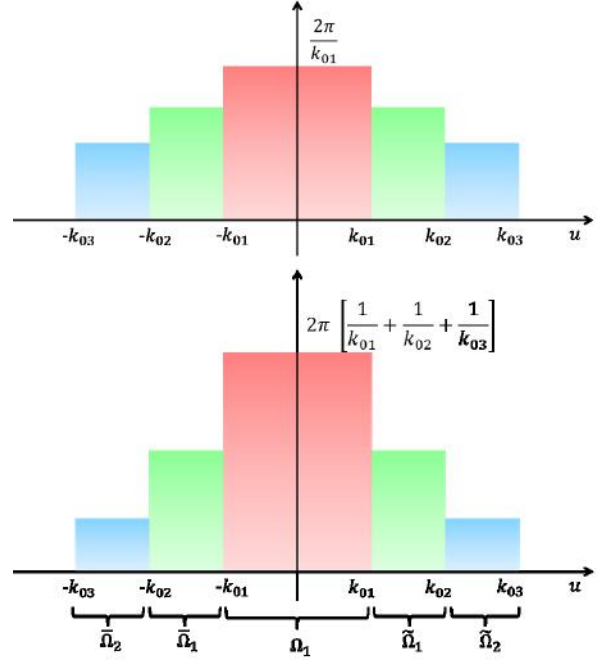


Figure 5: Illustration of how to rearrange the frequency bands to obtain (13).

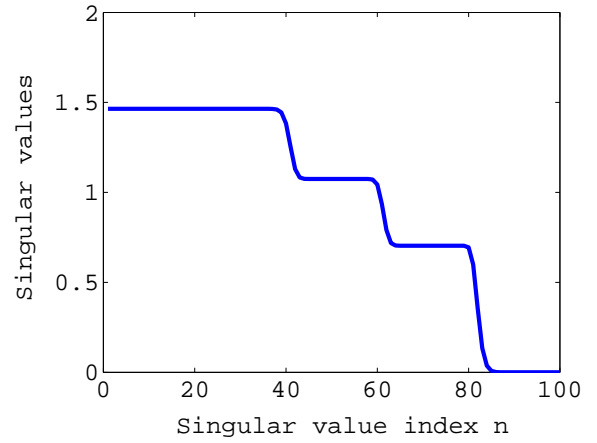


Figure 6: Singular value behavior of \mathcal{A}_f for the case of $M = 3$ frequencies $k_{0min}, 1.5k_{0min}$ and $2k_{0min}$, $k_{0min} = 2\pi m^{-1}$ and $a = 20\pi/k_{0min}$.

$$\begin{aligned} \mathcal{H}_{f\epsilon}/\mathcal{H}_\epsilon &\geq 1 + \frac{(k_{max} - k_{min})}{(M-1)k_{max}} \frac{\log_2 \prod_{m=2}^{M-1} \sqrt{1 + \sum_{l=m}^{M-1} \frac{k_{max}}{k_l}}}{\log_2 \frac{\sqrt{2\pi/k_{max}}}{\epsilon}} + \\ &+ \frac{k_{min}}{k_{max}} \frac{\log_2 \sqrt{\sum_{l=1}^M \frac{k_{max}}{k_l}}}{\log_2 \frac{\sqrt{2\pi/k_{max}}}{\epsilon}} \end{aligned} \quad (15)$$

In [12], it has been concluded that while the maximum number of measurements 'linearly independent' depends on the highest adopted frequency k_{max} , by using more frequencies (lower than the highest one) shapes the singular

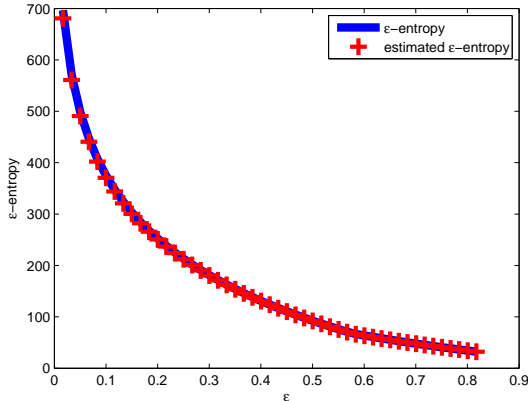


Figure 7: A comparison between the metric entropy estimated by the exact singular values and the one estimated by the equation (14) for the frequency diversity when $I = [-10, 10]$ m, $\Omega_o = [-1; 1]$, $M = 3$ and $\Omega_k = \{\pi, 6\pi\} m^{-1}$.

value behaviour so that it resemble a staircase. From equation (14), it can be observed that the presence of multiple frequencies yield an increasing of the ϵ -entropy and this improvement depends on the parameters of the configuration. Also here, an optimal collecting strategy of the field can be reached by illuminating the object at the frequency k_{max} and probing the scene more time at the same frequency. In this way a maximisation of the NDF and of the ϵ -entropy is obtained, contemporaneously.

4. Comparison between the diversities

The expressions obtained in the previous sections allow to obtain an estimation of the ϵ -entropy in terms of the scattering parameters. In this section, such results are used to compare the different configurations considered herein.

Assume that the bound about the norm of the noise ϵ is known and equal to $\epsilon = 0.21$ and that the observation domain is $\Omega_o = [-1, 1]$. For the single frequency case (which means for both the single-view /single-frequency and multi-view/single-frequency configurations) the object is illuminated at the spatial frequency $k_0 = k_{max}$.

Equation (9) normalised with respect to a becomes

$$\bar{\mathcal{H}}_\epsilon \geq \frac{2k_{max}}{\pi} \log_2 \frac{\sqrt{2\pi/k_{max}}}{\epsilon} \quad (16)$$

where $\bar{\mathcal{H}}_\epsilon$ denotes the normalised ϵ -entropy.

When the multi-view configuration is considered, the scattering scene is probed at M different angles of incidence. Accordingly, equation (8) normalised to a becomes

$$\bar{\mathcal{H}}_{v\epsilon} \geq \frac{4k_{max}}{(M-1)\pi} \sum_{m=1}^{M-1} \log_2 \frac{\sqrt{(M-m)(2\pi/k_{max})}}{\epsilon} \quad M \geq 2 \quad (17)$$

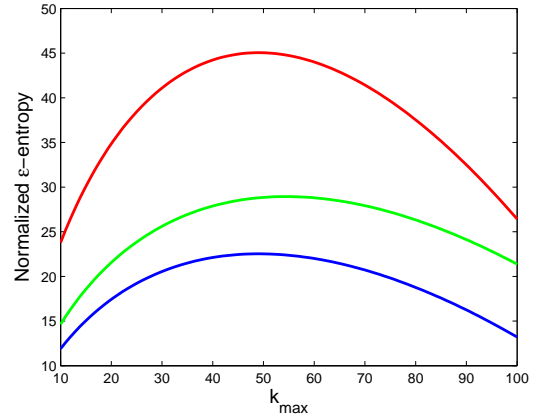


Figure 8: A comparison between the normalized upper bounds of the ϵ -entropy associated to the three different configurations, as k_{max} varies in the interval $[10, 100] m^{-1}$, when $M = 2$. The blue line refers to single view /single frequency configuration, the red and green line to multi-view and multi-frequency configuration, respectively .

From equation (17) it can be observed that in order to obtain better performance in terms of ϵ -entropy only k_{max} and M play a role. For multi-frequency configuration only normal incidence is considered. In this case, also k_{min} enters and affects the 'information'. Equation (14) normalised is

$$\bar{\mathcal{H}}_{f\epsilon} \geq \frac{2k_{min}}{\pi} \log_2 \frac{\sqrt{\sum_{l=1}^M (2\pi/k_l)}}{\epsilon} + \frac{2(k_{max} - k_{min})}{\pi(M-1)} \sum_{m=2}^M \log_2 \frac{\sqrt{\sum_{l=m}^M (2\pi/k_l)}}{\epsilon} \quad (18)$$

In order to perform the comparison let us assume $k_{min} = 2\pi m^{-1}$. This way, the different configurations can be compared by varying k_{max} and M only.

In figures 8 and 9, the normalised upper bound of the ϵ -entropy is shown as a function of k_{max} for each configuration, when $M = 2$ and $M = 3$, respectively. In particular, the blue line is associated to single view/ single frequency configuration (that is when no diversities are employed), while the red and the green lines are associated to the multi-view and multi-frequency configurations, respectively.

As expected, there is a gain in terms of ϵ -entropy obtained by exploiting the diversities with respect to the single-frequency/single-view configuration. This is always true as the scattering parameters vary .

Furthermore, as can be seen, the multi-view configuration allows to obtain better results than the multi-frequency one and this improvement increases as more views or frequencies are introduced.

However, this cannot allows to state that the multi-view configuration is the optimal one because in general the ϵ -entropy depends on the chosen k_{min} as well. Indeed, for

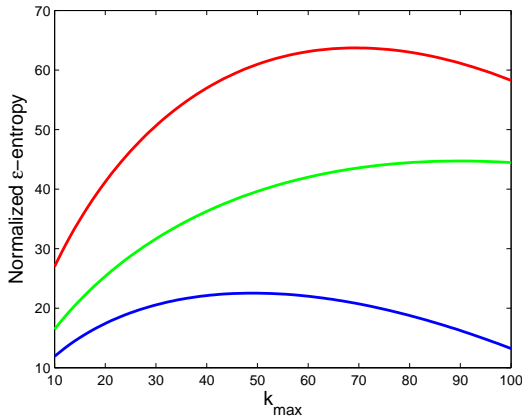


Figure 9: A comparison between the normalized upper bounds of the ϵ -entropy associated to the three different configurations, as k_{max} varies in the interval $[10, 100] m^{-1}$, when $M = 3$. The blue line refers to single view /single frequency configuration, the red and green line to multi-view and multi-frequency configuration, respectively .

some parameters the multi-view configuration can be better than the multi-frequency one (as in this case) and for other parameters the opposite is true.

So, the presented analytical analysis allows to get the answer to what is the optimal configuration when the parameters have been fixed according to some constraints that one may have.

5. Conclusion

The impact of view and frequency diversities on the Kolmogorov entropy measure has been studied in the framework of linear inverse scattering problems.

Canonical strip-like scatterers have been considered. This has allowed to determine and estimate the ϵ -entropy for all the considered configurations. Also, these expressions clearly make it evident the role of the scattering parameters (i.e., observation corner, number of views, frequencies, etc.). Numerical checks of such estimations showed that they are in very good agreement with the actual entropy.

As expected, the use of diversities increases the information content. Also, some numerical examples have been run to compare the view and the frequency diversities. It is shown that, for the considered parameters, view diversity outperforms the frequency one. However, in general this cannot be the case.

The main results of this paper is to provide a tool to foreseen the information content once the configuration parameters have been fixed. Conversely, the reported estimations can be used to set the configuration parameters in order to maximise the achievable information content.

Acknowledgement

This work was supported by the Italian Ministry of University and Research through the FIRB initiative under the project MICENEA (RBFR12A7CD).

References

- [1] A D.- L. Marks, A family of approximations spanning the Born and Rytov scattering series, *Opt. Exp.* 14: 8837–8847, 2006.
- [2] C. W. Groetch, *Inverse Problems in the Mathematical Sciences*, Vieweg, Braunschweig, 1993.
- [3] F. Riesz and B. Nagy, *Functional Analysis*, Dover, New York, 1990
- [4] M. Bertero and P. Boccacci, *Introduction to Inverse Problems in Imaging*, IOP, Bristol 1998.
- [5] A D.- L. Marks, N. Magnoli and G. A. Viano, On the eigenfunction expansions associated with Fredholm integral equation of first kind in the presence of noise, *J. Math. Anal. Appl.* 197: 188–206 (1996).
- [6] J. L. Harris, Diffraction and resolving power, *J. Opt. Soc. Am.* 54, 931–936 (1963).
- [7] G. Toraldo Di Francia, Degrees of freedom of an image *J. Opt. Soc. Am.* 59: 799–804 (1969).
- [8] G. Newsam and R. Barakat, Essential dimension as a well-defined number of degrees of freedom of finite-convolution operators appearing in optics, *J. Opt. Soc. Am. A* 2: 2040–2045 (1985).
- [9] E. De Micheli, G. A. Viano, Metric and probabilistic information associated with Fredholm integral equations of the first kind, *J. Int. Eq. Appl.* 14: 283–310 (2002).
- [10] C. Vogel, *Computational Methods for Inverse Problems*, SIAM - Frontiers in Applied Mathematics Series, N. 23, (2002).
- [11] E. De Micheli and G. A. Viano, Fredholm Integral Equations of the First Kind and Topological Information Theory, *Integr. Equ. Oper. Theory* 73: 553–571 (2012).
- [12] R. Solimene, M. A. Maisto, R. Pierri, The role of diversity on the singular values of linear scattering operators: the case of strip objects, *J. Opt. Soc. A* 30: 2266–2272 (2013).
- [13] R. Solimene, M. A. Maisto and R. Pierri, Inverse scattering in the presence of a reflecting plane, *Journal of Optics* 18: (2), 025603.
- [14] D. Slepian, H. O. Pollak, Prolate spheroidal wave function, Fourier analysis and uncertainty I, *Bell Syst. Tech. J.* 40: 43–63 (1961).

- [15] H. J. Landau and H. O. Pollak, Prolate spheroidal wave function, Fourier analysis and uncertainty II, *Bell Syst. Tech. J.* 40: 64–84 (1961).

Comparison between different decorrelation techniques in vital sign detection

Angela Dell'Aversano*, Andrea Natale and Raffaele Solimene

Dipartimento di Ingegneria Industriale e dell'Informazione,
Second University of Naples, Aversa, Italy

*corresponding author, E-mail: angela.dellaversano@unina2.it

Abstract

The problem of detecting the breath activities of a human subject is addressed. A CW signal is used to probe the scene and the MUSIC algorithm is exploited to detect frequency doppler modulation introduced by chest movements. For this particular measurement configuration, the correlation matrix results rank deficient. In order to restore the rank, two decorrelation techniques are compared by exploiting numerical data.

1. Introduction

The contactless heartbeat and respiration detection of a human subject via radar sensing is a problem that is relevant in medical as well as security contexts (e.g. for apnea syndrome and baby monitor)[1] or for detecting human beings trapped under snow or debris after avalanche or quake events [2].

The underlying principle upon which those methods are based is the Doppler shift. More in detail, once a human body is exposed to continuous-wave (CW) microwave fields, the arising reflected signals turn out to be modulated in frequency (or equivalently in phase) due to body movements. Now, if the subject is at rest for some reasons, the only relevant movement is the one due to chest displacement owing to the breathing and heart beating. These movements are essentially nearly periodic and hence can be detected starting from the reflected field by adopting a suitable demodulation/filtering scheme.

Vital signs' detection is a complex task due to many impairing factors. Leakage between the TX and RX channels, null point problem, stability of local oscillator and strong clutter coming from environment are among the problems to be faced [3].

Most of breath frequency estimation approaches are based on Fourier transform [4] algorithms which are often combined with proper demodulation schemes in order to avoid some of the drawbacks mentioned above [5].

In this paper, in order to detect the Doppler shift, a MUSIC [6] based algorithm is adopted. The key idea is to reach a particular spectral decomposition of the data correlation matrix into the so-called signal and noise subspaces. In particular, the noise subspace is employed to build the *pseudospectrum* which "peaks", in the unknown space, just in correspondence of the looked parameters.

Here, the MUSIC algorithm is properly tailored to take into account that for the case at hand the received signal is

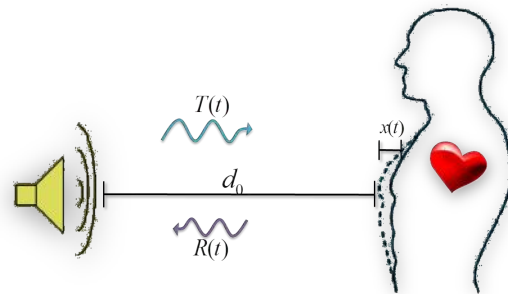


Figure 1: Scattering scenario: a human being is probed by a CW radio signal.

not a linear combination of complex exponentials. Moreover, as the signals representing the vital signs are correlated, a decorrelation stage has to be run before detection. Otherwise, the achievable performance rapidly decays so to cause missing detection.

In order to restore the *rank* of the correlation matrix, two decorrelation methods are compared: the spatial smoothing [7]-[8] and the Toeplitz based method [9].

Numerical examples are included in order to show how two methods work.

2. Mathematic model

Consider the scattering experiment schematically described in Figure 1. A human being is illuminated by the transmitted signal $T(t)$. Then the reflected modulated signal $R(t)$ arises and is collected in the receiving stage.

Neglecting amplitude variations, the transmitted signal $T(t)$ under CW regime can be expressed as

$$T(t) = \cos(2\pi ft + \phi(t)) \quad (1)$$

where t is elapsed time, f and $\phi(t)$ are the frequency and the phase noise of the local oscillator, respectively.

This signal impinges on a human target located at a nominal distance d_0 . The chest introduces a time-varying displacement denote by $x(t)$. Accordingly, after the transmitted signal propagates back and forth for a total distance (between the transmitter and the receiver) equal to $2d(t) = 2d_0 + 2x(t)$, the received signal is collected; its

expression is given by

$$R(t) \approx \cos \left[2\pi f t - \frac{4\pi(d_0 + x(t))}{\lambda} + \phi \left(t - \frac{2d_0}{c} \right) \right] \quad (2)$$

where c is the propagation velocity (the speed of light) and λ is the wavelength in air, which equals c/f .

Chest movements are of course embedded in the phase term related to $x(t)$. Therefore, this is the factor that has to be single out in order to detect (if any) and possibly characterize the breath activities. Accordingly, the received signal is processed by the receiving channel and a MUSIC-based algorithm as depicted in Figure 2.

Note that a quadrature demodulation scheme is exploited in order to avoid the null point problem. Hence, the signal to be processed is given by

$$B(t) = B_I(t) + jB_Q(t) = \exp \left(j \frac{4\pi x(t)}{\lambda} + j\theta(t) \right) \quad (3)$$

where $\theta(t) = \frac{4\pi d_0}{\lambda} + \Delta\phi(t)$ and $\Delta\phi(t)$ is the residual local oscillator phase noise, which usually can be neglected [10].

As the spatial displacement $x(t)$ is very small, it results that

$$B(t) \approx \exp(j\theta) \left(1 + j \frac{4\pi x(t)}{\lambda} \right)$$

Actually, besides the signal in Equation (3), clutter contributions are always present, specially when there is an obstacle (i.e., a wall, etc.) between the person and the antenna system.

Therefore, the actual demodulated signal is

$$B(t) = C + \exp(j\theta) \left(1 + j \frac{4\pi x(t)}{\lambda} \right) \quad (4)$$

where C stays for the *clutter* and is not function of time t .

Note that the clutter introduces a static contribution (after demodulation) that can be eliminated by filtering out the continuous component. This filtered signal is denoted as

$$\tilde{B}(t) = \exp(j\theta) j \frac{4\pi x(t)}{\lambda} \quad (5)$$

and represents the signal that is actually passed to the MUSIC stage.

From the theory of Fourier series, any time-varying periodic displacement $x(t)$ can be viewed as the combination of a series of single-tone signals. Therefore, for the ease of analysis and without loss of generality, it is assumed that the chest movement $x(t)$ is described as the sum of $x_h(t) = A_h \cos(2\pi f_h t)$, due to heartbeat, and $x_r(t) = A_r \cos(2\pi f_r t)$ due to respiration.

3. Multiple Signal Classification (MUSIC)

The MUSIC algorithm is a powerful method to estimate frequencies embedded in a signal.

The standard formulation applies to a linear combination of complex exponentials. Therefore, here, it is need to adapt this method to the problem at hand.

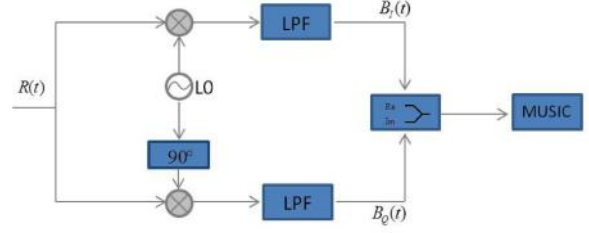


Figure 2: Schematic of the receiving stage.

Assume that the reflected signal is collected in correspondence of L instants of time t_n so that $t_{n+1} - t_n = \Delta t$ is the sampling interval. Say $\tilde{\mathbf{b}}$ the data column vector corresponding to the time vector \mathbf{t} . Then, Equation (5) can be recast in a matrix form as

$$\tilde{\mathbf{b}} = \mathbf{C}\mathbf{a} = [\cos(2\pi\mathbf{t}f_1) \dots \cos(2\pi\mathbf{t}f_d)]\mathbf{a} \quad (6)$$

where d is the number of harmonics and \mathbf{a} the coefficient column $a_i = \exp(j\theta)j \frac{4\pi A_i}{\lambda}$ (in our case $d = 2$ and $A_1 = A_h$ and $A_2 = A_r$).

In order to build the pseudospectrum, the data space is factorized in the so-called signal and noise subspaces. To this end, it is noted that the matrix \mathbf{C} can be expressed as $\mathbf{C} = \mathbf{E}^- + \mathbf{E}^+$ where $\mathbf{E}^- = [\exp(-j2\pi\mathbf{t}f_1) \dots \exp(-j2\pi\mathbf{t}f_d)]$ and $\mathbf{E}^+ = [\exp(j2\pi\mathbf{t}f_1) \dots \exp(j2\pi\mathbf{t}f_d)]$.

Accordingly, the signal subspace corresponds to that range of \mathbf{C} , i.e., $\mathcal{R}(\mathbf{C})$, which in turn $\mathcal{R}(\mathbf{C}) = \mathcal{R}(\mathbf{E}^-) \cup \mathcal{R}(\mathbf{E}^+)$. Therefore, $\mathcal{R}(\mathbf{C}) = \text{span}\{\exp(-j2\pi\mathbf{t}f_1), \dots, \exp(-j2\pi\mathbf{t}f_d), \exp(j2\pi\mathbf{t}f_1), \dots, \exp(j2\pi\mathbf{t}f_d)\}$. The noise subspace is orthogonal to both $\mathcal{R}(\mathbf{E}^-)$ and $\mathcal{R}(\mathbf{E}^+)$. Hence, also for the case at hand, the pseudospectrum can be achieved by considering as steering vector only exponential like vectors (as in usual MUSIC).

Formally, the pseudospectrum is as follows

$$\Phi(f) = \frac{1}{\|\mathcal{P}[\exp(j2\pi\mathbf{t}f)]\|^2} \quad (7)$$

where \mathcal{P} is the projection operator onto the noise subspace which depends on the adopted decorrelation algorithm.

4. Decorrelation methods

For the particular scenario addressed herein, it is obvious that the correlation matrix corresponding to (6) is rank deficient. So the rank need to be restored by some decorrelation techniques. In this section two different algorithms are described.

4.1. Spatial Smoothing

In Spatial Smoothing technique (SS) the data, consisting of L time samples, is separated in $M_d = L - N + 1$ overlapped sub-arrays composed by N samples, so that $\tilde{\mathbf{b}}_{\mathbf{k}} = \tilde{B}(t_k, \dots, t_{k+N})$, with $k \in [1, 2, \dots, M_d]$, M_d

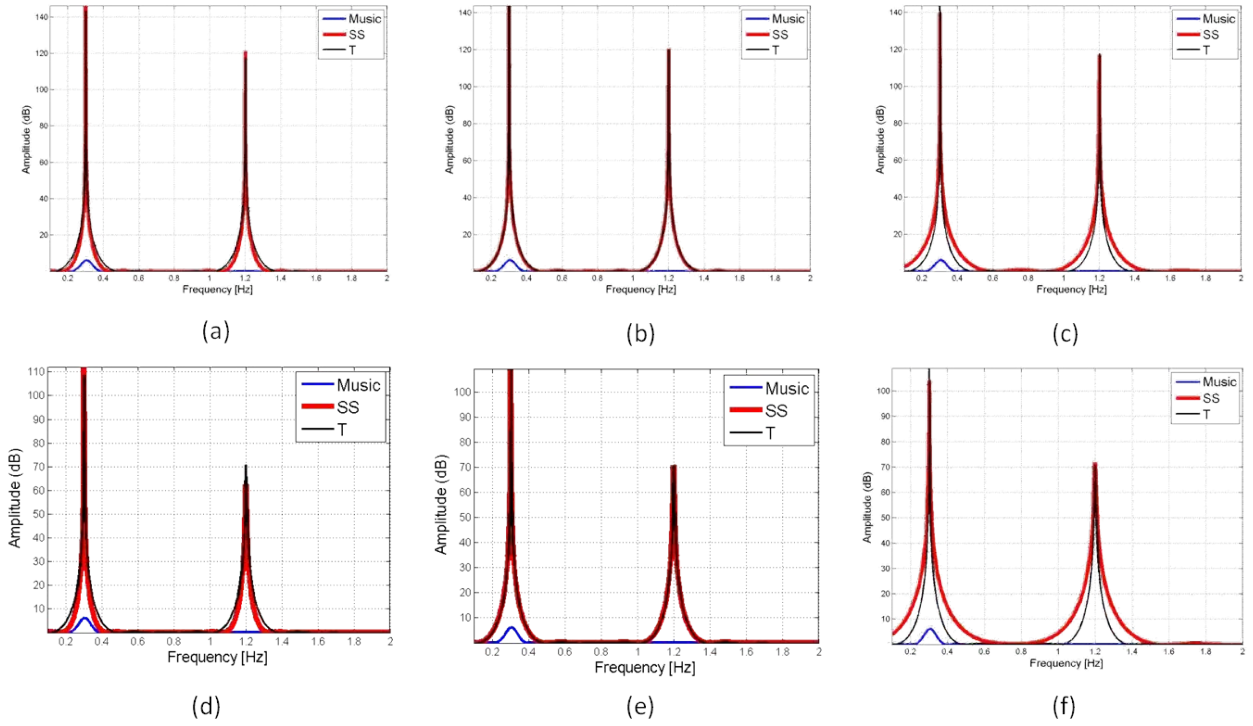


Figure 3: Synthetic data with acquisition time equal to 10s. Pseudospectrum comparison between SS (red line) and Toeplitz (black line) methods by varying the number of samples and the decorrelation index: (a) $L = 270$, $M_d = 53$, (b) $L = 270$, $M_d = L/2$, (c) $L = 270$, $M_d = 153$, (d) $L = 80$, $M_d = 21$, (e) $L = 80$, $M_d = L/2$, (f) $L = 80$, $M_d = 61$

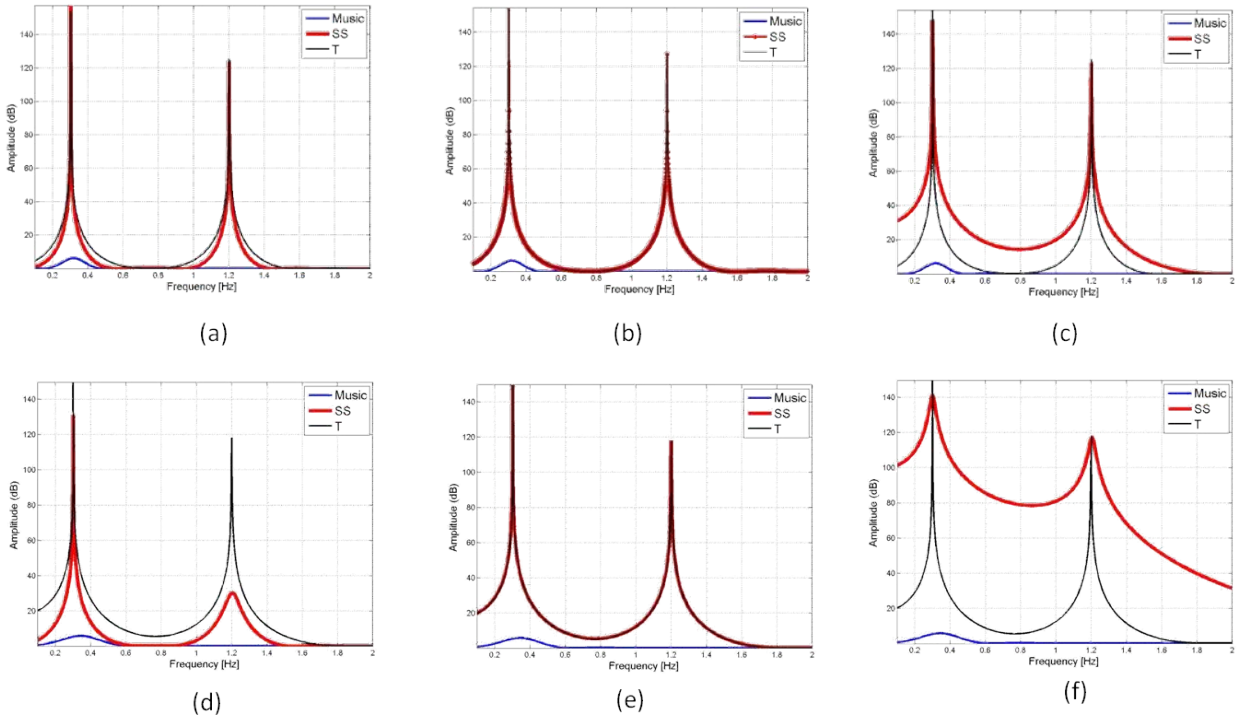


Figure 4: Synthetic data by varying the acquisition time and the decorrelation index. Pseudospectrum comparison between SS (red line) and Toeplitz (black line): (a) $\Delta tL = 5s$, $M_d = 51$, (b) $\Delta tL = 5s$, $M_d = L/2 = 100$, (c) $\Delta tL = 5s$, $M_d = 151$, (d) $\Delta tL = 3s$, $M_d = 11$, (e) $\Delta tL = 3s$, $M_d = L/2 = 60$, (f) $\Delta tL = 3s$, $M_d = 101$

being the decorrelation index. Accordingly, the correlation matrix is estimated as

$$S_{SS} = \frac{1}{M_d} \sum_{k=1}^{M_d} \mathbf{r}_k \quad (8)$$

where

$$\mathbf{r}_k = \tilde{\mathbf{b}}_k \tilde{\mathbf{b}}_k^H = \mathbf{D} \mathbf{H}_k \mathbf{D}^H \quad (9)$$

is the correlation matrix calculated for the k -th sub-array, $\mathbf{D} = [\cos(2\pi \mathbf{t}_i f_h), \cos(2\pi \mathbf{t}_r f_r), \sin(2\pi \mathbf{t}_i f_h), \sin(2\pi \mathbf{t}_r f_r)]$ and $(\cdot)^H$ denotes the complex conjugate transpose. \mathbf{H}_k is a 4×4 matrix. If the smoothing is properly achieved then the rank of $\sum_{k=1}^{M_d} \mathbf{H}_k$ should be 4.

In order to identify the signal and noise subspace, the Singular Value Decomposition (SVD) is applied to S_{SS} . By checking singular values, the noise subspace is defined as the set of singular values that get small with respect to the first one. In particular, note that for the case at hand, due to particular form of the matrix \mathbf{C} , the number of the relevant singular values (i.e., the signal subspace dimension) is twice as the number of frequencies. Finally, the projection operator \mathcal{P} picks the corresponding left singular function of S_{SS} in order to build the pseudospectrum. Note that after the smoothing, data is as it were collected only over the instants (7), with $\mathbf{t} = \mathbf{t}(1, \dots, N)$.

4.2. Toeplitz based algorithm

This method is based on building up Toeplitz matrices for each row of the correlation matrix $\mathbf{r} = \tilde{\mathbf{b}} \tilde{\mathbf{b}}^H$ [9]. Its introduction is motivated by the need to avoid reducing the time interval used while constructing the pseudospectrum that occurs in the Spatial Smoothing procedure.

The l -th Toeplitz matrix is defined as

$$\begin{aligned} \mathbf{R}_l = & \\ & \begin{bmatrix} \mathbf{r}(l, \frac{L}{2}) & \mathbf{r}(l, \frac{L}{2} + 1) & \cdots & \mathbf{r}(l, L - 1) \\ \mathbf{r}(l, \frac{L}{2} - 1) & \mathbf{r}(l, \frac{L}{2}) & \cdots & \mathbf{r}(l, L - 2) \\ \vdots & \cdots & \ddots & \vdots \\ \mathbf{r}(l, 1) & \mathbf{r}(l, 2) & \cdots & \mathbf{r}(l, \frac{L}{2}) \end{bmatrix} = \\ & = \mathbf{G} \mathbf{S}_l \mathbf{G}^H \end{aligned} \quad (10)$$

where $\mathbf{G} = [\mathbf{g}(f_r) \quad \mathbf{g}^*(f_r) \quad \mathbf{g}(f_h) \quad \mathbf{g}^*(f_h)]$ is the steering matrix where $\mathbf{g}(f_d) = [\exp(j2\pi t_{L/2} f_d), \exp(j2\pi t_{L/2-1} f_d), \dots, \exp(j2\pi t_1 f_d)]^T$ ($d = r, h$) and \mathbf{S}_l is 4×4 diagonal matrix that can be shown to be full rank.

Then the SVD factorization is applied to the following matrix

$$S_T = \sum_{l=1}^{L/2} \mathbf{R}_l^H \mathbf{R}_l \quad (11)$$

with $\mathbf{t} = \mathbf{t}(1, \dots, L/2)$ in (7).

It is noted that also this method entails a reduction of the time interval. But in this case only half the time interval is lost to achieve decorrelation.

It is interesting to compare both methods. This is the main aim of this paper and will be achieved numerically in the next section. However, we find interesting to show some analytical arguments we found that establish a clear link between them. More in detail, comparing the i, j -th entry of SS correlation matrix

$$\{S_{SS}\}_{ij} = \frac{1}{M_d} \sum_{k=1}^{M_d} b_{i+k-1} b_{j+k-1}^* \quad (12)$$

and that of Toeplitz correlation matrix

$$\{S_T\}_{ij} = F \sum_{k=1}^{L/2} b_{i+k-1} b_{j+k-1}^* \quad (13)$$

with $F = \sum_{k=1}^{L/2} |b_k|^2$, it is easy to note that, unless unessential constant, the entries of both matrices are the same when $M_d = L/2$. This means that for $M_d = L/2$ the two methods are practically the same. Also, this solves the problem connected to the choice of M_d in the SS algorithm. Indeed, by choosing $M_d = L/2$ one is sure that SS fully recovers the rank.

5. Numerical Results

In this section the analysis is conducted with numerical data. The comparison between the two decorrelation methods is carried out in terms of dynamic range and resolution and with respect to the signal to noise ratio (SNR), number of time samples and time interval duration.

The demodulated signal taken into account is

$$\tilde{\mathbf{b}} = A_r \cos(2\pi f_r \mathbf{t}) + A_h \cos(2\pi f_h \mathbf{t}) + n(\mathbf{t}) \quad (14)$$

with $A_r = 1.5mm$, $A_h = 0.001mm$, $f_r = 0.3Hz$ and $f_h = 1.2Hz$, $n(\mathbf{t})$ denotes the noise which is assumed to be AWGN.

In all the following examples, the pseudospectra are plotted in log-scale: the blue line indicates the MUSIC pseudospectrum without decorrelation step, instead, red and black lines show the pseudospectra with SS and Toeplitz decorrelation methods, respectively.

The reflected signal is collected at most over $L = 400$ samples for an interval of time of 10s.

As first example, noiseless data are considered while the number of samples is reduced at 270 (Figure 3(a)-(c)) and then at 80 (Figure 3(d)-(e)). The analysis is conducted by varying the correlation index M_d in the SS method (red line) in order to appreciate the differences with respect to Toeplitz technique (black line).

As can be noted, in panel (b) and (e), when M_d is chosen equal to $L/2$, the performance are the same in perfect agreement with the discussion reported above. On the other

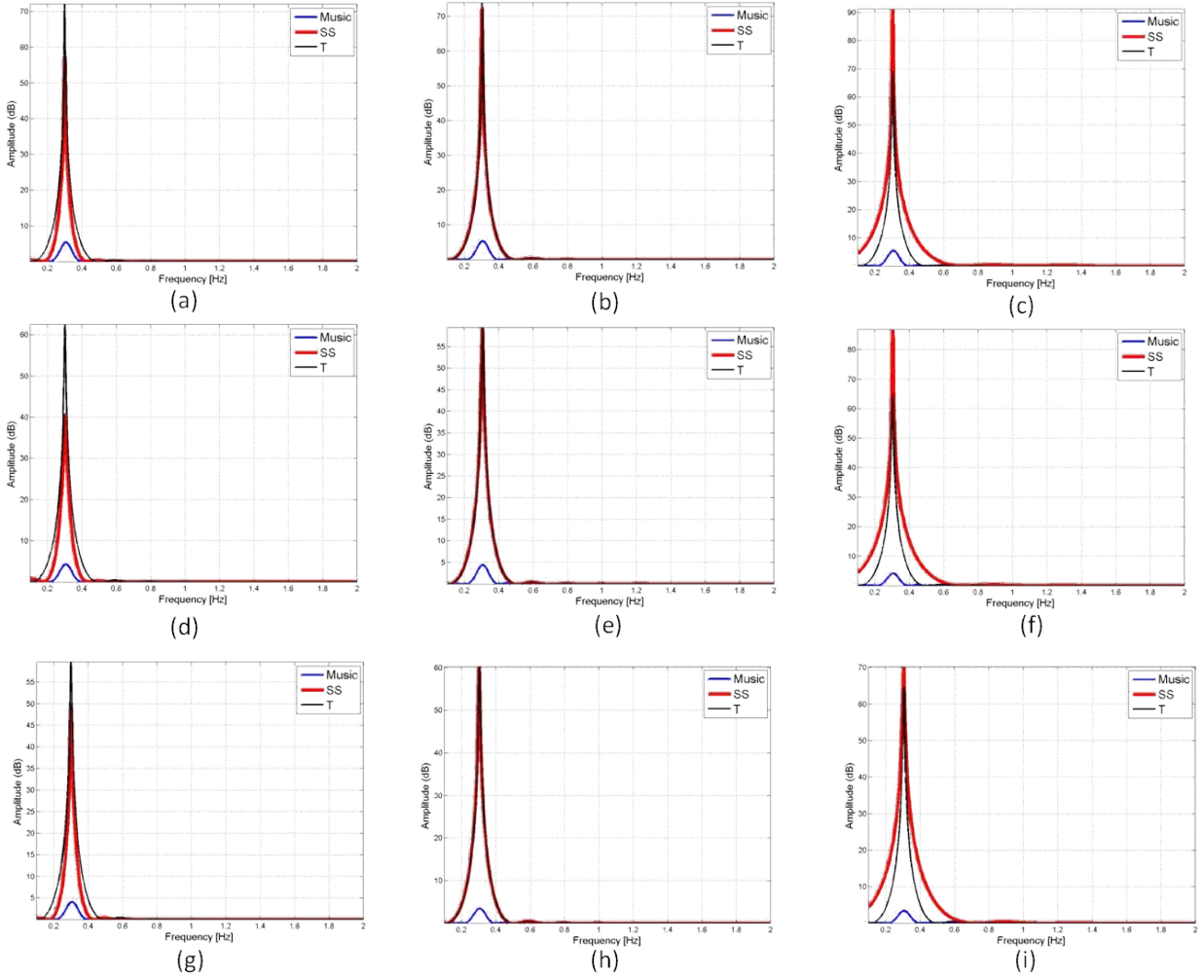


Figure 5: Synthetic data with $L\Delta t = 10s$ and $L = 400$. Comparing SS (red line) and Toeplitz (black line) methods by varying the SNR level and the correlation index: (a) $SNR = 20dB$, $M_d = 101$, (b) $SNR = 20dB$, $M_d = L/2$, (c) $SNR = 20dB$, $M_d = 301$, (d) $SNR = 10dB$, $M_d = 101$, (e) $SNR = 10dB$, $M_d = L/2$, (f) $SNR = 10dB$, $M_d = 301$, (g) $SNR = 5dB$, $M_d = 101$, (h) $SNR = 5dB$, $M_d = L/2$, (i) $SNR = 5dB$, $M_d = 301$

hand, when $M_d = 53 < L/2$ (panel (a), (d)) the SS decorrelation performs better than the Toeplitz method in terms of resolution, whereas when $M_d = 153 > L/2$ (panel (c), (f)) the opposite is true. This clearly occurs because M_d actually dictates the effective length of the time interval involved in the pseudospectrum formation.

In Figure 4 the role of time interval is studied keeping fixed the sampling step. In detail, in panels (a)-(c) the acquisition time is reduced to 5 seconds ($L = 200$) whereas in panels (d)-(f) to 3 seconds ($L = 120$). Of course, as the overall acquisition time has been reduced the pseudospectra tend to enlarge. Furthermore, the same trade as above as far as M_d is concerned is practically observed. However, now, when $M_d < L/2$ (here $M_d = 11$, see Figure 4(d)) the SS also exhibits a loss in the dynamic range. This is because in this case the smoothing procedure does not work perfectly. Whereas, when $M_d > L/2$ ($M_d = 101$, see Figure 4(f)), the SS shows a dramatic loss of resolution.

Finally, we turn to address the effect of noise on data.

In Figure 5 the results returned by the two methods at hand are displayed by varying the Signal to Noise Ratio (SNR). In particular, in the panels (a)-(c) SNR is equal to $20dB$, in (d)-(f) the $SNR = 10dB$ and in (g)-(i) $SNR = 5dB$.

As expected, the presence of noise does not allow to detect the heartbeat harmonic due to its very low amplitude A_h . Also, both the methods appears relatively stable against noise, even though the dynamic range reduces as compared to the noiseless case. Finally, it is noted that whether $M_d < L/2$ or $M_d > L/2$ the SS returns lower or higher (than the Toeplitz method) pseudospectra. This can be explained that when $M_d > L/2$ Equation (8) entails a more "strong" averaging that tends to reduce the noise. However, the cost to pay is a loss of resolution.

6. Conclusions

In this paper, two different decorrelation methods for vital sign detection have been compared. In particular, the analysis has been conducted in terms of dynamic range and resolution for Spatial Smoothing and Toeplitz methods.

It has been demonstrated that the SS and Toeplitz techniques show the same performance with a suitable choice of decorrelation index, in particular when it is equal to half of number of the available samples ($L/2$).

The performance of SS method depends by the choice of decorrelation index. Indeed, the results have shown that when $M_d < L/2$ the pseudospectrum have a loss of dynamic range and an increasing of resolution and for $M_d > L/2$ the opposite holds true.

References

- [1] A.-D. Droitcour, V.-M. Lubecke, J. Lin and O. Boric-Lubecke, A microwave radio for Doppler radar sensing of vital signs, *Microwave Symposium Digest, 2001 IEEE MTT-S International* 1:175–178, 2001.
- [2] K. M. Chen, J. Zhang and A. Norman, Microwave life-detection systems for searching human subjects under earthquake rubble and behind barrier, *IEEE Transactions on Biomedical Engineering* 47: 105–114, 2000.
- [3] C. Li, V. M. Lubecke, O. Boric-Lubecke, J. Lin, A Review on Recent Advances in Doppler Radar Sensors for Noncontact Healthcare Monitoring, *IEEE Transactions on Microwave Theory and Techniques* 61:2046–2060, 2013.
- [4] B. Lohman, O. Boric-Lubecke, V. M. Lubecke, P. W. Ong and M. M. Sondhi, A digital signal processor for Doppler radar sensing of vital signs, *IEEE Engineering in Medicine and Biology* 21: 161–164, 2002.
- [5] C. Li, Y. Xiao and J. Lin, Experiment and spectral analysis of a lowpower Ka-band heartbeat detector measuring from four sides of a human body, *IEEE Transactions on Microwave Theory and Techniques* 54:4464–4471, 2006.
- [6] R.O. Schmidt, Multiple emitter location and signal parameter estimation, *IEEE Transactions on Antennas and Propagation* 34:276–280, 1986.
- [7] S. Tie-Jun, W. Mati, K. Thomas, On Spatial Smoothing for Direction-of-Arrival Estimation of Coherent Signals, *IEEE Transaction on Acoustics, Speech and Signal Processing* 33: 806–811, 1985.
- [8] C. Qing, L. Ruonlun, On the Explanation of Spatial Smoothing in MUSIC Algorithm for Coherent Sources, *International Conference on Information Science and Technology*, Nanjing, China, pp.699-702, 2011.
- [9] Q. Cheng, H. Lei, Z. Wen-Jun and S. Hing Cheung, Direction of Arrival Estimation for Coherent Signals Without Knowledge of Source Number, *IEEE Sensors Journal* 14:3267–3273, 2014.
- [10] M. C. Budge, M. P. Burt, Range correlation effects on phase and amplitude noise, *IEEE Southeastcon '93, Proceedings*, Charlotte, NC, 1993.

Performance Evaluation of Linear Sampling Method for Mixed Boundary Objects in the Half-Space Scenario

Mallikarjun Erramshetty¹, Amitabha Bhattacharya²

¹Department of Electronics and Communication Engineering, National Institute of Technology Goa, India, 403401

²Department of Electronics and Electrical Communication Engineering, Indian Institute of Technology Kharagpur, India, 721302

*corresponding author, E-mail: emallikarjuna@nitgoa.ac.in

Abstract

This paper aims to investigate the performance of linear sampling method for mixed boundary (both dielectric and conducting) objects in the half-space domain. The study is based on the numerical evaluation of synthetic examples at different frequencies. It is shown that in half space scenario, dielectric objects are not detected at lower frequency whereas PEC objects do not suffer from such limitation. In order to improve the image reconstructions, a multifrequency approach is used.

1. Introduction

The Linear Sampling Method (LSM) is a simple, robust, and efficient method to detect the target's shapes and locations from the multi-view multi-static data collected around the target [1]. The method has been applied in the fields of biomedical, geophysical explorations, through-wall imaging, and so on [2, 3, 4]. Recently, in our work, it has been applied to the mixed boundary problems [5] where the behaviour of LSM for reconstructing the dielectric and the perfect electric conducting (PEC) objects were discussed in a full space measurement scenario. It is found that the LSM fails to detect low-permittivity objects at low frequencies and the reconstructions are improved either with increase in frequency or at higher permittivity values. In the case of PEC objects, good estimates are observed at lower frequencies. At higher frequencies, the chance of occurrence of eigenvalues is more for both dielectric and PEC objects which in-turn affects the target's shape. In extension to these works, this paper studies the reconstruction capabilities of LSM in the half space-domain. Conclusions are obtained from the numerical results evaluated at different frequencies. Moreover, a modified LSM indicator, based on multifrequency, is used to make the reconstructions more robust against limitations occurring at each operating frequency. The rest of the paper discusses brief view of linear sampling method, numerical results, and conclusions.

2. Linear sampling method

The LSM is able to retrieve the target's shape through the linear equation solved at each sampling point of investigating domain [1]. It is claimed that the solution assumes finite energy if sampling point belongs to the scatterer and

infinite elsewhere. While referring the reader to the literature for more mathematical details, the LSM equation in the half-space domain is written as [6, 7]

$$F[\xi] = \int_0^{2\pi} E^{scat}(\underline{r}, \varphi_i) \xi(\underline{z}_t, \varphi_i) d\varphi_i = \frac{1}{4j} \left(\frac{2k_2 \cos(\theta)}{k_2 \cos(\theta) + \sqrt{k_1^2 - k_2^2 \sin^2(\theta)}} \right) H_0^{(2)}(k_2 |\underline{z}_t - \underline{r}|) \quad (1)$$

Here scalar problem (two-dimensional) is assumed. E^{scat} is the scattered field, φ_i is the angle of incident field, $\underline{r} = (x, y)$ is the location of measured E^{scat} , ξ is the unknown complex function, $\underline{z}_t = (x, y)$ is the sampling point. $H_0^{(2)}(\cdot)$ is the Hankel function of 2nd kind and 0th order. k_1 and k_2 are the wavenumbers of region '1' and region '2' respectively, as shown in Fig. 1(a). θ is the angle between the propagation direction of the field and normal vector direction at the boundary.

To find the scatterer support, auxiliary linear equation (1) is to be solved at each \underline{z}_t . According to the principle of LSM, the solution in the energy form $\|\xi(\underline{z}_t)\|^2$ is finite if \underline{z}_t belongs to the scatterer and infinite elsewhere [1]. Here, $\|\cdot\|$ is the standard L^2 -norm. Hence, (1) is ill-posed [8] and requires regularization for a stable solution. While referring the reader to [1, 9] for mathematical details, the final form of regularized solution in the energy form based on the Singular Value Decomposition (SVD) technique [10] can be written as

$$\|\xi(\underline{z}_t)\|^2 = \sum_{n=1}^N \left(\frac{\lambda_n}{\lambda_n^2 + \alpha} \right)^2 |\mathbf{f} \cdot \boldsymbol{\mu}_n|^2 \quad (2)$$

where λ_n and $\boldsymbol{\mu}_n$ are singular-values and left-singular-vector of F , respectively. $\boldsymbol{\xi}$ is the vector of unknowns, vector \mathbf{f} is the far-field pattern radiated by the point source located in the half-space region at \underline{z}_t (right side of the LSM equation), N is the total number of non-zero singular values, and α is a regularization parameter. Therefore, the support of the scatterer is found by plotting $\|\xi(\underline{z}_t)\|^2$ over the investigating domain. Parameter α can be calculated using physics-based criteria as reported in [11], which does

not require knowledge about noise level present in the measured data. Based on the reasons reported in [11], the indicator function is to be modified to image the deeper parts of the probed region, and it is given by

$$\left\| \tilde{\xi}(z_t) \right\| = \frac{\left\| \xi(z_t) \right\|}{\left\| G(z_t) \right\|} \quad (3)$$

Next, we evaluate the performance of LSM by considering a few numerical examples.

3. Numerical results

In these synthetic examples, both dielectric and PEC objects are embedded in region '2' as shown in Fig. 1(a). It is assumed that the dimension of the objects along the z-axis is infinite. For image reconstruction, we consider two examples. In these examples, A total of 31 antennas are uniformly positioned from (-2 m, 0 m) to (2 m, 0 m). The spacing between the antennas is chosen such that it satisfies the minimum number of required measurements for the considered investigation area, up to 800 MHz [12]. The objects under investigation are buried in a lossy background medium of relative permittivity $\varepsilon_{r2} = 2$ and conductivity $\sigma_2 = 0.002$. An investigating domain of size 1 m \times 1 m with centre $d = -1.5$ m is considered and uniformly discretized into 201 \times 201 cells. Here, the synthetic data has been corrupted with additive Gaussian noise at the level of SNR ratio of 25 dB.

3.0.1. Example I

We consider one square dielectric object of $\varepsilon_r = 4$ and conductivity $\sigma = 0.004$ along with a PEC square object. The reference image is shown in Fig. 1(b). Both these objects have a length of 0.2 m. The reconstruction results of LSM at frequencies 200 MHz, 300 MHz, 500 MHz, and 800 MHz are shown in Fig. 2(a) through Fig. 2(d). Similar to the case of full space measurements [5], dielectric object is not detected at low frequency and when the frequency is increased, the image of dielectric object improve. However, in the case of PEC, good estimates are observed at all considered frequencies. Further, the shapes of the targets are not accurately retrieved due to limited input data. Moreover, the effect of eigenvalues [5] cannot be seen clearly due to limited number of measurements.

3.0.2. Example II

In this numerical example, we consider an image of one PEC cylinder of radius 0.15 m along with a square dielectric object of length 0.2 m and a dielectric cylinder of radius 0.15 m as shown in Fig. 1(c). Both dielectric objects are of $\varepsilon_r = 4$ and $\sigma = 0.004$. The reconstruction results of LSM at frequencies 200 MHz, 300 MHz, 500 MHz, and 800 MHz are shown in Fig. 3(a) through Fig. 3(d). In this case also, dielectric objects are not detected at low frequency, and when the frequency is increased, the images of dielectric objects improve.

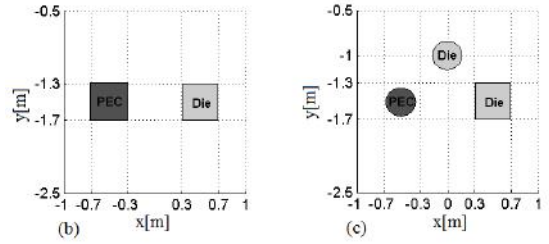
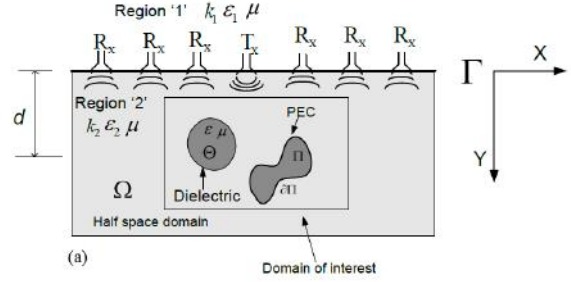


Figure 1: Image references. (a) Half-space scenario. (b) Example I. (c) Example II.

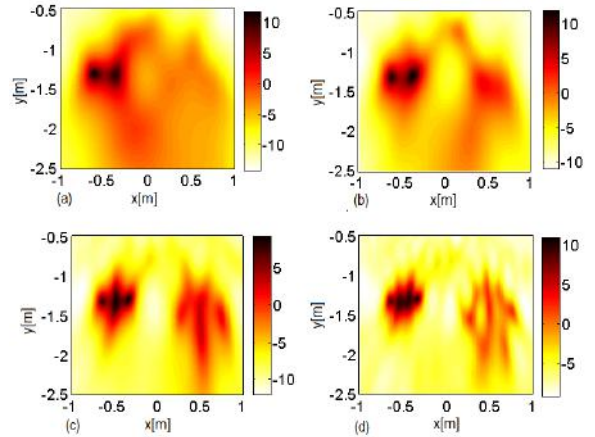


Figure 2: LSM results of Example I. (a) 200 MHz. (b) 300 MHz. (c) 500 MHz. (d) 800 MHz.

3.1. Modifications to the indicator function

From the numerical results, it is evident that the indicator function at the domain of PEC has larger values compared to the dielectrics. Hence, the dielectric objects are not visible in the result clearly. Target's better support is estimated with a simple modification to the indicator function. It can be achieved by restricting the maximum value of the indicator function to a particular value as given below:

$$Max = \max_{r \in \Omega} (-10 \log(\left\| \tilde{\xi}(r) \right\|^2)) \quad (4)$$

Here, the value of Max indicates the maximum value of indicator that is achieved over the entire investigating domain. We define a threshold value of $0.65Max$ such that the higher values of LSM output which are greater than the

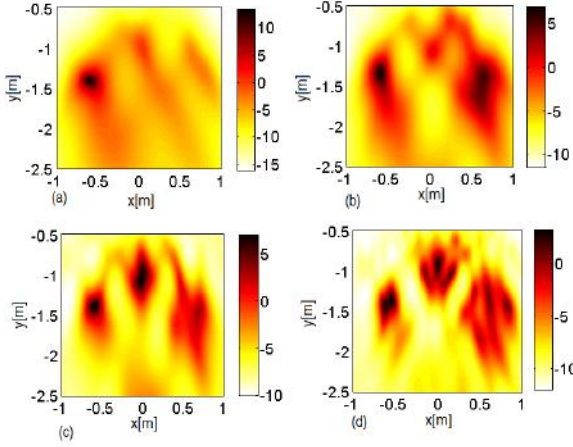


Figure 3: LSM results of Example II. (a) 200 MHz. (b) 300 MHz. (c) 500 MHz. (d) 800 MHz.

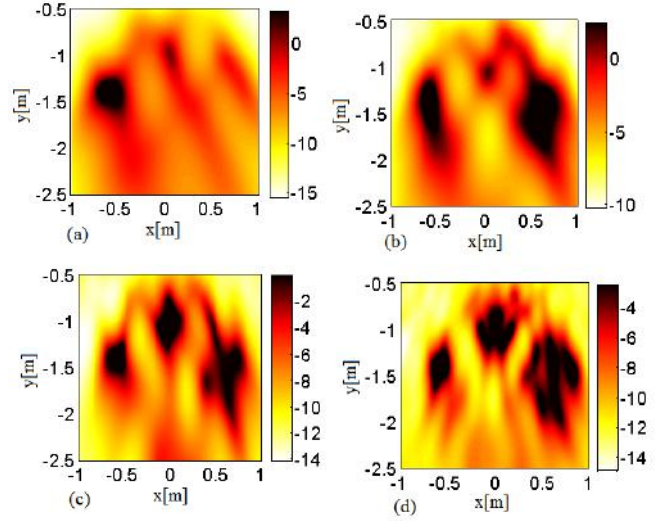


Figure 5: The modified LSM results for example II. (a) 200 MHz. (b) 300 MHz. (c) 500 MHz. (d) 800 MHz.

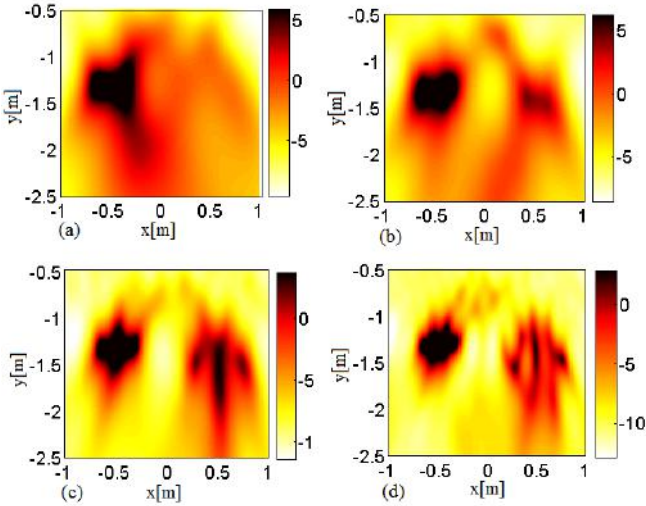


Figure 4: The modified LSM results for example I. (a) 200 MHz. (b) 300 MHz. (c) 500 MHz. (d) 800 MHz.

threshold, are replaced by the threshold value itself whereas lower values are unaltered. It can be written as

$$\begin{aligned}
 & \text{if } \left\{ -10 \log(\|\tilde{\xi}(z_t)\|^2) > 0.65 \text{Max} \right\} \\
 & \text{then} \\
 & -10 \log(\|\tilde{\xi}(z_t)\|^2) = \text{Max}
 \end{aligned} \tag{5}$$

Figs. 4 and 5 show the results of LSM with new modifications. It can be observed that the estimates of dielectric objects are improved. Further improvements can be achieved using multifrequency approach. From [5], the indicator function is given by

$$G_{mod}(z_t) = \frac{1}{N_F} \sum_{i=1}^{N_F} \left[\begin{array}{l} -10 \log(\|\xi(z_t, i)\|^2) \\ + \max_{r \in \Omega, j \in N_F} (-10 \log(\|\xi(r, j)\|^2)) \\ - \max_{r \in \Omega} (-10 \log(\|\xi(r, i)\|^2)) \end{array} \right] \tag{6}$$

where N_F is the number of frequencies that are considered for reconstruction. It should be noted that the considered frequency-band should be sufficiently large in order to accommodate and combine different kinds of maps in the low- and high-frequency regions. Here the LSM indicator is modified to exploit the reconstructions computed at each considered frequency. The strategy is to combine various single-frequency maps in such a way that the drawbacks of low and high frequencies are overcome. However, this procedure cannot completely eliminate the drawbacks of each frequency but certainly will produce a better estimation compared to individual frequencies. Fig. 6 shows the results of multifrequency approach. Here, 200 MHz to 800 MHz with a step size of 50 MHz is considered. It can be observed that a better reconstruction is obtained with the new indicator function. Notably, the new results are definitely better as compared to a single-frequency case. It is worth mentioning that, in the preceding examples, the LSM results were shown for simple structures. Our aim is to show the nature of LSM estimation for mixed boundary objects in the half space domain at various frequencies. In case of complicated objects, sophisticated LSM indicator similar to [11] should be adopted for accurate reconstructions.

4. Conclusions

The presented paper has discussed the reconstruction of LSM for mixed objects in the half space domain. It has been observed that the PEC objects are detected irrespective of the frequency. The reconstruction of dielectric ob-

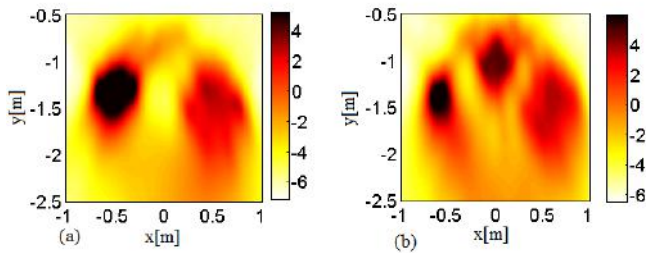


Figure 6: Results of LSM with multifrequency indicator function. (a) Example I. (b) Example II.

jects are improved at higher frequencies. The accuracy of reconstructions is less compared to the case of full space measurements due to the limited input data. Using multifrequency approach, the obtained results are found to be superior to the single-frequency case.

References

- [1] D. Colton, H. Haddar, and M. Piana, "The linear sampling method in inverse electromagnetic scattering theory," *Inv. Prob.*, Vol. 19, No. 6, pp. S105–S137, 2003.
- [2] Giovanni Bozza, Massimo Brignone and Matteo Pastorino, "Application of the no-sampling linear sampling method to breast cancer detection," *IEEE Trans. Antennas Propagat.*, Vol. 57, No. 10, pp. 2525–2534, 2010.
- [3] I. Catapano and L. Crocco, "An imaging method for concealed targets," *IEEE Trans. Geosci. Remote Sens.*, Vol. 47, No. 5, pp. 1301–1309, 2009.
- [4] I. Catapano and L. Crocco, "A qualitative inverse scattering method for through-the-wall imaging," *IEEE Geosci. Remote Sens. Lett.*, Vol. 7, No. 4, pp. 685–689, 2010.
- [5] E. Mallikarjun and A. Bhattacharya, "Shape reconstruction of mixed boundary objects by linear sampling method," *IEEE Trans. Antennas Propagat.*, Vol. 63, No. 7, pp. 3077–3086, 2015.
- [6] J. Munk, "An equivalent source inversion method for imaging complex structures," Ph.D dissertation, Ohio State University, USA, 1999.
- [7] I. Catapano *et al.*, "A tomographic approach for helicopter-borne ground penetrating radar imaging", *IEEE Geosci. Remote Sens. Lett.*, Vol. 9, No. 3, 2012.
- [8] M. Bertero and P. Boccacci, *Introduction to Inverse Problems in Imaging*. UK: IOP Publishing Ltd, 1998.
- [9] D. Colton and H. Haddar, "An application of the reciprocity gap functional to inverse scattering theory," *Inv. Prob.*, vol. 21, no. 1, pp. 383–398, 2005.
- [10] M. Pastorino, *Microwave Imaging*. New Jersey, USA: Wiley, 2010, pp. 82–91.
- [11] I. Catapano and L. Crocco, "An imaging method for concealed targets," *IEEE Trans. Geosci. Remote Sens.*, vol. 47, no. 5, pp. 1301–1309, May 2009.
- [12] O. M. Bucci and T. Isernia, "Electromagnetic inverse scattering: Retrievable information and a measurement strategies," *Radio Sci.*, vol. 32, pp. 2123–2138, 1997.

Recent Advances in Reconfigurable and Multiband Antenna Technology

Non-Foster Matched Reconfigurable Antenna in UHF band

D. S. Nagarkoti, Y. Hao, and K. Z. Rajab*

Antenna and Electromagnetics Research Group,
Queen Mary University of London, United Kingdom

*corresponding author: k.rajab@qmul.ac.uk

Abstract-

This paper discusses the RTD (resonant tunneling diode) based non-Foster matching with a tunable passive inductor to achieve reconfigurable, multiband and broadband performance of an ESA (electrically small antenna). A capacitive ESA ($\lambda/10$) exhibits high capacitance and very low radiation resistance. An RTD based capacitive negative impedance circuit is required to cancel the antenna capacitance and a tunable inductor based non-Foster based transformer circuit is used to reconfigure the operational bandwidth from 250 MHz to 2.5 GHz range.

The Quality factor (Q) of ESA is bound by Chu's limit [1] and the matching of a high Q antenna using a passive lossless network is limited by Bode-Fano limit [2]. A non-Foster circuit (NFC) based negative impedance elements offer a solution to the problem to a certain extent. An NFC is an active N-port network which disobeys Foster reactance theorem, according to that, the reactance or susceptance decreases with increasing frequency. The various approach based on transistors [3], operational amplifiers [4], CMOS integrated circuits [5] have been explored for achieving negative impedance. Recently, a RTD based NFC has been proposed [6] which highly reduces the complexity of the circuit realization. An RTD is a negative differential resistance device which offers negative resistance and negligible reactance with suitable biasing.

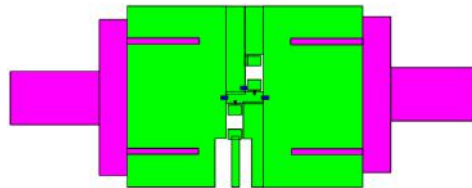


Figure 1: RTD evaluation board layout.

The topology shown in figure 2 is showing the matching of ESA which has self-resonance at 3.5 GHz, one can safely model as a 5 pF and frequency dependent radiation resistance with $k = 10^{-19} \text{ .sec}^2$. The antenna reactance has been cancelled by the negative capacitance circuit, leaving the frequency dependent radiation resistance. The tunable inductors, L_{TUNE} plays major role in the tunability of the matching and tune the frequency dependent radiation resistance of ESA to 50 Ω at difference frequencies from 300 MHz to 2.5 GHz. The upper matching frequency limited by the dominance of RTD reactive parasitics after 2.5 GHz [6].

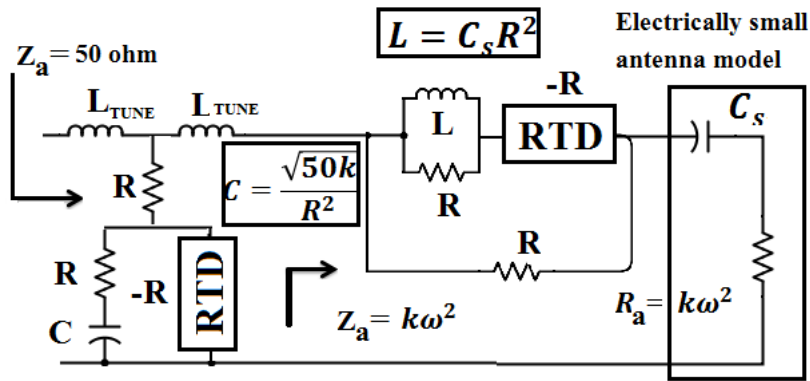


Figure 2: The topology for antenna matching with tunable inductor pair.

The tuning has been performed using Coilcraft 164 series inductors by means of an aluminum core. The possible inductance varies from 9 nH to 281 nH using this component. However, in this paper we are varying the inductance from 15 nH to 100nH range in order to achieve almost full UHF band reconfigurable antenna as shown in Figure 3.

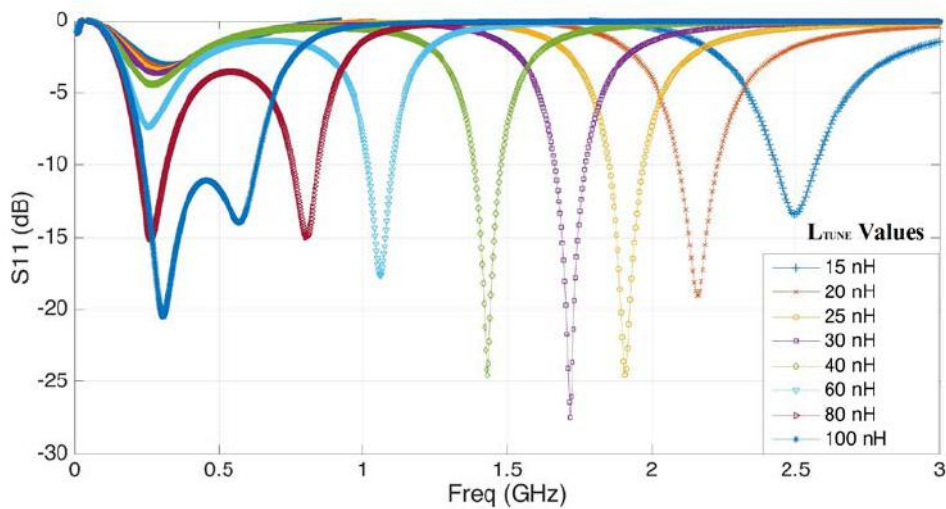


Figure 3: Reconfigurable antenna matching using tunable inductor.

The variation of inductance from 15 nH to 60 nH, the matching achieved from 2.5 GHz to nearly 1 GHz. A dual band operation has been obtained around 80 nH tuning and a broadband matching is noticed at 100 nH tuning of inductance. As the real impedance is very low at lower frequencies and around 50 Ohm at 3.5 GHz, a passive match is difficult to match at lower frequencies and offer matching near 3.5 GHz depending upon the value of constant k. Non-Foster matching has certain limitations in antenna apart from matching bandwidth. The noise introduce by active elements in receive mode and non-linear behavior in transmit mode are the issues needs to be addressed.

REFERENCES

1. Chu, L, Physical Limitations of Omnidirectional Antennas, *J. Appl. Phys.*, Vol. 19, 1163-1175, Dec.

1948.

2. Fano, R.M., Theoretical limitations on the broad-band matching of arbitrary impedances, *J. Franklin Institute*, Vol. 249, 57-83, Jan. 1950.
3. Linvill, J., Transistor negative impedance converters, *Proc. IRE*, Vol. 41, 725-729, June 1953.
4. Antonoiu, A., Floating negative-impedance converters, *IEEE transactions on circuit theory*, Vol. 19, No.2, March 1972.
5. Gregoire, D.J., C.R. White, J.S. Colburn, Wideband artificial magnetic conductors loaded With non-Foster negative inductors, *IEEE Antennas Wireless Propag. Lett.*, Vol. 10, 1586-1589, Dec 2011.
6. Nagarkoti, D.S., Y. Hao, D.P. Steenson, L. Li, E.H. Linfield, K.Z. Rajab, Design of Broadband non-Foster Circuits based on Resonant Tunneling Diodes, *IEEE Antennas Wireless Propag. Lett.*, Dec 2015 (*early access article*).

Applications of Nanoimprint in photonics and metamaterials

Sidewall relief gratings imprinted on optical fiber sidewall for sensing applications

Zhouyang Zhu and Wen-Di Li*

Department of Mechanical Engineering, Univ. of Hong Kong, Hong Kong, China;

*liwd@hku.hk

Nanoimprint lithography (NIL) is a promising method that can fabricate nanostructures with high resolution, high throughput and low cost [1]. Since this technology was developed, it has been used in many different fields such as photonics[2], bio-sensing[3], etc. Integration of NIL or other fabrication technology with optical fiber results in a new concept “lab-on-fiber” [4].

In this work, we proposed a fabrication method to create nanoscale structures on the sidewall of a plastic optical fiber (POF) to demonstrate a new form of “lab-on-fiber” for light-matter interaction. We then used this fiber sensor to detect the environment refractive index (RI) as an application demonstration. And a theoretical model was developed to explain the experimental phenomenon.

Fig. 1a showed the schematic of experimental setup for nanoimprinting on the sidewall of POF. The imprinting temperature was controlled by a hot wind gun. A copper stick was used to press POF into a silicon mold carrying grating patterns with period of 278nm, depth of 110nm and duty cycle of 1:1. Images of the POF after nanoimprint from top, side, and bottom view were provide in Fig. 1b. The transferred pattern was on the bottom side, and corresponding SEM images were showed in Fig. 1c. Thermal expansion and contraction of POF caused a little distortion of the grating lines.

In Fig. 2a, the reflection measurement setup (top) was illustrated. Light from a broadband source or a laser was guided into POF through a Y-shape fiber, the reflected light was collected by a spectrometer or a photodetector. Bottom figure showed the schematic of the model we developed to simulate the reflection caused by the imprinted region of POF. The measured and simulated reflectance of POF in air was plotted, and they agree well with each other. To construct a highly sensitive RI sensor, 30 nm gold was deposited on the POF for RI detection. The reflection spectrum in media with different RI was plotted in Fig. 2c with a schematic of the gold coated grating inserted. Linear fit and original peak position (blue) with RI was plotted in Fig. 2d. Besides this peak position method, another method was to measure reflection intensity with a 650nm laser as light source, and corresponding intensity (red) was also plotted in Fig. 2d.

In summary, we propose a NIL method to fabricate structures on sidewall of fibers, and a model was developed to explain the reflection at imprinted region. Finally, RI detection was conducted using this fiber as a probe.

- [1] S. Y. Chou, P. R. Krauss, and P. J. Renstrom, *Applied Physics Letters* **67**, 3114 (1995).
- [2] W.-D. Li, F. Ding, J. Hu, and S. Y. Chou, *Optics Express* **19**, 3925 (2011).
- [3] R. Alvarez-Puebla, B. Cui, J.-P. Bravo-Vasquez, T. Veres, and H. Fenniri, *The Journal of Physical Chemistry C* **111**, 6720 (2007).

[4] M. Consales, A. Ricciardi, A. Crescitelli, E. Esposito, A. Cutolo, and A. Cusano, ACS Nano **6**, 3163 (2012).

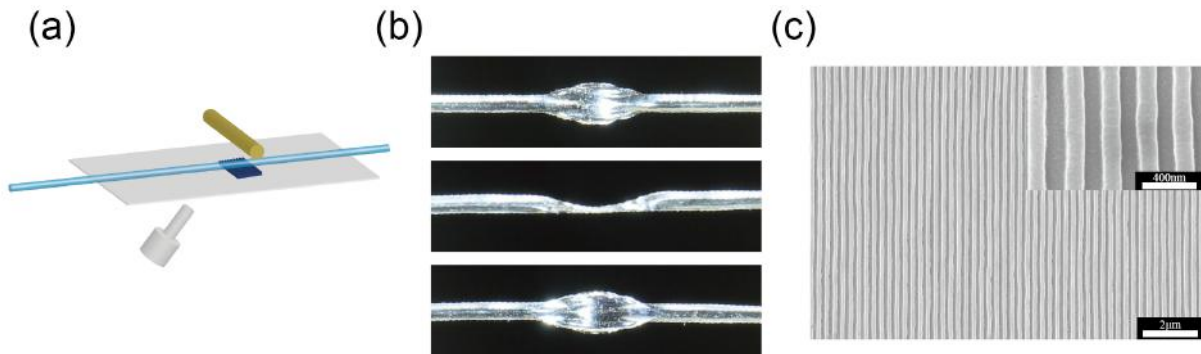


Fig.1 (a) Schematic of thermal nanoimprint setup for POF; (b) Images of POF after imprint from top, side and bottom view; (c) SEM images of the transferred grating pattern on the bottom of the POF

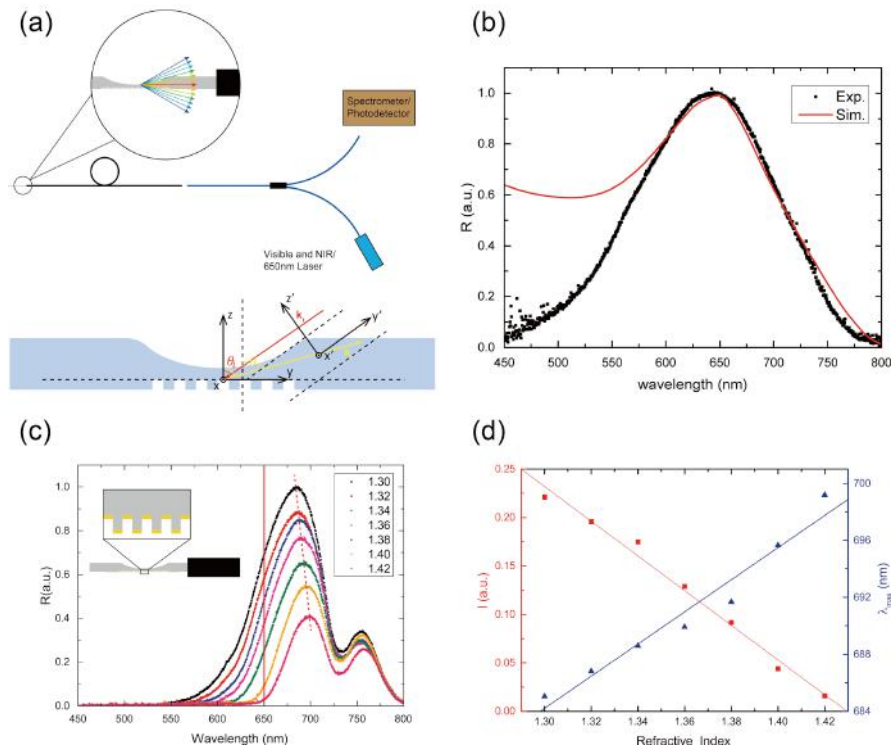


Fig.2 (a) Schematic of reflection measurement setup (top) and an analytical model used to investigate the reflection nature (bottom); (b) Measured and simulated reflectance of imprinted POF in air without any metal coating; (c) Reflection spectrum of POF after 30nm Au layer deposition, inset picture is a schematic of the gold deposited grating; (d) Refractive index detection result of monochromatic intensity method and peak position method.

High contrast gratings fabricated using Nanoimprint lithography for color reflective display

He Liu, Yuanrui Li, Yuhan Yao, Yifei Wang, and Wei Wu*

*Department of Electrical Engineering, University of Southern California,
Los Angeles, CA USA 90089*

* wu.w@usc.edu

Abstract-We proposed a color reflective display which can have unprecedented vivid color and brightness. It has a stacked tunable “color mirrors” architecture. Each “color mirror” is implemented with high contrast gratings fabricated by Nanoimprint lithography. The modulation of each “color mirror” will be realized using an electrowetting process. The working principle, design, fabrication and characterization of “color mirrors” will be presented.

Reflective display requires no internal light source, this gives them unique properties such as printing-like looking, low power consumption, and readability under sunlight. Those properties make them suitable for a number of potential applications like e-book reader, signage, electronic shelf-labels and display for wearable devices[1]. So far, several approaches have been reported and commercialized on reflective displays, e.g., electrophoretic displays[2], electrowetting displays [3, 4], and cholesteric liquid crystal displays[5]. However, most approaches are still suffering from some common drawbacks, like low brightness, low color saturation and small gamut volume[1], therefore commercial reflective displays are still dominantly black-and-white only. To solve the issues, we proposed a full color reflective display design based on stacked “color mirrors” (figure 1), which could exhibit high reflectance with large gamut area, as well as the ability to modulate the reflectance[6].

The “color mirrors” are implemented using 2-D high contrast gratings (HCGs) (figure 2). They are fabricated by combining interference lithography and nanoimprint lithography (NIL). The modulation of the reflectance is achieved by changing the index contrast between the grating and its surrounding. Figure 3 shows the blue and green mirrors and their reflection spectra in ON and OFF states. High resolution pixels and the combinations of colors by mirror stacking will be presented too.

Acknowledgements This work is supported in part by Huawei Technologies Co., Ltd.

[1] J. Heikenfeld, P. Drzaic, J.-S. Yeo, and T. Koch, “Review Paper: A critical review of the present and future prospects for electronic paper,” *Journal of the Society for Information Display*, vol. 19, no. 2, p. 129, 2011.

[2] I. Ota, J. Ohnishi, and M. Yoshiyama, “Electrophoretic image display (EPID) panel,” *Proceedings of the IEEE*, vol. 61, no. 7, pp. 832–836, 1973.

[3] G. Beni, “Electro-wetting displays,” *Applied Physics Letters*, vol. 38, no. 4, p. 207, 1981.

[4] R. A. Hayes and B. J. Feenstra, “Video-speed electronic paper based on electrowetting,” *Nature*, vol. 425, no. 6956, pp. 383–385, Sep. 2003.

[5] J. Yan, S.-T. Wu, K.-L. Cheng, and J.-W. Shiu, "A full-color reflective display using polymer-stabilized blue phase liquid crystal," *Applied Physics Letters*, vol. 102, no. 8, pp. 081102–081102, 2013.

[6] Liu, H., Yao, Y. H., Wang, Y. F., & Wu, W. (2014). Full-color reflective display system based on high contrast gratings. *Journal of Vacuum Science & Technology B*, 32(6). doi: Artn 06fe04

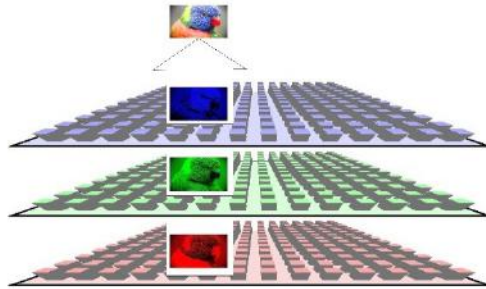


Figure 1 Three-layer architecture of a full color reflective display. Blue, green and red filters are stacked, reflecting blue, green and red light, respectively.

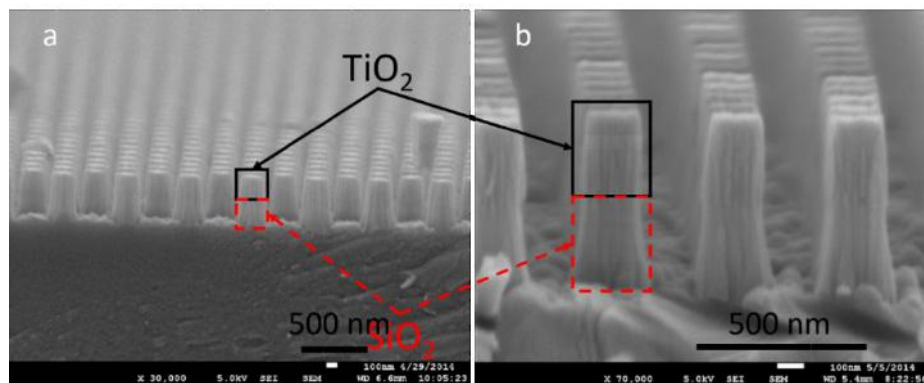


Figure 2 (a) SEM image of the 2D subwavelength grating reflecting blue light. (b) SEM image of the green mirror.

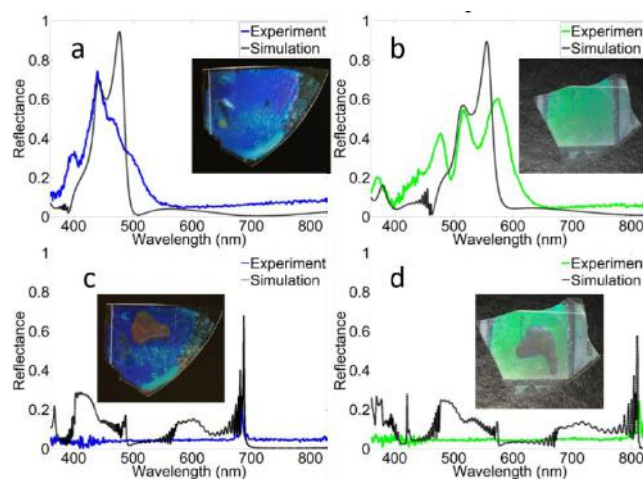


Figure 3 Both experimental (color lines) and theoretical reflection spectra of blue (a&c) and green (b&d) mirrors in ON state (a&b) and OFF state (c&d). The inserts are optical photos of the color mirrors.

Sub-10-nm Three-Dimensional Plasmonic Probes and sensors

G. Calafiore¹, A. Koshelev¹, T. Darlington², N. J. Borys², J. Schuck², A. Weber-Bargioni²,
S. Babin¹, K. Munechika¹, S. Cabrini²

¹1aBeam Technologies, 22290 Foothill Blvd, St. 2 Hayward, CA, 94541

²The Molecular Foundry, Lawrence Berkeley National Laboratory, Berkeley, CA 94720

Plasmonic antennas have been investigated as potential sensing element since long, but great part of the efforts on the nanofabrication have been devoted to the 2 dimensional patterning. Many times the the “sensing or probing” processes require geometries of the probe that are more complicated than the simple flat surface. In this paper we are going to show some example of three dimensional structures and their plasmonic properties as well as their application as sensors for IR spectroscopy and probes for Near-field scanning optical microscopy. We will present a series of structures and their characterization in IR as well as visible light. Particularly we will focus on the NSOM application. It is a powerful and unique approach to characterize the chemical, physical and biochemical properties of materials with the nanometer scale resolution in real-time [1]. One of the main challenges in using NSOM for a broad range of applications is the development of reproducible and efficient near-field probes. A novel class of nano-optical probes has been recently proposed, namely "campanile". Campanile tips consist of a 3-Dimensional (3D) tapered structure terminated by a plasmonic nano-antenna, which provides superior NSOM performance and decisive advantages [2]. We will present a novel approach to drastically simplify the fabrication of Campanile probes by ultraviolet nanoimprint lithography (UV-NIL) directly on the facet of commercial optical fibers, without the need to use FIB. The 3D mold is fabricated by a combination of polymer embossing and FIB lithography in a Helium Ion Beam.

We will show some characterization [3] measurement as well as some NSOM hyperspectral images

[1] JunHo Kim, Ki-Bong Song “Recent progress of nano-technology with NSOM” Micron 38, 409 (2007)

[2] Wei Bao, M. Melli, N. Caselli, F. Riboli, D. S. Wiersma, M. Staffaroni, H. Choo, D. F. Ogletree, S. Aloni, J. Bokor, S. Cabrini, F. Intonti, M. B. Salmeron, E. Yablonovitch, P. J. Schuck, and A. Weber-Bargioni

[3] Aleksandr Polyakov, Mauro Melli, Giuseppe Cantarella, Alexander Weber-Bargioni, P James Schuck and Stefano Cabrini: “Coupling model for an extended-range plasmonic optical transformer scanning probe”; Light: Science & Applications (2014) 3, e195

Nanoimprint-Assisted Shear Exfoliation + Transfer Printing (NASE+TP) for Producing Emerging Transition Metal Dichalcogenide Heterostructures

Xiaogan Liang*, Da Li, and Sungjin Wi

Mechanical Engineering Department, University of Michigan, Ann Arbor, MI 48109, USA

*corresponding author: xiaoganl@umich.edu

Abstract-Vertically stacked heterostructures of emerging layered materials are needed for modulating the band structures of new nanoelectronic/photonic devices based on layered materials. We present a nanofabrication route for producing arrays of such heterostructures, which uniquely combines nanoimprint-assisted shear exfoliation and transfer printing techniques. Using this route, we have demonstrated the fabrication of uniform arrays of heterostructures consisting of different multilayer transition metal dichalcogenides as well as photoresponse devices based on such structures.

Emerging layered transition metal dichalcogenides (TMDCs, *e.g.*, WSe₂ and MoS₂) are attractive materials for making new optoelectronic and nanoelectronic devices due to their superior electronic, photonic, and mechanical properties.^[1-2] In addition, TMDCs have high-quality 2D surfaces with extremely low densities of defects and dangling bonds. Therefore, heterostructures with high-quality interfaces free of charge traps can be made through the direct stacking of different TMDC layers. This simple stacking process does not need exquisite epitaxial growth tools (*e.g.*, molecular beam epitaxy (MBE)) and is potentially compatible with cost-effective roll-to-roll manufacturing processes. The produced vertically stacked TMDC heterostructures can be exploited for modulating the electronic band structures of various nanoelectronic and optoelectronic devices. One of the important applications is the generation of built-in potentials in TMDC-based photoresponse devices for facilitating the separation of photo-generated excitons and resulting in high photo-responsivity.^[3] However, we still lack a top-down nanofabrication approach capable of producing arrays of such attractive TMDC heterostructures.

We present an upscalable nanoimprint/nanoprint-based technique capable of producing uniform multilayer TMDC heterostructure arrays into device sites. Specifically, using this technique, we have demonstrated the fabrication of uniform multilayer WSe₂/MoS₂ heterostructure arrays. These heterostructures can be used for making photo-response devices.

Fig. 1 illustrates the presented nanofabrication technique, which involves two critical sub-processes. Firstly, our previously developed nanoimprint-assisted shear exfoliation (NASE) technique is used to exfoliate prepatterned TMDC features with uniform thicknesses from a bulk TMDC stamp onto a PDMS transfer stamp (Steps 1-4).^[4] These TMDC features on the PDMS stamp are subsequently transferred into the ordered device sites on the target substrate (Steps 5, 6) through a transfer-printing (TP) process. During the TP process, prepatterned metal contacts or already-printed TMDC layers can serve as effective adhesion layers for immobilizing as-printed TMDC flakes. The repetitive operation of this NASE+TP process for printing different

TMDC materials can generate vertically stacked TMDC heterostructure arrays. **Fig. 2** displays the optical micrographs (OMs) of (a) uniform WSe₂ mesa arrays exfoliated from a bulk WSe₂ stamp onto a PDMS transfer stamp, (b) the same WSe₂ mesa arrays transfer-printed onto prepatterned Au contacts on a SiO₂ substrate, and (c) MoS₂ mesa arrays subsequently transfer-printed on top of WSe₂ structures, forming uniform vertically-stacked multilayer WSe₂/MoS₂ heterostructure arrays. **Fig. 3** shows the AFM-acquired thickness data measured from (a) WSe₂ mesa arrays (the 1st layer) and (b) WSe₂/MoS₂ heterostructure arrays (total thicknesses for two layers). The relative standard deviation of the total thickness data measured from WSe₂/MoS₂ heterostructure flakes is estimated to be ~7%, which is much smaller than those of multilayer structures produced by previously reported exfoliation methods.[5] **Fig. 4a** shows the optical micrograph (OM) of a representative photo-response device consisting of vertically stacked Au/WSe₂/MoS₂/ITO layers. **Figs. 4b, 3c** exhibits the I-V characteristics of this device measured under dark condition and 532 nm laser illumination, respectively. Under the laser illumination, the device exhibits large photocurrents at negative biases, and also an observable photovoltaic effect.

This work advanced the critical nanofabrication technology to leverage the superior electronic and structural properties of TMDCs for practical device applications.

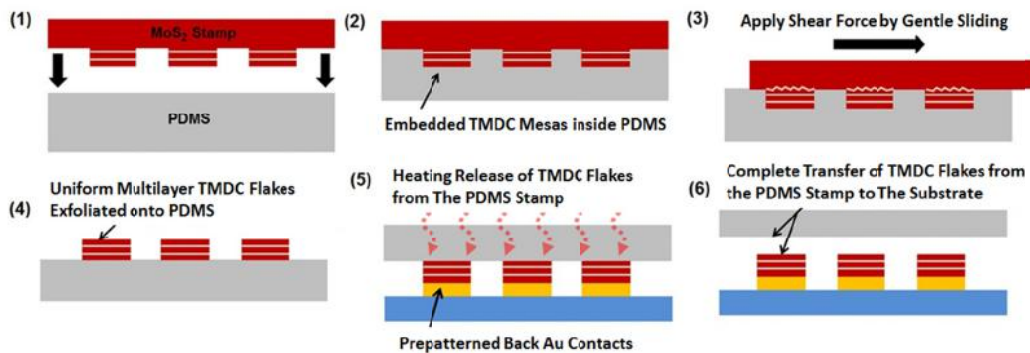


Fig. 1 Schematic steps for printing uniform multilayer TMDC arrays into device sites on the substrate: The whole process consists of two critical sub-processes – Steps (1)-(4): nanoimprint-assisted shear exfoliation (NASE) of pre-patterned TMDC mesas from a bulk TMDC stamp onto a PDMS transfer stamp; Steps (5) to (6): transfer-printing of TMDC mesas from the PDMS stamp onto the device sites on the final substrate. The repetitive application of this process for printing different TMDC flakes can generate vertically stacked TMDC heterostructures.

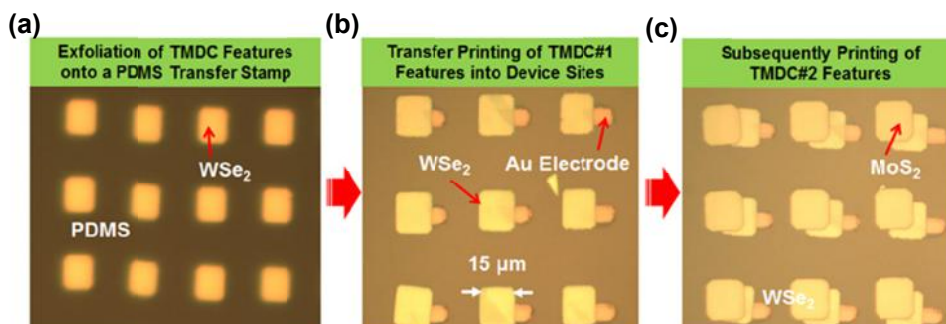


Fig. 2 Optical micrographs of (a) NASE-produced WSe₂ mesa arrays on a PDMS transfer stamp, (b) WSe₂ mesa arrays transfer-printed onto the prepatterned Au contacts on the final device substrate, and (c) MoS₂ mesas subsequently printed on top of WSe₂ mesas, resulting in vertically stacked WSe₂/MoS₂ heterostructure arrays.

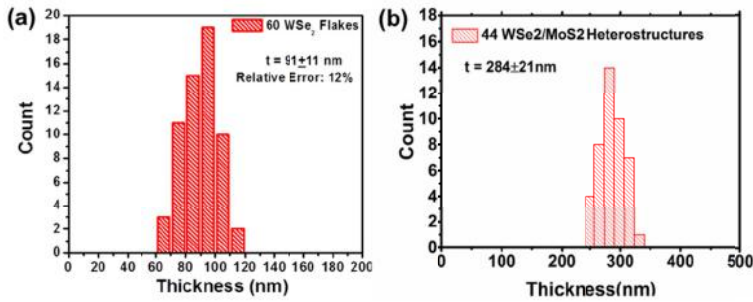


Fig. 3 AFM-acquired thickness data measured from (a) WSe₂ mesa arrays and (b) WSe₂/MoS₂ heterostructure arrays (total thicknesses for two layers). The relative standard deviation of the total thickness data measured from WSe₂/MoS₂ heterostructure flakes is estimated to be ~7%.

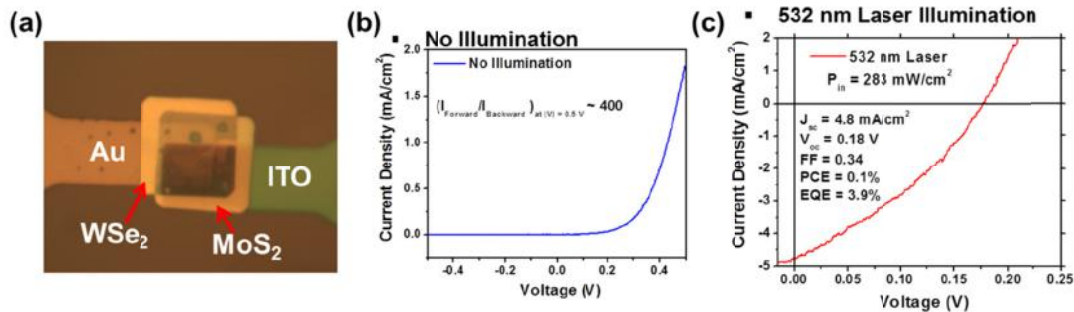


Fig. 4 (a) Optical micrograph of a vertically stacked Au/WSe₂/MoS₂/ITO photo-response device. I-V characteristics of this device measured (b) under no illumination and (c) under 532 nm laser illumination ($P = 200 \text{ mW/cm}^2$).

Acknowledgements: This work is supported by the NSF grant # ECCS-1307744.

REFERENCES

1. G. Eda and S. A. Maier, ACS Nano, **7**, 5660-5665 (2013)
2. L. Britnell, R. M. Ribeiro, A. Eckmann and A. H. C. Neto, Science, **340**, 1311-1314 (2013)
3. M. Furchi, A. Pospischil, F. Libisch, J. Burgdörfer, and T. Mueller, Nano Lett. **14**, 4785-4791 (2014)
4. M. Chen, H. Nam, H. Rokni, K. Kurabayashi, W. Lu and X. Liang, ACS Nano, **9**, 8773 (2015)
5. X. Liang, Z. Fu, and S. Chou, Nano Lett. **7**, 3774-3780 (2007)

Absorption and emission of electromagnetic radiation in 2D layered materials

Coherent absorption of N00N states

T. Roger¹, S. Restuccia², A. Lyons¹, D. Giovannini², J. Romero^{2*}, J. Jeffers³, M. Padgett², D. Faccio¹

¹School of Engineering and Physical Sciences, Heriot-Watt University, EH14 4AS Edinburgh, UK

²School of Physics and Astronomy, University of Glasgow, Glasgow G12 8QQ, UK

³Department of Physics, University of Strathclyde, Glasgow, G4 0NG, Scotland, UK

*present address: School of Mathematics and Physics, University of Queensland, St Lucia, 4072, Australia
t.w.roger@hw.ac.uk

Abstract— We experimentally investigate N00N state coherent absorption in a multilayer graphene film and show that coherent absorption may be used to selectively choose whether the sample undergoes one-photon or two-photon absorption.

A partial absorber placed in a standing wave may either completely transmit or coherently absorb light, depending on the relative phase of the counterpropagating fields. Recent results in deeply subwavelength thickness films hold the promise for coherent control and logical gate operations with both classical and single photon light sources [1, 2]. Here we experimentally investigate two-photon N00N state coherent absorption in a multilayer graphene film. Depending on the N00N state input phase, it is possible to selectively choose between *single* or *two* photon absorption of the input state in the graphene film [3]. These results demonstrate that coherent absorption in the quantum regime exhibits unique features with applications in multiphoton spectroscopy and imaging.

Recent experimental work has shown that coherent perfect absorption can occur when a single

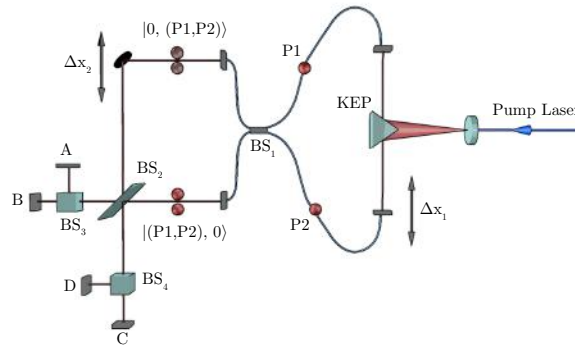


Figure 1: A frequency tripled Nd:YAG laser is used to pump a type 1 BBO crystal producing correlated photon pairs. The photons (P1, P2) are separated by a knife-edge prism (KEP) and coupled to single-mode polarisation-maintaining fibers. The photons are recombined onto a beamsplitter producing an N=2 N00N state. The quantum state is combined once again onto a second beam splitter BS₂, which either takes the form of either a lossless 50:50 beamsplitter or an absorptive graphene sample. The output states from the second beamsplitter are distributed over 4 SPADs, A, B, C and D via two further beamsplitters in order to measure the two-photon output states.

photon Fock state is input to a Sagnac interferometer into which a 50% absorbing film is placed, thus implying deterministic absorption of the single photon [4, 5]. More intriguing results are expected when non-trivial quantum states interact with a lossy beamsplitter. Fig. 1 shows the experimental layout for studying coherent absorption of N00N states; a Hong-Ou-Mandel (HOM) interferometer creates N00N states that are then used as input to a Mach-Zehnder interferometer (MZI). The output beamsplitter of the MZI is a $\sim 50\%$ absorbing multilayer graphene film. To explain the quantum coherent absorption process at the graphene beamsplitter, we use a theoretical model based on that developed in [6] and then compare the results to our experiments with N00N states incident on a graphene film and an ideal lossless beamsplitter. By changing the relative phases of the two arms of the MZI, we show the ability to modulate between two-photon output states and deterministic absorption of a single photon. In Fig. 2 we show that for a lossless beamsplitter the

output states are always two-photon states (as expected) and therefore show no overall modulation of the photon number. In contrast, when the output beamsplitter of the MZI is lossy, we observe a modulation of the total coincidence rate, indicating that absorption of *one* photon or *two* photons occurs for a specific phase of the interferometer. These results show that two photon absorption, although typically a nonlinear optical effect, may also occur in the linear regime as a result of the peculiar absorption regime and input photon states used in our experiments.

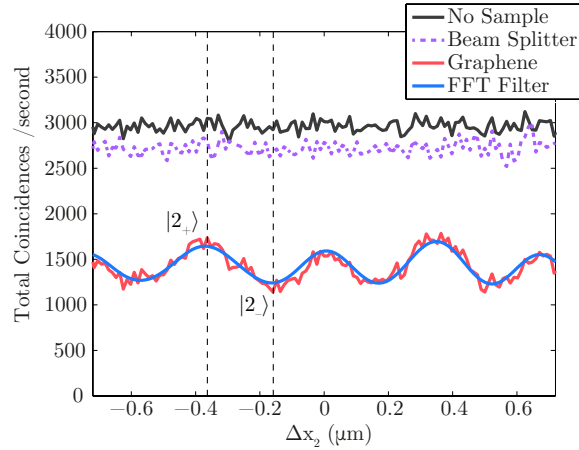


Figure 2: Total coincident rate counted with (i) no sample, black curve (ii) 50:50 lossless beamsplitter, purple curve (iii) lossy graphene beam splitter - graphene sample, red curve as a function of interferometer mirror position. The blue curve shows a fit to the oscillation at ω_2 . It can be seen that in (i) and (ii) no overall oscillation is seen inferring no modulation of the energy within the interferometer. In (iii) it can be seen that there are a series of minima and maxima corresponding to ‘nodes’ and ‘anti-nodes’ of the N00N state.

REFERENCES

1. Zhang, J. MacDonald, K. F. and Zheludev, N. I. “Controlling light-with-light without nonlinearity,” *Light: Sci. & Appl.*, Vol. 1, No. e18, 2012
2. Fang, X. MacDonald, K. F. and Zheludev, N. I. “Controlling light with light using coherent metadevices: all-optical transistor, summator and inverter,” *Light: Sci. & Appl.*, Vol. 4, No. e292, 2015
3. Jeffers, J. “Interference and the lossless lossy beam splitter,” *J. Mod. Opt.*, Vol.47, No.11, 1819–1824, 2000
4. Roger, T. Vezzoli, S. Bolduc, E. Valente, J. Heitz, J. J. F. Jeffers, J. Soci, C. Leach, J. Couteau, C. Zheludev, N. I. and Faccio, D. “Coherent perfect absorption in deeply subwavelength films in the single-photon regime,” *Nat. Comms.*, Vol. 6, No. 7031, 2015
5. Huang, S. Agarwal, G. S. “Coherent perfect absorption of path entangled single photons,” *Opt. Express* Vol. 22, No. 20936, 2014
6. Barnett, S. M. Jeffers, J. Gatti, A. and Loudon, R. “Quantum optics of lossy beam splitters,” *Phys. Rev. A.*, Vol. 57, No. 3, 1998

Nanoscale Terahertz Sensing and Imaging with Graphene and Arrayed Carbon Nanotubes

Yukio Kawano*

Quantum Nanoelectronics Research Center, Department of Physical Electronics, Tokyo Institute of Technology,
2-12-1 Ookayama, Meguro-ku, Tokyo 152-8552, Japan

*corresponding author: kawano@pe.titech.ac.jp

Abstract-Near-field terahertz (THz) imaging is indispensable to investigations in sub-wavelength regions down to the nanometer scale. This technology is particularly useful for examining objects such as nanomaterials, polymers, cells, and biomolecules. My talk will explain novel THz sensing and imaging technologies based on graphene and carbon nanotube devices, and their applications to materials and devices characterization.

The advantageous properties of terahertz (THz) waves - permeability through objects opaque for visible light, etc. - potentially enable various applications of imaging in this band. A promising approach for achieving high spatial resolution is to utilize near-field imaging technique. This method has been well established in visible, near-infrared and microwave regions. However, near-field imaging in the THz region remains to be fully explored. In particular, the development of passive near-field THz imaging is one of the important issues, which enables to provide clear information about inherent properties of samples without external THz source. For this realization, highly sensitive detection of the THz evanescent field alone is necessary. In this work, we have developed new devices for active and passive THz near-field imaging in which all components: an aperture, a probe, and a detector are integrated on a solid-state chip.

The first part of this talk explains our chip-based near-field imaging technology by utilizing two types of two-dimensional (2D) systems¹⁻⁸: GaAs/AlGaAs heterostructure and graphene. By scanning an evanescently-coupled THz detector closely across a sample surface (Fig. 1), we carried out collection-mode near-field THz imaging. The implementation of a magnetically-tunable THz detection method further allowed us to obtain frequency-selective, near-field THz images. As an application of this technology, cryogenic THz-emission imaging was demonstrated (Fig. 2), where THz radiation associated with energy dissipation in a

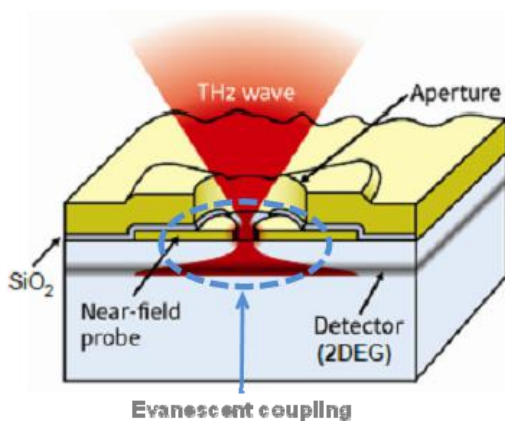


Fig. 1 Schematic view of the near-field THz imager.

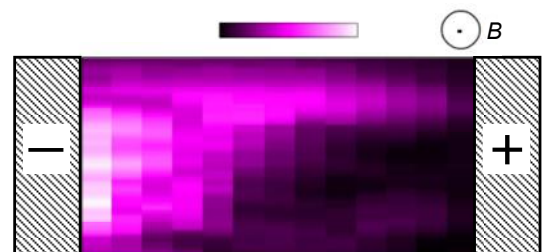


Fig. 2 Near-field image of THz emission distribution in a 2D semiconductor device, taken with the imager shown in Fig. 1. No external THz pump source was used.

2D semiconductor device was imaged without any THz pump sources. This observation offers direct information about electron injection into a 2D semiconductor channel.

The second part introduces THz sensing based on carbon nanotube devices⁹⁻¹². We found that the noise of this detector was close to the Johnson noise limit, indicating that this device works as a low-noise, highly sensitive THz detector.

Acknowledgements

This work was supported in part by the Japan Science and Technology Agency, the Funding Program for Next Generation World-Leading Researchers, MEXT/JSPS KAKENHI Grant Numbers 26286005, 26600010, 26103513, 26107516, and Support for Tokyotech Advanced Researchers (STAR).

REFERENCES

1. Y. Kawano et al., *Phys. Rev. Lett.* **95**, 166801 (2005).
2. Y. Kawano et al., *Nature Photonics* **2**, 618 (2008).
3. Y. Kawano et al., *Physica E* **42**, 1188 (2010).
4. Y. Kawano, *IEEE J. Selec. Top. Quantum Electronics* **17**, 67 (2011). (**Invited paper**)
5. D. Suzuki, S. Oda, and Y. Kawano, *Appl. Phys. Lett.* **102**, 122102 (2013).
6. Y. Kawano, *Contemporary Physics* **54**, 143 (2013). (**Cover**)
7. Y. Kawano, *Nanotechnology* **24**, 214004 (2013).
8. Y. Kawano, *J. Phys. Soc. Jpn.* **84**, 121010 (2015).
9. Y. Kawano et al., *Appl. Phys. Lett.* **95**, 083123 (2009).
10. Y. Kawano, *Laser & Photonics Reviews* (Wiley-VCH, Berlin) **6**, 246 (2012).
11. X. He et al., *Nano Lett.* **14**, 3953 (2014).
12. K. J. Erickson et al., *ACS Nano* **9**, 11618 (2015).

Growth and applications of 2D materials in electron emitters and renewable energy.

D.H.C. Chua

Department of Materials Science and Engineering, National University of Singapore, Singapore
Center for Advanced 2D Materials and Graphene Research Center, National University of Singapore, Singapore

*corresponding author: msechcd@nus.edu.sg

Carbon materials have attracted much attention due to their unique properties, ranging from low dimensional effects, good structural integrity, high electrical and thermal conductivity, and chemical stability. Increasingly, carbon-based materials have progressed from thin films to the nanoscale dimensions, such as graphite to graphene. There are many potential applications ranging from electronics to conductive coatings to biomedical technology. In order to obtain high quality materials as a precursor, the key focus has been in optimizing and finding the correct growth techniques.

Pulsed laser deposition (PLD) has been widely known for its ability to deposit high quality hydrogen free diamond-like carbon films. In this talk, I will focus on the lesser known fact that the PLD technique can be used to deposit high quality graphene films at relatively low temperatures of 700 °C. In addition, by modifying the growth process, one can obtain graphite nanodots and through the formation of nanocomposites, particles such as ZnO can be embedded into the carbon matrix. Some applications of the graphene, graphite nanodots and nanocomposites will also be shown. For example, with careful design, flat-film electron emitters can be engineered to be as effective as tube-like emitters. This forms the basis in fabricating these 2D materials on other forms of substrates for renewable energy such as Li-air batteries, Li-ion batteries, PEM fuel cells and Supercapacitors. The applications of the MoS₂ in Li-air battery will be discussed.

Acknowledgements, This research was supported by National Research Foundation, Prime Minister's Office, Singapore, under its Competitive Research Programme (CRP Award No. NRF-CRP 10-2012-6).

Strongly Coupled Graphene-Metamaterial Hybrids.

I. J. Luxmoore¹, P. Q. Liu², S. A. Mikhailov³, N. A. Savostiyanova³, F. Valmorra², P. Li¹, J. Faist² and G. R. Nash^{1*}

¹College of Engineering, Mathematics and Physical Sciences, University of Exeter, Exeter, United Kingdom

²Institute of Quantum Electronics, Department of Physics, ETH Zurich, Zurich, Switzerland

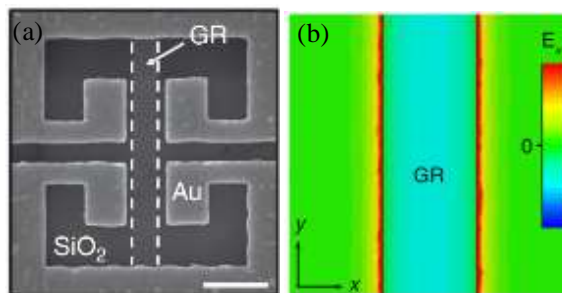
³Institute of Physics, University of Augsburg, Augsburg, Germany

*corresponding author: g.r.nash@exeter.ac.uk

Abstract-We introduce hybrid metamaterials consisting of split ring resonators and a graphene nanoribbon array and demonstrate their use for both modulation and integrated detection of electromagnetic radiation.

Research on metamaterials has progressed rapidly with substantial expansion of both the scope of novel functionalities and the operating frequency range enabled by different types of artificial structures. Many approaches are based on noble metals, but at mid-infrared wavelengths and longer the negative permittivity of noble metals means that the surface plasmons (SPs) are weakly bound to the metal-dielectric interface. Graphene has been shown to support tightly confined SPs in this spectral range [1], with the significant advantage that the SP resonance can be tuned by changing the conductivity of graphene, which can be modulated by two orders of magnitude using an applied gate voltage. We have recently demonstrated a novel type of tunable hybrid metamaterial employing graphene plasmonic resonators strongly coupled to conventional metal based metamaterials [2], as shown in Figure 1. Using this structure we were able to demonstrate a terahertz modulator exhibiting 60% transmission modulation and operating speed in excess of 40MHz.

Figure 1: (a) SEM image of a fabricated hybrid metamaterial unit cell (scale bar = 1 μ m) containing a graphene nano-ribbon (GR) (b) Simulated x-component of the electric field associated with the plasmon resonance in the graphene nano-ribbon.



As seen in the simulations in Figure 1(b) the hybrid metamaterial acts to concentrate the electric field component of incident radiation along the edge of the graphene ribbon. This effect can be used as a means of significantly enhancing the interaction of light with a sample under test and therefore, for example, potentially enhancing the sensitivity and resolution of infrared spectroscopy. As a first step towards this we have been able to reproduce the infrared transmission spectrum of a very thin (~20nm) layer of test polymer by integrating this metamaterial with graphene photodetectors [3]. Features associated with the vibrational modes within the polymer molecules then appear as minima in the measured photo-voltage. This is a key step towards the realization of a fully integrated, high spatial resolution, surface enhanced sensor and the ultimately could form the basis of a spectrometer-on-a-chip.

Acknowledgements. This research was supported by the European Union under the FET-open grant GOSFEL, and G.R.N. also gratefully acknowledges the support of the UK Engineering and Physical Sciences Research Council through a fellowship in Frontier Manufacturing (Grant No. EP/J018651/1).

REFERENCES

1. Low, T. and Avouris, P. “Graphene Plasmonics for Terahertz to Mid-Infrared Applications,” *ACS Nano*, Vol 8, 1086–1101, 2014.
2. Liu, P. Q., Luxmoore, I. J., Mikhailov, S.A., Savostianova, N.A., Valmorra, F., Faist, J., and Nash, G. R., “Highly tunable hybrid metamaterials employing split-ring resonators strongly coupled to graphene surface plasmons”, *Nat. Commun.* Vol. 6, 8969, 2015.
3. Luxmoore, I. J., Liu, P. Q., Li, P., Faist, J., and Nash, G. R., “Graphene-metamaterial photodetectors for integrated infrared sensing,” in preparation.

Spatio-temporal observation of photogenerated electron dynamics in twisted graphene

K. Fukumoto¹, M. Boutchich², H. Arezki², K. Sakurai³, K. Onda³, and S. Koshihara³

¹High Energy Accelerator Research Organization (KEK), 1-1 Oho, Tsukuba, Ibaraki 305-0801, Japan

²Group of electrical engineering Paris, UMR CNRS 8507, CentraleSuplec, Univ.Paris-Sud, Universit Paris-Saclay, Sorbonne Universits, UPMC Univ Paris 06

3 & 11 rue Joliot-Curie, Plateau de Moulon 91192 Gif-sur-Yvette CEDEX, France

³Tokyo Institute of Technology, 2-12-1 Ookayama, Meguro-ku, Tokyo 152-8550, Japan
keiki@post.kek.jp

Abstract— Graphene is one of the most studied 2D materials. However, the ultrafast carrier dynamics influenced by the crystallographic structures is not well studied, because of the instrumental limitations. Locally different twisting angle between graphene layers was detected by Raman spectro-microscopy. Photogenerated carrier lifetimes in these selected regions were estimated by time-resolved photoemission electron microscopy with 100 nm spatial and 100 fs temporal resolutions. We concluded that the interaction between layers and to the substrate influence the optoelectronic properties.

1. INTRODUCTION

Quasi-standing mono and multilayer graphene has attracted attention for a range of optoelectronic applications. The modulation of graphene’s properties for devices applications relies on the understanding of the carrier interactions and recombination dynamics. Indeed, stacked monolayer graphene, demonstrates tunable band stuctures that depends on the stacking orders, i.e. the rotation angles between two layers. In that regard, one expects the carrier dynamic to be angle dependent. Therefore, the ultrafast kinetics and their correlation with the number of layers as well as the stacking configuration is of particular interest. These relaxation mechanisms have been extensively studied in high quality exfoliated and SiC graphene using pump-probe techniques. Here we exploite a different technique coupling an optical pump-probe technique using femtosecond (fs) laser pulses and a photoemission electron microscopy with the spatial resolution of 100 nm (time-resolved photoemission electron micriscopy: TR-PEEM). On one hand the fs timescale helps to investigate the faster relaxation mechanisms, and on the other hand the simultaneous microscopic observation probes any particular region that may exhibit a given rotation angle.

We investigated a sample of CVD graphene with multilayer defects inherent to the growth process. These defects exhibit different stacking angles. Our spatial resolution permits to acquire in one shot the photoemission of all these defects. A subsequent analyzis performed on the pixelized image allows the extraction of the lifetime of the carrier within a particular region. As a result, we are able estimate lifetimes in multilayer regions which have a stronger interaction with the underlying substrate and other which seem decoupled from the substrate.

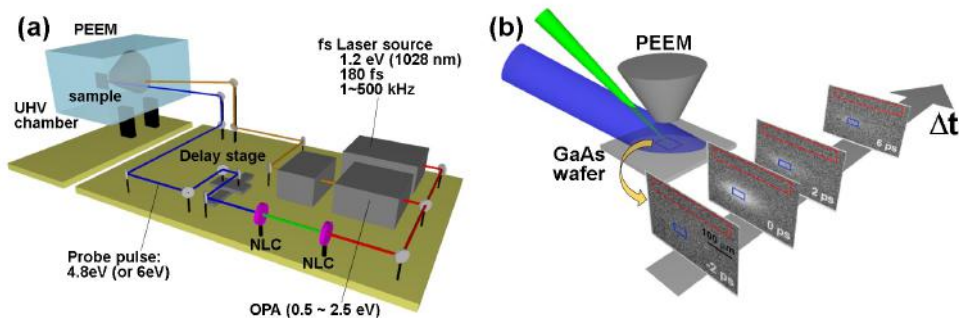


Figure 1: (a) Diagram of TR-PEEM. (b) Demonstration of TR-PEEM with a GaAs wafer.

2. TIME-RESOLVED PHOTOEMISSION ELECTRON MICROSCOPY

Figure 1(a) is a schematics of TR-PEEM setup. Figure 1(b) provides a diagram of demonstration of TR-PEEM with a GaAs wafer sample. A series of TR-PEEM images with different delay times between pump and probe pulses are shown. The pump pulse with 2.4 eV excite electrons over the band gap, and the probe pulse induce photoemission, whose intensity is proportional to the density of the excited electrons. The temporal evolution of the image contrast presents the relaxation and recombination of photogenerated carriers.

3. RESULTS AND DISCUSSION

We have isolated a sample containing CVD graphene superlattices with different orientations. Figure 2(a) shows a Raman microscopy image of the 2D peak over the G peak to enhance the structural information. The bilayered regions are marked with A, B, and C. Region A corresponds to a rotation angle of larger than 12 degree whereas region B and C correspond to around 12 degree and smaller, respectively. These angles have been determined from the Raman signatures. Figure 2(b) provides a PEEM image obtained at the same region to Figure 2(a). Slightly darker contrasts in the three regions indicate the higher workfunctions inherent to the different stacking orders. From the time-dependent photoemission intensity, we can determine the photogenerated carrier lifetime for each angle. Different stacking orientation give rise to a different band structure and therefore we expect different recombination lifetime for each region. Clearly, we observe a difference between the monolayer that is directly onto silicon dioxide and suffers from phonon interaction as opposed to the the bilayer superlattices, Fig. (d). The graphene layers decoupled from the substrate and longer lifetime are observed. The PEEM system presented here is able to precisely map in space and with fs time resolution the lifetime of photogenerated carrier in complex nanostructured materials.

ACKNOWLEDGMENT

This work was supported financially by KAKENHI (15K17677) and the JST-CREST project. M.Boutchich would like to thank the CNRS and the French Ministre des Affaires Etrangres et Europeennes for their financial support through the ICT-ASIA programme (3226/DGM/ATT/RECH).

REFERENCES

1. Fukumoto, K, *et al.*, "Direct imaging of electron recombination and transport on a semiconductor surface by femtosecond time-resolved photoemission electron microscopy," *Appl. Phys. Lett.*, Vol. 104, 053117–053121, 2014.
2. Fukumoto, K, *et al.*, "Femtosecond time-resolved photoemission electron microscopy for spatiotemporal imaging of photogenerated carrier dynamics in semiconductors," *Rev. Sci. Instrum.*, Vol. 85, 083705–083710, 2014.
3. Fukumoto, K, *et al.*, "Direct imaging of electron recombination and transport on a semiconductor surface by femtosecond time-resolved photoemission electron microscopy," *Appl. Phys. Exp.*, Vol. 8, 101201–101204, 2015.

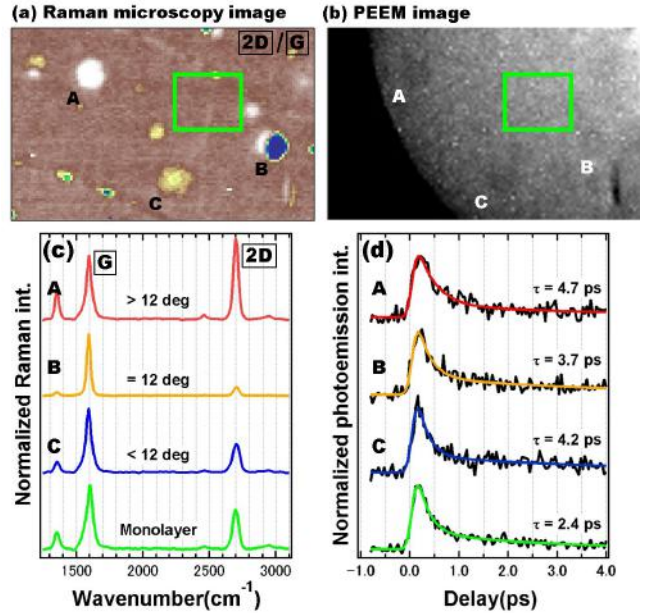


Figure 2: (a) Raman microscopy image. (b) PEEM image. (c) and (d) Raman spectra and time dependent carrier annihilation on different regions as indicated by A, B, C, and a green square in (a) and (b).

Generation and detection of light in 2D materials and heterostructures

Thomas Mueller

*Vienna University of Technology, Institute of Photonics,
Gußhausstraße 27-29, 1040 Vienna, Austria
E-mail: thomas.mueller@tuwien.ac.at*

Two-dimensional (2D) materials are currently receiving a lot of attention for applications in optoelectronics. In this talk, I will review our research activities on electrically driven light emission and photodetection in 2D materials and van der Waals heterostructures. In particular, I will present studies of electroluminescence from MoS₂ and WSe₂ monolayers and their heterojunctions. Further, I will discuss photoconductivity studies of 2D semiconductors, in which we find strong photoconductive gain. We envision that the efficient photon generation and detection, combined with the advantages of 2D semiconductors, such as flexibility, high mechanical stability and low costs of production, could lead to new optoelectronic technologies.

Homogenization and effective medium theories

High-frequency homogenization for layered hyperbolic metamaterials

A. A. Krokhin¹, J. Arriaga², L.N. Gumen³, and V. P. Drachev¹

¹University of North Texas, USA

²Instituto de Física, Universidad Autónoma de Puebla, Mexico

³Universidad Popular Autónoma del Estado de Puebla, Mexico
arkady@unt.edu

Abstract— We propose an analytical approach for calculation of the dielectric tensor of metal-dielectric superlattice (SL). The obtained formulas are valid at high frequencies near the points of topological transition from an elliptic to hyperbolic regime. We take into account the evanescent character of the plasmonic mode and oscillatory behavior of the waveguide modes. Our results show good correspondence to the exact solution of the dispersion equation and significant deviation from the widely used quasi-static formulas, which ignore spatial field inhomogeneity.

The most common geometry for artificial hyperbolic metamaterials is 1D periodic metal-dielectric SL [1]. The dielectric function of such structure becomes negative at sufficiently low frequencies when the contribution to polarization from the metallic layers overcomes the contribution from the dielectric constituent. Since polarizations along the layers and perpendicular to them are different, the elements of the dielectric tensor $\epsilon_{\parallel}(\omega)$ and $\epsilon_{\perp}(\omega)$ vanish at different frequencies, giving rise to the frequency bands with either elliptic or hyperbolic dispersion. Here the sub-indices \parallel and \perp refer to the propagation parallel or perpendicular to the optical axis, respectively.

The static values of the dielectric constants

$$\epsilon_{\parallel} = \bar{\epsilon} = f\epsilon_a + (1-f)\epsilon_b, \quad \frac{1}{\epsilon_{\perp}} = \frac{f}{\epsilon_a} + \frac{1-f}{\epsilon_b}. \quad (1)$$

with ϵ_a replaced by $\epsilon_a = 1 - \omega_p^2/\omega^2$ are widely used at optical frequencies. Here $f = a/d$ is the portion occupied by metal in a unit cell of length $a+b$. This oversimplified approach can be justified only if the width of the metal film a is less than the skin-depth $\delta(\omega) = c/(\omega|\epsilon_a(\omega)|)$. Otherwise, spatial variations of the fields in metal make the quasi-static approximation invalid, even if the homogenization condition $Kd \ll 1$ for the Bloch vector K is satisfied.

Here we propose relatively simple new analytical method of calculation of $\epsilon_{\parallel}(\omega)$ and $\epsilon_{\perp}(\omega)$ [3]. It is based on well-known formulas $V_{ph} = \frac{\omega}{k} = \frac{c}{n}$ and $V_g = \frac{d\omega}{dk} = \frac{c}{n(\omega) + \omega \frac{dn(\omega)}{d\omega}}$ for phase and group velocities respectively. Combining these formulas, a simple differential equation for the effective dielectric function $\epsilon_{eff} = n^2(\omega)$ can be obtained [3]:

$$\frac{c^2}{V_{ph}V_g} = n(n + \omega \frac{dn}{d\omega}) = \epsilon_{eff} + \frac{1}{2}\omega \frac{d\epsilon_{eff}}{d\omega} = F(\omega). \quad (2)$$

Solution of this equation gives frequency-dependent dielectric function of the equivalent homogeneous medium

$$\epsilon_{eff}(\omega) = \frac{2}{\omega^2} \int_{\omega_1}^{\omega} \omega' F(\omega') d\omega'. \quad (3)$$

Here ω_1 is the constant of integration, which is the frequency where the effective dielectric function vanishes, i.e. $\epsilon_{eff}(\omega_1) = 0$. Thus, Eq. (3) defines *exactly* the effective dielectric function if the group and the phase velocities are known within some interval of frequencies.

The proposed method of calculation of the effective dielectric function can be realized for metal-dielectric SL where the dispersion relation $\omega = \omega(K)$ is known implicitly from the Rytov's equation [2]. For propagation parallel to the lattice axis the following result has been obtained in the long-wavelength limit $Kd \ll 1$:

$$\epsilon_{\parallel}(\omega) \approx \frac{2c^2}{\omega^2 d^2} [1 - D_{\parallel}(\omega)], \quad (4)$$

$$D_{\parallel}(\omega) = \cosh\left(\frac{a}{\delta(\omega)}\right) \cos\left(\frac{\omega b}{c} \sqrt{\epsilon_b}\right) + \frac{1}{2} \left(\sqrt{\frac{|\epsilon(\omega)|}{\epsilon_b}} - \sqrt{\frac{\epsilon_b}{|\epsilon(\omega)|}} \right) \sinh\left(\frac{a}{\delta(\omega)}\right) \sin\left(\frac{\omega b}{c} \sqrt{\epsilon_b}\right).$$

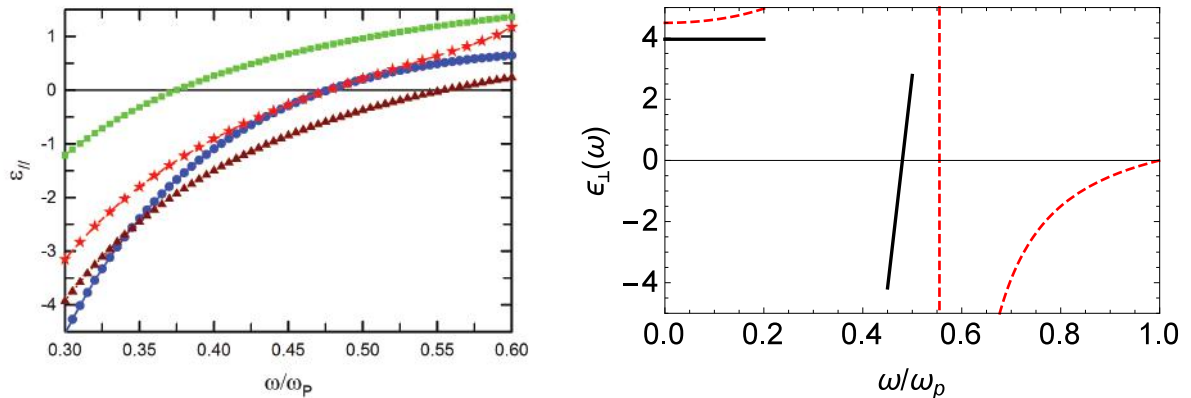


Figure 1: Left panel: Permittivity $\epsilon_{||}(\omega)$ for a SL with filling fraction $f = 1/2$. Red stars is the result obtained from the exact equation [2], blue circles is the effective permittivity obtained from Eq. (4), green squares plots the $\epsilon_{||}$ proposed in Ref. [4], and brown triangles is the dependence $\epsilon_{||}(\omega)$ obtained in the quasi-static limit (1). Right panel: Calculated effective permittivity $\epsilon_{\perp}(\omega)$, black solid line. The quasi-static approximation ϵ_{\perp} (1) is shown by dashed red line.

In Fig. 1 we plot the dielectric function (4) (blue circles) for a SL with $a = b = 2c/\omega_p$ and $\epsilon_b = 2.25$. The topological transition occurs at $\omega_1/\omega_p \approx 0.478$. For comparison we also plot the dielectric function (red stars) calculated from the exact dispersion equation. In the vicinity of topological transition $\epsilon_{||}(\omega)$ calculated from Eq. (4) is practically undistinguishable from the exact result. Unlike this, the dependence obtained from the quasi-static formula (1) (brown triangles) underestimates the value of the effective permittivity. This approach gives the position of the topological transition red shifted by 90 nm from the exact result. The dependence shown by green squares is calculated using the formula derived in Ref. [4]. The method of homogenization proposed there takes into account the skin-effect, however the effective permittivity is overestimated. The position of the topological transition is blue shifted by 35 nm. Thus, the accuracy of the method of homogenization proposed in Ref. [4], as well as the accuracy of the quasi-static approximation are not sufficient for modern optical studies.

The effective dielectric constant for propagation of the TM mode perpendicular to the lattice axis is shown by black solid line in Fig. 1 (right panel). At low frequencies the propagating mode is of plasmon-like nature. For this mode the fields are localized near the metal-dielectric boundaries. Our approach gives $\epsilon_{\perp}(\omega \rightarrow 0) = \epsilon_b [1 + 2c/(b\omega_p) \tanh(a\omega_p/2c)]$ for the homogenized dielectric function of this mode. For frequencies above the lowest cut-off frequency the spectrum of SL consists of waveguide modes. The corresponding permittivity vanishes linearly near each cut-off frequency, see Fig. 1. The graphs in Fig. 1 show that the quasi-static approximation (1) is not satisfactory for this component of the dielectric tensor as well.

In conclusion, we show that the quasi-static approximation is not valid near the frequencies of topological transitions and propose a new method of calculation of the effective dielectric tensor. This method takes into account rapid spatial variations of the fields within the unit cell and it is valid for high-frequencies in the long-wavelength limit $Kd \ll 1$. Some recent results for electrodynamics of hyperbolic metamaterials based on quasi-static approximation should be revised and recalculated.

ACKNOWLEDGMENT

V.P.D. thanks the ARO, Grant W911NF-11-1-0333, and J.A. thanks CONACyT, Grant 167939.

REFERENCES

1. Poddubny, A., *et al.*, “Hyperbolic metamaterials,” *Nat. Photonics*, Vol. 7, 948, 2013.
2. Rytov, S. M., “Electromagnetic properties of a finely stratified medium,” *Sov. Phys.-JETP*, Vol. 2, 466, 1956.
3. Krokhin, A. A., Arriaga, J., Gumen, L.N., and V. P. Drachev, “High-frequency homogenization for layered hyperbolic metamaterials,” *Phys. Rev. B*, Vol. 93, 075418, 2016.
4. Zenteno-Mateo, B., *et al.*, “Effective permittivity tensor for metal-dielectric superlattice,” *Prog. Electromagnet. Res. Lett.*, Vol. 22, 165, 2011.

Nonlocal effective medium theory for photonic crystals and metamaterials

Jie Luo¹, and Yun Lai^{1*}

¹College of Physics, Optoelectronics and Energy & Collaborative Innovation Center of Suzhou Nano Science and Technology, Soochow University, Suzhou 215006, China

*corresponding author: laiyun@suda.edu.cn

Abstract—We propose a nonlocal effective medium theory for photonic crystals and metamaterials by matching of the dispersions and impedances of eigen-fields. Such nonlocal effective medium theory is capable of homogenizing periodic structures beyond the long wavelength limit. The conditions of the validity of the theory is also clarified. Moreover, with the nonlocal effective medium theory, we propose photonic crystals with omnidirectional impedance matching and the ability of formation of aberration-free virtual image, which we denote as “ultra-transparent” photonic crystals.

We consider that a structure with translational symmetry in the z direction is composed of periodic rectangular lattice in the xy plane. And the lattice constant is a_x (a_y) in the x (y) direction. For the waves propagating in xy plane, the effective parameters can be obtained by matching the dispersions and impedances of eigen-fields:

$$\varepsilon_z = \frac{k_y \eta_x^{TE} \Big|_{x=0} - k_x \eta_y^{TE} \Big|_{x=0}}{\omega \eta_x^{TE} \Big|_{x=0} \eta_y^{TE} \Big|_{x=0}}, \quad \mu_x = \frac{k_y \eta_y^{TE} \Big|_{x=0}}{\omega} \quad \text{and} \quad \mu_y = -\frac{k_x \eta_x^{TE} \Big|_{x=0}}{\omega} \quad (1)$$

where $\eta_{x,y}^{TE} \Big|_{x=0} = \frac{\langle E_z \rangle \Big|_{x=0}}{\langle H_{y,x} \rangle \Big|_{x=0}}$ and $\eta_{x,y}^{TM} \Big|_{x=0} = \frac{\langle H_z \rangle \Big|_{x=0}}{\langle E_{y,x} \rangle \Big|_{x=0}}$. Here, the electric and magnetic fields are the eigen-fields

obtained from the numerical calculations.

REFERENCES

1. Śmigaj, W., Gralak, B. “Validity of the effective-medium approximation of photonic crystals,” *Phys. Rev. B*, Vol. 77, 235445, 2008.
2. Lawrence, F. J., de Sterke, C. M., Botten, L. C., McPhedran, R. C., Dossou, K. B. “Modeling photonic crystal interfaces and stacks: impedance-based approaches,” *Adv. Opt. Photonics*, Vol. 5, 385, 2013.
3. Chebykin, A. V., Orlov, A. A., Simovski, C. R., Kivshar, Y. S., Belov, P. A. “Nonlocal effective parameters of multilayered metal-dielectric metamaterials,” *Phys. Rev. B*, Vol. 86, 115420, 2012.
4. Luo, J., Chen, H., Hou, B., Xu, P., Lai, Y. “Nonlocality-induced negative refraction and subwavelength imaging by parabolic dispersions in metal–dielectric multilayered structures with effective zero

permittivity,” *Plasmonics*, Vol. 8, 1095-1099, 2013.

5. Chern, R. L., Han, D. “Nonlocal optical properties in periodic lattice of graphene layers,” *Opt. Express*, Vol. 22, 4817-4829, 2014.

Boundary optical stress in metamaterial and effective-medium systems

Shubo Wang¹, and C. T. Chan^{1*}

¹ Department of Physics and Institute for Advanced Study,
The Hong Kong University of Science and Technology, Hong Kong.

*corresponding author: phchan@ust.hk

Abstract-Using a generic microscopic model, we show that the boundary stress induced by an electromagnetic plane wave in a negative-refractive-index metamaterial depends not only on the macroscopic effective permittivity and permeability but also on the microscopic lattice symmetry of the polarizable units that constitute the metamaterial. The lattice effect is attributed to electrostriction and magnetostriction which can be accounted for by the Helmholtz stress tensor within the context of effective medium theory.

It is well known that light carrying momentum $\hbar\mathbf{k}$ exerts a positive photon pressure on an object in vacuum. With the advent of metamaterials which can have negative refractive indices, does photon pressure become photon tension in such a kind of material?

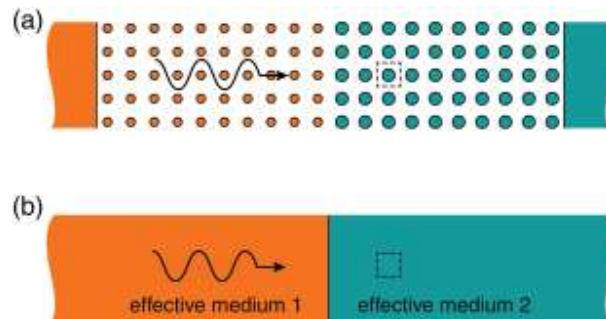


Figure 1. (a) The microscopic model system and (b) the effective medium system.

To answer the question we use a generic microscopic model as shown in Fig.1 (a), where two kinds of materials carrying different microstructures form a boundary in the middle. Near the boundary the materials are discretized into a lattice consisting of polarizable units (electric/magnetic dipoles), say for example, a square lattice here. The incident electromagnetic plane wave propagates from the left hand side to the right hand side and we are interested in the optical stress exerted on the boundary region. In the long wavelength limit the lattice system can be approximated as an effective medium system [Fig. 1(b)] characterized by the macroscopic effective permittivity and permeability. In the microscopic model system, the boundary stress is determined as follows. We first solve for the total field by using an analytical Green's function method. Then the optical force acting on each polarizable unit is calculated by using the Maxwell stress tensor approach. The boundary stress is obtained by summing the force acting all the units within the boundary region. We considered three kinds of lattice system: square lattice, triangle lattice and amorphous lattice and found that they have different boundary

stress, although they are designed to have the same effective permittivity and permeability and hence correspond to the same effective medium system. This means that the boundary stress is, in fact, indeterminate if only the macroscopic effective parameters are specified. Light can either push or pull a metamaterial boundary, depending also on the microscopic lattice structure of the polarizable units that constitute the medium.

Within the effective medium theory, the corresponding boundary stress can be determined using the Helmholtz stress tensor [1-3]:

$$\langle T_{ij}^H \rangle = \frac{1}{2} \text{Re} \left[\varepsilon_0 \varepsilon_{\text{eff}} E_i E_j^* + \mu_0 \mu_{\text{eff}} H_i H_j^* - \frac{1}{2} (\varepsilon_0 \varepsilon_{\text{eff}} E^2 + \mu_0 \mu_{\text{eff}} H^2) \delta_{ij} - \frac{1}{2} \left(\varepsilon_0 \frac{\partial \varepsilon_{\text{eff}}}{\partial u_{ij}} E^2 + \mu_0 \frac{\partial \mu_{\text{eff}}}{\partial u_{ij}} H^2 \right) \right], \quad (1)$$

where $\partial \varepsilon_{\text{eff}} / \partial u_{ij}, \partial \mu_{\text{eff}} / \partial u_{ij}$ are electrostriction and magnetostriction terms that take into account the microscopic lattice information and they can be analytically derived using multiple scattering theory or numerically retrieved based on the band structure of the lattice. Using this stress tensor one can predict the boundary stress that match the results of the microscopic model system very well. Other forms of stress tensors such as Abraham, Minkowski or Einstein-Laub cannot predict the correct results for boundary optical stresses due to the absence of lattice-structure dependent terms.

Our results may shed light on the study of optical force density inside dielectric medium and may find applications in the field of biophysics (e.g., how the electromagnetic stress will deform a biological cell).

Acknowledgements

We thank Prof. Z. Q. Zhang and Dr. W. J. Sun for their valuable comments and suggestions. This work was supported by the Hong Kong Research Grants Council (AoE/P-02/12).

REFERENCES

1. Landau, L. D., E. M. Lifshitz and L. P. Pitaevskii, *Electrodynamics of Continuous Media*, Elsevier, Singapore, 1960.
2. Sun, W. J., S. B. Wang, J. Ng, L. Zhou and C. T. Chan, "Analytic derivation of electrostrictive tensors and their application to optical force density calculations," *Phys. Rev. B*, Vol. 91, 235439, 2015.
3. Wang, S. B., J. Ng, M. Xiao and C. T. Chan, "Electromagnetic stress at the boundary: Photon pressure or tension?," *Sci. Adv.*, accepted.

A scheme to homogenize anisotropic metamaterials with elliptical inclusions

Xiujuan Zhang and Ying Wu

Division of Computer, Mathematical and Electrical Science and Engineering, King Abdullah University of Science and Technology, Saudi Arabia

*corresponding author: ying.wu@kaust.edu.sa

Abstract-We report a scheme, based on coherent potential approximation, to homogenize a type of metamaterial with elliptical inclusions beyond the long-wavelength limit. It offers an analytic solution to the anisotropic effective medium parameters. The theory serves as a tool in the design of new metamaterials. Here we present two examples, one can control energy flux arbitrarily and the other can perfectly absorb oblique incidence coherent waves.

By using coherent potential approximation, we found analytic solutions to the effective medium parameters of a rectangular array of dielectric elliptical cylinders embedded in air. The system and its microstructure are illustrated in Fig. 1.

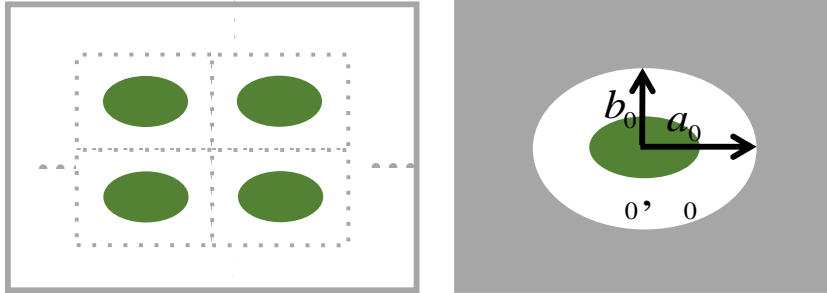


Figure 1: (left) Schematic of the system. (right) Microstructure of the unit.

The effective medium parameters are obtained as [1]:

$$\frac{\varepsilon_{eff} + 2\varepsilon_0 \frac{J'_{e0}(q_0; \xi_0)}{k_0^2 a_0 b_0 J_{e0}(q_0; \xi_0)}}{\varepsilon_{eff} + 2\varepsilon_0 \frac{Y'_{e0}(q_0; \xi_0)}{k_0^2 a_0 b_0 Y_{e0}(q_0; \xi_0)}} = \frac{Y_{e0}(q_0; \xi_0)}{iJ_{e0}(q_0; \xi_0)} \frac{D_{e0}(0)}{1 + D_{e0}(0)}$$

$$\frac{\mu_{effy} - \mu_0 \frac{b_0 J_{e1}(q_0; \xi_0)}{a_0 J'_{e1}(q_0; \xi_0)}}{\mu_{effy} - \mu_0 \frac{b_0 Y_{e1}(q_0; \xi_0)}{a_0 Y'_{e1}(q_0; \xi_0)}} = \frac{Y'_{e1}(q_0; \xi_0)}{iJ'_{e1}(q_0; \xi_0)} \frac{D_{e1}(0)}{1 + D_{e1}(0)}, \quad \frac{\mu_{effx} - \mu_0 \frac{J_{o1}(q_0; \xi_0) a_0}{J'_{o1}(q_0; \xi_0) b_0}}{\mu_{effx} - \mu_0 \frac{Y_{o1}(q_0; \xi_0) a_0}{Y'_{o1}(q_0; \xi_0) b_0}} = \frac{Y'_{o1}(q_0; \xi_0)}{iJ'_{o1}(q_0; \xi_0)} \frac{D_{o1}(0)}{1 + D_{o1}(0)}$$

In the quasi-static limit, the solution recovers the Maxwell-Garnett form [2] and in the limit of vanishing eccentricity, the solution converges to that of the isotropic case [3].

Guided by the effective medium theory, we design two types of anisotropic metamaterials. One can realize a theoretical proposal on arbitrarily controlling the energy flux [4] and the other can absorb the oblique incident coherent wave almost perfectly [5].

Acknowledgements The authors would like to thank financial supports from King Abdullah University of Science and Technology.

REFERENCES

1. Zhang X. J. and Wu Y. "Effective medium theories for anisotropic metamaterials," *Sci. Rep.*, Vol. 5, 7892, 2015.
2. Cohen, R. W., Cody, G. D., Coutts, M. D. & Abeles, B. "Optical Properties of Granular Silver and Gold Films." *Phys. Rev. B* 8, 3689 1973.
3. Wu, Y., Li, J., Zhang, Z. Q. & Chan, C. T. "Effective medium theory for magnetodielectric composites: Beyond the long-wavelength limit." *Phys. Rev. B* 74, 085111 (2006).
4. Luo, J. et al. "Arbitrary Control of Electromagnetic Flux in Inhomogeneous Anisotropic Media with Near-Zero Index." *Phys. Rev. Lett.* 112, 073903 2014.
5. Zhang X. J. and Wu Y (to be submitted)

Homogenization scheme for metamaterials in scalar waves

Min Yang,^{1,*} Guancong Ma,¹ Ying Wu,³ Zhiyu Yang,¹ and Ping Sheng^{1,2,†}

¹Department of Physics, Hong Kong University of Science and Technology, Clear Water Bay, Kowloon, Hong Kong, China

²Institute of Advanced Study, Hong Kong University of Science and Technology, Clear Water Bay, Kowloon, Hong Kong, China

³Division of Computer, Electrical and Mathematical Science and Engineering, King Abdullah University of Science and Technology, Thuwal, Saudi Arabia

*Corresponding author: pherwin@ust.hk, †Corresponding author: sheng@ust.hk

Abstract—We present a homogenization scheme for acoustic metamaterials that is based on reproducing the lowest orders of scattering amplitudes from a finite volume of metamaterials. This approach is noted to differ significantly from that of coherent potential approximation, which is based on adjusting the effective-medium parameters to minimize scatterings in the long-wavelength limit. With the aid of metamaterials' eigenstates, the effective parameters, such as mass density and elastic modulus can be obtained by matching the surface responses of a metamaterial's structural unit cell with a piece of homogenized material. From the Green's theorem applied to the exterior domain problem, matching the surface responses is noted to be the same as reproducing the scattering amplitudes. We verify our scheme by applying it to three different examples: a layered lattice, a two-dimensional hexagonal lattice, and a decorated-membrane system. It is shown that the predicted characteristics and wave fields agree almost exactly with numerical simulations and experiments and the scheme's validity is constrained by the number of dominant surface multipoles instead of the usual long-wavelength assumption. In particular, the validity extends to the full band in one dimension and to regimes near the boundaries of the Brillouin zone in two dimensions.

In this work, we propose an approach to homogenize acoustic metamaterials based on matching the lowest-order scattering amplitudes arising from a finite volume (or a structural unit) of the relevant metamaterial with that of a homogenized material whose material parameters are the desired quantities to be determined. From the Green's theorem applied to the exterior domain problem, matching the scattering amplitudes is the same as matching the interfacial responses of the relevant finite volume. The surface responses of a heterogeneous structural unit, in turn, may be formally calculated based on its eigenstates, which can be obtained numerically, e.g., such as by the finite element method (FEM). The problem can thereby be converted into a set of response equations for the unknown material parameters. We show that the relevant effective parameters can be explicitly solved as functions of frequency, and the homogenized effective medium provides an exact match to the motions at the boundaries of structural units and, hence, the scattering amplitudes with that of the actual metamaterial. The advantage of this approach is that it is conceptually clear cut and focuses on the resonant scatterings that are the source of metamaterials' exotic behaviors. It can ensure validity over a broad range of frequencies: In one dimension (1D), the theory is valid for all frequencies, and in two dimensions (2D), the validity of the theory is shown to be almost over the entire Brillouin zone, even when the effective wavelength is comparable to the size of the unit cell at the Brillouin-zone boundary. Such accuracy is achieved by matching only the lowest two orders of scattering amplitudes (surface motions).

We demonstrate the effectiveness of the proposed approach through three examples. The first is a two-phase layered lattice in which one phase is stiff and heavy while the other phase is an elastic medium. The wave propagation characteristics and the relevant wave fields, calculated from the homogenized effective parameters, are shown to yield excellent agreement with numerical simulations. The second example is a 2D hexagonal lattice of concentric cylinders. The homogenized

medium predictions are compared with numerical simulations from FEM and multiple-scattering theory with excellent agreement. The third example is the membrane-type metamaterial with a decorated-membrane resonator as the unit cell of a planar array. Again the comparison of the transmission/reflection characteristics with the experimental results from impedance tube measurements shows excellent agreement.

REFERENCE:

- [1] M. Yang, G. Ma, Z. Yang, and P. Sheng, *Phys. Rev. Lett.* **110**, 134301 (2013).
- [2] M. Yang, G. Ma, Y. Wu, Z. Yang, and P. Sheng, *Phys. Rev. B* **89**, 064309 (2014).
- [3] Y. Wu, J. Li, Z. Q. Zhang, and C. T. Chan, *Phys. Rev. B* **74**, 085111 (2006).
- [4] D. Torrent and J. Sanchez-Dehesa, *Phys. Rev. B* **74**, 224305 (2006).

Dynamic Homogenization of Metamaterials: Nonlocal Effects and Additional Constitutive Parameters

M. F. Ponge¹, O. Poncelet¹, and D. Torrent^{1,2*}

¹Université de Bordeaux, Institut de Mécanique et d'Ingénierie, UMR 5295, France

²Université de Bordeaux, Centre de Recherche Paul Pascal, UPR 8641, France

*corresponding author: torrent@crpp-bordeaux.cnrs.fr

Abstract—We present a dynamical homogenization method for acoustic and elastic metamaterials based on periodic arrangements of inclusions. The method allows for the calculation of the frequency-dependent effective parameters. It is shown that they are also spatially dispersive (nonlocal). Additionally, new constitutive parameters, which can also be accurately computed in the framework of the present theory, are found in the homogenization process. Several propagation regimes concerning these nonlocal effects are studied and some examples are given.

We present a homogenization method for periodic (elastic or acoustic) composites based on the well-known Plane Wave Expansion Method (PWE). A relationship between the averaged fields is found, from which we can obtain the effective constitutive parameters [1]. The method shows that the effective parameters are not only frequency-dependent, but also wavenumber-dependent. Metamaterials are then nonlocal structures whose dependence on the wavenumber can be very strong.

Additionally, it is found that metamaterials will require in general an additional constitutive parameter, called the Willis term in elasticity [2]. Willis term \mathbf{S} is also required for the accurate description of acoustic metamaterials, whose constitutive density ρ and bulk modulus B are found to be

$$\partial_t \mathbf{v} + \rho^{-1} \nabla P - i\mathbf{S} \partial_t P = 0 \quad (1)$$

$$\nabla \cdot \mathbf{v} + B^{-1} \partial_t P - i\mathbf{S} \cdot \nabla P = 0 \quad (2),$$

with \mathbf{v} and P , the velocity and pressure fields.

The consequences of these new equations for the propagation of acoustic waves in metamaterials will be analyzed, both in the local and nonlocal regimes. A comparison with elastic and electromagnetic metamaterials will be discussed, and possible consequences and applications of these effects will be presented.

REFERENCES

1. Torrent, D., Pennec, Y., & Djafari-Rouhani, B. (2015). Resonant and nonlocal properties of phononic metasolids. *Physical Review B*, 92(17), 174110.
2. Milton, G. W., & Willis, J. R. (2007, March). On modifications of Newton's second law and linear continuum elastodynamics. In *Proceedings of the Royal Society of London A: Mathematical, Physical and Engineering Sciences* (Vol. 463, No. 2079, pp. 855-880). The Royal Society.

Higher order terms and origin dependence in metamaterial homogenization

C. A. Dirdal¹, H. O. Hågenvik¹, and J. Skaar¹

¹Department of Electronics and Telecommunications, Norwegian University of Science and Technology, Norway
christopher.dirdal@iet.ntnu.no

Abstract— Surprising features of metamaterial homogenization are presented. The electric quadrupole *and* higher order terms in the expansion of macroscopic polarization can be significant. Origin dependence in the effective parameters can be used to adjust them towards e.g. making the effective parameters “more local”. These features are discussed in relation to the two classical *Agranovich & Ginzburg* and *Russakoff-Jackson* formulations, and the correspondence between them is made.

The rise in diversity and complexity of realizable metamaterial structures have spurred renewed interest into homogenization theories. These are theories that allow for the formulation of *effective* macroscopic Maxwell’s equations in structured media from the *exact* microscopic ones, and thereby allow for effective plane wave solutions in materials with complex structures, where dimensions are well below the wavelength. We aim to present some surprising features of metamaterial homogenization: That the electric quadrupole *and* higher order terms in the expansion of macroscopic polarization can be significant, ambiguity of the effective parameters, choices of coordinate origin that ensure desirable properties such as locality, and a discussion of alternative effective permeability parameter definitions.

Faced with the wide variety of proposed homogenization theories in the field, it makes sense to highlight such features in relation to the two classical formulations by *Agranovich & Ginzburg* and *Russakoff-Jackson* [1–5]. Consider the following definition of macroscopic (averaged) polarization, in which we expand the exponential function

$$\bar{\mathbf{P}} \equiv \frac{1}{V} \int \mathbf{P}(\mathbf{r}) e^{-i\mathbf{k}\cdot\mathbf{r}} d^3r, \quad (1a)$$

$$= \mathbf{P}_{\mathbf{E}} - \frac{1}{\omega\mu_0} \mathbf{k} \times \mathbf{M}_{\mathbf{E}} - i\mathbf{k} \cdot \bar{\mathbf{Q}}_{\mathbf{E}} - \frac{1}{2V} \int (\mathbf{k} \cdot \mathbf{r})^2 \mathbf{P}(\mathbf{r}) d^3r. \quad (1b)$$

The integrals are taken over the volume V of the unit cell, and the quantities $\mathbf{P}_{\mathbf{E}}$, $\mathbf{M}_{\mathbf{E}}$ and $\bar{\mathbf{Q}}_{\mathbf{E}}$ represent the averaged electric and magnetic dipoles and electric quadrupole, respectively, as defined in [5]:

$$\mathbf{P}_{\mathbf{E}} = \frac{1}{V} \int \mathbf{P}(\mathbf{r}) d^3r, \quad \mathbf{M}_{\mathbf{E}} = -\frac{i\omega\mu_0}{2V} \int \mathbf{r} \times \mathbf{P}(\mathbf{r}) d^3r, \quad \bar{\mathbf{Q}}_{\mathbf{E}} = \frac{1}{2V} \int [\mathbf{r}\mathbf{P}(\mathbf{r}) + \mathbf{P}(\mathbf{r})\mathbf{r}] d^3r. \quad (2)$$

The *Agranovich & Ginzburg* formulation, as used in Silveirinha’s homogenization [3], describes the entire averaged polarization by a single spatially dispersive effective permittivity $\bar{\epsilon}(\mathbf{k})$, defined as $\bar{\mathbf{P}} = \epsilon_0(\bar{\epsilon}(\mathbf{k}) - 1)\bar{\mathbf{E}}$, where $\bar{\mathbf{E}}$ represents the averaged electric field. The zeroth and second orders of $\bar{\epsilon}(\mathbf{k})$ may thereafter be assigned to local parameters $\bar{\epsilon}_s$ and $1 - \bar{\mu}_s^{-1}$, respectively. The *Russakoff-Jackson* formulation, as used in Alù’s homogenization [5], instead places the averaged polarization $\bar{\mathbf{P}}(\mathbf{r})$ into *both* a spatially dispersive effective permittivity $\bar{\epsilon}_a(\mathbf{k})$ *and* a spatially dispersive effective permeability $\bar{\mu}_a(\mathbf{k})$, that may in some cases tend to local parameters in the long wave limit $k \rightarrow 0$. Assuming we are dealing with a metamaterial without bianisotropy, consisting of non-magnetic constituents, the parameters may be expressed as $\mathbf{P}_{\mathbf{E}} = \epsilon_0(\bar{\epsilon}_a(\mathbf{k}) - 1)\bar{\mathbf{E}}$ and $\mathbf{M}_{\mathbf{E}} = \mu_0(1 - \bar{\mu}_a^{-1}(\mathbf{k}))\bar{\mathbf{H}}$, where $\bar{\mathbf{H}}$ is the averaged magnetic field and we have defined them to include dipole moments only.

The following correspondence between the effective parameters of the two homogenization methods can be written as an equation that operates on $\bar{\mathbf{E}}$

$$\bar{\epsilon} = \bar{\epsilon}_a - \frac{c^2}{\omega^2} \mathbf{k} \times (1 - \bar{\mu}_a^{-1}) \mathbf{k} \times, \quad (3)$$

when keeping first the dipole terms in (1b). While $\bar{\epsilon}$ is independent of the choice of origin, this is not the case¹ of $\bar{\epsilon}_{\mathbf{a}}$ and $\bar{\mu}_{\mathbf{a}}^{-1}$. A shift in coordinate origin therefore turns out to correspond with a shift between the amount of averaged polarization $\bar{\mathbf{P}}$ that is included in each of $\bar{\epsilon}_{\mathbf{a}}$ and $\bar{\mu}_{\mathbf{a}}^{-1}$. In other words, individually Alù's parameters are arbitrary unless the coordinate system is specified, while combined as in (3) they unambiguously describe a given physical system. Another difference between the two formulations is how much each of their respective effective parameters include of the expansion (1b). All terms are represented in $\bar{\epsilon}(\mathbf{k})$, whereas the electric quadrupole and higher order terms are excluded from $\bar{\epsilon}_{\mathbf{a}}$ and $\bar{\mu}_{\mathbf{a}}^{-1}$. This exclusion turns out to be problematic for certain metamaterials.

If $\mathbf{k} \perp \mathbf{P}$ one may rewrite $\mathbf{k} \cdot \bar{\mathbf{Q}}_{\mathbf{E}} \equiv \mathbf{k} \times \mathbf{Q}$ in (1b) where \mathbf{Q} is a vector which may be absorbed into $\mathbf{M}_{\mathbf{E}}$. The electric quadrupole will then have the exact same magnitude as the magnetic dipole, and may therefore be significant, as is already known for several metamaterial systems [6, 7]. Furthermore, despite corresponding to higher order multipoles which are usually disregarded, the last term in (1b) may too in some circumstances be significant. If we have a non-gyrotropic medium so that $\bar{\epsilon}(\omega, \mathbf{k}) = \bar{\epsilon}(\omega, -\mathbf{k})$, then the right hand side of (3) cannot be first order in \mathbf{k} . If it is second order in \mathbf{k} it seems intuitive that the last term of (1b) may, at least under certain circumstances, be significant. To observe a concrete example of this, we will consider a 1D photonic crystal where $\mathbf{k} \perp \mathbf{P} = \epsilon_0[\epsilon(x) - 1]\mathbf{E}$ for which (3) may be written

$$\epsilon(\omega, \kappa) = \epsilon_a(\omega, k) + \frac{2c^2 k^2}{\omega^2} \left(1 - \frac{1}{\mu_a}\right) - k^2 \frac{1}{2d\epsilon_0 \bar{E}} \int_0^d x^2 P dx, \quad (4)$$

when including all terms from (1b). Note that the electric quadrupole contribution is identical with the magnetic dipole contribution, which is why there is a factor 2 multiplied with the second term on the right hand side as compared with (3). Assuming a system with inversion symmetry we find that $M_E \rightarrow 0$ and $\bar{H} \rightarrow 0$ as $k, \omega \rightarrow 0$, so that $(1 - 1/\mu_a) = O(1)$, allowing us to express

$$1 - \frac{1}{\mu_s} \equiv \frac{\omega^2}{2c^2} \frac{\partial^2 \epsilon}{\partial k^2} \Big|_{k=0}, \quad (5a)$$

$$= \frac{\omega^2}{2c^2} \lim_{k \rightarrow 0} \left[\frac{\partial^2 \epsilon_a}{\partial k^2} + \frac{2c^2}{\omega^2} \left(1 - \frac{1}{\mu_a}\right) - \frac{1}{d\epsilon_0 \bar{E}} \int_0^d x^2 P dx \right], \quad (5b)$$

That is, for Silveirinha's local effective permeability the multipole term of order above the electric quadrupole in (4) may be significant. Numerical calculations verify that this is the case.

REFERENCES

1. Agranovich, V. M. and Ginzburg, V. L., *Crystal optics with spatial dispersion, and excitons*, Springer-Verlag, Berlin Heidelberg, 1984.
2. Landau, L. D. and Lifshitz, E. M., and Pitaevskii, L. P., *Electrodynamics of Continuous Media, 2nd ed., Course of Theoretical Physics, Vol. 8*, Elsevier Butterworth-Heinemann, Oxford, 2004.
3. Silveirinha, M. G., "Metamaterial homogenization approach with application to the characterization of microstructured composites with negative parameters", *Phys. Rev. B*, **75** 115104 (2007).
4. Jackson, J. D., *Classical Electrodynamics*, Wiley, New York, 1998.
5. Alù, A., "First-principles homogenization theory for periodic metamaterials", *Phys. Rev. B*, **84** 075153 (2011).
6. Cho, D. J. and Wang, F. and Zhang, X. and Shen, Y. R., "Contribution of the electric quadrupole resonance in optical metamaterials", *Phys. Rev. B*, **78** 121101(R) (2008).
7. Petschulat, J. and Menzel, C. and Chipouline, A. and Rockstuhl, C. and Tünnermann, A. and Lederer, F. and Pertsch, T., "Multipole approach to metamaterials", *Phys. Rev. A*, **78**, 043811 (2008).

¹It is readily seen that $\mathbf{M}_{\mathbf{E}}$ and $\bar{\mathbf{Q}}_{\mathbf{E}}$ depend on the origin from (2). Additionally, changing the coordinate origin to a point \mathbf{r}_0 introduces a phase factor $\exp(i\mathbf{k} \cdot \mathbf{r}_0)$ to the averaged quantities, as seen from (1a), which in turn leads also to a origin dependence in $\bar{\epsilon}_{\mathbf{a}}$.

Superluminal propagation of Dirac-cone modes in photonic crystal slabs.

K. Sakoda^{1,2}

¹National Institute for Materials Science, Japan

²University of Tsukuba, Japan
sakoda.kazuaki@nims.go.jp

Abstract— Apparent superluminal propagation characterized by a divergent group velocity is shown for the Dirac-cone modes in photonic crystal slabs by deriving their dispersion relation in the presence of diffraction loss. An analytical expression connecting the energy velocity to the group velocity is presented. It is shown that the former remains smaller than the speed of light even when the latter diverges.

Superluminal propagation in non-Hermitian systems, which often appears in optical physics, is an important and yet unsolved problem. A well-known example is the exciton polariton in the anomalous dispersion region [1]. The dispersion relation calculated for the complex dielectric constant with a damping term gives a group velocity that is larger than the speed of light, c , for certain frequencies, which contradicts special relativity. In Ref. [1], this problem was dealt with by taking into account the distortion of the wave packet during its propagation and evaluating the time necessary for the peak of the wave packet to reach the observation point that is sufficiently far from the starting point. The calculated value was an averaged velocity for a certain long distance, so it was not proven that the instantaneous group velocity was *always* smaller than c .

In this presentation, we show that the superluminal propagation is also present for the Dirac-cone modes in photonic crystal slabs with diffraction loss. We show this fact by deriving an analytical formula of the group velocity for photonic crystal slabs with the C_{4v} symmetry. We also derive an analytical expression for the energy velocity ($v_e = [\text{spatiotemporal average of Poynting's vector}]/[\text{that of the electromagnetic energy density}]$), which remains smaller than c , so the problem of the violation of special relativity is resolved. We show in particular that the non-Hermitian Dirac-cone dispersion is obtained by solving the eigenvalue problem of the 3×3 matrix,

$$\hat{D} = \begin{pmatrix} -iw & 0 & b'k_x \\ 0 & -iw & b'k_y \\ b'^*k_x & b'^*k_y & 0 \end{pmatrix}, \quad (1)$$

where b' is the slope of the Dirac cone in the absence of the diffraction loss, (k_x, k_y) is the in-plane wave vector, and w is the damping constant of an E mode due to the diffraction loss, which generates the Dirac cone with an A_1 mode [2]. Then, the dispersion relation is given by

$$\omega = \omega_\Gamma + \left(-iw + \sqrt{-w^2 + 4|b'|^2 k^2} \right) / 2, \quad (2)$$

where ω_Γ is the Dirac point frequency. The group velocity ($v_g = \partial\omega/\partial k$) is divergent at $k = w/2|b'|$. However, we can derive the relation between v_e and v_g :

$$v_e = v_g + w \text{Im} \left[A_k \frac{\partial A_k^*}{\partial k} \right], \quad (3)$$

where A_k is the complex amplitude of the E mode in the Dirac-cone mode. We can prove that v_e is always smaller than c even when v_g is divergent. In the presentation, we extend this finding to Dirac cones materialized by different mode combinations and different structural symmetries.

This study was supported by a Grant-in-Aid for Challenging Exploratory Research from Japan Society for the Promotion of Science (Grant number 26610090).

REFERENCES

1. Tanaka, M., Fujiwara, M., Ikegami, H., “Propagation of a Gaussian wave packet in an absorbing medium,” *Phys. Rev. A*, Vol. 34, 4851-4858, 1986.
2. Sakoda, K., “Proof of the universality of mode symmetries in creating photonic Dirac cones,” *Opt. Express*, Vol. 20, No. 22, 25181-25194, 2012.

An integral equation method for the homogenization of periodic inhomogeneous media with complex microstructure

William J. Parnell, Duncan Joyce, Raphael Assier and I. David Abrahams

School of Mathematics, University of Manchester, Oxford Road, Manchester, M13 9PL, UK
William.Parnell@manchester.ac.uk

Abstract— A new method to determine the effective properties of periodic composites is proposed, based on the integral equation form of the governing equations. For ease of illustration the scheme is presented here in the context of the two-dimensional potential problem, e.g. we determine the effective conductivity of a unidirectional fibre-reinforced composite. New, explicit formulae for effective properties are derived that are valid at arbitrary volume fraction, for general lattice configurations and for a wide range of fibre cross-sections.

1. INTRODUCTION

A classical problem in the mechanics of inhomogeneous media is to attempt to replace the two-dimensional potential problem $\nabla \cdot (\mu(\mathbf{x}) \nabla \Phi(\mathbf{x})) = 0$, where $\mathbf{x} = (x, y)$ and $\mu(\mathbf{x})$ is a periodic (scalar) function that varies rapidly with \mathbf{x} , with an equivalent problem of the form

$$\nabla \cdot (\boldsymbol{\mu}_* \nabla \Phi_*(\mathbf{x})) = 0, \quad (1)$$

assuming a so-called *separation of scales* and noting that in general $\boldsymbol{\mu}_*$ is a second order tensor. The process of obtaining (1) is *homogenization* and the problem posed is sufficiently general; μ here could refer to the electrical conductivity, electric permittivity or magnetic permeability in electromagnetic problems or more broadly it could be the antiplane shear modulus, thermal conductivity, etc.

Assume now that $\mu(\mathbf{x})$ is piecewise constant, and the medium takes the form as depicted in Fig. 1 so that the medium is a unidirectional fibre-reinforced composite (FRC), noting that we wish to consider general fibre cross-sections. A number of methods have proved extremely successful at predicting $\boldsymbol{\mu}_*$ including the method of asymptotic homogenization [1] and the equivalent inclusion method [2]. In [3] a new scheme was devised based on the integral equation form of the governing equation, and the leading order result was determined. Here we extend this to higher order terms (valid for higher volume fractions) and show that explicit forms for $\boldsymbol{\mu}_*$ can be determined. We restrict attention to orthotropic media so that $\boldsymbol{\mu}_* = \text{Diag}(\mu_1^*, \mu_2^*)$.

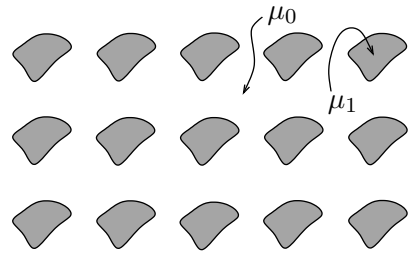


Figure 1: Inhomogeneous medium with piecewise constant $\mu(\mathbf{x})$. The unidirectional fibre reinforced composite medium depicted here has general microstructure, in particular the fibres have non-circular cross-sections.

2. METHODOLOGY AND RESULTS

The governing equation is written in integral equation form which includes a sum over all fibres on the periodic lattice. Taylor expanding the associated Green's function and generating moment averages of the potential gradient fields, coupled with an expansion of the effective properties in powers of the volume fraction leads to a linear system for the determination of the coefficients in this expansion. The shape of the cross-section is incorporated via terms that are akin to Hill polarization tensors and higher order moments of these tensors. It is determined that

$$\frac{\mu_j^*}{\mu_0} = \frac{1 + \mathcal{C}_{1j}\phi + \mathcal{C}_{2j}\phi^2 + \mathcal{C}_{3j}\phi^3 + \mathcal{C}_{4j}\phi^4 + \dots}{1 + \mathcal{D}_{1j}\phi + \mathcal{C}_{2j}\phi^2 + \mathcal{C}_{3j}\phi^3 + \mathcal{C}_{4j}\phi^4 + \dots}, \quad j = 1, 2 \quad (2)$$

where \mathcal{C}_{nj} and \mathcal{D}_{1j} , $j = 1, 2$ and $n = 1, 2, 3, \dots$ depend explicitly on the lattice geometry, the ratio $m = \mu_1/\mu_0$ and the shape of the fibre cross-section. The expression (2) will be called the *IEM order p* method where the expansion on both numerator and denominator includes terms up to $O(\phi^p)$.

We compare this scheme to the method of asymptotic homogenization (MAH) where [1]

$$\frac{\mu_j^*}{\mu_0} = 1 + (m - 1)(\phi + H_{jj}), \quad j = 1, 2, \quad (3)$$

in which H_{jj} is computed via the solution to the so-called *periodic cell problem*. This quantity can also be computed for the Integral Equation Method (IEM) by rearranging the expression in (3) for H_{jj} in terms of μ_j^* and using (2). It is as a convenient (sensitive) measure for method comparison and is plotted in Figs 2 and 3 below for the cases of fibres of circular and rectangular cross-sections. Effective properties for these cases and for elliptical cross-sections are shown on the right of Fig. 3.

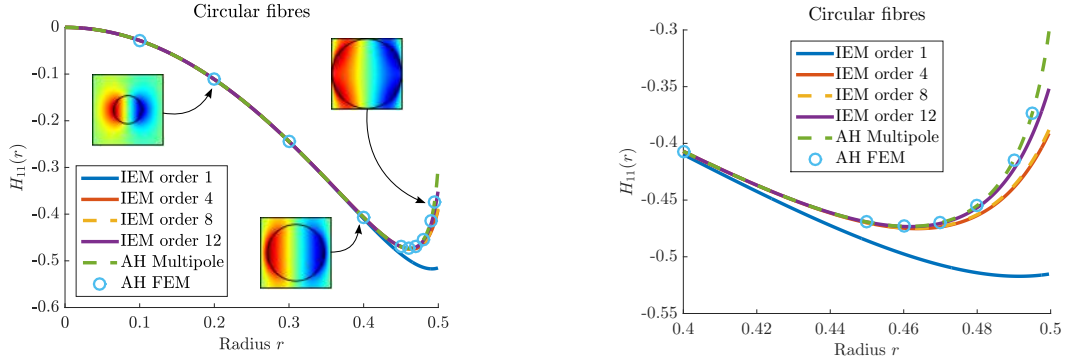


Figure 2: Plot of $H_{11}(r)$ when circular fibres are arranged on a square lattice, with associated solutions of the cell problem from the MAH inset (left) and a close-up for high radii (right).

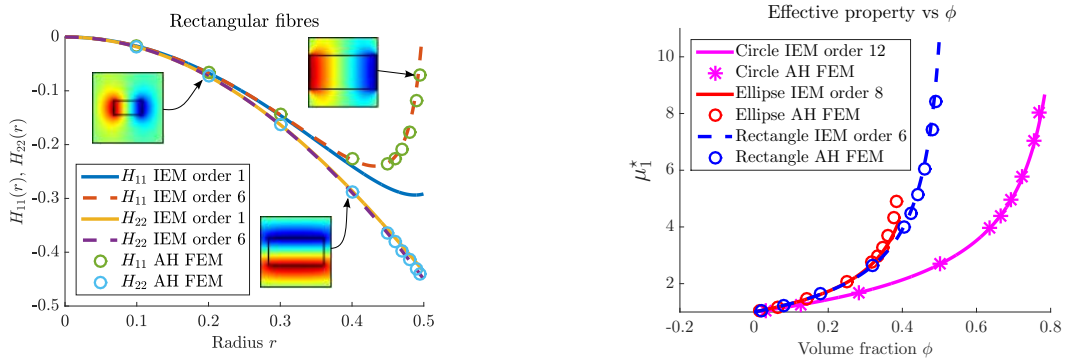


Figure 3: Plot of $H_{11}(r)$ for the situation when rectangular fibres are arranged on a square lattice, with associated solutions of the cell problem from the MAH inset (left) and a plot of the effective property μ_1^* for circular, rectangular and elliptical fibre cross-sections (right).

3. CONCLUSIONS

A new method for homogenization is proposed providing explicit expressions for effective properties of periodic media. Numerous applications reside in the fields of composite media and metamaterials.

ACKNOWLEDGMENT

Parnell is grateful to the EPSRC, for his research fellowship EP/L018039/1. Joyce thanks EPSRC and Thales Underwater Systems Ltd for funding his CASE PhD studentship. Abrahams acknowledges the support of the Royal Society via his Wolfson Research Merit Award (2013–2018).

REFERENCES

1. Parnell, W. J. and Abrahams, I. D. Dynamic homogenization in periodic fibre reinforced media. Quasi-static limit for SH waves, *Wave Motion* Vol. 43, No. 6, 474-498, 2006.
2. Nemat-Nasser, S. and Hori, M., *Micromechanics: Overall Properties of Heterogeneous Materials*. North-Holland, 1999.
3. Parnell, W. J. and Abrahams, I. D. A new integral equation approach to elastodynamic homogenization, *Proc. Roy. Soc. A* Vol. 464, No. 2094, 1461-1482, 2008.

Bounds on Eddy Current Losses Estimate for Soft Magnetic Composites

X. T. Ren^{1*}, R. Corcolle^{1,2}, and L. Daniel¹

¹GeePs | Group of electrical engineering-Paris, UMR CNRS 8507, CentraleSupélec, Univ. Paris-Sud,
Université Paris-Saclay, Sorbonne Universités, UPMC Univ Paris 06
3 & 11 rue Joliot-Curie, Plateau de Moulon 91192 Gif-sur-Yvette CEDEX, France

²NYU Shanghai, Shanghai, China

*corresponding author: xiaotao.ren@geeps.centralesupelec.fr

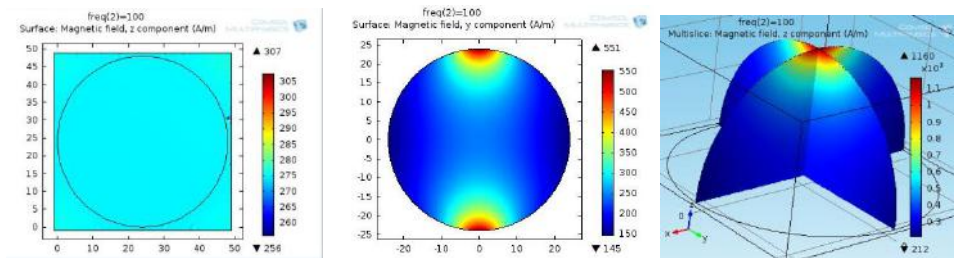
Abstract-Upper and lower bounds for eddy current losses in Soft Magnetic Composites (SMC) treated as a periodic pattern of circular fibers inside a matrix are analytically deduced. The model is validated using numerical simulations. The bounds are found to apply to 3D SMC with spherical inclusions.

Soft Magnetic Composites (SMC) are designed to reduce eddy current losses while maintaining high magnetic permeability. Several approaches can be found to estimate the effective magnetic permeability of composite materials [1-3]. As for Eddy Current (EC) losses, numerical [4] and analytical [5] approaches have been provided for 2D SMC with magnetic field perpendicular to the 2D plane. Under such condition at low frequency, the magnetic field in the whole domain is uniform, which greatly simplifies the problem. However, for 2D SMC with in-plane excitation, analytical deduction of EC losses is much more challenging, because there is no uniformity of the magnetic field. We propose to solve the problem using a homogenization approach to determine information about the distorted field, which leads to lower and upper bounds on EC losses. This method also applies to SMC with spherical inclusions.

Consider an inclusion (circle in 2D, sphere in 3D) of radius R_2 , with linear isotropic permeability μ_2 placed in an infinite medium. The medium is initially filled with a uniform field. Then the field inside the inclusion, \mathbf{H}_2 , is also uniform. At low frequency where the induced magnetic field is negligible, eddy current density in the inclusion can be deduced by solving Maxwell equation. The EC loss density U_2 in inclusion is given by (1) [6]:

$$U_2 = Kf\sigma_2R_2^2\mu_2^2H_2^2 \quad (1)$$

where f is the frequency, σ_2 the conductivity, and K the coefficient ($\pi^2/4$: for 2D case with normal field; $\pi^2/2$: for 2D case with in plane field; $\pi^2/5$: for 3D case).



(a) 2D with normal field (b) 2D with in plane field (c) 3D (Spherical inclusion)

Figure.1. Field Distribution of periodic SMC of square lattice (2D) or cubic lattice (3D)

For periodic SMC, the field inside each inclusion is affected by the neighboring inclusions, with the exception of 2D case with normal field excitation, as shown by numerical computations in Fig. 1.

In the following we focus on the 2D case with in plane field. To apply the homogenization strategy, H_2^2 in (1) is estimated by calculating either the average field ($H_2^2 = \langle \mathbf{H} \rangle_2^2$) or the second order moment ($H_2^2 = \langle \mathbf{H}^2 \rangle_2$). For a rectangular lattice of circular inclusions excited by an arbitrary field $\mathbf{H}=[H_x, H_y]$, noting $H=|\mathbf{H}|$ as average value over the periodic cell, the general solution for the potential in inclusions is [3],

$$\Phi(r, \theta) = H \cdot R_2 \sum_{n=0}^{\infty} (A_n \cos(2n+1)\theta + B_n \sin(2n+1)\theta) \left(\frac{r}{R_2}\right)^{2n+1} \quad (2)$$

where A_n, B_n are unknown real dimensionless coefficients. The average field and second order moment are respectively,

$$\begin{cases} \langle \mathbf{H} \rangle_2 = -H \cdot [A_0, B_0] \\ \langle \mathbf{H}^2 \rangle_2 = H^2 \sum_{n=0}^{\infty} (2n+1)(A_n^2 + B_n^2) \end{cases} \quad (3)$$

By substituting (3) into (1), we obtain

$$\begin{cases} U_{2,1} = \frac{\pi^2}{2} f \sigma_2 R_2^2 \mu_2^2 \langle \mathbf{H} \rangle_2^2 = \frac{\pi^2}{2} f \sigma_2 R_2^2 \mu_2^2 H^2 (A_0^2 + B_0^2) \\ U_{2,2} = \frac{\pi^2}{2} f \sigma_2 R_2^2 \mu_2^2 \langle \mathbf{H}^2 \rangle_2 = \frac{\pi^2}{2} f \sigma_2 R_2^2 \mu_2^2 H^2 \sum_{n=0}^{\infty} (2n+1)(A_n^2 + B_n^2) \end{cases} \quad (4)$$

Solving Maxwell equations, eddy current density can be deduced, and the exact EC loss density is obtained:

$$U_2 = \frac{\pi^2}{2} f \sigma_2 R_2^2 \mu_2^2 H^2 \sum_{n=0}^{\infty} \frac{A_n^2 + B_n^2}{n+1} \quad (5)$$

It is clear from (4) and (5) that

$$U_{2,1} \leq U_2 \leq U_{2,2} \quad (6)$$

Similar inequality applies for spherical inclusions. Numerical calculations of EC losses have been performed and compared to the analytical estimates.

The results show that the bounds on the EC losses in SMC can be obtained from homogenization information about the magnetic field distribution. The average field and second order moment of the magnetic field, which can be obtained from an effective permeability estimate, enable one to bound the EC losses in SMC with circular fibers or sphere inclusions.

REFERENCES

1. Lam, J., "Magnetic permeability of a simple cubic lattice of conducting magnetic spheres," *J. Appl. Phys.*, Vol. 60, No. 12, 4230-4235, 1986
2. Sihvola, A. H., *Electromagnetic Mixing Formulae and Applications*, The Institution of Engineering and Technology, London, 1999.
3. Godin, Y. A., "Effective complex permittivity tensor of a periodic array of cylinders," *J. Math. Phys.*, Vol. 54, No. 5, 053505, 2013.
4. Ren, X. T., R. Corcolle, and L. Daniel, "A 2D finite element study on the role of material properties on eddy current losses in soft magnetic composites," *Eur. Phys. J.-Appl. Phys.*, Vol. 73, No. 2, 20902, 2016
5. De la Barriere, O., M. LoBue, and F. Mazaleyrat. "Semianalytical and analytical formulas for the classical loss in granular materials with rectangular and elliptical grain shapes," *IEEE Trans. Magn.*, Vol. 50, No.10, 1-8, 2014.
6. Ren, X. T., R. Corcolle, and L. Daniel, "Homogenization of soft magnetic composites with the incorporation of eddy current losses into complex permeability," [In preparation]

Effective-medium theory for coated particles and magnetic metamaterials

Shiyang Liu^{1,2*}, Jialin Zhou¹, Xinning Yu¹, Huajin Chen², and Zhifang Lin²

¹Institute of Information Optics, Zhejiang Normal University, Jinhua, Zhejiang 321004, China

²State Key Laboratory of Surface Physics and Department of Physics, Fudan University, Shanghai 200433, China

*corresponding author, E-mail: syliu@zjnu.cn

Abstract

An effective-medium theory (EMT) is developed for the coated particles based on coherent potential approximation, which is then extended to the magnetic metamaterials (MMs). It is shown that a surface charged dielectric nanoparticle (CDNP) is equivalent to an equal-size neutral particle with different constitutive parameters, which is helpful for the understanding of the phenomena related to the CDNPs such as the vanishing scattering, the enhanced absorption, as well as the surface charge induced surface plasmon resonance. When applied to MMs, the EMT can take into account the anisotropy of the MMs exactly, which is instructive for the related nonreciprocal effects.

1. Introduction

In designing composite materials, including both structured materials and structured particles, in the long wavelength limit they can be considered equivalently as either homogeneous media or homogenous particles with effective constitutive parameters. Therefore, it is significantly important to retrieve these parameters (effective electric permittivity ϵ_{eff} and effective magnetic permeability μ_{eff}), for the understanding of exotic electromagnetic properties of metamaterials [1] such as negative index materials [2, 3] and zero index materials [4, 5], as well as the composite particles such as multilayered particles [6] and charged particles [7]. Based on the coherent potential approximation, we develop an effective-medium theory (EMT) for composite particles with regular boundaries, which can be generalized straightforwardly to the metamaterials consisting of regular sub-wavelength building blocks such as cylinders and spheres.

2. Theoretical framework

For the composite particles the typical configurations that can be solved analytically within the framework of the Mie theory and the coherent potential approximation are coated cylinders, coated spheres, and CDNPs, which are schematically illustrated in Fig. 1. As a typical paradigm, we concentrate our attention on CDNPs as shown in Fig. 1(c).

2.1. Mie coefficients for CDNP

For definiteness, it is supposed that a homogeneous spherical particle with the radius R , the permittivity ϵ_s , and the permeability μ_s in free space is concerned. Different from

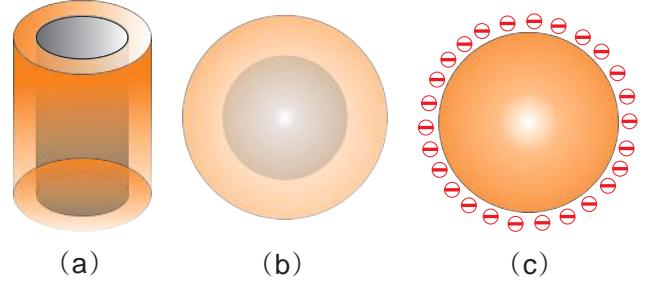


Figure 1: Schematic illustration of three typical composite particles (a) coated cylinder, (b) coated sphere, and (c) charged sphere.

a neutral particle, the electromagnetic field can drive a surface current for the charged particles, thus converting the boundary conditions. As a result, the tangential component of magnetic field is no longer continuous, which transforms the Mie coefficients to [8]

$$a_n = \frac{\mu_s k \psi'_n(mx) [\psi_n(x) - g \psi'_n(x)] - \mu_0 k_s \psi_n(mx) \psi'_n(x)}{\mu_s k \psi'_n(mx) [\xi_n(x) - g \xi'_n(x)] - \mu_0 k_s \psi_n(mx) \xi'_n(x)}, \quad (1a)$$

$$b_n = \frac{\mu_s k \psi_n(mx) [\psi'_n(x) + g \psi_n(x)] - \mu_0 k_s \psi'_n(mx) \psi_n(x)}{\mu_s k \psi_n(mx) [\xi'_n(x) + g \xi_n(x)] - \mu_0 k_s \psi'_n(mx) \xi_n(x)}, \quad (1b)$$

with

$$g = i\omega\mu_0 k^{-1} \sigma_s = i\omega\mu_0 k^{-1} \frac{i\eta e/m_e}{\omega + i\gamma_s} = -\frac{f\Phi}{x} \frac{\omega}{\omega + i\gamma_s}, \quad (2)$$

where $x = kR$ is the size parameter with $k = \omega\sqrt{\epsilon_0\mu_0}$ the wavenumber in the vacuum, $\psi_n(x) = xj_n(x)$, $\xi_n(x) = xh_n^{(1)}(x)$ are the Ricatti-Bessel functions, $m = k_s/k$ is the refractive index of the dielectric particle with $k_s = \omega\sqrt{\epsilon_s\mu_s}$ the wavenumber inside the particle, σ_s is the effective surface conductivity [8, 9], e/m_e is the charge-to-mass ratio of electron, $f = \frac{\epsilon_0\mu_0 e}{m_e} = 1.96 \times 10^{-6}$ is just a constant, $\Phi = |\eta|R/\epsilon_0$ is the electrostatic potential due to the surface charge with the static surface charge density η , and the parameter $\gamma_s \approx k_B T/\hbar$ [10] at room temperature $T = 300$ K with k_B the Boltzmann constant, T the thermodynamic temperature, and \hbar the Planck constant. For the special case with $g = 0$, the Mie coefficients in Eq. (1) are reduced to those for a neutral particle. Evidently, the surface charge can alter the scattering properties of a dielectric particle, alternatively, it can be concluded that by surface charging a

dielectric particle we can tailor its electromagnetic properties.

2.2. EMT for CDNP

On the condition that $x \ll 1$ and $mx \ll 1$, namely, in the long wavelength limit the scattering properties of the charged particles mainly arise from $n = 1$ terms, while the high order Mie coefficients are almost negligible. Based on the coherent potential approximation [11, 12], the effective permittivity ε_e and effective permeability μ_e of the charged sphere can be retrieved when treated as a neutral one. The process of the EMT is as follows: (i) Suppose we have a homogenous neutral background medium with constitutive parameters ε_e and μ_e ; (ii) We can then calculate the scattering efficiency Q_{sca} when the charged particle is immersed in the background; (iii) If the scattering efficiency Q_{sca} vanishes, it can be concluded that ε_e and μ_e are the effective constitutive parameters for the equivalent neutral particle. Mathematically, we should just replace k , ε_0 , μ_0 , and x in Eq. (1) with $k_e = \omega\sqrt{\varepsilon_e\mu_e}$, ε_e , μ_e , and $x\sqrt{\varepsilon_e\mu_e}$, namely, replacing the vacuum with the supposed background. The vanishment of Q_{sca} leads to the near-zero Mie coefficients, corresponding to $a_1 = 0$ and $b_1 = 0$ in the long wavelength limit. By taking $x \rightarrow 0$, the Riccati-Bessel functions and their derivatives can be further approximated to be $\psi_1(x) \cong x^2/3$, $\psi_1'(x) \cong 2x/3$, $\xi_1(x) \cong x^2/3 - i/x$, and $\xi_1'(x) \cong 2x/3 + i/x^2$. As a result, we can finally arrive at

$$\varepsilon_e = \varepsilon_s + \frac{2g\varepsilon_0}{x}, \quad \left(1 - \frac{gx\mu_s}{2\mu_0}\right)\mu_e = \mu_s. \quad (3)$$

It should be noted that the equations are reduced to $\varepsilon_e = \varepsilon_s$, $\mu_e = \mu_s$ for $g = 0$, corresponding to a neutral particle case as is certain. Considering the fact that $gx\mu_s \approx -f\Phi \frac{\omega}{\omega + i\gamma_s} \rightarrow 0$, the differences between the effective neutral particle and the charged particle $\Delta\varepsilon = \varepsilon_e - \varepsilon_s$ and $\Delta\mu = \mu_e - \mu_s$ can be deduced

$$\Delta\varepsilon = -\frac{2f\Phi}{x^2} \frac{\omega}{\omega + i\gamma_s} \varepsilon_0, \quad (4a)$$

$$\Delta\mu \approx -\frac{f\Phi}{2} \frac{\omega}{\omega + i\gamma_s} \frac{\mu_s^2}{\mu_0}. \quad (4b)$$

From Eq. (4), we can find that the permeability difference $\Delta\mu$ is usually negligible due to the fact that $f\Phi \ll 1$, while the permittivity difference $\Delta\varepsilon$ could be significantly large provided that the size of the spherical particle is very small compared to the wavelength for a sufficiently large surface potential Φ .

3. Discussion

3.1. CDNP related effects

We first examine the permittivity difference $\Delta\varepsilon$ for a CDNP with the fixed size parameter $x = 0.05$ versus the circular frequency. The numerical results are shown in Fig. 2(a), where we can find that the real part decreases fast in the first stage and then reaches a saturation value, while the

imaginary part exhibits an evident peak at a lower frequency range and then vanishes at higher frequency. These properties indicate that one can tailor the effective permittivity of a CDNP by adjusting its surface potential, especially at high frequency. The scattering properties of a CDNP can be precisely evaluated by calculating the scattering, extinction, and absorption efficiency [13]

$$Q_{sca} = \frac{2}{x^2} \sum_n (2n+1)(|a_n|^2 + |b_n|^2), \quad (5a)$$

$$Q_{ext} = \frac{2}{x^2} \sum_n (2n+1)\text{Re}\{a_n + b_n\}, \quad (5b)$$

and $Q_{abs} = Q_{ext} - Q_{sca}$. According to Eq. (4), the effective permittivity of a CDNP tends to ε_0 around optical frequency provided that the surface potential is equal to $\Phi \approx (\varepsilon_s - \varepsilon_0)x^2/2f\varepsilon_0$, thus leading to the vanishing of the scattering efficiency Q_{sca} of the CDNP. As illustrated in Fig. 2(b) by the red solid line, for the CDNP at the surface potential $\Phi \approx 637$ V the scattering efficiency is almost vanished in accord with the fact that the real part of effective permittivity $\text{Re}\{\varepsilon/\varepsilon_0\}$ is nearly equal to 1 as marked by blue dashed line in Fig. 2(b). In this case, the CDNP seems to be invisible to the incident light.

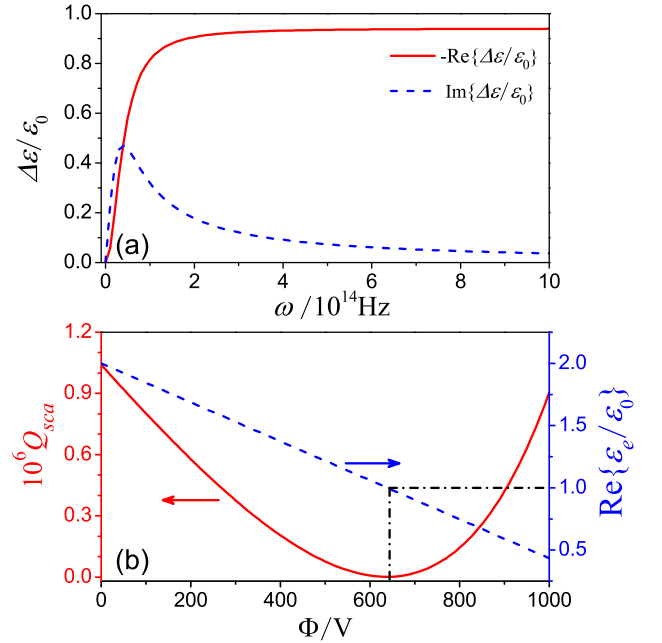


Figure 2: (a) The permittivity difference $\Delta\varepsilon$ versus circular frequency ω for the CDNP with the fixed size parameter $x = 0.05$ and the fixed surface potential $\Phi = 600$ V. (b) The scattering efficiency Q_{sca} and the effective permittivity ε_e as the function of the surface potential Φ at the fixed circular frequency $\omega = 1.5 \times 10^{15}$ Hz for the CDNP with $x = 0.05$, $\varepsilon_s = 2\varepsilon_0$, and $\mu_s = \mu_0$.

It is well known that the surface plasmon resonance of a spherical metal particle is located at $\varepsilon_s = -2\varepsilon_0$ in the long wavelength limit. Interestingly, a dielectric particle was also shown to exhibit such resonance via surface charging by

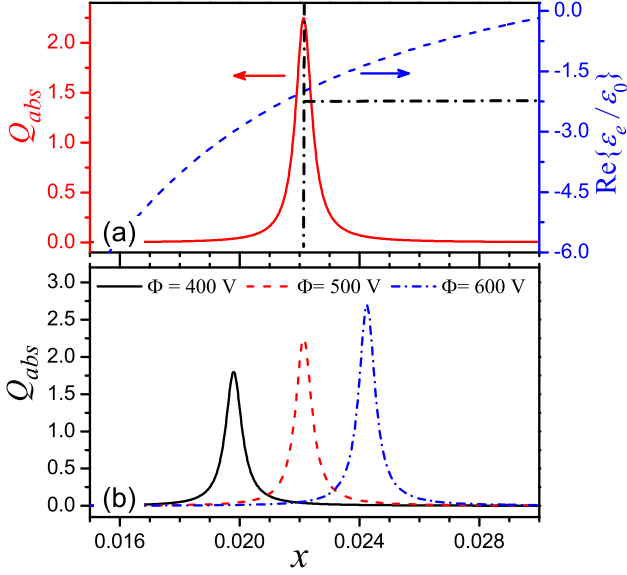


Figure 3: (a) The absorption efficiency Q_{abs} and the real part of effective permittivity ε_e are plotted as the functions of the size parameter x for a CDNP under a fixed surface potential $\Phi = 500$ V. (b) The absorption efficiency Q_{abs} versus the size parameter x under three different surface potentials $\Phi = 400$ V, $\Phi = 500$ V, and $\Phi = 600$ V. The frequency of the surface plasmon resonance can be tuned by surface potential as indicated by the peaks of the absorption efficiency Q_{abs} . The other parameters are $R = 5$ nm, $\varepsilon_s = 2\varepsilon_0$, and $\mu_s = \mu_0$.

Rosenkrantz and Arnon [7]. Since the effective permittivity of a dielectric sphere can be tailored significantly by surface charging, the surface plasmon resonance can be realized on the condition that the real part of the effective permittivity is equal to $-2\varepsilon_0$, which corresponds to $\frac{f\Phi}{x^2} \approx 1 + \frac{\text{Re}\{\varepsilon_s\}}{2\varepsilon_0}$ as can be acquired from Eq. (3). The numerical results are shown in Fig. 3(a), where we present the absorption efficiency Q_{abs} and the effective permittivity ε_e as the functions of size parameter x for a CDNP. The surface plasmon resonance can be determined by the peak of the absorption efficiency, which comes into appearance exactly at $\varepsilon_e = -2\varepsilon_0$ at a particular frequency for the fixed surface potential $\Phi = 500$ V. Moreover, the surface plasmon resonance can be tailored by the surface potential as illustrated in Fig. 3(b), where we can find the higher surface potential can shift the resonance to higher frequency, offering another freedom in manipulating the electromagnetic properties of the charged particles.

3.2. Generalization to MMs

The idea of coherent potential approximation can also be extended to consider the metamaterials composed of the building blocks with regular boundaries such as the cylindrical and spherical geometries [11, 12]. The scenarios of the corresponding EMT can be illustrated with the aid of the schematic diagram shown in Fig. 4 as follows: (i) Transfor-

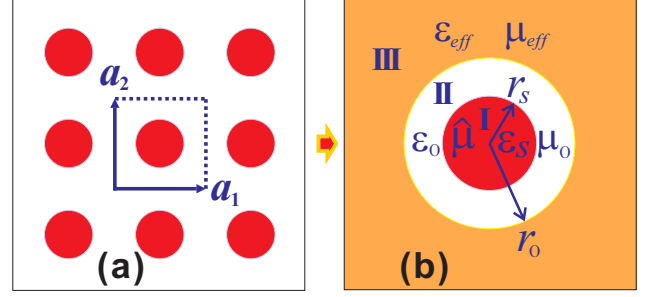


Figure 4: (a) A two-dimensional metamaterials consisting of the infinite long rods arranged periodically as square lattice in the air background, and (b) the corresponding geometry treated approximately in the EMT. The red circles, the white region, and the dark yellow region correspond to the infinite long rods, the isotropic homogeneous background, and the effective medium, respectively.

m the periodic metamaterial in Fig. 4(a) into the effective homogeneous medium with the effective permittivity ε_{eff} and the effective permeability μ_{eff} in Fig. 4(b); (ii) Take the unit cell of the metamaterial marked in Fig. 4(a) approximately as an equal-area coated rod with the rod as the inner core and the background medium as the coated layer with radius $r_0 = a/\sqrt{\pi}$ for the case of a square lattice. The metamaterial with hexagonal lattice can be considered similarly, but with a different radius of the coated layer $r_0 = \frac{\sqrt{3}}{\sqrt{2\pi}}a$; (iii) The effective constitutive parameters ε_{eff} and μ_{eff} can be retrieved on the condition that the total scattering of the coated rod in the effective medium vanishes in the long wavelength limit $k_0\sqrt{\varepsilon_{eff}}\sqrt{\mu_{eff}}r_0 \ll 1$ with k_0 the wave-number in the background medium.

Besides the composite particles and the electromagnetic metamaterials, the concept of coherent potential approximation based EMT can also be extended to acoustic metamaterials [14] and the elastic metamaterials [15] to retrieve the corresponding effective parameters. Here, our concentration is focused on the former case. As a typical example, we present the effective constitutive parameters for an MM composed of an array of ferrite rods of the radius $r_s = 2$ mm arranged periodically as square lattice with lattice constant $a = 8$ mm. The permittivity of the ferrite rods is $\varepsilon_s = 15$ and the saturation magnetization is $M_s = 1750$ Oe, operating under an external magnetic field (EMF) $H_0 = 500$ Oe. The effective permittivity ε_{eff} and permeability μ_{eff} acquired by the EMT are shown in Fig. 5(b), where ε_{eff} and μ_{eff} are denoted by the red solid line and the blue dashed line, respectively. The photonic band diagram are calculated as well as shown in Fig. 5(a) to confirm the validity of the effective constitutive parameters from the EMT. It should be pointed out that the simultaneous positive or negative effective constitutive parameters correspond to photonic bands, while the single negative or positive constitutive parameter corresponds to the photonic band gaps. Concretely, in the frequency range $0.05 < \omega a/2\pi c < 0.075$, simultaneous positive ε_{eff} and

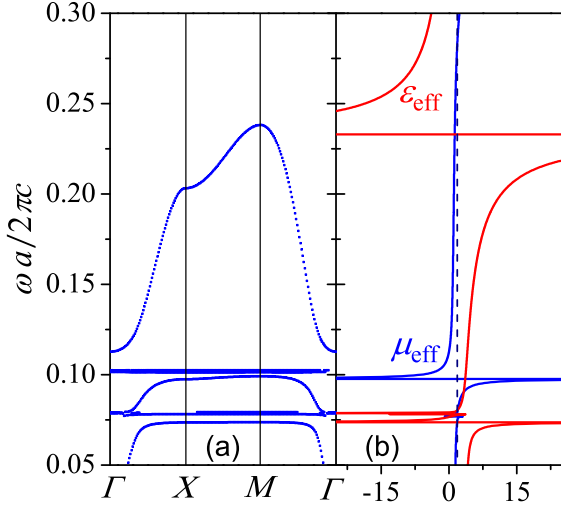


Figure 5: The photonic band diagram (a) and the effective constitutive parameters of the MM are calculated in the long wavelength range $a/\lambda \in [0.05, 0.3]$. The related parameters of the MM are $a = 8$ mm, $r_s = 2$ mm, $\epsilon_s = 15$, $M_s = 1750$ Oe, and the EMF satisfies $H_0 = 500$ Oe.

μ_{eff} appear, which implies a positive refractive index, corresponding to the first photonic band. In the vicinity of the frequency $\omega a/2\pi c = 0.075$ both electric and magnetic resonances appear, which leads to the formation of the photonic band gap and the flat bands, originating from the spin wave resonance [16]. Then, in the frequency range $0.08 < \omega a/2\pi c < 0.1$ simultaneous positive ϵ_{eff} and μ_{eff} appear again, corresponding to the photonic band. At the frequency near to $\omega a/2\pi c = 0.1$ another magnetic resonance appears, resulting in the form of a dense set of flat bands and the photonic band gaps. This resonance arises from the magnetic surface plasmon resonance of the ferrite rods, which can induce strong nonreciprocal effects such as unidirectional waveguiding [17] and reflection [18]. Above the magnetic surface plasmon resonance both μ_{eff} and ϵ_{eff} are positive until the emergence of the second electric resonance, which correspond to the photonic band in the frequency range $0.12 < \omega a/2\pi c < 0.24$ and the photonic band gap above, respectively.

4. Conclusions

In conclusion, we present an effective-medium theory based on coherent potential approximation, which can be used to retrieve the effective constitutive parameters for the surface charged dielectric nanoparticles. Some interesting phenomena such as the vanishing scattering, the remarkably enhanced absorption, and the tailorable surface plasmon resonance are demonstrated and interpreted based on the effective-medium theory. It is then extended to the metamaterial system and the effective constitutive parameters for magnetic metamaterials are acquired, which are in good agreement with the photonic band diagram calculation.

Acknowledgement

This work is supported by the China 973 Project (No. 2013CB632701), National Natural Science Foundation of China (Nos. 11274277, 11574055, and 11574275), MOE of China (B06011), Zhejiang Provincial Natural Science Foundation of China (LR16A040001), and the open project of State Key Laboratory of Surface Physics (KF2016_3) in Fudan University.

References

- [1] D. R. Smith, J. B. Pendry, M. C. K. Wiltshire, Metamaterials and negative refractive index, *Science* 305: 788–792, 2004.
- [2] J. B. Pendry, Negative refraction makes a perfect lens, *Phys. Rev. Lett.* 85: 3966–3969, 2000.
- [3] R. Shelby, D. R. Smith, S. Schultz, Experimental verification of a negative index of refraction, *Science* 292: 77–79, 2001.
- [4] M. G. Silveirinha, N. Engheta, Tunneling of electromagnetic energy through subwavelength channels and bends using ϵ -near-zero materials, *Phys. Rev. Lett.* 97: 157403, 2006.
- [5] X. Q. Huang, Y. Lai, Z. H. Hang, H. H. Zheng, C. T. Chan, Dirac cones induced by accidental degeneracy in photonic crystals and zero-refractive-index materials, *Nat. Mater.* 10: 582–586, 2011.
- [6] Y. Huang, Y. J. Feng, T. Jiang, Electromagnetic cloaking by layered structure of homogeneous isotropic materials, *Opt. Express* 15: 11133–11141, 2007.
- [7] E. Rosenkrantz, S. Arnon, Enhanced absorption of light by charged nanoparticles, *Opt. Lett.* 35: 1178–1180, (2010).
- [8] J. Klačka, M. Kocifaj, Scattering of electromagnetic waves by charged spheres and some physical consequences, *J. Quant. Spectrosc. Radiat. Transf.* 106: 170–183, 2007.
- [9] C. F. Bohren, A. J. Hunt, Scattering of electromagnetic waves by a charged sphere, *Can. J. Phys.* 55: 1930–1935, 1977.
- [10] J. Klačka, M. Kocifaj, On the scattering of electromagnetic waves by a charged sphere, *Prog. Electromagn. Res.* 109: 17–35, 2010.
- [11] Y. Wu, J. S. Li, Z. Q. Zhang, C. T. Chan, Effective medium theory for magnetodielectric composites: Beyond the long-wavelength limit, *Phys. Rev. B* 74: 085111, 2006.
- [12] J. F. Jin, S. Y. Liu, Z. F. Lin, S. T. Chui, Effective-medium theory for anisotropic magnetic metamaterials, *Phys. Rev. B* 80: 115101, 2009.

- [13] C. F. Bohren, D. R. Huffman, *Absorption and Scattering of Light by Small Particles*, John Wiley, 1983.
- [14] X. H. Hu, K. M. Ho, C. T. Chan, J. Zi, Homogenization of acoustic metamaterials of Helmholtz resonators in fluid, *Phys. Rev. B* 77: 172301, 2008.
- [15] Y. Wu, Y. Lai, Z. Q. Zhang, Effective medium theory for elastic metamaterials in two dimensions, *Phys. Rev. B* 76: 205313, 2007.
- [16] S. Y. Liu, J. J. Du, Z. F. Lin, R. X. Wu, S. T. Chui, Formation of robust and completely tunable resonant photonic band gaps, *Phys. Rev. B* 78: 155101, 2008.
- [17] S. Y. Liu, W. L. Lu, Z. F. Lin, S. T. Chui, Molding reflection from metamaterials based on magnetic surface plasmons, *Phys. Rev. B* 84: 045425, 2011.
- [18] J. J. Yu, H. J. Chen, Y. B. Wu, S. Y. Liu, Magnetically manipulable perfect unidirectional absorber based on nonreciprocal magnetic surface plasmon, *EPL* 100: 47007, 2012.

Photonics, Optics and Laser Technology

Novel platform for Optical Modulation Using Silicon Photonics

Mohamed A. Swillam

Department of Physics, School of Mathematics and Physics, The American University in Cairo, New Cairo,
Egypt, 11835

*corresponding author: m.swillam@aucegypt.edu.

Abstract-We propose novel platform for integrated sensing and modulations using silicon nanowires. The nanowires can be easily fabricated using metal assisted chemical etching (MACE). The dimensions of these nanowires can be easily controlled using the time and temperature of the etching process.

Silicon photonics attracts great attention in the last decade due to its ease of fabrication and high tolerance and fabrication yield which. However, silicon lacks good electro optic properties and depends on carrier diffusion process in order to change its optical characteristics. This process is slow and depends mainly on the speed of carrier generation and recombination. Hence the speed of modulation using this approach is limited to few giga Hertz only. Reaching higher modulation speed using silicon technology is a challenge that require the incorporation of other material that has fast electro optic response. In this work we utilize silicon organic hybrid platform using silicon nanowires (SiNWs) based optical waveguides [1].

These SiNWs allow for highly sensitive waveguide platform which require less switching power and faster response. Few novel designs using this platform have been proposed and discussed. These designs include, directional coupler configuration, and multimode interference devices. The proposed platform proved to be more sensitive to the change in the organic material than other configurations. It is also easy to fabricate and control. It also provide faster modulation speed.

Using this platform we are proposing novel components with superior performances including optical switches, modulators, and sensors. The enhanced performance of these components is mainly due to novel nature of the waveguides which becomes highly sensitive to any surrounding changes.

Acknowledgements This work was made possible by a NPRP award [NPRP7456-1-085] from the Qatar National Research Fund (member of the Qatar Foundation). The statements made herein are solely the responsibility of the authors.

REFERENCES

1. R. Gamal, Y Ismail, M. A. Swillam, " Optical biosensor based on a silicon nanowire ridge waveguide for lab on chip applications," *Journal of Optics*, 17 (4), 045802, 2015.

Plasma technology for industrial wastewater treatment and hydrogen production

Erik S. Lotfi

Qatar University, Qatar

Abstract. This study aims to review the previous research work taken towards this technology for the treatment of wastewater and hydrogen production that could guide for creating a new system that combines the two applications for the reduction of the consumed energy. The study will undertake all the related previous work in order to discuss the feasibility of the new proposed system for its application in the industrial scale.

Treatment of wastewater released from the industrial sector is an essential matter to achieve in order to overcome its negative impact on the environment and human being. As the industrial sector generates its wastewater with extremely hazardous pollutants, reaching highest efficiency for their removal is mandatory before sewage disposal to the aquatic life. Several treatment methods have been applied such as biological, chemical oxidation, adsorption and ion exchange, and filtration systems. However, these methods meet further limitations in their applicability including the system efficiency, capacity, running cost, and area required for installation. Among the treatment technologies, several studies were taken towards the applicability of plasma technology for sewage treatment. This radiation system is highly efficient for the removal of contaminants in limited time, while high energy consumption limits its applicability in the industrial scale. Alternatively, plasma technology has further application in providing clean energy from the vaporized water in which the mechanism depends on the electrolysis process for hydrogen production. Plasma application for radiation treatment has several methods including glow discharge electrolysis, dielectric barrier discharge, and pulsed corona discharge. Several studies recommend the dielectric barrier discharge (DBD) method for water purification that could be applicable for large scales since the system produces non-equilibrium plasma without rising in temperature. Therefore, there is no cooling system required for this method which is recommended for the reduction of the consumed energy. The treatment method takes place through the transformation of liquid water to plasma in which the sewage is accelerated to high speed and converted to liquid/gas mixture with applying high voltage for electric discharge. This conversion leads to the release of UV radiation, electric fields, and shockwaves that aids in the removal of hazardous pollutants and killing of microorganisms. This study aims to review the previous research work taken towards this technology for the treatment of wastewater and hydrogen production that could guide for creating a new system that combines the two applications for the reduction of the consumed energy. The study will undertake all the related previous work in order to discuss the feasibility of the new proposed system for its application in the industrial scale. This new system will be taken through a prototype model in which the study will consider the operational parameters that control the process of treatment and hydrogen production. These parameters include but are not limited to the reactor geometry and design, flowrate, power supply, and control system. The study will continue to undertake the optimization of the operational parameters for its scalability in the future works. The generated sewage will be selected according to the characteristics of the wastewater that contains high amount of hydrocarbons and aromatic compounds since they are good donors for hydrogen production.

Recent progresses for EMC applications: numerical and experimental tools

Optimization of EMC shielding procedures by means of statistical re-sampling: from mean trends to reliability assessments

S. Lall ch re¹, C. Kasmi², J. Lopes-Esteves², S. Girard¹, P. Bonnet¹, and F. Paladian¹

¹UBP, Institut Pascal CNRS UMR 6602, France

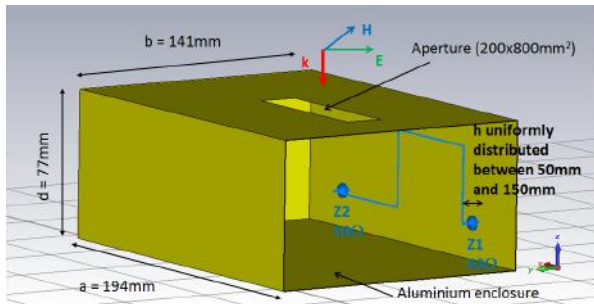
²ANSSI, Wireless Security Lab, France
sebastien.lallechere@univ-bpclermont.fr

Abstract— This proposal aims to demonstrate the benefit that could be expected from re-sampling methods for electromagnetic compatibility (EMC) test cases subject to random variations. Based upon Monte Carlo simulations, the use of bootstrap-like approaches will provide optimized confidence levels for stochastic assessments. Based upon statistical assumptions, the optimization process is validated and quantified in view of electromagnetic field-to-wire coupling inside EMC enclosure.

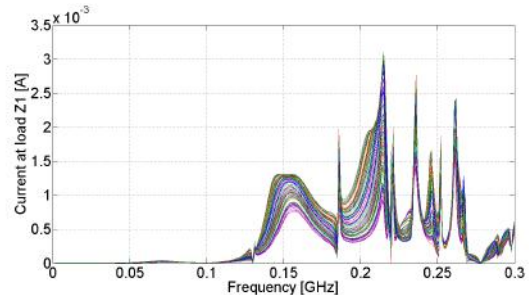
1. EMC CONTEXT AND MOTIVATIONS

The importance of stochastic susceptibility testing for electronic systems has been demonstrated regarding transmission lines (TLs) in several recent works [1, 2, 3, 4]. Although a large diversity of electromagnetic (EM) tools and test devices exist to model above systems, their structure and/or EM environment (enclosures, sources) lead to the inadequacy of purely deterministic strategies. Indeed, the variability is inherent to a huge number of EMC issues, e.g. due to environmental drifts (thermal, mechanical, EM), ignorance of inputs parameters (such as the geometries and/or materials of TLs). In this framework, the ElectroMagnetic Interference/Compatibility (EMI/EMC) communities have shown a growing interest over the past years for the assessment of the maximum confidence in simulation [1, 2, 3, 4] and also experiments [5]. To this end and without exhaustiveness, uncertainty quantification and propagation techniques such as Polynomial Chaos Expansion (PCE) [1], Stochastic Collocation (SC) [2], Extreme Values Theory [3] (EVT), stochastic fields decomposition [4] have provided interesting results. Despite all, EMC analysis, for technical and industrial constraints (mainly costs), naturally requires the minimization of the number of experiments.

2. STATEMENT OF THE PROBLEM



(a)



(b)

Figure 1: (a): Mock-up of the simulation set-up with CST . (b): MC simulations with several random realizations (heights of TLs).

This proposal is focusing on the statistical assessment of the penetration of EM field inside a cabinet, e.g. see Fig. 1a (several examples will be presented in the final paper): the height (h) is assumed to be uniformly distributed between 50 and 150 mm inside the enclosure that is illuminated by an arbitrarily chosen plane wave. Monte Carlo (MC) simulations [4] are often considered as reference approach; in this proposal, time domain simulations (using finite integral

technique, CST©) are serially achieved based upon MC set of inputs. Since MC methods are known for their low convergence rate, the aim of this work is to propose advanced strategy for assessing precise statistics and safe margins with reduced number of simulations. Fig. 1b gives an overview of the statistical dispersion of the results considering dozens of MC simulations, justifying the importance of computing maximum confidence levels. We propose to optimize use of re-sampling techniques [6] in this context.

3. EMC OPTIMIZATION OF CLASSICAL AND BAYESIAN BOOTSTRAPS

Bootstrapping procedures are based on new observations obtained by randomly taking sets of the original data, increasing sequentially the size m of samples. Since it was firstly introduced by Efron in 1979, many paradigms of the technique exist (e.g. Bayesian Bootstrap (BB) [6]), but few criteria are available to ensure the quality of bootstrapping replications. The final paper will give details about re-sampling methods used in this work and their optimization in EMC framework.

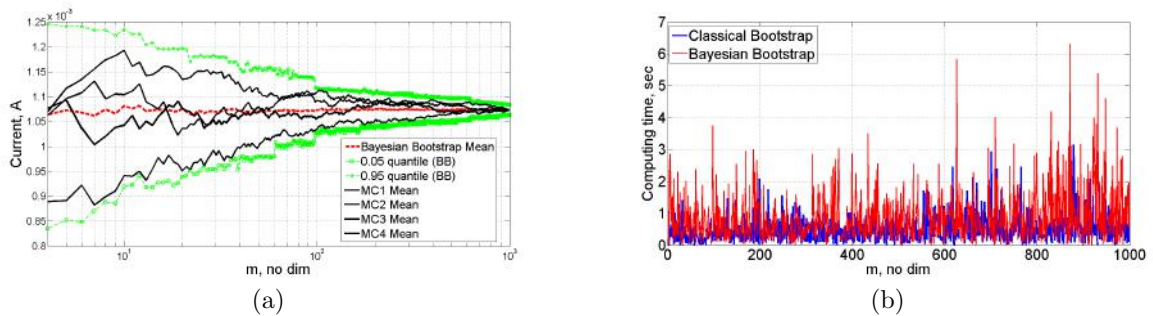


Figure 2: (a): BB assessments of mean and confidence levels VS MC results for current at load $Z1$ and $f = 210$ MHz. (b): Re-sampling computing time (sec) following classical and Bayesian bootstraps (Fig. 2a).

Fig. 2a shows the precision and quick convergence of BB procedure for the evaluation of the mean current at load $Z1$ (Fig. 1a) comparatively to MC simulations. Results are given in function of parameter m that stands for the number of bootstrapping samples [6]. The efficiency of the proposed approach is validated in Fig. 2b both regarding the similar computing time (several seconds for different sizes of sampling m) of bootstrap and BB in comparison with simulation time needed for one MC realization (here about 230 sec). This justifies the benefit expected from the real-time inclusion of bootstrapping procedures since convergence rates are improved with more than 30% gain relatively to crude MC approach. In the final paper, we will demonstrate the robustness of bootstrapping procedures for several EMC applications and the assessment of high-orders statistics (e.g. quantiles), and lay emphasis on the interests of BB in comparison to classical re-sampling.

REFERENCES

1. Manfredi, P. and Canavero, F. C., “Efficient Statistical Extraction of Per-Unit-Length Capacitance and Inductance Matrices of Cables with Random Parameters,” *Advanced Electromagnetics, AEM*, Vol. 4, No. 1, 22–30, 2015.
2. Lall ch re, S., Jannet, B., Bonnet, P. and Paladian, F., “Sensitivity Analysis to compute stochastic problems in uncertain and complex electromagnetic environments,” *Advanced Electromagnetics, AEM*, Vol. 1, No. 3, 13–23, 2012.
3. Kasmi, C., H lier, M., Darces, M., and Prouff, E., “Generalised Pareto distribution for extreme value modelling in Electromagnetic Compatibility,” *Electronics Letters*, Vol. 5, No. 49, 334–335, 2013.
4. Magdowski, M. and Wick, R., “Numerical Simulation of the Stochastic Electromagnetic Field Coupling to Transmission Line Networks,” in *Proceedings of the Joint IEEE Int. Symp. on EMC and EMC Europe*, Dresden, Germany, Aug. 2015, 818-823.
5. Kasmi, C., Lall ch re, S., Girard, S., Prouff, E., Bonnet, P. and Paladian, F., “Real-Time Radiated Tests Optimization using Bottstrap Module,” in *Proceedings of the Asia Electromagnetics Symposium (ASIAEM)*, Jeju, Republic of Korea, Aug. 2015.
6. Rubin, D. B., “The Bayesian Bootstrap,” *The Ann. of Stat.*, Vol. 9, No. 1, 130–134, 1981.

Microwave microscopy: Effect of material deposition on the distributions of E/H-fields in the vicinity of electronic circuits

J. Rossignol¹, D. Stuerger¹, G. Bailly¹, V. Colin¹, J. Dufresne¹, S. Lall  ch  re², and S. Girard²

¹Laboratoire interdisciplinaire Carnot Bourgogne, UMR 6303, UBFC, France

²UBP, Institut Pascal CNRS UMR 6602, France

*corresponding author: jerome.rossignol@u-bourgogne.fr

Abstract— This proposal is devoted to a collaborative approach dealing with microwave microscopy experiments. The application is dedicated to electromagnetic field cartography above circuits and the influence of nanometric material layer deposition on the circuits. The first application is associated to microstrip circuits. The results are in agreement with the simulated fields. The second application is focused on the effects of a dielectric layer deposited on the circuit and its impact in terms of electric modes propagation and shielding effectiveness.

1. INTRODUCTION

Recent functionalities in microelectronic have induced an increasing development of new materials inside integrated circuit (IC) and particular systems to characterize them [1]. Only few studies about the electromagnetic interferences have combined material science and electromagnetic compatibility (EMC) fields [2], even if the importance of material science in EMC is known for a long time [3]. The authors develop a collaborative project which associates these disciplines, using the microwave microscopy [4] along with numerical simulation comparisons. The objectives are to explore the influence of new materials (such as nanometric layers) on circuits and their effects on the distribution of electromagnetic (EM) fields.

2. EXPERIMENTAL SETUP

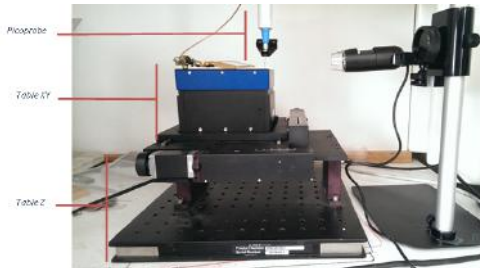


Figure 1: Experimental set-up of the microwave imager.

As shown in Fig. 1, the experimental set-up is composed of a positioning stage including XY- and Z-components with respectively spatial resolutions of 20 μm and 5 nm at horizontal (XY) and vertical (Z) levels. The device under test is placed on the XYZ stage in order to move the circuit under the electric probe (fixed with its own cable). Thus, the analysis system excludes all mechanical stress on the probe which would induce significant perturbations during the measurements. It is composed of home-made E- and H-fields probes connected to a spectrum analyzer which may be replaced by a vector network analyzer (VNA). The whole set-up is monitored by LabVIEW  interface.

3. FIRST RESULTS AND EM(C) IMPACT OF

MATERIAL DEPOSITION

The first experiments are focused on the E/H-fields mapping of usual circuits. A micro-strip resonant ring structure is used (Fig. 2, left); the resonance is estimated at 2.67 GHz by VNA (ZVB) measurements. Circuit feed is achieved with a signal generator (−10 dBm). According to the theoretical models the electromagnetic propagation is a transverse magnetic mode. The numerical simulation of H-field confirms this hypothesis since two symmetric lobes are observed (Fig. 2, right). Figure 3 shows the results of the numerical simulation (right) and the experimental measurements (left) of normalized Hx field at 3 mm above the circuit. The estimated values agree well between simulations and experiments.

The second part of this work will be associated to the effect of a dielectric layer composed of nanometric particles. In this case, we chose TiO_2 particles (specifically Degussa P25) which is a mixture of two TiO_2 crystallographic (anatase and rutile). TiO_2 [5] material is widely used

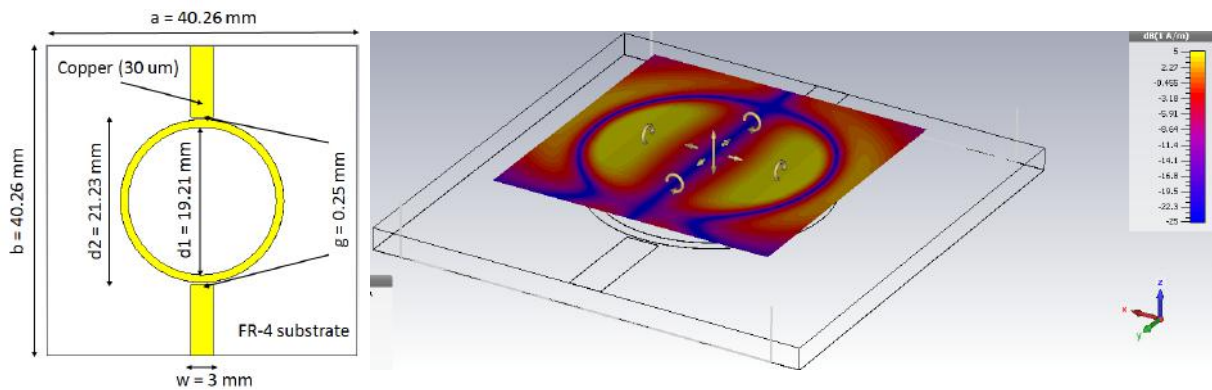


Figure 2: Mock-up of micro-strip ring resonator (left). Simulated normal H-field at $z = 3$ mm (right).

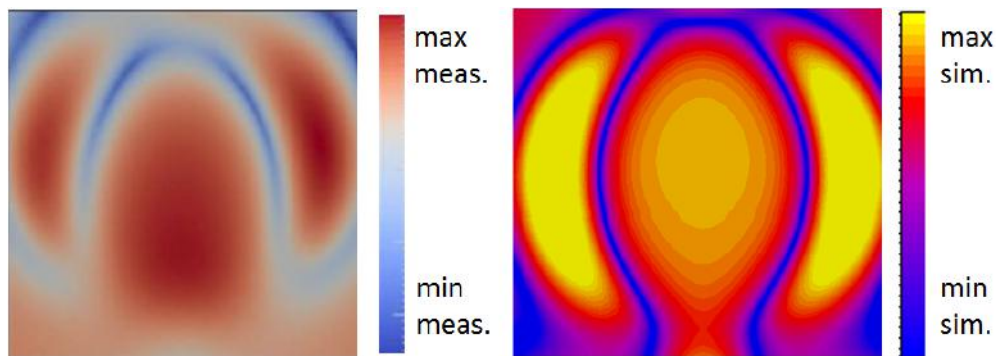


Figure 3: Normalized Hx component from measurements (left) and CST simulations (right) at 2.67 GHz.

in photovoltaic cells, white paintings and EMC shielding [6]. The mean crystallite sizes are respectively 49 nm (rutile) and 26 nm (anatase). The layer is obtained according to a simple doctor blade protocol with a thickness estimated around 25 μm (mechanical profilometer). The microwave circuit under investigation is here a classical patch antenna designed at 2.4 GHz (VNA measurements). The comparison of the simulation and the experimental results will be discussed in the final paper and will allow to assess the shielding effectiveness of the proposed structures.

REFERENCES

1. Geetha, S., Kumar, K. K. S., Rao, C. R. K., Vijayan, M., and Trivedi, D. C., "EMI shielding: Methods and materials - A review," *Journal of Applied Polymer Science*, vol. 112, 2073–2086, 2009.
2. Land, S. O., Tereshchenko, O., Ramdani, M., Leferink, F., and Perdirau, R., "Printed Circuit Board Permittivity Measurement Using Waveguide and Resonator Rings," *Proceedings of EMC'14*, Tokyo, Japan, 777–780, 2014.
3. Dixon, D. S. and Masi, J., "Thin Coatings Can Provide Significant Shielding Against Low Frequency EMF Magnetic Fields," *Proceedings of IEEE International Symposium on EMC*, Denver, USA, 1035–1040, Aug. 1998.
4. Rossignol, J., Plassard, C., Bourilot, E., Calonne, O., Foucault, M., Lesniewska, E. "Non-destructive technique to detect local buried defects in metal sample by scanning microwave microscopy," *Sensors and actuators A: Physical*, vol. 186, 219–222, 2011.
5. Gressel-Michel, E., Chaumont, D., Stuerga, D. "From a microwave flash-synthesized TiO₂ colloidal suspension to TiO₂ thin films," *Journal of colloid and interface Science*, vol. 285, 674–9, 2005.
6. Sarto, F., Sarto, M. S., Larciprete, M.C., Sibilia, C. "Transparent films for electromagnetic shielding of plastics," *Reviews on advanced materials science*, vol. 5, 329–336, 2005.

Kapton-based 1x2 passive antenna array physical parameters sensitivity analysis

Y. G. Rabobason, B. Ravelo*, and N. Benjelloun

IRSEEM EA 4353, ESIGELEC, Avenue Galilée, 76801 Saint Etienne du Rouvray, France

*corresponding author, E-mail: ravelo@esigelec.fr

Abstract

This paper describes a multivariable sensitivity analysis of Kapton-based flexible antenna versus the design physical parameters. The proposed analysis is focused on the 1x2 antenna array integrating microstrip Tee-power divider. The antenna reflection loss variation in function of the substrate relative permittivity and the microstrip antenna physical parameters varied randomly in normal distribution with +/- 5% standard deviation under 20 trials is performed. This numerical investigation is based on the Monte Carlo statistical analysis. The performed Monte Carlo trials quantify the combined effects due to the antenna length and width associated with the Kapton HN substrate relative permittivity.

1. Introduction

Recent investigation reveals a great interest on the flexible antenna design [1]. This emerging technology will be undeniably implemented into the wearable and embedded wireless communication devices. This future generation of antenna is particularly promising for the implementation on low cost substrate as plastic and paper. Those substrates offer a possibility to design bended electronic printed circuits [2-5].

Nowadays, various applications of flexible antenna system can be widely envisaged. Thanks to the flexible properties and its miniature ability, a compact size antenna for WLAN operation was proposed in [2]. Furthermore, with flexible Hilbert-curve loop antenna targeted exhibiting triple-band and omnidirectional pattern, WLAN/WiMAX applications were also introduced in [3]. More generally, telemedicine [4] and RFID [5] applications were also developed. Design methodologies of passive and switching 1x2 antenna arrays implemented on flexible Kapton substrate were recently proposed in [6-7]. However, so far, the sensitivity of the plastic or Kapton based antenna remains an open question of the RF design and fabrication engineers. Similar to all emerging technology, the flexible antenna performances can be considerably modified in function of the design and fabrication parameter uncertainties.

As a concrete real case, it was pointed out in [6] that the flexible Kapton based antenna resonance frequency and matching level can be outstandingly different between the simulations and measurements. For the numerical

understanding, the antenna array sensitivity analysis versus design physical parameters must be conducted. In the present paper, the deep analysis on the deviation between the simulated and measured return loss of the flexible antenna structure implemented in [6] will be investigated based on the Monte Carlo approach.

2. Description of the Kapton-based 1x2 antenna array under study

The 1x2 antenna array proposed in [6] is considered as the test structure investigated in the present paper. Basically, it can be assumed as a planar distributed circuit comprised of couple of patch antenna associated with a microstrip Tee-power divider (T-PWD).

2.1. Characteristic of the flexible substrate

The flexible dielectric substrate used for the tested circuit is consisted of a polyimide substrate layer synthesized by the polymerization between an aromatic di-anhydride and a diamine [8]. The considered Kapton HN type presents physical characteristics recapitulated in Table 1.

Table 1: Characteristics of the dielectric substrate and the metallization used to design the antenna structure.

Designation	Parameter name	Value
Dielectric constant	ϵ_r	3.3
Dielectric Loss tangent	$\tan(\delta)$	0.007
Substrate thickness	h	125 μ m
Cu metallization conductivity	σ	5.8 $\times 10^7$ S/m
Cu metallization thickness	t	17 μ m

This dielectric substrate can maintain its excellent physical, electrical and mechanical properties over a temperature range of several hundred °C. Furthermore, it offers excellent resistance to chemicals, there is no known organic solvent, does not melt, does not burn and can be used in high or low temperatures.

2.2. Design of the passive antenna array

The designed and simulated flexible 1x2 antenna array design under study is depicted in Fig. 1(a). The photograph of the flexible antenna prototype is displayed in Fig. 1(b). The nominal parameters addressed in Table 2 were obtained after synthesis of the T-PWD and the patch antenna parameters.

Table 2: Nominal physical parameters of the antenna structure proof of concept.

Parameter	Value [mm]
$W_p = W_{patch}$	17.84
$L_p = L_{patch}$	13.79
W_{sub}	92.26
L_{sub}	51.30
W_1	0.34
W_2	0.30
d_1	11.05
d_2	35.76

In the first view, it acts as planar circuit implemented in microstrip technology. However, the entire printed circuit board (PCB) can be bended geometrically on arbitrary shape structures as highlighted in Fig. 1(b).

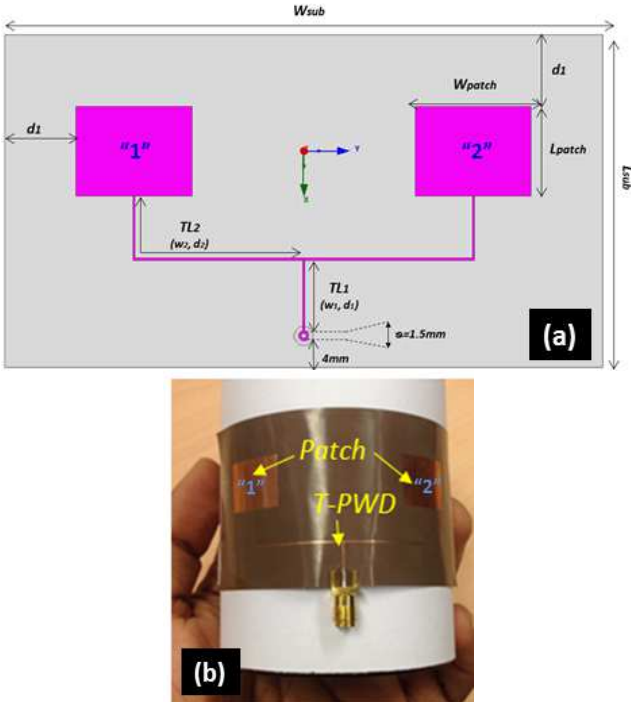


Figure 1: (a) Design and (b) photograph of the flexible 1x2 antenna array under study.

This flexible 1x2 antenna array was simulated by using the microwave circuit design and simulator ADS®. Comparison between simulated and measured return loss S_{11} in the work frequency from 5.75GHz to 6.25GHz was realized in Fig. 2 [6]. It can be pointed out that that among the differences, the resonance frequency shift was occurred.

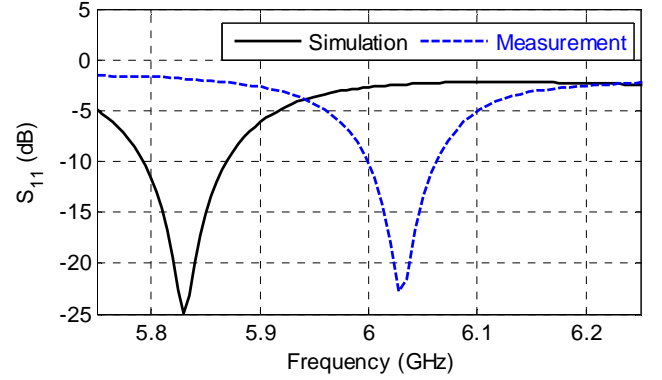


Figure 2: Simulated and measured return losses from the flexible antenna structure introduced in Fig. 1.

For the further understanding on the sources of the discrepancies, a multivariable sensitivity analysis is conducted in the next section.

3. Multivariable parameters Monte Carlo sensitivity analysis

The present Monte Carlo analysis is carried out with the random statistical approach. It materializes the antenna structure sensitivity analysis with respect to the different parameters L_{p_1} , L_{p_2} , W_{p_1} , W_{p_2} and ϵ_r .

3.1. Analytical methodology

The purpose of the Monte Carlo analysis is the investigation of the return loss and the resonant frequency in function of the mechanical fabrication uncertainties and the substrate material variations. To do this, the following multivariable approach materialized by the following functions envisaged:

$$S_{11} = \psi_{S_{11}}(L_{p_1}, L_{p_2}, W_{p_1}, W_{p_2}, \epsilon_r), \quad (1)$$

and

$$f_r = \psi_f(L_{p_1}, L_{p_2}, W_{p_1}, W_{p_2}, \epsilon_r). \quad (2)$$

In these expressions, subscripts “1” and “2” correspond respectively to antennas “1” and “2” as illustrated in Fig. 1. The modelling of the analytical functions is out of the scope of the present work. However, the trends of the antenna structure matching will be numerically investigated in the next paragraph.

3.2. Sensitivity analysis results

The numerical computation of the performed sensitivity analyses was run with +/-5% standard deviation of the multivariate parameters L_p and W_p constituting each antenna element.

The present sensitivity methodology lies on the random statistical simultaneous variations of the assumed antenna physical parameters. The generated numerical variables explored in this study were realized with 20 Monte Carlo trials. For each combination of the parameters corresponding to each trial, the antenna structure return loss S_{11} was computed with the randomly chosen independent variables. The standard values of the patch antenna variables L_p and W_p and ϵ_r for the different trials are plotted in Fig. 3. The corresponding computed numerical results are displayed in Fig. 4. For the further insight on the matching positions and levels in function of the input parameters, the resulting numerical values are addressed in Table 3.

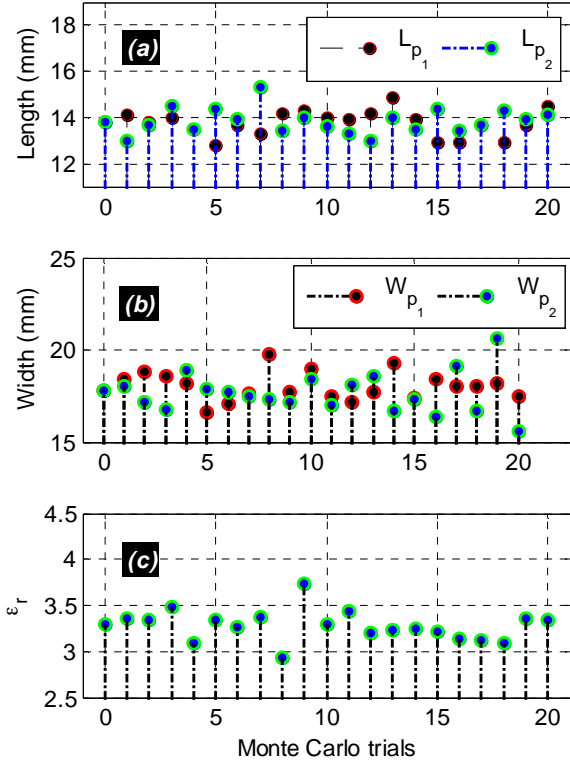


Figure 3: Monte Carlo analysis variables corresponding to the patch antennas (a) length L_{patch} and (b) width W_{patch} and the substrate permittivity ϵ_r .

With 20 trials Monte Carlo analysis, it can be emphasized that the resonance frequency f_r of the overall structure under study are shifted from 5.44GHz to 6.40GHz. Moreover, this frequency shift is due to both the effective permittivity variation and the physical length L_p . Moreover, the return loss matching is varied from -35.26dB to -9.89dB. The observed effect can be interpreted with the variation of the terminal antenna input impedance in function of W_p . In addition, it can be observed that with the random normal values of L_p also that the antenna array structure is susceptible to generate a couple of resonance frequency between approximately 5GHz and 6GHz.

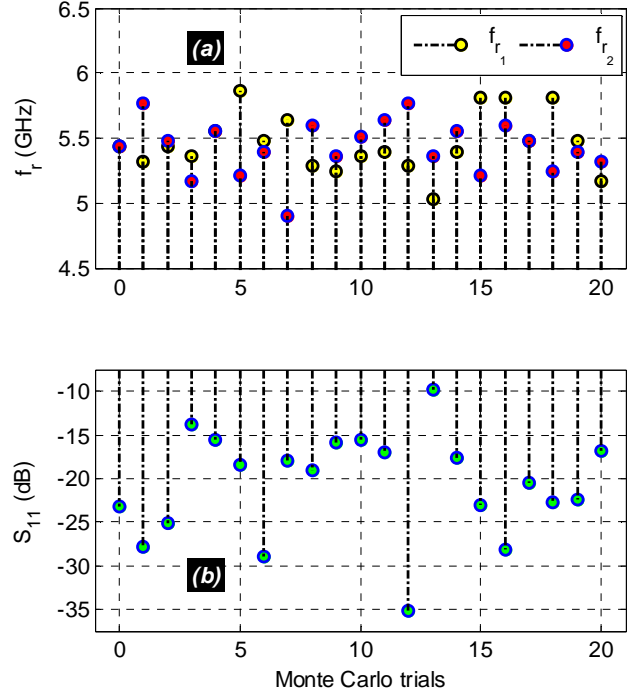


Figure 4: (a) Resonance frequency and (b) return loss Monte Carlo analysis results from the structure shown in Fig. 1(a) under 20 trials.

Table 3: Monte Carlo analysis results from the structure shown in Fig. 1(a) under 20 trials of (a) W_{p_1} [mm] and W_{p_2} [mm] and ϵ_r , and (b) L_{p_1} [mm] and L_{p_2} [mm] and S_{11} [dB].

Trial	ϵ_r	L_{p1}	L_{p2}	W_{p1}	W_{p2}	S_{11}
0	3.300	13.8	13.8	17.8	17.8	-23.25
1	3.355	14.1	13	18.4	18	-27.83
2	3.346	13.8	13.7	18.8	17.2	-25.07
3	3.491	14	14.5	18.6	16.8	-13.81
4	3.097	13.5	13.5	18.2	18.9	-15.53
5	3.342	12.8	14.4	16.6	17.9	-18.46
6	3.263	13.7	13.9	17.1	17.7	-28.96
7	3.378	13.3	15.3	17.6	17.5	-17.91
8	2.938	14.2	13.4	19.8	17.3	-18.99
9	3.742	14.3	14	17.7	17.2	-15.93
10	3.301	14	13.6	19	18.4	-15.49
11	3.444	13.9	13.3	17.5	17	-17.06
12	3.202	14.2	13	17.2	18.1	-35.26
13	3.231	14.9	14	17.7	18.6	-9.89
14	3.249	13.9	13.5	19.3	16.7	-17.69
15	3.210	12.9	14.4	17.4	17.3	-23.04
16	3.144	12.9	13.4	18.4	16.4	-28.20
17	3.126	13.7	13.7	18	19.1	-20.58
18	3.086	12.9	14.3	18	16.7	-22.75
19	3.354	13.7	13.9	18.2	20.6	-22.48
20	3.350	14.5	14.1	17.5	15.6	-16.82

4. Conclusions

A sensitivity analysis of flexible 1x2 passive antenna array printed on the Kapton substrate is examined. It acts as a microstrip structure. The proof of concept circuit was designed to operate at 5.8GHz [6]. The difference between the simulations and measurements of the return loss exhibited by this proof of concept motivated us to realize sensitivity analysis. It was highlighted with Monte Carlo statistical analysis that the antenna structure is particularly sensitive to the Kapton substrate relative permittivity and the physical size with only +/-5% standard deviation.

In the future, the proposed methodology can be considered by the antenna designers to predict the influence of the manufacturing imperfection and the material parameters variation. In function of the mechanical fabrication uncertainties and the dielectric substrate relative permittivity variations, the antenna performance can be estimated and optimized.

Acknowledgements

This research work was supported by Euripides²-Eureka Program funded by the research project "Embedded Die Design Environment & Methodology for Automotive Applications (EDDEMA)", 2015-2018.

References

- [1] A. C. Durgun, M. S. Reese, C. A. Balanis, C. R. Birtcher, D. R. Allee, S. Venugopal, Design, simulation, fabrication and testing of flexible bow-tie antennas, *IEEE Trans. Ant. Prop.*, Vol. 59, No. 12, pp. 4425–4435, Dec. 2011.
- [2] H.-Y. Chien, C.-Y.-D. Sim, C.-H. Lee, Compact size dual-band antenna printed on flexible substrate for WLAN operation, *Proc. Int. Symp. on Antennas and Propagation (ISAP) 2012*, Nagoya, Japan, pp. 1047–1050, 29 Oct. - 2 Nov. 2012.
- [3] D. O. Kim, C. Y. Kim, D. G. Yang, Flexible Hilbert-curve loop antenna having a triple-band and omnidirectional pattern for WLAN/WiMAX applications, *Int. Journal Antenna and Propagation*, Vol. 2012, pp. 1–9, 2012.
- [4] H. R. Raad, A. I. Abbosh, H. M. Al-Rizzo, D. G. Rucker, Flexible and compact AMC based antenna for telemedicine applications, *IEEE Trans. on Ant. and Propag.*, Vol. 61, No. 2, pp. 524–531, Feb. 2013.
- [5] D. L. Paul, L. Zhang, L. Zheng, Flexible dual-band LCP antenna for RFID applications, *Proc. URSI International Symposium on Electromagnetic Theory (EMTS) 2013*, Hiroshima, Japan, pp. 973–976, 20-24 May 2013.
- [6] Y. G. Rabobason, G. P. Rigas, S. Swaisaenyakorn, B. Mirkhaydarov, B. Ravelo, M. Shkunov, P. R. Young, N. Benjelloun, Design of flexible passive antenna array on Kapton substrate, *Progress In Electromagnetics Research (PIER) C*, Vol. 63, pp. 105-117, 2016.
- [7] Y. G. Rabobason, G. P. Rigas, S. Swaisaenyakorn, B. Mirkhaydarov, B. Ravelo, M. Shkunov, P. R. Young, N. Benjelloun, Design and synthesis of flexible switching 1x2 antenna array on Kapton substrate, *To be published in Eur. Phys. J. Appl. Phys. (EPJAP)*, 2016, pp. 1-10.
- [8] Available Online, http://www2.dupont.com/Kapton/en_US/assets/downloads/pdf/HN_datasheet.pdf, Accessed 2014.

Silicon photonic devices and integration

Demonstration of integrated optical matrix-vector multiplier based on two-dimensional silicon microring resonator array

Lei Zhang, Hao Jia, Jianfeng Ding, and Lin Yang*

State Key Laboratory on Integrated Optoelectronics, Institute of Semiconductors, CAS, Beijing, China

*corresponding author: oip@semi.ac.cn

Abstract—We report the proposal and demonstration of an integrated optical matrix-vector multiplier. We introduce the principle and show the advantages compared with its free-space counterpart. We present the latest experimental results and evaluate the limit of performance.

Matrix-vector multiplication (MVM) is one of the most common operations that are widely used in modern digital signal processing. MVM is mainly employed in digital image processing, radar and sonar signal processing, coherent optical communication, etc. Due to the inherent architecture of very large scale integrated circuit (VLSI), MVM implemented using VLSI is time-consuming and energy-intensive. Inspired by the intrinsic parallelism offered by optical information processing, many efforts have been made to develop optical systems that can implement such a parallelizable operation. The Stanford multiplier proposed in [1] is one of these examples. It uses a light source array (LSA) to represent the vector and a two-dimensional spatial light modulator (SLM) to represent the matrix. Two lens systems are employed to deliver light from the LSA to the SLM and collect them to a photodetector array in a specific way.

There are mainly three limitations that impede the scalability and performance of the Stanford multiplier. Firstly and apparently, the discrete elements used in the system makes it extremely sensitive to vibration and hard to calibrate. Secondly, it's quite difficult to get large-scale SLM with high switching elements. Thirdly and most importantly, the optical system design for large-size SLM is quite difficult.

To overcome these limitations, we have proposed an integrated optical MVM using wavelength-selective modulator array as the SLM, which is a two-dimensional silicon microring resonator array [2, 3]. Compared with the Stanford multiplier, discrete elements can be potentially eliminated and the fabrication of large-scale SLM with high switching elements is feasible. Most importantly, we employ a new degree of freedom—the wavelength to avoid the free-space propagation and thus no related design problems. The delivery of optical signals to the SLM is within the SLM plane, which cannot be done in traditional Stanford multiplier. Here in this report, we will present the latest experimental results with high-speed silicon microring resonator modulators and evaluate the limit of performance of the system due to the material characteristics and fabrication accuracy.

REFERENCES

1. J. W. Goodman, A. R. Dias, L. M. Woody, “Fully parallel, high-speed incoherent optical method for performing discrete Fourier transforms,” *Opt. Lett.* 2(1), 1–3 (1978).
2. L. Zhang, M. Geng, L. Yang, L. Jia, H. Tian, P. Chen, T. Wang, and Y. Liu, “A silicon-based integrated optical vector-matrix multiplier,” CN patent #2011/10116741.0.
3. L. Yang, R. Ji, L. Zhang, J. Ding, and Q. Xu, “On-chip CMOS-compatible optical signal processor,” *Opt. Express* 20(12), 13560–13565 (2012).

Fano resonance photonic crystal Si membrane photonics

Weidong Zhou^{1*}, Deyin Zhao¹, Hongjun Yang¹, Zhenqiang Ma² and Mattias Hammar³

¹Department of Electrical Engineering, University of Texas at Arlington, TX 76019, USA

²Department of Electrical and Computer Engineering, University of Wisconsin-Madison, WI 53706, USA

³KTH-Royal Institute of Technology, School of Information and Communication Technology, Elecctrum 229,
164 40 Kista, Sweden

*corresponding author: wzhou@uta.edu

Abstract- We review surface-normal Fano resonance photonic crystal membrane photonic devices based on heterogeneously integrated crystalline semiconductor nanomembranes on both Silicon and flexible substrates. Devices to be reviewed include two types of photonic crystal surface emitting membrane lasers on silicon substrates, close to unity absorption from monolayer graphene based on critically coupled photonic crystal cavities, and multi-band multi-color imaging arrays. Finally nanomembrane enabled flexible RF electronics/optoelectronics will also be introduced.

Crystalline semiconductor nanomembranes (NMs), which are transferable, stackable, bondable and manufacturable, offer unprecedented opportunities for unique electronic and photonic devices for vertically stacked high density photonic/electronic integration, high performance flexible electronics, and adaptive flexible/conformal photonics. Over the last few years, we have been carrying out research on various photonic and electronic devices, based on transfer printing techniques and heterogeneous integration of III-V/Si material systems.[1] In this talk, we will review some of the research accomplishments we made over the last few years on this emerging and exciting field, with focuses on stamp-assisted transfer-printed photonic crystal nanomembrane lasers on Si for Si photonics[2], Fano resonance photonic crystal membrane reflectors, critical coupling enhanced absorption [3], and ultra-high Q optical filters, based on coupled bi-layer photonic crystals with lattice displacements.[4, 5]

Work is supported by US ARO (W911NF-15-1-0431), NSF (ECCS-1308520), and AFOSR (FA9550-16-1-0010).

REFERENCES

1. Zhou, W., Zhao, D., Shuai, Y.-C., Yang, H., Chuwongin, S., Chadha, A., Seo, J.-H., Wang, K.X., Liu, V., and Ma, Z., 'Progress in 2d Photonic Crystal Fano Resonance Photonics', *Progress in Quantum Electronics*, 2014, 38, (1), pp. 1-74.
2. Yang, H., Zhao, D., Chuwongin, S., Seo, J.-H., Yang, W., Shuai, Y., Berggren, J., Hammar, M., Ma, Z., and Zhou, W., 'Transfer-Printed Stacked Nanomembrane Lasers on Silicon', *Nature Photonics*, 2012, 6, (9), pp. 617-622.
3. Liu, Y., Chadha, A., Zhao, D., Piper, J.R., Jia, Y., Shuai, Y., Menon, L., Yang, H., Ma, Z., and Fan, S., 'Approaching Total Absorption at near Infrared in a Large Area Monolayer Graphene by Critical Coupling', *Applied Physics Letters*, 2014, 105, (18), p. 181105.
4. Shuai, Y., Zhao, D., Tian, Z., Seo, J.-H., Plant, D.V., Ma, Z., Fan, S., and Zhou, W., 'Double-Layer Fano Resonance Photonic Crystal Filters', *Optics Express*, 2013, 21, (21), pp. 24582-24589.
5. Shuai, Y., Zhao, D., Chadha, A.S., Seo, J.-H., Yang, H., Fan, S., Ma, Z., and Zhou, W., 'Coupled Double-Layer Fano Resonance Photonic Crystal Filters with Lattice-Displacement', *Applied Physics Letters*, 2013, 103, (24), p. 241106.

Novel Application and Design for Silicon Photonic Devices

Xiao-Ping Liu*, Ming-Hui Lu, and Yan-Feng Chen

National Laboratory of Solid State Microstructures, Nanjing University, Nanjing, Jiangsu 210093, China

*corresponding author: xpliu@nju.edu.cn

Abstract- After decades of development, silicon photonic platform is becoming one of the most influential platforms for exploring novel concepts of photonic applications and device designs. In this talk, we will first present an investigation of Bloch oscillations (BO) on a silicon photonic lattice under the parity-time symmetry modulation, and we show that the dynamic of traditional BO can be largely altered and the resulted parity-time symmetry BO is accompanied with a strong secondary emission. Next, we will present an object oriented device design for various integrated photonic devices. In particular, we show that novel, high performance ultra-compact waveguide crossing and mode converter are possible.

The research of silicon photonic, although inspired by the need of on-chip optical interconnection, has evolved rapidly with its touch in various multidisciplinary field. A strong example is that there is a large portion of recent research interest being devoted into the field of optics physics on a fully integrated platform. BO is a fundamental transport phenomenon originated from solid-state physics. It is characterized by a coherent oscillatory motion of electron in a periodic potential driven by an external DC electric field¹. BO has also been observed in other wave systems, e.g., matter waves, optical waves, acoustical waves and surface plasmon polariton(SPP) waves. Recently, it has been shown that parity-time symmetric modulation of a wave system can has a profound effect on its wave dynamics². In this talk, we present our experimental investigation of parity-time symmetry BO in a silicon photonic lattice composed by an array of bent dissipative silicon waveguides shown in the inset of Fig. 1a). By directly visualizing the BO in real space, we show that there exists secondary emission due to the parity-time symmetry breaking, which is evident from the our simulation in Fig. 1b) and from the near field image in Fig. 1c).

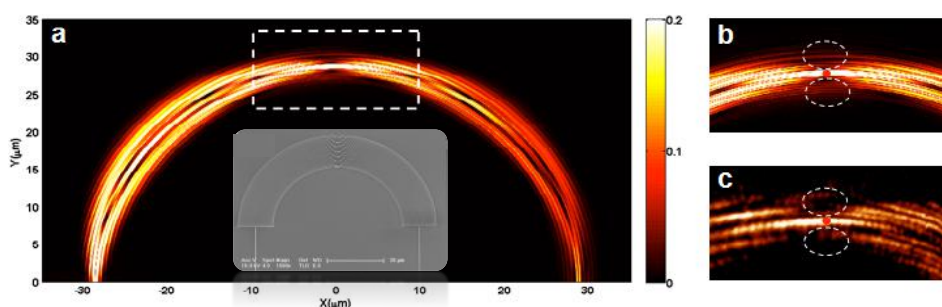


Figure 1 a) FDTD simulation of BO with inset showing the fabricated sample, b) zoom-in view of the simulated first Bloch period point, c) near field image of the first Bloch period point

Next, inspired by the recent concept of inverse design for photonic devices, we show that key devices like waveguide crossing, mode converter, etc can be designed with ultra-compact footprint while maintaining very high performance metrics. For example as shown below in Fig. 2, by simply incorporating a lens-like structure into a

waveguide crossing section and optimizing its geometry, a waveguide crossing structure with a transmission $>96\%$ and cross-talk $<25\text{dB}$ in the C-band can be confidently designed with footprint less than $1\mu\text{m}^2$. This kind of devices may find potential applications in future dense silicon photonic integration technology.

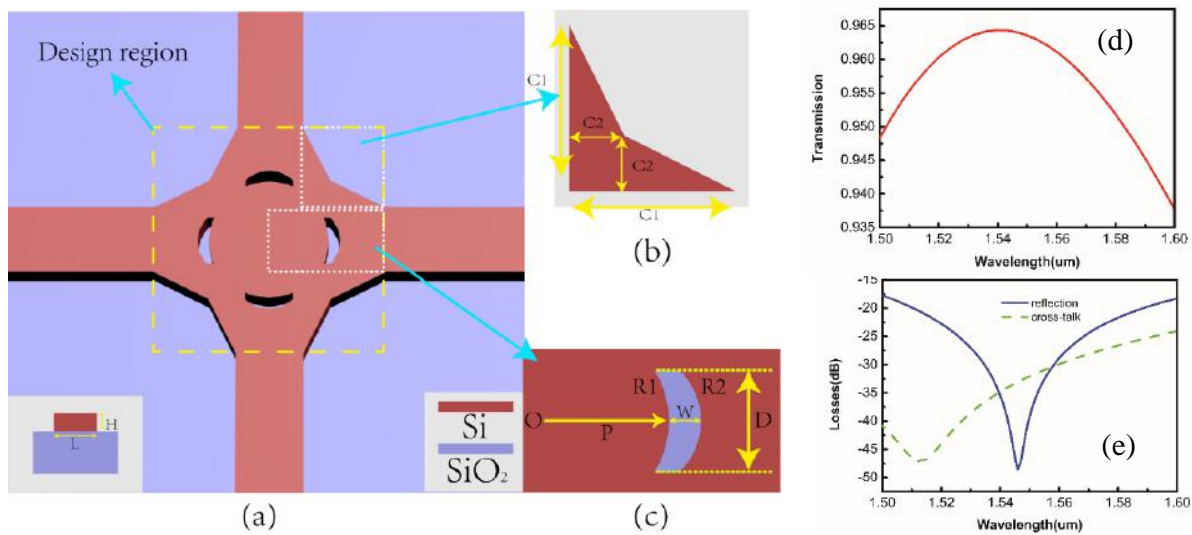


Figure 2 (a) Schematic of our proposed waveguide crossing structure, (b) a zoom-in view of the first piece around the corner of the crossing waveguides, (c) a zoom-in view of the lens-like structure, (d) transmission spectrum, and (e) reflection and cross-talk spectrum.

REFERENCES

1. Bloch, F. Quantum mechanics of electrons in crystal lattices. *Zeitschrift fur Physik* **52**, 555-600 (1928)
2. Regensburger, A. *et al.* Parity-time synthetic photonic lattices. *Nature* **488**, 167-171 (2012).
3. Piggott A.Y. *et al.*, Inverse design and demonstration of a compact and broadband on-chip wavelength demultiplexer. *Nature Photonics* **9**, 374-377 (2015).
4. Shen B. *et al.*, An integrated-nanophotonics polarization beamsplitter with $2.4 \times 2.4 \mu\text{m}^2$ footprint. *Nature Photonics* **9**, 378-382 (2015).

Chirp-free silicon ring optical modulator with a dual-ring push-pull coupler

X. M. Sun*¹, L. J. Zhou², L. Zimmermann^{1,3}, and K. Petermann¹

¹Fachgebiet Hochfrequenztechnik, Technische Universität Berlin, Berlin 10587, Germany;

²State Key Laboratory of Advanced Optical Communication Systems and Networks,
Department of Electronic Engineering, Shanghai Jiao Tong University, Shanghai, 200240, China;

³IHP, Im Technologiepark 25, 15236 Frankfurt (Oder), Germany

* xiaomeng.sun@tu-berlin.de

Abstract-We present a novel design of chirp-free silicon ring optical modulator. A parallel dual-ring coupler structure is introduced to control the coupling between the silicon ring resonator and the input bus waveguide. The push-pull drive of the coupler can suppress the frequency chirp of the modulated signal.

Silicon ring modulators are one of the most critical components among various energy-efficient devices for photonic integrated circuits, due to its small footprint and low power operation [1-6]. However, it is challenging to obtain chirp-free modulation with the refractive index modulation directly imposed on the ring resonator. Introducing multiple rings can increase the speed and modulation depth of the silicon ring modulator [6, 7]. Here, we propose to use a novel dual-ring coupler structure to control the ring-waveguide coupling coefficient. With the dual-ring coupler structure, the coupling coefficient could be easily varied with slight resonance detuning of the two small rings. The critical-coupling of the major ring would be achieved when the coupling coefficient matches with the major ring loss, resulting in a deep notch in the transmission spectrum. The coupling can be adjusted to the under-coupling region, leading to transparent transmission in the spectrum. The frequency chirp of the modulated signal is highly suppressed upon push-pull drive of the dual-ring coupler.

Figure 1(a) shows the schematic structure of our proposed ring modulator. Refractive index modulation based on the free-carrier plasma dispersion effect is performed to the two small rings with a push-pull drive scheme, so that the resonance of one small ring is blue-shifted while the other is red-shifted. t_i and k_i ($i=1, 2, 3, 4$) are the transmission and coupling coefficients of the four couplers of the two small rings (R_1 and R_2), respectively. t_5 and k_5 are the effective transmission and coupling coefficients of the dual-ring coupler. t_6 and k_6 are the transmission and coupling coefficients of the major ring (R_3) output coupler. a is the resonator loss factor and r_i ($i=1, 2$) is the small ring radius. The device parameters are set as $a=0.995$, $r_1=r_2=5\ \mu\text{m}$, $t_2=t_4=0.99$. Both small rings are designed to work at critical coupling, i.e., $t_2=at_1$ and $t_4=at_3$. The small ring waveguide refractive index change (Δn_{eff}) is assumed to be ± 0.0002 during the push-pull modulation.

At the first modulation state ($\Delta n_{\text{eff}}=0$), the resonances of the two small rings are slightly detuned ($\Delta\lambda=0.16\ \text{nm}$ under thermo-optic effect for example), an EIT-like resonance line-shape [6, 8] is generated in the coupler transmission (t_5) spectrum, as shown in Fig. 1(b). By setting $t_6=t_5/a$, a deep notch is present in the modulator output spectrum (through port) shown in Fig. 1(c), corresponding to the “0” state of the modulated signal (operating at the notch wavelength). At the other modulation state, the resonances of the small rings shift further apart, leading to a higher EIT peak. This makes the major ring work in the under-coupling regime. The transmission at the operation wavelength becomes high, corresponding to the “1” state. Therefore, on-off keying modulation can be realized by a small resonance detuning of the two small rings under push-pull drive. Figure 1(d) shows the output optical phase in response to the refractive index change. The end points of the output phase curve correspond to the two modulation levels. The output phase variation is approximately equal to zero, resulting in nearly chirp-free modulation.

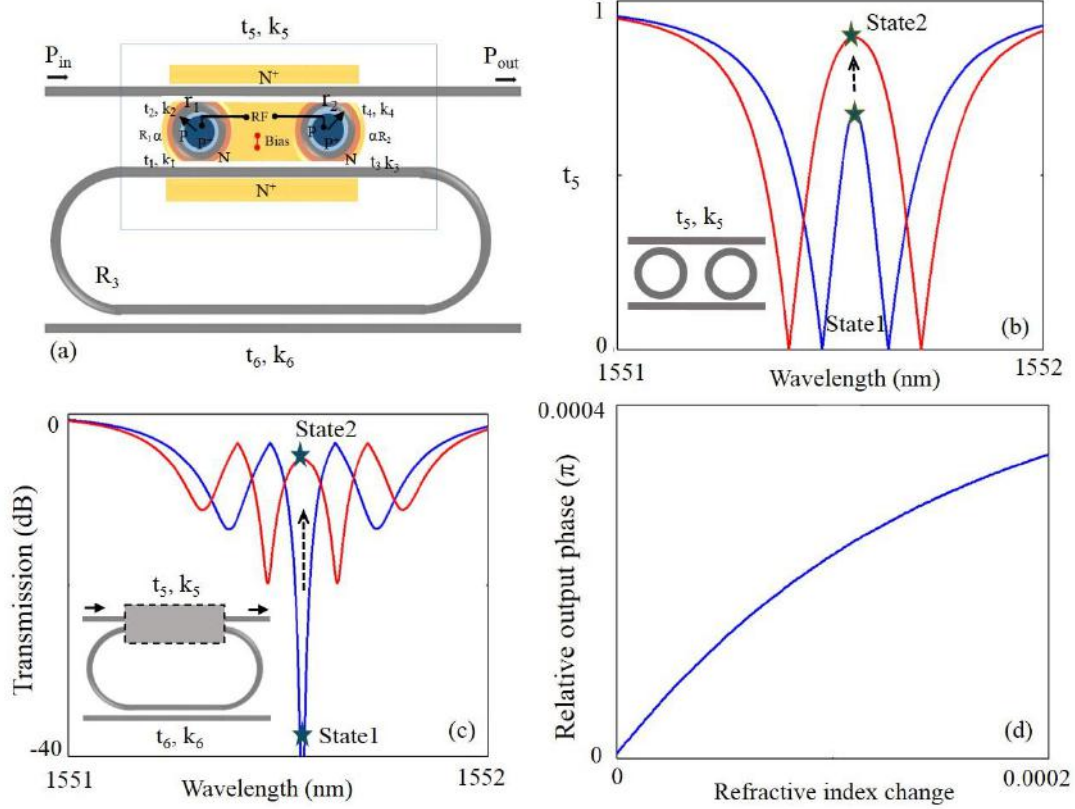


Figure 1. (a) Schematic diagram of the proposed ring modulator where the input coupling is enabled by a dual-ring coupler delineated by the dashed box. (b) Optical transmission spectra of the dual-ring coupler at two modulation states. (c) Optical transmission spectra at the through-port (P_{out}) of the ring modulator. (d) Output phase in response to the refractive index modulation of the two small rings in the input coupler under a push-pull drive scheme.

ACKNOWLEDGMENT

This work was supported by the Alexander von Humboldt Foundation.

REFERENCES

- [1]. Reed, G. T., Mashanovich, G., Gardes, F. Y. and Thomson, D. J., "Silicon optical modulators," *Nature photonics* 4, 518-526 (2010).
- [2]. Li, Z. Y., Xu, D. X., McKinnon, W. R., Janz, S., Schmid, J. H., Cheben, P. and Yu, J. Z., "Silicon waveguide modulator based on carrier depletion in periodically interleaved PN junctions," *Optics Express* 17, 15947-15958 (2009).
- [3]. Ding, J. F., Chen, H. T., Yang, L., Zhang, L., Ji, R. Q., Tian, Y. H., Zhu, W. W., Lu, Y. Y., Zhou, P., Min, R. and Yu, M. B., "Ultra-low-power carrier-depletion Mach-Zehnder silicon optical modulator," *Optics Express* 20, 7081-7087 (2012).
- [4]. Saadi, A. A., Franke, B. A., Kupijai, S., Theiss, C., Rhee, H., Mahdi, S., Zimmermann, L., Stolarek, D., Richter, H. H., Eichler, H. J., Woggon, U., Meister, S., "Performance improvement of silicon micro-cavity modulators by iteration of the p-i-n intrinsic region width," in *Proceedings of ECOC 2013, London*, paper We.1.B.3 (2013).
- [5]. Zhou, L. J., and Poon, A. W., "Silicon electro-optic modulators using pin diodes embedded 10-micron-diameter microdisk resonators," *Optics Express* 14, 6851-6857 (2006).
- [6]. Sun, X. M., Zhou, L.J., Jäger, M., Petousi, D., Zimmermann, L., and Pertermann, K., "Silicon dual-ring resonator-based push-pull modulators," in *proceeding of SPIE. Photonics west 2016*, paper 9752-7, the Moscone Center, Francisco, California United States, 2016.
- [7]. Gu, T. Y., Chen, Y. K., Wong, C. W., Dong, P., "Cascaded uncoupled dual-ring modulator," *Optics letters*, 39, 4974-7 (2014).
- [8]. Zhou, L.J., Ye, T. and Chen, J. P., "Coherent interference induced transparency in self-coupled optical waveguide-based resonators," *Optics letters*, 36, 13-15 (2011).

Low-voltage monolithic silicon optical modulators for high-capacity optical-fiber communications

Kensuke Ogawa

Advanced Technology Laboratory, Fujikura Ltd., 1440 Mutsuzaki, Sakura, Chiba 285-8550, Japan
kensuke.ogawa@jp.fujikura.com

Abstract- The paper describes monolithic silicon modulators having high-efficiency vertical PN-junction rib-waveguide phase shifters in the light of energy-efficient small-footprint modulators for high-capacity optical fiber communications. Characteristics of intensity modulation and phase modulation using the monolithic silicon modulators are reviewed.

Small-footprint monolithic silicon optical modulators operating in broad spectral ranges have been widely interested for applications to high-capacity optical-fiber communications such as integrated optical transceivers in datacenter/optical-interconnect networks and compact-form-factor pluggable digital coherent transceivers in core/metro networks. Energy efficiency is one of the major concerns in the high-capacity optical-fiber networks, and there have been extensive research and development efforts to realize drive-voltage reduction in high-speed silicon optical modulators [1-4].

The paper focuses on low-voltage monolithic carrier-depletion silicon Mach-Zehnder (MZ) optical modulators in applications to the high-capacity optical-fiber communications. Vertical PN-junction silicon rib-waveguide phase shifters [5] have been incorporated to the high-speed silicon MZ modulators. The vertical PN-junction phase shifters operate with DC half-waves shift voltage as low as 2.5 V, which is a record low voltage for reverse-biased carrier-depletion silicon-based waveguide phase shifters [6]. High-speed silicon MZ modulators for two major applications are presented here: one for single-polarization (SP) intensity modulation and the other for dual-polarization (DP) in-phase and quadrature (IQ) phase modulation. A silicon modulator having single MZ interferometer is suitable to a small-footprint modulator for SP intensity modulation in high on-off contrast, while a monolithic silicon modulator having nested IQ MZ interferometers and waveguides of polarization-division multiplexing (PDM) is suitable to an ultrasmall-footprint modulator for DP phase modulation at high symbol rates.

Nonreturn-to-zero on-off keying (NRZ-OOK) at 10 Gb/s has been achieved by using the former silicon MZ modulator with single-end RF drive voltage as low as 3.3 V_{PP} for SP intensity modulation as shown in Fig. 1. High-efficiency intensity modulation with on-off contrast (extinction ratio) higher than 10 dB is verified at high temperatures up to 130 C without thermo-electric cooling. DP phase modulation at 128 Gb/s and beyond is achieved by using the latter silicon MZ modulator with differential-end RF drive voltage as low as 2 V_{PPD} in the modulation formats of DP quadrature phase-shift keying QPSK, DP-16/32 quadrature amplitude modulation.

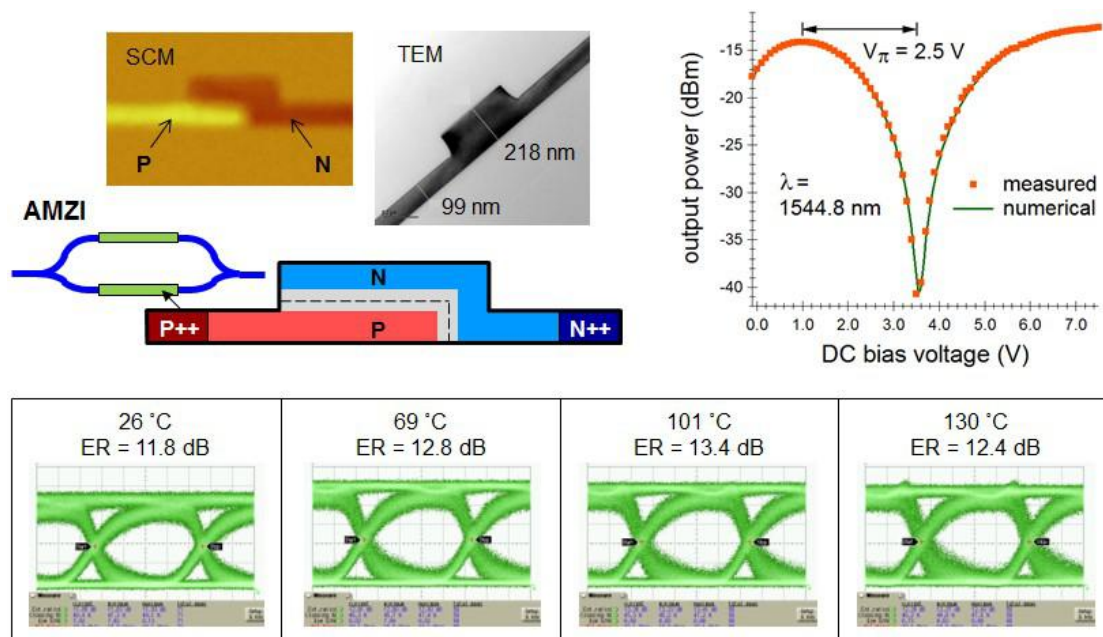


Fig. 1. Silicon Mach-Zehnder optical modulator having vertical PN-junction phase shifters.

REFERENCES

1. Dong, P., Chen, L. and Y.-K. Chen, "High-speed low-voltage single-drive push-pull silicon Mach-Zehnder modulators," *Opt. Express* Vol. 20, No. 6, 6163-616, 2012.
2. Webster, M., Appel, C., Gothoskar, P., Sunder, S., Dama, B. and K. Shastri, "Silicon photonic modulator based on a MOS-capacitor and a CMOS driver," *2014 IEEE Compound Semiconductor Integrated Circuit Symposium*, E3, 2014.
3. Akiyama, S., Baba, T., Imai, M., Akagawa, T., Takahashi, M., Hirayama, N., Takahashi, H., Noguchi, Y., Okayama, H., Horikawa, T. and T. Usuki, "12.5-Gb/s operation with 0.29-V·cm $V_{\pi}L$ using silicon Mach-Zehnder modulator based-on forward-biased pin diode," *Opt. Express* Vol. 20, No. 3, 2911-2923, 2012.
4. Ogawa, K., Ishihara, H., Goi, K., Mashiko, Y., Lim, S. T., Sun, M. J., Seah, S., Png, C. E., Liow, T.-Y., Tu, X., Lo, G.-Q. and D.-L. Kwong, "Fundamental characteristics and high-speed applications of carrier-depletion silicon Mach-Zehnder modulators," *IEICE Electron. Express* Vol. 11, No. 12, 20142010, 2014
5. Reed, G. T., Mashanovich, G. Z., Gardes, F. Y., Nedeljkovic, M., Hu, Y., Thomson, D. J., Li, K., Wilson, P. R., Chen, S.-W. and S. S. Hsu, "Recent breakthroughs in carrier depletion based silicon optical modulators," *Nanophotonics* Vol. 3, No. 4-5, 229-245, 2013.
6. Goi, K., Ishikura, N., Ishihara, H., Sakamoto, S., Ogawa, K., Liow, T.-Y., Tu, X., Lo G.-Q., and D.-L. Kwong, "Low-voltage silicon Mach-Zehnder modulator operating at high temperatures without thermo-electric cooling," *Optical Fiber Communication Conference and Exposition (OFC), (The Optical Society, (OSA), Washington, DC, 2016), W2A.23.*

Diffraction Grating theories as applied to nanophotonics, plasmonics and metamaterials

Full-wave approach for modeling cylindrical microresonators with aperiodic Fourier modal method

Haitao Liu^{1*}, Ying Li^{1,2}, Hongwei Jia¹, Fang Bo², Guoquan Zhang², and Jingjun Xu²

¹Key Laboratory of Optical Information Science and Technology, Ministry of Education, Institute of Modern Optics, Nankai University, Tianjin, 300071, China

²Key Laboratory of Weak Light Nonlinear Photonics, Ministry of Education, School of Physics and TEDA Applied Physics Institute, Nankai University, Tianjin 300071, China

*corresponding author: liuht@nankai.edu.cn

Abstract—A full-wave approach for solving the whispering-gallery modes (WGMs) of cylindrical microresonators based on the aperiodic Fourier modal method (a-FMM) is proposed. The approach allows efficient and accurate calculations of the resonant wavelength, the quality factor, and the field of the WGMs of rotationally-symmetric resonators. The validity and the efficiency of the method are confirmed by the numerical results with microdisk and microring resonators as examples in comparison with other approaches.

Benefiting from the developed fabrication techniques, WGM resonators with high quality factors have been demonstrated with various shapes of rotational symmetry such as microsphere, microdisk, microring and microtoroid [1]. They provide a platform for fundamental studies including cavity optomechanics, nonlinear optics and cavity quantum electrodynamics. They have also shown the ability to be used for various applications, such as low-threshold lasing and highly sensitive sensing.

There have been a great variety of numerical methods used for modeling cylindrical microresonators such as the finite-difference time-domain (FDTD) method, the finite element method (FEM) and the boundary element method (BEM). The FDTD and the FEM requires a large amount of computation for a full discretization of the Maxwell's equations along orthogonal spatial directions. A uniform distribution of refractive index within the cavity region is required for applying the BEM.

To achieve semi-analyticity in certain spatial direction, the a-FMM has been used for the analysis of cylindrical resonators [2–4]. The a-FMM is a generalization of the well-developed rigorous coupled wave analysis (RCWA, also called Fourier modal method). In RCWA, the field is expanded upon Fourier basis along the transversal x and y directions, and is expressed analytically along the propagation z direction as the waveguide eigenmodes. By introducing perfectly matched layers (PMLs) along the transversal directions to build up artificial periodicity, the algorithm of RCWA can be used as well for modeling aperiodic systems, which is called the a-FMM. Through an artificial periodization along both radial and axial directions with the use of PMLs, Bucci et al [2] solved WGMs that are expressed as the waveguide modes propagating along the azimuthal direction. The electromagnetic field of the waveguide modes is expressed in terms of double Fourier series along radial and axial directions, which leads to considerable amount of computation. Armaroli et al [3] expanded the field upon Fourier basis in the axial z direction by introducing PMLs, and expressed the field analytically along the radial direction as the eigen modes of cylindrical Bessel functions. With similar method, Bigourdan et al [4] modeled the field in rotationally-symmetric structures illuminated by a circular line source.

In this talk, an efficient full-wave method based on the a-FMM is developed to analyze the WGMs of rotationally-symmetric resonators [5]. The field is expanded upon Fourier basis along the radial direction by introducing PMLs, and is expressed analytically along the axial z direction as the waveguide eigenmodes. The eigen modes are expressed with the elementary exponential function, which is different from the method in [3,4] where the eigen modes are expressed as the special function of Bessel functions and thus are more computationally consuming. Single Fourier series is used in our method for the expansion of field in the radial direction. This requires much less computation amount in comparison with the method in [2] that adopts double Fourier series for solving the waveguide modes. The validity of our method is confirmed by the numerical results as shown in Table 1 and Figure 1 in comparison with other methods.

Mode	3D-FDTD		C-RCWA		a-FMM	
	$\text{Re}(\lambda_c)$ (μm)	Q	$\text{Re}(\lambda_c)$ (μm)	Q	$\text{Re}(\lambda_c)$ (μm)	Q
TM _{1,11}	1.3344	657	1.3899	721	1.3326	675
TM _{1,12}	1.2769	1916	1.2700	1814	1.2751	1977
TM _{1,13}	1.2248	4303	1.2512	5226	1.2228	6108
TM _{1,14}	1.1770	11369	1.1697	7632	1.1745	20679
TM _{1,15}	1.1313	12109	1.1372	9042	1.1296	69729

Table 1. Resonant wavelength $\text{Re}(\lambda_c)$ and quality factor Q for fundamental quasi-TM WGMs with different azimuthal order m for a microring resonator. The resonator is of silicon material, with internal and external radii of $1\mu\text{m}$ and $1.2\mu\text{m}$, thickness 300nm , and refractive index 3.48. The refractive index of the surrounding medium is 1.44. The results of 3D-FDTD and C-RCWA are taken from Table 2 in [3] for comparison.

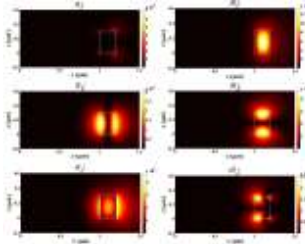


Figure 1. Electromagnetic field distribution for the fundamental quasi-TE WGM of $m=12$ for the microring resonator, with $\text{Re}(\lambda_c)=1.16846\mu\text{m}$ and $Q=395$. The result is consistent with that in Fig. 3 of [3].

Acknowledgements Financial support from the 973 Program (2013CB328701, 2011CB922003, 2013CB328702) and Natural Science Foundation of China (61322508, 11374165, 11174153) is acknowledged.

REFERENCES

1. Armani, D. K. et al., “Ultra-high-Q toroid microcavity on a chip,” *Nature*, Vol. 421, 925–928, 2003.
2. Bucci, D., B. Martin and A. Morand, “Application of the three-dimensional aperiodic Fourier modal method using arc elements in curvilinear coordinates,” *J. Opt. Soc. Am. A*, Vol. 29, 367–373, 2012.
3. Armaroli, A. et al., “Three-dimensional analysis of cylindrical microresonators based on the aperiodic Fourier modal method,” *J. Opt. Soc. Am. A*, Vol. 25, 667–675, 2008.
4. Bigourdan, F., J. P. Hugonin and P. Lalanne, “Aperiodic-Fourier modal method for analysis of body-of-revolution photonic structures,” *J. Opt. Soc. Am. A*, Vol. 31, 1303–1311, 2014.
5. Li, Y. et al., “Fully vectorial modeling of cylindrical microresonators with aperiodic Fourier modal method,” *J. Opt. Soc. Am. A*, Vol. 31, 2459–2466, 2014.

Efficient Fourier representation of complex crossed grating corrugations within the Generalized Source Method

A. A. Shcherbakov¹, and A. V. Tishchenko²

¹Moscow Institute of Physics and Technology, Russia

²University Jean Monnet, France

*corresponding author: shcherbakov.aa@mipt.ru

Abstract-In this work we provide a unified approach for description of a wide variety of complex shape crossed grating corrugations in terms of polygons and polyhedrons within the framework of the Generalized Source Method. We use analytical expressions for both spatial permittivity function Fourier decomposition, and normal vector field Fourier decomposition. The proposed approach is implemented on graphical processing units allowing one to obtain a significant calculation time gain.

Reliable grating diffraction simulation is important for many applications in diffractive and integrated optics. In our previous work we have developed the Generalized Source Method (GSM) for grating diffraction simulation with linear time and memory consumption relative to grating complexity [1,2]. The GSM exhibits the utmost performance for high-NA diffractive optical elements and photolithography masks with complex fine structure and complex geometry of interfaces. Thus, with a view of transforming the GSM into a convenient ready-to-use tool in this work we develop a unified approach for treatment of complex corrugation profiles and material interfaces. Our consideration concerns both GSM applications to crossed grating diffraction simulation [1], and to eigen mode calculation in 3D periodic dielectric composites [3]. The treatment is based on representation of complex 2D top-view shapes of binary diffractive structures as polygons and complex 3D surfaces being constituents of 3D periodic lattices as polyhedra. In this case Fourier integral of spatial permittivity function $\varepsilon(\mathbf{r})$

$$I_{\mathbf{m}} = \sum_k \varepsilon_k \int_{D_k} \exp(-2\pi i \mathbf{m} \cdot \mathbf{r}) dD_k \quad (1)$$

can be taken analytically for arbitrary polygon or polyhedron (see, e.g., [4,5]). Here \mathbf{m} stands either for two-dimensional or three-dimensional Fourier index, \mathbf{r} is two or three-dimensional coordinate vector, and D_k is either k -th polygon surface or k -th polyhedron volume. Moreover, one can define normal vector field to polygon boundary and polyhedron surface via some point \mathbf{r}_c inside volume D_k

$$\mathbf{n}_l = \mathbf{n}_l \frac{\mathbf{n}_l \cdot (\mathbf{r} - \mathbf{r}_c)}{\mathbf{n}_l \cdot (\mathbf{r}_{l0} - \mathbf{r}_c)} \quad (2)$$

providing that all vertices are seen from point \mathbf{r}_c . \mathbf{r}_{l0} in Eq. (2) is an arbitrary point on l -th edge of a polygon or on l -th face of a polyhedron. Functions (2) also admit analytical Fourier representation thus allowing us to apply correct formulation of the GSM as the Fourier space method.

Within the proposed approach a period of a crossed binary grating should be divided into a dense set of

convex polygons in such a way that curved interfaces between different materials should coincide with some polygon edges. Analogously for electromagnetic analysis of 3D lattices a period is divided into a set of polyhedra. The talk will demonstrate the convergence analysis of the GSM with such unified geometrical representation of complex structures, as well as implementation of the method on graphical processing units.

Acknowledgements

The work was supported by the Russian Ministry of Education and Science (within the framework of the program “5stop100”).

REFERENCES

1. Shcherbakov, A. A., and A. V. Tishchenko, “New fast and memory-sparing method for rigorous electromagnetic analysis of 2D periodic dielectric structures,” *JQSRT*, Vol. 113, 158–171, 2012.
2. Shcherbakov, A. A., and A. V. Tishchenko, “Fast numerical method for modelling one-dimensional diffraction gratings,” *Quant. Electron.*, Vol. 40, No. 6, 538-544, 2010.
3. Shcherbakov, A. A., and A. V. Tishchenko, “3D periodic dielectric composite homogenization based on the Generalized Source Method,” *J. Opt.*, Vol. 17, 065101, 2015.
4. McInturff K., and P. Simon, “The Fourier transform of linearly varying functions with polygonal support,” *IEEE Trans. Ant. Propagat.*, Vol. 39, No. 9, 1441-1443, 1991.
5. Lee, S.-W., and R. Mittra, “Fourier transform of a polygonal shape function and its application in electromagnetics,” *IEEE Trans. Ant. Propagat.*, Vol. 31, No. 1, 99-103, 1983.

On the stability of modal methods when dealing with lamellar structures with extreme filling ratios

B. Guizal^{1*}, M. Ben Rhouma² and K. Edee³

¹University of Montpellier, Laboratoire Charles Coulomb, France

²University Blaise Pascal, Institut Pascal, France

³Unit of Nanomaterials et Photonics, Faculty of Sciences of Tunis, Tunisia

*Corresponding author: brahim.guizal@umontpellier.fr

Abstract- Behind the appellation “modal methods”, for diffraction gratings, one can find a variety of methods sharing in common the development of the fields in terms of basis functions that can be either Fourier exponentials hence the name Fourier Modal Method (FMM), or polynomials leading to the family of Polynomial Modal Methods (Legendre, Tchebychev, and Gegenbauer). These approaches may not behave in the same way when dealing with gratings with extreme features such as a very low or very high filling ratios. In the present work, we address such a problem and compare the performances of the different Modal Methods.

One of the major advantages of modal methods for diffraction gratings [1-2] is their versatility and ability to model many plasmonic and metamaterials based devices with a relatively low computational cost. However, in certain special situations, the geometry of the structures under study can be pathological. This is the case of lamellar diffraction gratings with a very low/high aspect ratio. It is not difficult to figure out that for such a structure, the classical FMM [1] is likely to fail in describing the situation since the Fourier representation of the actual electromagnetic field will be very poor. On the contrary, polynomial modal methods [2] describe the spatial transitions through the appropriate boundary conditions after slicing the period into homogeneous subdomains. We will show that this last family of methods is

REFERENCES

1. B. Guizal, H. Yala and D. Felbacq, “Reformulation of the eigenvalue problem in the Fourier modal method with spatial adaptive resolution,” *Optics Letters*, Vol. 34, N°18, pp 2790-2792, September 2009
2. K. Edee and B. Guizal, “Modal Method based on subsectional Gegenbauer polynomial Expansion for non-periodic structures: complex coordinates implementation”, *J. Opt. Soc. Am. A*, Vol. 30, No.4, 631-639, 2013.

Graphene surface plasmons excited through diffraction gratings

M. Ben Rhouma^{1*}, M. Ouseslati¹ and B. Guizal²

¹Université de Tunis El Manar, Faculté des sciences de Tunis, Unité des Nanomatériaux et Photonique,
2092, El Manar, Tunisie

²University of Montpellier, Laboratoire Charles Coulomb, France

*Corresponding author: maha.physique@gmail.com

Abstract- We propose a model taking into account the periodic spatial modulation of a doped graphene sheet conductivity influenced by a dielectric grating. We obtain the dispersion relation through the Fourier Modal Method (FMM) and study the excitation of surface plasmons on such structures. We compute and study the spatially localized fields on the graphene sheet.

In the last decades, graphene has emerged as a new material with outstanding physical properties [1]. Among them, one of the most interesting and promising is the possibility of guiding both transverse magnetic (TM) and transverse electric (TE) surface plasmons polaritons (SPP) with striking advantages over those of noble metals (confinement, long range...) [2]. Unfortunately, the excitation of SPP over graphene is handicapped by the fact that its dispersion relation is very flat which necessitates, for a given frequency, a very long wave-vector. With the common techniques like that of Otto or Krestchmann, this implies the use of dielectrics with high permittivity, which is not always available. To alleviate this limitation, many approaches have been proposed one of which consists of putting the graphene over a diffraction grating. From the modeling point of view, the major part of published works treat the graphene sheet, as a homogeneous conducting film while it should be considered as periodic. In the present work, we propose an approach that puts into play the periodicity through a simple model based on the parallel plate capacitor.

REFERENCES

1. A. K. Geim, K. S. Novoselov, "The rise of graphene" Nature Materials, Vol. 6 183–191, 2007.
2. P. Tassin, T. Koschny, M. Kafesaki, C. M. Soukoulis, " A comparison of graphene, superconductors and metals for metamaterials and plasmonics," Nature Photonics, Vol 6, 259–264, 2012.

Hypersingularity of transverse electric field at sharp edges: a case study of the simplest lamellar grating problem

Lifeng Li

Department of Precision Instrument, Tsinghua University, Beijing 100084, CHINA
lifengli@mail.tsinghua.edu.cn

Abstract - A lamellar grating model is set up to study hypersingularity of transverse electric field component at a sharp edge formed with lossless dielectric and metallic media. The model is the simplest, keeping only the essential features of hypersingularity and simplifying all other aspects, and it allows asymptotic expression of the final system of linear equations of an infinite number of unknowns resulted from the matching boundary conditions. A detailed study of this expression may shed light on understanding numerical divergence due to hypersingularity.

Hypersingularity (HS) refers to the extremely singular behavior of the electric field near the edge of a wedge formed with a lossless dielectric and a lossless metal. There are three necessary conditions for HS to appear: (1) The edge is mathematically sharp; (2) the medium permittivity is real and changes sign along a circle enclosing the edge; (3) the electric field has a component transverse to edge. Near the edge, the magnitude of the transverse electric field component diverges to infinity at a rate of $1/r$, where r is the distance from the edge, and its phase oscillates with a frequency tending to infinity at a rate proportional to $\log(r)$. The study of HS is relatively recent largely due to the recent research in plasmonics, meta-materials, and nano-optics. So far, many facts about HS are known. For example, the most important parameter that characterizes HS is the singularity exponent that is solely determined by the medium permittivity function and wedge angles. Ample numerical experiments have shown that whenever HS is excited no numerical methods for modeling electromagnetic scattering can produce converged results. Introducing absorption loss to the wedge medium weakens the singularity from hyper to regular. Rounding off the sharp edge completely removes any singularity but as the rounding radius tends to zero the sequence of converged numerical results does not have a limit. However, many questions still remain. For example, is the HS problem physical and worth studying? Is the HS problem well defined? Is there a convergent numerical method? An attempt to answer these questions is made in [1]. Here it suffices to say that the problem is worth studying because in some practical cases an electromagnetic scattering problem is near hypersingular. Having a better understanding of the HS problem may help to find a better solution to some practical problems. The objective of this work is study as analytically as possible how a numerical method diverges in presence of HS in a simplest possible model. Such zoomed-in examination may shed some light on the essence of the HS problem.

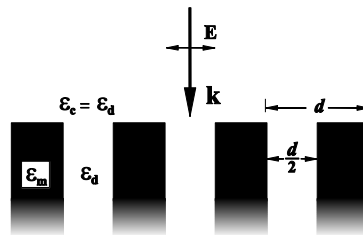


Fig. 1. The simplest lamellar grating model to study hypersingularity.

The physical model for this work is optical diffraction by a semi-infinite lamellar grating as shown in Fig. 1. The selection of this model is based on the principle of keeping the essential features of HS while

simplifying all other aspects. Using a grating model reduces the edge scattering problem from the open space to one Brillouin zone. Using the analytical modal method allows access to analytical expressions of eigenvalues and field representations. Using a semi-infinite grating reduces the number of boundary conditions to the minimum, two. Assuming normal incidence simplifies the eigenvalue solution and cuts the numbers of unknown Rayleigh and modal amplitudes by half. Assuming a 50% duty cycle further simplifies the eigenvalue solution.

The eigenvalue problem of the present lamellar grating case has some peculiarities in comparison with the ordinary cases because the permittivity function $\varepsilon(x)$ changes sign within a grating period (x is in the horizontal direction). The basis functions cannot be made orthonormal because the boundary value problem is non-self-adjoint. However, biorthonormality can be achieved with respect to basis functions of the boundary value problem that is adjoint to the original problem. The eigenvalues ρ_m are not necessarily real even though $\varepsilon(x)$ is real. I have proved that when the duty cycle of the grating is 50%, the number of truly complex eigenvalues is finite. In other words, ρ_m is real when m is sufficiently large. This is an important result; without it general asymptotic expressions to be mentioned below cannot be easily obtained. With these preliminary precautions the asymptotic expressions of the eigenvalues ρ_m , the overlap integrals a_{mq} between the modal basis functions ϕ_q and Rayleigh basis functions ψ_m , and the matrix elements Ω_{mq} of the final system of linear equations resulted from matching boundary conditions along the upper boundary of the grating, can all be found, keeping the leading orders in $1/m$ and $1/q$, for $m \gg 1$ and $q \gg 1$, respectively.

The result of the asymptotic modal analysis of the lamellar grating problem is a final system of linear equations $\sum_q \Omega_{mq} x_q = b_m$ of infinitely many unknowns x_q , where Ω_{mq} is a rational function of m and q for $m \gg 1$ and (or) $q \gg 1$, and b_m has only one nonzero element. To solve this system of equations it is customary to use the reduction method, i.e., to truncate the linear system to a finite size N and verify that as $N \rightarrow \infty$ the solution $x_m^{(N)}$ converges. The legitimacy of using this method requires convergence of the infinite series in q for every m . There are mathematical criteria for testing absolute convergence of an infinite determinant. If the determinant is convergent, Cramer's rule can be used to express the solution $\{x_m^{(N)}\}$. Unfortunately, the determinant of the present infinite matrix $[\Omega_{mq}]$ is not absolutely convergent and I have not found an applicable convergence criterion in the mathematics literature that can distinguish the convergence and divergence of the linear system depending on the permittivity function $\varepsilon(x)$.

As a stopgap I resort to numerical means. The infinite linear equation system is replaced with $\sum_{q=1}^{q=N} \Omega'_{mq} x_q^{(N)} = b_m$ and solved numerically, where the elements of Ω' are given by the asymptotic expressions of Ω_{mq} for $m \gg 1$ and $q \gg 1$. In all cases tested, $x_q^{(N)}$ converges or diverges as N increases depending on $-\varepsilon_d/\varepsilon_m \in (1/3, 3)$ or $-\varepsilon_d/\varepsilon_m \notin (1/3, 3)$, as expected for a right-angle edge.

In conclusion, I have set up perhaps the simplest model of a grating diffraction problem for studying hypersingularity and successfully derived a simple, asymptotic (algebraic) expression of the coefficient matrix of the final system of infinite linear equations. This expression may allow a close-up examination of how HS leads to divergence of expansion coefficients of the transverse electric component and serve as a stepping-stone to achieve the final solution of the HS problem. The next step is to find a mathematical criterion for testing the convergence or divergence of the final linear system.

REFERENCE

1. L. Li, "Hypersingularity, electromagnetic edge condition, and an analytic hyperbolic wedge model," *J. Opt. Soc. Am. A*, Vol. 31, No. 4, 808-817, 2014.

Derivation of the radiation pattern of a spheroidal particle with the Aperiodic Fourier Modal Method

M. Abboud^{1,2}, H. Saleh^{3,4}, J. Charon^{1,5,6,7}, K. Edee^{1,2}, J. M. Geffrin³, J. F. Cornet^{1,8}, J. Dauchet^{1,8}, and G. Granet^{1,2}

¹CNRS, UMR 6602, Institut Pascal, F-63171 Aubière, France

²Université Clermont Auvergne, Université Blaise Pascal, Institut Pascal, BP 10488, F-63000 Clermont-Ferrand, France

³Aix Marseille Université, CNRS, Centrale Marseille, Institut Fresnel, UMR 7249, 13013 Marseille, France

⁴Centre Commun de Ressources en Microondes CCRM, 5 rue Enrico Fermi, 13013 Marseille, France

⁵Université Fédérale de Toulouse Midi-Pyrénées, Mines Albi, UMR CNRS 5302, Centre RAPSODEE, Campus Jarlard, F-81013 Albi CT Cedex 09, France

⁶CNRS, UMR 5302, RAPSODEE, F-81013 Albi, France

⁷Université Perpignan Via Domitia, ED 305, 52 av. Paul Alduy, 66860 Perpignan Cedex 9, France

⁸Université Clermont Auvergne, ENSCCF, Institut Pascal, BP 10488, F-63000 Clermont-Ferrand, France
Mira.Kaissar_Abboud@univ-bpclermont.fr

Abstract— A novel approach based on the Aperiodic Fourier Modal Method is presented to compute the radiative properties of a spheroidal particle. A parametric study in which we vary the different parameters specific to the method is performed. The computed radiation patterns show good agreement with experimental data made at Fresnel Institute and with the results of the T-Matrix method.

Our aim is to model the light transfer within photosynthetic micro-organism suspensions in order to optimize the photosynthesis engineering in a photobioreactor devoted to biofuel production [1, 2]. Light scattering by small particles is an old problem whose analytical solutions exist in the case of canonical shapes [3]. The numerical resolution of the Helmholtz equation is a challenging problem for such diverse disciplines as atmospheric science, oceanography, astronomy and engineering sciences [1, 4].

In this presentation, we explore a new approach based on a modal formalism for solving the electromagnetic scattering problem. Our technique is based on the Fourier Modal Method which has a several decades long history in the field of rigorous diffraction modeling. The Fourier Modal Method was originally built for periodic structures such as diffraction gratings [5]. Nevertheless, by incorporating perfectly matched layers [6], it became possible to address the scattering by a single spheroidal object [7].

The results of our analysis were successfully compared with those obtained by the T-Matrix method and the measurements [8].

ACKNOWLEDGMENT

This work was funded by grants from the *European Commission* (Auvergne FEDER funds) and the *Region Auvergne* in the framework of the LabEx IMobS³. We would also like to thank the *Auvergne Regional Council* for the financial support.

REFERENCES

1. Dauchet, J. and al., “Calculation of the radiative properties of photosynthetic microorganisms,” *J Quant Spectrosc Radiat Transfer*, No. 161, 60–84, 2015.
2. Pruvost, J. and J. F. Cornet, *Knowledge models for the engineering and optimization of photobioreactors*, in Posten W. C., De Gruyter C., editors, *Microalgal biotechnology: potential and production*, 181–224, 2012.
3. Bohren, C. F. and D. R. Huffman, *Absorption and scattering of light by small particles*, John Wiley & Sons, New York, 1983.
4. Charon, J. and al., “Monte Carlo implementation of Schiff’s approximation for estimating radiative properties of homogeneous, simple-shaped and optically soft particles: Application to photosynthetic micro-organisms,” *J Quant Spectrosc Radiat Transfer*, No. 172, 3–23, 2016.

5. Moharam, M. G. and T. K. Gaylord, "Rigorous coupled-wave analysis of planar-grating diffraction," *Journal of the Optical Society of America A*, Vol. 71, Issue 7, 811–818, 1981.
6. Teixeira F. L. and W. C. Chew, "General closed-form PML constitutive tensors to match arbitrary bianisotropic and dispersive linear media," *IEEE Microwave and Guided Wave Letters*, Vol. 8, Issue 4, 223–225, 1998
7. Abboud, M. and al., "Computation of spheroidal micro-organisms cross sections using the aperiodic Fourier modal method," in *PIERS proceedings*, Prague, Czech Republic, July 2015, 1942-1946.
8. Mishchenko, M. I., L. D. Travis and A. A. Lacis, *Scattering, absorption and emission of light by small particles*, Cambridge: Cambridge University Press, 2002, URL http://www.giss.nasa.gov/staff/mmishchenko/t_matrix.html.

Modal analysis of V-groove plasmonic waveguides

G.Granet^{1,2}

¹Clermont Universités, Université Blaise Pascal,
Institut Pascal, BP10448, F-63000 Clermont- Ferrand, France

²CNRS UMR 6602, F-63177 Aubière, France
granet@univ-bpclermont.fr

Abstract— An original modal method is derived for the analysis of V-groove plasmonic waveguides. The problem is formulated with Maxwell's equations written under the covariant form and matched coordinates. The numerical solution is obtained by using the method of moments and sub-domain basis functions.

Among the diverse Surface Plasmon Polariton waveguide type, V-shaped dielectric gap waveguides achieve subwavelength confinement and low propagation losses. Numerical modelling of these waveguides is challenging and requires advanced numerical methods with high efficiency and accuracy especially when they include materials with negative permittivity as in the present case. The problem comes from the difficulty to enforce accurately boundary conditions with complicated geometries which in turn determines the overall effectiveness of the solver. In linear numerical methods, the waveguide cross section is discretized and a linear matrix eigenvalue problem is derived by using the method of moments. The effectiveness of any numerical modal method is linked with the mesh that is used to describe the geometry and by the expansion and test basis chosen in the computation. Matched coordinates [1] allow to make the boundary of the waveguide coincide with surfaces of coordinates which facilitates the writing of boundary conditions. Adaptive spatial resolution have also shown to be a powerful tool to improve the effectiveness of various numerical modal methods. In addition to the above geometrical aspects, using sub-domain basis functions like polynomials [2] or splines [3] allow to enforce boundary conditions rigorously. In our presentation we shall describe our code and use it to determine the dispersion relations of diverse V-groove plasmonic waveguides.

REFERENCES

1. T.Weiss, G. Granet , N. A. Gippius, S. G. Tikhodeev , H. Giessen ,” Matched coordinates and adaptive spatial resolution in the Fourier modal method”,*Opt. Ex.* 17, 8051-8061,(2009).
2. K.Edee,”Modal method based on subsectional Gegenbauer polynomial expansion for lamellar gratings”,*J.Soc.Opt.Soc.Am. A*,28 2006-2013,(2011)
3. G.Granet, ”Efficient implementation of the B-spline modal method for lamellar gratings”,*J.Soc.Opt.Soc.Am. A*, 31, 332-337,(2014).

Optical investigations of the quality and optical processes of photonic and plasmonic nanostructures

R. Antos¹, M. Veis¹, L. Beran¹, K. Palka², J. Mistrik², P. Janicek², and Mir. Vlcek²

¹Institute of Physics, Charles University in Prague, Ke Karlovu 5, 12116 Prague 2, Czech Republic

²Faculty of Chemical Technology, University of Pardubice, Studentska 95, 53210 Pardubice, Czech Republic
antos@karlov.mff.cuni.cz

Abstract— Optical scatterometry based on spectroscopic ellipsometry and other measurement techniques together with optical simulations are used to analyze the quality of various nanostructure patterns and to study the optical behavior of selected photonic and plasmonic devices.

Various optical responses and processes observed on periodic nanostructures (gratings, photonic and plasmonic crystals, and selected devices based on them) are demonstrated by a joint theoretical and experimental analysis, referred to as scatterometry [1]. For the theoretical treatment, the rigorous coupled wave analysis (RCWA) is used and explained in detail. For the experimental treatment, the spectroscopic ellipsometry (SE) and power reflectance and transmittance are used in wide spectral and incidence angle ranges.

The RCWA is based on treating the electromagnetic fields and the space distributions of material parameters in the Fourier space. The method uses various recent improvements including a modified Airy-like series approach (which enables visualization of space-dependent fields in deep structures) and proper Fourier factorization (which enables fast convergence or short calculation time).

Ellipsometric measurements carried out in a wide spectral range and various incidence geometries are used to determine the geometric properties of periodic textures with high accuracy and to analyze plasmonic processes occurring in metallic metasurfaces or optical processes occurring in common metasurfaces. Indirect observation of the surface plasmon propagation via ellipsometric spectra is demonstrated.

As an example, a sine-like relief profile created on an Ni plane surface, with a developed native NiO overlayer, is investigated in detail. The SE spectra in a near-IR/visible/near-UV spectral range are analyzed to determine the depth and precise shape of the NiO/Ni relief. The precise knowledge of the relief structure and the Ni dielectric function (determined on a reference thin film sample) is then used to simulate the propagation of surface plasmon polaritons along the metasurface at the SE-measurement configuration and to identify this process with the measured spectra. As another example, the quality of rectangular and embossed-relief gratings fabricated on chalcogenide glass surfaces is analogously investigated by scatterometry.

Various optical responses of shallow rectangular patterns are theoretically analyzed by the RCWA and an approximate local modes method (LMM) based on scalar diffraction theory. The diffraction effects of the edges of nanoscale elements patterned within the metasurfaces are investigated with respect to the spectroscopic response. A numerical modification of the LMM is proposed, taking into account the edges' diffraction effects. The modified LMM is then used to demonstrate how the edge effects affect the ellipsometric spectra and the holographic images reconstructed via an aperiodic metasurface working as a spatial light modulator.

The method can help in evaluating the quality of the lithographic techniques, evaluating the performance and reliability of the imaging techniques, and proposing novel optical and plasmonic devices.

ACKNOWLEDGMENT

The work was supported by the Czech Science Foundation, project No. 16-13876S.

REFERENCES

1. Veis, R. and Antos, R., "Advances in optical and magneto-optical scatterometry of periodically ordered nanostructured arrays," *J. Nanomater.*, Vol. 2013, 621531, 2013.

Leaky Modes and Plasmonics - The Impact of Layered Structures

S. R. J. Brueck* and S. C. Lee
Center for High Technology Materials
University of New Mexico, USA

*sbrueck@chtm.unm.edu

Abstract-Plasmonic structures are of great interest particularly for infrared detectors where strong enhancements $\sim 100\times$ have been reported as compared with bare detectors. Detectors are complex layered structures including absorption, contact and possibly other layers. This layer structure can impact the plasmonic effects and give rise to leaky modes that couple energy to propagating modes in the substrate reducing the surface plasmon detectivity.

There has been extensive work on the impact of metal photonic crystals (MPC) on the responsivity of infrared detectors.¹⁻⁵ Enhancements as high as $100\times$, depending on detector configuration, have been reported.⁶ While most evaluations of plasmonic effects deal with a metal film on a homogeneous substrate, detectors are more complex layered structures with absorption and contact regions at a minimum. These layers impact the optical interaction leading to the enhanced detectivity. In particular, contact layers because they are heavily doped typically have a lower refractive index than the bulk semiconductor as a result of free-carrier effects. This lower index can establish a leaky mode that suppresses the coupling to the surface plasma wave and leads to enhanced transmission into the substrate. In some cases this can be used to enhance coupling into the substrate and to a detection region deeper in the material; in others it results in a loss of the surface resonance and a degradation in the detector performance.

An experimental example (from Ref. 6) is shown in Fig. 1(a), where the only difference between the two detectors is the thickness of an n^+ contact layer located just below the MPC. There is a clear shift and weakening of the plasmon resonance enhanced detectivity. Fig. 1(b) shows an RCWA model of the absorption qualitatively replicating the experimental observations. These changes are due to leaky mode effects. Fig. 2 shows a modal calculation as a function of the thickness of the lower index n^+ layer.

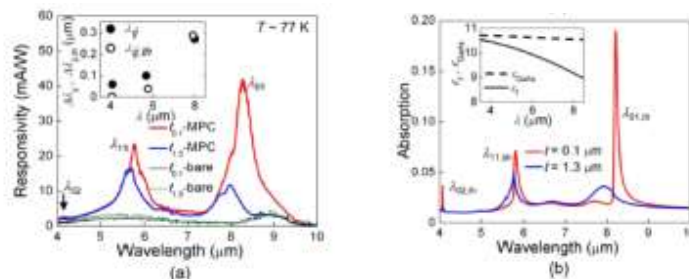


Fig. 1: a) Experimental and b) RCWA modeling results for four photodetectors. Two photodetectors are bare, with no MPC one with a $0.1\ \mu\text{m}$ thick top contact layer (black) and one with a $1.3\ \mu\text{m}$ thick top contact layer (green). Two have a MPC film, red for the $0.1\ \mu\text{m}$ thick and blue for the $1.3\ \mu\text{m}$ thick top contact layers. Note in particular the shift of the SPW resonance between the two MPC cases and the change in the absorption due to leaky mode effects. (from Ref. 6).

For a thin top contact layer the standard bound SPW mode is found (black crosses). (Note that this mode is bound in the absence of a grating structure, the addition of a grating allows coupling to the SPW which is then a leaky mode.) There is also an unphysical mode on the improper sheet (black dots). As the thickness of the top contact layer is increased, the modal index crosses the branch cut and emerges on the improper sheet as a backward wave (red dots). The thickness where this cross over occurs is much less than the SPW evanescent field decay. As the thickness is increased further, these modes have complex conjugates modal index solutions, both on the leaky mode sheet, with very high losses corresponding into enhanced far field transmission into the substrate. As the top contact layer is further increased, the two modes become degenerate, one on either Reimann sheet at a value consistent with the index of the contact layer.

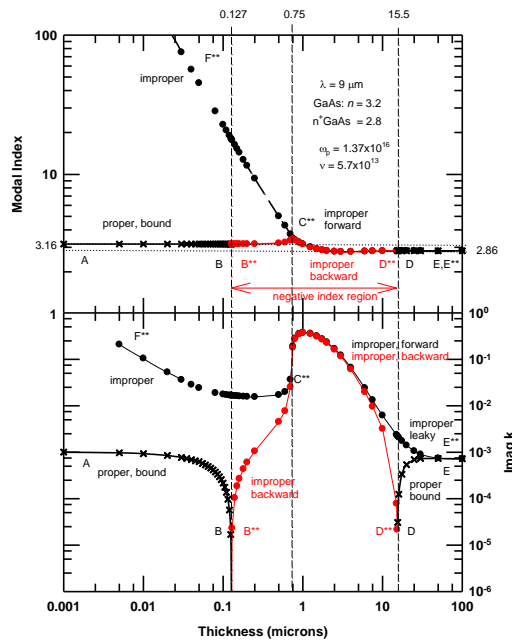


Fig. 2: Modal indices as the thickness of the top contact layer is varied.

Acknowledgment: Support for this work was provided by the Air Force Office of Scientific Research.

REFERENCES

1. Lee, S. C., Krishna, S., & Brueck, S.R.J., Quantum dot infrared photodetector enhanced by surface plasma wave excitation, *Opt. Exp.* Vol. 17, pp. 23160-23168, 2009.
2. Chang, C-C., Sharma, Y.D., Kim, Y.-S., Bur, J.A., Shenoi, R.V., Krishna, S., Huang, D., & Lin, S-Y., A surface plasmon enhanced infrared photodetector based on InAs quantum dots, *Nano Lett.* Vol. 10, pp. 1704-1709, 2010.
3. Wu, W., Bonakdar, A., & Mosheni, H., Plasmonic enhanced quantum well infrared photodetector with high detectivity, *Appl. Phys. Lett.* Vol. 96, Art. 161107, 2010.
4. Lee, S.J., Ku, Z., Barve, A., Montoya, J., Jang, W-J., Brueck, S.R.J., Sundaram, M., Reisinger, A., Krishna, S. & Noh, S.K., A monolithically integrated plasmonic infrared quantum dot camera, *Nature Commun.* Vol. 2, Art. 286, 2011.
5. Lee, S.C., Sharma, Y.D., Krishna, S., & Brueck, S.R.J., Leaky-mode effects in plasmonic-coupled quantum dot infrared photodetectors, *Appl. Phys. Lett.* Vol. 100, Art. 011110, 2012.
6. Lee, S.C., Sharma, Y.D., Krishna, S., & Brueck, S.R.J., Light direction-dependent plasmonic enhancement in quantum dot infrared photodetectors, *Appl. Phys. Lett.* Vol. 97, Art. 021112, 2010.

Casimir Interaction between a sphere and a grating

M. Antezza^{1*}, R. Messina¹, P. Maia Neto² and B. Guizal¹

²University of Montpellier, Laboratoire Charles Coulomb, France

²Universidade Federal do Rio de Janeiro, Brazil

*Corresponding author: mauro.antezza@umontpellier.fr

Abstract- We derive the explicit expression for the Casimir energy between a sphere and a 1D grating under thermal equilibrium, in terms of the sphere and grating reflection matrices, and valid for arbitrary materials, sphere radius, and grating geometric parameters.

We calculate numerically the Casimir energy between a metallic (gold) sphere and a dielectric (fused silica) lamellar grating at room temperature, and explore its dependence on the sphere radius, grating-sphere separation, and lateral displacement [1]. We quantitatively investigate the geometrical dependence of the interaction, which is sensitive to the grating height and filling factor, and show how the sphere can be used as a local sensor of the Casimir force geometric features. To this purpose we mostly concentrate on separations and sphere radii of the same order of the grating parameters (here of the order of one micrometer). We also investigate the lateral component of the Casimir force, resulting from the absence of translational invariance. We compare our results with those obtained within the proximity force approximation (PFA). When applied to the sphere only, PFA overestimates the strength of the attractive interaction, and we find that the discrepancy is larger in the sphere-grating than in the sphere-plane geometry.

REFERENCES

1. R. Messina, P. A. Maia Neto, B. Guizal, and M. Antezza, “Casimir Interaction between a sphere and a grating,” *Physical Review A*, Vol 92, 062504, 2015.

Wide angle boundary models for periodic structures with subwavelength periods

Ya Yan Lu

Department of Mathematics, City University of Hong Kong, Hong Kong
mayylu@cityu.edu.hk

Abstract— For periodic structures with subwavelength periods, wide-angle boundary models are developed by matching the reflection and transmission coefficients for incident waves with different incident angles. For non-periodic structures with slowly varying subwavelength elements, such as some metasurfaces, rigorous numerical simulations are expensive, if the size of the structure is much larger than the wavelength. The wide-angle boundary models with spatially-varying coefficients may be used to speed up the numerical simulations.

For a periodic structure, a fundamental problem is to analyze the diffraction of plane incident waves. If the reflection and transmission coefficients are calculated for plane incident waves of all incident angles and polarizations, then the diffraction problem of an arbitrary incident wave can be easily solved. This is so, because a general incident wave can be written as a superposition of plane waves. Metasurfaces appeared in recent years are mostly non-periodic structures with subwavelength scattering elements [1, 2]. These structures have been modeled by theories based on geometric optics [1] or relatively simple impedance conditions [2]. However, the size of the subwavelength elements in metasurfaces are not significantly smaller than the wavelength. Therefore, the geometric optics approaches may have limited accuracy, and modeling a complicated metasurface by an impedance condition is likely to be inadequate.

We propose to model a non-periodic metasurface in two steps. In the first step, for each subwavelength element, we consider a periodic structure where each period contains that element, calculate the reflection and transmission coefficients of that periodic structure for incident waves of all angles and polarizations, and approximate the periodic structure by a wide-angle boundary condition. In the second step, we model a non-periodic metasurface by a wide-angle boundary condition with position-dependent coefficients, so that the boundary condition at a subwavelength element is exactly that for the corresponding periodic structure. In the following, we show how to find wide-angle boundary conditions for periodic arrays of circular metallic rods.

We consider a one-dimensional periodic array of infinitely long circular metallic rods, with their axes parallel to the y axis and their centers located on the x axis. The array is periodic in x with period L and surrounded by air. The radius and the refractive index of the rods are a and $n_1 = 0.2 + 5i$, respectively. For the E polarization, we calculate the reflection coefficient R (the complex amplitude of the zeroth reflection order) for different values of a , different incident angles, and for $L/\lambda = 0.26$, where λ is the freespace wavelength. The case for $a = 0.1L$ and $a = 0.4L$ are shown in Fig. 1 as the solid lines. Our objective is to find a boundary condition at $z = L/2$, so

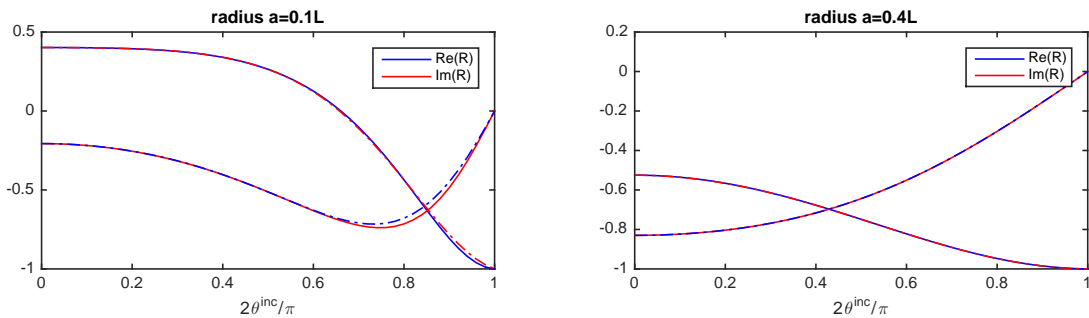


Figure 1: Reflection coefficient R (amplitude of the zeroth reflection order) as function of the incident angle θ^{inc} of a periodic array of metallic rods in the E polarization. The solid curves are the exact solution. The dash-dot curves are wide-angle boundary models.

that its reflection coefficient R_{bc} approximates R for all incident angles. The simplest boundary condition is $\partial_z E_y = a_0 E_y$, but it is not sufficiently accurate. We consider the wide-angle mode

$$\frac{\partial E_y}{\partial z} = a_0 E_y + b_0 \frac{\partial^2 E_y}{\partial x^2}, \quad z = \frac{L}{2}. \quad (1)$$

The coefficient a_0 can be determined from the exact R for normal incidence ($\theta^{inc} = 0$). We choose to determine b_0 by matching R at $\theta^{inc} = \pi/4$. The dash-dot curves in Fig. 1 show R_{bc} as functions of θ^{inc} . It can be seen that the approximation is good for $a = 0.4L$, slightly less so for $a = 0.1L$ when the incident angle is large. The coefficients a_0 and b_0 depend on a , and are shown in Fig. 2. It

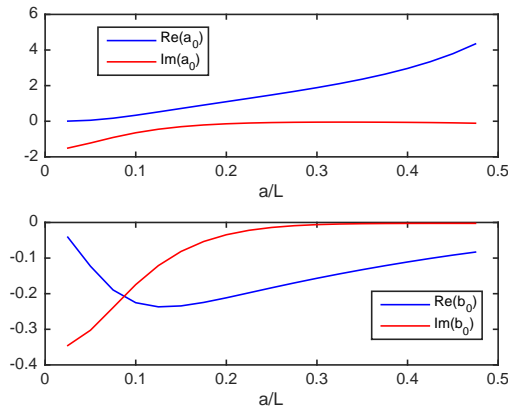


Figure 2: Coefficients a_0 and b_0 (actually, $a_0 L$ and b_0/L) for the wide-angle boundary model Eq. (1).

is possible to further increase the accuracy of the boundary models. For example, we may consider the following more complicated condition

$$\partial_z E_y = a_0 E_y + \sum_{j=1}^J b_j (1 + c_j \partial_x^2)^{-1} E_y, \quad (2)$$

where a_0 , b_j , c_j for $1 \leq j \leq J$ can be chosen to match R for various incident angles. Notice that the above boundary condition can be implemented if we introduce w_j satisfying $(1 + c_j \partial_x^2) w_j = E_y$.

We believe that boundary condition (1) can be used to model non-periodic slowly varying structures, if a_0 and b_0 are allowed to change with the spatial variable x . For an array of rods with different radii, but the fixed center-to-center distance L , if x is the center of a rod, we let $a_0(x)$ and $b_0(x)$ be the coefficients corresponding to the radius of that rod. For other x , we define $a_0(x)$ and $b_0(x)$ by linear interpolation or cubic spline. With such a boundary condition, the reflection of an arbitrary incident wave by the non-periodic structure can be easily analyzed. Furthermore, it is also possible to design metasurfaces for applications by considering the required boundary conditions.

ACKNOWLEDGMENT

The work is partially supported by the Research Grants Council of Hong Kong Special Administrative Region, China, under project CityU 11301914.

REFERENCES

1. Yu, N. *et al.*, “Light propagation with phase discontinuities: generalized laws of reflection and refraction,” *Science*, Vol. 334, 333–337, 2011.
2. Zhao, Y., X. X. Liu and A. Alù, “Recent advances on optical metasurfaces,” *J. Opt.*, Vol. 16, 123001, 2014.

Efficient statistical analysis of plasmonic devices response with a stochastic collocation method.

K. Edee^{1,2} and P. Bonnet^{1,2}

¹Clermont Université, Université Blaise Pascal, Institut Pascal, BP 10488
F-63000 CLERMONT-FERRAND

²CNRS, UMR 6602, Institut Pascal, F-63177 AUBIÈRE
kofi.edee@univ-bpclermont.fr

Abstract— We present an efficient numerical tool allowing to analysis the electromagnetic response of plasmonic guiding devices when some geometrical parameters of these structures are considered as random variables characterized by a given statistical distribution law. The deterministic responses *i.e.* the transmittivity and the reflectivity of the devices are successfully calculated with the modal method based on a subsectionnal Gegenbauer basis functions. Then statistical moments of these observables are computed thanks to a stochastic collocation method. The results are successfully compared with those obtained from some crude Monte Carlo simulations.

Miniaturized and integrated of opto-electronic high speed devices based on surface-plasmon or gap-plasmon devices is a rapidly growing research area because plasmon waveguiding structures provide high subwavelength scale confinement and low propagation loss. Plasmonic waveguides based on metal-insulator-metal (MIM), plasmonic light-emitting devices (light transmission enhancement through a metallic subwavelength square coaxial aperture), etc, have been tremendously studied nowadays. In one hand, some techniques such as electron-beam lithography allow to create complex nano-structures with impressive spatial control; however, small-scale manufacturing structure raises questions about the variability of the geometric parameters of these structures and how these variations influence the electromagnetic response of these plasmonic structures. In the other hand, since the study of these devices is often linked to a plasmon resonances, this phenomenon may be successfully treated as an eigenvalue problem with specific boundary conditions. Generally the numerical modal analysis of metal/dielectric junctions is deemed very tedious but some efficient numerical tools have been developed in order to provide both very accurate numerical results and short-computation time consuming.

it is worthwhile to examine the correlation of these accurate numerical results and the reality of the manufacturing that necessary involved some variabilities on certain geometrical parameters. Our goal in this paper is to provide an efficient statistical tool coupled with an accurate numerical algorithm in order to integrate stochastic parameters in a plasmonic device simulation. The structure under study is a plasmonic waveguiding consisting of 2D Metal-Insulator-Metal (MIM) waveguide coupled with a square-shaped ring resonator for filtering purposes.

The electromagnetic numerical model of the structure is based on the MMGE (modal method based on a subsectionnal Gegenbauer basis functions) [1] in its non-periodic version [2]. Some geometrical parameters of the plasmonic device are considered as random variables characterized by a given statistical distribution law. We are interested in the statistical moments (mean, variance, etc) of the some output parameters *i.e.* the transmittivity and the reflectivity of the structure, with respect to the wavelength. For that purpose, a non-intrusive stochastic collocation method [3] is implemented and successfully compared with some crude Monte Carlo simulations.

REFERENCES

1. K. Edee, "Modal method based on subsectional Gegenbauer polynomial expansion for lamellar gratings", *JOSA A* Vol. 28, Iss. 10, 2006-2013 (2011).
2. K. Edee, B. Guizal, "Modal method based on subsectional Gegenbauer polynomial expansion for nonperiodic structures: complex coordinates implementation" *JOSA A* Vol. 30, Iss. 4, 631-639 (2013).
3. P. Bonnet, F. Diouf, C. Chauvière, S. Lalléchère, M. Flogli, F. Paladian, "Numerical simulation of a reverberation chamber with a stochastic collocation method" *CR Acad Sci Phys*, 54-64 (2009).

Rigorous and extremely fast electromagnetic methods for diffraction problems

W. Iff¹, T. Kämpfe¹, Y. Jourlin¹, and A. V. Tishchenko^{1*}

¹ Université Jean Monnet, Laboratoire Hubert Curien UMR CNRS 5516, Bât. F, 18 rue Benoit Lauras, 42000, Saint-Etienne, France

*corresponding author, E-mail: alexandre.tishchenko@univ-st-etienne.fr

Abstract

With feature sizes becoming smaller and patterns becoming increasingly complex in lithography, diffractive optics and nanophotonics, there is a growing demand for and lack of ultrafast, memory sparing but rigorous light scattering calculation techniques at large planar 2D diffracting objects. Examples include diffraction in OPC and in real-time scatterometry. A good approach to these requirements is the Generalized Source Method (GSM) formulated in Fourier space [1] and its ongoing improvement. In this conference contribution, we report on recent success by switching from CPU to GPU computations and by application of the scattering-vector (S-vector) algorithm [2, 3].

1. Introduction: Review of GSM, status quo and improvable points

With the development of the GSM [1] in 2012, a large step towards the ultrafast, memory sparing and rigorous calculation at large diffracting objects has been made (see figure 1 and 2). Nevertheless, the calculation time of GSM on a CPU related to the time for a double FFT as the sim-

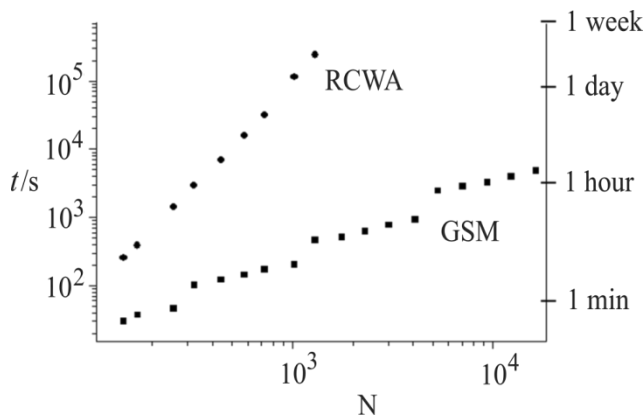


Figure 1: $O(N \cdot \ln(N))$ -complexity of GSM in time compared to $O(N)$ – complexity of RCWA, N being the number of harmonics.

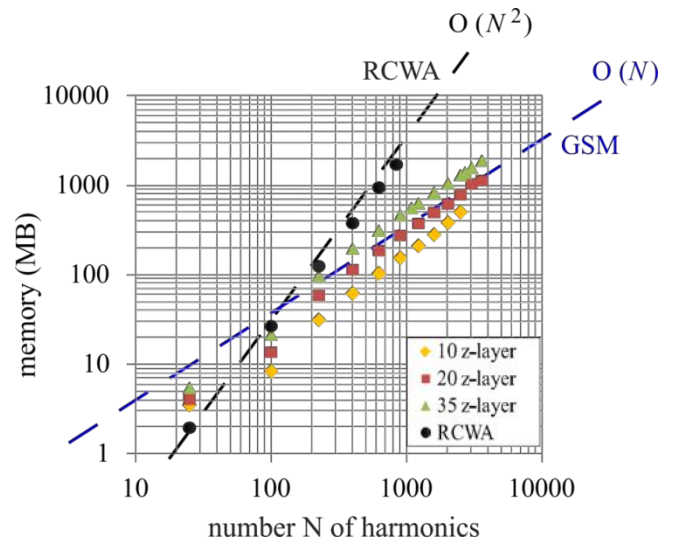


Figure 2: Linear memory consumption of GSM compared to $O(N)$ – memory consumption of RCWA.

plest approximate method is about $t(\text{GSM})/t(\text{double FFT}) \approx 10 \cdot \text{no. of iterations} \cdot \text{no. of layers} \approx 10\,000$, where the no. of iterations is between several tens and several hundreds; the pre-factor in the order of 10 originates from having to apply several Toeplitz matrices related to permittivities and normal vector components at each layer in each iteration and coincides with experiences from numerical experiments. So, the computational load is still too much for being competitive in time and memory with non-rigorous methods. Additionally, with GSM being integral equation based, there is a need of allowing more flexibility, facilitating the combination of layers of different materials and properties.

2. Acceleration by GPU computations

Nowadays, GPUs become increasingly superior to CPUs regarding computations. With GSM allowing parallel computations at the slices and FFTs being particularly suited for conduction on GPUs, GSM is well-suited for GPU applications. Having implemented GSM on GPUs, we observe an acceleration by a factor of about 400 at the state of the art. So, we report a reduction of the computation time

down to $t(\text{GSM on a GPU})/t(\text{double FFT on a CPU}) \approx 25$. We perform the reference double FFT on a CPU here, since the conduction of a single double FFT on a GPU would not allow a significant acceleration due to the time consumption for the data exchange between RAM and GPU.

Yet, with the employment of GPUs, a need of the reduction of the memory consumption arises. Data exchanges between GPU and RAM are realizable, however take a considerable fraction of the overall computation time (see figure 3).

As well, an acceleration of the convergence of the iterative solver employed by GSM – here GMRES [4] – is desirable since high numbers of GMRES iterations do not only require the storage of a high number of GMRES basis vectors but also increase the computational load for the Arnoldi process (ortho-normalization of GMRES basis vectors versus each other) [4].

As the number of GMRES iterations as well as the memory demand of GSM decrease with the thickness of diffracting objects, the division of thick gratings into several thinner layers to be computed separately is appealing. Yet, the task of the combination of several scattering layers arises.

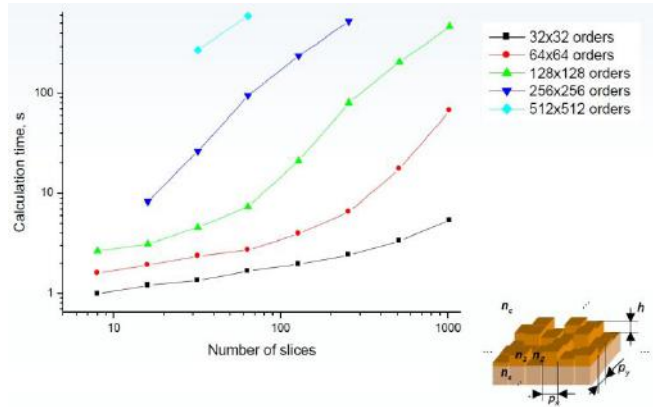


Figure 3: Computation time in seconds for the pixelated grating depicted in the lower right corner (refractive index of substrate and grating material made of glass: 1.46; medium of incidence: air, height: 770 nm, wavelength: 532 nm, size of the pixels: 500 nm \times 500 nm). For low numbers of slices, the memory on the graphic card is sufficient for the entire computation; thus, the computation time increases linearly with the number of slices here. For high numbers of slices however, the memory on the graphic card becomes insufficient, requiring data exchanges between RAM and GPU; thus, the overall computation time increases faster than linearly with the number of slices here.

3. Progress by the S-vector algorithm

As a remedy to the challenges arising in the sections 2 and 3, we present the S-vector algorithm. The S-vector algorithm follows a divide and conquer strategy; it models the interaction of subsystems and allows the calculation of their collective scattering behavior, provided a method for the scattering calculations at the

subsystems exists. A typical application example for the S-vector algorithm is the combination of grating layers of different profile or material to be calculated separately. The GPU memory consumption is restricted to the memory consumption for a single layer.

The prerequisites for the S-vector algorithm are illustrated in figure 4: division of the diffracting object into items (slicing), representation of the field in terms of S-vectors of up and down waves at the boundaries of the items and a rigorous method of linear complexity for scattering calculations at the items.

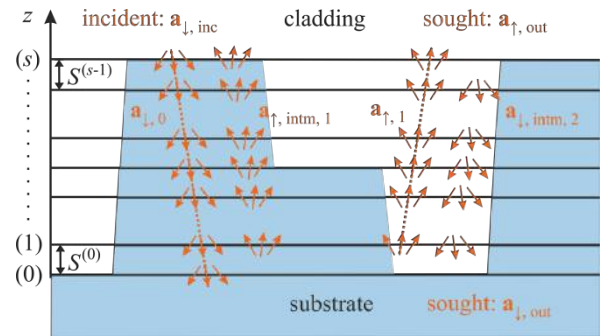


Figure 4: Illustration of the prerequisites for the application of the S-vector algorithm and the first two steps of the algorithm. On the left: coupling of the incident light $\mathbf{a}_{l, inc}$ into a stack of “S-vector layers” $S^{(0)}, \dots, S^{(s-1)}$ and propagation downwards to the substrate (step 0). Reflections $\mathbf{a}_{r, intm, 1}$ (“intermediate up-waves”) appearing at the layers are buffered for the subsequent step 1. On the right: collection of the buffered reflections $\mathbf{a}_{r, intm, 1}$ and propagation upwards to the cladding (step 1).

There is an explicit and an implicit variant of the S-vector algorithm: The explicit variant is a Bremmer series [5] or rather a multiple reflection series method [6, 7], but with a *fast* rigorous method at the single items. A drawback of the explicit variant is its modest and non-reliable convergence. Neviere and Montiel reported divergence of the multiple reflection series when combining it with the differential method [7]. This motivates the implicit variant: The multiple reflection series, which is a Neumann series, can be expressed by an inverse matrix; this introduces an inversion to be solved by an iterative solver like GMRES. *This* variant converges fast and reliably. We have tested the novel algorithm on the basis of many examples. For one of them, the convergence of the S-vector algorithm variants is illustrated in figure 5. Superior convergence of the implicit

variant can be seen in contrast to a trend towards stagnation in case of the explicit variant. Having combined the implicit variant with GSM in many test cases, we have never experienced an absence of convergence.

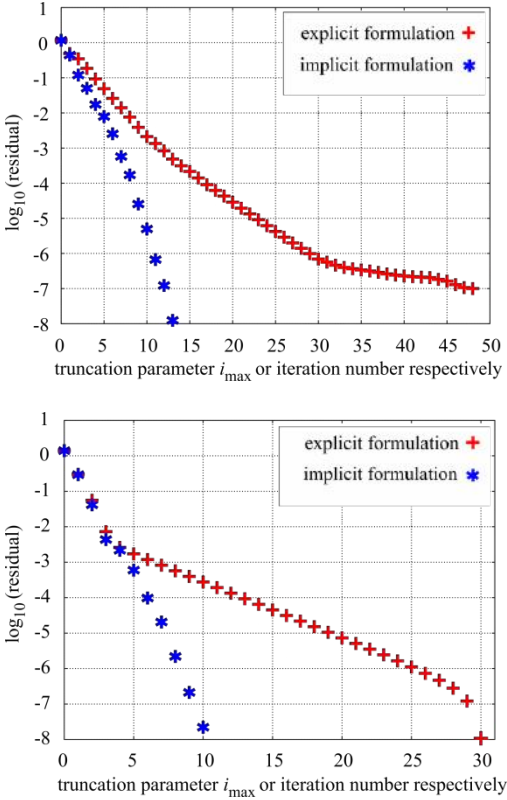


Figure 5: Convergence of the explicit variant (red crosses) and the implicit one (blue asterisks) in the case of non-conical incidence onto a 1D binary grating of glass divided into layers, using GSM at the single layers. The truncation parameter i_{\max} refers to the explicit formulation truncating the multiple reflection series; the iteration number refers to the implicit variant solving the underlying equation iteratively by GMRES. Upper figure: TE-polarization, lower figure: TM-polarization. For both polarizations, there is a trend towards stagnation in case of the explicit variant in contrast to super-linear convergence in case of the implicit variant.

4. Conclusions

The performance and versatility of ultrafast, memory sparing but rigorous light scattering calculation techniques at large planar 2D diffracting objects can be further pushed forwards by the use of graphic cards and the application of the scattering-vector (S-vector) algorithm [2, 3].

GSM is very well-suited for GPU computations; at the state of the art, one graphic card allows accelerations by more than a factor of 10 compared to CPU computations. However, the restricted memory on graphic cards and

consequently the time-consuming data transfer between GPUs and motherboard downgrades the computational performance in the case of large numbers of basis functions. A way of overcoming these limitations is offered by the S-vector algorithm. This algorithm enables the scattering-based combination of diffraction computation results at single layers and reduces the memory consumption to the memory consumption at a single layer. As well, it allows the computation of layers of various shape and materials by individually adapted methods and enhances the flexibility of ultrafast, memory sparing methods in this way.

References

- [1] A. Shcherbakov, A. V. Tishchenko, New and fast method for rigorous electromagnetic analysis of 2D periodic dielectric structures, *J. Quant. Spectrosc. and Radiat. Transfer*, 113 (2): pp. 158–171, 2012.
- [2] A. V. Tishchenko, W. Iff, Procédé de calcul numérique de la diffraction d' une structure, *patent application*, 2015.
- [3] W. Iff, *Rigorous Fourier methods based on numerical integration for the calculation of diffractive optical systems*, PhD Thesis, University of Erlangen, chapter 6, 2016.
- [4] Y. Saad, M. H. Schultz, GMRES: A Generalized Minimal Residual Algorithm for Solving Nonsymmetric Linear Systems, *SIAM J. Sci. Stat. Comp.*, 7: 856–869, 1986
- [5] H. Bremmer, The W.K.B. approximation as the first term of a geometric-optical series, *Commun. Pure Appl. Math.*, 4: pp. 105–115, 1951.
- [6] D. M. Pai, K. A. Awada, Analysis of gratings of arbitrary profiles and thicknesses, *J. Opt. Soc. Am. A*, 8: pp.: 755–762, 1991
- [7] M. Neviere, F. Montiel, Deep gratings: a combination of the differential theory and the multiple reflection series, *Opt. Commun.*, 108: pp. 1–7, 1994

Reliability and failures in electronic devices

GaN heterostructures for next generation of highly robust RF power electronics: from growth design to devices

E. Dogmus, A. Linge, M. Zegaoui, and F. Medjdoub*

Institute of Electronics, Microelectronics and Nanotechnology (IEMN), UMR-CNRS 8520, Villeneuve d'Ascq, France

*corresponding author: farid.medjdoub@iemn.univ-lille1.fr

Abstract- We report on a novel ultrathin high polarization AlN/GaN heterostructure for millimeter-wave applications that allows achieving unique combination of high performance and high robustness. A key feature has been the implementation of a thick in-situ SiN cap layer. A full description from growth design to major electrical data with respect to device reliability will be provided in the presentation.

GaN-based High Electron Mobility Transistors (HEMTs) devices have superior performance for high frequency, high power and high temperature applications compared to other competing technologies based on GaAs and Si [1] due to its unique material characteristics such as wide bandgap, high electron mobility and high thermal conductivity. Indeed, GaN heterostructures possess high breakdown voltage, which allows large drain voltages to be used, leading to high output impedance per watt of RF power, and resulting in lower loss matching circuits. The high sheet charge density leads to large current densities and transistor area can be reduced resulting in high watts per millimeter of gate periphery. In turn, this leads to lower capacitances per watt of output power. Low output capacitance and drain-to-source resistance per watt also make GaN HEMTs suitable for switch-mode amplifiers.

For instance, mobile base stations require high-output and high-efficiency power devices of a 100 W class. To achieve such high output power, a parallel configuration of multiple devices is needed if conventional GaAs MESFET or Si LD-MOSFET is used. On the other hand, owing to its high-output power performance, GaN HEMTs can achieve 100 W or higher with just a single device, making high-efficiency and energy-saving power. As a matter of fact, if for example we need to bias the 100 W Ku-band GaAs power amplifier (PA) at +12 VDC, we need to design a power supply able to generate 120 Amps. This is by no mean a trivial task, considering the small real estate available, the component ratings, and the limited cooling capabilities. By comparison, the same power supply, when designed for GaN-based PAs, will need to operate at +48 VDC, and hence generate only 30 Amps. This will greatly benefit the power supply design, and will have a major improvement in reliability. The second major benefit of using GaN transistors is the fact that they are much more efficient. As an example, a 100W Ku-band GaAs based SSPA, will consume at least 30% more energy than the equivalent GaN based design. Higher efficiency, combined with low operating bias current, provide a major improvement in the overall reliability of the power supply module in GaN based SSPAs.

Furthermore, as GaN devices can handle now up to 25°C higher temperature with no degradation in performance, it is expected the final RF Power Amplifier MTBF to increase by at least 60%. In summary, GaN offers a rugged and reliable technology capable of high-voltage and high-temperature operation. This opens up many industrial, defense, medical, and commercial applications that can be covered with GaN material systems.

Several major companies such as Qorvo, Fujitsu or UMS have qualified GaN-based products with gate length down to 0.25 μm for RF applications up to Ku band [2]. At higher frequency (millimeter-wave range), high reliability of GaN HEMTs requires specific innovative epilayers design as well as careful associated process in order to fully benefit from the potential of this outstanding material. Indeed, in this case, shorter gate lengths are needed to increase the frequency performance, however inducing much stronger electric field into the heterostructure.

This generates among others the following source of device instability under high electric field:

- Current Collapse, which manifests as drain current decreases under specific temperature, drain voltage, RF drive levels. This phenomenon could be reversible, as a function of drain voltage, or irreversible, when permanent damage occurred. The cause was studied in the scientific community and was associated to “Electron Trapping” in the dielectric interface. Due to the high energy levels (high RF fields and high Drain Voltage), high energy electrons would get trapped into the dielectric, causing drain current decrease.
- Gate Leakage degradation mechanisms. Under High Drain Voltage bias, and high RF drive levels, the peak voltage on the drain can get very high. That high voltage will cause quantum mechanical electron tunneling. The electric field at the gate edge will increase enough to cause leakage current, or electron trapping. This translates into a severe degradation of DC current and low output RF power.
- Inverse Piezoelectric Effects. High voltage bias on the gate edge under drain bias can generate inverse piezoelectric effects. These high electric fields can induce strain in the crystal structure of the GaN device. When a critical gate-drain voltage is reached, defects could develop in the crystal, which will lead to electron trapping and gate leakage current.

We have developed a novel AlN/GaN heterostructure that allows addressing the above-mentioned challenges. Key features have been the implementation of an ultrathin high polarization AlN barrier layer together with a thick in-situ SiN cap layer. This technology is therefore promising to achieve unique combination of high performance and high robustness in the Ka band and above [3-5].

Acknowledgement, This work was supported in part by the French Defense Ministry (DGA) and the French RENATECH network.

REFERENCES

1. U. K. Mishra *et al*, “AlGaIn/GaN HEMTs: An overview of device operations and applications,” *Proc. of the IEEE*, vol. 90, no. 6, pp. 1022–1031, 2002.
2. D. Floriot GH25-10 : New qualified power GaN HEMT process From Technology to Product overview,” *Proc. of the 9th European Microwave Integrated Circuits Conference*, Rome (Italy), p. 225, 2014.
3. F. Medjdoub *et al*, “Above 600 mS/mm transconductance with 2.3 A/mm drain current density AlN/GaN high-electron-mobility transistors grown on silicon,” *Appl. phys. express* 4 (6), 064106, 2011.
4. F. Medjdoub *et al*, “Beyond 100 GHz AlN/GaN HEMTs on silicon substrate,” *Electronics letters* 47 (24), 1345-1346, 2011
5. F. Medjdoub *et al*, “Preliminary reliability at 50 V of state-of-the-art RF power GaN-on-Si HEMTs,” *Proc. of Device Research Conference (DRC)*, pp. 195-196, 2010

Measuring and Improving Reliability in Today's Consumer Electronics Industry

Martin Shaw

MD Reliability Solutions

www.reliabilitysolutions.co.uk

Abstract- Understanding and predicting Reliability in the fast moving consumer electronics industry is becoming more and more difficult, while pressure is increasing to maintain low warranty failure costs while developing new products in very short design cycles. The old approach of concentrating purely on Parts Count / Stress, Design Reliability and Design Margin simply do not protect the manufacturer from possible excessive warranty costs. Increased focus on Early Life Reliability testing and assessment is now more critical than ever.

In today's consumer electronics appliances, the customer needs performance first and foremost but assumes Reliability as a given. Since 2004 the average 3-5 year failure incidence has grown steadily for consumer items while electronic content has also risen. Many designers and manufacturers simply do not place sufficient focus on early life reliability and maintain very old and traditional reliability test and prediction practices which provide virtually no correlation with real life failure rates. The traditional test methodology has low defect stimulation capability, hence many 'latent' defects are simply not detected and functional reliability is simply not stressed enough to understand Design Quality. This presentation explains clearly how Early Life can be optimized using short duration sub system reliability stress testing and several other key reliability indicators such as manufacturing process yield, assembly component failure rates, design maturity measurement. Combined the measures from each provide a new holistic approach to early life reliability prediction which correlates to real life. A range of actual case study material is presented to illustrate the power of this approach

Thermal Management of GaN Electronics

J.W. Pomeroy and M. Kuball

H.H. Wills Physics Laboratory, University of Bristol, UK

*corresponding author: james.pomeroy@bristol.ac.uk

Abstract-Gallium nitride based transistors are a disruptive technology in high-power RF and power conversion applications. Maintaining device temperatures within a safe operating area is critically important to ensure reliable long term operation, although this becomes ever more challenging as increasing power densities are required. We review recent developments in thermal management, from understanding where heat is generated during different modes of transistor operation (DC versus RF), to near junction thermal management strategies, including high thermal conductivity diamond substrates.

GaN high-power RF amplifiers are being developed for the most demanding high-power applications, such as communication or radar. To ensure reliable operation over the required lifespan, it is critical that transistor channel temperature is maintained within a safe operating area, since temperature is one of the main drivers of device degradation. Thermal management is therefore a critical aspect of device design. Very high temperature gradients are generated in the transistor channel during operation. Although device temperature can be estimated by using simulation only, uncertainties in some input parameters can lead to large errors in mean time to failure (MTTF) predictions, owing to the exponential relationship between temperature and failure rate. A better approach is to combine device modelling with temperature measurement, although this is challenging if using conventional thermal measurement techniques such as IR thermography, due to their finite spatial resolution. We have used a combination of laser based measurement techniques with submicron and nanosecond resolution, including Raman thermography [1] and thermoreflectance, to perform temperature measurements as close as possible to the peak temperature location (Fig. 1), validating detailed device simulations.

We use this combined measurement and simulation approach to investigate various aspects of self-heating and thermal management in GaN HEMTs. We address whether channel temperature is equivalent during RF versus DC only operation, which has been an outstanding question in the reliability testing community [2]. This has important implications for the cost and complexity of transistor accelerated life testing. Near junction thermal management is also crucial to ensure efficient heat extraction. By integrating GaN transistors with high thermal conductivity diamond substrates, we show that a $>3\times$ increase in RF power density can be achieved at the same channel temperature with respect to SiC, which is the current standard for high power GaN devices [3]. We also discuss how device design, novel die attach and packaging materials can be used to improve thermal management.

Acknowledgements

We gratefully acknowledge the support of the MCM ITP, DARPA and EPSRC.

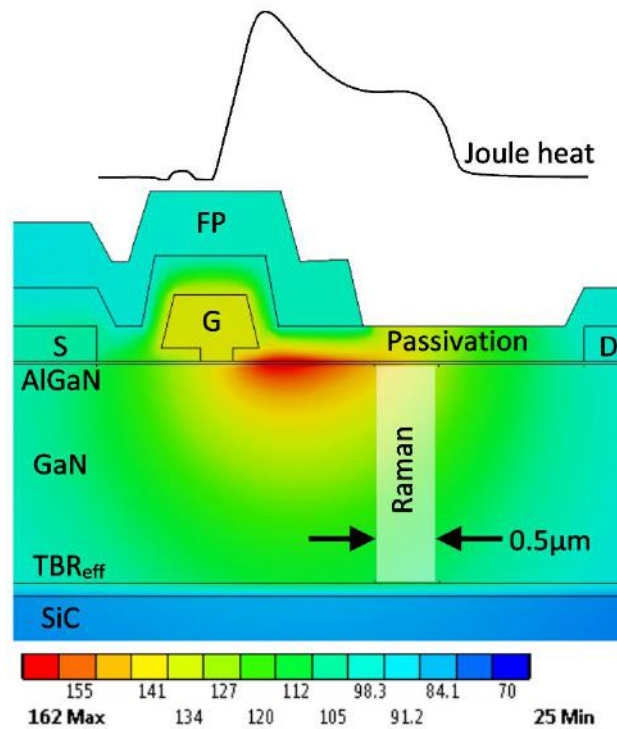


Figure 1: Cross section through a combined drift-diffusion / 3-D finite element thermal model of a packaged GaN RF HEMT operated with a 50 V_{DS} bias, 11W/mm power dissipation density, at an ambient temperature of 25°C; only the active region is shown for clarity. The S, G, D and FP labels indicate the source, drain, gate and field plate, respectively. The channel Joule heating profile close to the AlGa_N/Ga_N interface is also shown (upper plot) for visual reference. The peak temperature location close to the gate is evident in the temperature contour illustration (lower plot). The experimental Raman temperature measurement location is highlighted.

REFERENCES

1. G. J. Riedel, J. W. Pomeroy, K. P. Hilton, J. O. Maclean, D. J. Wallis, M. J. Uren, T. Martin, and M. Kuball, "Nanosecond Timescale Thermal Dynamics of AlGa_N/Ga_N Electronic Devices," *IEEE Electron Dev. Lett.*, Vol. 29, No. 5, 416–418, 2008.
2. J.W. Pomeroy, M.J. Uren, B. Lambert, M. Kuball, "Operating channel temperature in GaN HEMTs: DC versus RF accelerated life testing," *Microelectronics Reliab.*, Vol. 55, No. 12, 2505–2510, 2015.
3. J. W. Pomeroy, M. Bernardoni, D. C. Dumka, D. M. Fanning and M. Kuball, "Low thermal resistance GaN-on-diamond transistors characterized by three-dimensional Raman thermography mapping," *Appl. Phys. Lett.*, Vol. 104, No. 10, 083512-1–5, 2014.

Reliability study of mechatronic power components using spectral photon emission microscopy

Niemat Moulitif, Eric Joubert, Olivier Latry

Normandy University, University of Rouen, Groupe Physique des Matériaux, UMR CNRS 6634
Site de Madrillet, Avenue de l'Université – B.P 12. St Etienne de Rouvray 76801 France

*corresponding author: eric.joubert@univ-rouen.fr

Abstract

In this paper, we present one of the most important failure analysis tools that permits the localizing and the identification of the failure mechanisms. It is a new spectral photon emission system, enabling to localize the failure and quickly get the photon emission spectra that characterize the failure with high resolution. A diffraction grating is used as a spectrometer in the system. Application results on mechatronic power devices such as HEMT AlGaIn/GAN and SiC MOSFETs are reported.

1. Introduction

Failure analysis (FA) is becoming a crucial part of the integrated circuit (IC) design development and manufacturing. The microelectronic failure analysis process consists of five main steps, namely: failure validation, fault localization, sample preparation and defect tracing, defect characterization and root cause determination [1].

Fault localization is the step where the defective area is isolated to a smaller area. Photon emission microscopy (PEM) has been and still remains one of the most important localization techniques in the FA of semiconductor ICs. The major advantage of this technique is that it does not damage healthy devices nor further degrade existing defects. It is a non-destructive technique that requires the units to be in a fully functional state. But PEM technique has its limitation. It can only be used to indicate the place of the failure. In most cases it is not enough to allow an identification of the failure [2].

However, the study of spectral PE signatures gives a characterization of the defects, because each failure mechanism has its own unique spectral signature. Actually, the spectrum for a particular failure mechanism is distinguished from that of other mechanisms by its wavelength-dependent spectral shape and the wavelength range [3].

This paper introduces firstly the basics of PE phenomena, and a state of the art on the spectral photon emission systems (SPEMS). Next, the system developed is described. Then, the application results are presented on two technologies of semi-conductors devices.

2. PE distribution characterization

The PE technique is generally implanted on an optical microscope using a high sensitive camera enabling the detection of the weak emissions from semiconductor devices. Fig. 1 shows the quantum efficiency of the best detector candidates used for observing photon emissions (Si-CCD, MCT and InGaAs).

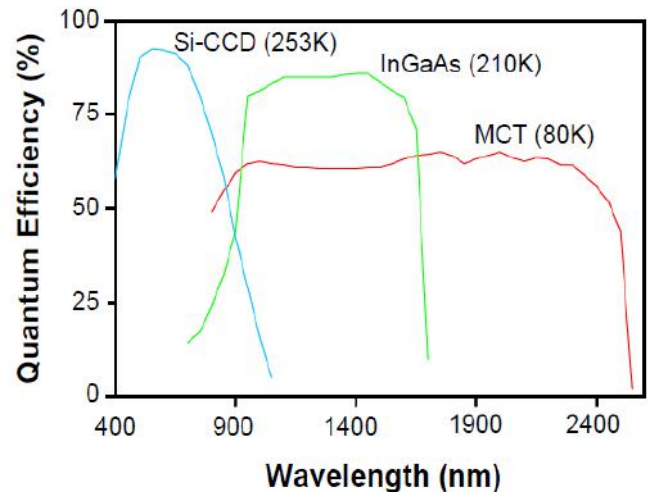


Fig. 1. Quantum efficiency of typical Si-CCD, MCT and InGaAs focal plane arrays [4]

In our system, PEM observations are performed using the microscope PHEMOS 1000 of HAMAMTSU. The system is equipped with a cooled Si-CCD detector with spectral sensitivity in the visible and near infrared range. The test procedure consists of three separate acquisitions:

- Visible pattern image of the device under test (DUT), is obtained by illumination the DUT with an external light source Fig. (2-a).
- Noise image aim at measuring the interference. It is obtained when the DUT and the external light source are in the idle mode.
- Emission image, which is the result of the acquisition of the biased DUT emissions without illumination, under dark conditions (Fig. 2-b).

The result of subtraction of the emission image by the noise image is superimposed with the visible image to localize the defective region of the DUT (Fig. 2-c).

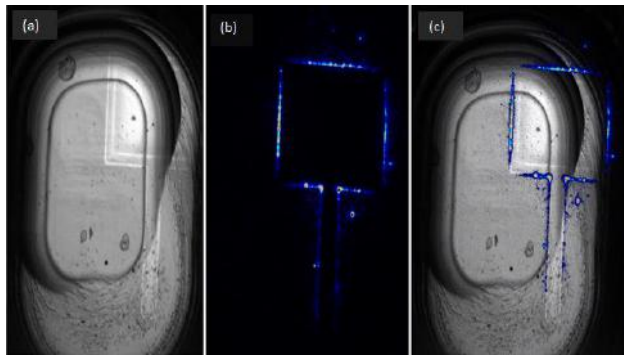


Fig. 2. (a) Pattern image of a backside opened Power MOSFET with the (x5) power lens. (b) Emission image. (c) Superimposed image.

The PE technique requires a detector view of the active surface. So, sample preparation and decapsulation of packaged devices are essential. Conventional frontside PE analysis is facing severe limitations with the growing use of multi-level metals and bridges, which prevent photon emission of the defects from reaching the detector. To overcome this problem we access the device from the backside, through the substrate. Since the transmission rate of light in the most conventional substrate (Si, SiC, and GaN) is a function of wavelength, substrate thickness and the dopant concentration, backside analysis requires proper backside sample preparation and substrate thinning (less than 180 μm thick) [5].

The PE process in a semiconductor occurs when there is a radiative emission of electromagnetic waves as a result of transition of carriers from a higher energy state to a lower energy state. There are different kinds of transition: Hot electron, hot hole, donor level, acceptor level, and deep level (Fig. 3).

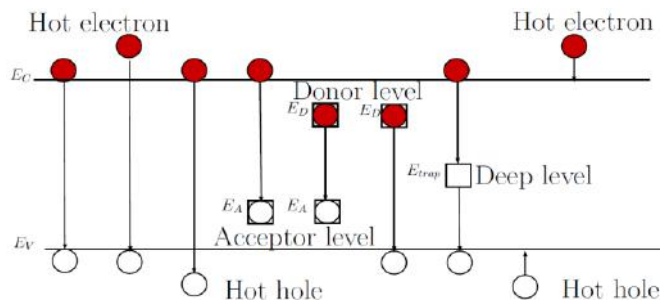


Fig. 3. Type of transitions

Since the wavelengths or energy of these emitted photons are related to the type of transitions of the carriers, this information can be a mean to determine the type of failure mechanisms that are emitting these photons. Whence comes the interest in extracting the spectral photon emission signature.

3. PE Spectrum analysis

3.1. Failure analysis

The light emission phenomena may be classified largely into three groups namely Oxide radiation, hot carrier radiation and recombination radiation. Each group is characterized by different spectral distributions [6] (Fig 4). In fact, each failure mechanism such as those caused by weak oxides, hot-carrier effects, leaky junctions, IC latch-up, or other current leakage problems has a unique spectral signature.

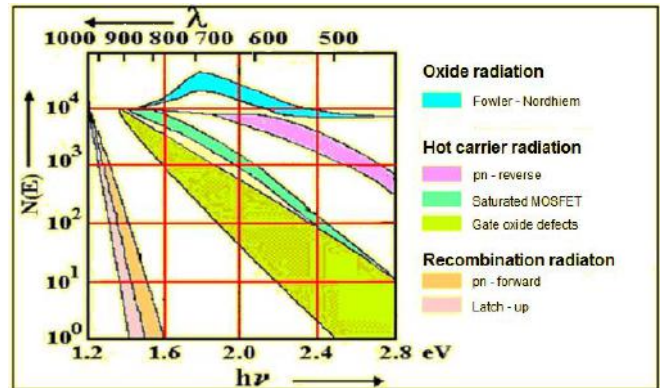


Fig. 4. Typical emission spectrum of most defects [6]

3.2. Existing SPEM systems

Using information obtained with a SPE system (SPES), it is possible to extract the fingerprint of the defect emissions of the DUT which can be correlated with the failure mechanism.

The oldest and the simplest approach for spectral analysis is the use of a serie of discrete bandpass filters of different wavelength range, to cover the whole spectrum in the detector spectral range response. By inserting different filters in the light path of the PEM, acquisition time becomes longer which may degrade further the device [6]. This represents a major disadvantage of this method. Moreover, these filters have low transmittance which makes the system less sensitive to weak emissions.

Other methods for spectroscopic analysis with the PEM include the use of an elliptical mirror [7, 8]. In the elliptical mirror method, Liu et al. used two separate detectors (one coupled to the spectrometer and one for the emission microscope) which make this method too expensive. In fact, the elliptical mirror is positioned between the sample and the microscope, to collect the light emitted from the sample and guided by an optical fiber to a monochromator. However, the system has a short working distance, making it difficult to work on encapsulated devices and unpackaged devices where probing are needed.

Another configuration is the in-lens method: a light dispersing element such as prism [9, 11, 12, 13] is positioned in the optical microscope to disperse the light emitted from the device to obtain a continuous wavelength

spectrum. Many studies used the prism as spectrometer. De Kort et al. used a prism/lens system to focus the spectrum of the emitted light on the detector [9, 10]. In this case, a beamsplitter is inserted between the objectives of the PEM and the detector. The reflected light is directed through a direct vision prism coupled by a focusing lens to a second detector.

A simplification of this method is presented by M S. Rasras et al. who used only one detector for both conventional failure analysis and continuous wavelength spectroscopy [11]. However, this system needs physical movement of the detector when switching between imaging and spectroscopic analysis.

An improved system based on a three element prism was realized by SL Tan et al. The three prisms are positioned in the path of the optical microscope, between the objective and the tube lens [12]. A more advanced system is proposed by P. Scholz et al. who used only one prism placed in the optical path of the microscope [13]. The major disadvantage of the prism is its incapability to show the original emission position and the spectra at the same time. Moreover, this device is difficult to insert in the optical path due to the volume taken by it.

As a compromise between the prism and band pass filters, a diffraction grating was chosen for our system.

3.2. System Description

A diffraction grating was used as a spectrometer and placed in the optical path of the microscope, between the objective lenses and the Si-CCD detector (Fig. 5). The choice of a transmission grating was mainly motivated by its shape, high resolution and one shot continuous acquisition. In fact, the device is flat, easy to insert into the optical path and provides continuous registration between the origin of the emissions and the spectral distribution. Single emission images are treated to obtain the spectrum by expansion of the emission spot to a spectral tail.

The system calibration is performed in two phases. The first phase aims to convert the raw PE spectrum as read out from the image into the real spectrum. This was obtained by founding the relation between the pixel number in the PEM image and the wavelength of the light. While the second phase has as purpose, the correction of the raw PE intensity spectrum by the known spectral response of the detector Si-CCD.

The grating chosen is a 100 lines/mm transmission diffraction grating, blazed in the first order.

The PE spectrum is extracted from the diffraction line. This line is drawn automatically by linking the centers of gravity of the points of orders '0' and '1' or based on average of the maximum intensity. The image processing is performed using personal software developed on Matlab.

3.3. Spectral PEM experimental results

3.3.1 Reliability study of an AlGaIn/GaN HEMT

The first device studied in this work by the spectral PEM technique, is an AlGaIn/GaN high electron mobility transistor (HEMT) power bars on SiC substrate (European technology).

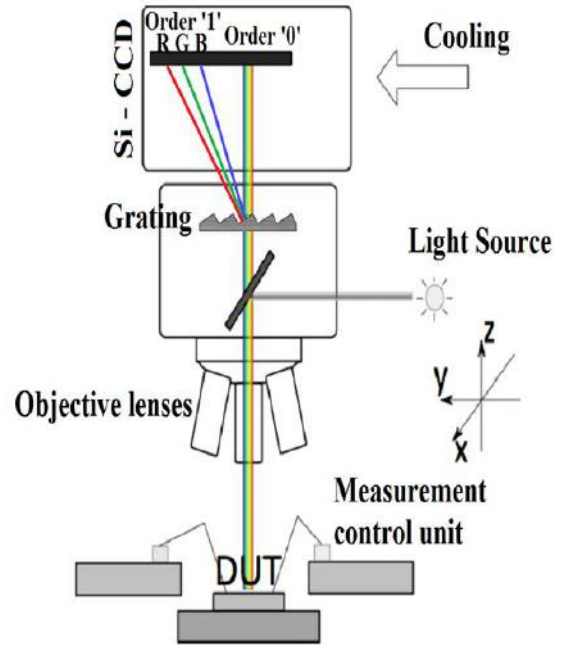


Fig. 5. Insertion of a grating in the optical path of the microscope.

PE Characterizations have been realized on the transistor mode (V_{gs}, V_{ds}) = (-7V, 30V). The current I_{ds} is extremely low since the transistor is strongly pinched off.

The PE signatures are localized in this device along the gate fingers due to gate current flow. The PE inhomogeneity is visible in this pinched off mode when no significant current flows through the device. In fact, there are plenty of locations characterized by stronger PE intensity and have a spot shape. These peaks maximum has been analyzed in spectral.

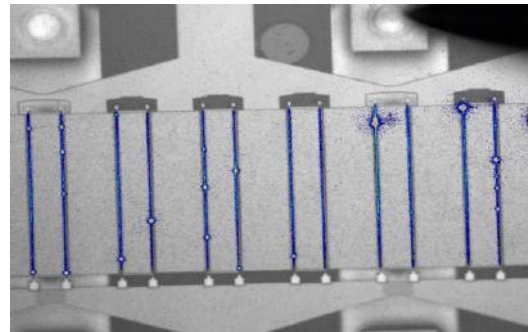


Fig. 6. PE signature of a fresh device in transistor mode: (V_{gs}, V_{ds})=(-7V, 30V).

Each spot measured showed no spread of its first order. Thus this is was monochromatic emission. The measured

wavelength was about 930 nm, corresponding to 1.35 eV level energy.

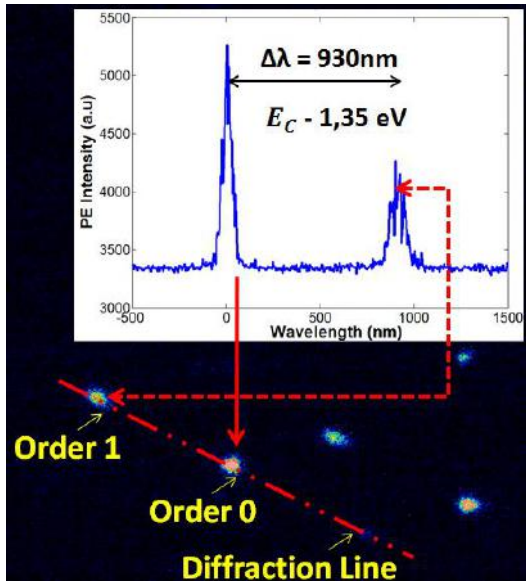


Fig. 7. Photo emission spectrum: Extracting a fresh device spot wavelength in the transistor mode (VGS, VDS) = (-7V, 50V).

According to literature this deep level energy corresponds either to an interstitial carbon defect that forms along dislocations [14], or an omnipresent defect such as C or possibly dislocations [15].

3.3.2 Reliability study on a SiC MOSFET: HTGB Stress

The second device studied in this work is a second generation Cree silicon carbide MOSFETs, having a D-MOSFET structure (Fig. 8), available in the market with the voltage and current of 1200 V and 19 A respectively.

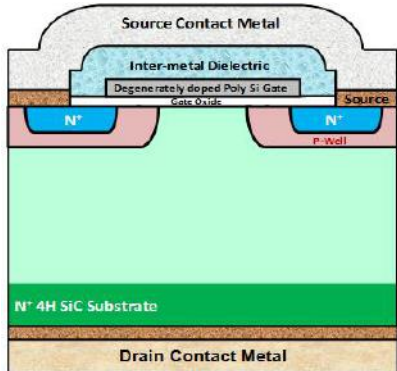


Fig. 8. 2nd Generation SiC Cree MOSFET: D-MOSFET Structure [16]

A device has been aged by high temperature gate bias (HTGB) test with (Vds ; Vgs) = (960 V ; -5V) for 26 days. It is a step stress temperature increasing from 120°C to 190°C. Following this aging test, there was an increase of Rds (on), drain leakage current (Idss) and threshold voltage (Vth).

A study by spectral PEM is performed on the aged and the fresh devices (Fig 9). The spectrum of the two devices shown in Fig. 10, presents a decrease in the intensity of PE for the aged component, and a slight shift in the decreasing wavelengths.

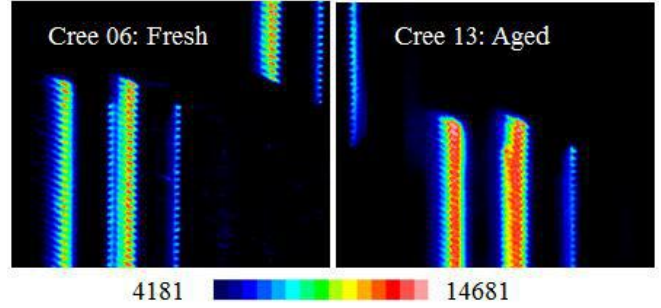


Fig. 9 Spectral PEM analysis of the fresh and the aged devices

It is believed that following the aging test, the surface between the gate oxide and the semi-conductor is damaged. This has degraded the gate command, which explain the decrease of the threshold voltage and the spectrum shift towards the decreasing wavelengths. In order to prove this hypothesis further analysis in focused ion beam and scanning electron microscopy are planned.

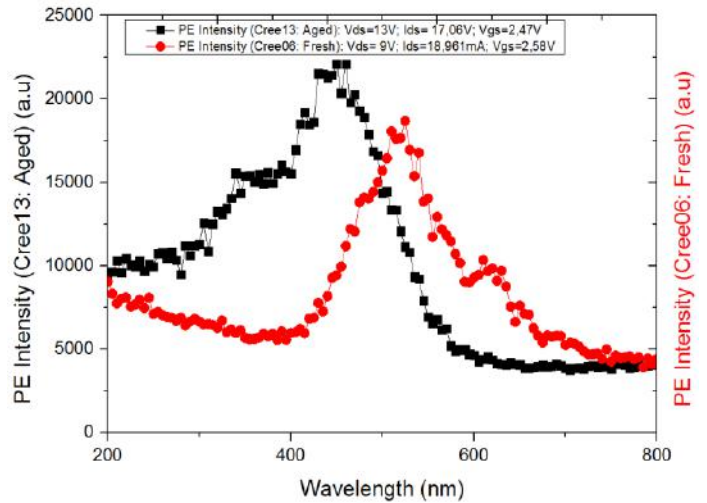


Fig. 10. PE spectrum of the fresh and the HTGB aged devices

3.3.3 Robustness Study on a SiC MOSFET: ESD Stress

In this paper, we are interested not only by studying the reliability of this SiC MOSFET devices with the HTGB test, but also in evaluating their robustness to ESD stress, using the spectral PEM technique.

We studied the spectral PE signature of both the fresh and the ESD degraded devices. The PE spectrums obtained are in the frequency range of the visible and near infrared (Fig. 11). A spectrum shift in the increasing wavelengths was noticed, in addition to a decrease in the intensity of light emission between the fresh and the degraded devices.

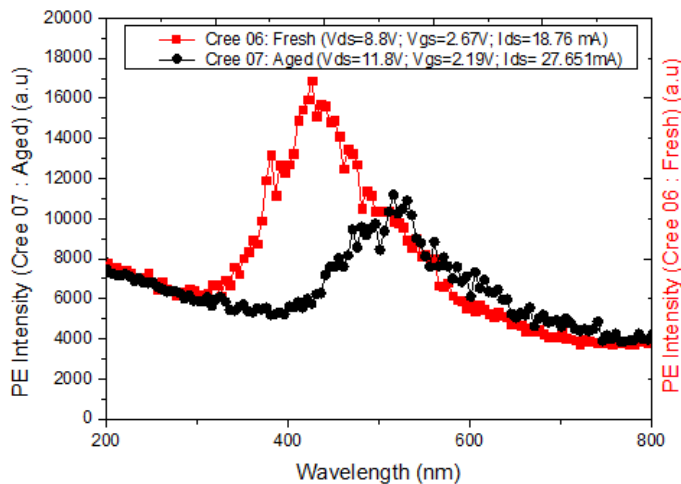


Fig. 11. PE spectrum of the fresh and the ESD aged devices

Following the ESD stress, diffusion at this junction is suspected, which has generated an increase in leakage current, and has caused a spectral gap between the fresh and the degraded device. To confirm this hypothesis Nano-SIMS analyses will be performed.

4. Conclusions

In this paper, photon emission microscopy and spectroscopy for microelectronic failure analysis are presented together with the instrumentation developments that allow these techniques to be effectively deployed for microelectronic fault localizing and defect characterization. We introduced in this paper a new spectral photon emission system. We demonstrate its application on a variety of high power mechatronic devices. The failure mechanisms related to the results spectrums are discussed and further analysis are in perspectives.

Acknowledgements

This work is funded by the French MFP FIRST project.

References

[1] S.M. Kudva et al. , The SEMATECH Failure Analysis Roadmap, Proc Int Symp Testing & Failure Analysis (ISTFA 1995), 6-10 Nov 95, Santa Clara, California, USA, pg 1-5, 1995

[2] I. De Wolf and M.S. Rasras. Spectroscopic photon emission microscopy: a unique tool for failure analysis of microelectronics devices. *Microelectronics Reliability*, 41(8):1161-1169, August 2001.

[3] J.M. Tao et al. , Analysis And Quantification Of Device Spectral Signatures Observed Using A Spectroscopic Photon Emission Microscope, Proceedings of 6th IPFA '97, Singapore 1997.

[4] J. C. H. Phang, D. S. H. Chan, et al. A review of near infrared photon emission microscopy and spectroscopy. In *Physical and Failure Analysis of Integrated Circuits*, 2005. IPFA 2005. Proceedings of the 12th International Symposium on the, pages 275-281. IEEE, June 2005.

[5] J. Tao, P. Fang, and J. Wang. Backside IR photon emission microscopy (IR-PEM) observation in failure analysis of the packaged devices. In *Electronic Packaging Technology*, 2007. ICEPT 2007. 8th International Conference on, pages 1-4. IEEE, August 2007.

[6] J. Kolzer, C. Boit, A. Dallmann, G. Deboy, J. Otto, D. Weinmann, "Quantitative Emission Microscopy", *J Appl Phys*, Vol 70, No 11, pg 23-41,1992.

[7] Y. Y. Liu, J. M. Tao, D. S. H. Chan, J. C. H. Phang, and W. K. Chim. A new spectroscopic photon emission microscope system for semiconductor device analysis. In *Physical and Failure Analysis of Integrated Circuits*, 1995., Proceedings of the 1995 5th International Symposium on the, pages 60-65. IEEE, November 1995.

[8] D. S. H. Chan, J. C. H. Phang, W. K. Chim, et al. Design and performance of a new spectroscopic photon emission microscope system for the physical analysis of semiconductor devices. *Review of Scientific Instruments*, 67(7):2576-2583, July 1996.

[9] K.. De Kort, P. Damink ,H. Boots, Spectrum Emitted by Hot Electrons in p-i-n Cold Cathodes, *Physical B*, Vol 48, No 16,pg 11912-11920, 1993.

[10] K. De Kort and P. Damink, The spectroscopic signature of light emitted by integrated circuits, *Proceeding of the European Symposium on Reliability of Electron Devices, Failure Physics and Analysis (ESREF'90)*, p. 45, 1990.

[11] M.S Rasras, I. De Wolf, G. Groeseneken, and H. E. Maes. Spectroscopic identification of light emitted from defects in silicon devices. *Journal of Applied Physics*, 89(1):249-258, January 2001.

[12] S.C. Tan, K. Toh, J. Phang, D. Chan, et al. . A Near-Infrared, continuous wavelength, In-Lens spectroscopic photon emission microscope system. In *Physical and Failure Analysis of Integrated Circuits*, 2007. IPFA 2007. 14th International Symposium on the. IEEE, July 2007.

[13] P. Scholz, A. Glowacki, U. Kerst, C. Boitet al. , Single image spectral electroluminescence (photon emission) of GaN HEMTs. In *Reliability Physics Symposium (IRPS)*, 2013 IEEE International, pages CD.3.1-CD.3.7. IEEE, April 2013.

[14] M. Armstrong, Investigation of deep level defects in GaN:C,GaN:Mg AND Pseudomorphic AlGaIn/GaN Films; Thesis dissertation University of Ohio, 2006.

[15] A. Armstrong, A. R. Arehart, Impact of carbon on trap states in n-type GaN grown by metalorganic chemical vapor deposition, *App. Phy Vol 84*, Num 3. 2004.

[16] J. Casady, J. Palmour, High Megawatt Direct-Drive Motors and Front-End Power Electronics Workshop - Sept 2014, Panel: WBG Devices Cost and Development Roadmap: http://www.nist.gov/pml/high_megawatt/sept2014_presentations.cfm

Reliability and Failure Analysis of UHF-RFID Tags for Harsh Environments Applications

S. Taoufik(1,2,3), A. El Oualkadi(1), P. Dherbécourt(2), F. Temcamani(3), B. Delacressonniere(3)

¹Laboratory of Information and Communication Technologies
National School of Applied Sciences of Tangier, Abdelmalek Essaadi University, Morocco

²Materials Physics Group, UMR CNRS 6634 university of Rouen
Avenue de l'université B.P 12 76801 Saint Etienne du Rouvray, France
Email: sanae.taou@gmail.com

³QUARTZ laboratory EA3649 National School of Electronics and its applications
6 Avenue du Ponceau 95014 Cergy Pontoise, France

Abstract- Nowadays, the RFID technologies are used in many domains such as aeronautics, automotives, pharmaceuticals and smart cards [1-2]. UHF passive RFID tags are especially suitable for these purposes because they are inexpensive, compact, mechanically robust, and their read range is several meters [3].

Due to their numerous different applications, RFID tags may be exposed to various environmental conditions during their lifetime. Different stresses from the environment may affect the reliability of a tag. The environmental stresses may, for example, include high temperature or humidity levels, and mechanical vibration [4]. Accelerated environmental tests can be used to study the effects of environmental stresses on reliability of passive tags [5-7].

In this work we have chosen to study the high temperature effect on the performance of passive UHF-RFID system. Therefore, a measurement bench was developed, and a thermal storage testing at various extreme temperatures (140 ° C, 160 ° C and 180 ° C) were made.

The results for the thermal storage test at a temperature of 160 °C are shown in Figure 1.

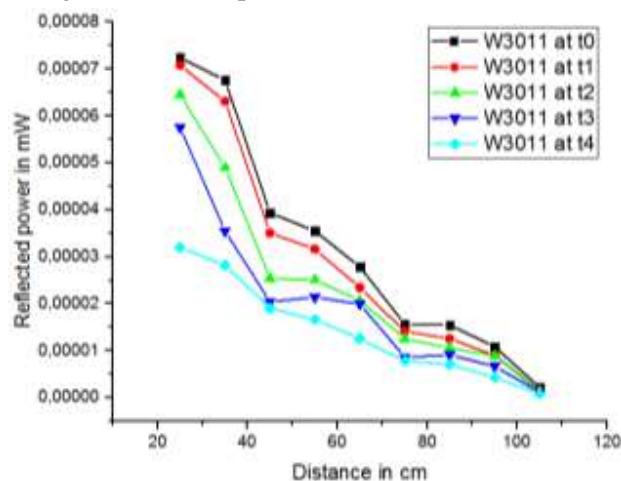


Fig.1. Reflected powers by the tag “W3011” versus distances for different aging times

The performance parameters of the tag are significantly changed during the tests, the reflected power decreases after each test which strongly influences the range of the tag.

Clear differences in the time to failure (TTF) depending on the selected temperature were observed. Statistical analyzes using the predicted reliability calculation tools are implemented to estimate the lifetime of this type of tag for nominal operating temperatures. Also a physical analysis of the aged tags, using the optical microscopy and SEM (Scanning Electron Microscopy), are implemented to reveal the failure mechanisms.

REFERENCES

1. B.Nath, F.Reynolds, and R. Want, « RFID technology an applications », IEEE Pervasive Comput., Vol 5, no.1, pp 22-24, Jan.-Mar. 2006.
2. Ming K. Lim, Witold Bahr, Stephen C.H. Leung, "RFID in the warehouse: A literature analysis (1995–2010) of its applications, benefits, challenges and future trends." International Journal of Production Economics, Volume 145, Issue 1, Pages 409–430, September 2013.
3. D. Dobkin, The RF in RFID—Passive UHF RFID in Practice. San Jose, CA: WJ Communications, 2007, 504 pp.
4. K.V.S.Rao, P.V.Nikitin and S.F.Lam, « Antenna design for UHF RFID tags, a review and a practical application», IEEE Trans. Antennas Propag., Vol 53, no.12, pp 3870-3876, Dec. 2005.
5. E. Suhir, “Accelerated life testing (ALT) in microelectronics and photonics: Its role, attributes, challenges, pitfalls, and interaction with qualification tests,” ASME J. Electron. Packag., vol. 124, no. 3, pp. 281–291, 2002.
6. Lahokallio,S, Saarinen-Pulli K,Frisk L. Effects of different test profiles of temperature cycling tests on the reliability of RFID tags . Microelectron Reliab 2015;55(1):93–100.
7. Saarinen-Pulli K, Lahokallio S, ,Frisk L. Effects of different anisotropically conductive adhesives on the reliability of UHF RFID tags . International Journal of Adhesion & Adhesives 64(2016)52–59.

Overview on Zener diode pulsed EOS characterization

F. Zhu¹, F. Fouquet¹, B. Ravelo^{1*}, B. Domenges², and M. Kadi¹

¹IRSEEM EA 4353, ESIGELEC, Avenue Galilée, 76801 Saint Etienne du Rouvray, France

²LaMIPS, CNRS, Campus Efficienc 2 Esplanade Anton Philips BP 20000, 14906 COLOMBELLES, France

*corresponding author, E-mail: ravelo@esigelec.fr

Abstract

The electrical overstress (EOS) is assumed as one of misinterpreted electrical phenomena susceptible to degrade electronic components. This paper deals with the failure analysis of a Zener diode under EOS. The experimentation enabling to investigate the tested component EOS signature with typically millisecond-duration square wave voltage pulse is described. Based on the transient responses of the stressed diode, the predictive model reproducing the degradation mechanism is presented.

1. Introduction

Beyond the classical ElectroMagnetic Compatibility (EMC) and ElectroStatic Discharge (ESD) phenomena, the Electrical Over Stress (EOS) or over voltage/current impact threatens the modern integrated circuits and electronic devices reliability [1]. The correlation between the EOS and electronic product failures attracted electronic engineer special attention [2]. Despite this preliminary observation, the electronic component degradation mechanism caused by EOS effect requires further technical analysis. Empirical study [3] and tentative modelling [4] of the Zener diode BZX84B6V8 degraded by EOS pulse are introduced. The overview on the research work for the further understanding of the EOS characterization applied to this diode is elaborated in this paper.

2. EOS effect failure analysis

The circuit diagram of the experimental setup corresponding to the diode or device under test (DUT) characterization is depicted in Fig. 1(a). The overall circuit is stressed by the time-dependent square wave voltage $V_{eos}(t)$. The stress signal V_{eos} presents amplitude of about 17V and duration equal to 4ms. The protection resistance $R_{test}=5\Omega$ was inserted in the circuit to control the current I_{eos} . In order to check the relevance of the DUT equivalent model, it was integrated in the circuit as shown in Fig. 1(b).

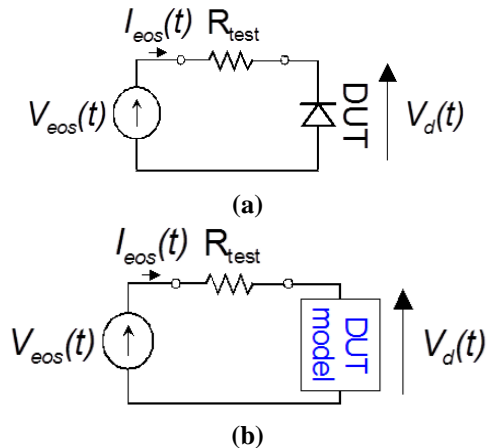


Figure 1: Schematic of the considered EOS test setup.

As seen in Fig. 2, a voltage breakdown of V_d is occurred across the DUT. More importantly, this phenomenon appears earlier for the periodical pulse EOS substantially materialized by the shift of the critical times t_{c1} , t_{c2} and t_{c3} .

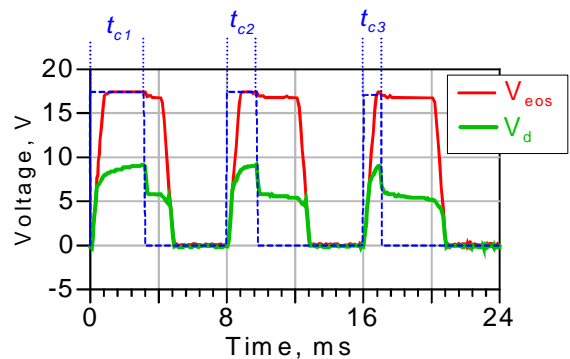


Figure 2: EOS test transient results.

This observation reveals that the EOS transient signature is inherently linked to the heat transfer through the diode junction. The EOS effect can be visibly understood by the degraded area with the X ray imaging of the stressed diode sample displayed in Fig. 3. With the progressive increase of the EOS amplitude, the EOS signature can be physically highlighted. It is observed that the wire bound junction is melted seemingly due to the increase of the junction temperature corresponding to the energy deposited via EOS onto the semiconductor material.

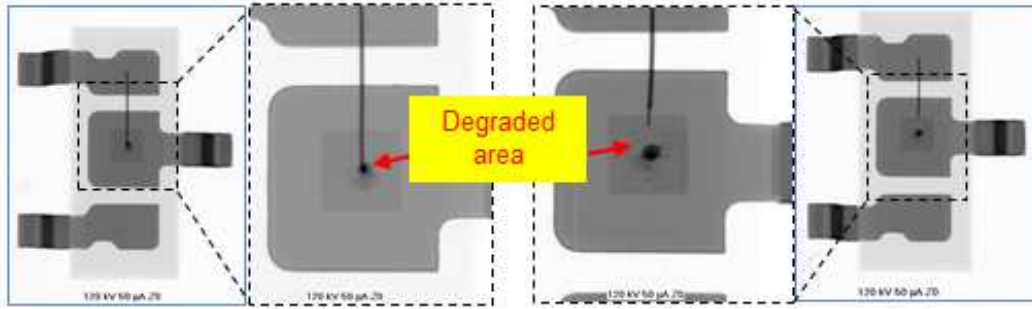


Figure 3: EOS signature with X ray imaging.

The electrical modelling highlighting this EOS mechanism will be examined in the next section.

3. EOS effect predictive modelling

The predictive model of the diode under EOS is presented in Fig. 4. Let us denote θ the temperature variable. It acts as an electro-thermal circuit with the equivalent circuit constituted by $R_{eos}(\theta)$ and $C_{eos}(\theta)$ and the Zener voltage $V_z(\theta)$ by considering the diode internal relative temperature $\Delta\theta$ which is in turn changing with respect to the instantaneous dissipated power $P_{eos}(t)$.

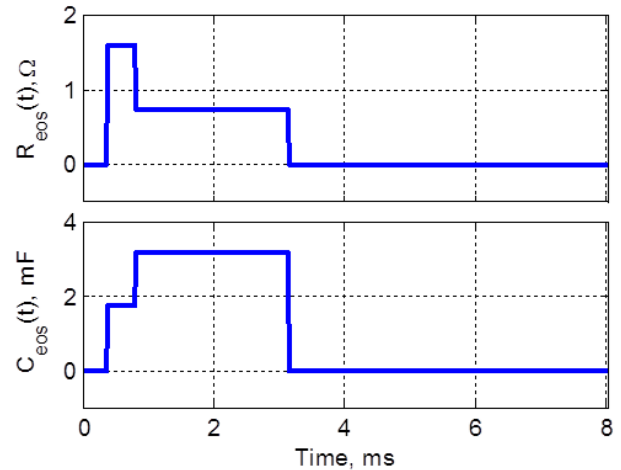


Figure 5: Time-dependent variation of the stress resistance R_{eos} and capacitor C_{eos} .

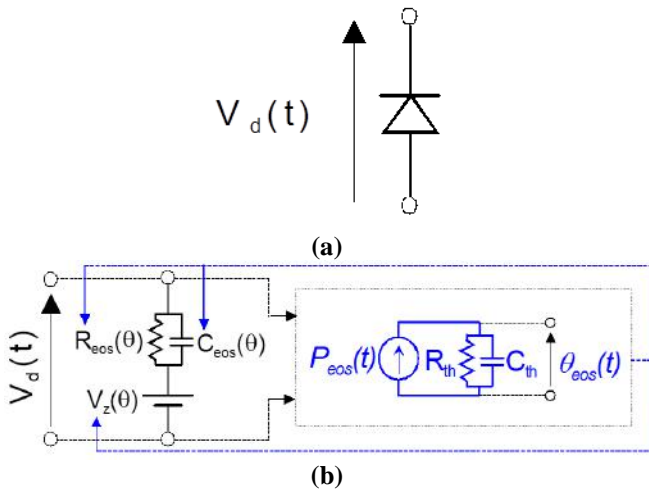


Figure 4: EOS predictive electro-thermal model.

With the EOS voltage plotted in Fig. 2, it can be emphasized that the stress resistance $R_{eos}(\theta)$ and capacitor $C_{eos}(\theta)$ vary in time-dependent as displayed in Fig. 5. This estimation can be deployed with the transient responses of V_d with the three periodical pulses shown in Fig. 2. The numerical implementation with Matlab of the transfer function responses corresponding to the electro-thermal model introduced in Fig. 4 enables to estimate the electro-thermal parameters R_{th} and C_{th} . Accordingly, the thermal circuit presents a constant time equal to $\tau_{th} \approx 5.4$ ms. Meanwhile, one assesses the critical temperature variation of about $\Delta\theta_c$.

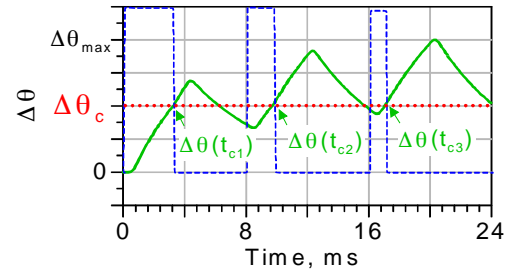


Figure 6: Transient temperature variation of the diode junction.

Despite this tentative predictive model, deep investigation is still needed for more precise deduction of the electro-thermal parameter variation in function of the EOS signal shape.

4. Conclusions

The EOS characterization applied to a Zener diode and the experimental analysis enabling to demonstrate the EOS signature are investigated. It is found that the EOS degradation mechanism is inherently due to the heat transfer which affects the physical characteristics of materials constituting the stressed component. The electrical behavior of the degraded component is illustrated with the predictive model integrating the instantaneous electro-thermal phenomenon between each element constituting the diode.

Acknowledgements

This research work was supported by Euripides²-Eureka Program funded by the research project “Embedded Die Design Environment & Methodology for Automotive Applications (EDDEMA)”, 2015-2018.

References

- [1] K. T. Kaschani, R. Gärtner, The impact of electrical overstress on the design, handling and application of integrated circuits, *Proc. of 33rd Electrical Overstress/Electrostatic Discharge Symposium (EOS/ESD)*, Anaheim, CA, pp. 11–16, 11-16 Sept. 2011.
- [2] J. L. Lefebvre, C. Gautier, F. Barbier, Correlation between EOS customer return failure cases and Over Voltage Stress (OVS) test method, *Microelectronics Reliability*, Vol. 49, No. 9-11, pp. 952–957, Sept.–Nov. 2009.
- [3] F. Zhu, F. Fouquet, B. Ravelo, M. Kadi, A. Alaeddine, Experimental investigation of Zener diode reliability under pulsed Electrical Overstress (EOS), *Microelectronics Reliability*, Vol. 53, No. 9–11, pp. 1288–1292, Sept.–Nov. 2013.
- [4] F. Zhu, B. Ravelo, F. Fouquet, M. Kadi, Electrical predictive model of Zener diode under pulsed EOS, *Electronics letters*, Vol. 51, No. 4, pp. 327–328, Feb. 2015.

Biomedical Applications of Electromagnetics

Microwave Antennas for Cancer Ablation Therapy: Backward Heating Problem.

H. Acikgoz

KTO Karatay University, Turkey

hulusi.acikgoz@karatay.edu.tr

Abstract- During this presentation, some important developments on the use of microwave coaxial antennas for cancer ablation therapy will be detailed. Particularly, we will focus on the problem of backward heating where surface currents propagate on the antenna outer conductor and overheat regions far away from the cancerous tissue.

The most frequently used methods for cancer treatment are chemotherapy, radiotherapy, surgery and ablation techniques. Each method has its own advantages and disadvantages depending on the patient specific situation or the size of the tumor tissue. For example, surgery may not be suitable for deep-seated or very big tumors. In addition, only between 10% and 20% of liver cancer patients having also cirrhosis can be treated by surgery. Additionally the most commonly used ablation method is the radio frequency (RF) ablation. By this method, the cancerous tissue is eradicated using 500 kHz alternating current. RF ablation is effective in tissues with a radius of 1-2 mm. The importance of microwave ablation technique arises from its shorter treatment time and relatively wider effective area with respect to RF ablation. Microwave ablation method is based on eradicating or minimizing of tumors by microwave heating, especially at 2.45 GHz, without causing damage to the healthy tissue. The microwave energy transfer is frequently performed by coaxial antennas with a slot opening to radiate the energy in the tissue. Fortunately, the physical properties of biological tissues ease the spatial distribution of thermal energy resulting from electromagnetic (EM) fields and make the treatment possible for larger lesions. However, the academic research on this topic still draw attention from antenna selection to clinical tests since there are some unsolved problems such as backward heating due to surface currents propagating from the slot towards the feedline of the antenna. This issue causes the high backward thermal energy distribution to healthy region resulting in healthy tissue damage.

In this presentation, a review of the microwave cancer ablation therapy as well as different microwave antennas used for this purpose will be presented. Especially, particular attention will be paid to the well-known backward heating problem due to surface currents flowing on the outer conductor of the antenna towards the feed-line. Important techniques that have been proposed to stop these surface currents will be exposed. Emphasis will be placed on the recent developments carried out over the last few years [1, 2].

REFERENCES

1. Acikgoz, H., Mitra R., "Suppression of Surface Currents at Microwave Frequency Using Graphene -Application to Microwave Cancer Treatment", accepted for publication in ACES, The Applied Computational Electromagnetic Society Journal, 2016.
2. Acikgoz, H., Mitra R., "Microwave Coaxial Antenna for Cancer Treatment: Reducing the Backward Heating Using a Double Choke," in *Proceedings of International Symposium on Antennas and Propagation*, Hobart, Tasmania, Australia, November 2015.

Magnetic Particle Imaging for Probing Viscosity

E. U. Saritas^{1,2,*}

¹Department of Electrical & Electronics Engineering, Bilkent University, Ankara, Turkey

²National Magnetic Resonance Research Center (UMRAM), Bilkent University, Ankara, Turkey

*corresponding author: saritas@ee.bilkent.edu.tr

Abstract-Magnetic Particle Imaging (MPI) is a recently introduced biomedical imaging modality that takes advantage of the nonlinear magnetization response of superparamagnetic iron oxide (SPIO) nanoparticles to image their distribution in vivo. As a “hot spot” imaging modality, MPI has shown promise for various applications such as angiography, stem cell tracking, and cancer imaging. Here, we show the potential of MPI for probing viscosity in vivo.

First introduced in 2005, Magnetic Particle Imaging (MPI) enables high contrast imaging of the distribution of superparamagnetic iron oxide (SPIO) nanoparticles [1-2]. These nanoparticles are utilized as tracers in MPI, and there is no background signal from the human body. While there is no commercially available human-size MPI scanners yet, numerous small animal imaging MPI scanners have been constructed in research laboratories worldwide and a few leading companies in the field. Current potential applications of MPI include angiographic imaging, stem cell tracking, and cancer imaging. It has been shown that the response of SPIO nanoparticles to the applied magnetic fields in MPI is delayed due to so-called relaxation effects [3-4]. While relaxation blurs the MPI image (an unwanted side effect), one can also take advantage of it for probing the local environment of the SPIO nanoparticles. Here, we show the potential of MPI for probing viscosity in vivo [5-6]. This potential application will play an important role in cancer imaging and for understanding the effects of viscosity for drug delivery to cancerous tissue.

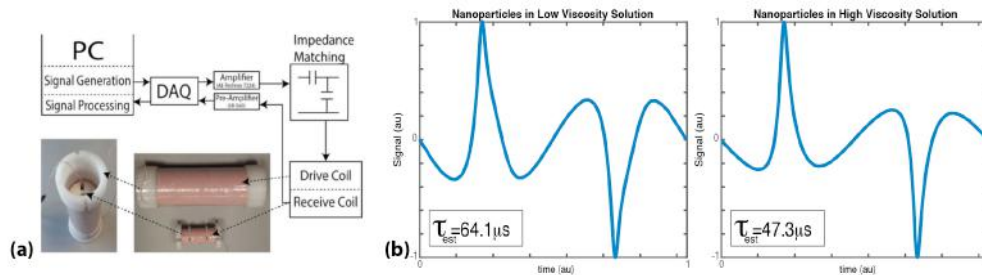


Figure 1: (a) Our custom magnetic particle spectrometer setup. This setup provides time-domain magnetization response signal of the SPIO nanoparticles to kHz range AC magnetic fields. (b) Nanoparticles in low and high viscosity solutions reveal significantly different time constants in their responses. Similarly, by calculating the time constant for every pixel in an MPI image, one can probe viscosity in vivo.

Acknowledgements: This work was supported by the Scientific and Technological Research Council of Turkey (through TUBITAK 114E167), by the ERA.Net RUS PLUS Program (215E198), by the European Commission through an FP7 Marie Curie Career Integration Grant (PCIG13-GA-2013-618834), by the Turkish Academy of Sciences through TUBA-GEBIP 2015 program, and by the BAGEP Award of the Science Academy.

REFERENCES

1. Gleich, B. and J. Weizenecker. "Tomographic Imaging Using the Nonlinear Response of Magnetic Particles," *Nature*, Vol. 435, No. 30, 1214–1217, 2005.
2. Saritas, E. U., P. W. Goodwill, L. R. Croft, J. J. Konkle, K. Lu, B. Zheng and S. M. Conolly. "Magnetic Particle Imaging (MPI) for NMR and MRI Researchers," *J Magn Reson*, Vol. 229, 116-126, 2013.
3. Croft, L. R., P. W. Goodwill and S. M. Conolly. "Relaxation in X-Space Magnetic Particle Imaging," *IEEE Trans Med Imag*, Vol. 31, No. 12, 2335-2342, 2015.
4. Croft, L. R., H. Arami, D. A. Price, A. X. Li, E. U. Saritas and S. M. Conolly. "Low Drive Field Amplitude for Improved Image Resolution in Magnetic Particle Imaging," *Med Phys*, Vol. 43, No. 1, 424-435, 2016.
5. Muslu, Y., M. Utkur, O. B. Demirel and E. U. Saritas. "Calibration-Free Color MPI," in *Proceedings of the 6th International Workshop on Magnetic Particle Imaging (IWMPI)*, Luebeck, Germany, March 2016.
6. Utkur, M., Y. Muslu, A. Alacaoglu, A. A. Ozaslan and E. U. Saritas. "Effect of Viscosity on Nanoparticle Relaxation Time Constant," in *Proceedings of the 6th International Workshop on Magnetic Particle Imaging (IWMPI)*, Luebeck, Germany, March 2016.

Wideband electromagnetic nearfield imaging using compressed sensing

Ibrahim Elshafiey* and Md Anowar Hossain

Electrical Engineering Department, King Saud University, Riyadh, Saudi Arabia

*corresponding author, E-mail: ishafiey@ksu.edu.sa

Abstract

Nearfield electromagnetic imaging (EMI) provides an attractive and simple medical imaging tool to reconstruct maps of tissue properties. This research aims at dealing with resolution limitations of EMI by implementing wideband multichannel system for energy excitation, and adopting compressed sensing approach in image reconstruction. Simulation is conducted assuming cylindrical head model with tumor anomalies. Inversion techniques are developed using greedy algorithm based orthogonal matching pursuit (OMP) and sparse Bayesian learning (SBL) technique. The performance of these two methods is found to depend on the signal to noise ratio level. Results reveal the potential of this system in detecting tissue properties inside the human body.

1. Introduction

Nearfield electromagnetic imaging (EMI) is an important research area for various disciplines. In particular, EMI provides simple tool for biomedical imaging compared to other imaging modalities. The contrast of dielectric properties for cancerous and surrounding healthy tissues can be used to detect tumors in applications such as breast imaging [1-3]. Initiative research has also emerged for implementing EMI in imaging the human head [4-8].

Although advanced systems are currently available to monitor and treat cancerous tumors, researchers continue to develop innovative tools for use into this battle. This research joins these efforts, by seeking to develop a wideband system for nearfield imaging that can be conducted along with hyperthermia treatment. Hyperthermia have the potential to enhance cancer treatment and reduce the associated side effects. By monitoring and processing the scattered energy during treatment, nearfield imaging can be integrated with hyperthermia to enhance energy localization efficiency.

Limitations of imaging resolution of EMI are addressed in this research by two approaches. Wideband system is implemented as discussed in [9-11]. Compressed sensing (CS) techniques are adopted for efficient formulation of image reconstruction. CS concepts is used for the reduction of sampling rate requirement and the number of spatial positions for data acquisition [12, 13].

Scattered signals at the applicator ports are sensed and preprocessed to maximize information extraction. A dictionary is formed and then implemented in CS based inverse problem analysis for efficient image reconstruction. Image reconstruction depends on identifying the dictionary element that matches acquired signal.

The remaining part of the paper is organized as follows. The forward problem formulation is described in Section 2. The inverse problem solution using compressed sensing is discussed in Section 3. Imaging results are discussed in Section 4. Final conclusion is provided in Section 5.

2. Forward Problem Formulation

The forward problem is performed considering a cylindrical head model with tumor anomaly using CST Microwave Studio [14]. An applicator array of eight elements is used as shown in Fig. 1. A Gaussian input signal pulse is used for the excitation of applicator array. The operational frequency range is selected to be 300-3000 MHz, providing a good compromise on resolution of the reconstructed image, signal penetration and the applicator element size. Figure 2 presents the used excitation signal in time and frequency domains.

Eight ports are used to excite and acquire the EM signal at each element of the array. The arrangement for head model consists of four layered cylindrical shapes. The first (inner) layer represents average brain tissue with a radius of 80 mm. The other layers represent the gray matter, cerebrospinal fluid (CSF) and skull, as shown in Fig. 1. The corresponding radii are 84, 89 and 94 mm, respectively.

The head configuration is assumed to contain tumor anomalies. The dielectric properties are assigned to the tumor according to the contrast reported in [15], which is 2:1 relative to the surrounding brain tissue in the electrical conductivity, and 1.6:1 in the relative permittivity.

The tissue materials used tumor anomaly and gray matter are assumed to be dispersive. The forward problem model is used to develop an imaging dictionary. The dictionary is created at discrete target space to obtain the scattered signal at a finite set of possible tumor locations with different tumor sizes.

Each dictionary element is comprised of the 64 signals. For each excitation signal, there are eight received signals from port. As an example, four output signals corresponding to excitation in port 1 are shown in Fig. 3.

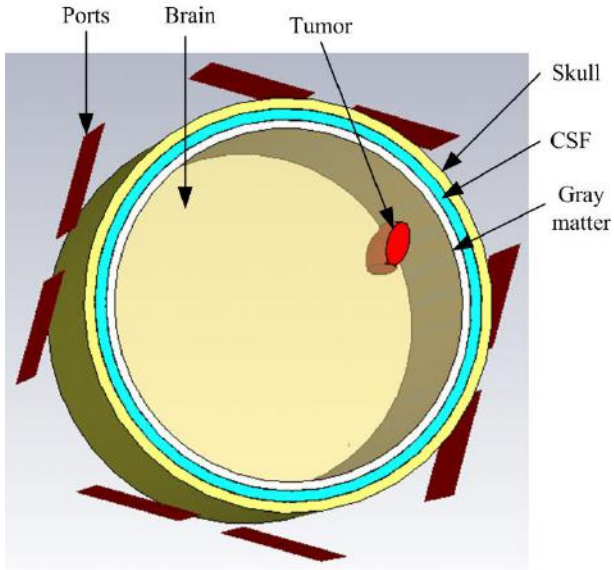
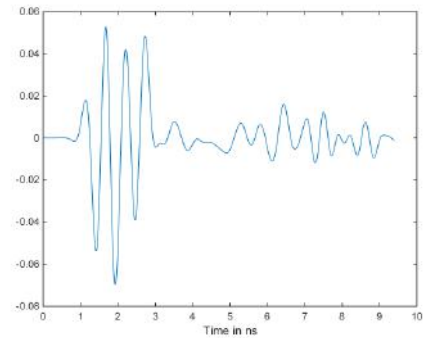
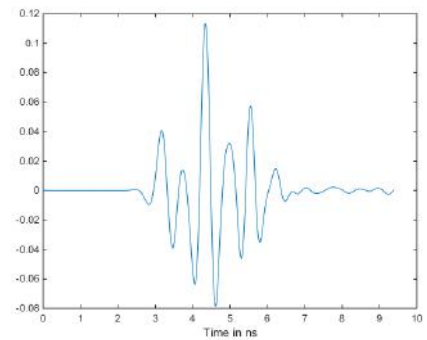


Figure 1: Forward problem using four-layered head model

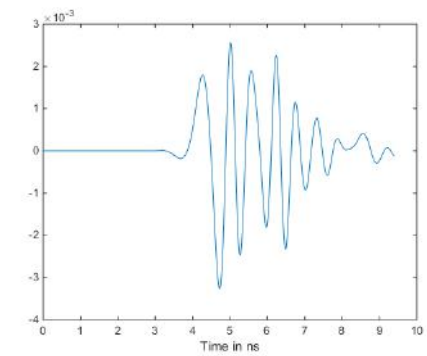
Figure 2: Excitation signal in time domain (a) and frequency domain (b).



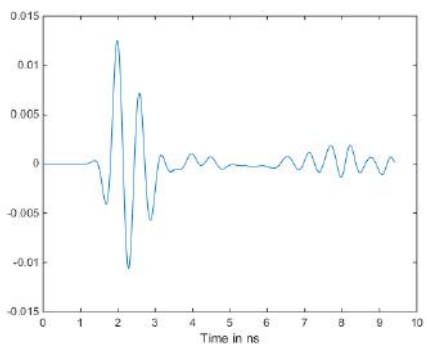
(a)



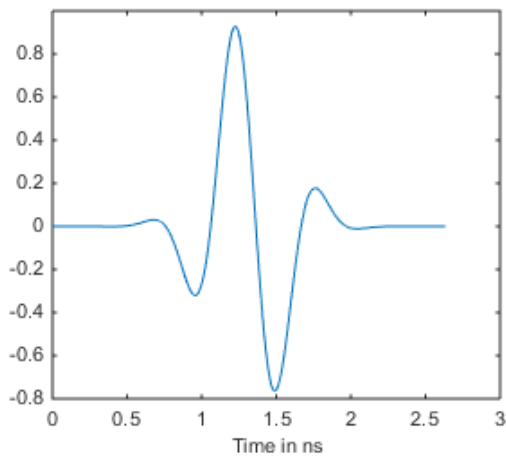
(b)



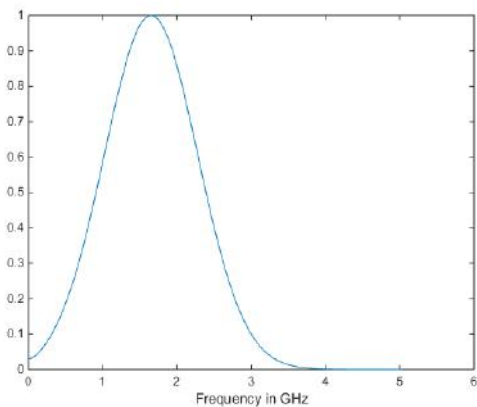
(c)



(d)



(a)



(b)

Figure 3: Samples of retrieved signals corresponding to excitation at port 1. Scattered signal (a) is acquired at

port 1, (b) is at port 2, (c) is at port 7, and (d) is at port 8

Frequency analysis is conducted of the acquired time domain signals to reduce signal dimension and simplify inverse problem analysis. The raw received signals contain background and other reflection signals. Preprocessing of raw signals can enhance useful information of tumor anomalies, by subtracting the received scattered signal corresponding to background tissues. This however is an unrealistic approach requiring full knowledge of scattered signal for no tumor case. An effective preprocessing method is introduced in [16].

3. Compressed sensing based Inverse Solution

High-resolution imaging of human head can be achieved by using wideband waveforms. Sparse signal recovery using CS theory is used in this research, by which only limited information of scattered signals is used for image reconstruction. The sample size of scattered signals can thus be reduced considerably.

According to the compressed sensing theory for a given dictionary Ψ of dimension $M \times N$, the recovery algorithm can reconstruct the sparse target \mathbf{x} , which maps the tumor distribution from a relatively small number of measurements as a vector \mathbf{y} by

$$\mathbf{y} = \Psi\mathbf{x} + \boldsymbol{\varepsilon} \quad (1)$$

where, $\boldsymbol{\varepsilon}$ represents the level of noise.

The raw scattered signals signal can be processed for image reconstruction using various algorithms. Two techniques are adopted here based on OMP, and SBL algorithms as discussed next.

3.1 Orthogonal Matching Pursuit (OMP)

Among many recovery algorithms in the literature, greedy methods receive significant attention for practical benefits. In particular, OMP algorithm has received significant interest because of its simplicity and efficient recovery performance.

OMP is an iterative greedy algorithm that uses the least-squares step at each iteration to update the residual vector in order to improve the approximation [16]. OMP leads to selecting the column which is most correlated with the current residuals at each step [17-19]. For a given measurement matrix, the CS recovery algorithm generates an estimate of K -sparse vector \mathbf{x} from a set of linear measurements given in (1). It has also been shown that OMP is reliable for reconstructing both sparse and near-sparse signals [20].

3.2 Sparse Bayesian learning (SBL)

Sparse Bayesian learning (SBL) framework is used to find robust solutions to problems in the context of regression and

classification. The canonical form of this problem can be given as

$$\mathbf{t} = \Phi\boldsymbol{\omega} + \boldsymbol{\varepsilon} \quad (2)$$

where, $\Phi \in \mathcal{R}^{N \times M}$ is a matrix whose columns represent a possibly over-complete basis (i.e., $\text{rank}(\Phi) = N$ and $M > N$). $\boldsymbol{\omega} = [\omega_1, \omega_2 \dots \omega_N]^T$ is the vector of weights to be learned, $\boldsymbol{\varepsilon}$ denotes the noise and $\mathbf{t} = [t_1, t_2 \dots t_N]^T$ is a vector of targets.

A key feature of this method that is related to the basis selection problem. If Φ is square and formed from a positive-definite kernel function, we obtain the relevance vector machine (RVM), which is a Bayesian competitor of the support vector machine (SVM) with several significant advantages [21, 22].

4. Imaging Results and Discussion

We consider various tumors in the developed cylindrical head model. OMP and SBL are applied to detect the tumor location using the developed dictionary data. In terms of, tumor detection without noise, these algorithms exhibit almost similar performance. However, these algorithms provide varying run-time and recovery ability with noise. We consider here three tumors with different sizes at the positions (0, -4, 0) cm, (0, 0, 4) cm and (-4, 0, -4) cm, respectively.

Figure 4 shows the imaging results with three tumor localization using SBL. The algorithm converges in reasonable computation time, and guarantees the stability of the results. No false targets appear on the reconstructed image if noise is not considered.

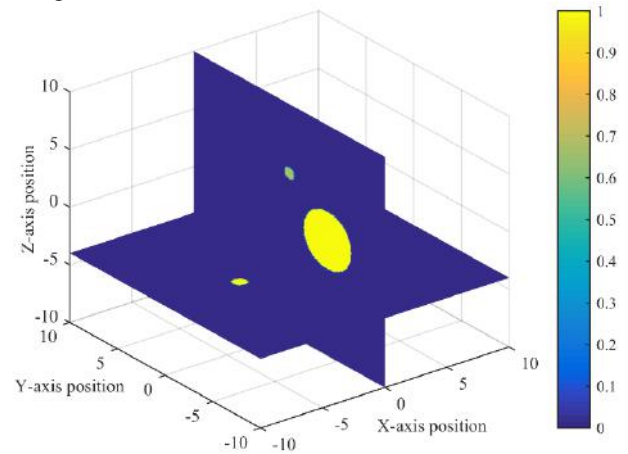


Figure 4: Tumor localization based on SBL (without noise).

Figure 5 shows the imaging results when noise is added corresponding to 10 dB SNR. It is observed that some false target appears in the reconstructed image but with lower intensity values. The actual tumors can still be recognized with higher intensity levels.

Figure 6 shows the imaging results with multiple tumor localization using OMP without noise. OMP converges quite

faster, but it doesn't guarantee the stability of the results, missing target and false target appears on the reconstructed image in some trials. It is observed that one target is missing in the reconstructed image.

Figure 7 shows the imaging results using OMP when noise is added. It is observed that significant number of false target appears in the reconstructed image with closer intensity values of actual tumors.

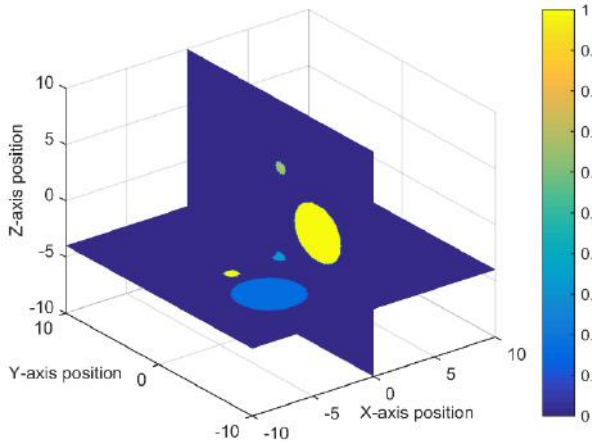


Figure5: Tumor localization based on SBL (SNR = 10 dB).

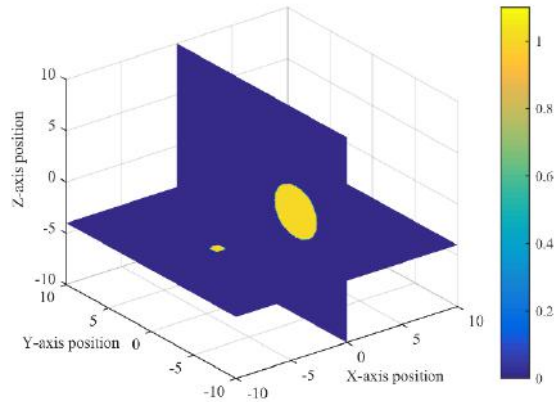


Figure 6: Tumor localization based on OMP (without noise).

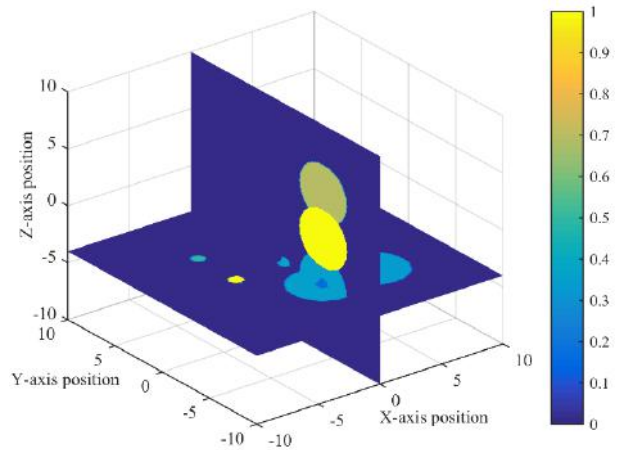


Figure 7: Tumor localization based on OMP (SNR =10 dB).

To analyze the effect of noise, imaging results of a point target for CS methods with various SNR are analyzed based on peak side-lobe ratio (PSLR). PSLR is defined as the ratio of maximum amplitude of the side-lobe to the main-lobe. The results of PSLR shown in Fig. 8 reveal that the SBL algorithm outperforms the OMP. However, OMP provides slightly faster convergence of results as compared to SBL. An ideal algorithm in compressed sensing should possess properties such as stability in providing results and uniform guarantee to function correctly for various conditions. Based on the imaging results, we can summarize that SBL provides stability and uniform guarantee to function correctly. The greedy approach is quite fast both in theory and in practice. It exhibits however lack of stability.

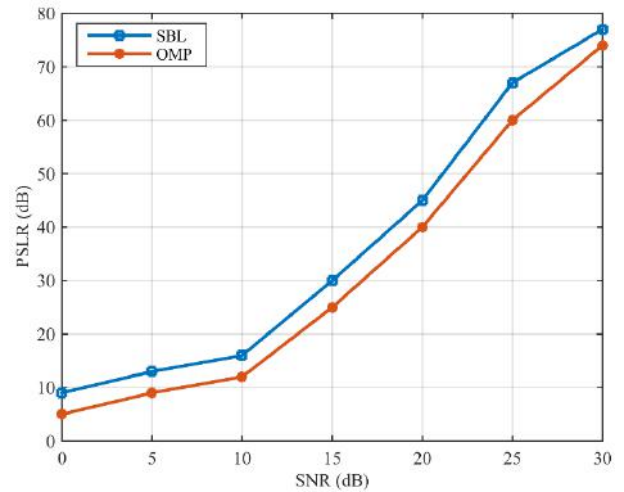


Figure 8: Comparison of PSLR at different SNR.

5. Conclusions

Nearfield EMI is proposed and investigated for the detection of tumors in the human head. A cylindrical head model with tumor anomalies is simulated in the forward problem, assuming the use of eight-element array to transmit electromagnetic signals and record the received scattered time-domain signals. The inverse problem implements CS

based techniques using SBL and OMP algorithms. Images for the target space with multiple tumors are found to be reconstructed successfully.

The obtained results reveal that high resolution nearfield imaging can be obtained by CS methods. Combining nearfield imaging with hyperthermia treatment can be used to enhance energy localization and efficiency of hyperthermia therapeutic plans.

Acknowledgements

This project is supported by research grant from King Abdulaziz City for Science and Technology (KACST), General Administration for Research Grants, Research Project AT 35-210.

References

- [1] T. Henriksson, N. Joachimowicz, C. Conessa, and J.-C. Bolomey, "Quantitative microwave imaging for breast cancer detection using a planar 2.45 GHz system," *IEEE Transactions on Instrumentation and Measurement*, vol. 59, pp. 2691-2699, 2010.
- [2] G. Ruvio, R. Solimene, A. D'Alterio, M. J. Ammann, and R. Pierri, "RF breast cancer detection employing a noncharacterized vivaldi antenna and a MUSIC - inspired algorithm," *International Journal of RF and Microwave Computer - Aided Engineering*, vol. 23, pp. 598-609, 2013.
- [3] X. Guo, M. R. Casu, M. Graziano, and M. Zamboni, "Simulation and design of an UWB imaging system for breast cancer detection," *Integration, the VLSI Journal*, vol. 47, pp. 548-559, 2014.
- [4] B. J. Mohammed, A. M. Abbosh, S. Mustafa, and D. Ireland, "Microwave system for head imaging," *IEEE Transactions on Instrumentation and Measurement*, vol. 63, pp. 117-123, 2014.
- [5] A. T. Mobashsher, A. M. Abbosh, and Y. Wang, "Microwave system to detect traumatic brain injuries using compact unidirectional antenna and wideband transceiver with verification on realistic head phantom," *IEEE Transactions on Microwave Theory and Techniques*, vol. 62, pp. 1826-1836, 2014.
- [6] I. Gouzouasis, I. Karanasiou, and N. Uzunoglu, "Exploring the enhancement of the imaging properties of a microwave radiometry system for possible functional imaging using a realistic human head model," *Journal of Instrumentation*, vol. 4, p. P06006, 2009.
- [7] S. Y. Semenov and D. R. Corfield, "Microwave tomography for brain imaging: Feasibility assessment for stroke detection," *International Journal of Antennas and Propagation*, 2008.
- [8] R. Scapaticci, L. Di Donato, I. Catapano, and L. Crocco, "A feasibility study on microwave imaging for brain stroke monitoring," *Progress In Electromagnetics Research B*, vol. 40, pp. 305-324, 2012.
- [9] I. Elshafiey, A.-F. Sheta, Z. Siddiqui, and M. A. Alkanhal, "Ultra-wideband applicator for brain-tumor ablation and imaging system," in *IEEE International Symposium on Signal Processing and Information Technology (ISSPIT)*, 2012, pp. 000310-000314.
- [10] A. F. Sheta, I. Elshafiey, A. Mohra, Z. Siddiqui, and A. R. Sebak, "A compact antenna for microwave imaging and hyperthermia treatment of brain tumor," in *15th International Symposium on Antenna Technology and Applied Electromagnetics (ANTEM)*, 2012, pp. 1-4.
- [11] M. Aldhaeabi, M. Alzabidi, I. Elshafiey, and Z. Siddiqui, "Antipodal Vivaldi antenna for hyperthermia treatment," in *Antennas and Propagation Conference (LAPC), Loughborough*, 2013, pp. 37-42.
- [12] J. Romberg, "Imaging via compressive sampling [introduction to compressive sampling and recovery via convex programming]," *IEEE Signal Processing Magazine*, vol. 25, pp. 14-20, 2008.
- [13] M. N. Tabassum, I. Elshafiey, and M. Alam, "Enhanced noninvasive imaging system for dispersive highly coherent space," in *IEEE International Conference on Acoustics, Speech and Signal Processing (ICASSP)*, 2015, pp. 912-916.
- [14] CST Microwave Studio, "Computer simulation technology," Available at <https://www.cst.com>.
- [15] S. M. Yacoob and N. S. Hassan, "FDTD analysis of a noninvasive hyperthermia system for brain tumors," *Biomedical engineering online*, vol. 11, p. 47, 2012.
- [16] M. N. Tabassum, I. Elshafiey, and M. Alam, "Efficient techniques to enhance nearfield imaging of human head for anomaly detection," in *IEEE International Symposium on Medical Measurements and Applications (MeMeA)*, 2015, pp. 565-569.
- [17] T. T. Cai and L. Wang, "Orthogonal matching pursuit for sparse signal recovery with noise," *IEEE Transactions on Information Theory*, vol. 57, pp. 4680-4688, 2011.
- [18] J. A. Tropp, "Greed is good: Algorithmic results for sparse approximation," *IEEE Transactions on Information Theory*, vol. 50, pp. 2231-2242, 2004.
- [19] J. A. Tropp and A. C. Gilbert, "Signal recovery from random measurements via orthogonal matching pursuit," *IEEE Transactions on Information Theory*, vol. 53, pp. 4655-4666, 2007.
- [20] N. Aravind, K. Abhinandan, V. Acharya, and D. Sumam, "Comparison of OMP and SOMP in the reconstruction of compressively sensed hyperspectral images," in *International Conference on Communications and Signal Processing (ICCCSP)*, 2011, pp. 188-192.
- [21] D. P. Wipf and B. D. Rao, "Sparse Bayesian learning for basis selection," *IEEE Transactions on Signal Processing*, vol. 52, pp. 2153-2164, 2004.
- [22] D. P. Wipf and B. D. Rao, "An empirical Bayesian strategy for solving the simultaneous sparse approximation problem," *IEEE Transactions on Signal Processing*, vol. 55, pp. 3704-3716, 2007.

Computational Techniques for Plasmonics, metamaterial and Graphene

Pseudospectral modal method for analyzing bent waveguides

Dawei Song¹, Ya Yan Lu²

¹Nanjing University of Aeronautics and Astronautics, Nanjing, China

²City University of Hong Kong, Hong Kong
dwsmath@nuaa.edu.cn

Abstract— The pseudospectral modal method (PSMM) is mode expansion method based on solving the one-dimensional modes numerically using the Chebyshev pseudospectral method. It was originally developed for analyzing diffraction gratings, later reformulated as a waveguide mode solver. The method is capable of producing very accurate solutions. In this paper, the PSMM is further extended as a mode solver for bent waveguides.

Waveguide bends are fundamental structures in photonic integrated circuits. For circular bends, the most important problem is to calculate the leaky modes with complex propagation constants. If the waveguide bend has a sufficiently small loss for practical use, the imaginary part of the complex propagation constant must be quite small. Therefore, high accuracy is needed in the numerical computation of bent waveguide modes. If the waveguide cross section only has vertical and horizontal material interfaces (assuming the substrate is parallel to the horizontal plane), mode solvers based on one-dimensional (1D) mode expansions are often more efficient than general methods, such as the finite element method.

In previous works [1, 2], we developed a waveguide mode solver (called pseudospectral modal method, PSMM) based on solving the 1D modes using a Chebyshev pseudospectral method. The method is called PSMM, since it is related to a method for analyzing diffraction gratings [3]. The PSMM (as a mode solver) is more convenient to use than traditional method based on analytic solutions of the 1D modes, is more accurate than related methods based on Fourier series, and it has been applied to compute leaky modes [2]. Accurate solutions for two difficult benchmark problems are reported in [2]. For a silicon wire with a $0.5\ \mu\text{m} \times 0.22\ \mu\text{m}$ cross section on a $1\ \mu\text{m}$ SiO_2 buffer layer with an infinite silicon substrate, we obtained $\beta/k_0 = 2.412371982 + i2.9135 \times 10^{-8}$, where β is the propagation constant and k_0 is the free space wavenumber (for wavelength $1.55\ \mu\text{m}$). Another difficult leaky mode appears in the classical rib waveguide, where the width and the height of the rib are $3\ \mu\text{m}$ and $1\ \mu\text{m}$, respectively, the height of the slab is $0.9\ \mu\text{m}$. Assuming the refractive indices of the guiding layer, the substrate and cladding are $n_g = 3.44$, $n_s = 3.4$ and $n_c = 1$, respectively, the fundamental quasi-TM mode is leaky. We obtained $\beta/k_0 = 3.413872819 + i6.718 \times 10^{-7}$, where k_0 corresponds to wavelength $1.15\ \mu\text{m}$.

In this work, we extend the PSMM as a mode solver for circularly bent waveguides, assuming the waveguide core has a rectangular cross section. Although mode solvers based on 1D mode expansions have been developed for bent waveguides before [4], our PSMM is more accurate similar to the cases demonstrated in our previous works [1, 2]. Using the cylindrical coordinate system $\{r, \theta, z\}$, where z is the vertical coordinate perpendicular to the substrate, r and θ are the horizontal radial and angle variables, and assuming the center of the waveguide core is located at $r = R$, then the θ variable can be separated as $\exp(i\beta R\theta)$, where β is the propagation constant. If the vertical interfaces are located at $r = r_1$ and $r = r_2$, then the structure has 1D material profiles in three different regions corresponding to $r < r_1$, $r_1 < r < r_2$ and $r > r_2$, respectively. The PSMM involves the following steps.

1. Truncate z by perfectly matched layers, solve the 1D modes in the three regions using the Chebyshev pseudospectral method.
2. For a given β which is complex in general, express H_z , E_z , H_θ and E_θ based on mode expansions using the 1D modes in each region. Bessel and Hankel functions of complex order appear in these expressions. These functions may be calculated numerically.
3. Formulate a homogeneous linear system $\mathbf{F}(\beta)\mathbf{u} = \mathbf{0}$, based on the continuity of H_z , E_z , H_θ and E_θ at $r = r_1$ and $r = r_2$ for all z .
4. Solve β from the condition that $\mathbf{F}(\beta)$ is a singular matrix, find a non-zero vector \mathbf{u} , and construct the wave field of the mode from the expansions developed in Step 2.

ACKNOWLEDGMENT

The work is partially supported by the National Natural Science Foundation of China under Project 11301265 and by the Research Grants Council of Hong Kong Special Administrative Region, China, under project CityU 11301914.

REFERENCES

1. Song, D. and Y. Y. Lu, "Pseudospectral modal method for computing optical waveguide modes," *J. Lightw. Technol.*, Vol. 32, 1624–1630, 2014.
2. Song, D. and Y. Y. Lu, "Analyzing leaky waveguide modes by pseudospectral modal method," *IEEE Photon. Technol. Lett.*, vol. 27, no. 9, pp. 955–958, 2015.
3. Song, D., L. Yuan, and Y. Y. Lu, "Fourier-matching pseudospectral modal method for diffraction gratings," *J. Opt. Soc. Am. A*, Vol. 28, No. 4, 613–620, 2011.
4. Prkna, L., M. Hubalek, and J. Ctyroky, "Vectorial eigenmode solver for bent waveguides based on mode matching," *IEEE Photon. Technol. Lett.*, Vol. 16, No. 9, 2057–2059, 2004.

Sensitivity analysis for photonic crystal microcavities.

Zhen Hu¹, Ya Yan Lu²

¹College of Science, Hohai University, Nanjing, China

²Department of Mathematics, City University of Hong Kong, Hong Kong, China
huzhen1230@gmail.com

Abstract— We develop an efficient sensitivity analysis technique to analyze two-dimensional (2D) photonic crystal (PhC) microcavities. By using the Dirichlet-to-Neumann (DtN) map method, the resonant frequencies of the PhC microcavities could be written as an implicit function of the design parameters. Then the partial derivatives of the resonant frequencies with respect to the design parameters could be calculated. Based on this technique, we can predict the resonant frequencies and the peak frequencies of the transmission spectra.

Sensitivity analysis is important for providing valuable information about fabrication tolerance. It is also very useful in the optimal design process. In a recent paper [1], we developed an efficient sensitivity analysis technique for analyzing the transmission coefficients of two-dimensional (2D) photonic crystal (PhC) devices. This technique is based on the Dirichlet-to-Neumann (DtN) map method, which is a particularly efficient numerical method for modelling the 2D PhC devices. In this paper, we extend the sensitivity analysis technique to analyze the resonant frequencies of PhC microcavities.

For the E polarization, the governing equation is the Helmholtz equation

$$\partial_x^2 u + \partial_y^2 u + k_0^2 n^2(x, y)u = 0, \quad (1)$$

where k_0 is the free space wavenumber, $n(x, y)$ is the refractive index function and u is the z component of the electric field. The DtN map method was used to analyze the PhC microcavities in [2]. The DtN map of a unit cell is an operator which maps the wave field on the edges of the unit cell to its normal derivatives. By using the DtN map method, the Helmholtz equation could be replaced by the following linear system

$$A(\omega_*)\vec{u} = 0. \quad (2)$$

where ω_* is the normalised frequency $\omega a/(2\pi c)$, the system matrix A depends on the frequency ω_* , and it is constructed by the DtN maps of the unit cells in the computational domain and the boundary conditions to truncate the PhC waveguides, \vec{u} is the column vector for u on all edges of the unit cells in the region. A non-zero solution \vec{u} only exists when the matrix A is singular. Therefore, we can solve ω_* from a nonlinear equation where the eigenvalue of A with the smallest magnitude is zero.

For sensitivity analysis of the resonant frequencies with respect to design parameters, such as the radii a_i of the cylinders in the unit cells Ω_i , for $i = 1, 2, \dots$. We take partial derivatives with respect to a_i for both sides of Eq. 2, and get

$$\frac{\partial \omega_*}{\partial a_i} = -\frac{\vec{y}^T \frac{\partial A}{\partial a_i} \vec{u}}{\vec{y}^T \frac{\partial A}{\partial \omega_*} \vec{u}}, \quad (3)$$

where \vec{y} satisfies $\vec{y}^T A = 0$, $\partial_{\omega_*} A$ and $\partial_{a_i} A$ can be evaluated based on the partial derivatives of the DtN maps.

We consider a 2D PhC microcavity as shown in Fig. 1. The background PhC is an infinite square lattice of dielectric rods surrounded by air. Its lattice constant is L . The radius and refractive index of the rods are $a = 0.2L$ and $n = \sqrt{11.4}$, respectively. Let a_1 be the radius of the rod whose number is 1 and assume only the radius of rod 1 is varied, we calculate the partial derivative of the resonant frequency with respect to a_1 from Eq. (3). The result is $\partial_{a_1} \omega_* = -0.0971298 + 0.0000192i$. Based on the partial derivative, we can predict resonant frequencies near the design point by Taylor expansions. For $a_1 = a + 0.01L$, the resonant frequency obtained by first order Taylor expansion is $\omega_* = 0.3779045 - 0.0000415i$, where the exact value is $0.3778495 - 0.0000419i$.

Since the peak frequency of transmission spectrum is exactly the real part of resonant frequency, we can also use the Taylor expansion for its predication. For different a_1 , the shift of the peak could be seen clearly in the right panel of Fig. 1.

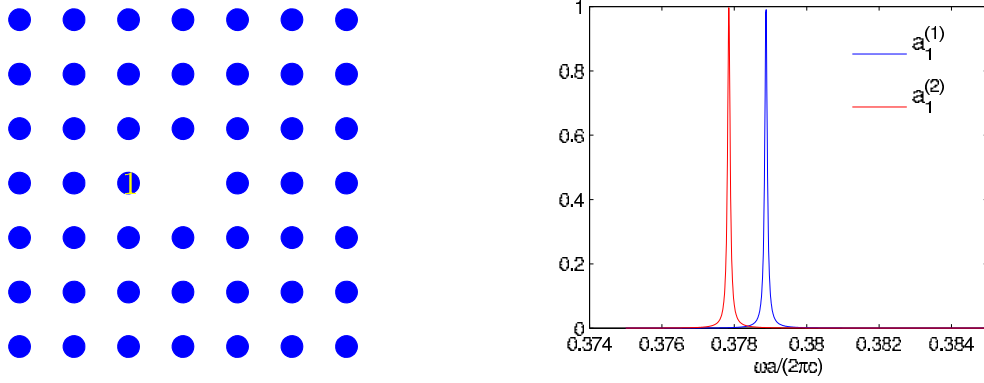


Figure 1: Left: a PhC microcavity. Right: transmission spectra of the PhC microcavity with $a_1^{(1)} = a$ and $a_1^{(2)} = a + 0.01L$.

ACKNOWLEDGMENT

This work is partially supported by the Fundamental Research Funds for the Central Universities (Project No. 2015B19614) and the Research Grants Council of Hong Kong Special Administrative Region (Project No. CityU 11301914).

REFERENCES

1. Hu, Z. and Y. Y. Lu, "Second order sensitivity analysis for a photonic crystal waveguide bend," *J. Opt. Soc. Am. B*, Vol. 32, No. 1, 69–75, 2015.
2. Li, S. J. and Y. Y. Lu, "Efficient method for analyzing leaky cavities in two-dimensional photonic crystals," *J. Opt. Soc. Am. B*, Vol. 26, No. 12, 2427–2433, 2009.

Time Domain Modelling of Parity-Time Symmetric Structure with Dispersive Gain/Loss

S. Phang¹, A. Vukovic², S. C. Creagh¹, G. Gradoni^{1,2}, P. D. Sewell² and T. M. Benson^{2*}

¹School of Mathematical Sciences, University of Nottingham, Nottingham, UK

²The George Green Institute for Electromagnetics Research, University of Nottingham, Nottingham, UK

*corresponding author: trevor.benson@nottingham.ac.uk

Abstract-A time-domain method based on the Transmission-Line Modelling (TLM) method is developed with a homogeneously broadened dispersion gain/loss material profile. It is used to model Parity-Time (PT) symmetric structures such as a Bragg gratings and coupled cylindrical resonators. Different applications of interest, such as a memory device and a laser in a loss-dominated structure, are studied. Results show that if the dispersion of gain/loss is considered then PT-symmetry can only be achieved at a single frequency.

Modelling a realistic material, taking account its dispersion and non-linear properties, is becoming increasingly important in photonics as structures become geometrically smaller, operate over a broader and higher frequency bands, and at stronger intensity. Although time-domain modelling is well-suited to model non-linear and time-dependent material parameters, modelling dispersive material is not as straightforward.

In our recent work, we have developed a model of a dispersive gain and non-linear material within the time-domain Transmission-Line Modelling (TLM) framework, using the alternative formulation of Maxwell's equation in the discrete time Z -domain, to model a new class of photonic metamaterials namely Parity-Time (PT)-symmetric structures. In the context of a PT-symmetric structure, a judicious design of gain and loss is required which results in a structure with balanced gain/loss with a main characteristic of a threshold point; as such operation beyond this point leads to an unstable system [1]. Previously we also have reported a Boundary Integral Equation (BIE) method [2] to demonstrate the importance of dispersion in modelling PT-symmetric structures [1, 2]; in the presence of dispersion, PT-symmetry can only be practically observed at a single frequency and device performance is sensitive to a mismatching condition.

In this contribution, we present our development of the time-domain Transmission Line Modelling (TLM) method with a homogeneously-broadened gain/loss dispersion model and use it to model PT-symmetric structures; in principle the model is appropriate for a broad range of other applications. The PT-symmetric structures studied include PT-symmetric Bragg gratings and PT-symmetric coupled resonators. The temporal dynamics of different applications of interest are studied including the use of a non-linear PT-symmetric Bragg grating as a memory device and of PT-coupled resonators structures as a laser in a loss dominated structure.

REFERENCES

1. Phang, S., Vukovic, A., Susanto, H., Benson, T. M. and Sewell, P. D. "Impact of dispersive and saturable gain/loss on bistability of nonlinear parity-time Bragg gratings" *Opt. Letts.* Vol. 39, No. 11, 2603-06, 2014
2. Phang, S., Vukovic, A., Creagh, S. C., Benson, T. M., Sewell, P. D., Gradoni, G. "Parity-time symmetric coupled microresonators with a dispersive gain/loss," *Opt. Express*, Vol. 23, No. 9, 11493-11507, 2015.

A Surface Integral Equation Solver for Transient Analysis of Graphene Devices

Y. Shi¹, P. Li^{1,2}, I. E. Uysal¹, H. A. Ulku³, and H. Bagci¹

¹Division of Computer, Electrical, and Mathematical Sciences and Engineering, King Abdullah University of Science and Technology, Thuwal, 23955-6900, Saudi Arabia

²School of Electrical and Computer Engineering, Purdue University, West Lafayette, IN 47907, USA

³Department of Electronics Engineering, Gebze Technical University, Kocaeli, Gebze, Turkey
emails: {yifei.shi, ping.li, ismail.uysal, huseyin.ulku, hakan.bagci}@kaust.edu.sa

Abstract— A surface integral equation solver for analyzing transient electromagnetic wave interactions on composite graphene-based devices is described. The time domain resistive boundary condition (TD-RBC) and the Poggio-Miller-Chang-Harrington-Wu-Tsai (TD-PMCHWT) integral equation, which are enforced on the surfaces of the graphene and dielectric substrates, respectively, are discretized using the well-known marching-on-in-time (MOT) scheme. The expressions of the time domain resistivity and conductivity of the graphene sheet are obtained analytically from the intra-band contribution formulated in frequency domain. Numerical results demonstrating the accuracy and the applicability of the proposed scheme, will be presented.

Graphene is a monolayer of carbon atoms structured in the form of a honeycomb lattice [1]. Graphene's dispersive conductivity provides a mechanism for generation of surface plasmons on graphene surfaces at Terahertz frequencies. Additionally, these plasmons can be dynamically tuned via electrostatic gating of the graphene sheet [1]. These properties suggest that graphene can be used as a building block for novel electromagnetic and photonic devices with applications in the fields of photovoltaics, bio-chemical sensing, all-optical computing, and flexible electronics. Device design calls for accurate and efficient simulation tools. However, numerical characterization of electromagnetic fields on graphene-based devices is not an easy task: The thickness of the graphene sheet is orders of magnitude smaller than any other geometrical dimension of the device. Consequently, fully volumetric discretization of the device leads to significantly large number of unknowns and/or an ill-conditioned matrix system.

In this work, an integral equation based scheme is developed to alleviate these problems. The proposed approach enforces the time domain resistive boundary condition (TD-RBC) [2, 3, 4, 5] on the graphene sheet and the time domain Poggio-Miller-Chang-Harrington-Wu-Tsai surface integral equation (PMCHWT-SIE) [6] on the surfaces of the substrate's dielectric volumes. This approach calls for introducing electric and magnetic equivalent current densities on both sides of a given surface. For dielectric-only surfaces there is only a sign difference between both sets of currents. When a graphene sheet coincides with a dielectric surface, the same applies for the magnetic current sets, but the relation between electric currents on both sides of the common surface is governed by the TD-RBC.

To numerically solve the coupled system of TD-RBC and PMCHWT equations, unknown equivalent current densities are expanded using Rao-Wilton-Glisson (RWG) basis functions [7] in space and shifted Lagrange interpolators [8] in time. Inserting this expansion into the coupled system and Galerkin testing the resulting equations at discrete times yield a system of equations. This system is solved for the unknown current expansion coefficients using a marching on-in-time (MOT) scheme. The MOT scheme requires time samples of graphene's surface resistivity to be computed. Those are obtained analytically from the intra-band contribution formulated in frequency domain [3].

Numerical results, which demonstrate the applicability of the proposed MOT solver to the analysis of transient electromagnetic interactions on graphene-based devices, will be presented.

REFERENCES

1. Novoselov, K. S., Geim, A. K., Morozov, S. V., Jiang, D., Zhang, Y., Dubonos, S. V., Grigorieva, I. V., and Firsov, A. A., "Electric field effect in atomically thin carbon films," *Science*, Vol. 306, No. 5696, 666–669, 2004.
2. Chen, Q., Lu, M., and Michielssen, E., "Integral-equation-based analysis of transient scattering from surfaces with an impedance boundary condition," *Microw. Opt. Tech. Lett.*, Vol. 42, No. 3, 213–220, 2004.
3. Nayyeri, V., Soleimani, M., and Ramahi, O. M., "Modeling graphene in the FDTD method using a surface boundary condition," *IEEE Trans. Antennas Propag.*, Vol. 61, No. 8, 4176–4182, 2013.
4. Shi, Y., Uysal, I. E., Li, P., Ulku, H. A., and Bagci, H., "Analysis of electromagnetic wave interactions on graphene sheets using time domain integral equations," in *Proceedings of ACES 2015*, Williamsburg, VA, USA, March 2015, 52–53.
5. Li, P., Jiang, L. J., and Bagci, H., "A resistive boundary condition enhanced DGTD scheme for the transient analysis of graphene," *IEEE Trans. Antennas Propag.*, Vol. 63, No. 7, 3065–3076, 2015.
6. Shanker, B., Lu, M., Yuan, J., and Michielssen, E., "TDIE analysis of scattering from composite bodies via exact evaluation of radiation fields," *IEEE Trans. Antennas Propag.*, Vol. 57, No. 5, 1506–1520, 2009.
7. Rao, S. M., Wilton, D. R., and Glisson, A. W., "Electromagnetic scattering by surfaces of arbitrary shape," *IEEE Trans. Antennas Propag.*, Vol. 30, No 3, 409–418, 1982.
8. Manara, G., Monorchio, A., and Reggiannini, R., "A space-time discretization criterion for a stable time-marching solution of the EFIE," *IEEE Trans. Antennas Propag.*, Vol. 45, No. 3, 527–532, 1997.

Novel Design of High Directivity Hybrid Yagi-Uda Antenna

AbdelRahman M Ghanim¹, Mohamed Hussein^{1,2}, Mohamed Farhat. O. Hameed^{2,3}, Ashraf Yahia¹,
and S. S. A. Obayya^{2,*}

¹Department of Physics, Faculty of Science, Ain Shams University, Abbassia 11566, Cairo, Egypt

²Centre for Photonics and Smart Materials, Zewail City of Science and Technology, Sheikh Zayed District,
6th of October City, Giza, Egypt

³Mathematics and Engineering Physics Department, Faculty of Engineering, Mansoura University,
Mansoura, Daqahlia 35516, Egypt.

*Corresponding author: sobayya@zewailcity.edu.eg

Abstract- In this paper, a novel design of broadband optical antenna with high directivity is introduced and analyzed using finite integration method (FIT). The proposed design consists of cylindrical nanoantenna with silver core surrounded by silicon cladding. The different geometrical parameters have been tuned to maximize the directivity. The proposed design offers high directivity of 14.8 which exceeds those of silicon nanospheres counterparts of directivity 12 with enhancement of 23 % at wavelength of 500 nm.

Recently, optical nanoantennas (OAs) attract a great attention in nanophotonics research due to their ability for monitoring the light beam link as well as the impedance and size mismatch between nanoparticles and the free space radiation. The main task of the optical antennas can to convert free propagating radiation energy into localized energy and vice-versa [1]. The OA can also enhance the efficiency of light matter interaction in different applications [1] such as optical sensors, solar cells, quantum communication systems and molecular spectroscopy techniques[2]. The performance of nanoantenna design is further enhanced by connecting an emitter to optical Yagi–Uda antenna. The Yagi–Uda design has higher gain and directionality than other conventional optical antenna designs. This enhancement could be attributed to the concept of inductively and capacitively detuned elements with an active feed. The main advantageous of unidirectional emission and reception are the novel opportunities for sub wavelength light manipulation as well as quantum communication with improved performance of photoactive devices such as photovoltaic detectors, light-emitting diodes, and solar cells. The relation between directivity and the radiation power is as follows

$$D(\theta, \phi) = 4\pi \frac{P(\theta, \phi)}{\int P(\theta, \phi) d\Omega} \quad (1)$$

where $P(\theta, \phi)$ is the power per unit solid angle radiated in a specific direction divided by the radiated power per solid angle from an isotropic source[3]. Previously, several studies have been carried out to enhance the directivity of nanoantenna. In 2008, Taminiou *et al.* [4][4] have enhanced the directivity by using four elements of aluminum nanorods[4]. Four years later, Kivshar *et al.*[5] have increased the directivity up to 12 by using five silicon nanospheres at wavelength of 500nm [5]. Further, Xiaoyan *et al.* have obtained directivity of 6.5 at $\lambda=780$ nm using spherical Yagi-Uda Nanoantennas made from dielectric (TiO_2) with gold feed element [6].

Figure. 1 (a) shows the proposed optical Yagi-Uda nanoantenna that consists of an array of hybrid cylindrical nanorods. Each element has a silver core surrounded by silicon cladding. In this study, the silver permittivity is taken from Johnson and Christy data [1]. The length of the feed element (dipole source) is equal to $L_f=160$ nm with a reflector length of $L_r=1.25 L_f$ to reflect the backward radiation to the specific direction. Additionally, four directors of length $L_d=0.9 L_f$ have been used. The radii of the reflector and directors nanorods are equal to 75nm and 70 nm, respectively. Further, the distance between two adjacent directors is equal to $D=70$ nm [3]. Fig.1(b) shows the directivity of conventional dielectric sphere nanoantennas[5] and the proposed hybrid nanoantennas. It is evident from this figure that the proposed design increases the directivity up to 14.8 which exceeds the silicon nanospheres counterpart by 23%.

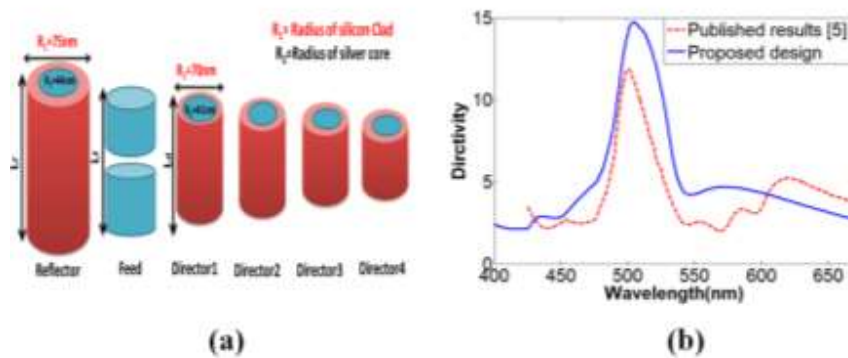


Figure 1.(a) Schematic diagram of proposed hybrid Yagi-Uda nanoantenna,(b)Variation of the directivity of the proposed nanoantenna and the dielectric nanosphere [5] versus the wavelength

REFERENCES

1. Goyal, K. and A. Srivastava. 3D U-shaped yagi uda nantenna for nanoscale applications. in Signal Processing and Communication (ICSC), 2015 International Conference on. 2015. IEEE.
2. Maksymov, I.S., Maksymov, I. S., Staude, I., Miroshnichenko, A. E. and Kivshar, Y. S., Optical yagi-uda nanoantennas. Nanophotonics, 2012. 1(1): p. 65-81.
- 3.Dregely, D., Taubert, R., Dorfmüller, J., Vogelgesang, R., Kern, K. and Giessen, H., 3D optical Yagi-Uda nanoantenna array. Nature communications, 2011. 2: p. 267.
- 4.Taminiau, T.H., F.D. Stefani, and N.F. van Hulst, Enhanced directional excitation and emission of single emitters by a nano-optical Yagi-Uda antenna. Optics express, 2008. 16(14): p. 10858-10866.
- 5.Krasnok, A.E., A. E., Miroshnichenko, A. E., Belov, P. A. and Kivshar, Y. S., All-dielectric optical nanoantennas. Optics Express, 2012. 20(18): p. 20599-20604.
- 6.Xiong, X.Y., X. Y., Jiang, L. J., Sha, W. E., Lo, Y. H. and Chew, W. C., Compact Nonlinear Yagi-Uda Nanoantennas. Scientific reports, 2016. 6.

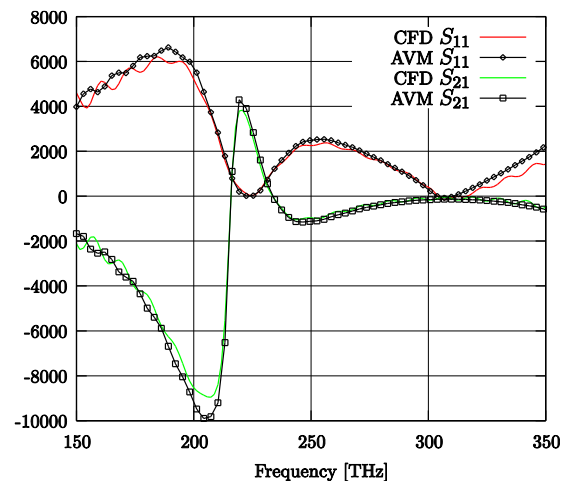
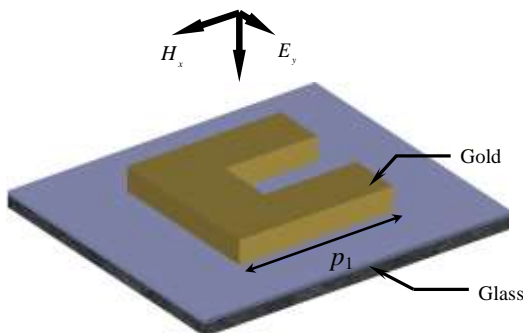
Efficient Wideband Adjoint Sensitivity Analysis of Dispersive Structures using FDTD

Mohamed H. Bakr¹, Yu Zhang, and Osman Ahmed

¹McMaster University, Hamilton, Ontario, Canada

*mbakr@mcmaster.ca

Abstract-We review in this paper efficient approaches for wideband sensitivity analysis of dispersive electromagnetic structures using FDTD. We show that to estimate the sensitivities of the desired response over the band of interest relative to all material and geometrical parameters, only one extra adjoint simulation is needed. This can be contrasted with the $2n$ extra simulations required to estimate the gradient using the accurate central finite difference (CFD) approaches, where n is the number of parameters. This approach is particularly suited for electrically long dispersive structures such as nano structures and for structures with large number of parameters. We show that this approach is applicable to models with different dispersion profiles such as the Lorentz, Drude, Debye, and Cole-Cole models [1]. The Auxiliary Equation (AE) method is used to derive the adjoint variable equations. Fig. 1 shows a dispersive gold nano antenna and one of the sensitivities of the response. The sensitivities of the response relative to all 8 parameters are estimated using only one extra FDTD simulation [2]. The estimated sensitivities can be utilized in gradient-based optimization [3].



REFERENCES

1. A. Taflove and S. C. Hagness, Computational Electrodynamics: The Finite Difference Time Domain Method (3rd edition). Norwood, MA: Artech House, 2005.
2. Y. Zhang, O.S. Ahmed, and M.H. Bakr "Wideband FDTD-based adjoint sensitivity analysis for problems with dispersive materials," *IEEE Trans. Microwave Theory Tech.*, vol. 62, No. 5, pp. 1122 – 1134, 2014.
3. M.H. Bakr, Nonlinear Optimization in Electrical Engineering with Applications in MATLAB, IET, September 2013.

Novel Wide Band Smoothed Finite Element Time Domain Analysis of Resonant modes in Photonic Bandgap Cavities

Khaled S. R. Atia¹, A. M. Heikal^{1,2}, and S. S. Obayya^{1*}

¹Center for Photonics and Smart Materials, Zewail City of Science and Technology, Egypt

²Department of Electronics and Communication Engineering, Mansoura University, Egypt

*corresponding author: sobayya@zewailcity.edu.eg

Abstract-this paper aims to develop novel smoothed finite element method (SFEM) for the analysis of photonic bandgap cavities through the application of the imaginary time beam propagation technique. The imaginary time beam propagation formula is also extended to include wide-band optical pulses. A 5×5 photonic bandgap cavity is simulated to test the performance of the proposed method.

Photonic bandgap (PBG) devices could be designed so that light can propagate in only the desired direction within a certain frequency range termed as the ‘bandgap’ region. This distinguishing feature strongly promoted the use of PBG in the design of laser due to the narrow selectivity of the localized resonant modes and the high quality factor in the bandgap region. Hence, it become a necessity to accurately model the localized modes in resonant PBG cavities. Therefore, several attempts have been made for the sake of this problem.

The efficiency and the versatility of the finite difference time domain method (FDTD) permitted the analysis of PBG cavities [1]. Also, a frequency domain solution has been proposed through the application of the finite element method (FEM) [2]. Due to the flexibility of FEM in modeling curved geometries, the research has been extended to analyze PBG cavity using time domain beam propagation based FEM (FETD-BPM). Unfortunately, high quality factor cavities require many time steps before the steady state mode is formed. Hence, an alternative time domain approach termed ‘imaginary time domain’ has been proposed [3]. This approach is inspired by the imaginary distance beam propagation method. Such approach can find the steady state mode formed inside the cavity after few iterations (4 or 5 iterations). However, this method uses a paraxial approximation.

In this paper, the SFEM is adopted to the imaginary time domain beam propagation approach to combine the efficiency of the imaginary time domain method and the outstanding performance of the SFEM. Also, dissimilar to [3], Padé approximation is used to permit the simulation of wide band optical pulses.

The governing scalar smoothed finite element beam propagation equation including the perfectly matched layer (PML) can be written as

$$\frac{-1}{c^2} [M] \frac{d^2\{\emptyset\}}{dt^2} - \frac{2j\omega_0^2}{c^2} [M] \frac{d\{\emptyset\}}{dt} + \left([K] + \frac{\omega_0^2}{c^2} [M] \right) \{\emptyset\} = \{0\} \quad (1)$$

where $[M]$ and $[K]$ are respectively the FEM mass matrix and SFEM stiffness matrix [4]. ω_0 is the reference angular frequency, c is the speed of light, $\emptyset = E_x$ for TE mode and H_x for TM mode. $[K]$ is given by

$$[K] = - \int_{\Omega_s} \{B\} [D] \{B\}^T d\Omega_s \quad (2)$$

with

$$\{B\} = \{\nabla N\} \approx \frac{1}{A_s} \int_{\Gamma_s} \{N\} \vec{a} d\Gamma_s \quad (2)$$

where Ω_s is the smoothing domain created by connecting the mid-point of each triangular element to the two end-points of adjacent edge, Γ_s is the outer boundary of the smoothing domain, \vec{a} is the outward unit normal vector on Γ_s , A_s is the area of Ω_s , and $[D]$ is the PML parameter. By utilizing Padé approximation, Eq. (1) is reduced to

$$-\frac{2j\omega_0^2}{c^2} [\tilde{M}] \frac{d\{\phi\}}{dt} + \left([K] + \frac{\omega_0^2}{c^2} [M] \right) \{\phi\} = \{0\} \quad (3)$$

where $[\tilde{M}]$ is given in [4]. The previous equation is divided in time using Crank-Nicholson algorithm. Allowing the time step size to take adaptive imaginary values as in [3,4], and by assuming an initial field of a Gaussian shape similar to the cavity mode, the proposed algorithm converges to the steady state resonant mode after few iterations.

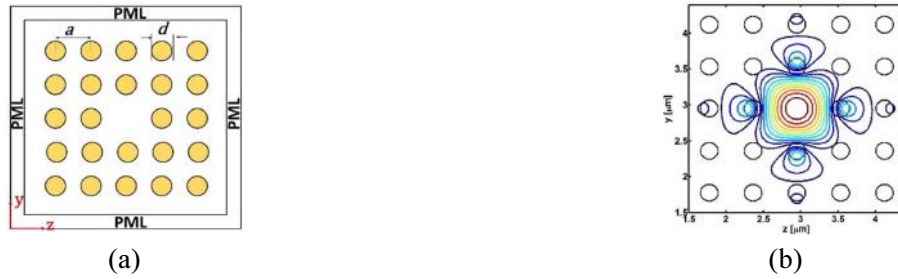


Fig. 1. (a) Schematic diagram of the simulated PBG cavity. (b) The steady state mode formed inside the cavity.

The 5×5 PBG cavity shown in Fig. 1a is analyzed using the proposed method to assess its performance. Figure 1b shows the steady state mode formed inside the cavity. The normalized frequency ($F = a/\lambda$), where a is the lattice constant and λ is the resonance wavelength, computed using the presented method is 0.37907. Whereas, under the same assumption, the normalized frequency computed using the conventional FEM equals .37942. Hence, the error produced using the proposed method with respect to the time domain method [6] is $6.3e-4$, while for the conventional FEM is $9.8e-4$ which is higher than our proposed method. The quality factor calculated using the proposed method equals 191 whereas for the conventional FEM is 175.

Conclusion—This paper presents a novel imaginary time beam propagation method based on the newly developed smoothed finite element method. The resonance frequency results indicate that the relative error produced by the proposed method is less than the conventional FEM.

REFERENCES

1. Watts, M. R., S. G. Johnson, H. A. Haus, and J. D. Joannopoulos, “Electromagnetic cavity with arbitrary Q and small modal volume without a complete photonic bandgap,” *Optics letters*, Vol. 27, No. 20, 1785–1787, 2002.
2. Hwang J. K., S. B. Hyun, H. Y. Ryu, and Y. H. Lee, “Resonant modes of two-dimensional photonic bandgap cavities determined by the finite-element method and by use of the anisotropic perfectly matched layer boundary condition.” *J. Opt. Soc. Am. B*, Vol. 15, No. 8, 2316–2324, 1998.
3. S. S. A. Obayya, “Finite element time domain solution of resonant modes in photonic bandgap cavities,” *Optical and quantum electronics*, Vol. 37, No. 9, 865-873, 2005.
4. Atia K. S. R., A. M. Heikal, and S. S. A. Obayya. “Efficient smoothed finite element time domain analysis for photonic devices,” *Optics express*, Vol. 23, No. 17, 22199-22213, 2015.

Recent Advances in Optical Micro-cavities

Phase matched SHG in an on-chip crystalline microresonator

Jintian Lin¹, Yingxin Xu², Zhiwei Fang¹, Min Wang¹, Wei Fang², and Y. Cheng^{1*}

¹State Key Laboratory of High Field Laser Physics, Shanghai Institute of Optics and Fine Mechanics, Chinese Academy of Sciences, China

²State Key Laboratory of Modern Optical Instrumentation, College of Optical Science and Engineering, Zhejiang University, Hangzhou 310027, China

*corresponding author: ya.cheng@siom.ac.cn

Abstract- We demonstrate phase matched SHG in an on-chip lithium niobate (LN) microresonator fabricated by femtosecond laser direct writing followed by focused ion beam milling. We achieve a normalized conversion efficiency of $1.1 \times 10^{-3}/\text{mW}$ in the LN microdisk with a diameter of $\sim 102 \mu\text{m}$.

Owing to a strong confinement of light in a small volume via total internal reflection, a high-Q whispering-gallery-mode (WGM) microresonator can dramatically enhance the nonlinear interaction between the light and the resonator material [1]. Recently, we have demonstrated fabrication of high-Q lithium niobate (LN or LiNbO₃) microresonators on a LN thin film wafer [2]. Applications such as second-harmonic generation (SHG) and electro-optic modulation have been preliminarily demonstrated in the LN microresonators because of the large second-order nonlinear optical coefficient and electro-optic coefficient of LN crystal. It should be stressed that for high-Q microresonators of small sizes, maintaining the coherent double resonance condition in the phase matched SHG is extremely challenging because of the sparse frequency distributions of high-Q modes for both the fundamental and second harmonic waves. Here, we employ the cyclic semi-phase matching (CSPM) for phase matched SHG in an on-chip LN microresonator with a diameter of only $\sim 100 \mu\text{m}$ [3]. The results are shown in Fig. 1. The technique opens new possibilities for modern classical and quantum optical applications by enabling ultralow threshold, efficient on-chip nonlinear wavelength conversion.

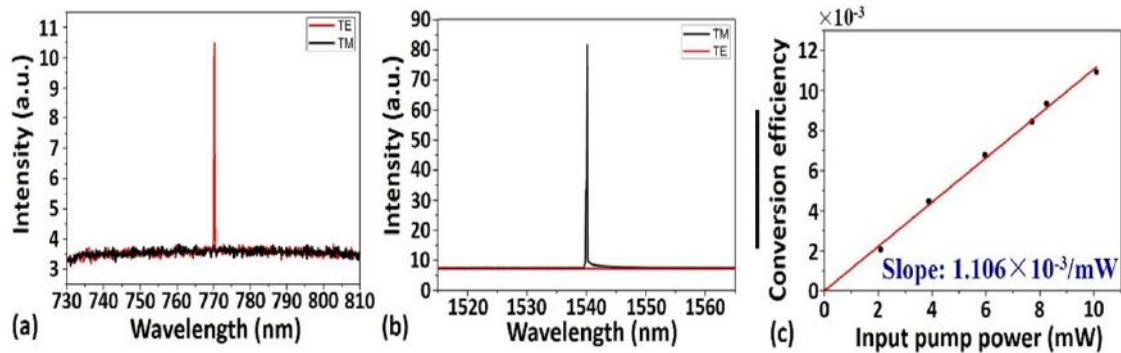


Fig. 1: The spectra of (a) the TE-polarized second harmonic generated from the microresonator and (b) the TM-polarized pump light. (c) The SHG conversion efficiency plotted as a function of the pump power.

REFERENCES

1. K. J. Vahala, "Optical microcavities," *Nature* **424**, 839-846 (2003).
2. J. Lin, Y. Xu, Z. Fang, M. Wang, J. Song, N. Wang, L. Qiao, W. Fang, and Y. Cheng, "Fabrication of high-Q lithium niobate microresonators using femtosecond laser micromachining," *Sci. Rep.* **5**, 8072 (2015).
3. G. Lin, J. U. Fürst, D. V. Strekalov, and N. Yu, "Wide-range cyclic phase matching and second harmonic generation in whispering gallery resonators," *Appl. Phys. Lett.* **103**, 181107 (2013).

Electro-optical modulator with 0.1% quantum efficiency

A. R. Rueda^{1,2,3}, F. Sedlmeir^{1,2,3}, and H.G.L. Schwefel⁴

¹Max Planck Institute for the Science of Light, Guenther-Scharowsky-Strasse 1/Building 24, 90158 Erlangen, Germany

²Institute for Optics, Information and Photonics, University Erlangen-Nuernberg, Staudtstr. 7/B2, 91058 Erlangen, Germany

³SAOT, School in Advanced Optical Technologies, Paul-Gordan-Str. 6, 91052 Erlangen, Germany

⁴Department of Physics, University of Otago, Dunedin, New Zealand
alfredo.rueda@mpl.mpg.de

Abstract— Conversion of microwave qubits into the optical regime is one of the next big steps in quantum information technology. It provides the link between electronic quantum devices via low-loss optical telecommunication networks. We present a novel system for coherent frequency upconversion of weak microwave signals to the telecom band based on the electro-optical effect using a high quality crystalline WGM-resonator coupled to a 3D microwave cavity, achieving high photon conversion efficiency of 0.1% with MHz bandwidth at room temperature.

The experimental realization of a device that can link superconducting microwave circuits to the optical domain has become of relevant importance in the quantum community. It will establish the possibility to implement hybrid systems in which diverse well developed optical quantum frameworks can be implemented such as long-lived quantum memories and quantum networks, among others. Currently the coherent exchange of information between microwave quantum circuits in different locations is not possible. As soon as a microwave qubit leaves the cryogenic fridge, it faces high decoherence and transmission losses at room temperature leading to complete information loss. In the optical domain however, these effects are negligible due to the high energy of optical photons. Frequency upconversion into the optical regime is the most suitable way to enable long distance information exchanges between diverse quantum systems.

In the past years many attempts have been undertaken to develop an efficient noiseless conversion channel where the so far highest microwave to optical conversion efficiency was reached via electro-optomechanical coupling, where nearly 10% photon conversion efficiency in a cryogenic environment was reported [1]. The bandwidth of this approach, however, is fundamentally limited to the mechanical resonance frequency and recent implementations reach only several tens of kHz. Electro-optic modulation is another approach for coherent microwave to optical conversion. The process can be described by sum-frequency (SFG) and difference-frequency generation (DFG). We focus on the SFG process because it is fundamentally noiseless and hence does not lead to decoherence if the photon conversion efficiency approaches unity.

Resonant electro-optic modulation was already realized in high Q whispering gallery mode resonators (WGM) coupled to a microwave resonator [2, 3]. These implementations could however only achieve single SFG or DFG by detuning the involved optical and microwave pump, resulting in an increase of the required optical pump power. Electro-optic single-sideband conversion has been demonstrated in a lithium tantalate WGM resonator, where the optical pump and the optical signal were orthogonally polarized (type-I conversion) [4]. We present a new take on the classical electro-optical (type-0) modulation within a lithium niobate WGM-resonator, where single sideband operation is made possible without detuning. Hereby we reach a photon conversion efficiency three orders of magnitude higher than in previous works [2, 3]. This significant increase of the conversion efficiency is due to better optical and microwave Q factors as well as improvements in the geometry of the microwave cavity, which strongly focuses the microwave field into the optical mode volume. Furthermore, our system has a bandwidth of a couple of MHz and is fully compatible with circuit QED.

The system consists in a z-cut lithium niobate WGM resonator which is placed inside a 3D microwave copper cavity as depicted in Fig. 1a) where it is clamped by two metallic rings that are designed to maximize the field overlap between the microwave and the optical modes. A silicon prism is placed within the cavity to evanescently couple light into the WGM resonator. Two holes

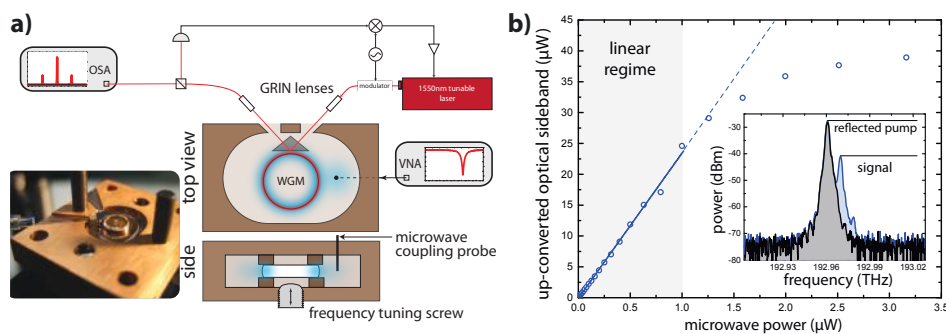


Figure 1: a) In top view, schematic of the optical coupling system. In the side view, schematic of the coaxial pin coupler and the metallic screw used to perturb the microwave mode. Photograph of the open microwave cavity. b) Up-converted sideband power vs. microwave power delivered into the cavity.

in the copper cavity allow the optical pump light ($\lambda \approx 1550$ nm) to enter and the light reflected from the prism, as well as emitted from the WGM resonator, to leave the cavity. This light is collected and analyzed by an optical spectrum analyzer (OSA) and a photodiode which allows us to extract information about the loaded optical Q ($> 10^8$) and the optical free spectral ranges (~ 8.95 GHz). The microwave signal is coupled into the cavity via a coaxial pin coupler mounted close to the WGM resonator. A metallic screw is used to perturb the microwave field for fine adjustment of its resonance frequency from 8.90 to 9.07 GHz. We find a loaded $Q_\Omega = 246$ for the undisturbed mode, which decreases to $Q_\Omega = 174$ for maximum perturbation by the screw. The whole setup is thermally stabilized at room temperature.

We are able to switch between sum- and difference frequency generation by employing avoided crossings of the optical modes, which lead to an asymmetric spectral distance between three neighboring resonances. Since the mode crossings are temperature dependent, they can be used to tune the microwave frequency of the converter over several tens of MHz. To estimate the single sideband photon conversion efficiency we maximize the upconversion and minimize the downconversion channel. Then, we measure the upconverted signal at different microwave pump powers as shown in figure 1b). From the slope of a linear fit in the undepleted regime (grey) we can extract a photon conversion efficiency of $\eta_+ = (1.09 \pm 0.02) \times 10^{-3}$ with 1 MHz bandwidth[5]. This efficiency is three orders of magnitude better than previous electro-optical attempts. We will report which enhancements of our system can lead to efficiencies reaching unity [5].

REFERENCES

1. R. W. Andrews, R. W. Peterson, T. P. Purdy, K. Cicak, R. W. Simmonds, C. A. Regal, and K. W. Lehnert, “Bidirectional and efficient conversion between microwave and optical light,” *Science* **30**, 321–326 (2014).
2. V. S. Ilchenko, A. A. Savchenkov, A. B. Matsko, and L. Maleki, “Whispering-gallery-mode electro-optic modulator and photonic microwave receiver,” *Journal of the Optical Society of America B* **20**, 333–342 (2003).
3. D. V. Strekalov, H. G. L. Schwefel, A. A. Savchenkov, A. B. Matsko, L. J. Wang, and N. Yu, “Microwave whispering-gallery resonator for efficient optical up-conversion,” *Physical Review A* **80**, 033,810–5 (2009).
4. A. A. Savchenkov, W. Liang, A. B. Matsko, V. S. Ilchenko, D. Seidel, and L. Maleki, “Tunable optical single-sideband modulator with complete sideband suppression,” *Optics Letters* **34**, 1300–1302 (2009).
5. A. Rueda, F. Sedlmeir, M. C. Collodo, U. Vogl, B. Stiller, G. Schunk, D. V. Strekalov, C. Marquardt, J. M. Fink, O. Painter, G. Leuchs, and H. G. Schwefel, “Efficient single sideband microwave to optical conversion using an electro-optical whispering gallery mode resonator,” arXiv:1601.07261 [quant-ph] (2016).

Electrically tunable silicon dual-ring assisted Mach-Zehnder interferometer switches

Linjie Zhou^{*}, Liangjun Lu, Shuoyi Zhao, and Jianping Chen

State Key Laboratory of Advanced Optical Communication Systems and Networks

Department of Electronic Engineering, Shanghai Jiao Tong University, Shanghai 200240, China

^{*}corresponding author: ljzhou@sjtu.edu.cn

Abstract-We report our recent progress on 16×16 optical switches based on dual-ring assisted Mach-Zehnder interferometers. TiN microheaters and p-i-n diodes are integrated in microring resonators for thermo-optic phase correction and electro-optic switching, respectively. Optical signal can be routed from an input port to any output port with low power consumption.

Optical switches have received considerable research interest in recent years. They can be used in optical interconnect networks for datacenters and supercomputers. Compared to conventional electrical switching, optical switching is more power efficient and low cost due to the absence of Optical-Electrical-Optical conversion. Optical switches can be implemented on various material platforms, such as silica-on-silicon, InP, silicon-on-insulator (SOI) etc. The SOI platform is very attractive because of its high index contrast which can make devices more compact and low power. In our previous work, we have demonstrated 2×2 and 4×4 optical switches based on Mach-Zehnder interferometers (MZIs) [1], multimode interferometers (MMIs) [2, 3], and dual-ring assisted MZIs (DR-MZIs) [4, 5]. A novel design of a two-bus coupled-rings 2×2 switch with inter-ring coupling enabled by a three-waveguide directional coupler was also proposed, in which resonance selective switching is achieved [6]. Here we report our recent progress on the more complicated 16×16 optical switch with the DR-MZI as the elementary switching unit.

Figure 1(a) shows the topological structure of the 16×16 optical switch. It is based on a Benes architecture, which is reconfigurably non-blocking. The 16 input ports can be connected to the 16 output ports in a one-to-one manner for any combination upon proper configuration of each switch element. The switch element, as shown in Fig. 1(b), is composed of a MZI side-coupled with two microring resonators. TiN micro-heaters are integrated in both rings and a p-i-n diode is integrated only in the top ring. Therefore, both thermal and electrical switching are possible by using the two types of electrodes. In our switch design, the thermal tuners are mainly used to correct the phase errors generated by the imperfect fabrication and the electrical tuner is for fast switching.

Figure 2 shows the preliminary measurement results. The input is from port I4 and the output spectra from I9 to I12 are measured. Initially, all switch elements are in the “cross” state after phase correction, and therefore, the destination port is O12, as indicated by the red line in Fig. 1(a). This is confirmed by the measured spectra in Fig. 2(a), where the path I4-O12 has high output power while the other three are much lower. The small dip in I4-O12 spectrum is caused by the ring resonator loss. As light passes 7 DR-MZIs along its routing paths, the extra loss per ring is calculated to be around 0.7 dB. The routing destination can be changed by turning on any switch element along its path. When SE(6, 7) is turned on, the optical transmission to O12 is reduced and transmission to O11 rises up at the operation wavelength of ~ 1562 nm. Therefore, it demonstrates that the optical path can be switched between O4-O11 and O4-O12 by tuning on/off SE(6, 7). The electrical switching power is

less than 1 mW.

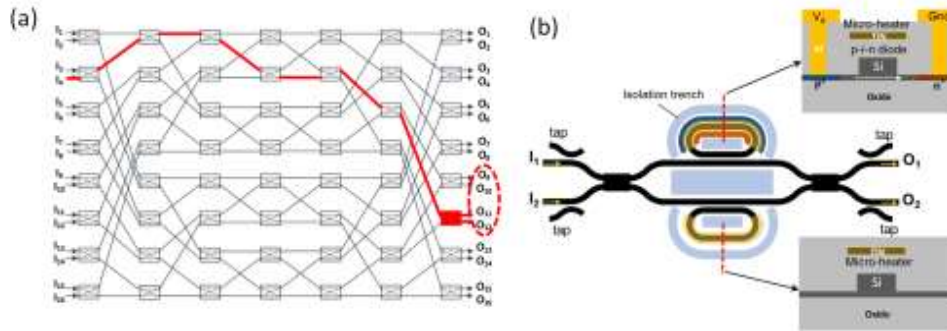


Figure 1. (a) Benes switch architecture for the 16×16 DR-MZI switch. Two optical paths from I_4 to O_{11} and O_{12} are highlighted. (b) 2×2 DR-MZI switching element. The insets show the cross-sections of the active ring waveguides.

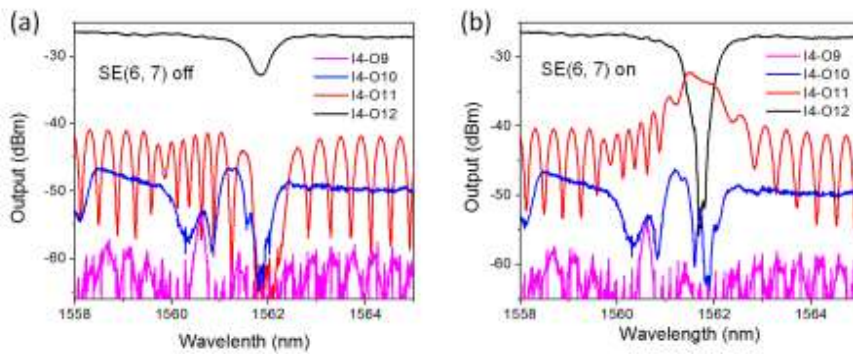


Figure 2. Measured transmission spectra of the 16×16 DR-MZI switch for optical paths from input I_4 to output O_9 - O_{12} when (a) no SE turned on, (b) SE(6,7) turned on.

Acknowledgements This work was supported in part by the 863 program (2013AA014402), the National Natural Science Foundation of China (NSFC) (61422508), and the Shanghai Rising-Star Program (14QA1402600).

REFERENCES

- [1] L. Lu, L. Zhou, Z. Li, X. Li, and J. Chen, "Broadband 4×4 non-blocking silicon electro-optic switches based on Mach-Zehnder interferometers," *IEEE Photon. J.*, vol. 7, p. 7800108, 2015.
- [2] Z. Li, L. Zhou, L. Lu, S. Zhao, D. Li, and J. Chen, " 4×4 nonblocking optical switch fabric based on cascaded multimode interferometers," *Photon. Res.*, vol. 4, pp. 21-26, 2016/02/01 2016.
- [3] L. Lu, L. Zhou, S. Li, Z. Li, X. Li, and J. Chen, " 4×4 non-blocking silicon thermo-optic switches based on multimode interferometers," *J. Lightwave Technol.*, vol. 33, pp. 857-864, 2015.
- [4] L. Lu, L. Zhou, Z. Li, D. Li, S. Zhao, X. Li, *et al.*, " 4×4 silicon optical switch based on double-ring assisted Mach-Zehnder interferometers," *IEEE Photon. Technol. Lett.*, vol. 27, pp. 2457-2460, 2015.
- [5] L. Lu, L. Zhou, X. Li, and J. Chen, "Low-power 2×2 silicon electro-optic switches based on double-ring assisted Mach-Zehnder interferometers," *Opt. Lett.*, vol. 39, pp. 1633-1636, 2014.
- [6] L. Zhou, R. Soref, and J. Chen, "Wavelength-selective switching using double-ring resonators coupled by a three-waveguide directional coupler," *Opt. Express*, vol. 23, pp. 13488-13498, 2015.

High-Q Micro/Nanoresonators for Nonlinear/Quantum Photonics and Sensing

Qiang Lin

Department of Electrical and Computer Engineering and Institute of Optics,
University of Rochester, Rochester, NY 14627, USA

*corresponding author, E-mail: qiang.lin@rochester.edu

Abstract

In this talk, we will discuss our recent progress in developing high-quality micro/nanoresonators on material platforms such as silicon, silicon carbide, and lithium niobate, whose outstanding material properties exhibit great potential for broad photonic applications. We will focus on our recent efforts in applying them for nonlinear and quantum photonics, and for sensing applications.

1. Summary

High-Q optical micro-/nano-resonators, with an exceptional capability of dramatically enhancing optical fields inside a small volume, are critical foundations for many areas of optical science, such as integrated nonlinear optics [1], cavity quantum electrodynamics [2], cavity optomechanics [3], and biomedical sensing [4]. In general, the underlying materials play a crucial role since most applications rely on the linear/nonlinear optical property [1], the mechanical property [3], the quantum confinement effect [2], defect characteristics [5], or thermal stability for proper operation [4]. In recent years, significant interest has been focused on developing micro-/nano-resonators on various material platforms, including dielectrics, semiconductors, and polymers.

Silicon carbide (SiC) is a semiconductor [6] with a wide band gap (2.3–3.4 eV), a large refractive index (~ 2.6), extremely large Young's modulus (~ 450 GPa), exceptionally low mechanical damping, a significant thermal conductivity (~ 490 W/(m · K)), very high hardness and chemical inertness, and unique point defect characteristics [7]. Moreover, SiC exhibit many crystal forms with various material isotropy and anisotropy. Therefore, SiC is outstanding material for broad quantum photonic and optomechanical applications, particularly for sensing applications in harsh environment.

Lithium niobate (LiNbO₃), instead, exhibits exceptional nonlinear optical, electro-optical, piezoelectric, photoelastic, and ferroelectric properties [8], with great potential as a universal material platform for making hybrid nanophotonic circuits for high-speed electro-optic and all optical signal processing, nonlinear wave generation, and photonic quantum state engineering.

Their great potential for micro/nanophotonics has attracted significant interest in the past few years [9–19]. Unfortunately, the device development along these lines

faces significant challenge due to the difficult in fabricating high-quality chip-scale photonic devices. We recently devoted considerable efforts in developing high-quality micro/nanophotonic devices in these material platforms. These devices allow us to observe intriguing nonlinear dynamics in thermal, optical, and mechanical degrees of freedom. Moreover, we have applied these devices for novel functionalities in nonlinear photonics, photonic signal processing, optomechanical sensing, and photonic quantum states generation. In this talk, we will discuss our recent progress along these lines.

2. Acknowledgement

This work is supported in part by NSF under grants numbers ECCS-1509749 and ECCS-1408517 and by the DARPA SCOUT program through grant number W31P4Q-15-1-0007 from AMRDEC.

References

- [1] K. J. Vahala, *Nature* **424**, 839 (2003).
- [2] K. Kennessy, *et al*, *Nature* **445**, 896 (2007).
- [3] M. Aspelmeyer, *et al*, *Rev. Mod. Phys.* **86**, 1391 (2014).
- [4] X. Fan, *et al*, *Ana. Chem. Acta* **620**, 8 (2008).
- [5] A. Faraon, *et al*, *Nature. Photon.* **5**, 301 (2011).
- [6] G. L. Harris, *Properties of Silicon Carbide*. (INSPEC, 1995).
- [7] W. F. Koehl, *et al*, *Nature* **479**, 85 (2011).
- [8] K. K. Wong, Ed., *Properties of lithium niobate*, (IEE, INSPEC, 2002).
- [9] B.-S. Song, *et al*, *Opt. Express* **19**, 11084 (2011).
- [10] X. Lu, *et al*, *Opt. Lett.* **38**, 1304 (2013).
- [11] J. Cardenas, *et al*, *Opt. Express* **21**, 16882 (2013).
- [12] M. Radulaski, *et al*, *Opt. Express* **21**, 32623 (2013).
- [13] G. Calusine, *et al*, *Appl. Phys. Lett.* **105**, 011123 (2014).
- [14] A. P. Magyar, *et al*, *Appl. Phys. Lett.* **104**, 051109 (2014).
- [15] T. Wang, *et al*, *Opt. Express* **20**, 28119 (2012).
- [16] C. Wang, *et al*, *Opt. Express* **22**, 30924 (2014).
- [17] J. Lin, *et al*, *Sci. Rep.* **5**, 8072 (2015).
- [18] R. Geiss, *et al*, *Opt. Lett.* **40**, 2715 (2015).
- [19] J. Wang, *et al*, *Opt. Express* **23**, 23072 (2015).

Electromagnetic Theory

Electromagnetic Nuclear Physics

Bernard Schaeffer

7, rue de l'Ambroisie, 75012 Paris, France
E-mail: bschaeffer@wanadoo.fr

Abstract

The so-called Coulomb force, repulsive between protons, discovered by Rutherford, is the only electromagnetic interaction recognized in nuclear physics for scattering and energy. A singularity was observed, falsely attributed to an attractive phenomenological strong interaction. In contrast, at high kinetic energy, it needs only to replace, above the singularity, in the Rutherford formula, the electrostatic -2 by -6 , magnetic. In log-log coordinates, one obtains two straight lines with slopes -2 , and -6 , going through the experimental points, crossing at the singularity. At kinetic energies higher than 28 MeV, the -28 MeV binding energy of the alpha particle is annihilated, freeing the magnetic moments of the nucleons. The nuclear binding energy is also electromagnetic. Indeed, the electrostatic attraction between a proton and a not so neutral neutron, as between amber and dust, equilibrates statically the magnetic repulsion. The precision of the calculation is of a few percent for the simplest bound nucleus, the deuteron. In contrast with the electromagnetic theory, the hypothetical strong force cannot be used to calculate nuclear scattering and binding energy. With protons and not so neutral neutrons fundamental constants, it is easy to calculate electromagnetically normal and not so anomalous Rutherford scattering and also binding energy, at least for light nuclei.

1. Introduction

According to conventional nuclear physics, a hypothetical strong force is assumed to hold the nucleons against the **repulsive** "Coulomb force" due to the positive charges of the protons. To publish a paper in nuclear physics journals, the belief that the "strong force" exists is mandatory. In contrast, it will be shown in this paper that the nuclear interaction is entirely and only electromagnetic:

1 - Rutherford scattering is well known to be *electrostatic* at low kinetic energy, with a -2 slope in log-log coordinates. At high kinetic energies, the slope has been discovered to be -6 , *magnetic*.

2 - The binding energy of a nucleus has never been calculated successfully, the fundamental laws of the strong force being unknown. In contrast, *electromagnetically*, one is able to calculate the binding energy of at least light nuclei, without fit, with a precision of a few percent for the deuteron. Indeed, there is an *electrostatic attraction* between a proton and a not so neutral neutron as amber *attracts* light bodies, ignored in nuclear physics. The magnetic **repulsion** equilibrates the *electrostatic attraction*.

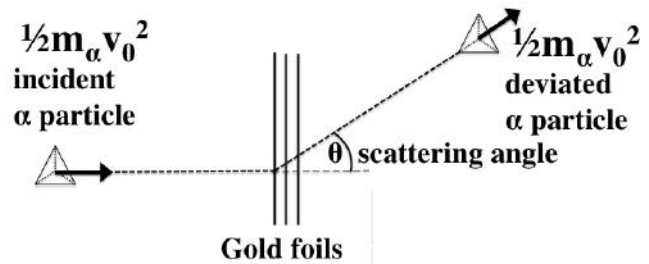


Figure 1: Geiger-Marsden Experiment - The α particles are emitted by radium, impacting thin gold, lead or other metal foils. The number of deflected α particles depends upon the scattering angle and the metal foils determining their velocity. The experiment consists to count the number of flashes viewed through the microscope during a given time and for a fixed solid angle. The α particles are scattered all around, even backwards, astonishing Rutherford [1, 2, 3, 4].

The purpose of this paper is to solve electromagnetically the "anomalous" α particle scattering problem and, in a second part, the nuclear binding energy problem. Up to know these two problems were only described empirically, without fundamental laws.

2. Scattering Theories

2.1. Rutherford Scattering

Rutherford discovered that an impacting *electrostatically* charged α particle is deviated by the **repulsive electrostatic** "Coulomb force" of an impacted nucleus. The origin of the concept of strong force comes from the observation of the discrepancy between Rutherford theory and experiment at high kinetic energies.

Alpha particles, from a radioactive source, are deviated by thin gold foils, producing a tiny, but visible flash of light when they strike a fluorescent screen (Fig. 1). Surprisingly, α particles were found at large angles of deflexion and, unexpectedly, some of the particles are scattered back in the direction of the incidence. They back penetrate so close to the central charge, that the field due to the uniform distribution of negative *electricity* may be neglected [1, 2], disproving the J. J. Thomson plum-pudding model.

Rutherford developed the *electrostatic* scattering formula relating the cross-section and the kinetic energy of the α particles. He explained why some alpha particles projected on an atom were reflected by a small nucleus: "As-

suming classical trajectories for the scattered alpha particles, Coulomb's law was found to hold for encounters between alpha particles and nuclei" [2]. The first evidence of departures from Coulomb's law other than those in alpha scattering by H and He was observed by Bieler [4].

The discontinuity appearing near the total absolute value of the α particle binding energy, 28 MeV, is called Rutherford singularity. For kinetic energies larger than 23 MeV [3, 5], the relative cross section decreases anomalously faster than predicted by the *electrostatic* Rutherford formula (Fig. 2). *Magnetic* interpretations have been tempted without success [4, 6], due to the wrong assumption of an *attractive*, negative *magnetic* moment.

2.2. Strong Force Potential (Chadwick)

Geiger [1] observed that, at high kinetic energies, "the deviation was larger than predicted by the *electrostatic* force". Chadwick and Bieler [3, 7] determined that forces of very great intensity hold the nucleus together, a force distinct from the *electromagnetism* [3, 8, 9]. The *electrostatic* potential is **repulsive** as discovered by Rutherford. The hypothetical "strong force", was assumed to be negative, thus *attractive* [3, 10]:

$$V(r) = +\frac{2Ze^2}{4\pi\epsilon_0 r} - \frac{B}{r^n} \quad (\mathbf{n} > 1) \quad (1)$$

The first term of equation (1) corresponds to the "normal" *electrostatic* Rutherford scattering and the second term to the "anomalous" scattering, *magnetic* if $\mathbf{n} = 3$. The sign of B, not specified, seems to be *positive* [10]. Many empirical theories have been developed. The first one is Yukawa's with two empirical parameters [11]. Up to now, the fundamental laws of the "strong force" remained unknown.

2.3. Electromagnetic Potential (Bieler)

Using formula (1) Bieler hypothesized the existence of *attractive magnetic* moments combined with the *electrostatic repulsion*, thus with $\mathbf{n} = 3$ for the potential [3, 4]:

$$V(r) = +\frac{2Ze^2}{4\pi\epsilon_0 r} - \frac{2Z|\mu_0\mu_n\mu_p|}{4\pi r^3} \quad (2)$$

Nuclear scattering became entirely and only electromagnetic. Unfortunately, with the *attractive* negative sign of the *magnetic* potential and a combined electromagnetic formula, Bieler was unable to solve the problem.

2.4. Electrostatic and Magnetic Potentials Separated

At low kinetic energies, r being large, the interaction is governed by the Rutherford *electrostatic* formula with a $1/r$ potential. In log-log coordinates, the experimental points are aligned on straight lines with slopes -2 and -6 (fig. 2). The intersection of these two straight lines, at 23 MeV, coincides approximately with the binding energy of the α particles -28 MeV, except for the sign. At kinetic energies higher than 28 MeV, the α particles are thus broken into protons and neutrons.

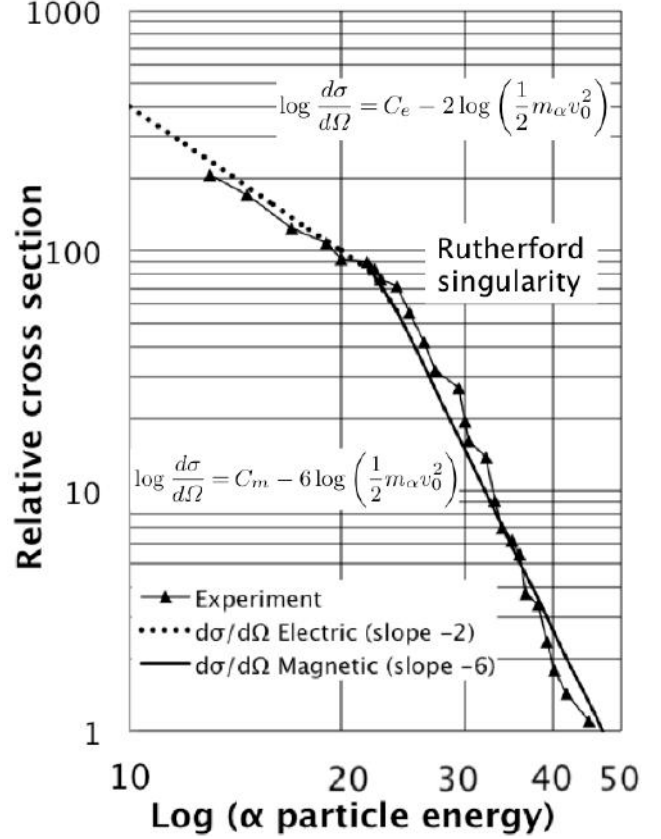


Figure 2: Applying Coulomb [12] and Poisson [13] potentials - The relative differential cross section $\frac{d\sigma}{d\Omega}$ is a targeted area per solid angle per unit time. In other words, it is the differential ratio between the geometrical area divided by the corresponding solid angle, multiplied by the ratio between potential and kinetic energies. The α particles are projected on Ta foils at a fixed scattering angle $\theta = 60^\circ$ with initial kinetic energies varying between 13 and 42 MeV [6]. The α particles are **repulsed** and deviated by the Ta nucleus *electrostatic* force in the direction of the particle exit trajectory (Fig. 1). The Rutherford singularity appears for a kinetic energy near 23 MeV. At higher kinetic energies, the curve deviates, wrongly assumed to be due to an attractive strong force [3]. Bieler assumed, also wrongly, an attractive magnetic force [4]. In contrast, with a **repulsive magnetic** force one obtains a straight line with a -6 slope going through the experimental points. The Rutherford formula works fine, even for the so called anomalous scattering, provided that the *electric* -2 shall be replaced by the *magnetic* -6 at kinetic energy able to annihilate the α particle around its total binding energy -28 MeV.

The separation distance r between impacting α particles and impacted heavy nuclei decreases with increasing kinetic energy. The *electrostatic* interaction between the protons of the impacting α particles and of the impacted Z nuclei is given by the Coulomb potential formula:

$$V(r_e) = + \frac{2Ze^2}{4\pi\epsilon_0 r} \quad (3)$$

At high kinetic energy, e.g. near or above 28 MeV , the total nuclear binding energy of the α particles, -28 MeV , is annihilated, freeing the *magnetic* moments of the nucleons. The Poisson potential in $1/r^3$ [13] replaces the Coulomb potential in $1/r$ [12], due to the small separation distance r between nucleons. Thus, the *magnetic* moments of the nucleons interact with those of the impacted nuclei. The -3 *magnetic* potential replaces the -1 *electrostatic* potential:

$$V(r_m) = + \frac{2Z|\mu_0\mu_n\mu_p|}{4\pi r^3} \quad (4)$$

2.5. Differential cross-section

The differential cross-section $\frac{d\sigma}{d\Omega}$ is defined as the ratio of the number of particles scattered into a constant direction θ , per unit time and per unit solid angle $d\Omega$. Squaring the initial kinetic energy of the α particle, $\frac{1}{2}m_\alpha v_0^2$, gives the so-called differential cross-section $\frac{d\sigma}{d\Omega}$, only relatively known. The complete Rutherford formula [2],

$$\frac{d\sigma}{d\Omega} = \left(\frac{1}{4 \sin^2 \frac{\theta}{2}} \times \frac{zZe^2}{4\pi\epsilon_0} \times \frac{1}{\frac{1}{2}m_\alpha v_0^2} \right)^2 \quad (5)$$

may be simplified for constant m_α , θ , z and Z :

$$\frac{d\sigma}{d\Omega} \propto \left(\frac{1}{2}m_\alpha v_0^2 \right)^{-2} \quad (6)$$

The exponent -2 , due to the *electrostatic* interaction cross-section, becomes, logarithmically, the coefficient -2 :

$$\log \frac{d\sigma}{d\Omega} = C_e - 2 \log \left(\frac{1}{2}m_\alpha v_0^2 \right) \quad (7)$$

where C_e , only relatively known, is adjusted to the singularity. The log-log graph shows two straight lines on Fig. 2, Coulomb *electrostatic*, slope -2 , and Poisson *magnetic*, with slope -6 [13, 14].

$$\log \frac{d\sigma}{d\Omega} = C_m - 6 \log \left(\frac{1}{2}m_\alpha v_0^2 \right) \quad (8)$$

The variables are the differential cross section $\frac{d\sigma}{d\Omega}$ and the initial α particle velocity v_0 . C_e and C_m are adjusted to make coincide the intersection between the *electrostatic* and *magnetic* straight lines (in log-log coordinates) with the Rutherford singularity. At the singularity, experimentally, the initial kinetic energy, $|-23| \text{ MeV}$, coincides nearly with the absolute value of the α particle total binding energy, $|-28| \text{ MeV}$ (Fig. 2). We have now one formula for *electrostatic* scattering (eq. 7) and another one

for *magnetic* scattering (eq. 8). The difference between “normal” and “anomalous” scattering is the potential exponent, -3 , *magnetic*, instead of -1 , *electrostatic*. The slopes are -6 , *magnetic*, and -2 , *electrostatic*, due to the cross sections in a log-log graph. The constant is defined at the Rutherford singularity, 23 MeV on Fig. 2, experimentally smaller than the ^4He binding energy, 28 MeV , taken positive, probably not significant.

The kinetic energy at the Rutherford singularity is somewhat less than the experimental value of the total binding energy of the α particle, in absolute value, $|-28| \text{ MeV}$ (Fig. 2).

2.6. Conclusion on Nuclear scattering

Rutherford discovered the electrostatic part of the nuclear interaction. The **repulsion** between protons was improperly called “Coulomb force”.

Indeed, the Coulomb force may be *attractive* or *repulsive*. Chadwick [3] choose an *attractive* strong force interacting indistinctly between nucleons (NN). Instead of being **repulsive** (equation 3), as for Rutherford’s *electric* scattering, Bieler assumed the interaction to be *electromagnetic* with a *magnetic* part (equation 2), falsely *attractive*[4]:

$$V(r) = - \frac{2Z|\mu_0\mu_n\mu_p|}{4\pi r^3} \quad (9)$$

Bieler was thus unable to solve the problem of the high energy scattering. As far as I know, nobody tried a *magnetic repulsive* force.

At short r , at high kinetic energy, the **repulsive magnetic** potential in r^{-3} replaces the Rutherford also repulsive electrostatic potential in r^{-1} . As the Rutherford model overturned Thomson’s model, the *magnetic* interaction overturns Chadwick’s *attractive* strong force hypothesis [3, 7]. Bieler had almost solved the problem *magnetically*: unfortunately, the sign was wrong, falsely assumed to be negative, *attractive*. In log-log coordinates, it suffices to replace the -2 of the Rutherford *electrostatic* formula by the -6 , *magnetic*, to obtain two straight lines coinciding respectively with the *electrostatic* and *magnetic* scattering curves (figure 2) crossing at the singularity. Except for the position of the singularity, slightly adjusted near to the total α particle binding energy, there is no adjustment, only fundamental laws and constants.

No need of relativity and/or quantum mechanics, both unable to explain the not so anomalous scattering. *Electric* and *magnetic* interactions explain nuclear scattering, both original Rutherford, *electric* and so anomalous anomalous scattering, *magnetic*. We may say that there is an extended Rutherford scattering theory, *electric* at low kinetic energy and not so anomalous *magnetic* scattering at high kinetic energy, both **repulsive**.

3. Nuclear Binding Energy

The neutron, discovered in 1931 by Chadwick, seeming to be uncharged, the *electromagnetic* hypothesis for the nuclear interaction was unfortunately abandoned. The *magnetic* moments of the proton and of the deuteron were discovered in 1932 by Stern and the *magnetic* moment of the neutron in 1938 by Bloch. Except for the proton-proton repulsion, in spite of the discovery of the neutron *magnetic* moment and its *electrostatic* charges with no net charge, *electrostatic* and *magnetic* interactions between nucleons are generally ignored in nuclear physics.

Thales discovered, two millenaries ago that amber ($\eta\lambda\epsilon\kappa\tau\rho\omega\nu$) *attracts* light objects. Similarly, a proton *attracts* a not so neutral neutron. In other words, an electric dipole is induced into a not so neutral neutron by a nearby proton. The principle can be found in the book by Feynman [15].

Greeks also discovered the *magnetic* properties of *magnetite* from mount *Magnetos* that may be *attractive* or *repulsive*. Coulomb [12] and Poisson [13] discovered the formulas of the *electrostatic* and *magnetic* fundamental laws, ignored in nuclear physics except the so-called “Coulomb force”, between protons, only *repulsive*.

In the deuteron, the Coulomb *electrostatic attraction* between a proton and a not so neutral neutron can be equilibrated statically by the *repulsive* Poisson *magnetic* moments of the proton and of the neutron. First results have been obtained for hydrogen and helium isotopes [16, 17, 18].

3.1. Calculation of Electromagnetic Potential Energies

In contrast with scattering, the *electrostatic* Coulomb [12] and *magnetic* Poisson [13] potential energies between nucleons may be united into a single formula [19, 20, 21]:

$$U_{em} = \sum_i \sum_{i \neq j} \frac{q_i q_j}{4\pi\epsilon_0 r_{ij}} + \sum_i \sum_{i \neq j} \frac{\mu_0}{4\pi r_{ij}^3} \left[\vec{\mu}_i \cdot \vec{\mu}_j - \frac{3(\vec{\mu}_i \cdot \vec{r}_{ij})(\vec{\mu}_j \cdot \vec{r}_{ij})}{r_{ij}^2} \right] \quad (10)$$

The first term is the sum of Coulomb’s *electrostatic* interaction energy potential between *electrostatic* charges q_i and q_j separated by r_{ij} (no need of hypothetical quarks). The second term is Poisson’s *magnetic* interaction energy potential between nucleons with *magnetic* moments $\vec{\mu}_i$ and $\vec{\mu}_j$, separated by r_{ij} .

3.1.1. Total Deuteron Electrostatic Energy Potential (Coulomb)

The *electrostatic* potential energy U_e of this system of three point charges is, from formula (10):

$$U_e = \frac{1}{4\pi\epsilon_0} \left(\frac{q_1 q_2}{r_{12}} + \frac{q_2 q_3}{r_{23}} + \frac{q_3 q_1}{r_{31}} \right) \quad (11)$$

where q_1 , q_2 , and q_3 are the three electrostatic charges. r_{12} , r_{23} , and r_{31} are their separation distances along their com-

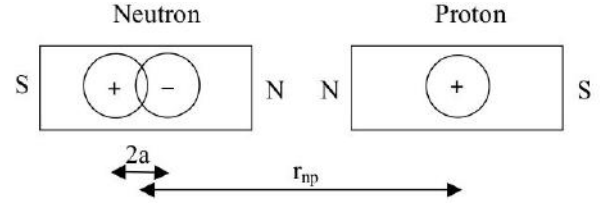


Figure 3: Schematic deuteron structure. - The elementary charges are assumed to be punctual. The proton contains an elementary charge $+e$ in the proton. The neutron contains *electrostatic* charges with no net charge, assumed to be $+e$ and $-e$. The *electrostatic* field of the proton produces a separation distance of $2a$ between the *electrostatic* charges of the neutron, distant by r_{np} from the proton. The proton attracts *electrically* the neutron as a rubbed plastic pen attracts small pieces of paper. The *magnetic* moments of the proton and the neutron are collinear and opposite, North against North (or South against South). Their *magnetic* interaction equilibrates the *electrostatic* attraction.

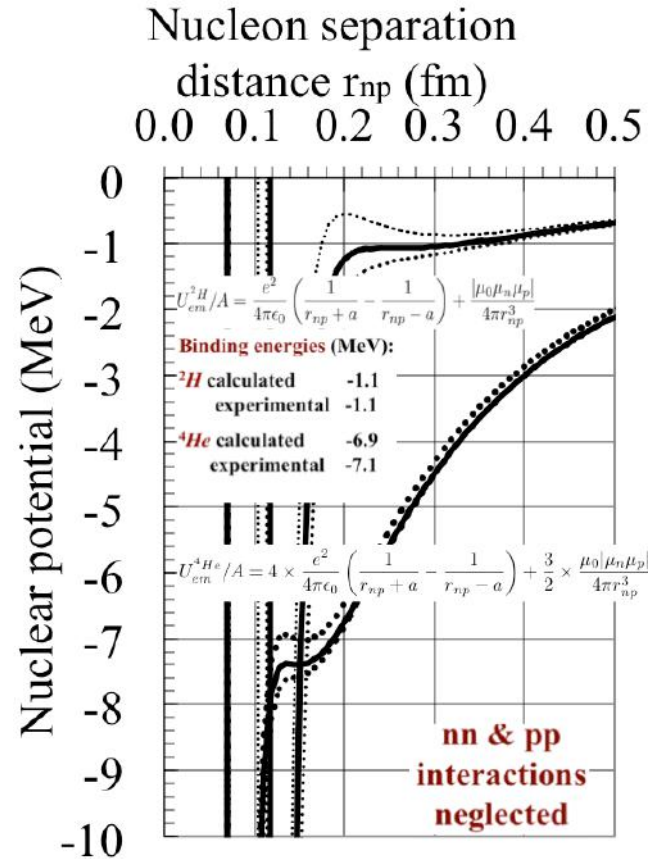


Figure 4: Calculated deuteron (${}^2\text{H}$ or heavy hydrogen, with one proton-neutron bond) and helium (${}^4\text{He}$ or α particles). - The *electrostatic* interaction between a proton and a not so neutral neutron is not negligible. Calculated helium (${}^4\text{He}$ or α particles) On helium, one has 6 bonds, 4 neutron-proton bonds, one neutron-neutron bond and one proton-proton bond. The proton-proton and neutron-neutron bonds may be neglected in a first approximation.

mon axis. The electrostatic energy potential between the 3 electrostatic charges of the deuteron (equation 11) becomes (r_{np} and a are defined on figure 3):

$$U_e = \frac{e^2}{4\pi\epsilon_0} \left(\frac{1}{r_{np} + a} - \frac{1}{r_{np} - a} - \frac{1}{2a} \right) \quad (12)$$

The usual dipole formula, $\frac{2a}{r_{np}^2}$ for $a \ll r_{np}$ doesn't work because a and r_{np} are of similar size. This can be solved by changing $\frac{1}{2a}$ by $\frac{1}{r_{np}+a} - \frac{1}{r_{np}-a}$. Although hypothesized, this gives the most precise result for the *electrostatic* dipole formula [15, 16], used instead of the usual approximate formula, $\frac{2a}{r_{np}^2}$. With this change one obtains a formula giving a zero dipole for both $r_{np} = 0$ and $r_{np} = \infty$:

$$U_e = \frac{e^2}{4\pi\epsilon_0} \left(\frac{2}{r_{np} + a} - \frac{2}{r_{np} - a} \right) < 0 \quad (13)$$

Although it is not rigorous, this **attractive** approximation gives a good result for 2H and 4He (Fig. 4).

3.1.2. Total Deuteron Magnetic Energy Potential (Poisson)

According to formula (10), the *magnetic* potential energy of the deuteron is:

$$U_m = \frac{\mu_0}{4\pi r_{np}^3} \left[\vec{\mu}_n \cdot \vec{\mu}_p - \frac{3(\vec{\mu}_n \cdot \vec{r}_{np})(\vec{\mu}_p \cdot \vec{r}_{np})}{r_{np}^2} \right] \quad (14)$$

The *magnetic* potential is positive, **repulsive**, assuming that the *magnetic* moments of the proton and of the neutron in the deuteron are collinear and opposite ($\vec{\mu}_n \cdot \vec{\mu}_p < 0$) as shown on figure 3. The coefficient in the brackets is thus equal to $2|\mu_n\mu_p|$. The *magnetic* potential is thus:

$$U_m = \frac{\mu_0}{4\pi} \frac{2|\mu_n\mu_p|}{r_{np}^3} > 0 \quad (15)$$

3.1.3. Total Deuteron Electrostatic and Magnetic Energy Potentials Added

Adding the total **attractive electrostatic** (equation 13) and **repulsive magnetic** (equation 15) components of the *electromagnetic* potential formula (10) becomes:

$$U_{em} = \frac{e^2}{4\pi\epsilon_0} \left(\frac{2}{r_{np} + a} - \frac{2}{r_{np} - a} \right) + \frac{\mu_0}{4\pi} \left(\frac{2|\mu_n\mu_p|}{r_{np}^3} \right) \quad (16)$$

or, numerically:

$$U_{em} = 1.442 \left(\frac{2}{r_{np} + a} - \frac{2}{r_{np} - a} \right) + \frac{0.170}{r_{np}^3} \text{ MeV} \quad (17)$$

There is one variable r_{np} and one parameter a in formula (17). In order to find the binding energy it is necessary to adjust the parameter a of the curve to obtain a potential minimum for both r_{np} and a . This is not to be confused with fitting to adjust the binding energy. Due to the Coulomb singularity, the potential has only one local minimum, a horizontal inflection point due to the point-like

assumption of the *electric* charges. A real minimum [22] would be better, of course, but, needing an empirical parameter, would break the fundamental nature of the theory. The curve of the *electromagnetic* potential is shown on figure 4, continuous dark line, calculated with formula (17). The horizontal inflection part of the curve corresponds to the deuteron binding energy. The result, obtained by applying *electrostatic* Coulomb's law and *magnetic* Poisson's law with the corresponding fundamental constants, is in accord with the experimental value of the deuteron binding energy -2.225 MeV for -2.13 MeV calculated (4% weaker).

3.2. Conclusion on Nuclear Energy

The binding energy of the deuteron has been calculated by applying the *electrostatic* and *magnetic* laws, knowing that the deuteron contains the electrostatic charge $+e$ of the proton, plus the neutron electrostatic charges with no net charge, assumed to be $+e$ and $-e$ (no need of hypothetical quarks). The magnetic moments of the proton and of the neutron being opposite in the deuteron (figure 3), the *electrostatic attraction* (equation 13) between a proton and a neutron is equilibrated statically by their *magnetic repulsion* (equation 15). On the graph (figure 4), the continuous dark curve shows the calculated nuclear potential of the deuteron where the horizontal inflection point matches with the binding energy of 2H and 4He with less than 5 % error. Although less precise, similar results have been obtained for H and He isotopes and $N = Z$ nuclei [16, 17, 18, 23, 24, 26, 27]. Agreement between theory and experiment proves the *electromagnetic* nature of the nuclear binding energy, contradicting the conventional theory, based on a hypothetical strong force whose fundamental laws and constants remain unknown even after one century of nuclear physics.

4. Conclusion on Nuclear Interaction

Chadwick et Bieler have recognised in 1921: "The present experiments do not seem to throw any light on the nature of the law of variation of the forces at the seat of an electrostatic charge, but merely show that the forces are of very great intensity"[7]. Indeed, the radius of a nucleus being one million times smaller than for an atom, according to Coulomb's potential energy, the nuclear binding energy is, inversely, one million times stronger.

Bieler, assuming that the *magnetic* force is **attractive**, missed the discovery [4]. To solve the not so anomalous scattering problem, it needs only to reuse Rutherford formula where the **repulsive electrostatic** -2 exponent is replaced, at high kinetic energies, by the also **repulsive magnetic** -6 exponent as shown on figure 2.

For the binding energy, the problem is different. Inside the nucleus, at zero kinetic energy, the **attractive electrostatic** force between a not so neutral neutron and a proton equilibrates statically the **repulsive magnetic** force, allowing the calculation of the binding energy of nuclei, never

obtained before with fundamental laws and constants only.

Strong Force, Strong Interaction and QCD are obsolete as Plum pudding model, Aether, Hollow Earth, Phlogiston theory, Flat Earth, Geocentric model. . .

In a few words, the main nuclear physics interactions are:

- Nuclear scattering: dynamic **repulsion** between nucleons, *electrostatic* at low kinetic energy and *magnetic* at high kinetic energy.

- Nuclear binding energy: *electrostatic attraction* between protons and neutrons equilibrated statically by their *magnetic repulsion*.

Acknowledgement

Thanks to persons at Dubna for their interest to my electromagnetic theory of the nuclear energy. The first question was about scattering. I said I don't know. Now I know: the anomalous Rutherford scattering is magnetic. The second question was: "*The strong force doesn't exist?*" and a third one about orbiting nucleons.

References

- [1] H. Geiger and E. Marsden, "On a Diffuse Reflection of the α -Particles", *Proc. Roy. Soc.* 82, 495, 1909.
- [2] E. Rutherford, "The scattering of alpha and beta particles by matter and the structure of the atom", *Phil. Mag.*, 21, 669 vol. A83, pp.492-504, 1911.
- [3] E. Rutherford, J. Chadwick, C. D. Ellis, *Radiations from Radioactive Substances*, Cambridge University Press, 1951, 2010.
- [4] E. S. Bieler, "Large-Angle Scattering of Alpha-Particles by Light Nuclei", *Proc. R. Soc. Lond. A* 105, pp.434-450, 1924.
- [5] H. Paetz, *Nuclear Reactions: An Introduction*, Springer, 2014.
- [6] R. M. Eisberg, C. E. Porter, "Scattering of Alpha Particles", *Rev. Mod. Phys.*, vol. 33, Issue 2, pp.190-230, 1961.
- [7] J. Chadwick and E. S. Bieler, "The Collisions of Alpha Particles with Hydrogen Nuclei", *Phil. Mag.*, 42: 923, 1921.
- [8] G. Farwell, H. E. Wegner, "Elastic scattering of Intermediate Energy Alpha Particles by Heavy Nuclei", *Phys. Rev.*, 95, Nb 5, 1954.
- [9] C. E. Burkhardt, J. J. Leventhal, *Foundations of Quantum Physics*, Springer Science, 2008.
- [10] G. Gamow, C. L. Critchfield, *Theory of Atomic Nucleus and Nuclear Energy-Sources*, Oxford at the Clarendon Press, p. 9, 1949.
- [11] H. Yukawa, "On the Interaction of Elementary Particles", *Proc. Phy. Math. Soc. Japan* 17, pp. 48-57, 1935.
- [12] Coulomb, Second Mémoire sur l'Electricité et le Magnétisme, *Mémoires de l'Académie Royale des Sciences de Paris*, 1785.
- [13] Poisson, Théorie du magnétisme, *Mémoires de l'Académie Royale des Sciences de Paris*, 1824.
- [14] B. Schaeffer, "Anomalous Rutherford Scattering Solved Magnetically", *World Journal of Nuclear Science and Technology*, 2016, 6, 96-102.
- [15] R. Feynman, R. B. Leighton, M. Sands, *The Feynman Lectures on Physics 2*, Pearson/Addison-Wesley, Reading, Mass, 2006.
- [16] B. Schaeffer, "Electric and Magnetic Coulomb Potentials in the Deuteron", *Advanced Electromagnetics*, Vol. 2, No. 1, 2013.
- [17] B. Schaeffer, "Electromagnetic theory of the nuclear interaction. Application to the deuteron 2H ", *Frontiers of Fundamental Physics*, 6-9 July 2010, Paris, France, AIP Conf. Proc. 1446, 123-131, 2012.
- [18] B. Schaeffer, "Electromagnetic Theory of the Binding Energy of the Hydrogen Isotopes", *Journal of Fusion Energy*, 30:377-381, 2011.
- [19] J.C. Maxwell, *A treatise on electricity and magnetism*, Vol.2, Oxford University Press, 1998.
- [20] G.E. Owen, *Introduction to Electromagnetic Theory*, Courier Dover Publications, Oxford, 2003.
- [21] K. Yosida, *Theory of magnetism*, Springer-Verlag, Berlin, 1996.
- [22] A. Bobesko, "Electromagnetic Interaction In Deuteron, Potential energy of electric and magnetic dipoles", January 2015
<http://www.tetrahedralsymmetry.talktalk.net/eid.pdf>.
- [23] B. Schaeffer, "Ab Initio Calculation of 2H and 4He Binding Energies", *Journal of Modern Physics*, 3, pp.1709-1715, 2012.
- [24] B. Schaeffer, "Electromagnetic Nature of Nuclear Energy: Application to H and He Isotopes", *World J. Nucl. Sci. Techn.*, 3, pp.1-8, 2013.
- [25] B. Schaeffer, "Proton-neutron electromagnetic interaction", *ISINN-22*, Dubna, pp.27-30, 2014.
- [26] B. Schaeffer "Binding Energy Curve of $N = Z$ Atomic Nuclei", *25th Int. Nuclear Physics Conf., INPC 2013*, Firenze (Italy), 2-7 June 2013.
- [27] B. Schaeffer, "Pairing Effect on the Binding Energy Curve of $N = Z$ Atomic Nuclei", *World Journal of Nuclear Science and Technology*, 3, pp.19-22, 2013.

Electromagnetic Field Visualization with Jefimenko's Equations

Brandon Gore^{1,2}, Peng Ye^{1,3}, Paul Huray¹

¹College of Engineering and Computing, University of South Carolina, Columbia, SC, USA

²Intel Corporation, Columbia, SC, USA

³Oracle Corporation, Redwood City, CA, USA

*corresponding author, E-mail: Brandon.Gore@intel.com

Abstract

Jefimenko's Equations, [1], also known as the Retarded Solution of Electromagnetic Fields, are one set of the analytical equations that can be used to solve electromagnetic fields. Derived from Maxwell's Equations, Jefimenko's Equations address the time retardation of Electromagnetic fields due to the finite propagation velocity. This paper presents intermediate results of the authors' study of Electromagnetic fields and their propagation using Jefimenko's equations. In addition to the application of Jefimenko's Equation in solving electromagnetic problems, this study also shows a visual view of how Electromagnetic fields near a simple transmission line propagate at 10GHz and 100GHz.

1. Introduction

Derived from Maxwell's Equations, the Retarded Solutions of electromagnetic fields for a point source in time domain, also known as the Jefimenko's Equations, are given below:

$$\vec{E}(\vec{x}, t) = \frac{1}{4\pi\epsilon} \left[\frac{\vec{r}}{R^2} [\rho(\vec{x}', t')]_{ret} + \frac{\vec{r}}{vR} \left[\frac{\partial \rho(\vec{x}', t')}{\partial t} \right]_{ret} - \frac{1}{v^2 R} \left[\frac{\partial \vec{J}(\vec{x}', t')}{\partial t} \right]_{ret} \right], (1)$$

$$\vec{B}(\vec{x}, t) = \frac{\mu}{4\pi} \left[\frac{1}{R^2} [\vec{J}(\vec{x}', t')]_{ret} \times \vec{r} + \frac{1}{vR} \left[\frac{\partial \vec{J}(\vec{x}', t')}{\partial t} \right]_{ret} \times \vec{r} \right], (2)$$

where $[\]_{ret}$ denotes the evaluation at retarded time $t' = t - R/v$, $\rho(\vec{x}', t)$ and $\vec{J}(\vec{x}', t)$ are the charge density current density of the point source.

Taking the Fourier Transform and integrating the contribution of a single point source solution, the following equations describe the Electromagnetic fields of a line source in the frequency domain:

$$\vec{E}(\vec{x}, \omega) = \frac{1}{4\pi\epsilon} \iiint \left[\frac{\vec{r}}{R^2} \left(1 + j \frac{\omega R}{v} \right) \rho(\vec{x}', \omega) - j \frac{\omega}{v^2 R} \vec{J}(\vec{x}', \omega) \right] e^{-j\omega R/v} d^3 x', (3)$$

$$\vec{B}(\vec{x}, \omega) = \frac{\mu}{4\pi} \iiint \left[\frac{1}{R^2} \left(1 + j \frac{\omega R}{v} \right) [\vec{J}(\vec{x}', \omega) e^{-j\omega R/v} \times \vec{r}] \right] d^3 x', (4)$$

If $\omega R/v \ll 1$, Equation (3) and (4) can be simplified to the Quasi-static Solutions:

$$\vec{E}(\vec{x}, \omega) = \frac{1}{4\pi\epsilon} \iiint \left[\vec{r} \frac{1}{R^2} \rho(\vec{x}', \omega) - j \frac{\omega}{Rv^2} \vec{J}(\vec{x}', \omega) \right] e^{-j\omega R/v} d^3 x'$$

$$\vec{B}(\vec{x}, \omega) = \frac{\mu}{4\pi} \iiint \left[\frac{1}{R^2} [\vec{J}(\vec{x}', \omega) \times \vec{r}] \right] e^{-j\omega R/v} d^3 x'$$

For a typical printed circuit board (PCB) environment ($\epsilon_0 = 4\epsilon, \mu_0 = \mu$), two reasonable PCB dimensions are $R = 5mils$ [PCB transmission line height above its reference plane] and $R = 20mils$ [distance between two PCB transmission lines]. High speed signaling requires simulation bandwidth to be beyond 10 GHz therefore the error introduced by quasi-static assumptions should be explored. For $f < 10GHz$ then $\omega R/v \ll 1$. Table 1 gives the values of $\omega R/v$ versus several frequencies. This relates the error introduced for equations (3) and (4) as frequency increase beyond 10 GHz.

Table 1: Values of $\omega R/v$ in typical PCB environment

f (Hz)	$\omega R/v$ with $R = 20$ mils	$\omega R/v$ with $R = 5$ mils
DC	0	0.000
10 MHz	1.0×10^8	0.002
1 GHz	1.0×10^9	0.021
10 GHz	1.0×10^{10}	0.213
20 GHz	2.0×10^{10}	0.426
100 GHz	1.0×10^{11}	2.129

2. Field Visualizations

To demonstrate the Electromagnetic fields and their propagation, a test case is introduced where a thin cylindrical transmission line lies along z-direction 100 mils above a flat reference plane. Here a simplification is made by the transmission line and reference plane as being perfect electrical conductors (PEC), and the surrounding medium is assigned lossless dielectric material with relative permittivity $\epsilon=4.0$. The structure is illustrated in Figure 1.

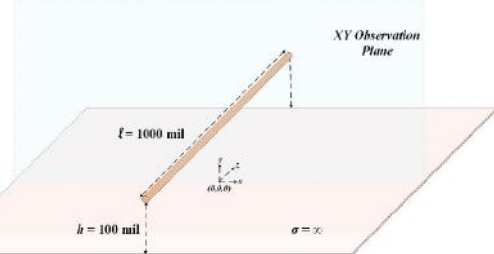


Figure 1: Line source above a PEC reference plane showing the observation plane location [not to scale].

Several source excitations and visualizations of the electromagnetic fields are available, due to the brevity of the summary paper, we only show the electromagnetic fields at 10GHz and 100GHz on an observation plane of XY cross-section where the line source is set to propagating towards the viewer [out of the page], as shown in Figure 2 and Figure 3. In these figures, the background color indicates the magnitude of the field, where peak magnitude is red and minimum magnitude is blue. The red arrows indicate the direction of the \vec{E}_{xy} field (on the x - y plane) and the blue arrows indicate the direction of the \vec{B}_{xy} field. Additionally, the electric field magnitude at $y=100\text{mils}$ is plotted below the graph.

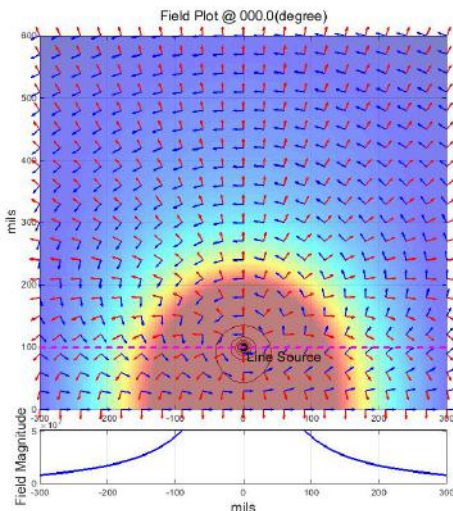


Figure 2: Electromagnetic Fields on XY cross-section plane of a line source at 10GHz.

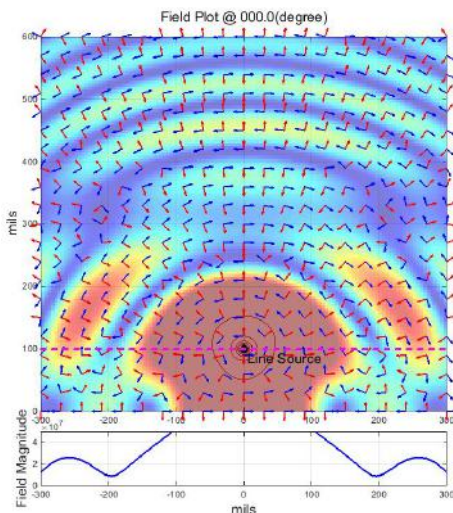


Figure 3: Electromagnetic Fields on XY cross-section plane of a line source at 100GHz.

The field at any observation location is a sum of the field contribution from the line source and the reflected field from the reference plane. The reflective field travels along a different and longer path thus it has a separate field retardation than the original. At higher frequencies where the retardation is more apparent, the total field becomes a complicated interaction between source and reference fields. This is unlike the fields at lower frequencies which fall off smoothly as seen in Figure 2.

The field at higher frequencies shows more irregular ripples. Another aspect for fields at high frequencies is the non-uniform direction. It appears that the field does not obey the Right-Hand Rule for the source current at the instance captured in the plot which is propagating towards [out of the page] with source phase of 0 degrees. This is expected as the field does obey the Right-Hand Rule to the source current that generated them. This effect produced by the time retardation is not sufficiently captured in the plot.

Many additional animations of the electromagnetic fields at different angles are available and will be provided in the full paper or in conference presentation. It will give the audience a direct visual impression of the electromagnetic fields near a line source. A comparison to the result of a well-accepted 3D FEM field solver will also be provided.

3. Conclusions

Electromagnetic fields are the fundamental of any analysis to electromagnetic problems. Through the study of a simple transmission line using Jefimenko's Equation, the electromagnetic fields are visualized and the difference of fields at lower and higher frequencies are demonstrated. The difference in electromagnetic fields indicates different electrical behavior of transmission line at low and high frequency and motivates a refinement of the transmission line's modeled electrical parameters which are based on the electromagnetic fields.

References

- [1] Oleg D. Jefimenko, "Causality Electromagnetic Induction and Gravitation", Electret Scientific Co; 2nd edition, 2000 Peng Dissertation
- [2] Peng Ye, "Applying the Retarded Solution of Fields to PCB Transmission Line RLGC Modeling", Ph.D. dissertation, College of Engineering and Computing, University of South Carolina, Columbia, SC, 2015.
- [3] John David Jackson, "Classical Electrodynamics", Wiley; 3rd edition, 1998.
- [4] Paul G. Huray, "The Foundations of Signal Integrity", Wiley-IEEE Press, 1st edition, 2010.
- [5] Richard P. Feynman, Robert B. Leighton, Matthew Sands, "The Feynman Lectures on Physics, Volume 2", Addison-Wesley, 1977.
- [6] Rosa, E.B. "The Self and Mutual Inductances of Linear Conductors", Bulletin of the Bureau of Standards 4 (2): 301–344

Analyzing the properties of quantized electromagnetic waves in time-varying media

Jeong Ryeol Choi

Department of Radiologic Technology, Daegu Health College, Yeongsong-ro 15, Buk-gu, Daegu 41453,
Republic of Korea
choiardor@hanmail.net

Abstract— The field quantization in time-varying media is fulfilled via complex classical solutions in this research. The characteristics of the quantized electromagnetic fields are analyzed in detail through the results of such quantization scheme.

It may be natural to extend the quantum electrodynamics in free space to more general cases such as the propagation of electromagnetic fields in weakly conductive media, in time-varying (complex) media, and in nonlinear media. In particular, the research associated with quantum electromagnetic fields in time-varying media have attained a considerable interest in quantum optics due to its potential applicability in analyzing and diagnosing electromagnetic properties of nonstationary media such as plasma[1] and in other broad areas of electromagnetic phenomena[2]. Quantized fields in such media are in general described in terms of classical solutions of the system. For instance, the quantization reported in Ref. [3] is carried out using real classical solutions. It is known that quantization of a time-dependent Hamiltonian system can also be performed in terms of complex classical solutions (CCSs) instead of real ones (see, for example, Ref. [6] and some of references therein). We will use CCSs in order to quantize the electromagnetic fields in time-varying media in this research.

Plasma media which reveal many unique features in their various situations are typical examples of time-varying media[1]. Theoretical research of electromagnetic wave propagation in such media is known as a very difficult task and still only its preliminary analysis is possible[7]. Nonstationary and inhomogeneous characteristics of the plasma medium may disturb electromagnetic signal and it is important to analyze this disturbance in order to understand field propagation in such media. Among wide application of wave propagation in plasma technology, the diagnosis of the change of plasma state in tokamak, where nuclear fusion takes place, in a nuclear fusion generation is important[1].

The purpose of this paper is to analyze the properties of quantizes electromagnetic waves in time-varying media. We will use the Lewis-Riesenfeld invariant method[5] in order to quantize the system in terms of CCSs. Invariant operator method enables us to derive exact quantum solutions for time-dependent Hamiltonian systems so far as the complete solutions of their classical equation of motion are known or derivable. We will find generalized quantization method that is not only very interesting task but also important for advancement of theoretical study of electromagnetics[8]. It is believed that the most generalized quantization scheme could be developed in terms of CCSs since a real number is just a particular case of a complex number. We will consider the Fock state which is the most fundamental quantum state in this research. Quantum features of electromagnetic fields beyond in the Fock state, such as in the coherent state, in the squeezed state, and in the thermal state, may also be investigated.

ACKNOWLEDGMENT

This research was supported by the Basic Science Research Program of the year 2015 through the National Research Foundation of Korea (NRF) funded by the Ministry of Education (Grant No.: NRF-2013R1A1A2062907)

REFERENCES

1. Kalluri, D. K., *Electromagnetics of Time Varying Complex Media*, CRC Press, Boca Raton, 2010. 2nd Ed.
2. Malkin, I. A., V. I. Man'ko, and D. A. Trifonov, "Coherent states and transition probabilities in a time-dependent electromagnetic field," *Phys. Rev. D*, Vol. 2, No. 8, 1371-1385, 1970.

3. Choi, J. R., "Nonclassical properties of superpositions of coherent and squeezed states for electromagnetic fields in time-varying media," *Quantum Optics and Laser Experiments*, InTech, Rijeka, 2012, Chap. 2, pp, 25-48.
4. Choi, J. R., "Interpreting quantum states of electromagnetic field in time-dependent linear media," *Phys. Rev. A*, Vol, 82, No. 5, 055803, 2010.
5. Lewis, H. R. Jr. and W. B. Riesenfeld, "An exact quantum theory of the time-dependent harmonic oscillator and of a charged particle in a time-dependent electromagnetic field," *J. Math. Phys*, Vol. 10, No. 8, 1458-1473, 1969.
6. Angelow, A. K. and D. A. Trifonov, "Dynamical invariants and Robertson-Schrödinger correlated states of electromagnetic field in nonstationary linear media," arXiv:1009.5593v1 [quant-ph] 2010.
7. Yu, P., Q. Liu, and L. Yang, "Analysis of frequency characteristics for ID electromagnetic wave in time-varying plasma," in *Cross Strait Quad-Regional Radio Science and Wireless Technology Conference*, Harbin, China, July, 2011, 100-103.
8. Choi, J. R., K. H. Yeon, I. H. Nahm, and S. S. Kim, "Do the generalized Fock-state wave functions have some relations with classical initial condition?," *Pramana-J. Phys*, Vol. 73, No. 5, 821-828, 2009.

Electromagnetic and material contributions to stress, energy, and momentum in metamaterials

Brandon A. Kemp¹ and Cheyenne J. Sheppard²

¹College of Engineering, Arkansas State University, Jonesboro, AR, USA

²College of Sciences and Mathematics, Arkansas State University, Jonesboro, AR, USA

*corresponding author, E-mail: bkemp@astate.edu

Abstract

We demonstrate modeling of the field-kinetic and material response subsystem for various media and extend the models to dispersive negative index metamaterials. It is shown that neither the Minkowski or Abraham models are universally correct, as demonstrated to describe metamaterials under both the field-kinetic and wave SEM models for various applications such as negative refraction, perfect lensing, and invisibility cloaking.

1. Introduction

Electromagnetic momentum has been debated since the early 20th century. The so-called Abraham-Minkowski debate is attributed to two independent stress-energy-momentum (SEM) tensors postulated for mathematically modeling electrodynamics of media [1]. Significant attention has been given to the momentum density expressions associated with the rival SEM tensors. The momentum density expressions were defined as being either $\bar{D} \times \bar{B}$ from the Minkowski tensor or $\epsilon_0 \mu_0 \bar{E} \times \bar{H}$ from the Abraham tensor, where \bar{D} and \bar{B} represent the electric displacement and magnetic induction fields, \bar{E} and \bar{H} are the electric and magnetic fields, and ϵ_0 and μ_0 are the permittivity and permeability of vacuum, respectively. Barnett presented a resolution to the photon momentum controversy in 2010, which related the Abraham density to the kinetic momentum of light and the Minkowski density to the canonical momentum of light [2]. However, the original debate was in regard to the relativistic invariance of the 4×4 SEM tensors; Barnett's partial resolution only identified the kinetic and canonical momentum densities.

Three other well-known SEM tensors have been proposed over the past century, and have found significant use in scientific and engineering modeling applications [3]. First, the Einstein-Laub tensor, like the Abraham and Minkowski tensors, utilizes the Minkowski fields, and it shares the Abraham momentum density. Second, the Amperian or "Lorentz" tensor derives from the Amperian formulation or EB -representation and utilizes the Amperian fields. Third, the Chu formulation or EH -representation was developed in the 1960's, and the Chu SEM tensor utilizes the Chu fields. It is important to note that the latter two formulations uniquely define the fields within matter, while the Abraham, Minkowski, and Einstein-Lab tensors

all use the common Minkowski fields.

In this correspondence, we demonstrate modeling of the field-kinetic and material response subsystem for dielectric media and extend the models to negative index metamaterials, which necessarily include dispersion and loss. In this model, we consider the total SEM tensor as a conservation of energy and momentum such that

$$\mathfrak{T}_{total} = \mathfrak{T}_{mech} + \mathfrak{T}_{can} = \mathfrak{T}_{mech} + \mathfrak{T}_{mat} + \mathfrak{T}_{F_k}, \quad (1)$$

where \mathfrak{T}_{mech} represents an external mechanical input of work, \mathfrak{T}_{mat} is the material response subsystem, and \mathfrak{T}_{F_k} is the field-kinetic subsystem. We show that the field-kinetic subsystem as given by the Chu formulation represents the energy and momentum contained within the fields [4], and the sum of the field-kinetic and material response subsystems represent the wave or canonical subsystem [5], which reduces to the Minkowski subsystem only under negligible dispersion [6]. Our conclusion is that neither the Minkowski or Abraham models are universally correct. We demonstrate our view applied to the physics of negative index materials under both the field-kinetic and canonical SEM models for applications such as negative refraction, which is fundamental to perfect lensing and invisibility cloaking. First, we review the mathematical framework of SEM tensors, relativistic invariance requirements, and applicability to electrodynamics in Section 2. Second, the field-kinetic and canonical SEM tensors are determined for a broad class of causal, isotropic media in Section 3. Then, we discuss the implications of negative refraction in Section 4. Conclusions are presented in Section 5.

2. SEM Tensors

Energy and momentum continuity for a given system can be divided into subsystems and mathematically represented as [1, 3]

$$\varphi_j(\bar{r}, t) = -\nabla \cdot \bar{S}_j(\bar{r}, t) - \frac{\partial W_j(\bar{r}, t)}{\partial t} \quad (2a)$$

$$\bar{f}_j(\bar{r}, t) = -\nabla \cdot \bar{T}_j(\bar{r}, t) - \frac{\partial \bar{G}_j(\bar{r}, t)}{\partial t} \quad (2b)$$

where \bar{f}_j is the force density, φ_j is the power density, \bar{T}_j is the momentum flux or stress tensor, \bar{S}_j is the power flux, \bar{G}_j is the momentum density, and W_j is the energy density.

Each j may represent any subsystem. Closing the overall system, such that $\sum_j \vec{f}_j = 0$ and $\sum_j \varphi_j = 0$ indicates momentum and energy conservation, respectively.

The choice of which momentum density, stress tensor, and force density are applied in any given problem are inherently tied to the formulation of electrodynamics being considered and the interpretation rendered. It is impossible to sidestep the momentum controversy by employing a Lorentz force density since, as the theoretical construction implies, each force density is tied to a momentum density and stress tensor through a formulation of Maxwell's equations [3]. One may rearrange the continuity equations, but such mathematical exercises should not be taken as reason for interpretation [4, 7]. For reference, Table 1 lists the leading electromagnetic momentum densities and stress tensors from the literature. The corresponding force densities for the stationary [1] and fully relativistic formulations [3] can also be found in the literature.

Table 1: Leading electromagnetic momentum densities and stress tensors.

	\vec{G}	\vec{T}
Abr.	$\epsilon_0 \mu_0 \vec{\mathcal{E}} \times \vec{\mathcal{H}}$	$\frac{1}{2} (\vec{\mathcal{D}} \cdot \vec{\mathcal{E}} + \vec{\mathcal{B}} \cdot \vec{\mathcal{H}}) \vec{I} - \vec{\mathcal{D}}\vec{\mathcal{E}} - \vec{\mathcal{B}}\vec{\mathcal{H}}$
Min.	$\vec{\mathcal{D}} \times \vec{\mathcal{B}}$	$\frac{1}{2} (\vec{\mathcal{D}} \cdot \vec{\mathcal{E}} + \vec{\mathcal{B}} \cdot \vec{\mathcal{H}}) \vec{I} - \vec{\mathcal{D}}\vec{\mathcal{E}} - \vec{\mathcal{B}}\vec{\mathcal{H}}$
Amp.	$\epsilon_0 \vec{\mathcal{E}} \times \vec{\mathcal{B}}$	$\frac{1}{2} (\epsilon_0 \vec{\mathcal{E}} \cdot \vec{\mathcal{E}} + \mu_0^{-1} \vec{\mathcal{B}} \cdot \vec{\mathcal{B}}) \vec{I} - \epsilon_0 \vec{\mathcal{E}}\vec{\mathcal{E}} - \mu_0^{-1} \vec{\mathcal{B}}\vec{\mathcal{B}}$
E-L	$\epsilon_0 \mu_0 \vec{\mathcal{E}} \times \vec{\mathcal{H}}$	$\frac{1}{2} (\epsilon_0 \vec{\mathcal{E}} \cdot \vec{\mathcal{E}} + \mu_0 \vec{\mathcal{H}} \cdot \vec{\mathcal{H}}) \vec{I} - \vec{\mathcal{D}}\vec{\mathcal{E}} - \vec{\mathcal{B}}\vec{\mathcal{H}}$
Chu	$\epsilon_0 \mu_0 \vec{\mathcal{E}} \times \vec{\mathcal{H}}$	$\frac{1}{2} (\epsilon_0 \vec{\mathcal{E}} \cdot \vec{\mathcal{E}} + \mu_0 \vec{\mathcal{H}} \cdot \vec{\mathcal{H}}) \vec{I} - \epsilon_0 \vec{\mathcal{E}}\vec{\mathcal{E}} - \mu_0 \vec{\mathcal{H}}\vec{\mathcal{H}}$

As one considers the amount of work being done on the system, one also sees that the momentum and stress are explicitly tied to the energy density and flux. This can be illustrated using the work-energy relation or the Relativistic Principle of Virtual Power (RPVP) [4, 5]. In Section 2.2 it will be demonstrated, instead, using a straightforward application of the Lorentz transformation. For now, we list for reference in Table 2 the leading electromagnetic energy densities and power flows corresponding to the momentum quantities in Table 1.

Table 2: Leading electromagnetic energy densities and power flows.

	\vec{S}	W
Abr.	$\vec{\mathcal{E}} \times \vec{\mathcal{H}}$	$\frac{1}{2} (\vec{\mathcal{D}} \cdot \vec{\mathcal{E}} + \vec{\mathcal{B}} \cdot \vec{\mathcal{H}})$
Min.	$\vec{\mathcal{E}} \times \vec{\mathcal{H}}$	$\frac{1}{2} (\vec{\mathcal{D}} \cdot \vec{\mathcal{E}} + \vec{\mathcal{B}} \cdot \vec{\mathcal{H}})$
Amp.	$\mu_0^{-1} \vec{\mathcal{E}} \times \vec{\mathcal{B}}$	$\frac{1}{2} (\epsilon_0 \vec{\mathcal{E}} \cdot \vec{\mathcal{E}} + \mu_0^{-1} \vec{\mathcal{B}} \cdot \vec{\mathcal{B}})$
E-L	$\vec{\mathcal{E}} \times \vec{\mathcal{H}}$	$\frac{1}{2} (\epsilon_0 \vec{\mathcal{E}} \cdot \vec{\mathcal{E}} + \mu_0 \vec{\mathcal{H}} \cdot \vec{\mathcal{H}})$
Chu	$\vec{\mathcal{E}} \times \vec{\mathcal{H}}$	$\frac{1}{2} (\epsilon_0 \vec{\mathcal{E}} \cdot \vec{\mathcal{E}} + \mu_0 \vec{\mathcal{H}} \cdot \vec{\mathcal{H}})$

The continuity equations can be rewritten in four-dimensional coordinates (\vec{r}, ict) so that

$$\vec{f}_j = \square \cdot [\vec{T}_j, -ic\vec{G}_j] \quad (3a)$$

$$-i\frac{\varphi_j}{c} = \square \cdot \left[-i\frac{\vec{S}_j}{c}, W_j \right] \quad (3b)$$

so that $\square \cdot \vec{\mathfrak{F}}_j = \vec{\mathfrak{F}}_j$, where $\square = [\nabla, \partial/\partial(ict)]$, $\vec{\mathfrak{F}}_j = [-\vec{f}_j, -i\varphi_j/c]$, and the SEM tensor is

$$\vec{\mathfrak{F}}_j = \begin{bmatrix} \vec{T}_j & -ic\vec{G}_j \\ -i\vec{S}_j & W_j \end{bmatrix}. \quad (4)$$

Here, we have defined $\vec{T}_j \equiv -\vec{T}_j$.

2.1. Equivalence of total force

The electromagnetic force density \vec{f} and power density φ inside an object depend upon formulation applied. In general, the equations take the form of Eqs. (2), where the force densities are defined by the corresponding momentum density \vec{G} and stress tensor \vec{T} given in Table 1 and the power densities φ are defined by the corresponding energy density W and power flux \vec{S} given in Table 2. The total electromagnetic force $\vec{F}(t)$ on an object can be computed by integrating an electromagnetic force density $\vec{f}(\vec{r}, t)$ over the volume V of the object. An exact, mathematically equivalent approach is to apply the divergence theorem to reduce the contribution of an electromagnetic stress tensor \vec{T} to an integral over the surface A with outward pointing area element $d\vec{A}$ enclosing the volume V so that the total force is calculated equivalently by

$$\vec{F}(t) = - \int_V dV \frac{\partial}{\partial t} \vec{G}(\vec{r}, t) - \oint_A d\vec{A} \cdot \vec{T}(\vec{r}, t). \quad (5)$$

In some cases, the total force may be equivalent between formulations although the force densities differ. The same argument may be applied to the transfer of energy since the energy continuity equation takes the same form.

2.1.1. Equivalence of Total Force

Fig. 1 (a) depicts an object surrounded by vacuum illustrating which total force equations are equivalent at any point in time. Integrating the electromagnetic force density $\vec{f}(\vec{r}, t)$ over the volume enclosing the object as depicted by the dashed line yields the total force and is given by Eq. (5), where the tensor reduces to the unambiguous vacuum Maxwell stress tensor since the surface of integration is outside the material. However, the momentum density \vec{G} still depends on the electromagnetic formulation applied. Therefore, any formulations which share a common momentum density will produce identical results for the total force on an object at all points in time. The implication is that the Chu, Einstein-Laub, and Abraham force densities are equivalent in terms of total force and the Amperian formulation differs only in the modeling of magnetic media. The Minkowski SEM tensor will yield a different time varying force for dielectric and magnetic media.

A second example is an object submerged inside another medium such as a dielectric fluid as shown in Fig. 1 (b). The total force remains the same for two formulations if their momentum densities are identical. However, we must clarify how the force is computed. The electromagnetic force is determined by volume integration of the

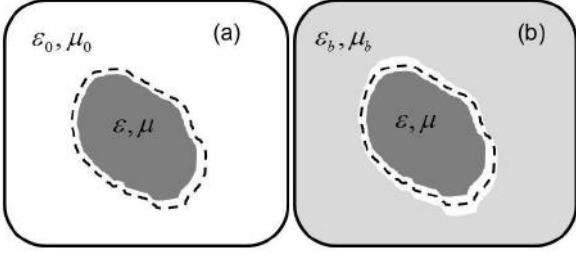


Figure 1: Illustration of total force calculation within a volume V within the dashed line. The total force on (a) an object in vacuum is computed by volume integration of a force density within a region which completely encloses the material object and (b) an object embedded is computed in a similar way by considering a thin vacuum region between the two materials.

force density $\bar{f}(\bar{r}, t)$, and there will generally be both volume and surface forces at the boundary, the latter due to material discontinuities at the boundaries [8, 9]. Any ambiguity as to which of the materials to which the surface forces should be assigned is removed by mathematically introducing a thin layer of vacuum separating the two materials. The volume integration is then applied to the submerged material. The tensor reduces to the vacuum stress tensor since the surface of the integration is in the vacuum region, and the forces applied to the two media are unambiguous. Taking the limit of the vacuum region to zero yields the unperturbed field problem with the surface forces applied correctly to the corresponding media [10]. In general, forces will be distributed to both the submerged object and the submerging fluid. The conclusion is unchanged. The total calculated time-domain force on an object is the same with any electromagnetic subsystem that share a common momentum density [3]. We will find that another conclusion from this thought exercise is important; once we identify the correct subsystem separation of field and matter it is necessary to assign a force on the embedded object and the embedding material [10, 11, 12].

When materials are excited by monochromatic waves, the time-average force is generally the observable quantity of interest. The total average force on a material object due to time-harmonic fields is

$$\langle \bar{F} \rangle = - \oint_A d\bar{A} \cdot \langle \bar{T} \rangle, \quad (6)$$

where the momentum density does not contribute to the time-average force of time-harmonic fields [3].

The total average force is the integration of the average force density over a volume that includes the entire object. All such computations will yield identical results regardless of the force density applied. This statement is a result of the condition that all electromagnetic SEM tensors must be consistent with Maxwell's equations [1]. To illustrate this fact, one must only consider again the problem in Fig. 1 under time-averaged conditions. Since the momentum den-

sity averages to zero, both computations in Fig 1 (a) and (b) reduce to the divergence of the vacuum stress tensor and the force is unambiguously independent of the formulation applied [3, 5]. As a result, it is generally not possible to determine the time-domain force or energy equations from only the time-average quantities [13].

2.2. Relativistic invariance

The total force on an object is often measured in experiment. However, this quantity is insufficient for determining the correct interpretations of electrodynamics as was demonstrated in the previous section. Moreover, the force densities differ between the various formulations [14], but it has been shown that many experimental observations can be modeled in the stationary limit (i.e. material velocity goes to zero $v \rightarrow 0$) by closing the system using a variety of subsystems [15]. In fact, the problem with the stationary approximation is the work-energy relation is always satisfied in a trivial manner [4]; $\bar{F} \cdot \bar{v} = \bar{\Phi} = 0$ since the velocity is zero in the limit. To determine which tensors are truly valid in a physical sense, we must look at relativistic invariance.

It is a fundamental tenet of modern physics that tensors which are not relativistic invariant cannot be energy momentum tensors. As an example, consider a region of space occupied by media described mathematically by a local mass density and a velocity field. The local momentum vector may vary with position and time regardless of how the coordinate system is assigned. Our inability to measure relativistic effects in any experiment may only be due to our limited measurement capabilities. This limitation does not prevent the fundamental laws of physics from holding [4].

For example, consider two frames of reference \mathcal{S} and \mathcal{S}' , whereas \mathcal{S}' moves with constant velocity $\bar{v} = \hat{x}v$ with respect to \mathcal{S} . The SEM tensor in \mathcal{S} is

$$\bar{\mathfrak{T}}_j = \begin{bmatrix} \mathcal{T}_{xx} & \mathcal{T}_{xy} & \mathcal{T}_{xz} & icG_x \\ \mathcal{T}_{yx} & \mathcal{T}_{yy} & \mathcal{T}_{yz} & icG_y \\ \mathcal{T}_{zx} & \mathcal{T}_{zy} & \mathcal{T}_{zz} & icG_z \\ iS_x/c & iS_y/c & iS_z/c & W \end{bmatrix}. \quad (7)$$

We want to know if the tensor is invariant under certain electrodynamic hypotheses. As a simple demonstration, we consider the Lorentz transform of the component

$$\mathcal{T}'_{xx} = \gamma^2 [\mathcal{T}_{xx} + \beta (S_x/c + cG_x) - \beta^2 W], \quad (8)$$

where $\beta = v/c$ and $\gamma = (1 - \beta^2)^{-1/2}$. To consider the five different hypotheses (i.e. Abraham, Minkowski, Amperian, Einstein-Laub, and Chu), we must consider the Lorentz transformation laws for the field variables within each field framework.

The Lorentz transformation laws for the Minkowski

field variables \bar{E} , \bar{H} , \bar{D} , and \bar{B} are [16]

$$\bar{\mathcal{E}}' = \bar{\mathcal{E}}_{\parallel} + \gamma (\bar{\mathcal{E}}_{\perp} + \bar{v} \times \bar{\mathcal{B}}), \quad (9a)$$

$$\bar{\mathcal{H}}' = \bar{\mathcal{H}}_{\parallel} + \gamma (\bar{\mathcal{H}}_{\perp} - \bar{v} \times \bar{\mathcal{D}}), \quad (9b)$$

$$\bar{\mathcal{D}}' = \bar{\mathcal{D}}_{\parallel} + \gamma \left(\bar{\mathcal{D}}_{\perp} + \frac{\bar{v} \times \bar{\mathcal{H}}}{c^2} \right), \quad (9c)$$

$$\bar{\mathcal{B}}' = \bar{\mathcal{B}}_{\parallel} + \gamma \left(\bar{\mathcal{B}}_{\perp} - \frac{\bar{v} \times \bar{\mathcal{E}}}{c^2} \right), \quad (9d)$$

where the subscripts \parallel and \perp denote parallel and perpendicular components to the velocity \bar{v} . These transformation laws are applied for the Abraham, Minkowski, and Einstein-Laub formulations, which utilize the Minkowski fields. The Lorentz transformation laws for the Chu field variables $\bar{\mathcal{E}}$, $\bar{\mathcal{H}}$, $\bar{\mathcal{P}}$, and $\bar{\mathcal{M}}$ are [16]

$$\bar{\mathcal{E}}' = \bar{\mathcal{E}}_{\parallel} + \gamma (\bar{\mathcal{E}}_{\perp} + \bar{v} \times \mu_0 \bar{\mathcal{H}}), \quad (10a)$$

$$\bar{\mathcal{H}}' = \bar{\mathcal{H}}_{\parallel} + \gamma (\bar{\mathcal{H}}_{\perp} - \bar{v} \times \epsilon_0 \bar{\mathcal{E}}), \quad (10b)$$

$$\bar{\mathcal{P}}' = \bar{\mathcal{P}}_{\parallel} + \gamma \left(\bar{\mathcal{P}}_{\perp} - \frac{\bar{v} \times (\bar{\mathcal{P}} \times \bar{v})}{c^2} \right), \quad (10c)$$

$$\bar{\mathcal{M}}' = \bar{\mathcal{M}}_{\parallel} + \gamma \left(\bar{\mathcal{M}}_{\perp} - \frac{\bar{v} \times (\bar{\mathcal{M}} \times \bar{v})}{c^2} \right), \quad (10d)$$

where it is important to note that the Chu field values $\bar{\mathcal{E}}$ and $\bar{\mathcal{H}}$ differ from the Minkowski ones. We will make clear which field values are being applied within a given context. The Lorentz transformation laws for the Amperian field variables $\bar{\mathcal{E}}$, $\bar{\mathcal{B}}$, $\bar{\mathcal{P}}$, and $\bar{\mathcal{M}}$ are [16]

$$\bar{\mathcal{E}}' = \bar{\mathcal{E}}_{\parallel} + \gamma (\bar{\mathcal{E}}_{\perp} + \bar{v} \times \bar{\mathcal{B}}), \quad (11a)$$

$$\bar{\mathcal{B}}' = \bar{\mathcal{B}}_{\parallel} + \gamma \left(\bar{\mathcal{B}}_{\perp} - \frac{\bar{v} \times \bar{\mathcal{E}}}{c^2} \right), \quad (11b)$$

$$\bar{\mathcal{P}}' = \bar{\mathcal{P}}_{\parallel} + \gamma \left(\bar{\mathcal{P}}_{\perp} - \frac{\bar{v} \times (\bar{\mathcal{P}} \times \bar{v})}{c^2} \right), \quad (11c)$$

$$\bar{\mathcal{M}}' = \bar{\mathcal{M}}_{\parallel} + \gamma \left(\bar{\mathcal{M}}_{\perp} - \frac{\bar{v} \times (\bar{\mathcal{M}} \times \bar{v})}{c^2} \right), \quad (11d)$$

Utilizing Eq. (8), we substitute the corresponding component values for \bar{S} , W , \bar{T} , and \bar{G} given in Tables 1 and 2 along with the field transformations for reference frame S to S' using Eq. (9) for the Abraham, Minkowski, and Einstein-Laub tensors, Eq. (10) for the Chu tensor, and Eq. (11) for the Amperian tensor. After some algebraic manipulation, the results are summarized in Table 3. It can be seen that only the Minkowski, Chu, and Amperian SEM tensors retain their form after transformation. Such mathematical exercises can be carried-out on the remaining tensor components with similar results. The conclusion is that the Abraham and Einstein-Laub tensors are not valid SEM tensors [4].

3. Energy and momentum in media

3.1. Field-kinetic subsystem

The Minkowski, Amperian, and Chu SEM tensors differ in many regards, but one significant difference is the momen-

Table 3: Transformed stress tensors.

	$T'_{xx} = -T'_{xx}$
Abr.	$\mathcal{D}'_x \mathcal{E}'_x + \mathcal{B}'_x \mathcal{H}'_x - \frac{1}{2} \delta_{xx} (\bar{\mathcal{D}}' \cdot \bar{\mathcal{E}}' + \bar{\mathcal{B}}' \cdot \bar{\mathcal{H}}') + \gamma^2 \beta [\epsilon_0 \mu_0 (\bar{\mathcal{E}}' \times \bar{\mathcal{H}}')_x - (\bar{\mathcal{D}}' \times \bar{\mathcal{B}}')_x]$
Min.	$\mathcal{D}'_x \mathcal{E}'_x + \mathcal{B}'_x \mathcal{H}'_x - \frac{1}{2} \delta_{xx} (\bar{\mathcal{D}}' \cdot \bar{\mathcal{E}}' + \bar{\mathcal{B}}' \cdot \bar{\mathcal{H}}')$
Amp.	$\epsilon_0 \mathcal{E}'_x \mathcal{E}'_x + \mu_0^{-1} \mathcal{B}'_x \mathcal{B}'_x - \frac{1}{2} \delta_{xx} (\epsilon_0 \bar{\mathcal{E}}' \cdot \bar{\mathcal{E}}' + \mu_0^{-1} \bar{\mathcal{B}}' \cdot \bar{\mathcal{B}}')$
E-L	$\gamma^2 [\mathcal{E}'_x \mathcal{D}'_x + \mathcal{H}'_x \mathcal{B}'_x + 2\gamma^2 \beta c^{-1} \{ (\bar{\mathcal{E}}' \times \bar{\mathcal{H}}')_x + c^2 \beta^2 (\bar{\mathcal{D}}' \times \bar{\mathcal{B}}')_x + c\beta (\mathcal{H}'_y \mathcal{B}'_y + \mathcal{H}'_z \mathcal{B}'_z + \mathcal{E}'_y \mathcal{D}'_y + \mathcal{E}'_z \mathcal{D}'_z) - \frac{1}{2} (1 + \beta^2) \{ \epsilon_0 \mathcal{E}'_x \mathcal{E}'_x + \mu_0 \mathcal{H}'_x \mathcal{H}'_x + \gamma^2 [(\epsilon_0 \mathcal{E}'_y \mathcal{E}'_y + \epsilon_0 \mathcal{E}'_z \mathcal{E}'_z + \mu_0 \mathcal{H}'_y \mathcal{H}'_y + \mu_0 \mathcal{H}'_z \mathcal{H}'_z) + c^2 \beta^2 (\epsilon_0 \mathcal{B}'_y \mathcal{B}'_y + \epsilon_0 \mathcal{B}'_z \mathcal{B}'_z + \mu_0 \mathcal{D}'_y \mathcal{D}'_y + \mu_0 \mathcal{D}'_z \mathcal{D}'_z) + 2c\beta \{ (\epsilon_0 \bar{\mathcal{E}}' \times \bar{\mathcal{B}}')_x + (\bar{\mathcal{D}}' \times \mu_0 \bar{\mathcal{H}}')_x \}] \}$
Chu	$\epsilon_0 \mathcal{E}'_x \mathcal{E}'_x + \mu_0 \mathcal{H}'_x \mathcal{H}'_x - \frac{1}{2} \delta_{xx} (\epsilon_0 \bar{\mathcal{E}}' \cdot \bar{\mathcal{E}}' + \mu_0 \bar{\mathcal{H}}' \cdot \bar{\mathcal{H}}')$

tum density \bar{G} . While each of the three SEM tensors are relativistically invariant, it is desirable to determine if one of the three is the kinetic momentum of light, which is the momentum representing only field contributions without contributions from the mass of the material. In 1953, Balazs developed a thought experiment that allows for the determination of the kinetic momentum by studying the center-of-mass displacement of a material slab as an electromagnetic pulse passes [17], and number of researchers have presented versions of this thought experiment [2, 3, 11, 18, 19].

We consider a slab of dispersive, impedance-matched material surrounded by vacuum. The slab is characterized by a group velocity $v_g = \partial\omega/\partial k$ and wave impedance is $\eta = \sqrt{\mu/\epsilon} = \sqrt{\mu_0/\epsilon_0}$. An electromagnetic wave pulse has an initial free space momentum \mathfrak{E}_i/c . The slab of thickness d delays the pulse with respect to the free space path by the distance $L = (n_g - 1)d$ since the group velocity in the material is $v_g = c/n_g$, where n_g is the group velocity index of refraction. The required kinetic momentum of the material while the pulse overlaps spatially with the slab is

$$p_m = \frac{\mathfrak{E}_i}{c} \left(1 - \frac{1}{n_g} \right), \quad (12)$$

which is necessary in order to maintain uniform motion of the center-of-mass energy. The momentum of the slab is the difference between the momentum of the incident pulse and the material momentum given by Eq. (12) as required by momentum conservation. Therefore, the electromagnetic momentum of the pulse is the field-kinetic momentum

$$p_{F_k} = \frac{1}{n_g} \frac{\mathfrak{E}_i}{c}. \quad (13)$$

This momentum corresponds to the Chu momentum, and we, therefore, take the Chu SEM tensor as the field-kinetic formulation [4]. Further discussion of this relationship is given in Section 4 of this correspondence.

The Maxwell-Chu equations [3, 16, 20]

$$\nabla \times \bar{\mathcal{H}} - \epsilon_0 \frac{\partial \bar{\mathcal{E}}}{\partial t} = \bar{\mathcal{J}}_e \quad (14a)$$

$$\nabla \times \bar{\mathcal{E}} + \mu_0 \frac{\partial \bar{\mathcal{H}}}{\partial t} = -\bar{\mathcal{J}}_h \quad (14b)$$

$$\epsilon_0 \nabla \cdot \bar{\mathcal{E}} = \rho_e \quad (14c)$$

$$\mu_0 \nabla \cdot \bar{\mathcal{H}} = \rho_h \quad (14d)$$

separate the electric and magnetic fields from the material response. The Chu formulation models the material responses by effective electric current density $\bar{\mathcal{J}}_e$, magnetic current density $\bar{\mathcal{J}}_h$, electric charge density ρ_e , and magnetic charge density ρ_h . These quantities for moving media with local velocity field \bar{v} are defined as [3, 16, 20]

$$\bar{\mathcal{J}}_e \equiv \frac{\partial \bar{\mathcal{P}}}{\partial t} + \nabla \times [\bar{\mathcal{P}} \times \bar{v}] + \bar{\mathcal{J}} \quad (15a)$$

$$\bar{\mathcal{J}}_h \equiv \mu_0 \frac{\partial \bar{\mathcal{M}}}{\partial t} + \mu_0 \nabla \times [\bar{\mathcal{M}} \times \bar{v}] \quad (15b)$$

$$\rho_e \equiv -\nabla \cdot \bar{\mathcal{P}} + \rho \quad (15c)$$

$$\rho_h \equiv -\mu_0 \nabla \cdot \bar{\mathcal{M}}, \quad (15d)$$

where $\bar{\mathcal{M}}$ is the magnetization, $\bar{\mathcal{P}}$ is the polarization, $\bar{\mathcal{J}}$ is the free current density, and ρ is the free charge density of the given medium. The energy and momentum continuity equations for the field-kinetic subsystem are completed by the interaction terms [3, 16, 20]

$$\bar{f}_{F_k} = \rho_e \bar{\mathcal{E}} + \rho_h \bar{\mathcal{H}} + \bar{\mathcal{J}}_e \times \mu_0 \bar{\mathcal{H}} - \bar{\mathcal{J}}_h \times \epsilon_0 \bar{\mathcal{E}} \quad (16a)$$

$$\varphi_{F_k} = \bar{\mathcal{J}}_e \cdot \bar{\mathcal{E}} + \bar{\mathcal{J}}_h \cdot \bar{\mathcal{H}} \quad (16b)$$

Next, we will derive the material response to the field-kinetic subsystem for dielectrics and isotropic metamaterials with electric and magnetic response.

3.2. Material response in dielectrics

Consider a harmonic oscillator describing the motion of a bound charge under excitation of a time-harmonic field \bar{E} . The motion can be used to determine the stationary dielectric response of the charge q given the damping factor γ and the electric resonant frequency ω_{e0} . The equation of motion for $\bar{r} = \hat{x}x + \hat{y}y + \hat{z}z$ is [20]

$$m \left(\frac{\partial^2}{\partial t^2} + \gamma_e \frac{\partial}{\partial t} + \omega_{e0}^2 \right) \bar{r} = q \bar{\mathcal{E}}. \quad (17)$$

If there are N such harmonic oscillators per volume of dielectric, the material subsystem is given by [21, 22, 23]

$$\bar{S}_{mat} = 0 \quad (18a)$$

$$\bar{W}_{mat} = N \left\{ \frac{1}{2} m \frac{\partial \bar{r}}{\partial t} \cdot \frac{\partial \bar{r}}{\partial t} + \frac{1}{2} \omega_{e0}^2 m \bar{r} \cdot \bar{r} \right\} \quad (18b)$$

$$\varphi_{mat} = -\varphi_{F_k} + N \left\{ \gamma_e \frac{\partial \bar{r}}{\partial t} \cdot \frac{\partial \bar{r}}{\partial t} \right\}. \quad (18c)$$

The energy terms consist of a kinetic energy term $\frac{1}{2} m \frac{\partial \bar{r}}{\partial t} \cdot \frac{\partial \bar{r}}{\partial t}$ and a potential energy term $\frac{1}{2} \omega_{e0}^2 m \bar{r} \cdot \bar{r}$ for each of N

charges in motion per-unit-volume. The momentum continuity equation for the material is [23]

$$\bar{T}_{mat} = N \left\{ \left[q \bar{r} \cdot \bar{E} + \frac{1}{2} m \frac{\partial \bar{r}}{\partial t} \cdot \frac{\partial \bar{r}}{\partial t} - \frac{1}{2} \omega_{e0}^2 m \bar{r} \cdot \bar{r} \right] \bar{I} - q \bar{r} \bar{E} \right\} \quad (19a)$$

$$\bar{G}_{mat} = N \left\{ q \bar{r} \times \mu_0 \bar{H} - m \frac{\partial \bar{r}}{\partial t} \right\} \quad (19b)$$

$$\bar{f}_{mat} = -\bar{f}_{F_k} + N \left\{ -\gamma_e m \frac{\partial \bar{r}}{\partial t} \right\}. \quad (19c)$$

Here, we recognize the terms proportional to $q \bar{r} \bar{E}$ as the energy of the charge in the electric field, $\frac{1}{2} m |\partial \bar{r} / \partial t|^2$ as the kinetic energy of the particle, and $\frac{\omega_{e0}^2}{2} m |\bar{r}|^2$ as the potential energy. This last term proportional to ω_{e0}^2 is due to the spring-like restoring nature between the electron and an oppositely charged nucleus, which is assumed to be much more massive.

Equation (17) can be written in terms of the macroscopic polarization definition by $\bar{\mathcal{P}} = Nq\bar{r}$, giving the equation of motion as

$$\left(\frac{\partial^2}{\partial t^2} + \gamma_e \frac{\partial}{\partial t} + \omega_{ep}^2 \right) \bar{\mathcal{P}} = \frac{Nq^2}{m} \bar{\mathcal{E}} = \epsilon_0 \omega_{ep}^2 \bar{\mathcal{E}}, \quad (20)$$

where $\omega_{ep} = \sqrt{\frac{Nq^2}{m\epsilon_0}}$ is the plasma frequency. The dielectric material contributions to the energy are [1, 3, 6]

$$\bar{S}_{mat} = 0 \quad (21a)$$

$$\bar{W}_{mat} = \frac{1}{2\epsilon_0 \omega_{ep}^2} \left[\frac{\partial \bar{\mathcal{P}}}{\partial t} \cdot \frac{\partial \bar{\mathcal{P}}}{\partial t} + \omega_{e0}^2 \bar{\mathcal{P}} \cdot \bar{\mathcal{P}} \right] \quad (21b)$$

$$\varphi_{mat} = -\varphi_{F_k} + \frac{\gamma}{\epsilon_0 \omega_{ep}^2} \frac{\partial \bar{\mathcal{P}}}{\partial t} \cdot \frac{\partial \bar{\mathcal{P}}}{\partial t} \quad (21c)$$

The dielectric material contributions to the momentum are [1, 3, 6]

$$\bar{T}_{mat} = \frac{1}{2} (\bar{\mathcal{P}} \cdot \bar{\mathcal{E}}) \bar{I} - \bar{\mathcal{P}} \bar{\mathcal{E}} \quad (22a)$$

$$+ \frac{1}{2} \left[\bar{\mathcal{P}} \cdot \bar{\mathcal{E}} + \frac{1}{\epsilon_0 \omega_{ep}^2} \left(\frac{\partial \bar{\mathcal{P}}}{\partial t} \cdot \frac{\partial \bar{\mathcal{P}}}{\partial t} - \omega_{e0}^2 \bar{\mathcal{P}} \cdot \bar{\mathcal{P}} \right) \right] \bar{I}$$

$$\bar{G}_{mat} = \bar{\mathcal{P}} \times \mu_0 \bar{\mathcal{H}} - \frac{1}{\epsilon_0 \omega_{ep}^2} \nabla \bar{\mathcal{P}} \cdot \frac{\partial \bar{\mathcal{P}}}{\partial t} \quad (22b)$$

$$\bar{f}_{mat} = -\bar{f}_{F_k} - \frac{\gamma_e}{\epsilon_0 \omega_{ep}^2} \nabla \bar{\mathcal{P}} \cdot \frac{\partial \bar{\mathcal{P}}}{\partial t}. \quad (22c)$$

The material subsystem and field-kinetic subsystem can be combined to form the canonical subsystem as described conceptually in Eq. (1).

3.3. Energy and momentum in NIMs

By duality of the field-kinetic (i.e Chu) subsystem, the causal dielectric and magnetic response of a stationary

isotropic system can be formulated as [6, 24]

$$\left(\frac{\partial^2}{\partial t^2} + \gamma_e \frac{\partial}{\partial t} + \omega_{e0}^2\right) \bar{\mathcal{P}} = \epsilon_0 \omega_{ep}^2 \bar{\mathcal{E}} \quad (23a)$$

$$\left(\frac{\partial^2}{\partial t^2} + \gamma_m \frac{\partial}{\partial t} + \omega_{m0}^2\right) \mu_0 \bar{\mathcal{M}} = \mu_0 \omega_{mp}^2 \bar{\mathcal{H}} \quad (23b)$$

The resulting material energy contributions are

$$\bar{S}_{mat} = 0 \quad (24a)$$

$$\begin{aligned} \bar{W}_{mat} &= \frac{1}{2\epsilon_0 \omega_{ep}^2} \left[\frac{\partial \bar{\mathcal{P}}}{\partial t} \cdot \frac{\partial \bar{\mathcal{P}}}{\partial t} + \omega_{e0}^2 \bar{\mathcal{P}} \cdot \bar{\mathcal{P}} \right] \\ &+ \frac{\mu_0}{2\omega_{mp}^2} \left[\frac{\partial \bar{\mathcal{M}}}{\partial t} \cdot \frac{\partial \bar{\mathcal{M}}}{\partial t} + \omega_{m0}^2 \bar{\mathcal{P}} \cdot \bar{\mathcal{P}} \right] \end{aligned} \quad (24b)$$

$$\begin{aligned} \varphi_{mat} &= -\varphi_{Fk} + \frac{\gamma_e}{\epsilon_0 \omega_{ep}^2} \frac{\partial \bar{\mathcal{P}}}{\partial t} \cdot \frac{\partial \bar{\mathcal{P}}}{\partial t} \\ &+ \frac{\gamma_m}{\epsilon_0 \omega_{mp}^2} \frac{\partial \bar{\mathcal{M}}}{\partial t} \cdot \frac{\partial \bar{\mathcal{M}}}{\partial t}, \end{aligned} \quad (24c)$$

and the momentum contributions are

$$\begin{aligned} \bar{T}_{mat} &= \frac{1}{2} (\bar{\mathcal{P}} \cdot \bar{\mathcal{E}} + \mu_0 \bar{\mathcal{M}} \cdot \bar{\mathcal{H}}) \bar{I} - \bar{\mathcal{P}} \bar{\mathcal{E}} - \mu_0 \bar{\mathcal{M}} \bar{\mathcal{H}} \\ &+ \frac{1}{2} \left\{ \bar{\mathcal{P}} \cdot \bar{\mathcal{E}} + \mu_0 \bar{\mathcal{M}} \cdot \bar{\mathcal{H}} \right. \end{aligned} \quad (25a)$$

$$\begin{aligned} &+ \frac{1}{\epsilon_0 \omega_{ep}^2} \left(\frac{\partial \bar{\mathcal{P}}}{\partial t} \cdot \frac{\partial \bar{\mathcal{P}}}{\partial t} - \omega_{e0}^2 \bar{\mathcal{P}} \cdot \bar{\mathcal{P}} \right) \\ &+ \frac{\mu_0}{\omega_{mp}^2} \left(\frac{\partial \bar{\mathcal{M}}}{\partial t} \cdot \frac{\partial \bar{\mathcal{M}}}{\partial t} - \omega_{m0}^2 \bar{\mathcal{M}} \cdot \bar{\mathcal{M}} \right) \left. \right\} \bar{I} \end{aligned}$$

$$\begin{aligned} \bar{G}_{mat} &= \bar{\mathcal{P}} \times \mu_0 \bar{\mathcal{H}} + \bar{\mathcal{E}} \times \mu_0 \bar{\mathcal{M}} + \bar{\mathcal{P}} \times \mu_0 \bar{\mathcal{M}} \\ &- \frac{1}{\epsilon_0 \omega_{ep}^2} \nabla \bar{\mathcal{P}} \cdot \frac{\partial \bar{\mathcal{P}}}{\partial t} - \frac{\mu_0}{\omega_{mp}^2} \nabla \bar{\mathcal{M}} \cdot \frac{\partial \bar{\mathcal{M}}}{\partial t} \end{aligned} \quad (25b)$$

$$\begin{aligned} \bar{f}_{mat} &= -\bar{f}_{Fk} - \frac{\gamma_e}{\epsilon_0 \omega_{ep}^2} \nabla \bar{\mathcal{P}} \cdot \frac{\partial \bar{\mathcal{P}}}{\partial t} \\ &- \frac{\mu_0 \gamma_m}{\omega_{mp}^2} \nabla \bar{\mathcal{M}} \cdot \frac{\partial \bar{\mathcal{M}}}{\partial t}. \end{aligned} \quad (25c)$$

Under time-harmonic excitation, the stationary (i.e. $\bar{v} \rightarrow 0$) Minkowski constitutive parameters can be approximated $\bar{D} = \epsilon(\omega) \bar{E}$ and $\bar{B} = \mu(\omega) \bar{H}$. Each field phaser follows the relation $\bar{\mathcal{A}} = \Re\{\bar{A} e^{-i\omega t}\}$. The constitutive parameters are

$$\epsilon(\omega) = \epsilon_0 \left(1 - \frac{\omega_{ep}^2}{\omega^2 - \omega_{e0}^2 + i\omega\gamma_e} \right) \quad (26a)$$

$$\mu(\omega) = \mu_0 \left(1 - \frac{\omega_{mp}^2}{\omega^2 - \omega_{m0}^2 + i\omega\gamma_m} \right). \quad (26b)$$

The time-averaged energy density is

$$\begin{aligned} \langle W_{can} \rangle &= \frac{\epsilon_0}{2} \left[1 + \frac{\omega_{ep}^2 (\omega^2 + \omega_{e0}^2)}{(\omega^2 - \omega_{e0}^2)^2 + \gamma_e^2 \omega^2} \right] |\bar{E}|^2 \\ &+ \frac{\mu_0}{2} \left[1 + \frac{\omega_{mp}^2 (\omega^2 + \omega_{m0}^2)}{(\omega^2 - \omega_{m0}^2)^2 + \gamma_m^2 \omega^2} \right] |\bar{H}|^2 \end{aligned} \quad (27)$$

In the limit of zero losses ($\gamma_e \rightarrow 0$ and $\gamma_m \rightarrow 0$) both $\epsilon_I = 0$ and $\mu_I = 0$ and the energy density satisfies the well-known relation [20, 21, 25, 26]

$$\langle W_{can} \rangle = \frac{1}{4} \frac{\partial(\epsilon\omega)}{\partial\omega} |\bar{E}|^2 + \frac{1}{4} \frac{\partial(\mu\omega)}{\partial\omega} |\bar{H}|^2. \quad (28)$$

It is the rate of change in energy that appears in the energy continuity equation, which tends to zero upon cycle averaging, and since $\langle \partial W / \partial t \rangle = 0$, the resulting conservation equation

$$-\langle \nabla \cdot \bar{S}_{can} \rangle = \frac{1}{2} [\omega \epsilon_I |\bar{E}|^2 + \omega \mu_I |\bar{H}|^2] \quad (29)$$

is generally regarded as the complex Poynting's theorem, where $\langle \bar{S}_{can} \rangle = \frac{1}{2} \Re\{\bar{E} \times \bar{H}^*\}$ is the time average Poynting power.

The average momentum density,

$$\begin{aligned} \langle \bar{G}_{can} \rangle &= \frac{1}{2} \Re \left\{ \bar{D} \times \bar{B}^* + \bar{k} \frac{\epsilon_0 \omega \omega_{ep}^2}{(\omega^2 - \omega_{e0}^2)^2 + \gamma_e^2 \omega^2} |\bar{E}|^2 \right. \\ &+ \left. \bar{k} \frac{\mu_0 \omega \omega_{mp}^2}{(\omega^2 - \omega_{m0}^2)^2 + \gamma_m^2 \omega^2} |\bar{H}|^2 \right\}, \end{aligned} \quad (30)$$

satisfies [27]

$$\begin{aligned} \langle \bar{G}_{can} \rangle &= \frac{1}{2} \Re \left\{ \bar{D} \times \bar{B}^* + \frac{\bar{k}}{2} \left(\frac{\partial \epsilon}{\partial \omega} |\bar{E}|^2 + \frac{\partial \mu}{\partial \omega} |\bar{H}|^2 \right) \right\} \\ &= \frac{1}{2} \left\{ \frac{1}{v_g v_p} \bar{E} \times \bar{H}^* \right\} \end{aligned} \quad (31)$$

when the losses approach zero, where $v_p = \omega/k$ and $v_g = \partial\omega/\partial k$ are the phase velocity and the group velocity, respectively. The time average stress tensor is found to be

$$\langle \bar{T}_{can} \rangle = \frac{1}{2} \Re \left\{ \frac{1}{2} (\bar{D} \cdot \bar{E}^* + \bar{B} \cdot \bar{H}^*) \bar{I} - \bar{D} \bar{E}^* - \bar{B} \bar{H}^* \right\} \quad (32)$$

since the dispersive terms average to zero. Because the average rate of change in momentum density is zero (i.e. $\langle \partial \bar{G} / \partial t \rangle = 0$), the momentum conservation theorem for a monochromatic wave becomes

$$-\langle \nabla \cdot \bar{T}_{can} \rangle = \frac{1}{2} \Re \left\{ \omega \epsilon_I \bar{E} \times \bar{B}^* - \omega \mu_I \bar{H} \times \bar{D}^* \right\} \quad (33)$$

where the tensor is the complex Minkowski tensor. The force terms in Eq. (33) have been defined as the force density on free currents [28, 29].

4. Discussion

For illustration purposes, we consider a couple of examples. First, we consider the momentum density contribution to an electromagnetic pulse. Then, we consider the momentum flux or stress tensor contribution to a continuous wave.

4.1. Electromagnetic Pulse

A pulse is incident upon a medium with constitutive parameters $\mu(\omega)$, $\epsilon(\omega)$. For simplicity, we consider the medium to be dispersive, but lossless. The excitation energy of the pulse is [1, 3]

$$\mathfrak{E}_{exc} \equiv \mathfrak{E}_i - \mathfrak{E}_r = \mathfrak{E}_i(1 - |R|^2), \quad (34)$$

where \mathfrak{E}_i is the incident energy, \mathfrak{E}_r is the reflected energy, and $|R|^2$ is the reflectivity. The excitation energy is unambiguously defined in terms of the vacuum quantities. The spatial length of the transmitted pulse is decreased proportional to the factor n_g^{-1} due to the change in velocity inside the medium. We can investigate the interpretation of the field-kinetic and canonical subsystems inside the medium.

If we assume the field-kinetic momentum density defined by the Chu SEM tensor, we see that the momentum inside the material is

$$\begin{aligned} \bar{p}_{F_k} &= \int_z dz \bar{G}_{F_k}(z) = \hat{z} \frac{1}{n_g} \frac{\mathfrak{E}_i}{c} (1 - R^2) \\ &= \hat{z} \frac{1}{n_g c} \mathfrak{E}_{exc}. \end{aligned} \quad (35)$$

This is the momentum derived in Balazs' thought experiment.

We may arrive at this result using another approach by viewing each photon as a particle with effective mass unchanged as it enters the material so that $m_0 = m = \mathfrak{E}/c^2$. In the vacuum region ($z < 0$), the velocity of the pulse is $\bar{v}_0 = \hat{z}c$. At $t = 0$, the pulse enters the material and the velocity becomes $\bar{v} = \hat{z}c/n_g$. The force on the material is due to the momentum exchange

$$\begin{aligned} \bar{p}_i - \bar{p}_{kin} &= m_0 \bar{v}_0 - m \bar{v} = \hat{z} \left(\frac{\mathfrak{E}}{c^2} c - \frac{\mathfrak{E}}{c^2} \frac{c}{n_g} \right) \\ &= \hat{z} \frac{\mathfrak{E}}{c} \left(1 - \frac{1}{n_g} \right). \end{aligned}$$

Therefore, the field-kinetic subsystem gives the interpretation of constant effective mass.

Alternately, if we assume the canonical momentum density defined for a dispersive, lossless material from Eq. (31)

$$\bar{G}_{can}(z) = \hat{z} n_g n_p \frac{W_i(z)}{c} (1 - |R|^2), \quad (36)$$

we see that the momentum inside the material is

$$\begin{aligned} \bar{p}_{can} &= \int_z dz \bar{G}_{can}(z) = \hat{z} n_p \frac{\mathfrak{E}_i}{c} (1 - R^2) \\ &= \hat{z} n_p \frac{\mathfrak{E}_{exc}}{c}. \end{aligned} \quad (37)$$

This momentum, which is proportional to the phase velocity index of refraction, is generally measured inside materials as a combination of field plus material contributions [12, 28, 30, 31, 32].

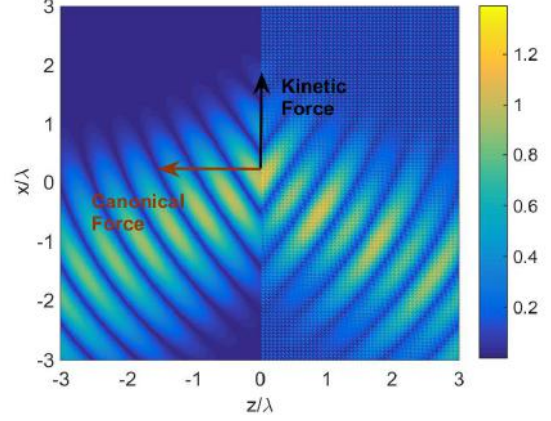


Figure 2: Demonstration of a refracted Gaussian beam at a matched negative refractive index boundary. The incident medium $z < 0$ is vacuum (μ_0, ϵ_0) and the transmitted is a matched left-handed medium ($-\epsilon_0, -\mu_0$). The parameters for incident TM field are amplitude $H_0 = 1$ A/m, incident wavelength $\lambda_0 = 1064$ nm, beam waist $w = \lambda_0$, and $NA = 0.8$.

We may arrive at this result using another approach by viewing each photon as a particle where the effective mass increases when it enters the material. The force on the material is due to the momentum exchange

$$\begin{aligned} \bar{p}_i - \bar{p}_{can} &= m_0 \bar{v}_0 - m \bar{v} = \hat{z} \left(\frac{\mathfrak{E}}{c^2} c - \frac{\mathfrak{E}}{c^2/(n_g n_p)} \frac{c}{n_g} \right) \\ &= \hat{z} \frac{\mathfrak{E}}{c} (1 - n_p). \end{aligned} \quad (38)$$

In this view, the momentum of the pulse entering a dielectric is increased due to the additional momentum of the material which is added to the electromagnetic pulse. These contributions were described in detail in Section 3.

It is interesting what happens to the two quantities in negative index media (NIM). Note that for NIM, $n_p < 0$, but $n_g > 0$. The field-kinetic momentum, being related to n_g , remains positive in negative index media. The canonical momentum on the other hand reverses direction due to its proportionality to n_p . Note, however that in the presence of losses, the direction of the canonical momentum can be parallel or anti-parallel to the energy flow [6].

4.2. Continuous Wave

Consider the problem of a continuous wave incident upon a negative index material ($-\epsilon_0, -\mu_0$) from vacuum (ϵ_0, μ_0). The wave shown in Fig. 2 is a TM Gaussian beam incident at $\pi/6$.

The field-kinetic force on the surface is $\bar{F}_{F_k} = \hat{x}1.6$ pN/m. The interpretation of this force is that there is an equal and opposite force $-\bar{F}_{F_k} = -\hat{x}1.6$ N/m that changes the direction of the incident photons from the $+\hat{z}$ and $+\hat{x}$ direction to the $+\hat{z}$ and $-\hat{x}$ direction. The transmitted electromagnetic momentum has an identical \hat{z} com-

ponent as the incident. Therefore, it is the equal and opposite force of the material on the electromagnetic waves at the surface that causes the change in momentum in the \hat{x} direction. The form of the field-kinetic momentum remains the same for all types of medium, and this description was previously applied to describe the optical dynamics of anisotropic metamaterial cloaks [33, 34]. Although the field-kinetic subsystem had yet to be uniquely identified, the Chu formulation was used to describe the optical dynamics of optical cloaks, which explains in retrospect how the forces on the optical paths were able to describe the transformed paths. Such a description is also useful for perfect lenses where planar surfaces are used to negatively refract images [24].

The canonical SEM tensor provides an alternate viewpoint. In this case, the time-averaged force reduces to the divergence of the Minkowski stress tensor. The canonical force on the surface is $\vec{F}_{can} = \hat{z}2.8 pN/m$. The zero force in the \hat{x} direction means that the tangential component of the wave momentum is conserved [6]. The change in the normal component of the wave momentum is due to the additional momentum from the material response as described in Section 3.

5. Conclusions

We have shown that the field-kinetic subsystem as given by the Chu formulation represents the energy and momentum contained within the fields, and the sum of the field-kinetic and material response subsystems represent the wave or canonical subsystem. The canonical subsystem reduces to the Minkowski subsystem only under negligible dispersion. We may conclude that neither the Minkowski or Abraham SEM tensors are universally correct. In fact, the Abraham SEM tensor violates the physical constraint of relativistic invariance. Our view was demonstrated the physics of negative index materials under both the field-kinetic and canonical or wave SEM models for negative refraction, which is fundamental to perfect lensing and invisibility cloaking.

Acknowledgement

This work was sponsored in part by the NSF Division of Electrical, Communications, and Cyber Systems (Award No. ECCS-1150514) through the Faculty Early Career Development (CAREER) program, the Arkansas EP-SCoR program provided by the National Science Foundations Research Infrastructure Improvement (Award No. OIA-1457888), and the Arkansas Research Alliance Fellows program.

References

[1] B. A. Kemp, "Resolution of the Abraham-Minkowski debate: Implications for the electromagnetic wave theory of light in matter," *J. Appl. Phys.*, vol. 109, p. 111101, 2011.

[2] S. M. Barnett, "Resolution of the Abraham-Minkowski dilemma," *Phys. Rev. Lett.*, vol. 104, p. 070401, 2010.

[3] B. A. Kemp, "Macroscopic theory of optical momentum," *Prog. Optics*, vol. 60, p. 437, 2015.

[4] C. J. Sheppard and B. A. Kemp, "Kinetic-energy-momentum tensor in electrodynamics," *Phys. Rev. A*, vol. 93, p. 013855, 2016.

[5] C. J. Sheppard and B. A. Kemp, "Relativistic analysis of field-kinetic and canonical electromagnetic systems," *Phys. Rev. A*, vol. 93, p. 053832, 2016.

[6] B. A. Kemp, J. A. Kong, and T. M. Grzegorzczuk, "Reversal of wave momentum in isotropic left-handed media," *Phys. Rev. A*, vol. 75, p. 053810, 2007.

[7] T. M. Grzegorzczuk and B. A. Kemp, "Transfer of optical momentum: reconciliations of the abraham and minkowski formulations," *Proc. SPIE*, vol. 7038, p. 70381S, 2008.

[8] M. Mansuripur, "Radiation pressure and the linear momentum of the electromagnetic field," *Opt. Express*, vol. 12, p. 5375, 2004.

[9] B. A. Kemp, T. M. Grzegorzczuk, and J. A. Kong, "Lorentz force on dielectric and magnetic particles," *J. of Electromagn. Waves and Appl.*, vol. 20, p. 827, 2006.

[10] B. A. Kemp and T. M. Grzegorzczuk, "The observable pressure of light in dielectric fluids," *Opt. Lett.*, vol. 36, no. 4, p. 493, 2011.

[11] C. J. Sheppard and B. A. Kemp, "Optical pressure deduced from energy relations within relativistic formulations of electrodynamics," *Phys. Rev. A*, vol. 89, no. 1, p. 013825, 2014.

[12] B. A. Kemp, "Subsystem approach to the electrodynamics in dielectric fluids," *Proc. SPIE*, vol. 8458, p. 845803, 2012.

[13] B. A. Kemp, "Comment on "revisiting the balazs thought experiment in the presence of loss: electromagnetic-pulse-induced displacement of a positive-index slab having arbitrary complex permittivity and permeability"," *Appl. Phys. A*, vol. 110, p. 517, 2013.

[14] M. Mansuripur, A. R. Zakharian, and E. W. Wright, "Electromagnetic-force distribution inside matter," *Phys. Rev. A*, vol. 88, p. 023826, 2013.

[15] N. G. C. Astrath, L. C. Malacarne, M. L. Baesso, G. V. B. Lukasiewicz, and S. E. Bialkowski, "Unravelling the effects of radiation forces in water," *Nat. Commun.*, vol. 5, p. 4363, 2014.

- [16] P. Penfield and H. A. Haus, *Electrodynamics of Moving Media*. Cambridge, MA: M.I.T. Press, 1967.
- [17] N. L. Balazs, *Phys. Rev.*, vol. 91, p. 408, 1954.
- [18] R. Loudon, "Radiation pressure and momentum in dielectrics," *Fortschr. Phys.*, vol. 52, p. 1134, 2004.
- [19] M. G. Scullion and S. M. Barnett, "Optical momentum in negative-index media," *J. Mod. Opt.*, vol. 55, p. 2301, 2008.
- [20] J. A. Kong, *Electromagnetic Wave Theory*. Cambridge, MA: EMW Publishing, 2005.
- [21] L. Brillouin, *Wave Propagation and Group Velocity*. New York: Academic Press, 1960.
- [22] R. Loudon, "The propagation of electromagnetic energy through an absorbing dielectric," *J. Phys. A*, vol. 3, p. 233, 1970.
- [23] R. Loudon, L. Allen, and D. F. Nelson, "Propagation of electromagnetic energy and momentum through an absorbing dielectric," *Phys. Rev. E*, vol. 55, p. 1071, 1997.
- [24] S. A. Ramakrishna and T. M. Grzegorzczuk, *Physics and Applications of Negative Refractive Index Materials*. CRC Press, 2008.
- [25] L. D. Landau, E. M. Lifshitz, and L. P. Pitaevskii, *Electrodynamics of Continuous Media, 2nd ed.* New York: Pergamon, 1984.
- [26] J. D. Jackson, *Classical Electrodynamics*. New York: John Wiley and Sons, 1999.
- [27] V. G. Veselago, "The electrodynamics of substances with simultaneously negative values of ϵ and μ ," *Sov. Phys. Usp.*, vol. 10, p. 509, 1968.
- [28] R. Loudon, S. M. Barnett, and C. Baxter, "Radiation pressure and momentum transfer in dielectrics: The photon drag effect," *Phys. Rev. A*, vol. 71, p. 063802, 2005.
- [29] B. A. Kemp, T. M. Grzegorzczuk, and J. A. Kong, "Optical momentum transfer to absorbing Mie particles," *Phys. Rev. Lett.*, vol. 97, p. 133902, 2006.
- [30] R. V. Jones and J. C. S. Richards, "The pressure of radiation in a refracting medium," *Proc. R. Soc. Lond. A.*, vol. 221, p. 480, 1954.
- [31] R. V. Jones and B. Leslie, "The measurement of optical radiation pressure in dispersive media," *Proc. R. Soc. Lond. A.*, vol. 360, p. 347, 1978.
- [32] G. K. Campbell, A. E. Leanhardt, J. Mun, M. Boyd, E. W. Streed, W. Ketterle, and D. E. Pritchard, "Photon recoil momentum in dispersive media," *Phys. Rev. Lett.*, vol. 94, p. 170403, 2005.
- [33] H. Chen, B. Zhang, Y. Luo, B. A. Kemp, J. Zhang, L. Ran, and B.-I. Wu, "Lorentz force and radiation pressure on a spherical cloak," *Phys. Rev. A*, vol. 80, p. 011808, 2009.
- [34] H. Chen, B. Zhang, B. A. Kemp, and B.-I. Wu, "Optical force on a cylindrical cloak under arbitrary wave illumination," *Opt. Lett.*, vol. 35, p. 667, March 2010.

Applying the Retarded Solutions of Electromagnetic Fields to Transmission Line RLGC Modeling

Peng Ye^{1,2}, Paul Huray¹, Brandon Gore^{1,3}

¹College of Engineering and Computing, University of South Carolina, Columbia, SC, USA

²Oracle Corporation, Redwood City, CA, USA

³Intel Corporation, Columbia, SC, USA

*corresponding author, E-mail: Brandon.Gore@intel.com

Abstract

The RLGC model, and its variations, is one of the most common techniques to simulate Transmission Lines. The RLGC model uses circuit network elements consisting of Resistance R, Inductance L, Conductance G and Capacitance C (per unit length) to represent a small segment of the Transmission Line, and then cascades multiple segments to simulate the Transmission Line of arbitrary length. Typically the parameters in RLGC model are extracted from the propagation constant γ and characteristic impedance Z_o of the transmission line, which are found using numerical simulation methods. These resulting RLGC parameters for multi-GHz signaling are usually frequency-dependent. This paper introduces an analytical approach to extract RLGC parameters to simulate transmission line, which results in a different model, the RLGC(p) model.

1. Introduction

Maxwell's Equations have been widely studied and used since their publication in 1861 by the Scottish physicist and mathematician James Clerk Maxwell. While Maxwell's Equations may appear in different forms, a common key aspect is that these equations specify the relationship of electric field intensity (\vec{E}), magnetic field intensity (\vec{H}), electric charge density (ρ) and electric current density (\vec{J}) at a particular space-time¹, (\vec{x}, t) . For example:

$$\vec{\nabla} \times \vec{E}(\vec{x}, t) = -\partial \vec{B}(\vec{x}, t) / \partial t$$

$$\vec{\nabla} \times \vec{B}(\vec{x}, t) = \mu \vec{J}(\vec{x}, t) + \mu \epsilon \partial \vec{E}(\vec{x}, t) / \partial t$$

$$\vec{\nabla} \cdot \vec{E}(\vec{x}, t) = \rho(\vec{x}, t) / \epsilon$$

$$\vec{\nabla} \cdot \vec{B}(\vec{x}, t) = 0$$

Where $\vec{B}(\vec{x}, t) = \mu \vec{H}(\vec{x}, t)$ is the magnetic flux density at point \vec{x} , time t , and μ is the permeability of the medium.

To analyze electromagnetic field propagation we need to find the causal relationship between different space-times

for the source (\vec{x}', t') and the observation point (\vec{x}, t) . Since electromagnetic fields propagate in the medium with a finite propagation speed, denoted as ν , there is a time difference in the relationship of electromagnetic fields at the source and the observation point. This phenomenon is known as Time Retardation and the time difference can be described as $t - t' = |\vec{x}' - \vec{x}| / \nu$.

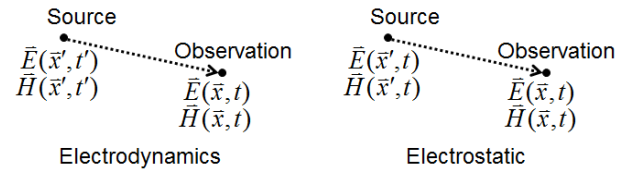


Figure 1: Time Retardation of Electromagnetic Fields

For *Electrostatic* fields where the source does not change over time: $\vec{E}(\vec{x}', t) = \vec{E}(\vec{x}', t')$ and $\vec{H}(\vec{x}', t) = \vec{H}(\vec{x}', t')$, therefore the electromagnetic fields at the source and the observation point can have the same time component t , which makes the propagation appear instantaneous and makes the Time Retardation irrelevant. However, for time-varying electromagnetic fields, the time component t' and t must be treated differently, and the derivative on t' will result in extra terms as t' is correlated to t, \vec{x}', \vec{x} . In other words, a comprehensive solution of electromagnetic fields that addresses Time Retardation must include these extra terms. We call such a solution the Retarded Solution of electromagnetic fields. It should be noted that the solution for *Electrostatic* fields is a special case of the Retarded Solution where the extra terms are zero due to $t' = t$.

The Retarded Solution of electromagnetic fields can be derived from Maxwell's Equations with a Green's Function. The Retarded Solution for point source, which is also known as the Jefimenko's Equations², can be found as:

$$\vec{E}(\vec{x}, t) = \frac{1}{4\pi\epsilon} \left[\frac{\vec{r}}{R^2} [\rho(\vec{x}', t')]_{ret} + \frac{\vec{r}}{\nu R} \left[\frac{\partial \rho(\vec{x}', t')}{\partial t} \right]_{ret} - \frac{1}{\nu^2 R} \left[\frac{\partial^2 \vec{J}(\vec{x}', t')}{\partial t^2} \right]_{ret} \right]$$

$$\vec{B}(\vec{x}, t) = \frac{\mu}{4\pi} \left[\frac{1}{R^2} [\vec{J}(\vec{x}', t')]_{ret} \times \vec{r} + \frac{1}{\nu R} \left[\frac{\partial \vec{J}(\vec{x}', t')}{\partial t} \right]_{ret} \times \vec{r} \right]$$

With a Fourier transform, this can be converted to Frequency Domain²:

$$\vec{E}(\vec{x}, \omega) = \frac{1}{4\pi\epsilon R^2} \left[\vec{r} \left(1 + j \frac{\omega R}{v}\right) \rho(\vec{x}', \omega) e^{-j\omega R/v} - j \frac{\omega R}{v^2} \vec{J}(\vec{x}', \omega) e^{-j\omega R/v} \right]$$

$$\vec{B}(\vec{x}, \omega) = \frac{\mu}{4\pi R^2} \left(1 + j \frac{\omega R}{v}\right) \left[\vec{J}(\vec{x}', \omega) e^{-j\omega R/v} \times \vec{r} \right]$$

The solution for other type of sources can be developed based on the solution for a point source.

2. Theoretical Case Study

The Retarded Solution of electromagnetic fields provides an analytical way to solve the electromagnetic fields. In this section we use it to solve the test case of a simplified transmission line. In this test case, we use a lossless thin straight line source along the z direction to represent the Transmission Line, and use a PEC flat plane at distance h away from the line source to represent the reference plane. We fill the entire space with uniform lossless medium in which the electromagnetic fields propagate at velocity, v . As a simplification, the model is extended to infinity to avoid the need of handling any boundary condition.

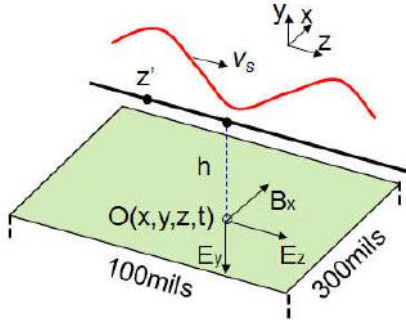
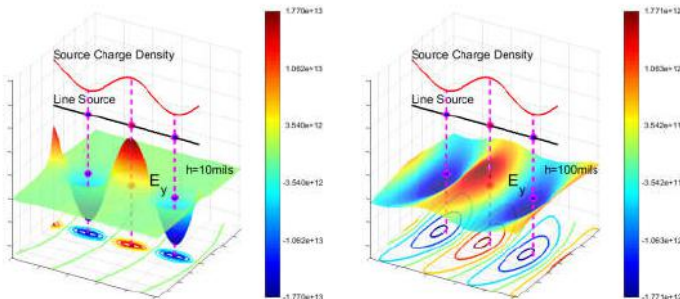
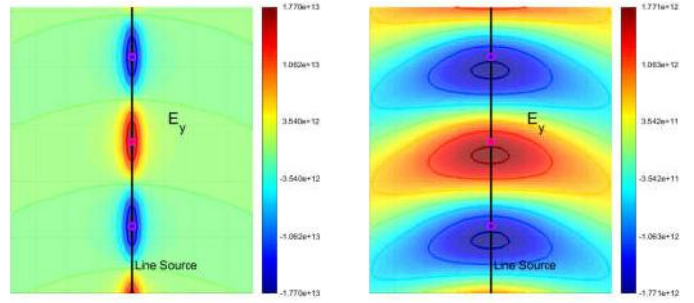


Figure 2: Case Study

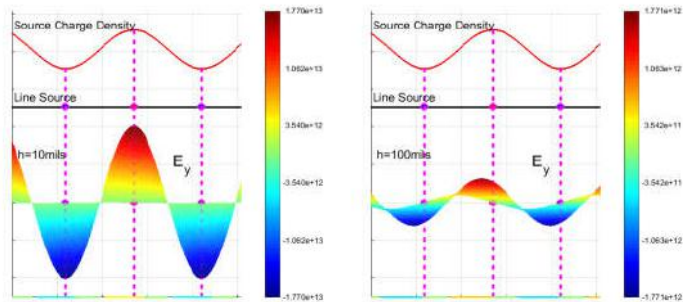
For demonstration purposes, we drive the source with 100GHz sinusoidal wave and observe the electromagnetic fields on the surface of the PEC reference plane, for $h=10\text{mils}$ and $h=100\text{mils}$, respectively. We plot the field magnitude of the fields in color where the positive peak is in red and the negative peak is in blue.



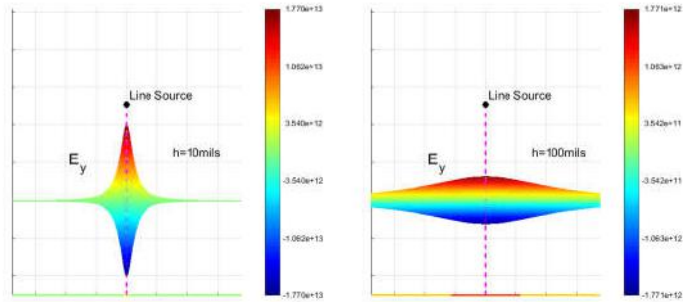
(a) $h=10\text{mils}$ (b) $h=100\text{mils}$
Figure 3: $|\vec{E}_y|$ magnitude plot, oblique view



(a) $h=10\text{mils}$ (b) $h=100\text{mils}$
Figure 4: $|\vec{E}_y|$ magnitude plot, top view



(a) $h=10\text{mils}$ (b) $h=100\text{mils}$
Figure 5: $|\vec{E}_y|$ magnitude plot, side view



(a) $h=10\text{mils}$ (b) $h=100\text{mils}$
Figure 6: \vec{E}_y magnitude plot, front view

In addition to showing that the magnitude of field intensity at \vec{x} is inversely proportional to its distance from \vec{x}' , these electric field intensity plots show the Time Retardation due to finite propagation velocity of fields. It is apparent that the peak of field intensity lags behind the peak of the source, and the delay is proportional to the distance, resulting in a “new moon” field pattern on the observation plane. This is more obvious with larger h as the field has been spread out further when it arrives at the reference plane such as in Figures 3(b) and 4(b).

For the same study case, we can observe the field magnitude on the cross section of the model, as indicated in Figure 7. In this case, we set $h=100\text{mils}$ and set source frequency to 100GHz and 10GHz, respectively in Figure 8 and Figure 9.

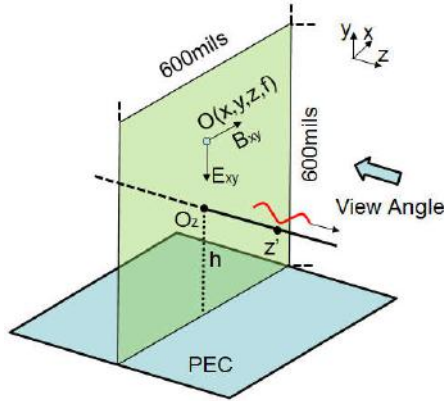


Figure 7: Case Study

In these field plots, the background color represents the magnitude of the field where peak magnitude is red and minimum magnitude is blue. The red arrows indicate the direction of the \vec{E}_{xy} field (electrical field on the x-y observation plane) and the blue arrows indicate the direction of the \vec{B}_{xy} field (magnetic field on the x-y observation plane).

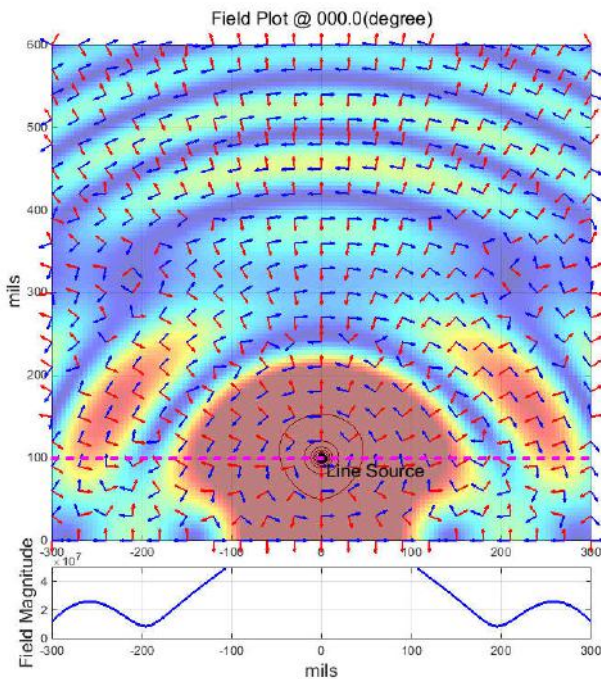


Figure 8: Field plot for 100GHz

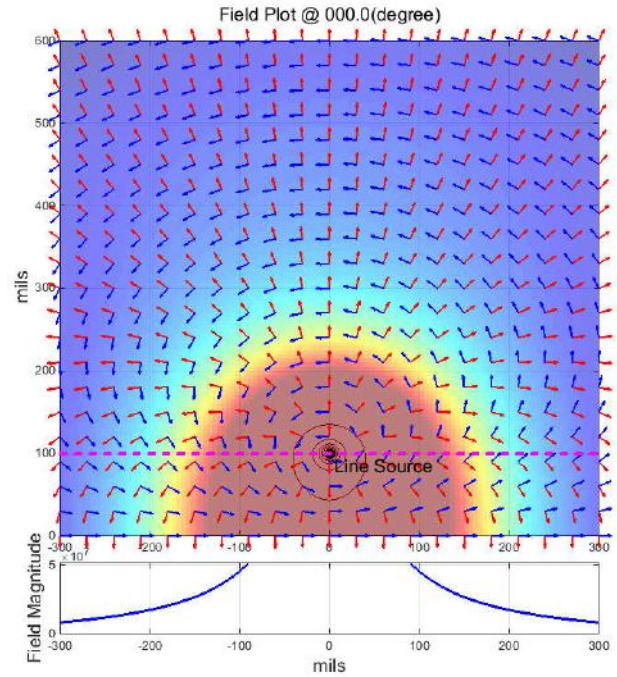


Figure 9: Field plot for 10GHz

The direction of \vec{E}_{xy} (red arrows) and \vec{B}_{xy} (blue arrows) in both figures shows that the energy is propagating in the same direction for any point on the observation plane; however, the direction of fields are not uniform for 100GHz. This is due to Time Retardation of fields. The total field is a sum of the original fields directly from the line source and the reflected field from the PEC reference plane. The total field at a given observation location is dominated by a certain section of the line source due to Time Retardation and the dominating section is related to the distance of the observation location to line source. If the source is varying at a very high frequency, there is more variation in the dominating sections on the line source for the observation area, some of which segments may even be on different parity, this creates an irregular field pattern and opposite direction of the fields for 100GHz source as shown in Figure 8. Conversely shown in Figure 9, if the source is varying slower, there is minor variation in the dominating sections on the line source for the observation area; therefore the total field is more uniform. Note that the direction of electric field intensity at the bottom of both Figure 8 and Figure 9 is perpendicular to the PEC as required.

Electromagnetic fields near the Transmission Line are the key to understanding the performance of the transmission line. As with field patterns in Figure 8 and Figure 9, there are unique characteristics for Transmission Line at high frequency. This can be studied analytically by using the Retarded Solution of Fields introduced in previous section of this paper and by using the simulation program developed by the authors.

3. Simulation Case Study

In the previous section, it was demonstrated how to solve the electromagnetic fields near a Transmission Line using the Retarded Solution. In this section, these field solutions will be used to study the RLGC model which is a common technique for representing Transmission Line behavior. As in Section 2, a simplified representation of a Transmission Line is assumed where a lossless, thin, and uniform line source along the z axis is placed above a flat, PEC plane at distance h away representing the reference plane.

To simulate a transmission line, the propagation constant γ and characteristic impedance Z_o are needed. For a uniform Transmission Line along the z direction, the voltage and current at a given location z is $V(z) = V_+ e^{-\gamma z} + V_- e^{+\gamma z}$ and $I(z) = I_+ e^{-\gamma z} + I_- e^{+\gamma z}$, where $V_+ e^{-\gamma z}$ and $I_+ e^{-\gamma z}$ are the voltage and current propagating in the $+z$ direction; $V_- e^{+\gamma z}$ and $I_- e^{+\gamma z}$ are the voltage and current propagating in the $-z$ direction. With this, the characteristic impedance is: $Z_o = V_+ / I_+ = -V_- / I_-$, which is the ratio of voltage and current propagating along one direction.

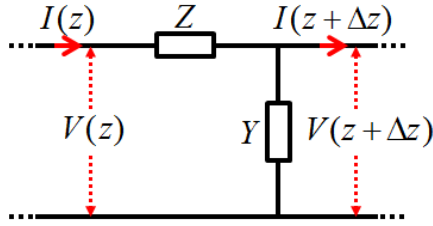


Figure 10: Impedance and Admittance network

As shown in Figure 10, the Transmission Line is divided into multiple equal segments of Δz in length, where γ and Z_o are found with the impedance, Z , and admittance, Y , of each segment:

$$\begin{cases} \frac{\partial V_{\pm} e^{\mp \gamma z}}{\partial z} = -Z \cdot I_{\pm} e^{\mp \gamma z} \\ \frac{\partial I_{\pm} e^{\mp \gamma z}}{\partial z} = -Y \cdot V_{\pm} e^{\mp \gamma z} \end{cases} \rightarrow \begin{cases} V_{\pm} = \frac{Z}{\pm \gamma} \cdot I_{\pm} \\ I_{\pm} = \frac{Y}{\pm \gamma} \cdot V_{\pm} \end{cases} \rightarrow \begin{cases} \gamma = \sqrt{Z \cdot Y} \\ Z_o = \sqrt{Z/Y} \end{cases} \text{ or } \begin{cases} Z = \gamma \cdot Z_o \\ Y = \gamma / Z_o \end{cases}$$

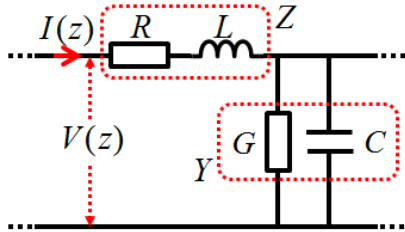


Figure 11: RLGC Transmission Line model segment

In a classical RLGC model, as shown in Figure 11, the impedance, Z , and admittance, Y , of each segment are represented by the Resistance R , Inductance L , Conductance G and Capacitance C , where $Z = R + j\omega L$, $Y = G + j\omega C$, with

the underlining assumption that R, L, G, C parameters are real positive values. One key assumption to make the cascaded segments a good representation of the Transmission Line is to keep each segment small enough compared to the wavelength of the frequency of interest which is application dependent. To resolve this, the classical RLGC modeling technique introduces the per unit length R, L, G, C parameters, $R_{pul}, L_{pul}, G_{pul}, C_{pul}$, and multiplies the length of segment Δz respectively to $R_{pul}, L_{pul}, G_{pul}, C_{pul}$ to obtain R, L, G, C values for an application. In summary, for classical RLGC model:

$$\begin{aligned} R \text{ parameter} &= \text{real}(Z) = \Delta z \cdot R_{pul} & Z &= R + j\omega L \\ L \text{ parameter} &= \text{imag}(Z)/\omega = \Delta z \cdot L_{pul} & \text{and } Y &= G + j\omega C \\ G \text{ parameter} &= \text{real}(Y) = \Delta z \cdot G_{pul} & \gamma &= \sqrt{Z \cdot Y} \\ C \text{ parameter} &= \text{imag}(Y)/\omega = \Delta z \cdot C_{pul} & Z_o &= \sqrt{Z/Y} \end{aligned}$$

With the electromagnetic fields near a Transmission Line solved by the Retarded Solution, applying their physical meaning to $R_{pul}, L_{pul}, G_{pul}, C_{pul}$ leads to a different result.

From a physical point of view, R_{pul} is often referred to as the electrical resistance due to the Transmission Line material's conductivity, and G_{pul} is referred to as the electrical loss due to surrounding material. In a simplified model with assumptions of lossless Transmission Line as well as lossless surrounding material, resistance and conductance can be assigned as $R_{pul} = 0$ and $G_{pul} = 0$. According to their definitions, L_{pul} is the ratio of the total magnetic flux surrounding a unit segment (perpendicular to the segment and extending to ∞) to the current on such segment and C_{pul} is the ratio of the charge on a unit segment over the voltage of such segment. Since the total magnetic flux and the voltage are integral products of the fields Transmission Line and such fields are solved by the Retarded Solution as demonstrated in Section 2, the L_{pul} and C_{pul} for the simplified Transmission Line model setup in Section 2 are:

$$\begin{aligned} L_{pul} &= \frac{\mu}{4\pi} \int_{L_1}^{\infty} \int_{L_1}^{L_2} (x-x') e^{-jkz'} \left[\left(\frac{e^{-jkR}}{R^3} - \frac{e^{-jkR_{img}}}{R_{img}^3} \right) + jk \left(\frac{e^{-jkR}}{R^2} - \frac{e^{-jkR_{img}}}{R_{img}^2} \right) \right] dz' dx \\ C_{pul} &= \frac{4\pi\epsilon}{\int_a^{\infty} \int_{L_1}^{L_2} (x-x') e^{-jkz'} \left[\left(\frac{e^{-jkR}}{R^3} - \frac{e^{-jkR_{img}}}{R_{img}^3} \right) + jk \left(\frac{e^{-jkR}}{R^2} - \frac{e^{-jkR_{img}}}{R_{img}^2} \right) \right] dz' dx} \end{aligned}$$

where a is the radius of the transmission line, L_1 and L_2 are the starting and ending location of the transmission line, and $k = \omega / v$. Additionally, we define R as the distance from the observation point to an integral segment, and R_{img} as the distance from the observation point to the mirror image of the same segment with respect to the reference plane. This image line source is used to assure that fields on the PEC are orthogonal to that reference plane.

For L_{pul} and C_{pul} , there is a common term in the solution:

$$\int_a^\infty \int_{L_1}^{L_2} (x-x') e^{-jkz'} \left[\left(\frac{e^{-jkR} - e^{-jkR_{img}}}{R^3} - \frac{e^{-jkR_{img}}}{R_{img}^3} \right) + jk \left(\frac{e^{-jkR}}{R^2} - \frac{e^{-jkR_{img}}}{R_{img}^2} \right) \right] dz' dx$$

It can be shown that this term is a complex value unless $k = \omega/v = 0$ (Static case), so the authors define this common term to be $|P|e^{j\phi}$, where $|P|$ is the magnitude and ϕ is the phase. It can also be shown that ϕ increases as $k = \omega/v$ increases. With this common term, we can see that L_{pul} and C_{pul} are also complex if the source is not static and we can write: $L_{pul} = |L_{pul}|e^{j\phi}$ and $C_{pul} = |C_{pul}|e^{-j\phi}$, where:

$$|L_{pul}| = \frac{\mu}{4\pi} |P| \text{ and } |C_{pul}| = 4\pi\epsilon / |P|. \text{ As a result we have:}$$

$$R \text{ parameter} = \text{real}(Z) = \Delta z \cdot R_{pul} - \omega |\Delta z \cdot L_{pul}| \sin \phi$$

$$L \text{ parameter} = \text{imag}(Z) / \omega = |\Delta z \cdot L_{pul}| \cos \phi$$

$$G \text{ parameter} = \text{real}(Y) = \Delta z \cdot G_{pul} + \omega |\Delta z \cdot C_{pul}| \sin \phi$$

$$C \text{ parameter} = \text{imag}(Y) / \omega = |\Delta z \cdot C_{pul}| \cos \phi$$

The authors refer to the model using these RLGC parameters as the RLGC(p) model, to distinguish from the classical RLGC model as described in the beginning of this section. A key characteristic of the RLGC(p) model is that it yields extra terms in R and G parameters from inductance and capacitance. This changes the “loss portfolio” in that C and L now contain energy loss components whereas the classical RLGC model considers only R and G parameters as representing energy loss. The extra terms $-\omega |\Delta z \cdot L_{pul}| \sin \phi$ and $\omega |\Delta z \cdot C_{pul}| \sin \phi$ (shown in red above) are in opposite polarity so one appears as an energy source and the other appears as an energy consumer. It must be noted that these terms are energy neutral in the sense that the energy “produced” by one is exactly the same as the energy “consumed” by the other. This phenomenon is due to Time Retardation and the definition of inductance and capacitance, which requires part of the energy generated by previous segments is accounted for by the current segment, and the same amount of energy generated by the current segment is accounted for by the next segment, so on and so forth. The RLGC(p) model is able to describe such behavior, in other words, it describes Time Retardation. It is also noted that the Classical RLGC model is a special case of the RLGC(p) model when $\phi = 0$.

For high loss transmission at low frequency, the extra terms in RLGC(p) model are small since ϕ is small; therefore, the difference between RLGC(p) model and classical RLGC model may be negligible. However, for low loss or no loss Transmission Lines or for Transmission Lines at high frequency, using a Classical RLGC model will result in error.

The simplified Transmission Line in Section 2 is an extreme case because no material loss is assumed in addition to a very high source frequency (100GHz); it is a good case to

demonstrate the difference between RLGC(p) model and classical RLGC model. As a comparison, the S parameter at 100GHz are plotted for a 500mils section using the RLGC(p) model generated by the author’s solutions to the Retarded Field equations (Case [1]), it is compared against the S parameters generated by a commercial 3D FEM field solver (Case [0]). Also added to the comparison are the S parameters generated from classical RLGC model extracted by a 2D field solver (no Time Retardation included) (Case [2]) and the S parameters generated from classical RLGC model extracted by the 3D field solver (Case [3]). Finally, Case [4] is added which is the S parameters generated from RLGC(p) model extracted from the modal data of the 3D FEM field solver.

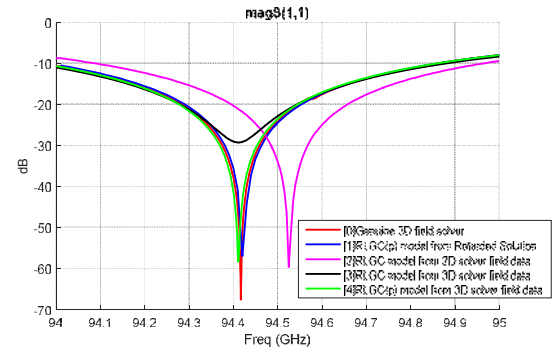


Figure 12: Magnitude of S11 from 94GHz to 95GHz

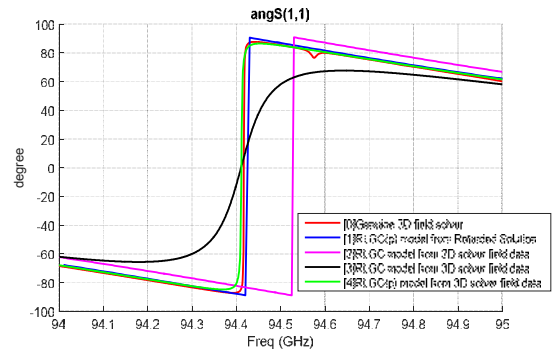


Figure 13: Phase of S11 from 94GHz to 95GHz

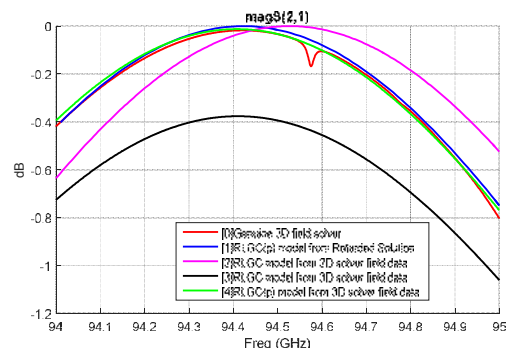


Figure 14: Magnitude of S21 from 94GHz to 95GHz

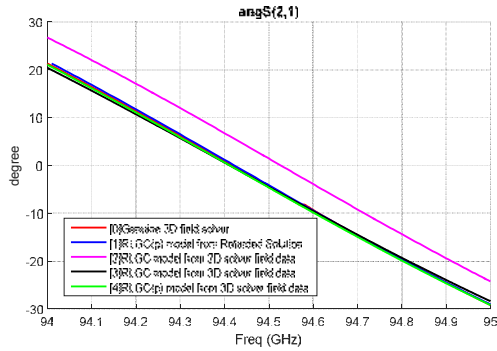


Figure 15: Phase of S21 from 94GHz to 95GHz

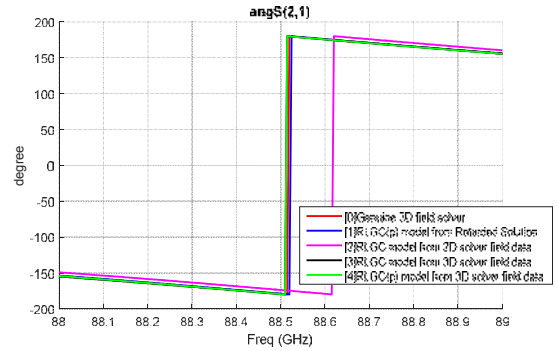


Figure 19: Phase of S12 from 88GHz to 89GHz

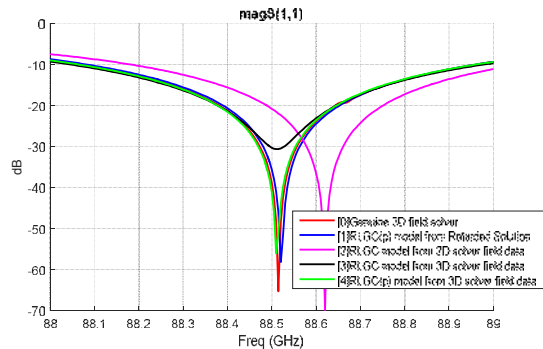


Figure 16: Magnitude of S11 from 88GHz to 89GHz

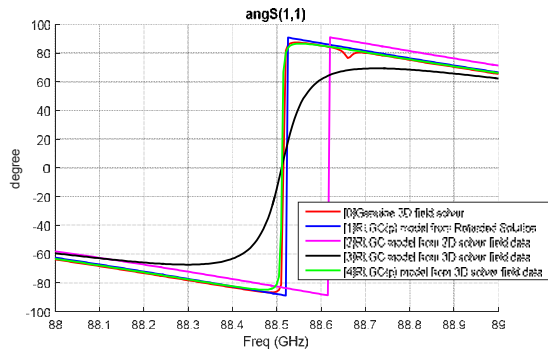


Figure 17: Phase of S11 from 88GHz to 89GHz

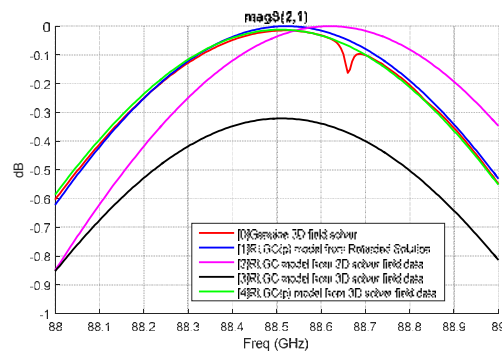


Figure 18: Magnitude of S12 from 88GHz to 89GHz

4. Discussion

From Figure 12 to Figure 19, it is shown that an RLGC(p) model is effective in representing the Transmission Line, its performance is similar to the S parameters of a commercial 3D FEM field solver (Case [0], Case [1] and Case [4]). Comparing Case [3] and Case [4] shows the differences between a classical RLGC model and a RLGC(p) model; in that, the classical RLGC model trends well but are not accurate when compared to the RLGC(p) model. It should be emphasized that Case [1] and Case [3] are generated from the same field data of the 3D FEM field solver. In Case [2], the classical RLGC model from 2D field solver is incorrect in the Propagation Constant and Characteristic Impedance due to not take into account Time Retardation. This tells us that ignoring Time Retardation at high frequency results in error.

Regarding the magnitude of S12 in Figure 14 and Figure 18, the insertion loss of the Transmission Line, Case [3] is drastically different from Case [0] because the 3D solver “corrects” the negative parameters, in this case the R parameter, for the classical RLGC model with the intention of preserving passivity. However, this “correction” disturbs the energy state as it eliminates the energy source, a negative R parameter, but preserves the energy consumer in G parameter. We cannot preserve the energy state by eliminating both the energy source and consumer in R and G parameter, because it is effectively ignoring Time Retardation, as shown in Case [2], it will create incorrect Propagation Constant and Characteristic Impedance. The best approach is to make no “correction” as done in RLGC(p) model. As explained in Section 3, Time Retardation will create a complementary energy source and energy consumer, the passivity enforcement should avoid correcting such an energy source.

5. Conclusions

Based on the study of the analytical solution, an RLGC(p) model is proposed. It is shown that this new model is more effective in simulating the Transmission Line compared to

the classical RLGC model. Unlike the classical RLGC model that uses the DC (static) definition for Capacitance and Inductance, this new model takes into account the time retardation between sources (charge and current density) and the electric and magnetic field intensities that appear at large separated locations, which leads to complex value of Capacitance and Inductance. In extreme cases (for example with a digital rapidly fluctuating source charge and current), traditional methods can even extract negative RLGC parameters from S parameters. We thus conclude that classical RLGC parameters at high frequencies are not consistent with their DC counterparts. This inconsistency is due to time retardation of propagating fields in the medium. The proposed RLGC(p) model can handle this inconsistency.

References

- [1] John David Jackson, "*Classical Electrodynamics*", Wiley; 3rd edition, 1998.
- [2] Oleg D. Jefimenko, "*Causality Electromagnetic Induction and Gravitation*", Electret Scientific Co; 2nd edition, 2000.
- [3] Paul G. Huray, "*The Foundations of Signal Integrity*", Wiley-IEEE Press, 1st edition, 2010.
- [4] Paul G. Huray, "*Maxwell's Equations*", Wiley-IEEE Press, 1st edition, 2010.
- [5] Richard P. Feynman, Robert B. Leighton, Matthew Sands, "*The Feynman Lectures on Physics, Volume 2*", Addison-Wesley, 1977.
- [6] Rosa, E.B. "*The Self and Mutual Inductances of Linear Conductors*", Bulletin of the Bureau of Standards 4 (2): 301–344.
- [7] Albert Ruehli, "*Partial element equivalent circuit (PEEC) method and its application in the frequency and time domain*", in Proc. Electromagn.Compat. Symp., Aug. 19–23, 1996, pp. 128–133.
- [8] Madhusudanan K. Sampath, "*On Addressing the Practical Issues in the Extraction of RLGC Parameters for Lossy Multiconductor Transmission Lines using S-parameter Models*", Proceedings of the 16th Topical Meeting on the Electrical Performance of Electronic Packaging, pp. 259-262 (Oct. 2008).

Antenna and Propagation

New Ultra Wide Band antenna design with innovative materials.

H. Nadir^{1*}, R. Negrier¹, N. Essaidi^{1,3}, E. Martinod¹, N. Feix¹, V. Bertrand², S. Rossignol³ and M. Lalande¹

¹XLIM, University of Limoges, Brive, France

²CISTEME, Brive, France

³SPCTS, Université de Limoges, Limoges, France

*houda.nadir@unilim.fr

Abstract- The limitation of the antenna dimensions is critical for radar applications, especially at low frequencies. We demonstrate the use of an appropriate dielectric material is an efficient way to optimize antenna behavior and to reduce its dimensions. The behavior of an antenna filled with resin intended for Ground Penetrating Radar is validated using the experimental results. We propose to develop a new dielectric material based on different test mixtures to significantly improve the material properties, especially in term of electromagnetic characteristics.

The limitation of the antenna size is critical for radar applications, especially at low frequencies. For example, a radar system installed on Tunnel Boring Machine (TBM) must provide identification of large obstacles which can obstruct during digging (e.g. other tunnels, cavities, boulders, foundations, archaeological remains, etc..) as well as soil changes (e.g. from gravel to fractured rock) (NETTUN Project). This radar system must radiate at low frequencies in order to achieve better penetration in the soil, ideally few decades of Megahertz.

A solution to reduce the size of antennas is to introduce a dielectric material to the radiating structure. The main antenna dimensions are divided by square root of the dielectric permittivity. Table I illustrates an example of a K antenna [1]-[2] designed for the frequency band of 200 MHz to 2 GHz. The relative permittivity of the dielectric is equal to 6.

TABLE I. ILLUSTRATIONS OF REDUCED ANTENNA DIMENSIONS

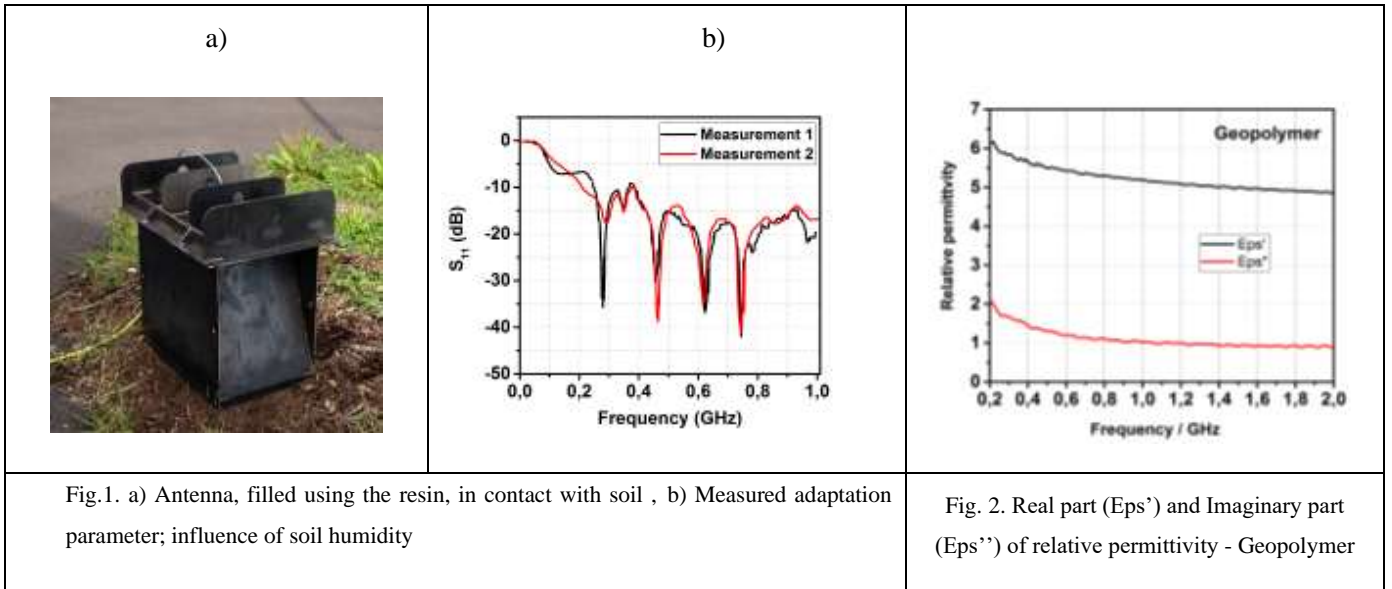
K antenna in air	K antenna with dielectric ($\epsilon_r=6$)
L=0.4m	L=0.16m
H=0.3m	H=0.12m
W=0.15m	W=0.06m

For NETTUN project [3], an UWB antenna, KHORN antenna which consists of the insertion of a K antenna into a metallic cavity. The selected filling material was a polyurethane dielectric resin from Axson Technologies (reference RE11880/RE1020).

We have measured the relative permittivity of resin using the Dielectric Assessment Kit (DAK-12) by Schmid & Partner Engineering AG which is ideal for all applications where high-precision dielectric parameter measurements (permittivity, conductivity, loss tangent) are required, including applications in electronic, chemical, food, and medical industries. The relative dielectric permittivity of resin is close to 4.

The designed KHORN antenna has been manufactured (Fig. 1.a) and test measurements have been performed on this structure when the antenna is in contact with the soil. The adaptation bandwidth strongly depends on the

nature of the soil and its humidity. To illustrate this dependence, measurements of reflection coefficients have been performed in the same location at two different times. The obtained results are depicted in Fig. 1.b. The lower adaptation frequency is 250MHz for this configuration.



For reducing the antenna dimensions, it is better to use dielectric materials with higher dielectric permittivity from which we are able to extract an accurate electromagnetic model.

New dielectric materials based on different test mixtures are currently designed [4]. This new class of materials called geopolymer are ill-organized, three-dimensional materials resulting from the activation of an aluminosilicate source using an alkaline solution. The aim of such research is to significantly improve the material properties, especially in term of electromagnetic characteristics. Relative dielectric permittivity for such material is presented in Fig. 2.

Acknowledgements: We greatly appreciate the European Commission Seventh Framework Programme for Research, for funding under Grant Agreement 280712 (NETTUN).

REFERENCES

1. Yu. A. Andreev, Yu. I. Buyanov and V. I. Koschelev, "Combined Antennas for High-Power Ultrawideband Pulse Radiation", *2nd International Congress on Radiation Physics, High Current Electronics, and modification of Materials*, Tomsk, September 10-16, 2006.
2. A. Godard, L. Desrumaux, V. Bertrand, J. Andrieu, M. Lalande, B. Jecko, M. Brishoual, V. Couderc and R. Guillerey, "A transient UWB antenna array used with complex impedance surfaces", *International Journal of Antennas and Propagation*, 2010.
3. G. Manacorda, A. Simi, M. Sow, E. Martinod, N. Feix, M. Lalande, S. Reynaud, V. Bertrand, D. Tran, H. Cetinkaya and A. Yarovoy, *International Workshop on Advanced Ground Penetrating Radar (IWAGPR2015)*, Florence, July 7-10, 2015.
4. E. Prud'homme, P. Michaud, E. Joussein, J.M. Clacens and S. Rossignol, 'Role of alkaline cations and water content on geomaterial foams: Monitoring during formation', *Journal of Non-crystalline Solids*, vol. 357, no. 4, pp. 1270-1278, 2011.

Low-Cost Transmit and Receive Reflectarray Antenna for Satellite Communications in Ka-Band

Eduardo Martinez-de-Rioja^{1*}, Jose A. Encinar¹, Rafael Florencio² and Rafael. R. Boix²

¹Dept. of Signals, Systems and Radiocommunications, Technical University of Madrid, Spain

²Dept. of Electronics and Electromagnetism, University of Seville, Spain

*corresponding author: emartinez@etc.upm.es

Abstract-This contribution describes the design of a printed reflectarray to generate a focused beam in dual polarization at 19.7 GHz and also at 29.5 GHz, which are downlink and uplink frequencies for Satcom terminal antennas in Ka-band. The proposed reflectarray allows dual-frequency and dual-polarization operation, as well as simple and low-cost manufacturing. The simulated radiation patterns for a 20-cm reflectarray show a gain better than 30 dBi in both bands, with low levels for cross-polar radiation and side lobes.

Introduction: Ka-band has become a major alternative for satellite systems to satisfy the growing demand for capacity and provide broadband services. Conventional reflectors and phased arrays have been proposed for transmit and receive terminal antennas; however, the different frequencies for uplink (30 GHz) and downlink (20 GHz) lead to a more complex antenna design. Otherwise, reflectarrays can be designed for multi-frequency operation using a single layer [1] or stacked layers for each frequency [2]. A reflectarray working at 20 GHz and 30 GHz in orthogonal linear polarization was proposed in [3], so that only one linear polarization could be used at each frequency. In this paper, the authors present the design of a reflectarray VSAT antenna to simultaneously operate in dual polarization (linear or circular) at receive (19.7 GHz) and transmit (29.5 GHz) frequencies.

Reflectarray cell: The unit-cell used to provide the phasing on the reflectarray consists of two orthogonal sets of five parallel dipoles printed on a dielectric layer, and two additional sets of three parallel dipoles stacked above the first sets and printed on the top of a second dielectric sheet (see Fig.1a). The period, $P_X = P_Y = 6.5$ mm, is chosen as $0.66 \cdot \lambda$ at the higher frequency (29.5 GHz) to avoid the appearance of grating lobes up to 30° incidence. This cell provides a smooth variation in phase response in a range greater than 360° at 19.7 GHz and 29.5 GHz. An independent phase control can be achieved based on the dipole lengths: upper dipoles will not disturb the phase response at 19.7 GHz, as they are shorter than the ones in bottom layer, while lower dipoles will behave as a ground plane at 29.5 GHz for higher layer elements. Thus, the dipole lengths can be first adjusted on the bottom layer to produce the required phase-shift at 19.7 GHz, and then, those on the top layer to provide the required phase at 29.5 GHz.

Antenna design: A 20-cm sided reflectarray, consisting of 900 elements arranged in a 30×30 grid, has been designed to generate a focused beam in the direction $\theta_b = 13^\circ$, $\phi_b = 0^\circ$ for the two orthogonal polarizations (with the electric field in the direction of the dipoles) at 19.7 and 29.5 GHz. Since the antenna is designed to provide the same radiation pattern for the two orthogonal components of the incident field, it will operate in dual Circular Polarization (CP) when it is illuminated by a dual-CP polarized feed. The phase center of the feed is placed at coordinates (-40, 0, 195) mm relative to the reflectarray center, and the radiated field is modeled using a cos-q distribution, with $q=10.5$ for 20 GHz band and $q=10.7$ for 30 GHz band. A home-made software analysis

routine, based on the Method of Moments in the Spectral Domain (MoM-SD) and the local periodicity approach, has been employed to optimize the dipole lengths in order to provide the phase-shift distributions shown in Figs. 1b and 1c for both polarizations at 19.7 GHz and 29.5 GHz, considering the real angle of incidence on each reflectarray element. The dimensions of all dipoles are optimized element-by-element to simultaneously match the phases at the central and extreme frequencies in lower (19.2-20.2 GHz) and higher (29-30 GHz) bands, following a procedure similar to that shown in [4].

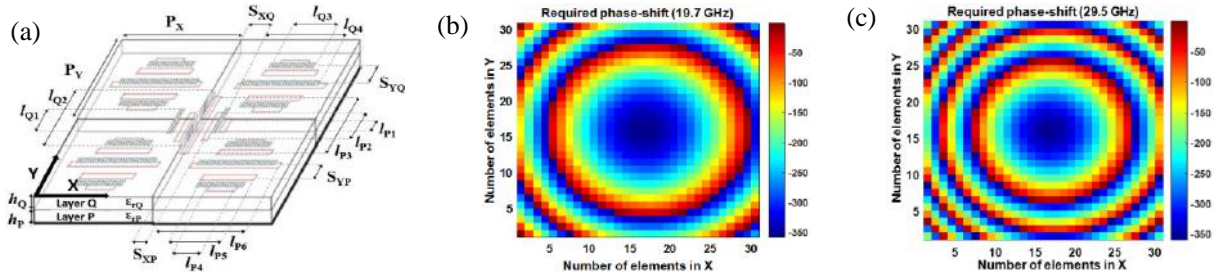


Figure 1. (a) View of reflectarray periodic structure. (b) Required phase-shift at 19.7 GHz and (c) at 29.5 GHz.

Results and conclusions: The simulated radiation patterns in gain (see Fig. 2), have been obtained from the tangential reflected field at each reflectarray cell, using the mentioned MoM-SD software. A gain of 31.4 dBi and 34.2 dBi is reached at 19.7 GHz and 29.5 GHz, respectively, with cross-polar radiation around -26.5 dB within a -3 dB main beam and side-lobe level close to -22 dB. An 8% and 5% bandwidth has been achieved in each band with a gain variation < 1 dB. The antenna efficiency can be estimated as 67% in lower band and 57% in higher band, considering illumination, spillover and dielectric losses. These results show the potential of reflectarrays for dual-frequency and dual-polarization operation as an alternative for Ka-band terminal antennas.

Acknowledgements: Authors are grateful to the Spanish Ministry of Economy and Competitiveness (project TEC2013-43345-P) and the Regional Government of Madrid (project SPADERADAR-CM, P2013/ICE-3000).

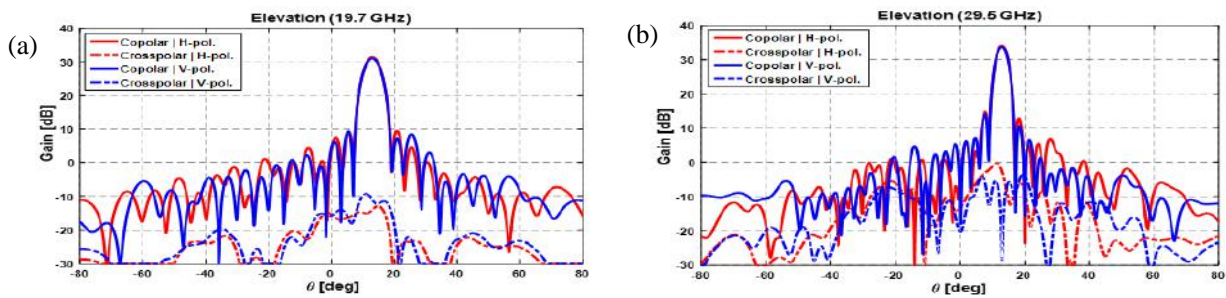


Figure 2. Simulated radiation patterns in gain (dBi): (a) XZ-plane at 19.7 GHz, (b) XZ-plane at 29.5 GHz.

REFERENCES

1. Hasani, H., C. Peixeiro et al., "Single-Layer Quad-Band Printed Reflectarray Antenna with Dual Linear Polarization," *IEEE Trans. on Antennas and Propag.*, Vol. 63, No. 12, 5522–5528, 2015.
2. Chaharmir, M. R., J. Shaker and H. Legay, "Dual-band Ka/X reflectarray with broadband loop elements," *IET Microwaves, Antennas & Propagation*, Vol. 4, No. 2, 225–231, 2010.
3. Encinar, J. A. and M. Barba, "Design manufacture and test of Ka-band reflectarray antenna for transmitting and receiving in orthogonal polarization," in *Int. Symp. on ANTEM-AMEREM*, Ottawa, Canada, July 2010.
4. Florencio, R., J. A. Encinar et al., "Reflectarray Antennas for Dual Polarization and Broadband Telecom Satellite Applications," *IEEE Trans. on Antennas and Propag.*, Vol. 63, No. 4, 1234–1246, 2015.

Study of the Complementary Strip-Slot with Circular Geometry

Y. Alonso-Roque*, E. Abdo-Sánchez, and C. Camacho-Peñalosa

Dpto. Ingeniería de Comunicaciones, E.T.S.I. Telecomunicación,
Universidad de Málaga, Andalucía Tech, Campus de Teatinos, Málaga, Spain

*yar@ic.uma.es, elenaabdo@ic.uma.es, ccp@ic.uma.es

Abstract- In this contribution the study of the complementary strip-slot with circular geometry is presented. Electromagnetic simulations of the S-Parameters and radiation characteristics were carried out. A matching bandwidth of more than 175% was obtained, which is explained by the circuit modeling using a lattice network. The circular strip-slot has a broadside and bidirectional radiation pattern appropriate for series-fed arrays.

The narrow bandwidth of microstrip antennas leads to the research of alternatives to solve this limitation. In [1] the complementary strip-slot was proposed as a planar radiator with broad matching and it was shown this structure can be modeled by a lattice network [2]. In this paper, the circular strip-slot structure is studied in order to analyze whether the strip-slot with this geometry has similar properties to the rectangular strip-slot and whether it can be modeled likewise with a lattice network.

The analyzed structure consists in a circular stub in the center of the two sections of a microstrip line constituting a two-port network. The structure was designed on the substrate GIL1032 ($\epsilon_r=3.2$ and $h=0.762\text{mm}$). A slot with circular geometry is located on the center of the ground plane and aligned with the stub, as shown in Fig. 1.

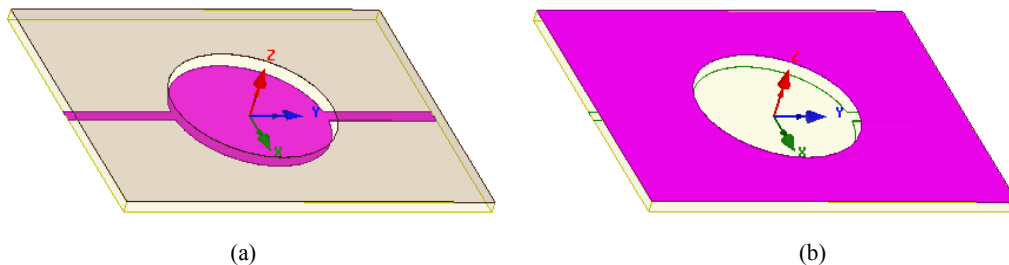


Figure 1. Geometry of strip-slot with circular geometry: (a) Microstrip layer highlighted, (b) Slot layer highlighted.

The influence of the dimensions of the slot and the stub on the scattering parameters and radiation characteristics was studied. The $|S_{11}|$ is shown in Fig. 2a for a stub radius of 10.42mm and a slot radius of 10.76mm. A return loss bandwidth of more than 175% was achieved, which shows that it is possible to obtain the inherent broad impedance bandwidth behavior of the rectangular strip-slot. In Fig. 2b, the phase of the S_{12} parameter is plotted with the reference planes at the borders of the circular stub.

The circuit modeling of circular strip-slot using a lattice network was performed. This study showed that the impedances of the series and cross branches have a complementary behavior like in the rectangular strip-slot, which justifies the broad impedance bandwidth of the circular strip-slot. The impedances of the series branch Z_a and of the cross branch Z_b are shown in Fig. 3a and 3b, respectively.

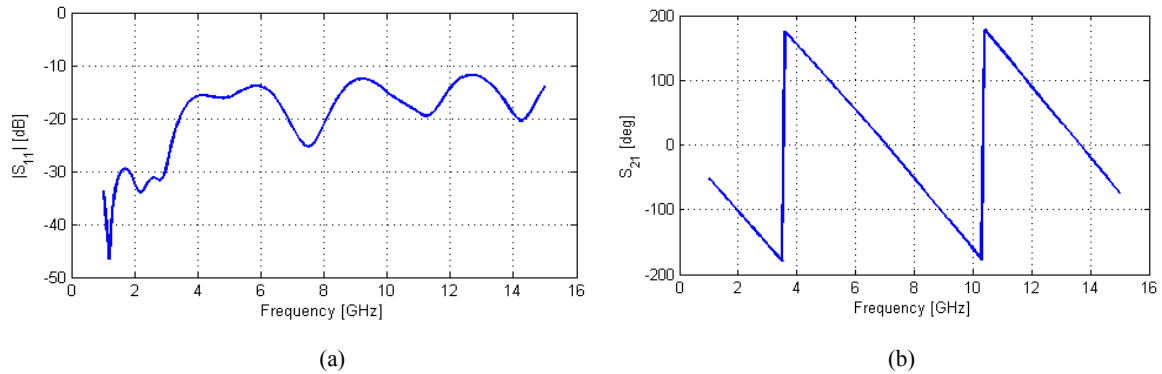


Figure 2. (a) Simulated $|S_{11}|$. (b) Simulated phase of S_{21} .

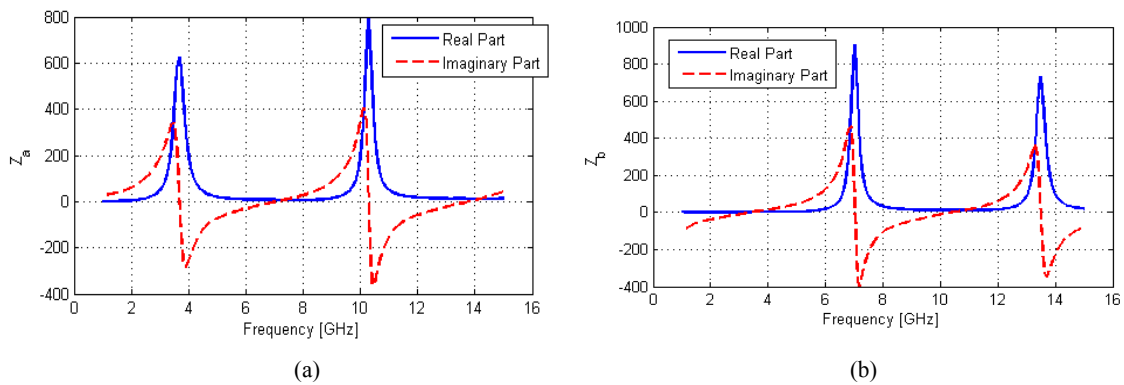


Figure 3. Simulated equivalent lattice network impedances: (a) Series branch Z_a , (b) Cross branch Z_b .

The studied structure has a broadside and bidirectional radiation pattern with more radiation into the stub half-space. Moreover, since significant amount of power is received at Port 2, this type of structure can be very appropriate for applications in series-fed arrays, as demonstrated for the rectangular strip-slot [3].

As conclusion, the study of the circular strip-slot reveals that it is possible to obtain broad matching bandwidth with this geometry. Its circuit modeling with a lattice network shows that the slot and the stub present complementary behavior, thus explaining the achieved wide impedance bandwidth. It was demonstrated that the circular strip-slot has similar characteristics to the rectangular strip-slot. The obtained radiation characteristics suggest that the studied circular strip-slot can be used as radiating element in the design of series-fed arrays. Measurements of the structure will be available at the time of the conference.

REFERENCES

1. E. Abdo-Sánchez, J.E. Page, T.M. Martín-Guerrero, J. Esteban, and C. Camacho-Peñalosa, "Planar broadband slot radiating element based on microstrip-slot coupling for series-fed arrays," *IEEE Trans. Antennas Prop.*, vol. 60, no. 12, pp. 6037–6042, Dec. 2012.
2. Valkenburg, M. E. V., *Introduction to Modern Network Synthesis*. New York: John Wiley & Sons, Inc., 1960.
3. E. Abdo-Sánchez, J. Esteban, T.M. Martín-Guerrero, C. Camacho-Peñalosa, and P.S. Hall, "A novel planar log-periodic array based on the wideband complementary strip-slot element," *IEEE Trans. Antennas Prop.*, vol. 62, no. 11, pp. 5572–5580, Nov. 2014.

Simple Design Procedure for 2D SWAs with Specified Sidelobe Levels and Inclined Coupling Slots

H. M. El Misilmani¹, M. Al-Husseini², and K. Y. Kabalan¹

¹ECE Department, American University of Beirut, Lebanon

²BRIC, Lebanese Center for Studies and Research, Lebanon
hilal.elmisilmani@ieee.org

Abstract— A simple procedure for the design of two-dimensional SWA array systems with desired sidelobe level ratio (SLR) is presented. The described procedure finds the slots length, width, locations and displacements from the centerline, for each branch waveguide. For a specified number of branch waveguides, the method also finds the rotation angle of each of the coupling slots. To explain the controllable SLR, two 2D SWA array systems designed for an SLR higher than 20 dB are illustrated and compared.

Slotted Waveguide Antennas (SWAs) radiate energy through slots cut in a broad or narrow wall of a rectangular waveguide. They offer clear advantages in terms of their design, weight, volume, power handling, directivity, and efficiency. For broad-wall SWAs, the slot displacements from the wall centerline determine the antenna's sidelobe level (SLL). In addition, the rotation angle of the coupling slot in a 2D system array of SWAs determines the power fed by each slot into each branch-line SWA. Inclined coupling slots have found their interest as the radiating elements used in the main feeder to couple the power to the SWA branch-lines in two-dimensional (2D) SWA array systems. Based on the procedure described by Elliott and Stevenson in [1, 2, 3], Bhatti *et al.* designed a planar slotted waveguide array antenna for X-band radar applications having a diamond shape[4].

In comparison to the previous work done, this paper presents a simple procedure for the design of a two-dimensional (2D) SWA array system with a desired sidelobe level ratio (SLR), and study the effect of having a diamond shape array system. The system proposed here consists of multiple branchline waveguides with broadwall radiating shunt slots, designed as per the guidelines described by the author in [5]. A main waveguide is used to feed the branch waveguides through a series of inclined coupling slots with well-defined rotation angles for low SLLs. For a specified number of identical longitudinal slots, the described procedure finds the slots length, width, locations along the length of the waveguide, and displacements from the centerline, for each branch waveguide. Furthermore, for a specified number of branch waveguides, the method finds the rotation angle of each of the coupling slots. To explain the controllable-sidelobe 2D SWA design procedure, two 2D SWA array designs are studied. An SWA with 8×8 elliptical slots, designed for an SLL lower than -20 dB, is taken as an example. An 8-element 1D SWA with a desired SLL is designed first. Eight identical such SWAs are then attached side by side in the first design. The proper design of the 1D SWAs ensures having the desired SLL in one principal plane. To enforce the same SLL over the whole 3D pattern, special care should be given to the design of the feed SWA, whose slots should power the radiating SWAs according to a correct distribution. For the taken example, the feed SWA should have 8 slots, separated consecutively by a distance related to the radiating SWA aperture width and wall thickness. The power fed by each slot in the feeder and fed to the branchline waveguide is controlled by the inclination angle of the coupling slot. The second design varies the design of the SWA branchlines and slots displacements and studies the comparison between the illustrated examples. The simulations results for both designs are reported and compared.

Designs 1 and 2 are shown in Figure 1, they both operate at a frequency of 4.021 GHz. The gain pattern comparison of the three designs are shown in Figure 2, with a detailed comparison listed in Table 1. As inspected, Designs 1 and 2 both achieve very low SLRs in both E- and H-planes compared to the uniform case. Studying the effect of having a planar diamond shape in Design 2, proposed in the literature such in [4], different observations have been depicted. For instance, Design 2 achieved better results in terms of SLR in H-plane, however, Design 1 outperforms Design 2 in terms of SLR in E-plane, and HPBW in both planes, and total gain. Hence, no valuable improvements have been seen as a result of using such diamond configurations. Nevertheless, the

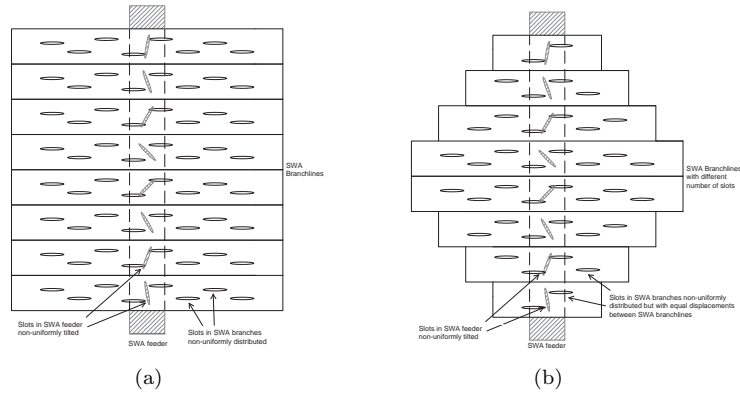


Figure 1: 2D Systems, (a) Design 1, (b) Design 2.

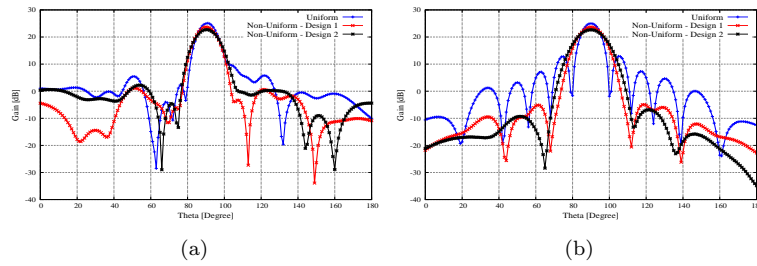


Figure 2: Compared gain pattern results of the uniform and non-uniform displacements and rotation angles Design 1 and Design 2 cases: (b) E-plane, (c) H-plane.

Table 1: Compared HPBW and SLR results of uniform case, Design 1 and Design 2 array designs

System	E-plane		H-plane		Gain (dB)
	HPBW ($^{\circ}$)	SLR (dB)	HPBW ($^{\circ}$)	SLR (dB)	
Design 1	10.2	22.5	12.6	28.8	23.7
Design 2	11.1	20.4	14.9	32	22.7
Uniform	7.9	19.6	9.2	12.3	25

increment of HPBW in the proposed designs here is higher than that of the uniform, and this is normal because of the decrement in the SLL values. Hence, in this paper, a simple design procedure for 2D SWA arrays with desired SLRs have been illustrated using non-uniform inclined coupling slots in the main feeder, and longitudinal shunt slots in the radiating branches. The two example illustrated resulted in SLR values of higher than 20 dB.

REFERENCES

1. Elliott, R. S., "An improved design procedure for small arrays of shunt slots," *IEEE Trans. Antennas Propagat.*, Vol. 31, 48–53, 1983.
2. Elliott, R. S., *Antenna theory and Design. Revised Edition.*, John Wiley & sons, 2003.
3. Stevenson, A. F., "Theory of slots in rectangular waveguides," *Journal of Applied Physics*, Vol. 19, pp. 24–38, 1948.
4. Bhatti, R. A., B.-Y. Park, Y.-T. Im, and S.-O. Park, "Design of a planar slotted waveguide array antenna for X-band radar applications," *Journal of the Korean Institute of Electromagnetic Engineering and Science*, Vol. 11, No. 2, 97–104, 2011.
5. El Misilmani, H. M., M. Al-Husseini, and K. Y. Kaban, "Design of slotted waveguide antennas with low sidelobes for high power microwave applications," *Progress In Electromagnetics Research C*, Vol. 56, pp. 15–28, 2015.

Simple Design Method for Dielectric-Filled Low-Sidelobe Slotted Waveguide Antennas

M. Al-Husseini^{1,2}, H. M. El-Misilmani², K. Y. Kabalan², A. El-Hajj², and E. Nassar³

¹Beirut Research and Innovation Center, Lebanese Center for Studies and Research, Lebanon

²Electrical and Computer Engineering Department, American University of Beirut, Lebanon

³Electrical, Computer and Communication Engineering Department, Notre Dame University, Lebanon
husseini@ieee.org

Abstract— A simple method for the design of dielectric-filled slotted waveguide antennas (SWAs) with sidelobes below a prescribed level is presented. The existing methods mostly deal with vacuum or air-filled SWAs and resort to numerical techniques or to already available design graphs to deduce the different lengths and positions of the slots. This presented method is based on slots with identical dimensions and uses closed-form equations to compute the uniform length of the slots, their distances from the waveguide's ends, and their offsets from the center line of the waveguide's broad face. The offsets are first computed for a larger air-filled SWA and then scaled for the SWA under design. Examples are given to show the proper operation of the presented design method.

Slotted Waveguide Antennas (SWAs) have been ideal solutions for applications such as radar, communications, and navigation. They benefit from a simple design, since their radiating elements (the slots) are an integral part of the feed system (the waveguide itself), and have the advantages of relatively low weight and small volume, high power handling, high efficiency, and good reflection coefficient [1]. The design of resonant vacuum or air-filled rectangular SWAs is usually based on the use of the graphs produced in 1951 by Stegen for X-band SWAs [2], or on numerical techniques, such as the Method of Moments (MoM). The design goal is to find the slots lengths and offsets to obtain a desired radiation pattern. The design procedure by Elliott [3] computes these slots lengths and offsets after setting the following guidelines: 1) the waveguide is short-circuited at a distance of a quarter-guide wavelength ($\lambda_g/4$) from the center of the last slot, and the inter-slot distance is $\lambda_g/2$.

An advantage of filling a waveguide with a dielectric material is the lowering of its cut-off frequency thus enabling it to operate at a smaller frequency. The cut-off frequency of a dielectric-filled waveguide having a large internal dimension a is given for the TE_{10} mode by:

$$f_{c(10)} = \frac{c}{2a\sqrt{\epsilon_r}}, \quad (1)$$

where c is the speed of light in vacuum, and ϵ_r is the dielectric constant of the material filling the waveguide. The guide wavelength inside a dielectric-filled waveguide is given by:

$$\lambda_g = \frac{1}{\sqrt{\frac{\epsilon_r}{\lambda_0^2} - \frac{1}{4a^2}}}, \quad (2)$$

where λ_0 is the free-space wavelength at the frequency of propagation.

Given a dielectric-filled SWA with N slots, where the SWA is shorted at one end and fed at the other end, the center of the first slot is at $n_1\lambda_g/2$ from the feed, and the center of the last slot is at $n_2\lambda_g/4$ from the shorted end, where n_1 and n_2 are integers ≥ 1 , and n_2 is odd. The distance between consecutive slots is $\lambda_g/2$ center to center. λ_g is as given in Eq. 2. These are equivalent to the guidelines in Elliott's procedure. The uniform length of the slots is given by:

$$L = 0.98 \times \frac{\lambda_0}{\sqrt{2(\epsilon_r + 1)}}. \quad (3)$$

To find the offsets of the slots, they first have to be computed for a virtual vacuum or air-filled SWA, which can support the same operation frequency, using the method detailed in [4]. Denoting

the offset of the n^{th} slot of the virtual SWA by d_{vn} , the offset of the corresponding slot in the dielectric-filled SWA under design will be equal to

$$d_n = d_{vn} \times \frac{a}{a_v}, \quad (4)$$

where a_v is the larger inner dimension of the waveguide making the virtual SWA. The virtual SWA should be designed for the same number of slots, and same desired sidelobe level ratio and distribution as the dielectric-filled SWA.

As an example, consider the design of an SWA with 10 rectangular slots based on a WR-284 waveguide filled with a dielectric material having $\epsilon_r = 2.2$. The SWA is to be operated at 2.45 GHz. The virtual SWA uses a vacuum or air-filled WR-340 waveguide, since an air-filled WR-284 is not operable at 2.45 GHz. Hence, $a = 2.84''$ and $a_v = 3.4''$. λ_g is computed from Eq. 2 for the dielectric-filled SWA. The 1st slot is positioned at $\lambda_g/2$ from the feed, and the 10th slot at $3\lambda_g/4$ from the shorted waveguide end. From Eq. 3, the length of each slot is 47.4 mm. The width of each slots is taken as 5 mm. For a sidelobe level ratio $\leq -20\text{dB}$, a 35-dB Chebyshev distribution is applied, as explained in [4], to obtain the d_{vn} 's of the virtual WR-340-based SWA. The d_{vn} 's and the corresponding d_n 's, computed from Eq. 4, are given in Table 1.

n	1	2	3	4	5	6	7	8	9	10
d_{vn} (mm)	6.22	-9.11	12.10	-14.51	15.88	-15.88	14.51	-12.10	9.11	-6.22
d_n (mm)	5.19	-7.61	10.11	-12.12	13.26	-13.26	12.12	-10.11	7.61	-5.19

Table 1: Offsets of the slots in the virtual air-filled SWA and dielectric-filled SWA

For the resulting SWA, the reflection coefficient and the H -plane gain pattern are plotted in Fig. 1. The plots show the soundness of the presented method. Compared to the uniform-offset case, the designed antenna also operates at 2.45 GHz and has very low sidelobes (more than 20 dB below the level of the main lobe). The back lobe is also lower in magnitude.

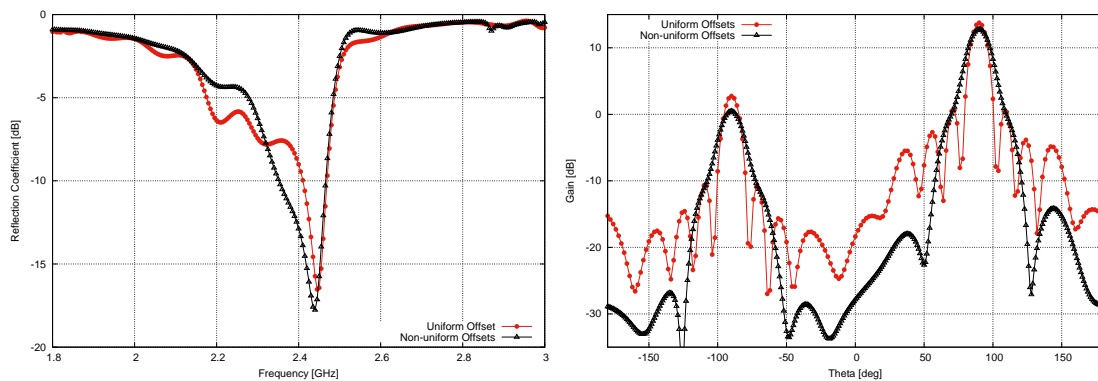


Figure 1: (Left) S_{11} plots and (right) H -plane gain patterns of the uniform- and nonuniform-offset cases

ACKNOWLEDGMENT

This work is partially supported by an Associated Research Unit (ARU) fund from the Lebanese National Council for Scientific Research.

REFERENCES

1. Mailloux, R. J., *Phased Array Antenna Handbook*, Artech House, 2005.
2. Stegen, R. J., "Longitudinal Shunt Slot Characteristics," Hughes Technical Memorandum No. 261, Culver City, CA, November 1951.
3. Elliott, R. S. and W. R. O'Loughlin, "The Design of Slot Arrays Including Internal Mutual Coupling," *IEEE Trans. Antennas Propagat.*, Vol. 34, 1149–1154, September 1986.
4. El Misilmani, H. M., M. Al-Husseini, and K. Y. Kabalan, "Design of Slotted Waveguide Antennas with Low Sidelobes for High Power Microwave Applications," *Progress In Electromagnetics Research C*, Vol. 56, 15–28, 2015.

Interesting Combinations of Phase and Group Velocities in the Transmission Line Negative Delay Metamaterials Explained by the Forward-Transmission-Matrix (FTM) Method

O. Siddiqui^{1*}

¹College of Engineering, Taibah University, Madinah, Saudi Arabia

*corresponding author : omarsiddiqui2@gmail.com

Abstract- A Negative delay metamaterial (NDMM) consists of a left-handed transmission line structure periodically loaded with a parallel RLC resonator. In this paper we analyze the NDMMs by employing the Forward-Transmission-Matrix (FTM) technique. It has been shown that the NDMMs demonstrate several interesting combinations of phase and group velocities. The relation between phase and group velocities is explained in frequency domain by generating Brillouin diagram and transmission coefficient plots. In time domain, the propagation behavior is shown by Gaussian pulse propagation simulations.

Keywords: *Left-handed transmission Lines, Negative delay, Negative Group velocity, Forward-Transmission-Matrix Method, Modified Kirchhoff's Current Rule, Metamaterials*

The negative delay metamaterials (NDMMs) are constructed by loaded a left-handed structure with a parallel RLC resonator, as shown in Fig. 1. The NDMMs possess a simultaneous negative phase and negative group delays [1]. In this paper, we present the microwave nodal analysis of the transmission line Negative Delay Metamaterials (NDMMs) which is performed by done by solving the Krichhoff's Current equations that are modified for high frequency circuits. Since the electromagnetic wave propagation is taken into account, the presented technique can be used to explain various interesting dispersive behaviors of the NDMMs in time and frequency domains. As depicted in Fig. 2, the NDMMs can possess very interesting behaviors of phase and group velocities over different frequency ranges on account of their strong dispersive properties. In particular, the phase and group velocities can become contra-directional and simultaneously negative. Moreover, it has been shown that a phenomenon analogous to Quantum wave tunneling can also take place in the NDMMs.

Keywords: Forward-Transmission-Matrix (FTM) Method, Node Voltage Analysis, Modified Kirchhoff's Current Rule, Forward Transmission Matrix, ABCD matrix, Metamaterials, Left-handed Lines, Negative group delay, negative phase delay, negative group velocity.

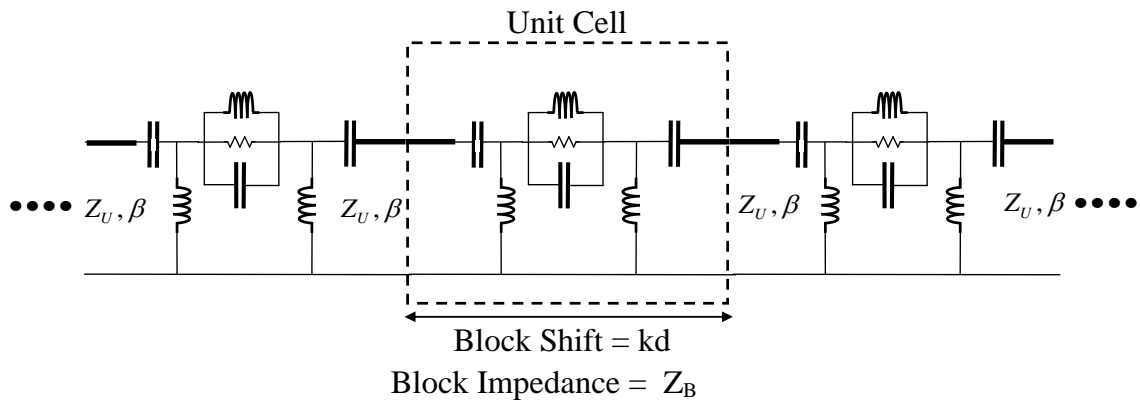


Figure 1: The negative delay metamaterial consists of a Left-handed transmission line periodically loaded with a parallel RLC resonator

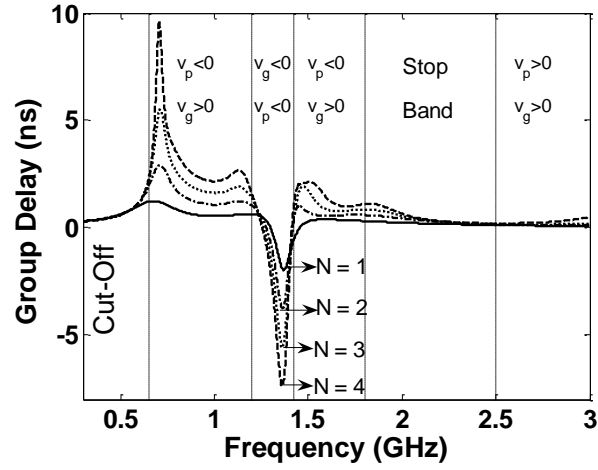


Figure 2: (a) The Phase and group Velocity relations in various frequency bands for truncated NDMMs that consist of different number of unit cells N .

REFERENCES

1. Siddiqui, O., Mojahedi, M., Eleftheriades, GV (2003), Periodically loaded transmission line with effective negative refractive index and negative group velocity, *IEEE Trans. on Antenn. and Propag.*, (51) 2619 – 2625

Performance Enhancement of Proximity Coupled Patch Antenna Using Fishnet Metamaterial

A. Yilmaz^{1*}, and C. Sabah²

¹KTO Karatay University, Department of Electrical and Electronics Engineering, Konya, Turkey

²Middle East Technical University, Northern Cyprus Campus, Department of Electrical and Electronics Engineering, Kalkanli, Guzelyurt, TRNC, Turkey

*corresponding author: adem.yilmaz@karatay.edu.tr

Abstract-This paper investigates the performance improvements of proximity coupled patch antenna by using metamaterial. The designed antenna is covered with metamaterial and a wider bandwidth is obtained. Also, dual mode response of antenna is obtained when using metamaterial.

A microstrip patch antenna consists of a dielectric substrate, where one side is covered with a ground plane and other side hosts a radiating patch. However, these antennas exhibit narrow bandwidth and bandwidth enhancement is crucial for most of applications. In order to obtain a wider bandwidth, a proximity coupled patch antenna (PCPA) covered with metamaterial (MTM) is proposed in this study.

A PCPA has two dielectrics, where radiating patch of desired geometrical shape is on one side of a dielectric substrate material and a feeding and ground plane are on each face of the other dielectric substrate. A PCPA, which operates at 2.4 GHz, is designed on FR4 substrates. As a MTM cover, previously proposed fishnet MTM design [2] is optimized and placed at top of the PCPA. The numerical results indicate that MTM cover enhances bandwidth of the PCPA with an insignificant shifting of resonance frequency, which is due to capacitive loading of MTM itself. Moreover, MTM design is modified in order to obtain a dual mode response of PCPA. The numerical results imply that MTM cover can alter the response of antenna successfully.

According to our best knowledge, PCPA covered with MTM has never been studied before. The numerical studies show that PCPA performance can be improved when a proper MTM design is applied to antenna. The numerical results will be supplied in full paper.

REFERENCES

1. Pozar, D. M. "Microstrip antennas," *Proceedings of the IEEE*, January 1992, 79-91.
2. Yilmaz, A. and C. Sabah, 'Diamond-shaped hole array in double-layer metal sheets for negative index of refraction,' *JEMWA*, Vol. 27, No. 4, 413-420, 2013.

Performance Evaluation of Conventional and Planar Feeds in Resonant Cavity Antennas

Arslan kiyani, Raheel M. Hashmi, Karu P. Esselle

Centre for Collaboration in Electromagnetic and Antenna Engineering
 Department of Engineering, Macquarie University
 Sydney, NSW 2109, Australia

*corresponding author, E-mail: arslan.kiyani@mq.edu.au

Abstract

A simple and planar feeding approach is evaluated for use in wideband Resonant Cavity Antennas (RCAs). Boresight directivity performance of the planar (aperture-coupled dual slot) and a conventional feeding technique (waveguide-fed slot) are investigated by placing each under an unprinted all-dielectric single-layer superstrate with transverse permittivity in lateral dimensions. The well-matched printed feed antenna is shown to achieve a peak directivity of 17 dBi over a wide 3dB directivity bandwidth of 16.2%. This type of planar feeding configuration is effective, particularly for the design of RCA arrays, to reduce the design complexities and fabrication cost.

1. Introduction

Given the progress towards future smart-wireless communication systems, Resonant Cavity Antennas (RCAs) have attracted significant research focus owing to their simple configuration, planar profile and extremely directive radiation nature [1]. Recently, these antennas are being viewed as the emerging candidates for use in satellite reception, short-range to medium-range directional communications, as well as for various millimeter-wave applications.

Rigorous research has led to the development of simple and wideband RCAs, which are capable of achieving directivities in the range of 15-20 dBi with excellent bandwidth exceeding 20% [2-6]. Despite excellent performance of these wideband RCAs, a major limitation prevails is their feeding mechanism. In order to achieve a wide 3dB gain-bandwidth in RCAs, it is imperative that the 3dB directivity-bandwidth of a particular RCA (often associated with the superstrate) is complemented by an equally wide impedance bandwidth (often associated with the feed). For this purpose most of the RCAs proposed recently rely on waveguide-based feeds, since they can support a wide bandwidth of operation. In this paper, we compare the performance of a planar dual aperture-coupled slot feed [7] with a wideband waveguide-fed slot feed. The key advantage of such a planar feeding approach is its flexibility of planar printed design, which is not only significantly cost effective than waveguide feeding but also reduces the overall height of the antenna. Moreover, such planar feeds allows for increased design scalability such as in case of compact wideband arrays of RCAs, where printed feeds are essential for use with a feeding network [8].

2. Design and Feed Antenna Specifications

In order to compare the performance of the two feed antennas judiciously, let us use a simple wideband RCA with a dielectric superstrate. This RCA is fed one by one using each feed antenna, and the performance is compared in the next section. The proposed configuration is shown in Fig. 1. The single-layer dielectric superstrate has a radius (R) of $1.15\lambda_{low}$ and its thickness (t) is 5.3 mm. The superstrate is suspended at a height (h) of $0.5\lambda_{low}$ above the metallic ground plane as shown in the Fig. 1. The wideband superstrate [9] is radially divided into three sections of equal widths and their dielectric constants from the innermost section to the outermost section are 9.8, 6.15 and 3.38, respectively.

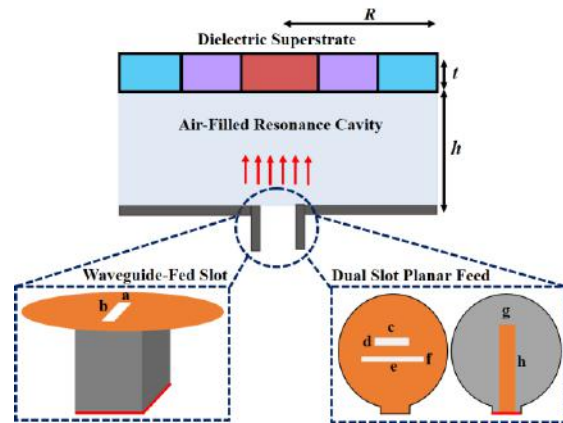


Figure 1: Configuration of the two feeds in a wideband RCA

Table 1: Waveguide-Fed Slot and Aperture Coupled Dual Slot Feed Antenna Dimensions

Waveguide-Fed Slot Antenna	Dual Slot Feed Antenna		
Slot (mm)	Slot1 (mm)	Slot2 (mm)	Transmission Line (mm)
a=4	c=5	e=13	g=3
b=7.5	d=1	f=1	h=20.41

The two feeding methods used, i.e. waveguide-fed slot and dual aperture-coupled slot, are also shown in Fig. 1. The detailed dimensions of each of these feeds are given in Table I. It can be seen from Fig. 1 that a single slot is made in the ground plane and it is fed by a WR-42 waveguide to coax

adaptor. Alternatively, the dual slot is etched on a 0.787 mm thick Rogers 5880 substrate, fed by a 50Ω transmission line. The use of dual aperture-coupled slot reduces the height of the RCA by approximately $0.6\lambda_{low}$, as compared to the waveguide-fed slot.

3. Numerical Results

Full wave simulations for both the cases discussed above were conducted in CST Microwave Studio. Fig. 2 compares the boresight directivity for each of the feeding configuration. It can be seen from Fig. 2 that, the waveguide-fed slot predicts a peak directivity of 18.6 dBi with 3dB directivity-bandwidth of more than 20%. For the dual aperture-coupled slot, the directivity reaches a maximum of 17 dBi along with a 3dB directivity bandwidth of 16.2%. Fig. 3 shows the far-field radiation patterns at 22.5 GHz in both *E*- and *H*-plane respectively.

The results predicts an approximate difference of 1.6 dBi in the maximum directivity for the two feeds. The difference is caused by the fact that the waveguide induces minimal losses as it is filled with air, whereas the printed feed is more prone to increased losses within the dielectric material. In addition, considering the small size of the ground plane, the printed transmission line may give rise to spurious radiation, which reduce the coupling of electromagnetic energy to the cavity, thereby reducing boresight directivity of the RCA. It is envisaged that this undesired radiation can be reduced by using a strip-line feed instead of a microstrip transmission line.

4. Conclusion

The performance of dual aperture-coupled slot feed is compared with conventional waveguide-fed slot feed when used in wideband RCAs. Dual slot planar feed antenna was shown to achieve $0.6\lambda_{low}$ RCA height reduction as compared to waveguide-fed slot. It also exhibits a peak directivity of 17 dBi with 3dB directivity bandwidth of 16.2%. The planar feeding technique addressed few limitations associated with the waveguide-fed slot by reducing the overall antenna profile and is cost effective. Moreover, it is well suited for the sparse arrays or switched-polarization array configurations.

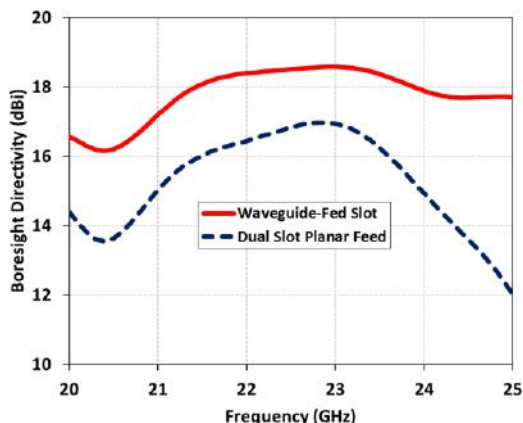
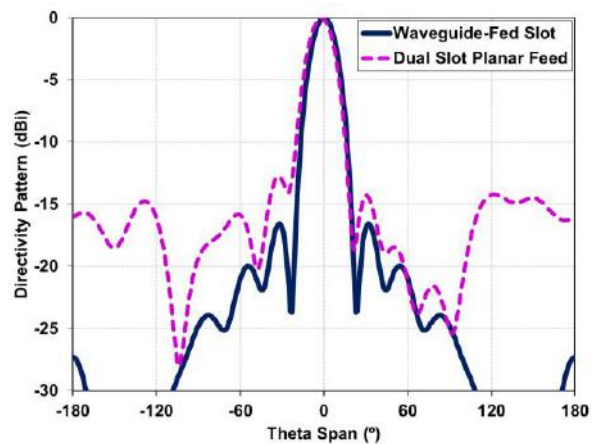
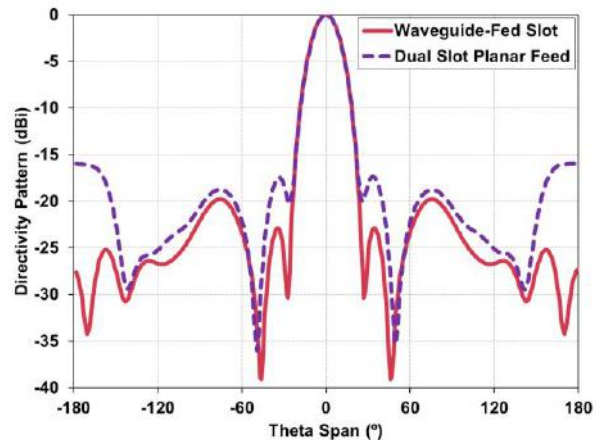


Figure 2: Comparison of boresight directivity for the two feedings methods



(a)



(b)

Figure 3: Normalized radiation patterns of the RCA with the two feeds (a) *E*-plane at 22.5 GHz (b) *H*-plane at 22.5 GHz

References

- [1] Y. J. Lee, J. Yeo, R. Mittra and W. S. Park, Application of electromagnetic bandgap (EBG) superstrates with controllable defects for a class of patch antennas as spatial angular filters, *IEEE Transactions on Antennas and Propagation*, vol. 53, no. 1, pp. 224-235, 2005.
- [2] Y. Ge, K. P. Esselle and T. S. Bird, The use of simple thin partially reflective surfaces with positive reflection phase gradients to design wideband, low-profile EBG resonator antennas, *IEEE Transactions on Antennas and Propagation*, vol. 60, no. 2, pp. 743-750, 2012.
- [3] R. M. Hashmi, B. A. Zeb, and K. P. Esselle, Wideband high-gain EBG resonator antennas with small footprints and all-dielectric superstructures, *IEEE Transactions on Antennas and Propagation*, vol. 62, no. 6, pp. 2970-2977, 2014.
- [4] K. Konstantinidis, A. P. Feresidis and P. S. Hall, Broadband sub-wavelength profile high-gain antennas based on multilayer metasurfaces, *IEEE Transactions on Antennas and Propagation*, vol. 63, no. 1, pp. 423-427, 2015.
- [5] B. A. Zeb, R. M. Hashmi and K. P. Esselle, Wideband gain enhancement of slot antenna using one unprinted dielectric superstrate, *Electronics Letter*, vol. 51, no. 15, pp. 1146-1148, 2015.
- [6] A. A. Baba, R. M. Hashmi and K. P. Esselle, Wideband gain enhancement of slot antenna using superstructure

- with optimised axial permittivity variation, *Electronics Letter*, 2016.
- [7] K. Konstantinidis, A. P. Feresidis and P. S. Hall, Dual-slot feeding technique for broadband Fabry-Perot cavity antennas, *IET Microwaves, Antennas and Propagation*, pp. 861-866, 2015.
 - [8] R. H. Hashmi and K. P. Esselle, Arrays of high aperture efficiency wideband EBG resonator antennas, *International Conference on Electromagnetics in Advanced Applications (ICEAA)*, 2015.
 - [9] R. M. Hashmi and K. P. Esselle, A class of extremely wideband resonant cavity antennas with large directivity-bandwidth products, *IEEE Transactions on Antennas and Propagation*, 2015.

Diffraction by a Lossless Dielectric Wedge on a Ground Plane: Time Domain Formulas

Marcello Frongillo¹, Gianluca Gennarelli², Giovanni Riccio^{1*}

¹D.I.E.M. – University of Salerno, Via Giovanni Paolo II 132, 84084 Fisciano (SA), Italy

²I.R.E.A. – C.N.R., Via Diocleziano 328, 80124 Naples, Italy

*corresponding author, E-mail: griccio@unisa.it

Abstract

Easy to handle expressions are proposed for evaluating the time domain diffraction coefficients associated to plane waves impacting a structure consisting of a tapered lossless dielectric wedge on a perfectly conducting surface. They are determined by applying the inverse Laplace transform to the Uniform Asymptotic Physical Optics diffraction coefficients in the frequency domain. No closed form solutions exist for the considered time domain problem.

1. Introduction

Ultra wide band communication and radar systems make research activities on transient electromagnetic scattering very attractive. Analytical techniques exist for solving scattering problems concerning a limited number of perfectly conducting (PEC) structures excited by an electromagnetic pulse (see [1]-[5] as reference). In this framework, the time domain (TD) version of the uniform geometrical theory of diffraction (UTD) [3]-[5] furnishes a simple physical representation for radiation and scattering phenomena since it uses the same rays (incident, reflected and diffracted contributions) as the frequency domain (FD-UTD) one [6]. The TD expressions are obtained by applying analytical transformations to the FD-UTD solutions.

Diffraction by dielectric wedges is a stimulating problem and closed form expressions are not available for evaluating the TD diffraction coefficients. The solutions to the canonical problems tackled in [7]-[9] are exceptions. They were obtained by applying the approach proposed in [3] to the corresponding frequency domain Uniform Asymptotic Physical Optics (FD-UAPO) diffraction coefficients [10]-[12]. The transient diffracted field originated by an arbitrary function plane wave was then evaluated via a convolution integral. The TD-UAPO formulation has the same advantages and limitations of the TD-UTD one. In addition, it retains the FD-UAPO limitations arising from a PO approximation of the electric and magnetic equivalent surface currents located on the internal and external faces of the wedge-shaped dielectric region. Anyway, the TD-UAPO approach is the only one able to offer analytical wave solutions to TD diffraction problems involving penetrable dielectric wedges with arbitrary apex angle.

The goal of this paper is to provide expressions of the TD-UAPO diffraction coefficients to be used for evaluating the transient diffracted field due to an arbitrary function plane wave impacting a structure formed by a tapered lossless dielectric wedge on a PEC ground plane. The junction is excited by E -polarized plane waves impinging at normal incidence with respect to the edge (see Fig.1), so that a two dimensional problem is considered. According to [3] and [7]-[9], the goal is attained by applying the inverse Laplace transform to the corresponding FD-UAPO diffraction coefficients. They have been determined by the authors in [13], where two separate diffraction problems relevant to the dielectric (internal) region and the surrounding space (external region) have been solved. For each observation domain, electric and magnetic equivalent PO surface currents have been located on the free-space/dielectric interface, and electric PO surface currents have been placed on the PEC ground plane. The surface radiation integrals using these sources have been assumed as starting point and manipulated for obtaining integrals able to be solved by means of the Steepest Descent Method and the Multiplicative Method. A UTD-like solution has been so obtained for the diffraction contribution due to each interface forming the boundary of the considered observation region.

2. The diffraction problem

A lossless non-magnetic wedge-shaped dielectric is placed on a PEC ground plane (see Fig. 1). Its apex angle α is less than 90° . The dielectric is characterized by the relative permittivity ϵ_r and the propagation constant $k_d = k_0 \sqrt{\epsilon_r}$, k_0 being the free-space wavenumber. The angle ϕ' controls the incidence direction of E -polarized plane waves ($\phi' = \alpha$ corresponds to the grazing incidence with respect to free-space/dielectric interface S_0). The corresponding FD-UAPO diffraction coefficients at the observation point $P(\rho, \phi)$ have been evaluated in [13] by considering two regions: the acute-angled dielectric wedge (internal region) and the surrounding space (external region). Note that the values assumed by α and ϕ' avoid the illumination of S_0 by reflection rays from the PEC surface and vice-versa.

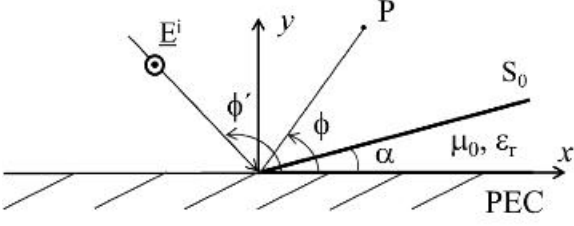


Figure 1: Geometry of the problem.

3. TD-UAPO diffracted field

The approach for obtaining the TD-UAPO diffraction coefficients d is that adopted in [7]-[9] and uses the inverse Laplace transform applied to the FD-UAPO diffraction coefficients determined in [13]. Note that the wedge permittivity is assumed independent on the frequency.

3.1. Internal region ($0 < \phi < \alpha$)

$$d^{in} = d_{S_0}^{in} + d_{S_{PEC}}^{in} \quad (1)$$

$$d_{S_0}^{in} = \frac{T_0}{2\sqrt{2\pi}} \left[\sin(\phi - \alpha) - \cos\theta_0^t \right] \times \frac{G\left(2\rho \cos^2\left(\frac{(2\pi - \phi + \alpha) + (\theta_0^t + \pi/2)}{2}\right), t\right)}{\cos(\phi - \alpha) + \cos(\theta_0^t + \pi/2)} + \sum_{\substack{m=1 \\ m \text{ even}}}^M \frac{G\left(2\rho \cos^2\left(\frac{(2\pi - \phi + \alpha) + (\theta_m^i + \pi/2)}{2}\right), t\right)}{\cos(\phi - \alpha) + \cos(\theta_m^i + \pi/2)} \times (-1)^{m/2} \left[(1 + R_m) \sin(\phi - \alpha) + (1 - R_m) \cos\theta_m^i \right] \prod_{\substack{p=1 \\ p \text{ even}}}^{m-1} R_p \quad (2)$$

$$d_{S_{PEC}}^{in} = \frac{T_0}{\sqrt{2\pi}} \sum_{\substack{m=1 \\ m \text{ odd}}}^M \prod_{\substack{p=1 \\ p \text{ even}}}^{m-1} R_p \times$$

$$(-1)^{(m-1)/2} \cos\theta_m^i \frac{G\left(2\rho \cos^2\left(\frac{(\phi - 2\pi) + (\theta_m^i + \pi/2)}{2}\right), t\right)}{\cos\phi + \cos(\theta_m^i + \pi/2)} \quad (3)$$

where $\theta_0^t = \sin^{-1}(\sin\theta_0^i/\sqrt{\epsilon_r})$, θ_0^i being the incidence angle with respect to S_0 , $M = \text{Int}[(\pi/2 - \theta_0^t)/\alpha]$, $\theta_m^i = m\alpha + \theta_0^t$,

$$T_0 = \frac{2\cos\theta_0^i}{\cos\theta_0^i + \sqrt{\epsilon_r} \cos\theta_0^t} \quad (4)$$

$$R_p = \frac{\sqrt{\epsilon_r} \cos\theta_p^i - \cos\theta_p^t}{\sqrt{\epsilon_r} \cos\theta_p^i + \cos\theta_p^t} \quad (5)$$

θ_p^t being the transmission angle at the p -th interaction, and

$$G(X, t) = \frac{X}{\sqrt{\pi ct}(t + X/c)} \quad (6)$$

3.2. External region ($\alpha < \phi < \pi$)

$$d^{ext} = d_{S_0}^{ext} + d_{S_{PEC}}^{ext} \quad (7)$$

$$d_{S_0}^{ext} = \frac{1}{2\sqrt{2\pi}} \left\{ \left[(1 - R_0) \sin(\phi' - \alpha) - (1 + R_0) \sin(\phi - \alpha) \right] \frac{G\left(2\rho \cos^2\left(\frac{(\phi - \alpha) + (\phi' - \alpha)}{2}\right)\right)}{\cos(\phi - \alpha) + \cos(\phi' - \alpha)} + \left. \begin{aligned} & -T_0 \sum_{\substack{m=1 \\ m \text{ even}}}^M (-1)^{m/2} T_m \left[\sin(\phi - \alpha) + \cos\theta_m^t \right] U(\theta_c - \theta_m^i) \times \\ & \prod_{\substack{p=1 \\ p \text{ even}}}^{m-1} R_p \frac{G\left(2\rho \cos^2\left(\frac{(\phi - \alpha) + (\theta_m^t + \pi/2)}{2}\right)\right)}{\cos(\phi - \alpha) + \cos(\theta_m^t + \pi/2)} \end{aligned} \right\} \quad (8)$$

$$d_{S_{PEC}}^{ext} = \frac{\sin\phi'}{\sqrt{2\pi}} \frac{G\left(2\rho \cos^2\left(\frac{(\pi - \phi) + (\pi - \phi')}{2}\right)\right)}{\cos(\pi - \phi) + \cos(\pi - \phi')} \quad (9)$$

where $U(\theta) = 1$ if $\theta > 0$ and $U(\theta) = 0$ elsewhere, θ_c is the internal critical angle and

$$R_0 = \frac{\cos\theta_0^i - \sqrt{\varepsilon_r} \cos\theta_0^t}{\cos\theta_0^i + \sqrt{\varepsilon_r} \cos\theta_0^t} \quad (10)$$

$$T_p = \frac{2\sqrt{\varepsilon_r} \cos\theta_p^i}{\sqrt{\varepsilon_r} \cos\theta_p^i + \cos\theta_p^t} \quad (11)$$

The above expressions can be used for calculating the TD electric field diffracted in each observation region by means of the following integral:

$$e^d(P,t) = \frac{1}{\sqrt{\rho}} \int_{t_0}^{t-\rho/c} d\left(t - \frac{\rho}{c} - \tau\right) e^i(Q,\tau) d\tau \quad (12)$$

with $t - \rho/c > t_0$. The forcing function is the incident field e^i at the diffraction point Q and c is the speed of light in the considered observation region.

4. Numerical results

The TD field behavior is analyzed in the following examples. The considered wedge is characterized by $\varepsilon_r = 2$ and $\alpha = 15^\circ$, and the incidence direction is $\phi' = 110^\circ$. Figure 2 shows the electric field arriving at $P(3m, 20^\circ)$. In order of arrival, it is possible to identify the Geometrical Optics (GO) contributions (solid line), i.e., incident, specular reflection by S_0 (SRS0), transmission-reflection-transmission (TRT) waveforms, and the diffraction one (dashed line). The specular reflection contribution due to S_{PEC} (SRPEC) is not present since the corresponding boundary is at $\phi = 70^\circ$. Figures 3 and 4 show the contributions arriving at observation points very close to the TRT shadow boundary ($\phi = 53.6^\circ$). Note that the incident field is not displayed since it arrives at P before reaching Q ($t = 0$). The diffraction and TRT waveforms arrive together

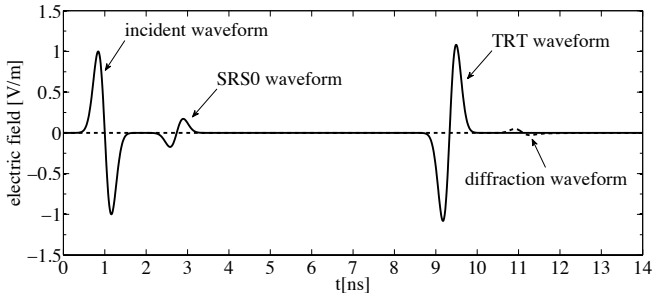


Figure 2: Electric field at $P(3m, 20^\circ)$.

at $P(3m, 53^\circ)$, but they possess opposite positivity (see Fig. 3). The TRT contribution vanishes when crossing the boundary and the positivity of the diffraction contribution changes (see Fig. 4).

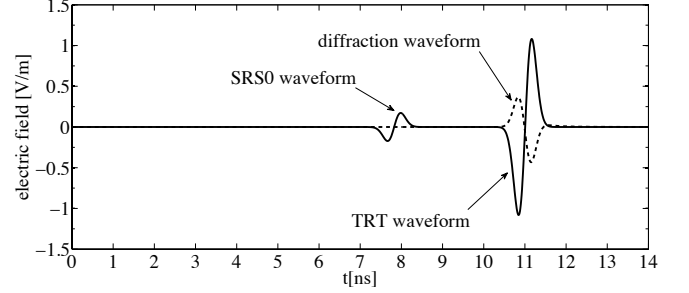


Figure 3: Electric field at $P(3m, 53^\circ)$.

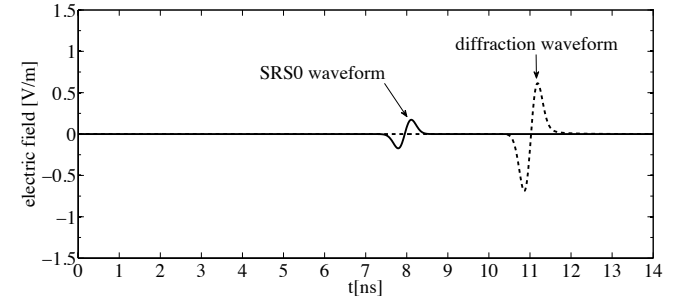


Figure 4: Electric field at $P(3m, 54^\circ)$.

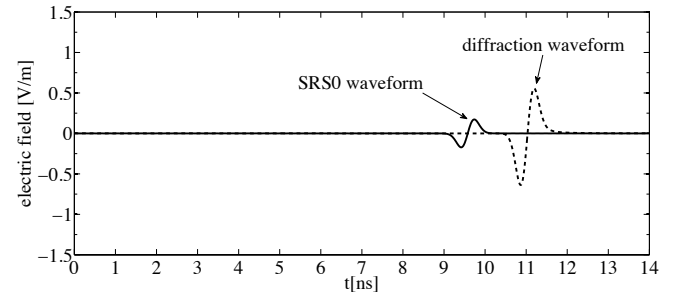


Figure 5: Electric field at $P(3m, 69^\circ)$.

5. Conclusions

Easy to handle TD-UAPO diffraction coefficients have been derived for evaluating the TD diffracted electric field in the free-space surrounding the structure, as well as within the lossless wedge-shaped dielectric. To the authors' knowledge, no other closed form expressions are available in literature.

References

- [1] P.M. Johansen, Time-domain version of the physical theory of diffraction, *IEEE Trans. Antennas Propag.* 47: 261–270, 1999.
- [2] C.G. Rego, F.J.V. Hasselmann, A Time-domain uniform asymptotic theory applied to the analysis of pulse-excited PEC wedges, *IEEE Antennas Wireless Propag. Lett.* 10: 955–958, 2011.
- [3] T.W. Veruttipong, Time domain version of the uniform GTD, *IEEE Trans. Antennas Propag.* 38: No. 11, 1757–1764, 1990.
- [4] P.R. Rousseau, P.H. Pathak, Time domain uniform geometrical theory of diffraction for a curved wedge, *IEEE Trans. Antennas Propag.* 43: 1375–1382, 1995.
- [5] P.R. Rousseau, P.H. Pathak, A time domain uniform geometrical theory of slope diffraction for a curved wedge, *Turk. J. Elec. Engin.* 2: 385–398, 2002.
- [6] R.G. Kouyoumjian, P.H. Pathak, A uniform geometrical theory of diffraction for an edge in a perfectly conducting surface, *Proc. IEEE* 62: 1448–1461, 1974.
- [7] G. Gennarelli, G. Riccio, Time domain diffraction by a right-angled penetrable wedge, *IEEE Trans. Antennas Propag.* 60: 2829–2833, 2012.
- [8] G. Gennarelli, G. Riccio, Obtuse-angled penetrable wedges: a time domain solution for the diffraction coefficients, *J. Electromagn. Waves Appl.* 27: 2020–2028, 2013.
- [9] M. Frongillo, G. Gennarelli, G. Riccio, TD-UAPO diffracted field evaluation for penetrable wedges with acute apex angle, *J. Opt. Soc. Am. A* 32: 1271–1275, 2015.
- [10] G. Gennarelli, G. Riccio, A uniform asymptotic solution for diffraction by a right-angled dielectric wedge, *IEEE Trans. Antennas Propag.* 59: 898–903, 2011.
- [11] G. Gennarelli, G. Riccio, Plane-wave diffraction by an obtuse-angled dielectric wedge, *J. Opt. Soc. Am. A* 28: 627–632, 2011.
- [12] G. Gennarelli, M. Frongillo, G. Riccio, High-frequency evaluation of the field inside and outside an acute-angled dielectric wedge, *IEEE Trans. Antennas Propag.* 63: 374–378, 2015.
- [13] M. Frongillo, G. Gennarelli, G. Riccio, FD-UAPO solutions for the diffraction by a penetrable wedge on a PEC ground plane, *Proc. LAPC 2015*, Loughborough, UK, 2015.

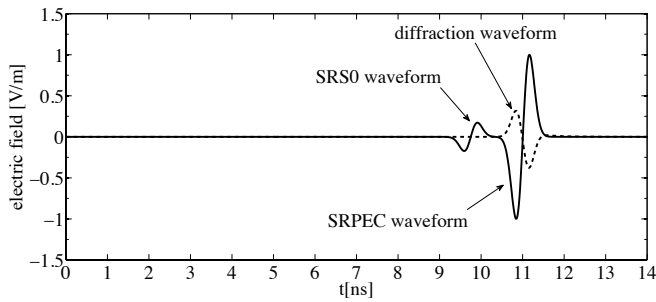


Figure 6: Electric field at $P(3m, 71^\circ)$.

The previous analysis is confirmed by the field evolution when crossing the SRPEC and SRS0 shadow boundaries (see from Fig. 5 to Fig. 8).

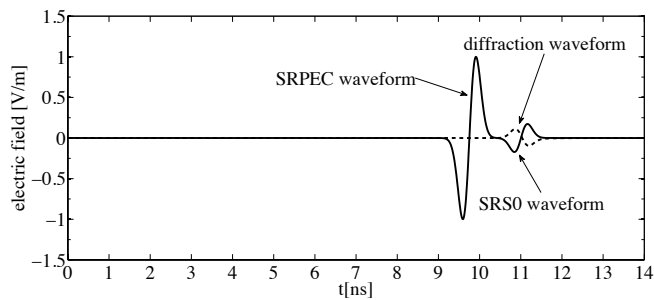


Figure 7: Electric field at $P(3m, 99^\circ)$.

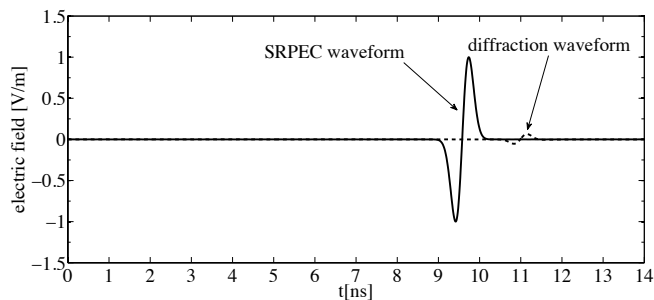


Figure 8: Electric field at $P(3m, 101^\circ)$.

The Complementary Dumbbell-Shaped Strip-Slot Radiating Element

Rocío Rodríguez-Cano, Elena Abdo-Sánchez, Teresa M. Martín-Guerrero and Carlos Camacho-Peñalosa

Departamento de Ingeniería de Comunicaciones, E.T.S.I. Telecomunicación,
Universidad de Málaga, Andalucía Tech, Bulevar Louis Pasteur 35, 29010 Málaga, Spain
{rocio, elenaabdo, teresa, ccp}@ic.uma.es

Abstract

The dumbbell-shaped strip-slot element is proposed to reduce the length of the rectangular-shaped element and still providing an extra broad bandwidth. Based on a simplified circuit model, it is demonstrated the possibility of theoretically achieving frequency independent-image impedance. Two different designs for the dumbbell-shaped structures and the equivalent rectangular counterpart have been manufactured. Simulations and measurements have validated the theory and it is shown the dumbbell-shaped geometry can improve the radiation efficiency around the third resonance, reaching even 100 %.

1. Introduction

The rectangular-shaped strip-slot element (Fig. 1a) is composed of a microstrip-fed slot with a complementary strip placed on the top layer of the microstrip and aligned with the slot. Previous research papers have shown that the image impedance can be theoretically made frequency independent if the electrical lengths of the strip and the slot are equal, resulting in vast impedance bandwidth [1].

The dumbbell-shaped geometry (Fig. 1b) is commonly used in filter design to reduce the length of the stepped impedance resonators (SIR) [2]-[5]. The structures depicted in Fig. 1 are supposed to behave similarly because of their complementary topology. The dumbbell-shaped strip-slot structure is analysed to assess the possibilities of reducing the length of the rectangular-shaped strip-slot element.

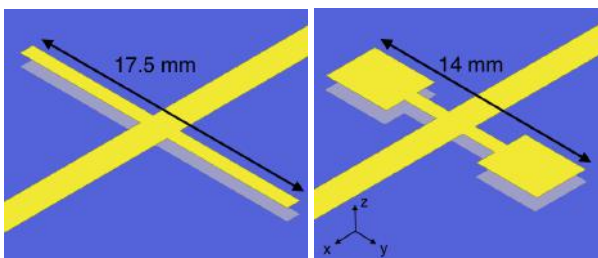


Figure 1: Geometry of: (a) Rectangular-shaped element, (b) Dumbbell-shaped element (first design manufactured).

This paper is divided into six sections. An analytical model to obtain frequency-independent impedance matching of the dumbbell-shaped element is proposed in Section 2. The designed rectangular and dumbbell structures

are presented together with their corresponding prototypes in Section 3. Section 4 deals with the behavioral comparison between the first dumbbell-shaped strip-slot design and the rectangular-shaped strip-slot. An enhancement of the radiation efficiency of the dumbbell-shaped geometry is achieved in Section 5. Finally, the conclusions are summarized in Section 6.

2. Analysis of the Dumbbell-Shaped Structure

The complementary strip-slot structure can be properly modelled with a lattice network, Fig. 2. A symmetrical lattice topology consists of two series branches, named Z_a , and two cross branches, Z_b [7, 6]. As shown in [8], it can be assumed that the series branches corresponds to the slot geometry and the cross branches are determined by the strip.

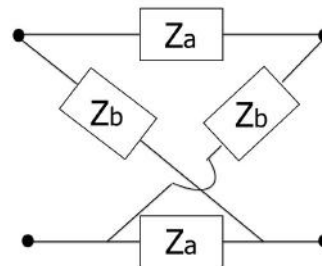


Figure 2: Symmetrical lattice network.

The lattice impedances can be obtained from the immittance parameters as

$$Z_a = Z_{11} - Z_{12} \quad (1)$$

$$Y_b = Y_{11} + Y_{12}, \quad (2)$$

and the image impedance in terms of the lattice impedances can be written

$$Z_{im} = \sqrt{Z_a Z_b}. \quad (3)$$

In order to check the feasibility of accomplishing broad-band matching with the dumbbell-shaped geometry, a simplified transmission line model (without considering the discontinuity effects) has been used to obtain the image impedance of this structure as done for the rectangular-shaped structure in [1]. Two cascaded transmission lines

sections of different widths are considered. The first section corresponds to the narrow part and the second section to the wide one.

The impedances of the series and shunt branches are calculated from the theoretical model. In the case of the strip, the input impedance is obtained considering that the second line is open-ended, while short-circuited for the slot. Once Z_a and Z_b are known, the image impedance is straightforwardly obtained from equation (3).

It can be proven that the following equations provide the design criteria to obtain a frequency independent image impedance in the dumbbell-shaped element (with m used to refer to the strip and s to the slot and the subindexes 1 and 2 to the narrow and wide sections respectively):

$$\theta_{s1} = \theta_{m1} \quad (4)$$

$$\theta_{s2} = \theta_{m2} \quad (5)$$

$$\frac{Z_{s1}}{Z_{s2}} = \tan \theta_{s2} \tan \theta_{s1} \quad (6)$$

$$\frac{Z_{m2}}{Z_{m1}} = \tan \theta_{m2} \tan \theta_{m1} \quad (7)$$

$$\frac{Z_{m2}}{Z_{m1}} = \frac{Z_{s1}}{Z_{s2}} \quad (8)$$

$$\frac{1}{2} \sqrt{Z_{m1} Z_{s1}} = Z_0 \quad (9)$$

The electrical lengths of the strip and the slot of equations (4) and (5) are set equal to reduce the number of unknown parameters and thus, achieve a closed-form expression for the image impedance.

The next step is to force the first resonances of the strip and the slot to be coincident, as shown in equations (6), (7) and (8).

Finally, the resultant image impedance is given by equation (9) and is set to Z_0 to match the structure.

3. Design

In the interest of confirming the soundness of the aforementioned approximations, a design has been carried out and simulated. The proposed dumbbell-shaped structure has been fabricated on RO4350B substrate, with $\epsilon_r = 3.48$ and 0.76 mm of thickness. The resonance frequency has been fixed to $f_r = 5.90 \text{ GHz}$ and the width of the microstrip-fed line is set to 1.74 mm to obtain 50Ω impedance matching. It is possible to represent the left part of the equation (9) as a function of the widths w_s and w_m as shown in Fig. 3.

Based on complementarity, the more similar the strip and the slot are, the better performance is expected to be achieved. Therefore, the widths of interest are those nearby 50Ω matching which have similar dimensions (intersection between the dashed line and the 50Ω isoline). Consequently, the chosen pairs of widths from Fig. 3 are $w_{s1} = 0.86 \text{ mm}$ and $w_{m1} = 0.83 \text{ mm}$ for the narrow

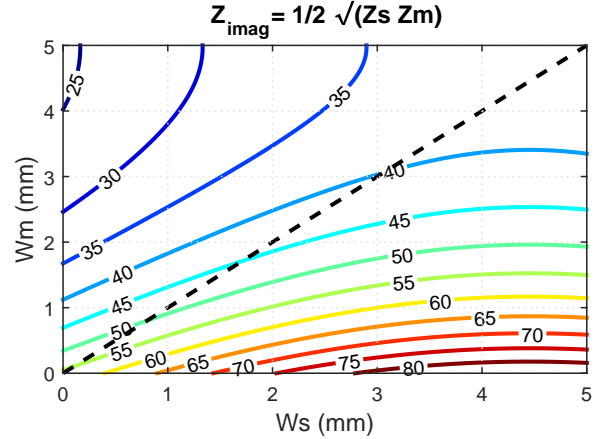


Figure 3: Isolines of the real part of the image impedance for the dumbbell-shaped element. The dashed line in the figure represents equal widths.

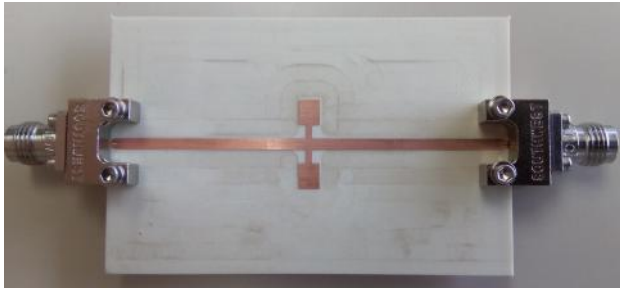
section, and $w_{s2} = 3.46 \text{ mm}$ and $w_{m2} = 3.23 \text{ mm}$ for the wide one. Then, the lengths have been adjusted to make the structure resonate at f_r and the resulting values are the same for the strip and the slot, $l_1 = 6.00 \text{ mm}$ and $l_2 = 4.00 \text{ mm}$ (equations (6) and (7)).

For the sake of completeness, a rectangular-shaped structure has been fabricated as well. The widths of the strip and the slot have been fixed to the value of the narrow part of the dumbbell geometry and the lengths have been enlarged until the first resonance frequencies of both structures were coincident. Pictures of the fabricated dumbbell and rectangular structures are shown in Fig. 4. The manufactured elements have been built in the LPKF ProtoMat S103 circuit board plotter.

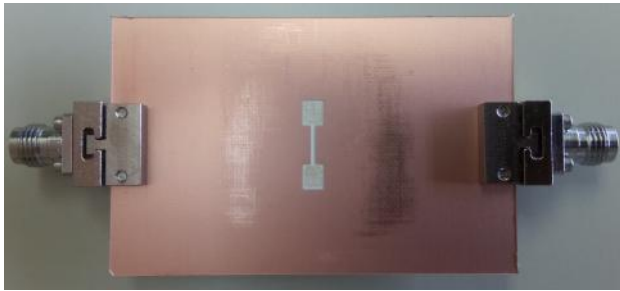
4. Comparison of the Dumbbell and the Rectangular-Shaped Strip-Slots

The simulations have been performed using the software HFSS (Ansys EM 16.0). In Fig. 5, a comparison between the reflection and transmission coefficients of the resulting dumbbell strip-slot and the rectangular-shaped strip-slot is plotted. The dumbbell-shaped structure accomplishes the -10 dB matching criterion on the whole bandwidth, whereas the rectangular structure does not fulfill the requirement at high frequencies. It is noticeable that the growth of the reflection coefficient ceases nearby the third resonance frequency to reach a minimum value of -40 dB and then continues to rise again.

The phase of the transmission parameter can be observed in Fig. 6, for which the reference planes have been set coincident at the middle of the structure. Both first and third resonance frequencies of the dumbbell and the rectangular-shaped structures coincide, but there is a 1 GHz difference around the second one. A frequency shift is found in the comparison of the frequency response between the simulated and the manufactured radiating elements, which can be attributed to fabrication inaccuracies.



(a) Dumbbell top view



(b) Dumbbell bottom view



(c) Rectangular top view



(d) Rectangular bottom view

Figure 4: Manufactured structures. The dumbbell-shaped geometry corresponds to the first design.

The image impedance of the dumbbell-shaped structure is plotted in Fig. 7 and can be considered real, with a value of 50Ω over the entire frequency range but around the resonance frequencies, where the response of the strip and the slot slightly differ and the resonant behavior is not completely compensated. This effect is more noticeable around the second resonance frequencies, where the reflection coefficient has a higher value. The 50Ω matching proves the validity of the design procedure, where the widths are cho-

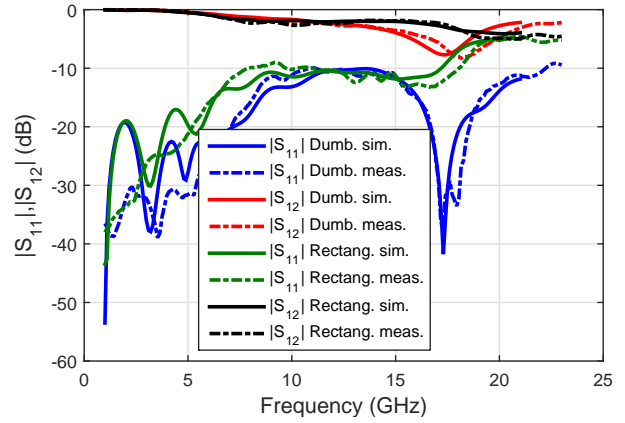


Figure 5: S-Parameters of the dumbbell-shaped element and the rectangular-shaped element.

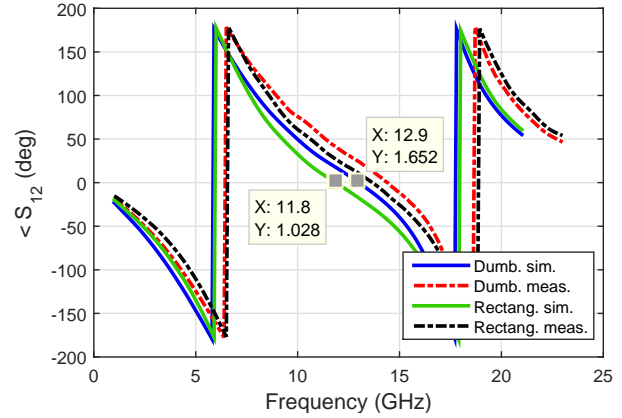


Figure 6: Comparison of S_{12} phase.

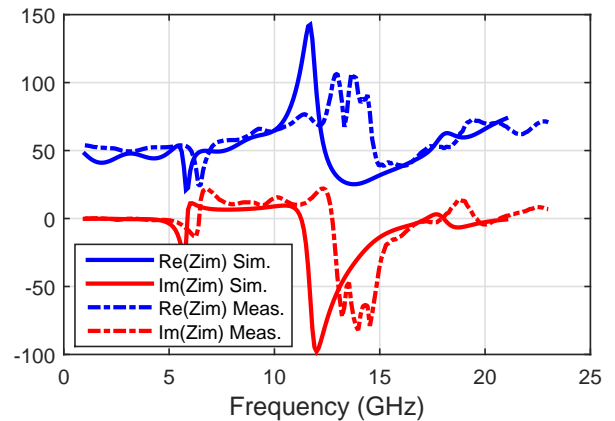


Figure 7: Image impedance of the dumbbell-shaped element.

sen from Fig. 3 and the lengths are calculated from equations (6), (7) and (8).

As can be observed in Fig. 8, the co-polar components

of the dumbbell and the rectangular elements have been plotted in two planes of the space: the ZX plane and the ZY plane. The radiation pattern shows almost the same shape for both structures, with its maximum at broadside.

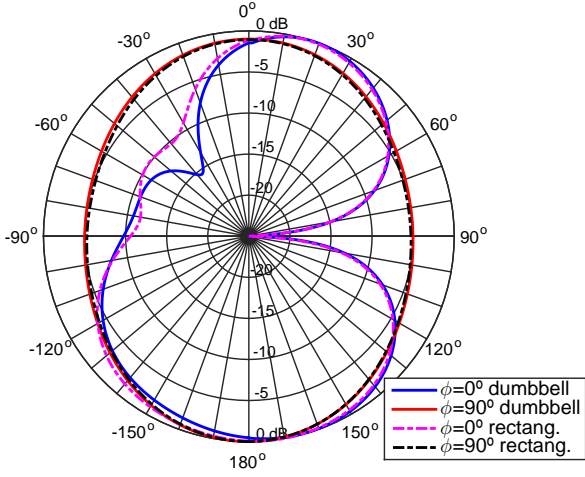


Figure 8: Radiation pattern of the dumbbell and the rectangular-shaped elements.

Fig. 9 plots the radiation efficiency of both prototypes, which is obtained from the S-parameters as the radiated power divided by the delivered power

$$\eta_{rad} = \frac{1 - |S_{11}|^2 - |S_{12}|^2}{1 - |S_{11}|^2}. \quad (10)$$

It shows that the behavior of the rectangular and dumbbell-shaped elements is similar around the two first resonances, but there is a significant increase of the dumbbell radiation efficiency in the third resonance frequency. This behavior demonstrates that the dumbbell-shaped geometry introduces an extra degree of freedom, with which it may be possible to modify certain parameters and attain higher radiation efficiency.

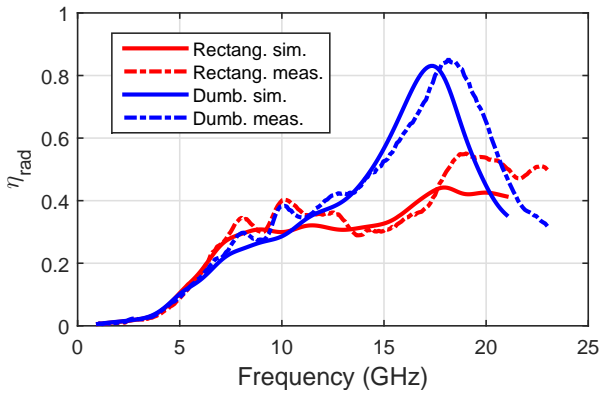


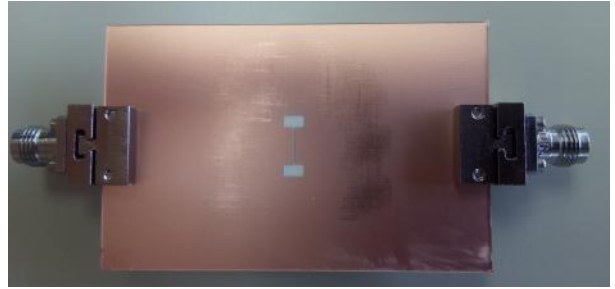
Figure 9: Radiation efficiency of the dumbbell and the rectangular geometries.

5. Radiation Efficiency Improvement

As highlighted in Section 4, the results in Fig. 9 show that it may be possible to achieve a 100 % of radiating efficiency from the dumbbell-shaped geometry. Thus, a second design has been carried out with that aim, trying to maintain the first resonance with the same frequency value than the first design. The modified dimensions of the dumbbell-shaped structure are $l_{m2} = l_{s2} = 2.00 \text{ mm}$ and $w_{m1} = w_{s1} = 0.30 \text{ mm}$, shown in Fig. 10.



(a) Dumbbell top view



(b) Dumbbell bottom view

Figure 10: Second manufactured dumbbell-shaped strip-slot design.

In Fig. 11, the comparison between the reflection and transmission coefficients of both dumbbell-shaped designs can be observed. The second design also achieves broadband matching with a similar response shape.

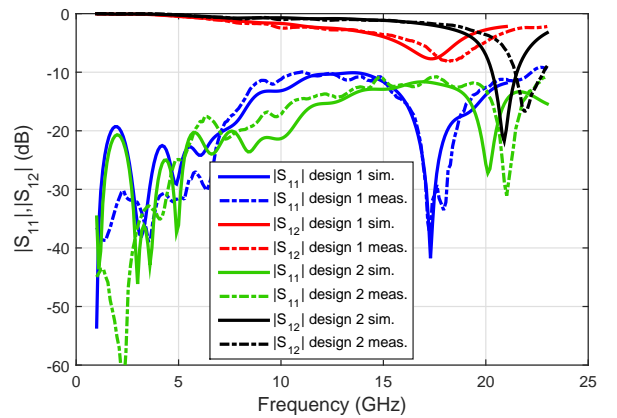


Figure 11: S-Parameters of the two dumbbell-shaped designs.

The phase of the transmission coefficient is shown in Fig. 12. The first resonance frequency is similar for both structures, but the separation between the first and the second resonance is higher in the second design.

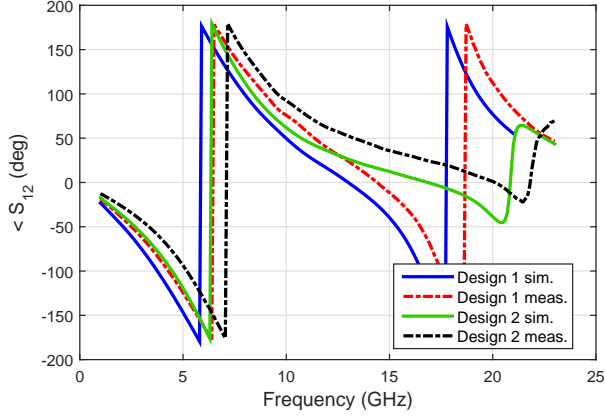


Figure 12: S_{12} phase of the two dumbbell designs manufactured.

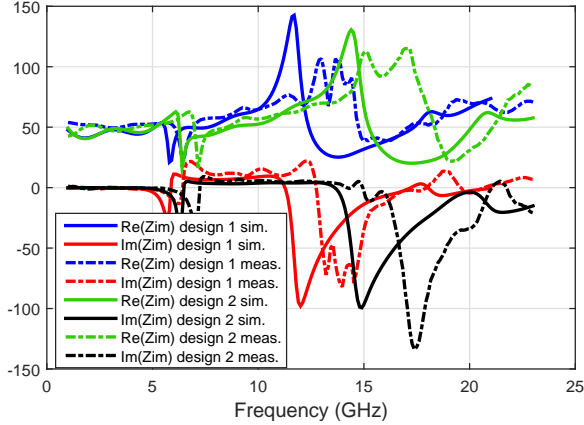


Figure 13: Image impedance of the two dumbbell-shaped designs.

The image impedance of the dumbbell-shaped designs is depicted in Fig. 13. The wider the separation between the first two resonance frequencies is, the flatter the image impedance is going to be. Therefore, the value of the image impedance of the structure within that frequency range is going to be closer to the one designed for matching, a resistive value of 50 Ω .

The radiation efficiency of both dumbbell designs can be seen in Fig. 14. It proves that the purpose of achieving a theoretical 100% radiation efficiency around the third resonance is feasible with the dumbbell-shaped structure if its parameters are properly adjusted.

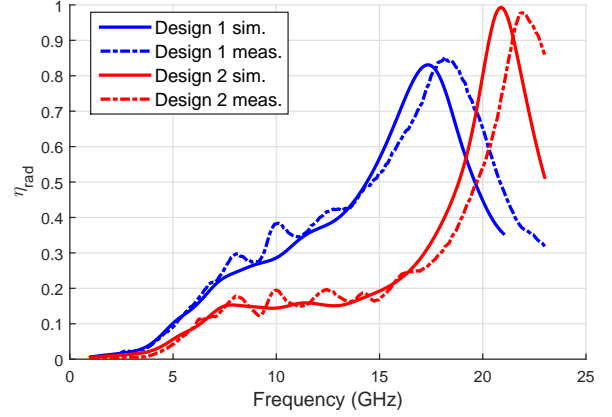


Figure 14: Radiation efficiency of the two dumbbell-shaped structures.

6. Conclusions

Complementary strip-slot structures behave as the conventional slot regarding radiation with the interesting property of broadband matching.

The dumbbell-shaped element can improve the characteristics achieved by using a rectangular-shaped structure with the advantage of reducing the length of the element. A simplified model of cascaded transmission lines has provided the design equations to achieve impedance matching. The design methodology has been validated with the manufactured designs, since good agreement between simulations and measurements has been found.

The comparison between the first design of the dumbbell geometry and the rectangular strip-slot has proved that the dumbbell is better matched in the whole bandwidth and reaches higher values of radiation efficiency. Furthermore, another dumbbell-shaped design has been carried out with an enhanced radiation efficiency of a 100 %.

In conclusion, the dumbbell-shaped element provides an extra degree of freedom with respect to the rectangular element, which allows the second resonance frequency to be tuned and the shape of the radiation efficiency to be designed to some extent. It is expected that this degree of freedom can be exploited to design series-fed arrays with a certain control of the element excitations.

Acknowledgement

This work was supported by Junta de Andalucía (Spain) under Grant P10-TIC-6883.

References

- [1] E. Abdo-Sánchez, J.E. Page, T.M. Martín-Guerrero, J. Esteban and C. Camacho-Peñalosa, Planar Broadband Slot Radiating Element Based on Microstrip-Slot Coupling for Series-fed Arrays, *Antennas and Propagation*, IEEE Transactions, vol.60, no.12, pp.6037-6042, Dec. 2012.

- [2] Duk-Jae Woo, Taek-Kyung Lee, Sangwook Nam, A Simple Model for a DGS Microstrip Line with Stepped Impedance Slot-Lines, *Journal of Electromagnetic Engineering and Science*, vol.15, no.1, pp.26-30, Jan. 2015.
- [3] P. Deng, M. Lai, S. Jeng and C. Chen, Design of Matching Circuits for Microstrip Triplexers Based on Stepped-Impedance Resonators, *Microwave Theory and Techniques*, IEEE Transactions, vol.54, no.12, pp.4185-4192, Dec. 2006.
- [4] Jia-Sheng Hong and M.J. Lancaster, "Theory and experiment of novel microstrip slow-wave open-loop resonator filters, *Microwave Theory and Techniques*, IEEE Transactions, vol. 45, no. 12, pp. 2358-2365, Dec 1997.
- [5] D. Ahn, J. S. Park, C. S. Kim, J. Kim, Y. Qian and T. Itoh, A design of the low-pass filter using the novel microstrip defected ground structure, *Microwave Theory and Techniques*, IEEE Transactions, vol. 49, no. 1, pp. 86-93, Jan 2001.
- [6] M.E.V Valkenburg, *Introduction to Modern Network Synthesis*, New York: John Wiley & Sons, Inc., 1960.
- [7] C.G. Montgomery, R.H. Dicke and E.M. Purcell, *Principles of microwave circuits*, Peter Peregrins on behalf of the Institution of Electrical Engineers, London,1987.
- [8] E. Abdo-Sánchez, T. M. Martín-Guerrero, J. Esteban and C. Camacho-Peñalosa, On the Radiation Properties of the Complementary Strip-Slot Element, *IEEE Antennas and Wireless Propagation Letters*, vol. 14, pp. 1389-1391, 2015.

Microwave and Millimeter Circuits and Systems

A generalized approach to analyze broadband arrow-shaped loaded-stub phase shifters

Badar Muneer^{1*}, An Sensong², Abdul Waheed Umrani¹, Faisal Karim Shaikh¹ and Umair Ahmed Korai¹

¹Dept. of Telecommunication Engineering, Mehran University of Engineering & Technology, Jamshoro, Pakistan.

² Dept. of EEIS, University of Science and Technology of China

Key Laboratory of Electromagnetic Space Information, Chinese Academy of Science

Hefei, 230027, China

*corresponding author: badar.muneer@faculty.muett.edu.pk

Abstract. *This paper discusses a simple and analysis-efficient approach to develop and design wideband loaded-stub (WB-LS) phase shifters. The WB-LS phase shifter achieves a uniform phase shift of $130^\circ \pm 5^\circ$ over a relatively wide bandwidth by utilizing a transmission line loaded with one or two arrow-shaped open stubs and a reference line. Measured insertion loss is less than 0.5 dB for a $90^\circ \pm 4^\circ$ dual-stub loaded phase shifter, whereas, a return loss of better than 10 dB is achieved over a wide bandwidth of nearly 80%. It is observed analytically that employing ideal open stubs, return loss performance of better than 10 dB can be achieved over around 100% of the bandwidth. The stumbling block here is the realization of open stubs that can provide a near-to-ideal value of impedance. An approach to realization of such stubs is proposed with an arrow-shaped stub. Furthermore, a few methods to control the impedance of such stubs are also discussed in this paper.*

Keywords

Arrow shaped stub, broadband phase shifter, analysis and design

1. Introduction

A phase shifter is central building block for phase controlled devices such as phase array antennas and smart antennas. It is often quite cumbersome to develop a phase shifter that can fulfil the needs of now-a-days communication systems that demand wide bandwidth and low losses.

Despite, there are worthy efforts from few researchers around the world to design broadband phase shifters. There are numerous approaches proposed to implement phase shifters with improved properties [1]-[3]. Most prominent of which include, a phase shifter comprising of a broadside coupling structure [4], [5], Schiffman's phase shifter [6]-[8] which is capable of providing as wide as 80% of the bandwidth with a differential phase shift and a phase

imbalance of less than 10° . A modification of Schiffman's phase shifters that uses cascaded coupled lines and double coupled lines to achieve broader bandwidth [7], [8]. However, the acquisition of better bandwidth performance for such phase shifters is strictly related to the microstrip lines that are very narrow in width as well as exceedingly narrow coupling gaps. This causes such phase shifters to be strictly dependent on fabrication constraints and limitation, making it tedious and sometimes even impossible to achieve such broader bandwidths and insertion loss in reality. An ultra-wideband phase shifter utilizing weak coupling technique was introduced in [4], this phase shifter is reported to perform well over a 110% of the bandwidth having a phase imbalance of better than $\pm 3^\circ$, but the differential phase shift it can achieve is limited to only 20° to 25° . An effort to improve the differential phase range of such phase shifters was proposed in [6] with the help of a multilayer structure, but range improvement on the other hand has also result in performance degradation in terms of phase imbalance ($\pm 10^\circ$) and insertion loss (1.85 dB). Moreover, multilayer structure makes the integration of this phase shifter with planar modules problematic. Another wideband phase shifter which incorporates open and short stubs to demonstrate a phase shifter providing up to 90° of phase shift was reported in [9]-[11].

Wideband behavior of loaded line phase shifter has caught great attentions when it comes to developing broadband phase shifter. Researchers have developed and reported few broadband loaded line phase shifters that reveal the usefulness of such phase shifters, but a lack of analysis methods and techniques available to design and properly analyze such phase shifter has brought a huge barrier in their proper utilization and application. Most of the design approaches still rely on 'cut-and-try' method to develop a wideband phase shifter. For instance, the phase shifter reported in [9] that uses dumbbell-shaped multi-section stub provides wide bandwidth, yet the optimization process is employed for the determination of stub dimensions. A shunt quarter-wavelength stub loaded transmission line phase shifter reported in [10], although the phase ripples exceed the acceptable limits for phase shifts greater than 60° but, straightforward relationships

between stub resistance and differential phase shift are provided, however, lack of information and proper explanation makes the effort less effective. Another design procedure for quick determination of design parameters for a phase shifter which is capable of achieving phase shift up to 90° is introduced [11] however, this can be proved that the constant value of resistance for all phase shifter reported in the design procedure may lead to inaccuracies in phase shift.

In this paper, the authors propose a numerical analytic approach to determine characteristic impedance of the loaded stub for all the frequencies of interest. This largely simplifies the designing process for class of loaded stub based phase shifters. The strengths of design procedure are highlighted with the help of a single arrow-shaped stub, furthermore, several impedance control methods are also discussed in the later sections. The proposed method is validated by designing and fabricating a broadband phase shifter composed of two open stubs which can achieve up to 90° of linear phase shift.

1.1 Design and analysis of Arrow-shaped stub

Design and realization of perfect open stub providing closest impedance to the ideal value is cumbersome. By analytical observations, it is concluded that an ideal stub can provide almost 100% 10-dB return loss performance. In the later sections, design approach to realize and control the impedance of open stubs of such capabilities is discussed. A technique to increase the impedance of open stub is also proposed.

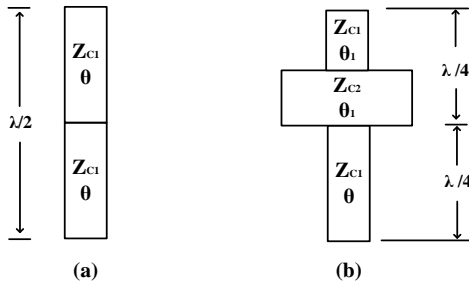


Fig. 1. Schematics of stubs; (a) conventional rectangular stub (b) stepped impedance rectangular patch stub

Input impedance equation of a transmission line suggests that,

$$Z_{in} = Z_0 \left[\frac{Z_L + jZ_0 \tan \theta}{Z_0 + jZ_L \tan \theta} \right]$$

$$Z_{in} = \frac{Z_L + jZ_0 \tan \theta}{1 + j(Z_L/Z_0) \tan \theta} \quad (1)$$

Similarly, the admittance equation for open stub can be obtained,

$$Y_{in} = \frac{1 + j(Z_L/Z_0) \tan \theta}{Z_L + jZ_0 \tan \theta}$$

Or

$$Y_{in} = j \left[\frac{\tan \theta}{Z_0} - \frac{1 + \tan^2 \theta}{Z_L + Z_0 \tan \theta} \right] \quad (2)$$

From above equation, it is obvious that smaller values of load impedance (Z_L) will help lower the value of input admittance (Y_{in}).

Modifying the geometric shape of loaded-line shown in Fig. 1 (a) from rectangular to stepped-rectangular geometry as shown in Fig. 1 (b), the equation for impedance can be modified as follows,

$$Z_L = Z_{C2} \left[\frac{Z_1 + jZ_{C2} \tan \theta_1}{Z_{C2} + jZ_1 \tan \theta_1} \right] \quad (3)$$

Where

$$Z_1 = Z_{C1} / j \tan \theta_1 \quad (4)$$

So

$$Z_L = j \left[\frac{Z_{C2} \tan \theta_1 - Z_{C1} / j \tan \theta_1}{1 + Z_{C1} / Z_{C2}} \right] \quad (5)$$

$$Z_L = \frac{Z_{C1}(1 - (Z_{C2}/Z_{C1}) \tan^2 \theta_1)}{j \tan \theta_1 (1 + Z_{C1}/Z_{C2})} \quad (6)$$

Comparing to the impedance of rectangular shaped patches,

$$Z'_L = \frac{Z_{C1}}{j \tan \theta} = \frac{Z_{C1}}{j \tan(2\theta_1)}$$

$$Z'_L = \frac{Z_{C1}(1 - \tan^2 \theta_1)}{2j \tan \theta_1} \quad (7)$$

A quick glance at eq. (6) and eq. (7) reveals the relationship of impedances as $Z_{C1} > Z_{C2}$ and $Z_L < Z'_L$. This suggests the possibility of using rectangular stepped impedance transmission line in place of conventional quarter-wave stub to lower the value of admittance. In this manner, difficulties and limitation associated with fabrication of high-impedance transmission lines can be eased.

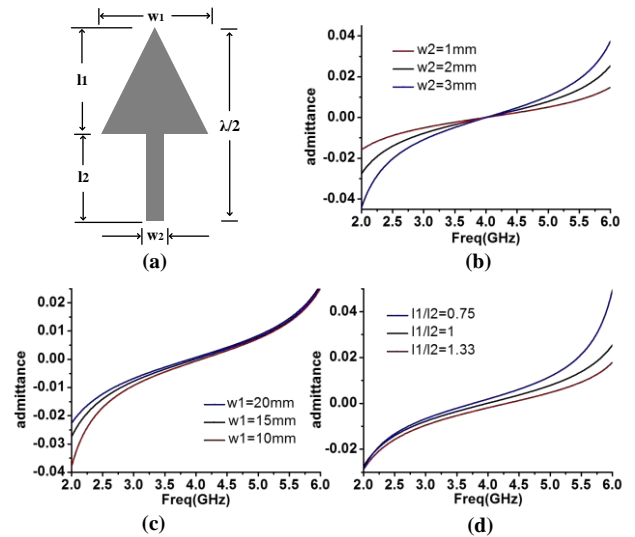


Fig. 2. Proposed arrow-shaped stub and its parametric study by changing several variables to control the impedance of stub (a) diagram of arrow-shaped stub (b) variation in width of line (w_2) (c) variation in width of stub (w_1) (d) varying the length ratio (l_1/l_2)

Fig. 2 (a) shows the schematic of an arrow-shaped stub having low impedance or high resistance. High resistance values are much simpler to achieve, leading to reduced fabrication complexities and limitation. On the other hand, this kind of stub can be controlled by varying stub parameters (w_1 , w_2 , l_1 and l_2) as shown in Fig. 2 (a, b and c). To ensure the better return loss performance at operating frequency, the total length of stub (l_1+l_2) is kept equal to half wavelength.

1.2 Demonstration and results

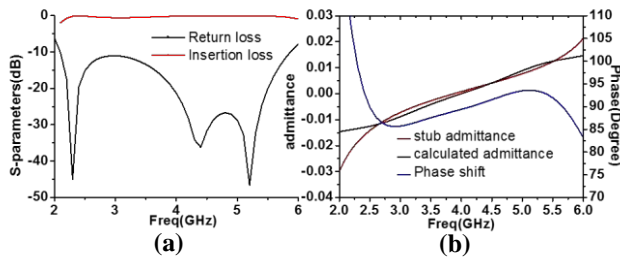


Fig. 3. Simulated S-parameters and comparison; (a) S-parameters (b) phase response and admittance comparison

As a demonstration and to validate the proposed approach, a phase shifter consisting of two such arrow-shaped stubs is designed and prototyped. The stubs are designed to offer admittances very close to the ideal values, this ensures a constant phase shifter for all values of frequency. Simulated and measured S-parameters and phase response is given in Fig. 3 and Fig. 4, respectively. It is observed that both results resemble quite accurately, offering a return loss of better than 13 dB and a low insertion loss of only 0.5 dB for a wide range of frequencies i.e. 2.5 GHz to 6 GHz. Phase imbalance is found to be less than $\pm 4^\circ$.

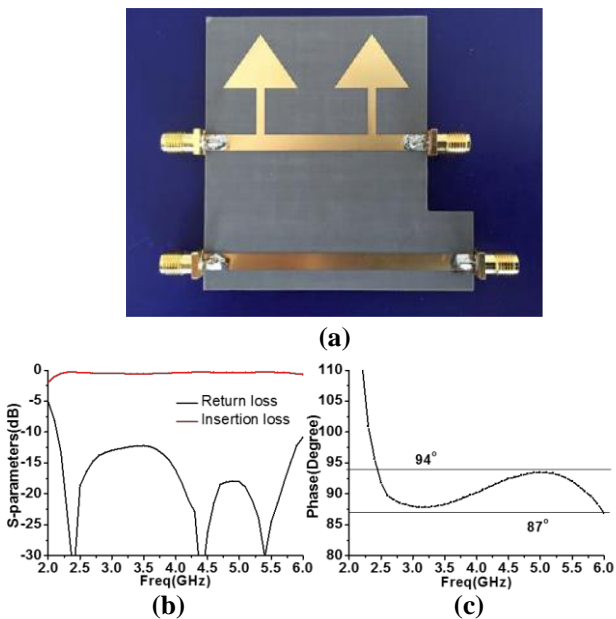


Fig. 4. Fabricated prototype and measured results; (a) prototype snapshot (b) S-parameters (c) phase response

2. Conclusion

In this paper, a generalized method to analyze phase shifter based on load stub technique is proposed. Using the proposed method, a phase shifter incorporating two arrow-shaped loaded stubs is developed. This phase shifter is capable of achieving 90° of constant phase shift over a wide bandwidth (approximately 85%) with the phase imbalance performance of better than $\pm 4^\circ$. Furthermore, it is demonstrated that the complexities related to designing and fabricating such type of phase shifters can be greatly reduced by using proposed design method.

Acknowledgements

This work is supported by the Higher Education Commission of Pakistan (HEC) under the grant SRGP# 772 and National Research Program for Universities (NRPU).

References

- [1] B. Muneer, Q. Zhu and S. Xu, "A Broadband Tunable Multilayer Substrate Integrated Waveguide Phase Shifter," *IEEE Microwave and Wireless Components Letters*, Vol 25 (4), pp. 220-222, 2015.
- [2] B. Muneer, Qi Zhu and Shanjia Xu Fellow, IEEE, "A Digital SIW Phase Shifter Implemented by Switching Transverse Slots via PIN Diodes," *Frequenz, Journal of RF-Engineering and Telecommunications*, Vol 69 (9-10), pp. 383-387, Jan 2015.
- [3] Badar Muneer and Qi Zhu, "A Novel Two-layer Electronically Controllable Substrate Integrated Waveguide Phase Shifter," 2015 German Microwave Conference (GeMic), Nurnberg, Germany, pp. 158-161 March 2015.
- [4] A. M. Abbosh, "Ultra-Wideband Phase Shifters," *IEEE Trans. Microw. Theory Tech.*, vol. 55, no. 9, pp. 1935-1941, Sep. 2007.
- [5] Y. Wang, M. E. Bialkowski, and A. M. Abbosh, "Double Microstrip-Slot Transitions for Broadband $\pm 90^\circ$ Microstrip Phase Shifters," *IEEE Microw. Wirel. Components Lett.*, vol. 22, no. 2, pp. 58-60, Feb. 2012.
- [6] B. M. Schiffman, "A New Class of Broad-Band Microwave 90-Degree Phase Shifters," *IEEE Trans. Microw. Theory Tech.*, vol. 6, no. 2, pp. 232-237, Apr. 1958.
- [7] J. L. R. Quirarte and J. P. Starski, "Novel Schiffman phase shifters," *IEEE Trans. Microw. Theory Tech.*, vol. 41, no. 1, pp. 9-14, 1993.
- [8] Y. X. Guo, Z. Y. Zhang, and L. C. Ong, "Improved wide-band schiffman phase shifter," *IEEE Trans. Microw. Theory Tech.*, vol. 54, no. 3, pp. 1196-1199, 2006.
- [9] S. Y. Zheng, S. H. Yeung, W. S. Chan, K. F. Man, and S. H. Leung, "Improved broadband dumb-bell-shaped phase shifter using multi-section stubs," *Electron. Lett.*, vol. 44, no. 7, p. 478, 2008.
- [10] X. Tang and K. Mouthaan, "Design of a UWB phase shifter using shunt $\lambda/4$ stubs," *IEEE MTT-S Int. Microw. Symp. Dig.*, pp. 1021-1024, 2009.
- [11] S. Y. Zheng, W. S. Chan, and K. F. Man, "Broadband phase shifter using loaded transmission line," *IEEE Microw. Wirel. Components Lett.*, vol. 20, no. 9, pp. 498-500, 2010.
- [12] D. M Pozar, *Microwave Engineering*, 3rd. 2005, p. 728.

Broadband TE₁₀ to TE₂₀ Mode Transformer for X Band

Davide Passi^{1*}, Alberto Leggieri¹, Rocco Citroni¹ and Franco Di Paolo¹

¹University of Rome Tor Vergata, Rome, Italy

*corresponding author, E-mail: davide.passi@uniroma2.it

Abstract

This paper deals with a broadband TE₁₀ to TE₂₀ mode transformer in a WR90 rectangular waveguide with more than 35 dB suppression of the fundamental mode and only 0.4 dB of maximum transformation loss. Two fin lines are employed with appropriate configuration in order to obtain a broadband mode transformation.

1. Introduction

Into waveguide systems, usually, only the fundamental propagation mode is used because the input power is not equally distributed for each mode and high order mode power may be lost. In some applications, instead, the high order modes fields' distribution is a requirement for best working and the fundamental mode is the unwanted one. In addition, only one mode may be preferred; thus others have to be suppressed. In such applications, the conversion efficiency and the suppression mode ratio are the key concepts. In this work, a broadband TE₁₀ to TE₂₀ mode transformer for the X band is presented. It employees the well-known fin line transitions in antipodal configuration, the standard WR90 waveguide and the WR90 waveguide with double width to allow the TE₂₀ mode to propagate. In final instance, the application of the mode converter to the spatial power combining technique is shown. This application is exemplificative of the innovation provided by the proposed approach and clearly shows its potentialities.

2. Mode Conversion

In a rectangular waveguide, the electric field of the first mode TE₁₀, has distribution like a half sine wave distribution; while that of instead the TE₂₀ follows an entire sine wave. Usually, the conversion mode is achieved with several dielectric rods placed along the waveguide [1]. In order to accomplish the mode conversion, the fundamental mode must be spatially divided in two equal parts, one shifted by 180° in phase with respect to the other. The innovation presented in is the strategy for achieving this phase shifting [2].

The dividing operation is obtained through two cards with single fin line in antipodal configuration. By means of the opportune field-rotating performance of the antipodal fin line, it is possible to get the right phase shifting. The two cards have different topology because they have different

tasks. One card (Figure 1) rotates the electric field (from left to right) first in the clockwise for 90° and then in the counter clockwise for 90° (hence, the output electric field has the same polarization of the input). The second card (Figure 2) rotates the electric field in the clockwise for 180°, obtaining the desired phase shifting between the two cards.



Figure 1: The card that rotates the electric field of 0°. Green trace is on the top of the substrate and the yellow one is on the bottom.



Figure 2: The card that rotates the electric field of 180°. Green trace is on the top of the substrate and the yellow one is on the bottom.

At this point, a TE₂₀ mode is formed and it can propagate only if the waveguide dimensions (or the operating frequencies) allows for. In this work, an oversized waveguide, where the long side of the waveguide is twice the standard value, it has been preferred. The fin lines have the same length, allowing for a so the broadband behavior.

3. Fin Lines and Waveguide Designs

The operation of this mode transformer (Figure 3) relies on opportune fin lines design. They have been designed starting from the exponential shape (1):

$$\begin{cases} W(x) = A \left[\exp\left(\frac{x \ln w_f}{L_{Fin}}\right) - 1 \right] \\ A = \frac{b + W}{2(w_f - 1)} \end{cases}, \quad (1)$$

where b is the waveguide height, W is the paired strip lines width, L_{Fin} is the transition length and w_f is the form factor. Two latter parameters are subjected to optimization process and their values are reported in Table 1.

Table 1: Optimized values of the fin line tapers

w_f	L_{Fin} [mm]	$/W(x)/$ [mm]
0.4	40	$10.13[\exp(-22.9 \cdot 10^{-3} x) - 1]$

The paired strips lines are needed to join the two fin line tapers and they are required to be as wide as possible in order to reduce losses. The upper limit is due to the high order modes propagation which is frequency- and dielectric permittivity-dependent. In fact, the line width must be lower than a quarter of the wavelength in the medium. For this work, it must agree with the (2) by assuming $W/H_{sub} > 1$, $H_{sub} = 0.508$ mm, $\epsilon_r = 9.8$ (Alumina substrate), $f = 12$ GHz. It has been approximated as a microstrip line [3].

$$\left\{ \begin{array}{l} W < \frac{\lambda}{4\sqrt{\epsilon_e}} = 2.27 \text{ mm} \\ \epsilon_e = \frac{\epsilon_r + 1}{2} + \frac{\epsilon_r - 1}{2} \left(1 + 12 \frac{H_{sub}}{W} \right)^{\frac{1}{2}} = 7.59 \end{array} \right. , \quad (2)$$

H_{sub} is the substrate thickness.

The width of the paired lines has been chosen with 2 mm to get a certain safety margin. The Bal-un has a semicircle shape with radius of 4.08mm.

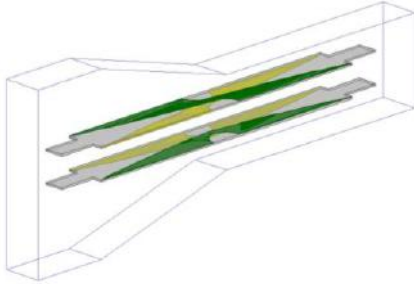


Figure 3: TE₁₀ to TE₂₀ mode transformer.

Two 8 mm length Quarter Wave Transformers (QWTs) have been implemented on the card topology in order to improve the return loss. The two cards have been placed at 4 mm of distance from the waveguide center in order to correctly distribute the dielectric load.

The waveguides design has been performed by joining two WR90 waveguides together: a standard 22.86x10.16 mm² waveguide and a 45.72x10.16 mm² one. The junction interface has been linearly tapered and its length has been chosen as the same as that of the fin line. Accordingly, the waveguides junction interfaces are placed in the middle of the paired lines. The performances obtained in X band show 15 dB of return loss in TE₁₀ and TE₂₀ terms, at the input and at the output ports respectively, with 0.3 dB ±0.1 dB of transformation loss (Figure 5), corresponding to the insertion loss. The efficiency mode conversion has a mean value of 96.6% in the whole X band, so a bandwidth of 40% has been achieved. At the output port, where only TE₂₀ mode is desired, TE₁₀ is 35 dB attenuated, TE₃₀ is 50 dB and TE₄₀ is 25 dB (Figure 6).

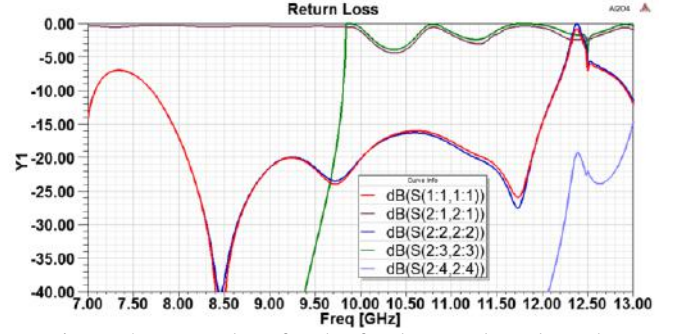


Figure 4: Return loss for the fundamental mode at the input port and for the first 4 modes at the output port (from TE₁₀ to TE₄₀). dB(S(PortX : ModeX, PortY : ModeY)) indicates the S(PortX,PortY) parameter considering ModeX presents at the PortX and ModeY presents at the PortY.



Figure 5: TE₁₀ to TE₂₀ transformation loss. It is the S₂₁ when at the port 1 there is the first mode and at the port 2 the second mode is wanted.

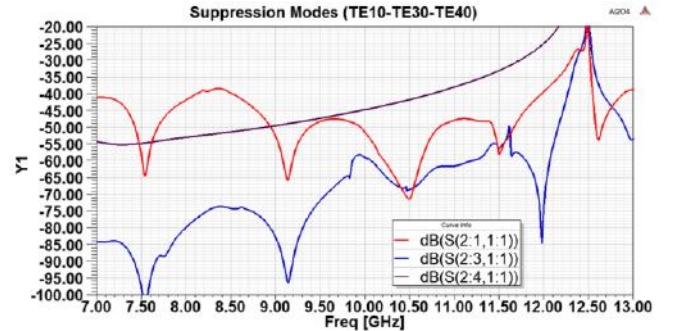


Figure 6: TE₁₀, TE₃₀ and TE₄₀ suppression at the output port. They are the S₂₁ parameters when at the input port the fundamental mode is excited and at the output port other modes are investigated.

4. Spatial Power Combiner application

The Spatial Power Combining (SPC) technique [4] is a suitable approach where the mode transformer (previously described) is used. When more cards are employed in a SPC, the feeding of each fin line must be seriously considered. In fact, the outermost fin lines capture less power than the innermost ones. In this way, the solid state power amplifiers placed on the fin lines work in different compression regions. The TE₂₀ mode, in a rectangular waveguide,

improves the feeding of the solid state power amplifiers placed far from the center of the waveguide (Figure 7).

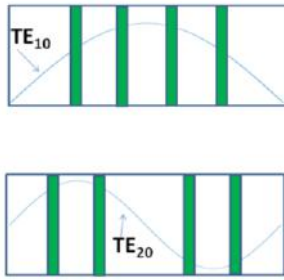


Figure 7: Field distribution for fundamental and second modes. Fin line cards are the green rectangular.

Several improvements are obtained on the feeding balance, which is each fin line receives the same power of the others. In addition, more space is available for MMICs placement. In order to assess the improvements achieved from the proposed approach, an SPC has been (Figure 9). It employs 4 Al_2O_3 cards with single fin lines printed on in antipodal configuration. The design procedure has been largely treated in [5] and it is frequency scalable. The propagation medium is a waveguide with the same dimensions of the mode transformer designed, which are $45.72 \times 10.16 \text{ mm}^2$.

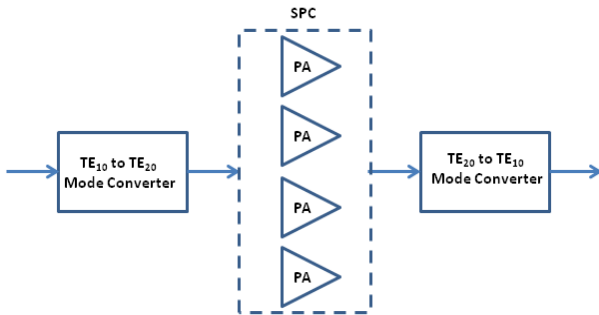


Figure 8: Blocks diagram of the SPC application.

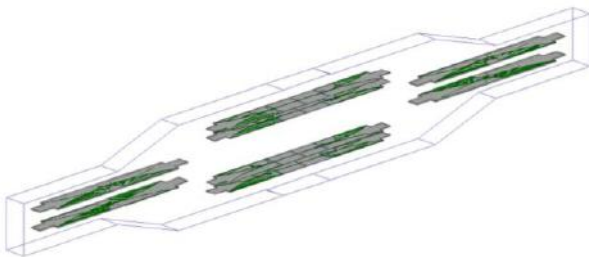


Figure 9: The SPC designed for the X band employing the broadband mode transformers.

The results of the simulation show a balanced power splitting within $\pm 0.1\text{dB}$ (Figure 10). The two minimum in the splitting scheme are due to the intrinsic limits of the mode transformer. Two semicircular metallic traces have been applied in the slots places in order to bring the resonances away from the operative band [6].

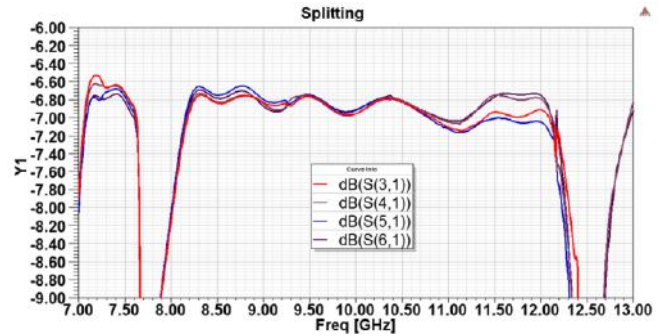


Figure 10: Balanced power splitting achieved by the Spatial Power Combiner fed by the TE_{10} to TE_{20} mode transformer.

5. Conclusions

In this paper, a new waveguide mode transformer has been presented. It operates in full X band applications with only 0.3 dB loss. An X-band SPC has been designed employing two mode transformers in order to proof the right behavior of the converters. Further improvements could be performed to reduce the length of the fin line taper in order to maximize efficiency in the transformation process. Moreover, the spatial combiner may be designed to eliminate the output transformer, by inverting the phase of two fin line cards. In this case, major attention should be given to the output waveguide section.

References

- [1] Y. Kokubo, Frequency Range Dependent TE_{10} to TE_{20} Mode Converter, *Microw. Opt. Technol. Lett.*, Vol. 52, No. 1, pp: 169–171, Jan. 2010.
- [2] M. Belaid, R. Martinez, K. Wu, A Mode Transformer Using Fin-Line Array for Spatial Power-Combiner Application, *IEEE MTT-Transaction*, Vol. 52, No. 4, pp: 1191-1197, Apr. 2004.
- [3] F. Di Paolo, Networks and Devices Using Planar Transmission Lines, *CRC Press LLC*, 2000, ISBN 0-8493-1835-1.
- [4] D. Passi, A. Leggieri, F. Di Paolo, M. Bartocci, A. Tafuto, Spatial Power Combiner Technology, *PIERS Proc.*, Czech Republic, pp: 932-938, Jul. 2015.
- [5] A. Leggieri, D. Passi, F. Di Paolo, M. Bartocci, A. Tafuto, A. Manna, A Novel Ka-band Spatial Combiner Amplifier: Global Design and Modelling, *PIERS Proc.*, Czech Republic, pp: 840-845, Jul. 2015.
- [6] G. E. Ponchak, A. N. Downey, A New Model for Broadband Waveguide to Microstrip Transition Design, *NASA Technical Memorandum 88905*, Lewis Research Center Cleveland, Ohio, Dec. 1986.

New Six-Way Waveguide to Microstrip Transition applied in X Band Spatial Power Combiner.

Davide Passi^{1*}, Alberto Leggieri¹, Rocco Citroni¹ and Franco Di Paolo¹

¹University of Rome Tor Vergata, Rome, Italy
 *corresponding author, E-mail: davide.passi@uniroma2.it

Abstract

A Spatial Power Combiner is proposed using an innovative waveguide to microstrip transition capable to divide the electric field in six equal parts per card. This device can combine 12 MMIC Solid State Power Amplifiers in the whole X Band with 13 dB of return loss and only 2.2 dB losses in a small size, high power and high efficiency system.

1. Introduction

Spatial Combining technique [1] is a suitable approach if several Solid State Power Amplifiers (SSPAs) have to be combined. It has high efficiency due its one shot dividing and combining ways and then losses are quite independent to the number of devices combined. Thus power dividing and combining are performed in a parallel way rather than in a serial way how the classical power combining approach does. At the state of the art only binary combinations were performed [2]-[3] and more than the necessary devices may be combined. In this work, an X band Spatial Power Combiner (SPC), employing the innovative hexa-Fin Line to microstrip (FLuS) transition is presented. The proposed structure allows to combine six-multiple SSPAs with low loss, until now impossible with SPC's at the actual state of the art. This limit has been overtaken by means of inserting six parallel 50 Ω microstrip lines into a WR90 waveguide, by relying on its cross sectional dimensions that has hallowed to place equally spaced 254 μm FluS on Alumina substrate (Figure 1).

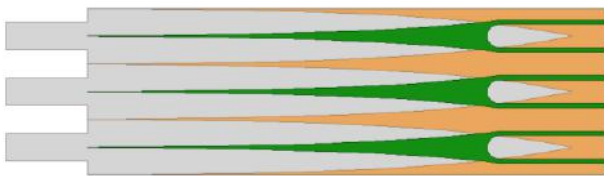


Figure 1: Proposed card with hexa-fin line to microstrip transition. Green traces are on the top of the substrate and orange ones are on the bottom.

2. Electromagnetic Design and Simulation

The design of hexa-fin lines involves an accurate material selection by considering all multiple physics aspects of their

properties: an Al₂O₃ substrate has been chosen with 254 μm of thickness, due its good thermal conductivity. This requirement is a key point to allow the system to dissipate high amount of heat generated by SSPAs. An exponential taper, in antipodal configuration, has been chosen for the fin line profile. Hence, two parameters have to be defined to obtain the right impedance transformation in (1), where b is the waveguide height, W_{50} is the 50 Ω microstrip line width, L_{Fin} is the transition length and w_f is the form factor. Two latter parameters are subjected to optimization process. After optimization w_f value is 20 with a L_{Fin} of 25 mm.

$$W(x) = A \left[\exp\left(\frac{x \ln w_f}{L_{Fin}}\right) - 1 \right] \quad \text{with} \quad A = \frac{b + 6W_{50}}{12(w_f - 1)}, \quad (1)$$

Hexa-fin is 25 mm length for full X band applications and it needs of triple Quarter Wave Transformer (QWT) with 5 mm length to improve return loss and to make symmetric currents in the substrate [4] (Figure 2). Each microstrip is anti-phase (180°) shifted with respect to the adjacent ones for intrinsic performance of the antipodal fin configuration. It catches and divides the electromagnetic field and while it transforms the impedance it rotates the electric fields in opposite directions. In adding a Bal-un has been designed in order to obtain minimum reflections in the fields transferring process. It has the same shape of the fin line but its length is 4.46 mm, hence the bottom plane, that is the ground one of the hexa-fin transition, is 29.46 mm length from the start of the fin line to the end of the Bal-un.

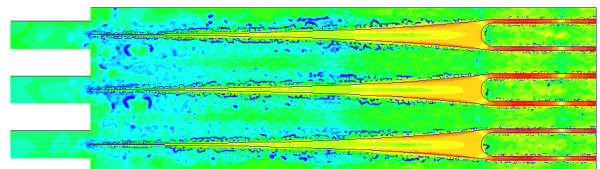


Figure 2: The symmetry of the current magnitude due to the triple QWT inside the hexa-fin line.

Two designed hexa-fin lines have been employed in a SPC so it is able to combine 12 MMIC SSPAs. Each MMIC spends 5x10 mm² areas but different sized one may be used with only few modifications. Transitions have been placed

at 6 mm of distance from each other to reduce coupling and to allow for the use a thick carrier with high dissipation capacity. Equalization lines have been designed on Al₂O₃ substrate obtaining a phase imbalance of 0.3° and maximum loss of 0.8 dB.

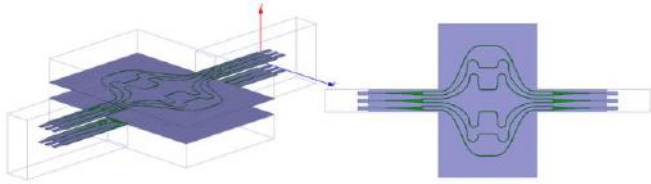


Figure 3: 3D model of the simulated Spatial Power Combiner employing 4 hexa-fins in the WR90 waveguide, 2 for dividing and 2 for combining, holding 12 MMICs (3D and top view).

Electromagnetic simulations have been performed using Ansys HFSS software of the model showed in Figure 3. The whole SPC has 13 dB return loss in the 8.2-12.4 GHz band, that is the WR90 operative band, and it has 1.9 dB of mean insertion loss with ripple of 0.3 dB but major losses are due to the equalization lines that bring electromagnetic fields from fin lines to MMIC SSPAs. Performances are reported in Figure 4. Thus two hexa-fin cards divide electromagnetic field in twelve parts with only 0.3 dB of loss; this corresponds to a 93.3 % of transformation efficiency calculated by (2). Instead the entire SPC has an efficiency of 60% calculated on the insertion loss basis.

$$\eta = 1/\text{Loss}, \quad \text{Loss is in linear} \quad (2)$$

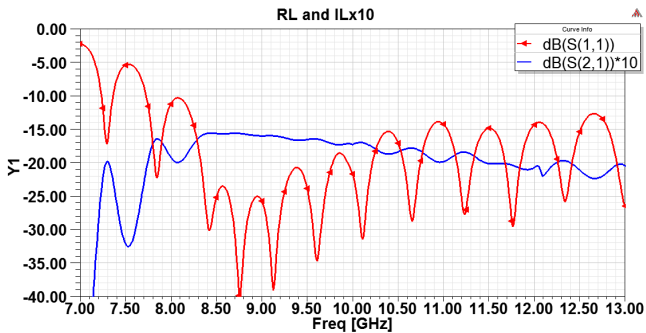


Figure 4: Return Loss and Insertion Loss (10 times magnified) of the SPC, in back to back configuration, holding two cards with the proposed new transition.

3. Technological Aspects

It has been mentioned that the major losses are induced on long equalization lines. In order to reduce such losses, it is possible to use low dissipation factor substrates or lower permittivity dielectric substrates than alumina (used in this work) may be used. Therefore two different materials should be used, one for the fin line and another one for the equalization lines but anyways the power dissipation of the lines has to be taken in account.

Minimum distance, from two microstrip lines, must be dimensioned in order to allow each one to not interfere with others. This requirement can be reached by dimensioning

the distance as about three times the width of the line. Anyhow, in this work two adjacent lines have been placed at more than the double of this minimum allowable distance. At least limit, in a WR90 waveguide is possible to use up to ten 50 Ω parallel lines, but more external lines are too close to the waveguide walls, so hexa-fin is a right compromise between maximum numbers allowable of parallel lines and maximum accepted coupling among them. Another solution, it may be the usage of higher impedance lines than 50 Ω but they come up with more losses and then impedance transformation is needed to interfacing with SSPAs.

The heat dissipated by the SSPAs warms up the fin line substrate reflecting in a line profile bend-up. Once it has been bended up, the fin line card can't capture (or launch) the electric field correctly. In this manner, the field is launched by the projection of line component parallel to the short waveguide side and not by the total line; which must be totally orthogonal to the long side, with no bend or rotations. This, thermo-mechanically induced, field shape alteration considerably reduces the capturing (or launching) efficiency of the global structure, so the right feeding of the fin line must be assured [5].

The last generation of SSPAs, with GaN technology, is capable of to delivering about 50 W in the X band with PAE around 30% [6]. This means that the power dissipated is higher than 100 W. The WR90 waveguide width, which is 22.86 mm, permits the use of a thick carrier, while ensuring for high power dissipation. In fact, the carrier is 6 mm thick and a heat-pipe liquid cooling system might also be provided.

Another very important aspect, in the SPC design, deals with the driver performance. Correctly driving 12 SSPAs is a design challenge, if it is considered that all these devices must be symmetrically combined at the input where a power at least 10.8 dB higher than that of what a SSPA needs is applied. A more expensive alternative solution is the usage of 12 gain amplifiers with at least 10.8 dB of gain placed before each SSPA.

4. Conclusions

In this paper, a new waveguide to microstrip transition has been presented. Hexa-fin breaks the binary combination constrains, by allowing for six-multiple combination approach showing good performances in the X band. A Spatial Power Combiner has been designed and simulated placing 12 solid state power amplifiers by means of the use of the new proposed transition: a maximum 2.2 dB losses have been obtained with maximum 13 dB return loss. Furthermore, some technological aspects have been discussed by the key importance of the underhand work that stands behind the electromagnetic modeling.

References

- [1] D. Passi, A. Leggieri, F. Di Paolo, M. Bartocci, A. Tafuto, Spatial Power Combiner Technology, in *PIERS 2015 Proceedings*, Prague, Czech Republic, 2015, pp. 932-938.

- [2] K. Chang, C. Sun, Millimeter-Wave Power Combining Techniques, *IEEE MTT Trans.*, vol. MTT-31, no. 2, pp. 91-107, 1983.
- [3] K.J.Russel, Microwave Power Combining Techniques, *IEEE MTT Trans.*, vol. MTT-27, no. 5, pp. 472-478, 1979.
- [4] D. Passi, A. Leggieri, F. Di Paolo, M. Bartocci, A. Tafuto and A. Manna, High Efficiency Ka-Band Spatial Combiner, *Advanced Electromagnetics*, vol. 3, no. 2, pp. 10-15, 2014.
- [5] A. Leggieri, D. Passi, G. Saggio and F. Di Paolo, Multiphysics Design Of A Spatial Combiner Predisposed For Thermo-Mechanically Affected Operation, in *Journal of Electromagnetic Waves and Applications*, vol. 28, no. 17, pp. 2153-2168, 2014.
- [6] Hae-Chang Jeong, Hyun-Seok Oh, Abdul-Rahman Ahmed, Kyung-Whan Yeom, Design of X-band 40 W Pulse-Driven GaN HEMT Power Amplifier, in *Proceedings of APMC 2012*, Taiwan, 2012, pp. 466-468.

Theoretical analysis of MSSW propagation in ferrimagnetic bilayer structures for band-stop zones in microwaves spectrum

J. R. Fragoso-Mora*, D. Matatagui and O. V. Kolokoltsev

CCADET, Universidad Nacional Autónoma de México (UNAM), Circuito Exterior s/n A.P. 70-186 - Ciudad Universitaria, 04510 México D.F., México
 fragosorob1@gmail.com

Abstract

Tunable band-stop zones in GHz frequency region was studied theoretically for magnetostatic surface waves (MSSWs) propagating along two-layer over-coupled magnonic waveguides. The analysis has revealed interesting peculiarities in periodical transversal re-distribution of MSSW energy within narrow frequency regions. Band-stop regions can be efficiently tunable by μm -scale displacements between the layers.

1. Introduction

Magnetostatic Waves (MSWs) in thin ferrimagnetic films have been widely used for microwave signal processing [1]. The main advantage of MSW is their short, μm -scale, wavelength, and high tunability. A single-film MSW-based microwave filters have been well studied and described [2]. In recent works main attention was paid to the so-called magnonic crystals (MC), as a basic candidate for reconfigurable microwave filters [3, 4]. These devices use periodic modulation of magnetic properties as an active area, to modify MSWs dispersion characteristics. An important issue of MC devices is the control of periodic active area for manipulation of MSWs transmission spectrum. The reconfigurable filters were realized, recently, by using a control *dc* currents [5], and optically induced magnetic gratings [6].

Alternative proposal is based on MSW coupling in multilayer structures. The directional couplers based on two magnetic layers was proposed by Sasaki and Mikoshiba [7]. Transmission characteristics of MSWs in different coupled multilayer magnonic structures has been analyzed in detail in [7-10]. Recently, the spectral characteristics of surface MSW (MSSW) was demonstrated experimentally in a *planar* structure consisted of two coupled magnonic waveguides [11]. This device has provided frequency-dependent directional coupling with prohibited bands in the transmission spectrum. However, the disadvantage of the planar coupler is its relatively small coupling coefficient, because the transversal in-plane microwave component of the magnetic field, induced by MSSW, is out-of-phase at adjacent ages of the waveguides.

Here, we consider a bi-layer structure based on yttrium iron garnet (YIG). Our analysis in this work is focused on the transformations in MSW transmission spectrum stop-bands caused by a variation in the distance between two ferrite layers. We suppose that this mechanism for the stop-band tuning can be realized by means of MEMS microactuators based, for example, on piezoceramic or thermal strain effects.

2. Theoretical analysis

The bilayer structure on Fig. 1 is constituted of two similar ferrimagnetic films (regions II and IV) with thickness d_1 . Separated (region III) and surrounded (region I and V) by non-magnetic dielectric gap. This layer has the thickness d_2 . Structure is supposed be infinite in the $x = 0$ plane. External dielectric media are also infinite in the x direction. Free space parameters for I, II and V regions are contemplated. External field \mathbf{H}_0 is applied along the z direction, and the spin wave, this geometry corresponds to MSSW, propagates in the y -direction.

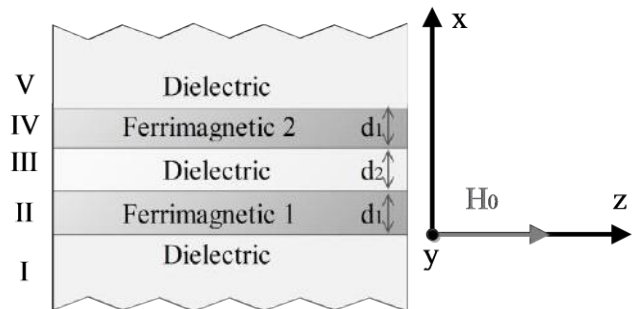


Figure 1: Magnetic bilayer structure magnetized in plane.

The gyrotropic properties of the ferrites in regions II and IV in Fig. 1 are described by the permeability tensor $\hat{\mu}$.

$$\hat{\mu} = \begin{pmatrix} \mu_1 & j\mu_a & 0 \\ -j\mu_a & \mu_1 & 0 \\ 0 & 0 & 1 \end{pmatrix}, \quad (1)$$

where

$$\mu_1 = \frac{\omega_H(\omega_H + \omega_M) - \omega^2}{\omega_H^2 - \omega^2}, \quad \mu_a = \frac{\omega\omega_M}{\omega_H^2 - \omega^2} \quad (2)$$

ω is the frequency, $\omega_H = \gamma H_0$, $\omega_M = 4\pi\gamma M_s$, γ is the gyromagnetic ratio and M_s is the saturation magnetization. The waveguide problem of the bilayer structure in Fig. 1 is solved by means of the Walker's equation (3) that describes the transverse distribution and propagation of MSSW magnetostatic potential (Ψ).

$$\nabla(\mu\nabla\Psi)=0 \quad (3)$$

Eq.(3) follows from magnetostatic approximation of the Maxwell equations, $\nabla\times\mathbf{H} = 0$, where Ψ defines the microwave magnetic field as $\mathbf{h} = -\nabla\Psi$. The dispersion relation for MSSWs in the two similar magnetic layers with in plane magnetization is (4):

$$e^{-2|k|d_2} = \frac{[2\mu_1 \coth(k|d_1) + (\mu_1^2 - \mu_a^2 + 1)]^2}{(\mu_1^2 - \mu_a^2 - 2\mu_a - 1)(\mu_1^2 - \mu_a^2 + 2\mu_a - 1)}, \quad (4)$$

where k is the wavenumber of MSSW. In the solution of the problem we consider two lowest order fundamental eigenmodes. Their wavenumbers $k_{1,2}(\omega)$ were obtained through numerical solution of Eq.(4) and the MSSW field \mathbf{h} was calculated from Eq.(3). The eigenmodes have quasi-symmetric and quasi-anti-symmetric transversal profiles. Superposition of both modes defines the \mathbf{h} -field of the structure. Its spatial evolution along the propagation direction can be interpreted as the energy exchange between the waveguides. Note, at a large gap d_2 , the \mathbf{h} -field can be described by means of the coupled modes perturbation theory [12].

3. Results

Fig. 2 illustrates the dispersion curves, corresponding to the fundamental eigenmodes. The parameters used in the simulations were the following: $H_0 = 170$ Oe, $4\pi M_s = 1750$ G, and $d_1 = 7$ μm . Fig.3 shows the MSSW power flux in the xy plane. It was calculated by the equation

$$\langle P \rangle = \frac{1}{2} \text{Re}(-j\omega\Psi\hat{\mu}H^*), \quad (5)$$

where P is the magnitude of Poynting vector that represents the average power flux per unit surface. In Fig. 3, the power exchange period along the y -direction can be calculated as $L = 2\pi/(\Delta k)$, $\Delta k = k_1 - k_2$. Here, k_2 is the wave number for quasi-symmetric mode and k_1 is the wave number for quasi-anti-symmetric mode.

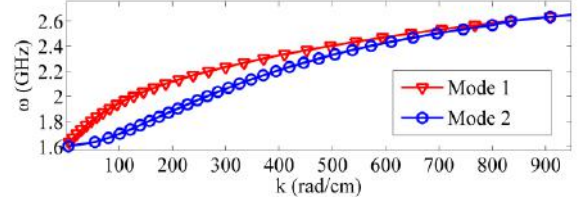


Figure 2: Dispersion curve and its branches for $d_2 = 50$ μm . Mode 1 is related to quasi-symmetric-mode and Mode 2 to quasi-anti-symmetric mode.

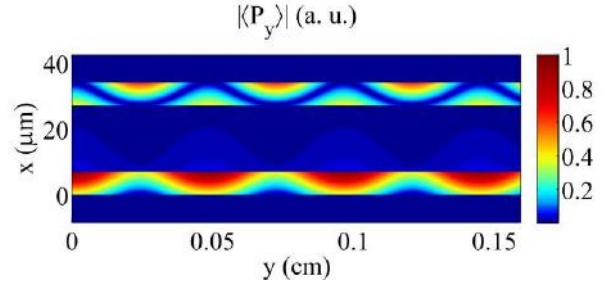


Figure 3: Power evolution in a bi-layer, at the gap $d_2 = 50$ μm and $\omega = 1.7$ GHz.

The principle of the formation of the required band-stop zones is the selection of a proper output propagation distance $y = L$ in one magnetic layer, taking into account that L is a function of the wave number difference $\Delta k(\omega)$. In turn, Δk strongly depends on the gap d_2 , therefore, variations in d_2 can be considered as a tuning mechanism for the system. A high efficiency of this mechanism was suggested by Sasaki and Mikoshiba [7].

Indeed, our numerical experiments have revealed a high sensitivity of the transmission band to d_2 variations. In Fig. 4 we compare two transmission spectrums for the cases when $d_2 = 40$ μm , and $d_2 = 45$ μm .

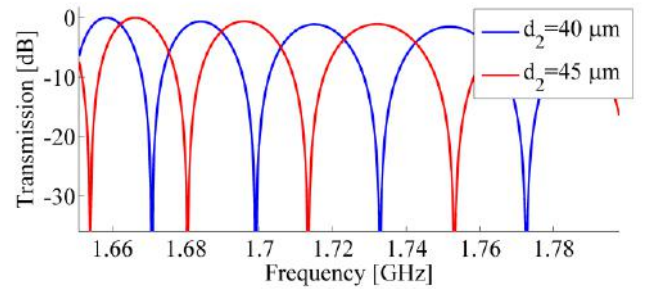


Figure 4: Band structure tuning due to the variation in d_2 . The results were obtained at a fixed L .

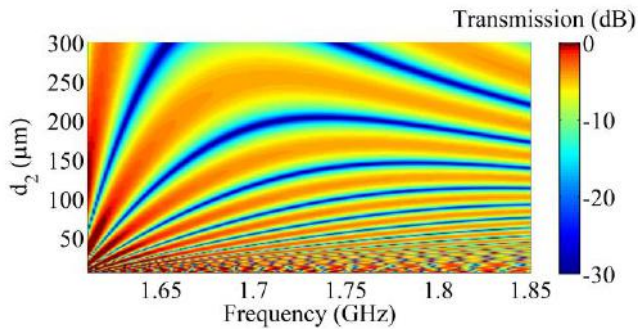


Figure 5: Band structure evolution in a reconfigurable structure as a function of the gap d_2 .

As seen in Fig.4, the variation $\Delta d_2 = 5 \mu\text{m}$ provides the $\approx 15 \text{ MHz}$ frequency shift of the narrow band-stop zones. The results in Fig.5 illustrate that the sensitive in the frequency shift with respect to Δd_2 increases, as d_2 decreases to the waveguide thickness Δd_1 .

Conclusions

The band-stop structure of the MSSW transmission spectra of the bi-layer magnonic waveguide can be efficiently tuned by micrometric scale variations of the gap between the layers. The structure provides a variety of the spectrum waveforms with narrow and tunable band-stop regions.

Acknowledgements

This work was supported through Programa de Apoyo a Proyectos de Investigación e Innovación Tecnológica (PAPIIT) UNAM projects IA103016 and IG100314, Conacyt student grant: 625515 and Coordinación de Estudios de Posgrado, UNAM.

References

- [1] A. A. Serga, A. V. Chumak, B. Hillebrands, YIG magnonics, *J. Phys. D: Appl. Phys.* 43:264002, 2010.
- [2] W. S. Ishak, Magnetostatic wave technology: a review, *Proc. IEEE* 76:171–187, 1988.
- [3] M. Krawczyk, D. Grundler, Review and prospects of magnonic crystals and devices with reprogrammable band structure, *J. Phys: Condens. Matter* 26: 123202, 2014.
- [4] V. V. Kruglyak, S. O. Demokritov, D. Grundler, Magnonics, *J. Phys. D: Appl. Phys.*, 43: 264001, 2010.
- [5] A. V. Chumak, T. Neumann, A. A. Serga, et al., A current-controlled, dynamic magnonic crystals, *J. Phys. D: Appl. Phys.* 42: 205005, 2009.
- [6] M. Vogel, A. V. Chumak, E. H. Waller, et al., Optically reconfigurable magnetic materials. *Nature Phys.* 11: 487–491, 2015.
- [7] H. Sasaki, N. Mikoshiba, Directional coupling of magnetostatic surface waves in layered structure of YIG films, *J. Appl. Phys.* 52: 3546–3552, 1981.
- [8] K. Sun, C. Vittoria, Magnetostatic wave propagation in YIG double layers, *IEEE Microw. Theory Techn.* 39: 339–345, 1991.
- [9] L. R. Adkins, H. L. Glass, Magnetostatic volume waves propagation in multiple ferrite layers, *J. Appl. Phys.* 53: 8928–8933, 1982.
- [10] P. Grünberg, Magnetostatic spinwaves modes of a ferromagnetic double layer, *J. Appl. Phys.* 51: 4338–4341, 1980.
- [11] A. V. Sadovnikov, E. N. Beginin, S. E. Sheshukova, et al., Directional multimode couplers for planar magnonics: Side-coupled magnetic stripes, *Appl. Phys. Lett.* 107: 202405, 2015.
- [12] H. Xi, X. Wang, Y. Zheng et al, Spinwave propagation and coupling in magnonic waveguides, *J. Appl. Phys.* 104:063921, 2008.

Electromagnetic Compatibility

Simulation of Upset of Electronic Systems from Intentional Electromagnetic Interference.

R. L. Gardner

Consultant, Alexandria, VA USA

corresponding author: Robert.L.Gardner@verizon.net

Abstract-Upset of electronic systems is a failure in the function of the system due to a tailored illumination of the system. Upset is difficult to simulate because it involves a complex interaction of the circuits and systems at threat current and voltage levels that are similar to the operating levels and frequencies of the electronics controlling the systems. This paper will demonstrate simulation of a number of interesting responses and system failure modes caused by tailored illumination. The simulations begin with a study of a number of interesting nonlinear, potentially chaotic circuits and their response to stimuli and concludes with a simulation of a mechanical system controlled by an electronic circuit.

Summary: In developing the tools necessary to predict upset in electronic systems due to IEMI illumination, we begin with the study of a number of interesting circuits. The circuits are all nonlinear and can show chaos for selected parameters and for certain excitations (Ref. 5,7). While chaos is an interesting failure mechanism, any system failure mechanism is interest. For example, if an illumination causes an engine to stop, the electronics behavior causing that failure would be of interest. The circuits considered are:

1. Circuits associated with rectification (typical illumination frequencies are often much higher than circuits operating frequencies) (Ref. 6).
2. Chua's Circuit (Ref 1) and driven Chua's Circuit (Ref. 5)
3. PT Symmetric circuits (Ref 2).
4. Buck Converter (Ref 5).
5. Phase locked loops (Ref. 3, 4).
6. PID controller.

Tools: While many of the problems in the first six circuits can be treated with general tools such as LTSpice, MathematicaTM, or even Fortran, our goal is to extend this work to very complex, hybrid and nonlinear systems, including thermal, mechanical, fluid and other types of systems. To accomplish this type of modeling we need more complex tools. For this study, we perform our studies using the Modelica® language. Modelica is an equation based language extensively used in industry for system simulation. For ease of use, we use Dymola® and Wolfram SystemModelerTM to edit the Modelica code and perform the simulations and presentations. Finally, since many extensive parameter studies are required we automate the simulation and plotting process using a Python script.

Final Simulation: The last demonstration will inject a signal onto a simplified auto engine bus that controls the spark advance of a simplified single cylinder engine. As the injected signal interferes with the pulse width modulated signal of the simplified electronic control unit, the advance will move until the combustion no longer can supply the pressure that moves the cylinder. This spark advance demonstration is different than the Inmarsat work in Ref. 3 since the failure mechanism is just a pulse width shift rather than a transition to chaos of an intermediate circuit.

REFERENCES

1. Chua, L. O., C. W. Wu, A. Huang and G. Q. Zhong, "A universal circuit for studying and generating chaos – Part I: Routes to chaos", *IEEE Tran. On Circuits and Systems – I: Fundamental Theory and Applications*, **40**, No 10, October 1993.
2. Schindler, J., L. Ang Li, Zheng, M. C., F. M. Ellis and T. Kottos, "Experimental study of active LRC circuits with PT symmetries", *Phys. Rev. A* **84**, 040101(R), October 2011.
3. Booker, S. M., P. D. Smith, P. V. Breman and R. J. Bullock, "Designing input signals to disrupt commercial systems in band – A nonlinear dynamics approach", *IEEE Trans. Circuits and Systems-I Fundamental Theory and Applications*, **49**, No. 5, May 2002.
4. Kandangath, A., S. Krinshnamoorthy, Y. C. Lai and J. A. Gaudet, "Inducing chaos in electronic circuits by resonant perturbations", *IEEE Trans. Circuits and Systems – I: Regular Papers*, **54**, No. 5, May 2007.
5. Gardner, R. L., "Response of a switched dynamical system to intentional EMI", in *Proc. Of the 10th Int. Symposium on Electromagnetic Compatibility (EMC Europe 2011)*, York, UK, September 26-30, 2011.
6. Triandaf, I., "Spatiotemporal chaotic dynamics in a transmission line model," in *Proc. of International Symposium on Advanced Applications Electromagnetics (ICEAA)*, pp.329-332, 7-11 Sept. 2015.
7. Gardner, R. L., "Nonlinear processes in infrastructure failure", in *Proc. of International Conference on Electromagnetics in Advanced Applications*, pp. 360-362, Turin, September 2013.

Investigation on EM radiations from Interconnects in Integrated Circuits

L. Belhimer,, A. Benfdila and A. Lakhlef*

*Microelectronics Research Group, Faculty of Electrical Engineering and Computer Sciences
University Mouloud Mammeri, Tizi-Ouzou, Algeria*

**Corresponding author. Email: benfdila@mail.ummt0.dz*

The present paper deals with the study and investigation of radiations produced by the interconnects inside an Integrated circuits operated at high frequencies.

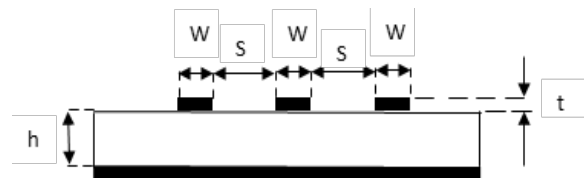
Interconnects are multiple strip and multilevel in ICs. This complicates the study of radiations the produce or receive. The radiations should be studied and modeled in order to secure the functioning of ICs in different media under varying electric and magnetic conditions.

In this first study, we consider a planar interconnects line including three strips isolated by a high k dielectric. The main parameter evidenced is the capacitance of the transmission line which will act as a filter and then attenuate to a worse level the digital signals that flow in these strips.

The work is carried out as modeling using a computation method which common in the field, the finite element method.

We simulated and modeled the interconnect capacitance in different situations. The case study is shown below:

The three microstrip lines are equidistant and mounted on a oxide grown on silicon substrate.



The computations are made based on the Resistance, capacitance and inductance for couples of lines and for their mutual interactions.

The main conclusions are drawn for the study of the influence of the dielectric width and permittivity. The transmission line length and geometry was also studied and the impedance per length is treated in order to estimate the losses and define the limit amplitude of the digital signal in use.

The results are found to comply with literature and encouraging for further investigations on dielectric separation.

Computational Electromagnetics

Accuracy of Norton Approximation Formulas for the Radiation of an Electric Current Element over a Homogeneous Ground.

J. Vincent¹, P. Borderies², V. Gobin², M. Lelong², and J. -R. Poirier¹,

¹LAPLACE - Research Group in Electromagnetism, Toulouse, France

²ONERA - Electromagnetism and Radar Department, Toulouse, France
vincent@laplace.univ-tlse.fr

Abstract— In this paper the problem of the radiation of an electric current element above a homogeneous infinite flat ground is solved with an adaptive algorithm to compute the numerical integration. This method ensures to obtain the correct values of all components of the electromagnetic field with a controlled accuracy. These values, computed in different scenes, are considered as references to analyse the approximation error in the propagation theory of Norton.

Introduction: Since Sommerfeld solved the problem of the radiation of a vertical current element above a homogeneous half-ground [1], many other formulations of the same problem have appeared in the literature [2, 3, 4], the mostly used is the Norton engineering approximation [5, 6]. Recently [7, 8], an adaptive algorithm was created to accurately compute Sommerfeld's integral in the case of a vertical electric current element. The main aim of this paper is to extend this algorithm to a horizontal electric current element and to evaluate the approximation error in the formulas given by Norton, considering different scenes (nearfield or farfield propagation, frequency of the source, different types of ground).

Numerical integration: In a previous work [7], the radiation of a vertical current element $I_0 dl$ located at height h above a homogeneous flat ground with wavenumber k_2 is considered. The observation point is located at radial distance r and height z in the air (wavenumber k_0). All components of the electromagnetic field are obtained everywhere above the ground. All these components are made up of three analytical terms: the direct radiation from the current element ($I_0 dl$), the negative image ($-I_0 dl$) at depth $-h$ in the ground and an integral which is the surface wave term. As an example, the vertical component of the electric field at $\omega = 2\pi f$ is written below in (1).

$$E_z(r, z, h) = E_0 \left[\left(\frac{\partial^2}{\partial z^2} + k_0^2 \right) \left(\frac{e^{-jk_0 R}}{R} - \frac{e^{-jk_0 R'}}{R'} \right) + \int_0^{+\infty} \frac{2k_2^2 J_0(\lambda r) e^{-(z+h)\sqrt{\lambda^2 - k_0^2}}}{k_2^2 \sqrt{\lambda^2 - k_0^2} + k_0^2 \sqrt{\lambda^2 - k_2^2}} \lambda^3 d\lambda \right] \quad (1)$$

Where $E_0 = -\frac{j\omega\mu_0 I_0 dl}{4\pi k_0^2}$, $R = \sqrt{r^2 + (z-h)^2}$, $R' = \sqrt{r^2 + (z+h)^2}$ and J_0 is the zero order Bessel function of the first kind.

Following [9], the analytical formulas has been written in the case of a horizontal electric current and implemented in the adaptive algorithm.

Accuracy of Norton's Approximation Formulas: Considering the results given by the adaptive algorithm as a reference solution, the errors in the approximation of Norton's formulas are computed in different scenes : a vertical and then a horizontal current element, radiating at different frequencies, above different types of infinite half-space (dry soil, wet soil and sea).

Conclusion: This study evaluates the errors in the approximation of Norton's propagation theory with an adaptive algorithm for numerical integration. The effects of the orientation of the current element, the radiating frequency and the type of the ground are observed on the accuracy of Norton's formulas.

REFERENCES

1. Sommerfeld, A. "Propagation of Waves in Wireless Telegraphy," *Annalen der Physik*, Vol. 28, 665–736, March 1909.
2. Van der Pol, B. "Theory of the Reflection of the Light From a Point Source by a Finitely Conducting Flat Mirror, with an Application to Radiotelegraphy," *Physica*, Vol. 2, 843–853, June 1935.
3. Wait, J., *Electromagnetic Waves in Stratified Media*, Pergamon Press, Oxford, 1970.
4. DeMinco, N. "Propagation Prediction Techniques and Antenna Modeling (170 to 1705 kHz) for Intelligent Transportation Systems (ITS) Broadcast Applications," *Antennas and Propagation, IEEE Transactions on*, Vol. 42, n. 4, 9–34, August 2000.
5. Norton, K. A., "The Propagation of Radio Waves over the Surface of the Earth and in the Upper Atmosphere," in *Proceeding of tghc IRE*, Vol. 25, n. 9, 1203–1236, September 1937.
6. Maclean, T. S. M. and Z., Wu *Radiowave Propagation Over Ground*, Chapman and Hall, London U.K., 1993.
7. Vincent, J., Borderies, P., Gobin, V. and J.R. Poirier, "Modelling the Effects of Realistic Environments in the Near-field and Far-field of Low Frequency Antennas with 3D FDTD Method," in *IEEE-NEMO, 2014 International Conference on*, 1–4, May 2014.
8. Vincent, J., Borderies, P., Gobin, V. and J.R. Poirier, "Long Range Ground Wave Scattering of Low Frequency Antennas due to Ground Discontinuities," in *Antennas and Propagation (APCAP), 2015 IEEE 4th Asia-Pacific Conference on*, Bali Island, Indonesia, June 2015, 345–346.
9. Robin, L. and P. Poincelot, "Rayonnement d'un Dipôle Électrique en Présence de Deux Milieux Séparés par un Plan," *Annales des Télécommunications*, Vol. 22, 243–248, September 1967.

Analysis of Optical Properties of Nanowires Using Surface Integral Equations and the Multilevel Fast Multipole Algorithm

Akif Yılmaz, Barışcan Karaosmanoğlu, Özgür Ergül

Department of Electrical and Electronics Engineering
Middle East Technical University, Ankara, Turkey

*corresponding author, E-mail: ozgur.ergul@eee.metu.edu.tr

Abstract

We present fast and accurate analysis of nanowires at optical frequencies. Plasmonic properties are investigated via the Lorentz-Drude model, where the metals are considered as penetrable bodies with negative permittivity values. Surface integral equations are used to formulate scattering and transmission problems, while strongly negative permittivity values bring computational challenges. A modified combined tangential formulation is developed and used for accurate solutions of transmission problems involving nanowires. Also a modified version of the multilevel fast multipole algorithm (MLFMA) is employed for accelerating numerical solutions, where quickly decaying interactions are dropped for improving the efficiency. Numerical examples are presented to demonstrate the capabilities of the developed implementation.

1. Introduction

Nanowires are important ingredients of optical metamaterials [1],[2]. Therefore, their computational analysis is essential to understand optical properties of these structures and their combinations with other metallic and dielectric objects. On the other hand, at optical frequencies, where plasmonic effects dominate for metals, conventional implementations that are developed for lower frequencies must be used carefully. This study is devoted to accurate and efficient analysis of nanowires via iterative solutions of surface integral equations. Since the conventional formulations become inaccurate, especially when the value of the negative permittivity is large, we propose and employ a modified tangential combined formulation (MCTF). In order to analyze large-scale (e.g., long) nanowires with respect to wavelength, we further employ a modified multilevel fast multipole algorithm (MLFMA) that allows for efficient full-wave simulations of three-dimensional models.

In the next section, we summarize different aspects of the developed implementation for rigorous solutions. As a new type of formulation, MCTF is detailed in Section 3. Section 4 includes numerical examples, followed by our concluding remarks in Section 5.

2. Full-Wave Analysis of Nanowires

We consider time-harmonic excitations of nanowires, which are analyzed in the frequency domain using the $\exp(-i\omega t)$ time convention. Nanowires are considered as three-dimensional structures with finite sizes.

2.1. Plasmonic Models

Lorentz-Drude models are available for modeling metals at optical frequencies. Experimental studies reveal effective electrical parameters of several important metals [3]. Interpolations can further be used to extract possible values of the relative permittivity with respect to frequency. In general, we investigate single-material nanowires with electrical parameters $\{\epsilon_p, \mu_p\}$ in free space $\{\epsilon_o, \mu_o\}$. Considering that large negative permittivity values are computationally difficult to handle, frequencies in the infrared region (that are particularly focused in this work) are usually more challenging than those in the visible region.

2.2. Formulation

Alternative options are available for surface formulations of penetrable objects, and the existing implementations can be converted into plasmonic solvers [4],[5]. On the other hand, many formulations are designed for ordinary dielectric materials and their behaviors may change significantly for very large negative values of the permittivity. Among several stable formulations, the electric and magnetic current combined-field integral equation (JMCFIE) and the combined tangential formulation (CTF) provide fast iterative convergences. However, CTF tends to break down in terms of accuracy as the negative permittivity increases. For example, at 250 THz, silver has an effective relative permittivity of $-60.67 + 4.303i$, for which CTF fails to provide accurate solutions in comparison to its performance for ordinary dielectrics. For such values, JMCFIE seems to provide more stable results, especially in the near zone. Unfortunately, with low-order discretizations, JMCFIE has well-known accuracy issues for all permittivity values, including plasmonics. These observations reveal that numerical comparisons with moderate permittivity values [4]–[8] (e.g., gold at visible frequencies) may need to be revised for different frequency ranges.

For plasmonic problems, it is also possible to resort

to more traditional integral equations, such as the Poggio-Miller-Chang-Harrington-Wu-Tsai (PMCHWT) formulation. On the other hand, most of the plasmonic structures are represented as high-contrast problems, leading to extremely difficult iterative solutions, especially if the number of unknowns is large. Alternatively, an investigation on the accurate breakdown of CTF demonstrates the source of the error as numerically unbalanced matrix blocks, which become extreme as the negative permittivity increases. Based on this observation, we propose a modified version of CTF, namely MCTF, that provides accurate solutions in wide ranges of permittivity values without deteriorating the efficiency of iterative solutions.

2.3. Discretization

Surface formulations usually allow for accurate solutions with $\lambda_o/10$ discretizations, where λ_o is the wavelength in the excitation (host) medium, provided that geometric discretization errors are minimized [9]. On the other hand, for plasmonic structures, where the electromagnetic power is restricted in the close proximity of structures, very dense discretizations may be required. Using the Rao-Wilton-Glisson (RWG) functions on triangular domains, $\lambda_o/80$ and even denser triangulations are needed to achieve a typical 1% error using CTF and JMCIE. For large permittivity values, however, CTF may break down without any indication in iterative solutions. Therefore, mesh convergence is often required for verifying the level of accuracy. As shown in Section 4, MCTF needs coarser discretizations (hence smaller numbers of unknowns) in comparison to both CTF and JMCIE, as an important advantage of this new formulation.

2.4. Iterative Solutions Using MLFMA

Interactions in plasmonic regions decay very fast and become negligible for large distances with respect to wavelength. Therefore, for ordinary host media, inner interactions can be eliminated systematically without deteriorating the accuracy. This corresponds to pruning the tree structure in MLFMA, leading to very fast matrix-vector multiplications, without dealing with large values of the absolute wavenumber. As detailed in [10], these eliminations can be performed before the iterative solution starts, by comparing the theoretical exponential decays for the given plasmonic medium with the target number of accurate digits. With those careful eliminations, the accuracy of the final simulation results are not affected, while the efficiency is significantly improved.

3. Modified Combined Tangential Formulation

Since the conventional formulations, such as the PMCHWT formulation, JMCIE, and CTF are well-known in the literature, we focus on MCTF in this paper. Two major integro-

differential operators in surface formulations are defined as

$$\begin{aligned} \mathcal{T}_u\{\mathbf{X}\}(\mathbf{r}) &= ik_u \int_{S_n} d\mathbf{r}' \mathbf{X}(\mathbf{r}') g_u(\mathbf{r}, \mathbf{r}') \\ &\quad + \frac{i}{k_u} \int_{S_n} d\mathbf{r}' \nabla' \cdot \mathbf{X}(\mathbf{r}') \nabla g_u(\mathbf{r}, \mathbf{r}') \end{aligned} \quad (1)$$

$$\mathcal{K}_u\{\mathbf{X}\}(\mathbf{r}) = \int_{PV, S_n} d\mathbf{r}' \mathbf{X}(\mathbf{r}') \times \nabla' g_u(\mathbf{r}, \mathbf{r}'), \quad (2)$$

where $k_u = \omega \sqrt{\mu_u} \sqrt{\epsilon_u}$ is the wavenumber and

$$g_u(\mathbf{r}, \mathbf{r}') = \frac{\exp(ik_u |\mathbf{r} - \mathbf{r}'|)}{4\pi |\mathbf{r} - \mathbf{r}'|} \quad (3)$$

is the three-dimensional Green's function for $u = \{o, p\}$. Discretizations of these operators with tangential (direct) testing can be written as

$$\bar{\mathbf{T}}_u^T[m, n] = \int_{S_m} d\mathbf{r} \mathbf{t}_m(\mathbf{r}) \cdot \mathcal{T}_u\{\mathbf{b}_n\}(\mathbf{r}) \quad (4)$$

$$\bar{\mathbf{K}}_u^T[m, n] = \int_{S_m} d\mathbf{r} \mathbf{t}_m(\mathbf{r}) \cdot \mathcal{K}_u\{\mathbf{b}_n\}(\mathbf{r}), \quad (5)$$

where \mathbf{t}_m and \mathbf{b}_n represent testing and basis functions, respectively. Using a Galerkin scheme, the testing and basis functions are selected as the same set of the RWG functions. Then, the discretization of MCTF leads to $2N \times 2N$ matrix equations, which can be written as

$$\begin{bmatrix} \bar{\mathbf{Z}}_{11}^{\text{MCTF}} & \bar{\mathbf{Z}}_{12}^{\text{MCTF}} \\ \bar{\mathbf{Z}}_{21}^{\text{MCTF}} & \bar{\mathbf{Z}}_{22}^{\text{MCTF}} \end{bmatrix} \cdot \begin{bmatrix} \mathbf{a}_J \\ \mathbf{a}_M \end{bmatrix} = \begin{bmatrix} \mathbf{w}_1^{\text{MCTF}} \\ \mathbf{w}_2^{\text{MCTF}} \end{bmatrix}. \quad (6)$$

In the above, the matrix blocks are defined as

$$\bar{\mathbf{Z}}_{11}^{\text{MCTF}} = \eta_o \bar{\mathbf{T}}_o^T + \eta_p \bar{\mathbf{T}}_p^T \quad (7)$$

$$\bar{\mathbf{Z}}_{12}^{\text{MCTF}} = -\bar{\mathbf{K}}_o^T - \bar{\mathbf{K}}_p^T \quad (8)$$

$$\bar{\mathbf{Z}}_{21}^{\text{MCTF}} = \eta_o \eta_p \bar{\mathbf{K}}_o^T + \eta_o \eta_p \bar{\mathbf{K}}_p^T \quad (9)$$

$$\bar{\mathbf{Z}}_{22}^{\text{MCTF}} = \eta_p \bar{\mathbf{T}}_o^T + \eta_o \bar{\mathbf{T}}_p^T, \quad (10)$$

where $\eta_u = \sqrt{\mu_u} / \sqrt{\epsilon_u}$ represents the wave impedance. Similarly, the right-hand-side vectors are derived as

$$\mathbf{w}_1^{\text{MCTF}} = - \int_{S_m} d\mathbf{r} \mathbf{t}_m(\mathbf{r}) \cdot \mathbf{E}^{\text{inc}}(\mathbf{r}) \quad (11)$$

$$\mathbf{w}_2^{\text{MCTF}} = -\eta_o \eta_p \int_{S_m} d\mathbf{r} \mathbf{t}_m(\mathbf{r}) \cdot \mathbf{H}^{\text{inc}}(\mathbf{r}), \quad (12)$$

where \mathbf{E}^{inc} and \mathbf{H}^{inc} are incident electric and magnetic fields. Solutions of the matrix equations in (6) lead to coefficients $\{\mathbf{a}_J, \mathbf{a}_M\}$, which are further used to compute the

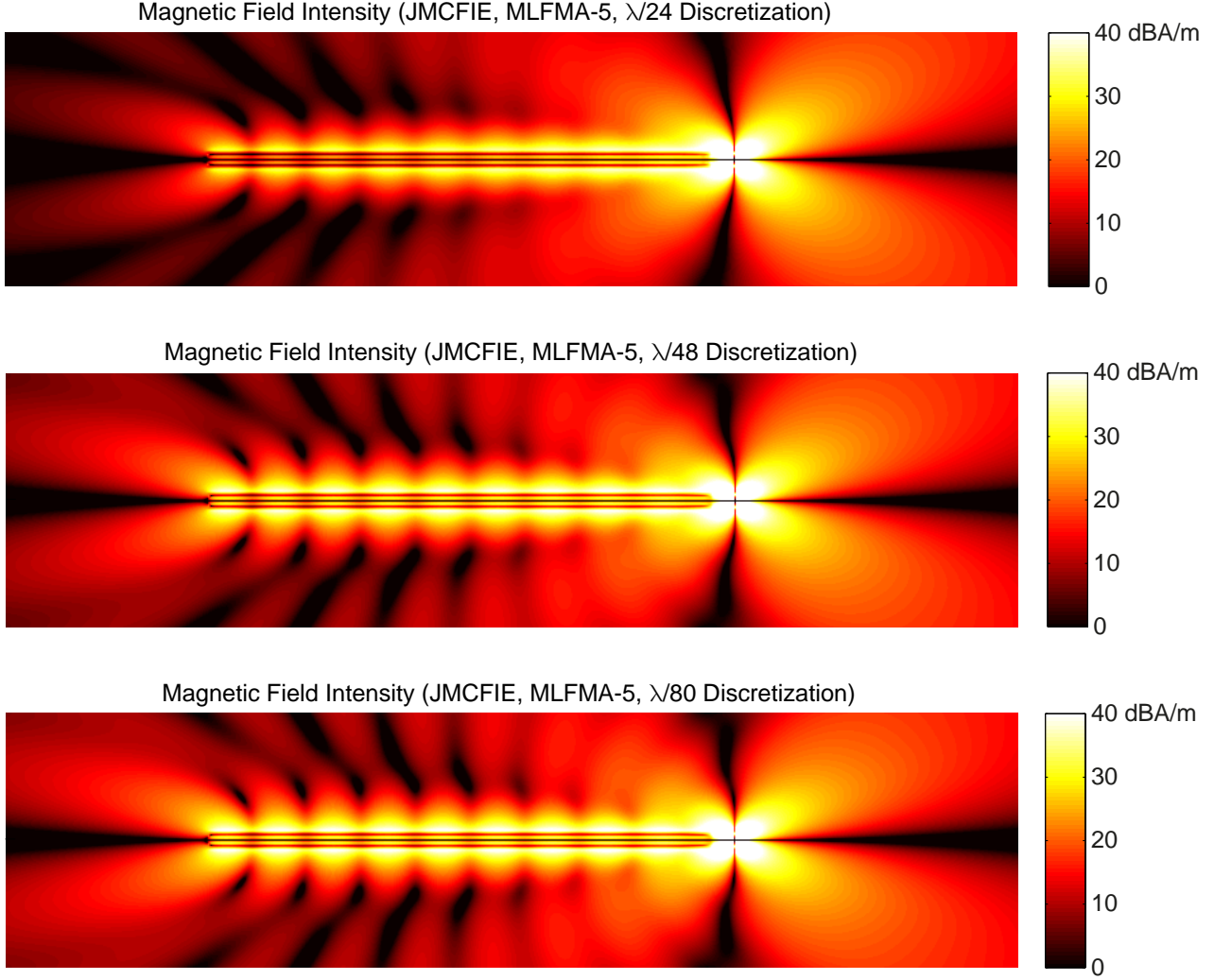


Figure 1: Magnetic field intensity in the vicinity of a dual nanowire transmitter made of silver and excited with two dipoles (located on the right-hand side) at 250 THz. Solutions are obtained by using JMC FIE discretized with $\lambda_o/24$, $\lambda_o/48$, and $\lambda_o/80$ triangles.

secondary electric and magnetic fields as

$$\begin{aligned} \mathbf{E}_u^{sec}(\mathbf{r}) &= ik_u \eta_u \sum_{n=1}^N a_n^J \int d\mathbf{r}' \mathbf{b}_n(\mathbf{r}') g_u(\mathbf{r}, \mathbf{r}') \\ &\quad - i \frac{\eta_u}{k_u} \sum_{n=1}^N a_n^J \int d\mathbf{r}' \nabla' \cdot \mathbf{b}_n(\mathbf{r}') \nabla' g_u(\mathbf{r}, \mathbf{r}') \\ &\quad - \sum_{n=1}^N a_n^M \int d\mathbf{r}' \mathbf{b}_n(\mathbf{r}') \times \nabla' g_u(\mathbf{r}, \mathbf{r}') \end{aligned} \quad (13)$$

$$\begin{aligned} \mathbf{H}_u^{sec}(\mathbf{r}) &= \frac{ik_u}{\eta_u} \sum_{n=1}^N a_n^M \int d\mathbf{r}' \mathbf{b}_n(\mathbf{r}') g_u(\mathbf{r}, \mathbf{r}') \\ &\quad - \frac{i}{k_u \eta_u} \sum_{n=1}^N a_n^M \int d\mathbf{r}' \nabla' \cdot \mathbf{b}_n(\mathbf{r}') \nabla' g_u(\mathbf{r}, \mathbf{r}') \\ &\quad + \sum_{n=1}^N a_n^J \int d\mathbf{r}' \mathbf{b}_n(\mathbf{r}') \times \nabla' g_u(\mathbf{r}, \mathbf{r}'). \end{aligned} \quad (14)$$

By selecting $u = \{o, i\}$, electromagnetic fields for the outer and inner problems are obtained, while their superpositions lead to the overall field distributions.

4. Numerical Examples

For numerical examples, we consider a system of two Ag nanowires excited by a pair of dipoles at 250 THz. The system can be considered as a transmitter, and field distributions in its vicinity are of particular interest. Each nanowire has $0.1 \times 0.1 \times 5 \mu\text{m}$ dimensions, and the distance between them is $0.1 \mu\text{m}$. Fig. 1 depicts the magnetic field intensity in the vicinity of the structure, when the problem is formulated with JMC FIE. For discretizations, the RWG functions on $\lambda_o/24$, $\lambda_o/48$, and $\lambda_o/80$ triangles are used, leading to matrix equations involving 9792, 38,784, and 113,064 unknowns, respectively. All solutions are performed by a five-level MLFMA with two digits of accuracy on a single core.

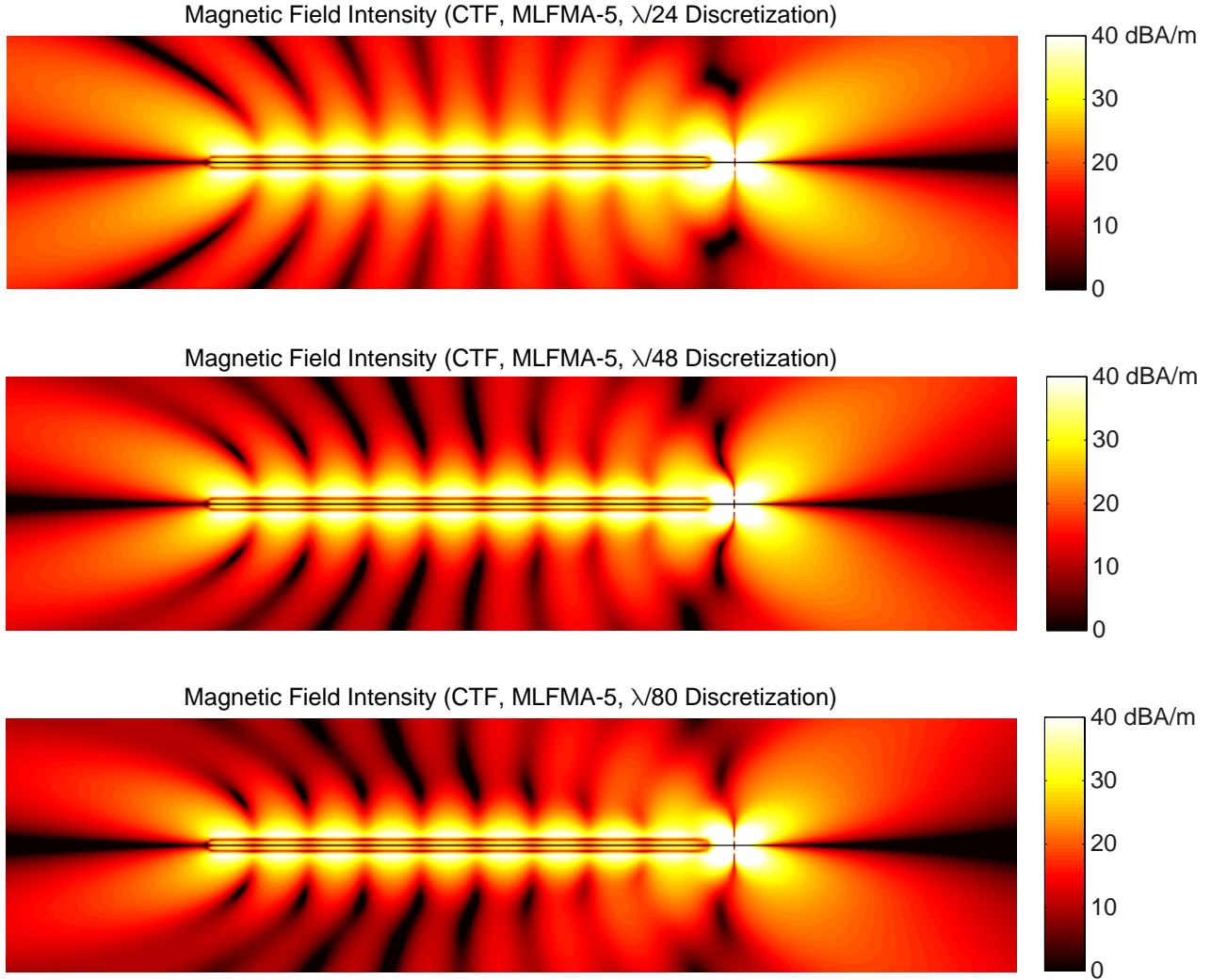


Figure 2: Magnetic field intensity in the vicinity of a dual nanowire transmitter made of silver and excited with two dipoles (located on the right-hand side) at 250 THz. Solutions are obtained by using CTF discretized with $\lambda_o/24$, $\lambda_o/48$, and $\lambda_o/80$ triangles.

Iterative solutions are carried out by using the generalized minimal residual (GMRES) method. As depicted in Fig. 1, the results obtained with JMCFIE change significantly as the discretization is improved. These comparisons reveal that $\lambda_o/24$ and even denser discretizations may not be sufficient if nanowire problems are formulated with JMCFIE.

Next, in Fig. 2, we present the magnetic-field results provided by CTF. Using this formulation instead of JMCFIE improves the accuracy, while there are still important discrepancies between the results obtained with different discretizations. As opposed to much better performance of CTF for low-order discretizations of ordinary materials, we observe that $\lambda_o/24$ discretization of CTF may not be sufficient for nanowires. As a comparison, Fig. 3 depicts the results when MCTF is used with $\lambda_o/24$ triangles. It can be observed that the field values obtained in this case are very similar to those obtained with JMCFIE and CTF using $\lambda_o/80$ discretization. Considering also the mesh conver-

gence for JMCFIE and CTF, we conclude that MCTF provides accurate results with coarser discretizations and less numbers of unknowns. Using MCTF, the number of iterations increases to 249 (from 134/145 for JMCFIE/CTF) for 10^{-4} residual error when $\lambda_o/24$ discretization is considered. Nevertheless, for a given level of accuracy, the decrease in the number of unknowns more than compensates for the increase in the iteration counts.

5. Conclusions

We present rigorous analysis of nanowires at optical frequencies. As important components of the developed simulation environment, we employ

- surface integral equations that require discretizations of only surfaces while enabling plasmonic modeling via effective electrical parameters,

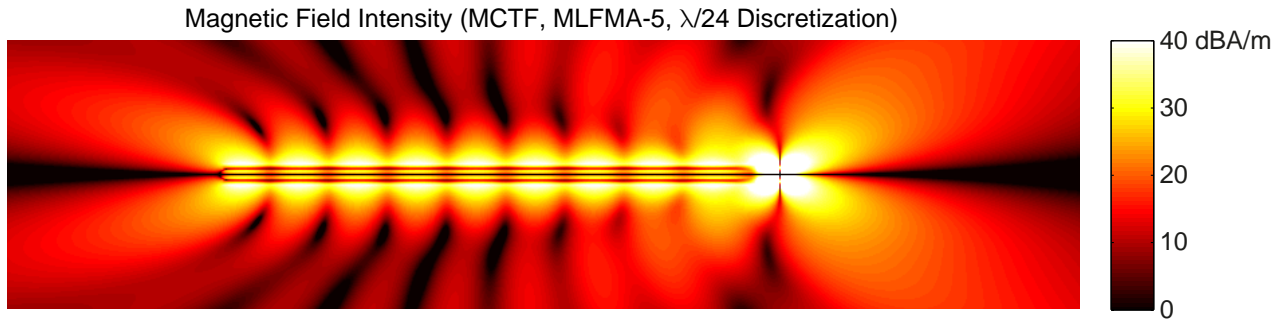


Figure 3: Magnetic field intensity in the vicinity of a dual nanowire transmitter made of silver and excited with two dipoles (located on the right-hand side) at 250 THz. The solution is obtained by using MCTF discretized with $\lambda_o/24$ triangles. A typical high-quality transmission of the electromagnetic power along the nanowire surfaces is observed. On the left-hand side, the transmitted power is coupled to free space and radiated as two beams.

- MLFMA that provides fast matrix-vector multiplications for iterative solutions of matrix equations.

Considering fast and accurate solutions of plasmonic problems, we improved the traditional versions of these components, by

- rebalancing matrix blocks in order to preserve the accuracy of surface integral equations for large negative permittivity values,
- eliminating quickly decaying inner interactions and avoiding their unnecessary computations for given error thresholds of the corresponding outer interactions in order to preserve the efficiency of MLFMA.

Accuracy of solutions for different surface formulations are focused in this paper. As an important advantage, the proposed solution mechanism provides the analysis of deformed nanowires (e.g., similar to [2]) in addition to regular structures.

Acknowledgement

This work was supported by the Scientific and Technical Research Council of Turkey (TUBITAK) under the Research Grant 113E129 and by the Turkish Academy of Sciences (TUBA) in the framework of the Young Scientist Award Program.

References

- [1] J. Yao, Z. Liu, Y. Liu, Y. Wang, C. Sun, G. Bartal, A. M. Stacy, and X. Zhang, Optical negative refraction in bulk metamaterials of nanowires, *Science*, 321: 930, 2008.
- [2] A. Yılmaz, B. Karaosmanoğlu, and Ö. Ergül, Computational electromagnetic analysis of deformed nanowires using the multilevel fast multipole algorithm, *Sci. Rep.*, 5: 8469, 2015.
- [3] P.B. Johnson and R.W. Christy, Optical constants of the noble metals, *Phys. Rev. B*, 6: 4370–4379, 1972.
- [4] M.G. Araujo, J.M. Taboada, D.M. Solis, J. Rivero, L. Landesa, and F. Obelleiro, Comparison of surface integral equation formulations for electromagnetic analysis of plasmonic nanoscatterers, *Opt. Express*, 20: 9161–9171, 2012.
- [5] Ö. Ergül, Analysis of composite nanoparticles with surface integral equations and the multilevel fast multipole algorithm, *J. Opt.*, 14: 062701, 2012.
- [6] Ö. Ergül, Fast and accurate solutions of electromagnetics problems involving lossy dielectric objects with the multilevel fast multipole algorithm, *Eng. Anal. Bound. Elem.*, 36: 423–432, 2012.
- [7] D.M. Solis, J.M. Taboada, O. Rubinos-Lopez, and F. Obelleiro, Improved combined tangential formulation for electromagnetic analysis of penetrable bodies, *J. Opt. Soc. Am. B.*, 32: 1780–1787, 2015.
- [8] H. Gomez-Sousa, O. Rubinos-Lopez, and J.A. Martinez-Lorenzo, Comparison of iterative solvers for electromagnetic analysis of plasmonic nanostructures using multiple surface integral equation formulations, Online: arXiv:1510.05337.
- [9] Ö. Ergül and L. Gürel, *The Multilevel Fast Multipole Algorithm (MLFMA) for Solving Large-Scale Computational Electromagnetics Problems*. Wiley-IEEE, 2014.
- [10] B. Karaosmanoğlu, A. Yılmaz, U.M. Gür, and Ö. Ergül, Solutions of plasmonic structures using the multilevel fast multipole algorithm,” *Special Issue on Challenges in RF and Microwave Defense Engineering, Int. J. RF Microwave Comput.-Aided. Eng.*, 26: 335–341, 2016.

Coupled Field Problems

Modeling and analysis of loaded multilayered magneto-electroelastic structures composite materials: Applications

M. Ajdour^{1*}, A. Bakkali², L. Azrar¹, A. El Omri³

¹ Mathematical Modeling and Control, Faculty of Sciences and Techniques of Tangier, AbdelMalek Essaadi University; Tangier; Morocco

² Mathematical Modeling and Control, Faculty of Sciences of Tetouan, AbdelMalek Essaadi University; Tetouan. Morocco

³ Laboratory Of Mechanics and Materials, Faculty of Sciences and Technology of Tangier, AbdelMalek Essaadi University; Tangier; Morocco

*corresponding author: majdour@hotmail.fr

Abstract- This paper presents the detailed analysis of fiber- reinforced Magneto-electroelastic composite plates. The work is divided into two major sections. The first one, deals with the homogenization of the properties of each layer based on the Mori-Tanaka mean field approach where all the needed effective coefficients of each layer are determined. Then in order to perform analysis of the considered, the Stroh formalism is used to provide solutions for multifunctional multilayered magneto-electroelastic composites, to predict exactly the mechanical and electrical behaviors near or across the interface of material layers.

We consider the linear magneto-electroelastic effect where the magnetic, electric and elastic fields are coupled through the following constitutive equations:

$$\begin{aligned}\sigma_{ij} &= C_{ijkl}\varepsilon_{kl} - e_{lij}E_l - h_{lij}H_l \\ D_i &= e_{ikl}\varepsilon_{kl} + \kappa_{il}E_l + \alpha_{il}H_l \\ B_i &= h_{ikl}\varepsilon_{kl} + \alpha_{il}E_l + \mu_{il}H_l\end{aligned}\quad (1)$$

Where the elastic strain ε_{kl} , electric fields E_l and the magnetic fields H_l are independent

variables related to stresses σ_{ij} , electric displacements D_i and magnetic inductions B_i . The tensors

C_{ijkl} , e_{lij} , h_{lij} , α_{il} , κ_{il} and μ_{il} are the elastic, piezoelectric, piezomagnetic, magnetoelectric, dielectric and magnetic permeability constants respectively. The following gradient expressions are used:

$$\varepsilon_{kl} = \frac{1}{2}(u_{k,l} + u_{l,k}), E_l = \varphi_{,l}^e \text{ and } H_l = \varphi_{,l}^m$$

Where u_k , φ^e and φ^m are the elastic displacements, electric and magnetic potentials respectively.

The magneto-electroelastic constant can be represented as follows:

$$E_{iJMn} = \begin{cases} C_{iJMn} & (J, M = 1, 2, 3) \\ e_{nij} & (J = 1, 2, 3; M = 4) \\ h_{nij} & (J = 1, 2, 3; M = 5) \\ e_{imn} & (J = 4; M = 1, 2, 3) \\ h_{imn} & (J = 5; M = 1, 2, 3) \\ -\kappa_{in} & (J = 4; M = 4) \\ -\alpha_{in} & (J = 4; M = 5 \text{ or } J = 5; M = 4) \\ -\mu_{in} & (J = 5; M = 5) \end{cases} \quad (2)$$

The homogeneous fictitious media called “reference media” has the magneto-electroelastic moduli E_{iJMn}^0 .

The expression of the local magneto-electroelastic moduli is given as follow:

$$E_{iJMn}(r) = E_{iJMn}^0 + \delta E_{iJMn}(r) \quad (3)$$

Where “r” is the position vector in the media considered and δE is the derivation part.

The equilibrium equation becomes [1,2]:

$$E_{iJMn}^0 U_{M,ni}(r) + (\delta E_{iJMn}(r) U_{M,n}(r))_{,i} = 0 \quad (4)$$

$$\text{Where } U_M = \begin{cases} u_m & (M = 1, 2, 3) \\ \varphi^e & (M = 4) \\ \varphi^m & (M = 5) \end{cases}$$

The Mori-Tanaka mean field approach takes into account the effect of other inhomogeneities by considering a finite concentration of inclusions embedded in an infinite matrix of magneto-electroelastic moduli and , and gives a straightforward explicit expression of the effective moduli. The corresponding concentration tensor is then given by the solution for a single inclusion embedded in an infinite matrix in the same manner as the heterogeneous inclusion problem of Eshelby.

Results are presented for a two-phase composite material with laminate or fibrous microstructure and compared with analytic solutions and finite-element results taken from the literature.

Using the Stroh formalism [3,4] associated with the propagation matrix, this will provide solutions for multifunctional multilayered plate, to predict exactly the mechanical and electrical behaviors near or across the interface of material layers

REFERENCES

1. Bakkali, A. Azrar, L. Aljinaidi, A.” Journal of Intelligent Material Systems and Structures” *JIMSS* doi:10.1177/1045389X16629552.
2. Azrar, L. Bakkali, A. Aljinaidi, A.” Composite Structures”, *CS*, Vol. 113 281-297, 2014
3. Pan, A. Journal of Applied Mechanics *JAM* Vol. 68, 608 - 618; 2001.
4. Ajdour, M. Azrar, L.” Advanced Materials Research” *AMR*, Vol. 682, 127-134, 2013.

RF and Wireless Communication

Exploiting Large-Scale Cooperative MIMO Approach in Relay-Assisted Next-Generation Cellular Systems

Mostafa Hefnawi

Department of Electrical and Computer Engineering, Royal Military College of Canada, Kingston, Canada

E-mail: hefnawi@rmc.ca

Abstract

This paper proposes a massive multiple-input multiple-output (MIMO) beamforming scheme for cooperative relay-assisted millimeter-wave cellular systems employing orthogonal frequency-division multiplexing (OFDM) such as the upcoming 5th generation (5G) systems. The relay nodes are divided into clusters, each consisting of cooperative nodes that form a virtual massive antenna array. Using particle swarm optimization (PSO), each cluster seeks the optimal transmit weight vectors that maximize the uplink cooperative MIMO channel capacity of each cluster. The PSO-based capacity-aware (PSO-CA) scheme is compared to the traditional capacity-aware gradient search scheme (GS-CA) and the results show that PSO-CA requires considerably less computational complexity while achieving essentially better or the same level of performance as the GS-CA.

1. Introduction

Recently, the use of millimeter-wave (mm-Wave) frequency bands of 30–300 GHz has gained attentions from system developers as a possible way forward for realizing gigabit data rate in the future 5G systems [1]. The mm-Wave spectrum is attractive because of the massive amount of bandwidth available but it suffers from heavy shadowing and often requires a line-of-sight between transmitter and receiver. In order to use the mm-Wave band more efficiently, various advanced technologies such as highly directional steerable antennas and relays are considered for use in 5G mobile communication networks. More specifically, base stations (BSs) equipped with a very large number of antennas (also called massive or large-scale MIMO system) that can simultaneously accommodate many co-channel users, has emerged as a promising solution to extend the coverage at longer ranges and to overcome the high mm-Wave path loss [2]. Also, at these frequencies, very large arrays can be created with a reasonable size that could be deployed at BSs and relay stations (RSs). Multiuser-MIMO (MU-MIMO) techniques have been successfully deployed in 4G cellular systems for traditional microwave spectrum bands and a vast number of multiuser detection algorithms are presently being tailored towards solving the MU-MIMO processing in mm-Wave networks

[3]-[7]. In particular, capacity-aware MU-MIMO schemes have been proposed for 4G systems using different multiuser detection schemes such as maximum ratio combining (MRC) and minimum mean-squared error (MMSE) [6], [7], and have shown the potential to exhibit better system capacity and provide better symbol error rate (SER) enhancement than traditional singular value decomposition (SVD)-based MU-MIMO systems [3], [4]. However, for most MIMO implementations in 4G, the base station typically employs only a few (i.e. < 10) antennas, and the corresponding improvement in spectral efficiency, while important, is still relatively modest, especially with the explosion of wireless mobile devices and services. On the other hand, the concept of massive MIMO was investigated for cellular networks and have shown significant performance improvement in terms of reliability, spectral efficiency, and energy efficiency [2]. Also, when using massive MIMO close to optimal performances can be achieved with the simplest forms of user detection and beamforming, i.e., MRC, and eigenbeamforming. Most of these works, however, have assumed large antenna array at the base station only and have focused on MIMO multiplexing as a major enabler for high-speed wireless transmission without considering MU-MIMO contexts. In this paper, therefore, we will be considering massive MIMO where both MSs and BSs are equipped with large antenna array. However, since it is difficult to integrate large antenna arrays in small devices due to space limitations and circuit complexity, a cooperative relay-assisted system, where a group of relay nodes (RNs) organize themselves into a virtual antenna array, is used to cooperatively relay the MS signal to the BS. Moreover, MU-MIMO approach is exploited by dividing the network into groups of RNs called clusters. Also, in the development of our capacity-aware beamforming scheme for large-scale cooperative MIMO (LS-CMIMO) we will be exploring free-derivative population-based training algorithms such as the particle swarm optimization (PSO) that are well known by their fast convergence, low complexity and simple implementation [8]. In this paper, PSO is used at the cluster side to seek iteratively the transmit beamforming weights that maximize the uplink MIMO channel capacity for each cluster (i.e. each MS), without involving any gradient search. The performance of the proposed PSO-based capacity-aware

(PSO-CA) is compared to the one based on the gradient search scheme (GS-CA) in terms of channel capacity and symbol error rate. The contribution of this paper includes the extension of the capacity-aware MU-MIMO to large-scale LS-MU-MIMO cellular system using clustered cooperative RNs and the use of the derivative-free PSO for channel maximization.

2. System Model

We consider the uplink multicluster access scenario shown in Fig. 1 where a group of RNs is divided into L_s clusters each connected to a MS.

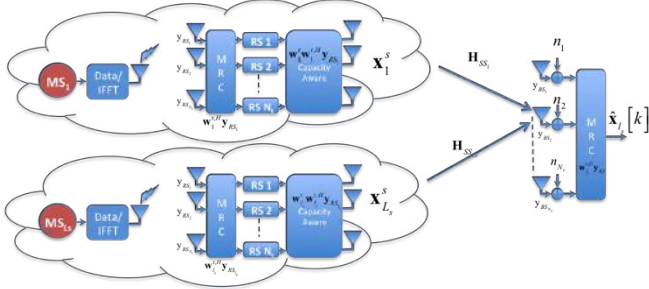


Figure 1: Cooperative relay-assisted MIMO-OFDM System.

Each cluster consists of N_s^t cooperative RNs that collect the data broadcasted by its MS using MRC detection and relay it to the BS using a capacity-aware beamforming scheme. In each cluster, the MS and its N_s^t cooperative RNs act as one MS user with N_s^t -element antenna array. It is also assumed that the BS detects independent OFDM data streams from multiple clusters simultaneously on the same time-frequency resources. Let $\mathbf{x}^s[k] = \{x_1^s, x_1^s, \dots, x_{L_s}^s\}$ denote the set of L_s signals transmitted during the second hop on each subcarrier, $k = 1, \dots, N_c$, where N_c denotes the number of subcarriers per OFDM symbol in the system. The expression for the array output at the base station in Fig. 1 can be written for each subcarrier as

$$\mathbf{y}_{\text{BS}}[k] = \sum_{l_s=1}^{L_s} \mathbf{H}_{ss,l_s}[k] \mathbf{w}_{l_s}^t[k] \mathbf{x}_{l_s}^s[k] + \mathbf{n}[k] \quad (1)$$

where $\mathbf{y}_{\text{BS}}[k]$ is the $N_s^r \times 1$ vector containing the outputs of the N_s^r -element array at the BS, with $(\cdot)^T$ denoting the transpose operation, \mathbf{H}_{ss,l_s} is the $N_s^r \times N_s^t$ frequency-domain channel matrix representing the transfer functions from the N_s^t nodes of cluster l_s to the BS's N_s^r -element antenna array, $\mathbf{w}_{l_s}^t[k]$ is the $N_s^t \times 1$ complex transmit weight vector for cluster l_s , $l_s = 1, \dots, L_s$, $\mathbf{n}[k]$ is the $N_s^r \times 1$ complex additive white Gaussian noise vector. Assuming that the spacing between relays is large enough, the entries of $\mathbf{H}_{ss,l_s}[k] \in \mathbb{C}^{N_s^r \times N_s^t}$ can be modeled as independent and identically distributed (i.i.d) complex Gaussian, with zero mean and unit variance. The BS detects all L_s clusters data, simultaneously at the multiuser detection module, by multiplying the output of the BS array with the $N_s^r \times 1$ receiving weight vectors, $\mathbf{w}_{l_s}^r[k]$, for each cluster l_s . The

detection of cluster l_s out of $L - 1$ interfering users can thus be depicted as

$$\hat{\mathbf{x}}_{l_s}[k] = \mathbf{w}_{l_s}^{r,H}[k] \mathbf{y}_{\text{BS}}[k] = \mathbf{S}_d[k] + \mathbf{S}_I[k] + \mathbf{N}[k] \quad (2)$$

where $\mathbf{N}[k] = \mathbf{w}_{l_s}^{r,H}[k] \mathbf{n}[k]$ is the noise signal at the array output of the BSN, $\mathbf{S}_d[k] = \mathbf{w}_{l_s}^{r,H}[k] \mathbf{H}_{ss,l_s}[k] \mathbf{w}_{l_s}^t[k] \mathbf{x}_{l_s}^s[k]$ is the desired signal for the detection of cluster l_s 's signal, $\mathbf{S}_I[k] = \mathbf{w}_{l_s}^r[k] \sum_{i=1, i \neq l_s}^{L_s} \mathbf{H}_{ss,i_s}[k] \mathbf{w}_{i_s}^t[k] \mathbf{x}_{i_s}^s[k]$ is the multiple-access interference contributed by the $L_s - 1$ other clusters. During the analysis, perfect channel estimation is assumed. This assumption is justified by the fact that when the number of antennas grows towards infinity, effects of noise, interference and imperfect channel state information (CSI) disappear.

3. PSO-based channel Maximization

Our objective is to find the optimal beamforming vector, $(\mathbf{w}_{l_s}^t[k])_{opt}$, that maximizes the Ergodic channel capacity of the MU-MIMO-OFDM channel for each cluster l_s while limiting its maximum transmission power to $P_{max,l}^t$. In mathematical terms, this can be expressed as follows:

$$\max_{\mathbf{w}_{l_s}^t[k]} \mathbb{C}(\mathbf{H}_{ss,l_s}, \mathbf{w}_{l_s}^t), \quad (3)$$

where $\mathbb{C}(\mathbf{H}_{ss,l_s}, \mathbf{w}_{l_s}^t)$ is the Ergodic capacity of the channel and is given by

$$\mathbb{C}(\mathbf{H}_{ss,l_s}, \mathbf{w}_{l_s}^t) = E \left(\log_2 \left\{ \mathbf{I} + \frac{\rho_{l_s}}{N_s^t} |\mathbf{B}_{l_s}[k]|^{-1/2} \tilde{\mathbf{H}}_{ss,l_s}^t[k] \right\}^2 \right), \quad (4)$$

where $E[\cdot]$ denotes the expectation operator,

$\tilde{\mathbf{H}}_{ss,l_s}^t[k] = \mathbf{H}_{ss,l_s}[k] \mathbf{w}_{l_s}^t[k]$, and

$$\mathbf{B}_{l_s}[k] = \sum_{i=1, i \neq l_s}^{L_s} \tilde{\mathbf{H}}_{ss,i_s}^t[k] \tilde{\mathbf{H}}_{ss,i_s}^{t,H}[k] + \sigma_n^2 \mathbf{I}_{N_s^r}[k].$$

As an alternative to the conventional gradient search-based capacity-aware algorithm (GS-CA) [6], [7] we employ the PSO free-derivative algorithm to optimize the transmit weight vector. PSO is a stochastic algorithm; where the birds or particles are mapped to the transmit beamforming weights, fly in the search space, aiming to optimize a given objective. In this paper, the beamforming weights are optimized towards maximizing the channel capacity given by Equation (4). First, the PSO generates B random particles for each cluster (i.e., random weight vector $\mathbf{w}_{l_s}^{t,(b)}$, $b = 1, \dots, B$ of length $N_s^t \times 1$) to form an initial population set S (swarm). The algorithm computes the channel capacity according to Eq. (4) for all particles $\mathbf{w}_{l_s}^{t,(b)}$ and then finds the particle that provides the global optimal channel capacity for this iteration, denoted $\mathbf{w}_{l_s}^{t,(b,gbest)}$. In addition, each particle b memorizes the position of its previous best performance, denoted $\mathbf{w}_{l_s}^{t,(b,pbest)}$. After finding these two best values, PSO updates its velocity $\mathbf{v}_{l_s}^{t,(b)}$

and its particle positions $\mathbf{w}_{l_s}^{t,(b)}$, respectively at each iteration n as follows:

$$\begin{aligned} \mathbf{v}_{l_s}^{t,(b)}(n+1) &= \omega \mathbf{v}_{l_s}^{t,(b)}(n) \\ &+ c_1 \varphi_1 \left(\mathbf{w}_{l_s}^{t,(b,pbest)}(n) - \mathbf{w}_{l_s}^{t,(b)}(n) \right) \\ &+ c_2 \varphi_2 \left(\mathbf{w}_{l_s}^{t,(b,gbest)}(n) - \mathbf{w}_{l_s}^{t,(b)}(n) \right), \quad (5) \end{aligned}$$

$$\mathbf{w}_{l_s}^{t,(b)}(n+1) = \mathbf{w}_{l_s}^{t,(b)}(n) + \mathbf{v}_{l_s}^{t,(b)}(n+1), \quad (6)$$

where c_1 and c_2 are acceleration coefficients towards the personal best position ($pbest$) and/or global best position ($gbest$), respectively, φ_1 and φ_2 are two random positive numbers in the range of $[0, 1]$, and ω is the inertia weight which is employed to control the exploration abilities of the swarm. Large inertia weights will allow the algorithm to explore the design space globally. Similarly, small inertia values will force the algorithms to concentrate in the nearby regions of the design space. This procedure is repeated until convergence (i.e., channel capacity remains constant for a several number of iterations or reaching maximum number of iterations). Note that since the update is done separately on each subcarrier, we dropped the frequency index $[k]$ and concentrate on the iteration index (n) in this recursion. Also, since random initialization does not guarantee a fast convergence, in our optimization procedure we consider that the initial value of $\mathbf{w}_{l_s}^{t,(b)}(n)$ at iteration index $n = 0$ is given by the eigen-beamforming (EBF) weight, i.e., $\mathbf{w}_{l_s}^{t,(b)}(0) = \mathbf{w}_{l_s}^{t,EBF} = \sqrt{P_{max,l_s}^t} \mathbf{u}_{max,l_s}$, where \mathbf{u}_{max,l_s} denotes the eigenvector corresponding to λ_{max,l_s} , the maximum eigenvalue of $\mathbf{H}_{SS,l_s}^H \mathbf{H}_{SS,l_s}$. This initial guess enables the algorithm to reach a more refined solution iteratively by ensuring fast convergence.

4. Simulation Results

In our simulation setups we consider a relay-assisted cellular system organized into five clusters ($L_s = 5$), each with N_s^t RNs (N_s^t varying from 8 to 50) and one MS. The number of antennas at the BS, N_s^r , is fixed at 200. We assume QPSK modulation and impose $P_{max,l}^t = 0$ dB. For the OFDM configurations, we assume the 256-OFDM system ($N_c = 256$), which is widely deployed in broadband wireless access services. We assume MRC at the receiving RNs for the first hop and at the receiving BS for the second hop. For the PSO parameters, the swarm size is 30, the maximum iteration number is 25 and the acceleration coefficients are $c_1 = c_2 = 2$. The inertia weight ω ranges from 0.9 to 0.4 and varies as the iteration goes on. Fig. 2 and Fig. 3 show, respectively, the SER performance and system capacity of the proposed PSO-CA and the traditional GS-CA schemes for different cluster size ($N_s^t = 8, 25, \text{ and } 50$) with $N_s^r = 200$. It is observed from the results that for all cases PSO-CA is outperforming GS-CA.

It is also noted that as we increase the cluster size, the performance gap between the two schemes is reduced. This means that when the number of base station antennas becomes large, PSO-CA is able to achieve the same level or better performance than GS-CA with less computational complexity.

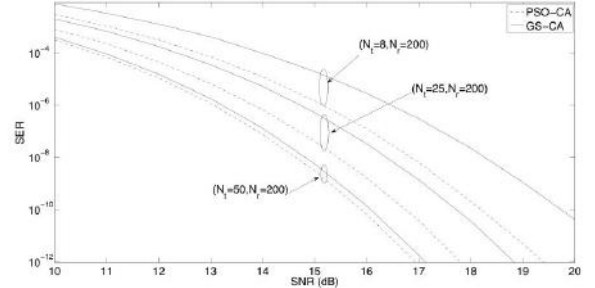


Figure 2: SER performance with PSO-CA and GS-CA for different clusters size

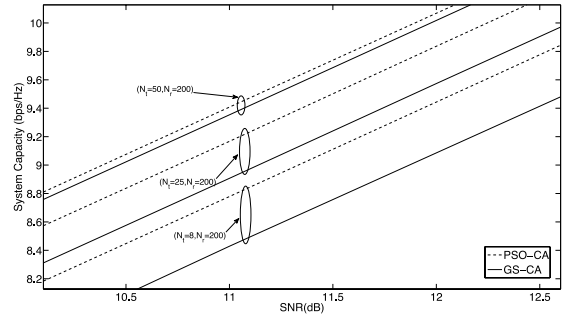


Figure 3: Channel capacity with PSO-CA and GS-CA for different clusters size

5. Conclusion

This paper proposes a PSO-based adaptive beamforming algorithm for multiuser access in large-scale cooperative relay-assisted cellular systems. The proposed algorithm iteratively seeks the optimal transmit weight vectors that maximize the channel capacity of each secondary user in the network without requiring a gradient search of the channel capacity. It was shown that the proposed system is able to achieve a low computational complexity with the same level or better performance than the conventional gradient search for channel maximization.

Acknowledgements

The author would like to thank the Canadian Microelectronics Corporation (CMC) for providing the Heterogeneous Parallel Platform to run the computationally intensive Monte-Carlo Simulations.

References

- [1] T. S. Rappaport et al., “Millimeter Wave Mobile Communications for 5G Cellular: It Will Work!,” *IEEE Access*, vol. 1, May 2013, pp. 335–49.
- [2] T. L. Marzetta, “Noncooperative cellular wireless with unlimited numbers of base station antennas,” *IEEE Tran. Wirel. Comm.*, vol. 9, no. 11, pp. 3590 – 3600, Nov. 2010.
- [3] M. Jiang, S. Ng, and L. Hanzo, “Hybrid Iterative Multiuser Detection for Channel Coded Space Division Multiple Access OFDM Systems,” *IEEE Trans. Veh. Technol.*, Vol.55, No1, Jan. 2006.
- [4] M. Munster and L. Hanzo, “Performance of SDMA Multi-User Detection Techniques for Walsh-Hadamard-Spread OFDM Schemes,” *IEEE-VTC’01*, Vol. 4, pp. 2319-2323, Oct. 2001.
- [5] M. Kang, “A comparative study on the performance of MIMO MRC systems with and without cochannel interference,” *IEEE Transactions on Communications*, Vol. 52 , Iss. 8, pp. 1417 – 1425, 2004.
- [6] A. I. Sulyman and M. Hefnawi, “Adaptive MIMO Beamforming Algorithm Based on Gradient Search of the Channel Capacity in OFDMSDMA System,” *IEEE Commun. Letters*, Vol. 12, No. 9, pp. 642-644, Sept. 2008.
- [7] A. I. Sulyman, and M. Hefnawi, “Performance Evaluation of Capacity-Aware MIMO Beamforming Schemes in OFDM-SDMA Systems,” *IEEE Trans. Commun.*, Vol. 58, No. 1, Jan. 2010.
- [8] J. Kennedy, RC. Eberhart, “Particle swarm optimization,” *Proceedings of the IEEE Conference on Neural Networks IV*, , pp. 1942–1948, 1999

Optics and Photonics

Optical Attenuators with Translational Risley Prisms

V.-F. Duma^{1,2,3}

¹3OM Optomechanics Group, Aurel Vlaicu University of Arad, 77 Revolutiei Ave., Arad, Romania

²Doctoral School, Polytechnics University of Timisoara, 1 Mihai Viteazu Ave., Timisoara, Romania

³Faculty of Physics, West University of Timisoara, 4 Vasile Parvan Ave., Timisoara, Romania

duma.virgil@osamember.org

Abstract-We study the three possible configurations of optical attenuators with translational Risley prisms. These devices are compared from the point of view of their relevant parameters: minimum transmission coefficient, attenuation range and interval, and sensitivity. The variant with two identical, symmetrically moving prisms is demonstrated to provide the best possible values of these optical parameters, as well as the best mechanical solution. Its designing calculus is developed and a prism angle of 10° is demonstrated to be the optimal one from the point of view of the maximum attenuation range that this device can provide.

A large variety of optical attenuators exist [1,2], including with diaphragms (iris or shutters), with polarization filters, with sets of neutral density (ND) or with continuously variable rotational filters. With regard to such solutions, attenuators with double wedges/Risley prisms have certain advantages: a constant diameter of the exit beam (as necessary for example in colorimeters) and a fine adjustment of the light transmission, therefore good sensitivity. Issues exist, such as obtaining a good transmission range and interval, while having a satisfactory minimum light flux. While rotational [3,4] and oscillatory [5] Risley prisms scanners have been developed extensively, devices with translational ND or colored double wedges have been just mentioned in literature, without being analyzed and optimized – to the best of our knowledge.

Three types of such devices can be designed [6]: (i) with one prism fixed and another one in translation along the hypotenuse of the first one; (ii) with both prisms mobile, moving symmetrically with respect to each other (Fig. 1); (iii) with one prism fixed and the other one in translation along the long cathetus of the first one. In the detailed analyses

made in [6] we demonstrated that configuration (ii) - Fig. 1 - is the best one from both the optical and the mechanical point of view, the latter aspect given by the contactless movement of the prisms.

The transmission coefficient of this attenuator is:

$$\tau = \Phi/\Phi_i, \quad (1)$$

$$\text{with } \Phi = \Phi_e (D/D_i)^2, \quad \Phi_e(x) = \Phi_i \exp(-\alpha d(x)) \quad (2)$$

where Φ_i and Φ_e are the incident and the emergent flux from the prisms, respectively, α is the absorption coefficient, and $d(x)$ is the thickness of the neutral filter formed. The emergent flux Φ also takes into account the exit diaphragm, of diameter $D=D_i-\delta(l)$, where D_i is the diameter of the

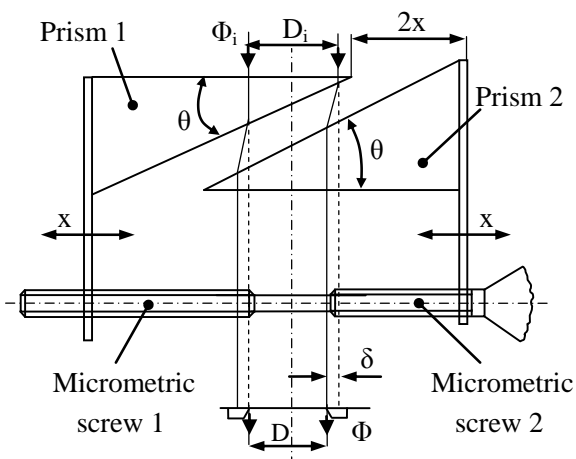


Fig. 1. Optical attenuator with Risley prisms [6].

incident beam, l is the maximum displacement of a prism, and $\delta(l) = \delta_{\max}$ is the maximum deviation of the emergent beam, obtained from:

$$\delta(x) = 2x \left(n \cos \theta / \sqrt{1 - n^2 \sin^2 \theta} - 1 \right) \sin^2 \theta. \quad (3)$$

As the current thickness of the ND filter plate formed is:

$$d(x) = d_0 - [2x + \delta(x)] \tan \theta. \quad (4)$$

The condition to have the incident beam completely on the first facet of the top prism is:

$$a \geq 2l + D + \delta_{\max}. \quad (5)$$

From Eqs. (1) to (5), the current transmission coefficient is:

$$\tau(x) = r_1 \tau_0 \exp[2\alpha r_2 \cdot x \cdot \tan \theta] \quad (6)$$

where $\tau_0 = \exp(-\alpha d_0)$ and

$$r_1 = \left(\frac{D}{D + \delta_{\max}} \right)^2; \quad r_2 = \left(\frac{n \sin^2 \theta}{\sqrt{1 - n^2 \sin^2 \theta}} + \cos \theta \right) \cos \theta. \quad (7)$$

The minimum and maximum transmission can thus be characterized (with) by:

$$\tau_{\min} = \tau(0) = r_1 \tau_0; \quad \tau_{\max} = \tau(l) = r_1 \tau_0^{1-r_2} C^{r_2}, \quad \text{where} \quad C = \exp(-\alpha \cdot D_i \cdot \tan \theta) \quad (8)$$

The adjustment/attenuation range, as well as the adjustment/attenuation interval can be finally obtained:

$$k = \tau_{\max} / \tau_{\min} = (C / \tau_0)^{r_2}, \quad \text{respectively} \quad \Delta \tau = \tau_{\max} - \tau_{\min} = r_1 \tau_0 \left[(C / \tau_0)^{r_2} - 1 \right]. \quad (9)$$

From the designing calculus of this device [6], the best solution is obtained (when the refractive index of the prisms is $n=1.517$) for $\theta=10^\circ$ and $l=15$ mm. For these values of the parameters of the device the attenuation range is $k=2.5$, which we have thus demonstrated to be the highest attenuation range this type of attenuator can provide [6].

Acknowledgements This work was supported by the Romanian National Authority for Scientific Research, CNDE-UEFISCDI project PN-II-PT-PCCA-2011-3.2-1682 (<http://3om-group-optomechatronics.ro/>).

REFERENCES

1. Bass, M., *Handbook of optics*, 3rd Edition, Mc. Graw-Hill Inc., New York, 2009.
2. Duma, V.-F., *Optomechatronic Modulators: Choppers, Attenuators and Scanners. Analysis and Design*, Habilitation Thesis - at the Polytechnics Univ. of Bucharest, 2013.
3. Marshall, G. F., "Risley Prism Scan Patterns," Proc. SPIE 3787, 74-86, 1999.
4. Li, Y., "Third-order theory of the Risley-prism-based beam steering system," Appl. Opt. 50, 679-686 (2011).
5. Li, A., Liu, L., Sun, J., Zhong, X., Wang, L., Liu, D., and Luan, Z., "Research on a scanner for tilting orthogonal double prisms," Appl. Opt. 45, 8063-8069, 2003.
6. Duma, V.-F. and Nicolov, M., "Neutral density filters with Risley prisms: analysis and design," Appl. Opt. 48(14), 2678-2685, 2009.

Family of paraxial Laguerre-Gaussian beams with complex shift in Cartesian coordinates

A. A. Kovalev^{1,2*}, V. V. Kotlyar^{1,2}, A. P. Porfirev^{1,2}, and D. S. Kalinkina²

¹Image Processing Systems Institute, Molodogvardeiskaya St. 151, Samara, Russia

²Samara State Aerospace University, Moskovskoe shosse 34, Samara, 443086, Russia

*corresponding author: alanko.ipsi@mail.ru

Abstract—We consider a family of asymmetrical paraxial Laguerre-Gaussian beams with complex shift in Cartesian coordinates. An expression for their orbital angular momentum (OAM) is derived. When the radial index is zero, we determine the coordinates of intensity maximum. We analytically and experimentally show rotation of the crescent-like diffraction pattern during propagation.

Laguerre-Gaussian (LG) modes are well-studied light fields used in optical manipulation, quantum optics, optical communications. Nevertheless, there still appear publications about their properties and applications [1-3]. Applying complex shift to LG beams in Cartesian coordinates, we theoretically and experimentally study asymmetrical LG beams (aLG-beams). In Cartesian coordinates, their complex amplitude reads as

$$E(x, y, z) = \frac{w(0)}{w(z)} \left[\frac{\sqrt{2}}{w(z)} \right]^n [(x-x_0) + i(y-y_0)]^n L_m^n \left[\frac{2\rho^2}{w^2(z)} \right] \exp \left[-\frac{\rho^2}{w^2(z)} + \frac{ik\rho^2}{2R(z)} - i(n+2m+1)\zeta(z) \right], \quad (1)$$

where x_0 and y_0 are transverse shifts, w_0 is the waist radius, n is the vortex topological charge, $\rho^2 = (x-x_0)^2 + (y-y_0)^2$, $k = 2\pi/\lambda$ is the wavenumber of light with the wavelength of λ , $w(z) = w_0[1 + (z/z_R)^2]^{1/2}$, $R(z) = z[1 + (z_R/z)^2]$, $\zeta(z) = \arctan(z/z_R)$, $z_R = kw_0^2/2$ is the Rayleigh range, $L_m^n(x)$ is the associated Laguerre polynomial. If x_0 and y_0 are complex, intensity has no radial symmetry (Fig. 1). On propagation, light crescent becomes almost a ring, while side rings are not restored. Beam energy goes from the crescent to side rings.

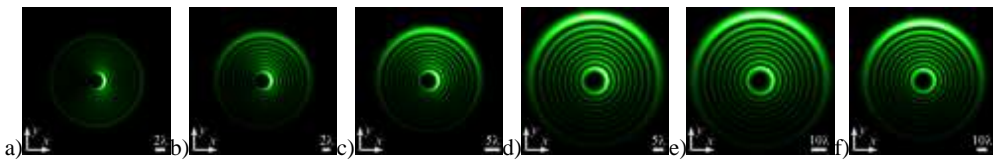


Figure 1. Intensity distribution of aLG-beam at wavelength $\lambda = 532$ nm, waist radius $w_0 = 2\lambda$, beam index $(m, n) = (8, 7)$, transverse shift $x_0 = 0$, $y_0 = 0.2\lambda i$, propagation distances $z = 0\lambda$ (a), 12λ (b), 20λ (c), 40λ (d), 60λ (e), 80λ (f).

The normalized OAM (OAM divided by the beam power) of the aLG-beam reads as $J_z/W = n + 2\text{Im}(x_0^*y_0)(Q_m + Q_{m+n} - 1)/w_0^2$, where $Q_m = L_m^1(-2D_0^2/w_0^2)/L_m(-2D_0^2/w_0^2)$, $D_0 = [(\text{Im } x_0)^2 + (\text{Im } y_0)^2]^{1/2}$.

If $m = 0$, Eq. (1) is simplified. There is an intensity maximum at the point (x_{\max}, y_{\max}) , which rotates by the angle α_0 at a distance of $z = z_R \tan(\alpha_0)$ around the intensity minimum $(x_{\min}, y_{\min}) = (\text{Re } x_0 - \text{Im } y_0, \text{Re } y_0 + \text{Im } x_0)$:

$$\begin{Bmatrix} x_{\max} \\ y_{\max} \end{Bmatrix} = \begin{Bmatrix} x_{\min} \\ y_{\min} \end{Bmatrix} + \frac{1}{2z_R} \left(\begin{Bmatrix} \text{Im } x_0 \\ \text{Im } y_0 \end{Bmatrix} z + \begin{Bmatrix} \text{Im } y_0 \\ -\text{Im } x_0 \end{Bmatrix} z_R \right) \left(1 + \sqrt{1 + \frac{2nw_0^2}{D_0^2}} \right). \quad (2)$$

Fig. 2(a) shows the experimental setup. Light from a laser L , collimated by lenses L_1 and L_2 , illuminated a

spatial light modulator SLM. Reflected first-order beam via lenses L_3 and L_4 illuminated a lens L_5 , focusing the beam onto the matrix of a CMOS-camera LOMO TC-1000. The diaphragm stopped the zero order of diffraction. Figs. 2(b-g) show that the crescent-like beam rotates around the axis (it also narrows due to the focusing).

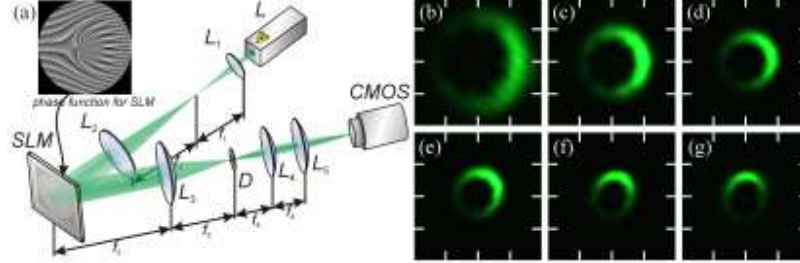


Figure 2. (a) Optical setup: L – solid-state laser ($\lambda = 532$ nm), L_1, L_2, L_3, L_4 и L_5 – lenses ($f_1 = 250$ mm, $f_2 = 500$ mm, $f_3 = 350$ mm, $f_4 = 150$ mm, $f_5 = 280$ mm), SLM – spatial light modulator PLUTO VIS (1920×1080 pixels, each of $8 \mu\text{m}$), D – diaphragm (spatial filter), CMOS - camera LOMO TC-1000 (3664×2740 pixels, each of $1.67 \mu\text{m}$). (b-g) Intensity at different distances from the lens L_5 : (b) 0 mm, (c) 100 mm, (d) 150 mm, (e) 200 mm, (f) 250 mm, (g) 280 mm. Size of area is 2×2 mm. Parameters are $w_0 = 1$ mm, $n = 8$, $x_0 = 0.2w_0$, $y_0 = 0.2w_0i$.

Superposition of aLG-beams with different D_0 ($D_0 \gg w_0$) looks like light spots. On propagation, these beams are rotated and almost do not interfere with each other. Fig. 3 shows two aLG-beams (one with $D_0 = 5w_0$, other with $D_0 = 8w_0$). It is seen that two-spot light beam rotates and has little change of its shape (only scaling).

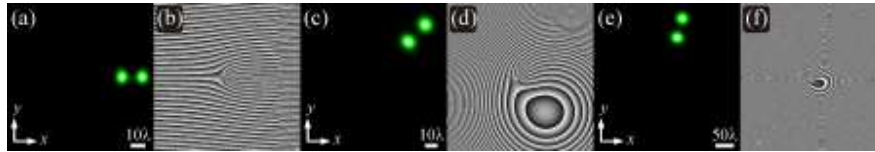


Figure 3. Intensity and phase of aLG-beams at wavelength $\lambda = 532$ nm, waist radius $w_0 = 5\lambda$, beam index $(m, n) = (0, 8)$, shifts of the 1st beam $x_0 = 5w_0$, $y_0 = 5w_0i$, shifts of the 2nd beam $x_0 = 8w_0$, $y_0 = 8w_0i$, propagation distances $z = 0$ (a, b), $z = z_R$ (c, d), $z = z_R \tan(5\pi/12)$ (e, f).

So, we considered asymmetric generalization of the LG beams. An expression for their OAM has been obtained. At zero radial index, the beams have a shape of a crescent. We determined the position of the crescent and shown its rotation on propagation, which was experimentally demonstrated by using a light modulator. Such crescent beams can be used for moving of biological objects [4], and for generation of entangled photons [5].

Acknowledgements. The work was partially funded by the Russian Federation Ministry of Education and Science, Russian Federation Presidential grants for support of leading scientific schools (NSh-9498.2016.9), and Russian Foundation of Basic Research grants ## 14-29-07133, 15-07-01174, 15-37-20723, and 15-47-02492.

REFERENCES

1. Plick, W.N., W.N. Plick, and M. Krenn, "Physical meaning of the radial index of Laguerre-Gauss beams," *Physical Review A*, Vol. 92, 063841, 2015.
2. Allocca, A., A. Gatto, M. Tacca, R.A. Day, M. Barsuglia, G. Pillant, C. Buy, and G. Vajente, "Higher-order Laguerre-Gauss interferometry for gravitational-wave detectors with in situ mirror defects compensation," *Physical Review D*, Vol. 92, 102002, 2015.
3. Sun, K., C. Qu, and C. Zhang, "Spin-orbital-angular-momentum coupling in Bose-Einstein condensates," *Physical Review A*, Vol. 91, 063627, 2015.
4. Rykov, M.A. and R.V. Skidanov, "Modifying the laser beam intensity distribution for obtaining improved strength characteristics of an optical trap," *Applied Optics*, Vol. 53, 156–164, 2014.
5. Mair, A., A. Vaziri, G. Weihs, and A. Zeilinger, "Entanglement of the orbital angular momentum states of photons," *Nature*, Vol. 412, 313–316, 2001.

Emergence of classicality from initial quantum world for dissipative optical waves

Jeong Ryeol Choi

Department of Radiologic Technology, Daegu Health College, Yeongsong-ro 15, Buk-gu, Daegu 41453,
Republic of Korea
choiardor@hanmail.net

Abstract— For light waves propagating in dissipative media, the emergence of classical characteristics from the initial quantum world is investigated. Two classicality measures of the system, which are the measure of the degree of (relative) classical correlation and that of the degree of quantum decoherence, are analyzed. We also investigated absolute classical correlations for the light in dissipative media.

For dissipative light waves, the transition to classicality from the initial quantum world is investigated. We have assumed for convenience that there is no net free charge in media, in addition that electric permittivity ϵ , magnetic permeability μ , and conductivity σ are real constants. Non-zero conductivity in a medium is, in general, responsible for the dissipation of light waves. The recent increasing interest in quantum behaviors of light waves and their reduction to classicality in dissipative media has accompanied active research on quantum optical properties of materials through advanced computational resources and developed algorithmic tools[2, 3, 4].

Useful criteria for determining whether the system behaves classically or not can be represented in terms of the classical correlation together with the quantum decoherence. The measures of the degree of classicality have been defined by Morikawa, which are the measure of the degree of (relative) classical correlation (MDRCC) and that of the degree of quantum decoherence (MDQD) in q -space[5]. Soon after, many researchers in this field studied the emergence of classicality from quantum world by means of MDRCC and MDQD. Due to the complementarity between q and p , it may also be possible to define these quantities in p -space. We study MDRCC and MDQD for dissipative optical waves in both q - and p -spaces and clarify whether their values in p -space are the same as those in q -space or not.

We can specify, from basic analysis of classical correlation, whether there is a well-defined classical trajectory in phase space. The condition for classicality through a classical correlation is satisfied when the Wigner function represented in phase space for a quantum state is sharply peaked along a classical trajectory. If a well-defined classical trajectory exists for a particular system, high precision measurements can be achievable. On the basis of fundamental quantum optics, it will be rigorously examined in this work that whether the value of MDRCC is uniquely determined irrelevant to the adopted space. We will also define the measure of the degree of absolute classical correlation (MDACC) and its relevant properties will be investigated in detail.

The classicality of a system cannot be entirely evaluated in terms of its classical correlation. Another factor that we can use for examining the classicality is quantum decoherence. The interaction of the system with the environment destroys coherence to their eigenstates, leading to the emergence of the classical structure of phase space. This means that a preferred set of states is singled out from superposed numerous ones.

Through the calculation of the evolution of the density operator for a light wave in dissipative media, the characteristics of classical correlation and quantum decoherence in both q - and p -spaces was investigated. We have managed MDRCC and MDQD separately for q - and p -spaces and showed that the results of their p -space analyses are the same as those of q -space analyses. Hence, we can conclude that both the MDRCC and MDQD have unique values for each. The classicality condition for classical correlation is satisfied under the limit that σ is sufficiently large. In other words, the system exhibits a strong classical correlation as σ increases. It is obvious that the MDRCC can be defined only when the conductivity is not zero. The classicality condition for quantum decoherence is also satisfied for a sufficient large value of σ . However, the dependence of MDQD on σ follows quite a different behavior from that of the classical correlation, MDRCC.

We also investigated MDACC in q -space ($\bar{\delta}_{CC,q}$) and in p -space ($\bar{\delta}_{CC,p}$). Notice that $\bar{\delta}_{CC,q}$ exponentially increases with time depending on the value of σ , whereas $\bar{\delta}_{CC,p}$ exponentially decreases.

These time variations are somewhat significant, especially when σ is large. In the meantime, we can confirm an interesting consequence that $\bar{\delta}_{CC,q}\bar{\delta}_{CC,p}$ does not vary with time. This reciprocal relation is very similar to that of the uncertainty relation that plays a central role in quantum mechanics. We can expect for a more general system that, if $\bar{\delta}_{CC,q}$ increases with time, $\bar{\delta}_{CC,p}$ decreases and vice versa. The values of not only q but also p , that correspond to non-zero MDACCs, span within specified ranges instead of posing precise ones. Of course, there is no way to avoid this intrinsic limitation for $\bar{\delta}_{CC,q}$ and $\bar{\delta}_{CC,p}$ in nature.

In general, the theory of measurement is finding the state of an object from its measured data. Because, in the case of the quantum state, the measuring apparatus complies with the law of classical mechanics while the object remains in a quantum state, various problems take place regarding their correspondence. The superposition of multiple state functions is possible for quantum states, whereas classical states can be represented with a pair of canonical conjugate variables, (q, p) . Accordingly, the main task in the quantum measurement theory is to demonstrate which steps under which conditions are to be followed from the results of a quantum process in the implementation toward classicality in measuring processes. Apparently, the reciprocal relation between $\bar{\delta}_{CC,q}$ and $\bar{\delta}_{CC,p}$, obtained in this work, may contribute to providing an insight not only for understanding the underlying mechanism for the fundamental quantum mechanics, but also the emergence of the classical characters from the initial quantum world. The absolute classical correlation in q -space would be enhanced as time goes by, provided that that in p -space decreases over time and vice versa.

ACKNOWLEDGMENT

This research was supported by the Basic Science Research Program of the year 2015 through the National Research Foundation of Korea (NRF) funded by the Ministry of Education (Grant No.: 2013R1A1A2062907).

REFERENCES

1. Blume-Kohout, R. and W. H. Zurek, "Quantum Darwinism: Entanglement, branches, and the emergent classicality of redundantly stored quantum information," *Phys. Rev. A*, Vol. 73, No. 6, 062310, 2006.
2. Lyagushyn, S. and A. Sokolovsky, "Description of field states with correlation functions and measurements in quantum optics," *Quantum Optics and Laser Experiments* (ed. Lyagushyn, S.) Chap. 1, pp. 3-24, Intech, Rijeka, 2012.
3. Choi, J. R., "Coherent and squeezed states for light in homogeneous conducting linear media by an invariant operator method," *Int. J. Theor. Phys.*, Vol. 43, No. 10, 2113-2136, 2004.
4. Servin, M. and G. Brodin, "Propagation of electromagnetically generated wake fields in inhomogeneous magnetized plasmas," *J. Plasma Phys.*, Vol. 67, No. 5, 339-351, 2002.
5. Morikawa, M., "Quantum decoherence and classical correlation in quantum mechanics," *Phys. Rev. D*, Vol. 42, No. 8, 2929-2932, 1990.

Remote Sensing, Inverse Problems, Imaging Radar

Polarization effects on 3D imaging from scattering measurements

C. Eyraud, J.-M. Geffrin, A. Litman, and H. Tortel

Aix-Marseille Université, CNRS, Centrale Marseille, Institut Fresnel UMR 7249, 13013 Marseille, France
christelle.eyraud@fresnel.fr

Abstract— This paper deals with the polarization aspect in microwave imaging for 3D targets. The vectorial information contained in the scattering matrix is often under-exploited in inverse scattering problems. In this work, a study on the influence of the polarization state on the reconstructed maps by inverse procedures will be presented. Reconstructions performed from measurements in different polarization cases will be compared and discussed.

Electromagnetic wave probing is an interesting tool to reach the physical features of unknown targets. The inverse scattering problem deals with the estimation of the physical features (permittivity map or a quantity linked to the permittivity map) of an unknown object from its scattered field and thus to obtain its position, shape, size, complex permittivity. Dealing with 3D targets generally increase the number of the characteristics that must be retrieve by the inverse procedure. In practice, when dealing with measurements, difficulties grow in particular due to the fact that we are almost every time faced with truncated data. Indeed, the complex amplitude scattering matrix can usually not be measured on an entire surface enclosing the target. It is thus important to exploit as much as possible all the available information.

The polarization of the electromagnetic wave contains useful information as studies in radar polarimetry [1] or light scattering communities [2] point it out. In inversion procedures, the different polarizations are generally considered to contain the same amount of information and the treatment of each polarization state are often performed in a similar way. The reconstruction results seem however to be greatly influenced by the polarizations state, as shown by the results obtained in [3]. In this work, we will present a study investigating the influence of the polarization state on the reconstructed maps. Reconstructions from scattered fields measured in an anechoic chamber in the microwave domain with different polarization cases will be shown and be discussed.

REFERENCES

1. Cloude, S., Pottier, E., A review of target decomposition theorems in radar polarimetry”, *IEEE Trans. Geosci. Remote Sens.*, Vol. 34, 498–518, 1996.
2. Mishchenko, M., Travis, L., Lacis, A., Scattering, ”Absorption, and Emission of Light by Small Particles”, *Cambridge University*, 2002.
3. Eyraud, C., Vaillon, R., Litman, A. Geffrin, J.-M., Merchiers, O., ”Polarization effects in 3D vectorial-induced current reconstructions” *JOSA A*, Vol. 30, No. 10, 1967–1974, 2013.

Identification of the electromagnetic scattering by dynamic sea surfaces with a stochastic differential equation model

Arnaud Coatanhay* and Alexandre Baussard

Lab-STICC UMR 6285, ENSTA-Bretagne, 2 rue François Verny, 29806 Brest cedex 9, France

*corresponding author, E-mail: arnaud.coatanhay@ensta-bretagne.fr

Abstract

This paper presents a Nonlinear Stochastic Differential Equation System (NLSDES) that can be used to model the electromagnetic scattering by time-varying sea surfaces. More precisely, we show how to identify the parameters of this generic stochastic model with the numerical simulations computed for different sea states.

1. Introduction

For remote sensing activities in maritime environment, the scattering of the radar electromagnetic waves by the sea surface is of a major importance to assess the weather conditions (wind speed and wind direction) and the sea dynamics (swell for instance). Due to complex non-linear fluid dynamics, sea surfaces can be considered as random rough surfaces. To model the electromagnetic field scattered by such boundaries, various theoretical approaches were developed: asymptotic approximations (two scale method, small slope approximation) [1, 2], Monte-Carlo simulations based upon numerical techniques, statistic models [3],...

However, most of the time, these models assume static sea surfaces. If a time variation is taken into account, the modeling issue becomes far more challenging. The most obvious way (Monte-Carlo approach) is to generate a great number deterministic sea surfaces, simulate the evolution in time using fluid mechanics and finally compute the scattered field using numerical methods (Method of Moments for instance). Unfortunately, this approach does not provide an efficient analytical model.

More recently, Field and al. developed a Stochastic Differential Equation (SDE) model that can be used for this purpose. Nevertheless, this model requires parameters that have to be identified with actual scattered fields. This papers presents the identification obtained from numerical simulations for different sea states.

2. Numerical simulations

2.1. Sea surface generation

To generate a realistic ocean surface associated to a given weather condition (wind speed and wind direction), we introduce the sea spectrum developed by Elfouhaily et al. [4] since it is very consistent with experimental data. This sea

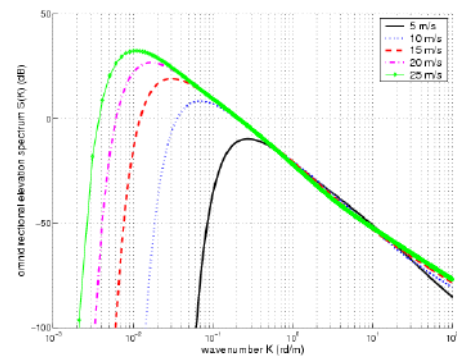


Figure 1: Elfouhaily sea surface spectra with different wind speeds (isotropic component).

spectrum is in the form:

$$S(K, \phi) = M(K)f(K, \phi) \quad (1)$$

where $M(K)$ represents the isotropic part of the spectrum modulated by the angular function $f(K, \phi)$, and where K and ϕ are respectively the spatial wave number and the wind direction, see figure (1). Then, the convolution of this spectrum with an unitary white Gaussian random signal generates a one-dimensional profile (a statistical realization for the sea surface) that represents an ocean surface for given weather conditions (see fig. 2).

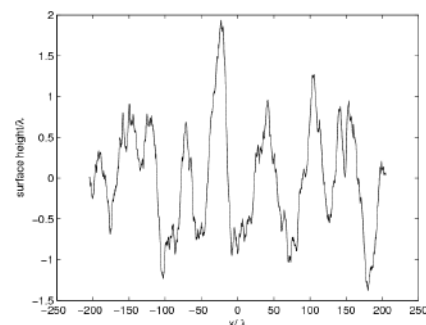


Figure 2: Example of an ocean surface profile generated where the wind speed is 10 m/s.

To introduce the movement of the so-generated random profiles, we must take into account the velocity of the sea waves that depends on the wave number [5]. The velocity of the longer wavelength waves is mainly influenced by

the gravity, whereas for the shorter wavelength waves the predominant effect in the velocity is the capillary. For non-shallow water, the dispersion relation can be approximated by:

$$\omega(k) \approx k \cdot \sqrt{\frac{g}{k} + \frac{\tau k}{\rho}} \quad (2)$$

where g is the gravitational acceleration, τ is the water surface tension and ρ is the density.

2.2. Electromagnetic scattering simulations

To compute the electromagnetic field scattered by the ocean-like profiles previously generated, we apply an accelerated Method of Moments (MoM). Then, using the so-computed scattered fields, we can numerically simulate the temporal stochastic process corresponding to the RCS for different weather conditions. In this way, the numerical data generated by a Monte-Carlo methodology can be seen as the realizations of the stochastic process related to the electromagnetic scattered field.

3. Stochastic differential equation model

Assuming that the sea surface is modeled by a set of random scatterers (phase screens), Field and al.[6, 7] proved that the dynamics of the normalized amplitude process $\Psi_t = \mathcal{E}_t^{(N)}/N^{1/2}$ and the continuous valued RCS x_t are given by the following set of nonlinearly coupled stochastic differential equations (NLSDES):

$$dx_t = \mathcal{A}(\alpha - x_t) dt + (2\mathcal{A}x_t)^{1/2} dW_t \quad (3a)$$

$$\begin{aligned} \frac{d\Psi_t}{\Psi_t} = & \left[\mathcal{A} \left(\frac{2(\alpha - x_t) - 1}{4x_t} \right) - \frac{1}{2}\mathcal{B} \right] dt \\ & + \left(\frac{\mathcal{A}}{2x_t} \right)^{1/2} dW_t^{(x)} + \frac{\mathcal{B}^{1/2}}{\gamma_t} d\xi_t \end{aligned} \quad (3b)$$

where \mathcal{A} and \mathcal{B} are constant. It should be noted that W_t and ξ_t are two independent Wiener processes.

Now, the major problem is to identify the both parameters (\mathcal{A} and \mathcal{B}) from electromagnetic scattered field previously simulated.

4. Identification of the parameters

The identification of a nonlinear stochastic model is usually a very delicate task, see for instance the recursive approach developed by D. Levanony et al. [8]. In the present study, we developed a more pragmatic approach adapted to the Field and al. stochastic model. The main idea is to decouple the identification of each parameters.

First, the numerical data are based upon a finite difference approximation $dt \approx \Delta t$ and $dx_t \approx x_{t+\Delta t} - x_t$. Based upon the analysis of averaging process for the first equation of the NLSDES, it is possible to provide an accurate estimation of the parameter \mathcal{A} . Then, the analytical properties

of Wiener process can be used to identify the characteristics of process W_t .

In a second step, following different calculus and mathematical transformations, we can obtain a decoupled identification of the NLSDES model. Moreover, our method also provides an estimated precision for the identified parameters.

5. Conclusion

From the computed data (numerical simulation), our algorithm can identify the parameters of the NLSDES model. Since the simulations are made for various sea states, the parameters of the dynamic stochastic model can be associated to the different sea states (wind speed and wind direction). Finally, our study highlight the relations between parameters \mathcal{A} and \mathcal{B} and the dynamic of the sea in different weather conditions.

References

- [1] A. Ishimaru, *Wave propagation and scattering in random media*. IEEE Press, 1997.
- [2] Y. Ayari, A. Khenchaf, and A. Coatanhay, "Bistatic Scattering by Sea Surface at Large Incident Angles : Two Scale Model Using the Unified Sea Spectrum," *J. Appl. Remote Sens.*, vol. 1013532, pp. 1–19, 2007.
- [3] K. Ward, R. Tough, and S. Watts, *Sea Clutter: Scattering, the K Distribution and Radar Performance*. Radar, Sonar, Navigation and Avionics, Institution of Engineering and Technology, 2006.
- [4] T. Elfouhaily, B. Chapron, K. Katsaros, and D. Vandemark, "A unified directional spectrum for long and short wind-driven waves," *Journal of Geophysical Research*, vol. 102, no. C7, pp. 15781–15796, 1997.
- [5] J. Miranda, A. Camps, J. Gmez, M. Vall-llossera, and R. Villarino, "Time-dependent sea surface numerical generation for remote sensing applications," in *IGARSS'05*, 2005.
- [6] T. R. Field and R. J. Tough, "Diffusion processes in electromagnetic scattering generating k-distributed noise," *Proceedings of the Royal Society of London A: Mathematical, Physical and Engineering Sciences*, vol. 459, no. 2037, pp. 2169–2193, 2003.
- [7] T. R. Field, *Electromagnetic scattering from random media*. Oxford Science Publications, 2009.
- [8] D. Levanony, A. Shwartz, and O. Zeitouni, "Recursive identification in continuous-time stochastic processes," *Stochastic Processes and their Applications*, vol. 49, no. 2, pp. 245 – 275, 1994.

EM and Nanophotonic Materials (metamaterials, plasmonics, etc)

Properties of isofrequency surfaces of 3D periodic dielectric composites with finite periods.

A. A. Ushkov¹, A. V. Tishchenko², and A. A. Shcherbakov^{1*}

¹ Moscow Institute of Physics and Technology, Russia

² University Jean Monnet, France

* corresponding author: shcherbakov.aa@mipt.ru

Abstract—In this work demonstrate effective optical properties of 3D periodic dielectric composites unusual to natural crystals when the period of such composites is only several times smaller than the vacuum wavelength. Numerical simulations demonstrates deformation of isofrequency surfaces and existence of additional optical axes unusual to natural crystals.

Artificial dielectric structures with spatial periodicity operating in the effective medium regime are promising for use in applied optics. Their potential in design miniature optical components have been demonstrated [1,2]. Wide range of possible applications follows from stronger anisotropic and chiral properties of designed composites than observed in natural materials as well as scalability and tunability of their optical parameters for specific operation regimes. The Direct Laser Writing method [3] is one the most popular techniques of producing 3D periodic dielectric microstructures. Usually it deals with dielectric materials which refractive index contrast is not very high. In this work we demonstrate than even with such structures one can obtain interesting effective optical properties.

Finite period composite structures possess spatial dispersion [4], and the period to wavelength ratio together with refractive index contrast define an accuracy of effective medium description with a constant permittivity tensor. Effect of spatial dispersion can be illustrated via isofrequency surface (IS) representation. Spatial dispersion leads to nonstandard optical properties not found in natural uniaxial and biaxial crystals. 3D periodic composites demonstrate nontrivial IS shapes most prominently when spatial periods of structures are only several times smaller than vacuum wavelength.

In this work we focus on edge regimes of such composites, when the period-wavelength ratio is of the order 0.1, and study IS characteristic deformations via rigorous calculating method in frequency domain [5]. The method possess a high proven accuracy, and allows for efficient propagation constant simulation. An example of structure under study consisting of isotropic spheres located periodically in 3D lattice sites is shown in Fig. 1a. Fig. 1b demonstrates composite's truncated IS (a constant is subtracted along each axis) when all spatial periods are equal to 0.2λ , and radius of spheres is 0.033λ . Intersections of this IS by planes $[1,0,0]$ and $[1,1,0]$ are provided in Figs. 1c,d, and demonstrate existence of seven optical axes in the structure [6]. In our research we also studied possible IS deformations for different ratios of periods and different types of experimentally realizable structures.

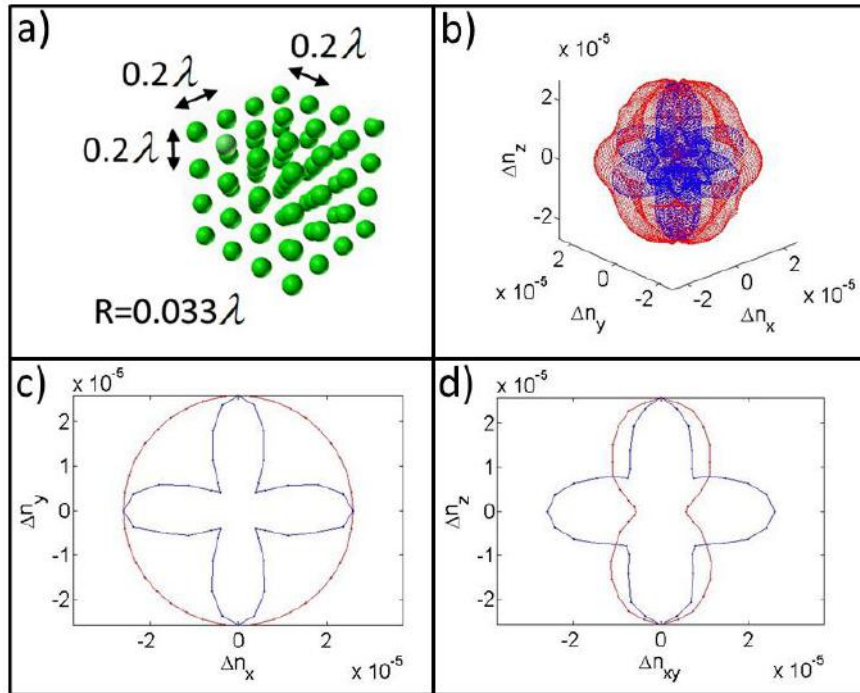


Figure 1. a) 3D infinitely periodic structure of spheres of refractive index 1.5; b) 3D view of truncated isofrequency surface (IS) for this structure; c) cross-section of truncated IS by plane $[1,0,0]$; d) cross-section of truncated IS by plane $[1,1,0]$.

Acknowledgements

The work was supported by the Russian Ministry of Education and Science (within the framework of the program “5top100”).

REFERENCES

1. Turner, M. D., et. al., “Miniature chiral beamsplitter based on gyroid photonic crystals,” *Nature Photon.*, Vol. 7, 801–805, 2013.
2. Funda, T.G., A. E. Serebryannikov, A. O. Cakmak, and E. Ozbay, “Asymmetric transmission in prisms using structures and materials with isotropic-type dispersion,” *Optics Express*, Vol. 23, 24120-24132, 2015.
3. Farsari, M., and B. N. Chichkov, “Materials processing: two-photon fabrication,” *Nature Photon.*, Vol. 3, 450-452, 2009.
4. Chebykin, A. V., M. A. Gorlach, and P. A. Belov, “Spatial-dispersion-induced birefringence in metamaterials with cubic symmetry,” *Phys. Rev. B*, Vol. 92, 045127, 2015.
5. Shcherbakov, A. A., and A. V. Tishchenko, “3D periodic dielectric composite homogenization based on the generalized source method,” *J. Opt.*, Vol. 17, 065101, 2015.
6. Feofilov, P. P., and A. A. Kaplyanskii, “Latent optical anisotropy of cubic crystals containing local centers, and methods of its study,” *Phys. Usp.*, Vol. 5, 79-103, 1962.

Competition between the antiferromagnetic phase and the superconducting state in underdoped $\text{BaFe}_{2-x}\text{Ni}_x\text{As}_2$ (RF measurements).

A. Abbassi^{1,3}, M. Saint-Paul², C. Guttin², M. R. Britel¹, R. Dkiouak³, Zhao-Sheng Wan^{2,4}, Huinqian Luo⁴, Xingye Lu⁴, Cong Ren⁴, Hai-Hu Wen^{4,5} and K. Hasselbach².

¹Laboratoire des Technologies Innovantes, ENSAT, Université Abdelmalek Essaâdi UAE, BP 1818 Tanger, Morocco.

² Université Grenoble Alpes, Institut Néel, F-38042 Grenoble ; CNRS, Institut Néel, F-38042 Grenoble France.

³ Faculté des Sciences et Techniques de Tanger, BP 416 Tanger, Université Abdelmalek Essaâdi, Morocco.

⁴ Institute of Physics and National Laboratory for Condensed Matter Physics, Chinese Academy of Sciences, P.O Box 603, Beijing 100190, People's Republic of China.

⁵ National Laboratory for solid State Microstructures, Department of Physics, Nanjing University, 210093 Nanjing, People's Republic of China.

*corresponding author, E-mail: abdellatif1966@hotmail.com

CSTM- Tanger/Direction de la Marine Marchande- Morocco.

Abstract

We report a comparison between the results obtained by three different measurements of the temperature and RF frequency dependence. These results concern the measurement of the surface impedance in the underdoped superconducting $\text{BaFe}_{2-x}\text{Ni}_x\text{As}_2$ crystal in the $5 < T < 30 \text{ K}$ temperature range using two methods based on the radiofrequency reflection technique and by Ultrasound technique. The measurements by induction were done with LC resonant circuit at 92 Mhz and with impedance measurement using impedance and network analyzers in the frequency range 10 MHz–1.5 GHz. The measurements were performed on superconducting $\text{BaFe}_{2-x}\text{Ni}_x\text{As}_2$ crystals with $x = 0.07$. The elastic constants C_{33} and C_{44} for the underdoped crystal ($x = 0.07$) show a large softening related to the structural phase transition at high temperatures. Anomalies in the sound velocity and the ultrasonic attenuation have been found at the superconducting phase transition $T_c = 17 \text{ K}$. Ultrasonic attenuation exhibits a peak at the superconducting transition in contrast with the attenuation in conventional superconductors and the overdoped. Unconventional behaviour of the ultrasonic attenuation is observed in the superconducting $\text{BaFe}_{2-x}\text{Ni}_x\text{As}_2$ crystals.

A similar behavior was observed by the magnetic induction measurements. With our two measurement techniques, we observed and highlighted the transition to the superconducting state of the underdoped sample. Strong anomalies are observed along the antiferromagnetic phase before reaching the superconducting state. The succession of variations in the two phases, confirms the competition between them.

The establishment of the antiferromagnetic order at $T_N \sim 50 \text{ K}$ gives rise to anomalous an increase of electron scattering time. Drude type conductivity yields X and R

differ from each other. The increase of the real conductivity σ_1 in the superconducting state is attributed to a rapid decrease of the σ_1 quasiparticle scattering time. This result gives evidence of coexistence of superconductivity and antiferromagnetism.

The temperature dependence of the London penetration depth follows a T^2 law. The conductivity σ_1 increases with decreasing temperature below T_c in agreement with the results obtained for the optimally Co doped $\text{BaFe}_{2-x}\text{Co}_x\text{As}_2$ crystals. The increase of σ_1 in the superconducting state is attributed to a rapidly decrease of the quasiparticle scattering rate.

1. INTRODUCTION

The recent discovery of iron based arsenide superconductors $\text{BaFe}_{2-x}\text{Ni}_x\text{As}_2$ has attracted much interest [1-2]. The compound parent BaFe_2As_2 exhibits simultaneous structural and magnetic phase transitions below $T_S = T_N = 140 \text{ K}$. Upon doping electrons via either Co or Ni substitution for Fe, the structural and magnetic phase transition are separated. A number of experimental works have been published recently concerning the surface impedance of iron based superconductors. Low frequency, radiofrequency, microwave and optical reflectivity performed on crystals and thin films give information about the pairing of the superconducting in these materials.

The underdoped $\text{BaFe}_{1.93}\text{Ni}_{0.07}\text{As}_2$ exhibits a structural transition at $T_S \sim 70 \text{ K}$, an antiferromagnetic transition at $T_N \sim 50 \text{ K}$ and a superconducting transition at $T_c \sim 16 \text{ K}$ [2-14]. NMR measurements give clear evidence of coexistence of superconductivity and antiferromagnetism [14]. The spin-lattice relaxation shows a critical slowing down around T_N and a further strong decrease around the superconducting transition. A number of surface impedance measurements have been published on iron based

superconductors. They give information on London penetration depth and quasiparticle scattering [5– 11] . The power temperature dependence of the London penetration depth in the ab plane $\lambda(T) - \lambda(0) \sim T^n$ with $n = 2 - 2.8$ is attributed to pair breaking scattering in the so-called $s \pm$ superconductivity [5–12]. The sharp increase of the real part of the conductivity below T_c was explained by a rapid decrease of the quasiparticle scattering rate for the optimally Co and Ni doped crystals [3– 11] .

The measurements of the surface impedance $Z_s = R_s + iX_s$ probe the complex conductivity [2-3]. The real part of the surface impedance is proportional to the loss of the radio frequency power and caused by the normal current carriers. The imaginary part is determined by the response of the superconducting current carriers and characterized the non dissipating energy stored in the superconducting surface layer. When the sample is superconducting magnetic field lines are excluded from the sample, the magnetic field is limited to the London penetration depth λ , which is approximately $1 \mu\text{m}$. After the sample passes from the superconducting to the normal state, the magnetic field penetrates into the sample on a much larger distance, the normal skin depth δ . For our samples, this distance is of the order of $70 \mu\text{m}$ at 100 MHz.

In the ultrasonic measurements technique approach, when a sound wave propagates through a metal, the microscopic electric field induced by the displacement of ions transfers the energy from the wave to the electrons. In a superconductor well below the superconducting transition T_c attenuation of sound waves are markedly lower than in a normal metal [4].

2. EXPERIMENT

We report measurements of the surface impedance in the (ab) plane of superconducting $\text{BaFe}_{1.93}\text{Ni}_{0.07}\text{As}_2$ crystals and relative variations of elastic constants and ultrasound attenuation.

2.1. Experimental set up

The crystals were grown using a Fe/Ni-As self flux method, details are given [2]. Typical crystals have dimensions of $7 \times 5 \times 0.2 \text{ mm}^3$. The crystallographic c-axis is perpendicular to the plane of plate-like crystals along the smallest dimension.

We selected samples with typical dimensions $(1000 \times 1000 \times 100) \mu\text{m}^3$, the smallest dimension is along the c axis. The 2.6 mm diameter, 18 turns, inductance 0.2 m Henry). The coil is situated at the end of a coaxial line inside a terminal adapter. Radiofrequency magnetic field is applied parallel to the ab plane. Incident radiofrequency power was fixed to -20 dBm . Non resonant measurements of the real (R) and imaginary (L) of the impedance of the coil were performed with an automated impedance analyzer Agilent 4395 in the frequency range 10–100 MHz. Measurements of the self LC resonant frequency and series resistance, $L = 0.2 \text{ mH}$, $C = 50 \text{ fF}$, quality factor ~ 80 were performed at 1.5 GHz with a Hewlett Packard 8720B network analyzer. Resistance and inductance were

measured separately in the absence of a sample and were subtracted from measurements with the sample present [5].

The formulation of the impedance of the coil surrounding the sample was obtained using the equivalent circuit based on a transformer analogy developed in [6].

In this model the primary of the transformer is the measuring coil L_0 . The secondary is defined by an inductance L_2 which is related to the eddy currents induced in the sample, L_2 is a geometrical factor and does not depend on the sample properties. The mutual inductance M depends on the sample properties. The mutual inductance M between the sample and the coil is defined by the mutual inductance between the primary and secondary,

$$M^2 = kL_0L_2 \quad (2)$$

, where k is the geometrical coupling factor between the primary and secondary. The inductance of the coil is given by

$$Z = R_0 + \frac{k^2 L_0 L_2 \omega^2 R}{|Z_2 + jL_2 \omega|^2} + j \left[L_0 - \frac{k^2 L_0 L_2 \omega \{X + L_2 \omega\}}{|Z_2 + jL_2 \omega|} \right] \omega \quad (3)$$

Where R_1 and L_1 are the resistance and the inductance of the empty coil.

In acoustics' approach, the ultrasonic waves were generated and detected at 15 and 45 MHz with LiNbO_3 transducers bounded to the crystal.

2.2. RESULTS

The elastic constants C_{33} and C_{44} for the underdoped crystal $\text{BaFe}_{1.93}\text{Ni}_{0.07}\text{As}_2$ shows a large softening related to the structural phase transition at high temperatures, (fig.1).

$$V = V_0 \left(1 - \frac{EJT}{2(T-\theta)} \right) \quad (4)$$

Where V_0 is the sound velocity value at high temperatures.

Anomalies in the sound velocity and the ultrasonic attenuation have been found at the superconducting phase transition $T_c = 17 \text{ K}$, (fig.2 and 3). Ultrasonic attenuation exhibits a peak at the superconducting transition in contrast with the attenuation in conventional superconductors [7]. The elastic properties of the underdoped crystal are strongly affected by the structural instabilities competing with the purely electronic effects in the elastic properties near the superconducting phase transition.

Unconventional behaviour of the ultrasonic attenuation is observed in the superconducting crystals $\text{BaFe}_{2-x}\text{Ni}_x\text{As}_2$. This result is in agreement with the softening of C_{66} observed in the $\text{BaFe}_{2-x}\text{Co}_x\text{As}_2$ crystals above the superconducting transition [8].

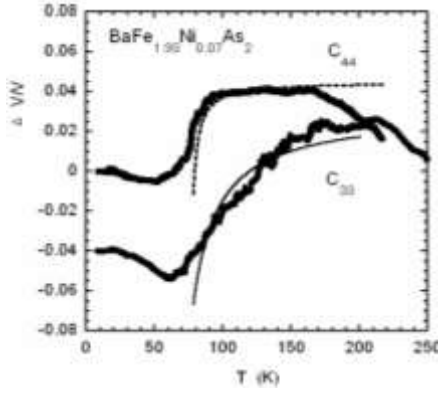


Figure 1: Relative change of the sound velocity of C_{33} longitudinal mode and C_{44} shear mode of underdoped $\text{BaFe}_{1.93}\text{Ni}_{0.07}\text{As}_2$ sample measured at 15 MHz [9].

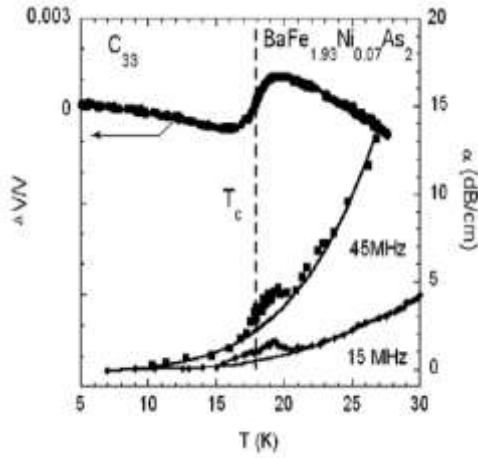


Fig.2. Relative change of the sound velocity and, ultrasonic attenuation α of the C_{33} longitudinal mode measured at 15 and 45 MHz of underdoped $\text{BaFe}_{1.93}\text{Ni}_{0.07}\text{As}_2$ sample around the superconducting transition. Zero decibel is normalized to the value at the lowest temperature, the solid lines are the high temperature background fits. [9]

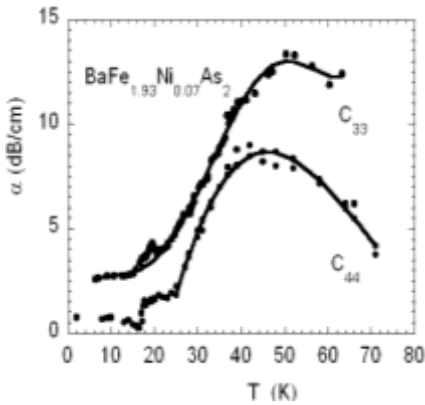


Fig.3. Relative change of ultrasonic attenuation α of the C_{33} and C_{44} modes measured at 15 MHz of underdoped $\text{BaFe}_{1.93}\text{Ni}_{0.07}\text{As}_2$ sample. For clarity the points of the C_{33} mode have been shifted [9].

A similar behavior was coarsely observed in the measurement LC resonant circuit. With this method, it's not possible to extract separately the own relative variations of the sample.

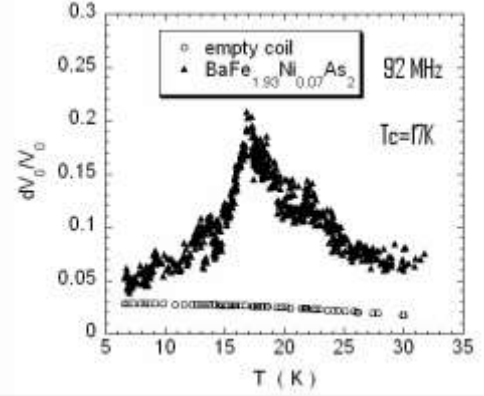


Figure 4: Temperature dependence of the relative change dV_0/V_0 , LC circuit measured at 92 MHz with $\text{BaFe}_{1.93}\text{Ni}_{0.07}\text{As}_2$ crystal dimensions $7 \times 5 \times 0.2 \text{ mm}^3$, superconducting phase transition $T_C = 17 \text{ K}$ and the empty coil [10].

Our second contribution reports measurements of the temperature dependence of the surface impedance and electrical conductivity in underdoped $\text{BaFe}_{1.93}\text{Ni}_{0.07}\text{As}_2$, in the frequency range 10 MHz– 1.5 GHz using a single coil technique. The temperature dependence of R and X normalized to the value R_N measured at 25 K are shown for underdoped $\text{BaFe}_{1.93}\text{Ni}_{0.07}\text{As}_2$ crystals in Figs. 5 and 6 [15].

In the underdoped crystal $\text{BaFe}_{1.93}\text{Ni}_{0.07}\text{As}_2$, the establishment of the antiferromagnetic order at $T_N \sim 50 \text{ K}$. gives rise to anomalous increase of electron scattering time. Drude type conductivity yields X and R differ from each other. This result gives evidence of coexistence of superconductivity and antiferromagnetism.

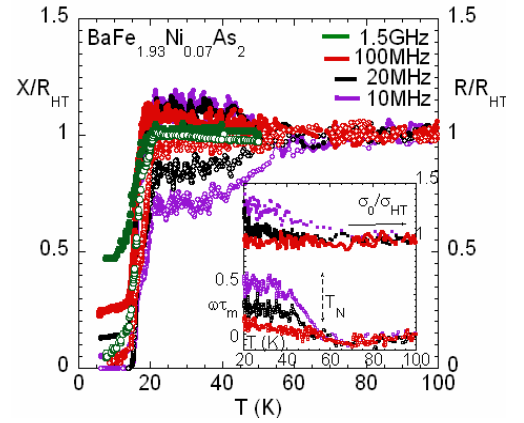


Figure 5: Temperature variation of X/R_{HT} (filled symbols) and R/R_{HT} (open symbols) of surface impedance at radio and high frequencies [15].

Inset: Temperature dependence of σ_0/σ_{HT} normalized to the value σ_{HT} of $\omega\tau_m$ with $\omega=2\pi f$, $f=10, 20$ and 100 MHz .

The increase of the conductivity σ_1 below T_c , measured by the magnetic induction using analysers, is attributed to the temperature dependence of the quasiparticle scattering rate.

A significant decrease of the electron scattering rate is observed around T_N (Fig. 3) when magnetic order sets in. Below T_C , strong decrease of the quasiparticle scattering rate

is found in the superconducting state. This result is similar to the temperature dependence of $1/T_1$ [14]. Evidence for coexistence of superconductivity and antiferromagnetism is given.

The superconducting transition is quite broadened in the temperature range 16–20 K for the underdoped crystals in contrast with the optimally and over doped crystals [11]. This result is in agreement with the broad elastic anomaly of the C_{33} mode observed with the same crystals [9]. The purely electronic effects are strongly affected by structural instabilities near the superconducting transition in the Ni and Co underdoped BaFe_2As_2 crystals [16].

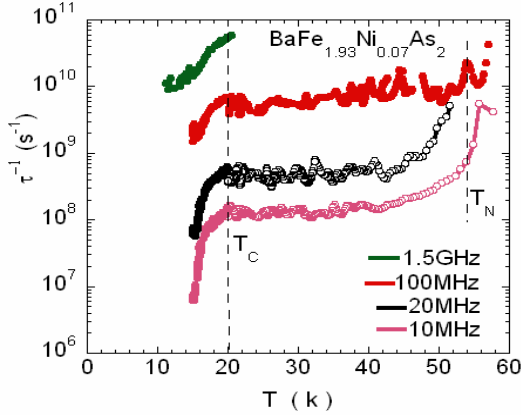


Fig.6. Temperature dependence of the electron scattering Rate τ_m^{-1} in the temperature range $20\text{ K} < T < T_N$ and of the quasiparticle scattering rate τ^{-1} , deduced from the conductivity σ_1 in the superconducting state for the underdoped $\text{BaFe}_{1.93}\text{Ni}_{0.07}\text{As}_2$. At each frequency we take $\tau^{-1}(20\text{K}) = \tau_m^{-1}(20\text{K})$. [15]

Conclusions

The elastic properties of the underdoped crystal are strongly affected by the structural instabilities competing with the purely electronic effects in the elastic properties near the superconducting phase transition.

The increase of the conductivity σ_1 below T_c , measured by the magnetic induction using analysers, is attributed to the temperature dependence of the quasiparticle scattering rate.

A similar behavior was observed in Co doped $\text{BaFe}_{2-x}\text{Co}_x\text{As}_2$. Strong temperature dependence of the quasi particle scattering time is observed in many unconventional superconductors [3,12].

References

- [1] H. Hosono, J. Phys.Soc.Jpn, **77**, 1–8, (2008).
- [2] Chen Yanchao, Xingye Lu, Meng Wang, Huiqian Luo and Shiliang Li, Supercond. Sci. Techno., **24**, 065004, (2011).
- [3] Barannick, N. T. Cherpak, M. A. Tanatar, S. Vitusevich, V. Skresanov, P. C. Canfield, and R. Prozorov. Phys. Rev. B **87** (2013) 014506.
- [4] G. Goll, Unconventional Superconductors Springer Tracks in Modern Physics Springer-Verlag Berlin (2006).
- [5] R. Prozorov, V.G. Kogan, Rep Prog. Phys.**74** (2011) 1245051–12450520
- [6] Yann Le Bihan, NDT&E Int. **36** (2003) 297–302.
- [7] X.F. Wang, T. Wu, R.H. Liu, H. Chen, Y.L. Xie, X.H. Chen, New J. Phys. **11** (2009) 045003–045011.
- [8] M.Yoshizawa and S. Simayi, Modern Physics Letters B Lett. B **2012.26**. by 196.12.241.147 on 02/14/13 on Vol. 26, No. 19 (2012) 1230011 World Scientific Publishing Company.
- [9] M. Saint-Paul, A. Abbassi, Zhao-Sheng Wang, Huiqian Luo, Xingy Lu, Cong Ren, Hai-Hu Wen, K. Hasselbach, Physica C **483**(2012) 207–212.
- [10] A. Abbassi, M. Saint-Paul, R. Dkiouak, M. R. Britel, Zhao Sheng Wan, Huiqian Luo, Xingye Lu, Cong Ren, and Hai-Hu Wen Advanced Electromagnetic, Vol.1, No.2, August 2012.(ISSN:2119-0275)]
- [11] M. Saint-Paul, C. Guttin, A. Abbassi, Z.S. wang, H. Luo, X. Lu, R. Cong, H.H. Wen, K. Hasselbach, Solid State Communications **185** (2014) 10-13.
- [12] J. S. Bobowski, and al. Phys. Rev. B, **52**, 094520, (2010).
- [13] D. A. Bonn and al. Phys. Rev. B **47** (1993) 11314.
- [14] R Zhou, Z. Li, J. Yang, D.L Sun, C.T. Lin, Guo-qing Zheng, Nat. Commun. **4** (2013) 2265.
- [15] M. Saint-Paul, C. Guttin, A. Abbassi, Z.S. wang, H. Luo, X. Lu, R. Cong, H.H. Wen, K. Hasselbach. Solid State Communications **192** (2014) 47-50.
- [16] M. Yoshizawa, Shalamujiang Simayi, Kohei Sakano, Yoshiki Nakanishi, K unihiro Kihou, Chul-Ho Lee, Akira Iyo, Hiroshi Eisaki, Masamichi Naka jima, Shin-Ichi Uchida, Solid State Commun. **152**(2012) 680–687.

Electroactive and Magnetoactive Materials

Engineering of giant magnetoimpedance effect of amorphous and nanocrystalline microwires

Valentina Zhukova^{1,2}, Ahmed Talaat^{1,2}, Mihail Ipatov^{1,2}, Alexandr Granovsky³ and Arcady Zhukov^{1,2,4*}

¹School of Energy and Power Engineering, Heat Transfer University, Xi'an, China

¹Dpto. de Fís. Mater., UPV/EHU San Sebastián 20009, Spain

²Dpto. de Física Aplicada, EUPDS, UPV/EHU, 20018, San Sebastian, Spain

³Moscow State “Lomonosov” University, Moscow, Russia

⁴IKERBASQUE, Basque Foundation for Science, 48011 Bilbao, Spain

*corresponding author, E-mail: arkadi.joukov@ehu.es

Abstract

Composite structural materials containing periodic or random arrays of metallic wires often referred to as wire metamaterials have a strong dispersion of the dielectric function in the GHz frequency band. These metamaterials utilising thin ferromagnetic wires exhibiting magnetoimpedance effect present tuneability of the effective permittivity, by a weak magnetic field or a mechanical stress. We present our studies of the factors affecting soft magnetic properties and giant magnetoimpedance effect in thin amorphous and nanocrystalline microwires. We showed that the magnetoelastic anisotropy is one of the most important parameters that determine magnetic softness and GMI effect of glass-coated microwires and annealing can be very effective for manipulation the magnetic properties of amorphous ferromagnetic glass-coated microwires. Considerable magnetic softening and increasing of the GMI effect is observed in Fe-rich nanocrystalline FINEMET-type glass-coated microwires after the nanocrystallization.

1. Introduction

Studies of innovative design of electromagnetic materials continue to be an important issue in microwave technology. A recent trend is to achieve adjustability in these structures. One of the perspective materials is the tuneable metamaterial utilising thin ferromagnetic wires exhibiting magnetoimpedance effect (MI) [1,2]. Our and some other groups work demonstrates that this leads to powerful adjustment of their electromagnetic properties, in particular, effective permittivity, by a weak magnetic field or a mechanical stress [1-3]. Composite structural materials containing periodic or random arrays of metallic wires often referred to as wire metamaterials have a strong dispersion of the dielectric function in the GHz frequency band. This behaviour could be of plasmonic or resonance type for long or short-cut wires, respectively [1,2]. In both cases, the real part of the permittivity can be negative in the dispersion region resulting in many fascinating effects including

negative refraction and frequency selective band-gap or band-pass regimes [1-3].

In thin conducting wires the currents that are responsible for effective permittivity are constrained with the associated resonances determined by the geometrical parameters. The current resonances are damped due to the wire impedance which may increase greatly when the wire magnetisation is changed. This is known as giant magnetoimpedance (GMI) effect [4-6]. In soft magnetic amorphous wires subjected to an external magnetic field GMI is in the range of 100% even at frequencies of few GHz [4-6]. Increase in magnetic losses results in increase in the relaxation parameter which determines the frequency dispersion of the effective permittivity. In the case of plasmonic wire arrays, this will result in considerable decrease in the absolute value of the permittivity and will enhance the wave propagation. Similarly, in cut-wire composites, the increase in relaxation broadens the permittivity dispersion which may even show transformation from resonance to relaxation behaviour [1-3]. Therefore, in composites containing ferromagnetic wires exhibiting GMI effect at GHz frequencies the effective permittivity will depend on the wire magnetic properties via the corresponding dependence of its impedance.

Consequently tailoring of the GMI effect in magnetic wires is essential for performance of the tuneable metamaterial utilising thin ferromagnetic wires.

Recent few years studies of glass-coated magnetic microwires exhibiting excellent soft magnetic properties and Giant magnetoimpedance effect gained considerable attention [5-7]. These properties are related to cylindrical symmetry as well as to crystalline structure of magnetic wires.

On the other hand GMI effect and its magnetic field dependence are closely related to the internal and applied stresses [8-10]. Therefore both GMI and magnetic softness can be tailored by magnetic wires processing.

Consequently we present our recent studies of the factors affecting soft magnetic properties and giant magnetoimpedance (GMI) effect in thin amorphous wires.

2. Experimental details

For the preparation of Co- and Fe-rich Finemet-type glass-coated microwires we employed modified Taylor-Ulitovsky technique and/or quenching-and-drawing method described elsewhere [5,6]. This method essentially consists of a simultaneous drawing of the composite microwire (metallic nucleus inside the glass capillary) through the quenching liquid (water or oil) jet onto rotating bobbins. More details on microwires preparation can be found elsewhere [5-8].

We studied glass-coated $\text{Co}_{50.69}\text{Fe}_{8.13}\text{Ni}_{17.55}\text{B}_{13.29}\text{Si}_{10.34}$ microwires ($d=12.8 \mu\text{m}$, $D=15.8 \mu\text{m}$, $\rho=0.81$) and $\text{Fe}_{70.8}\text{Cu}_1\text{Nb}_{3.1}\text{Si}_{14.5}\text{B}_{10.6}$ ($d=10.7 \mu\text{m}$, $D=16.4 \mu\text{m}$, $\rho=0.6$). We have measured the magnetic field dependence of impedance, Z , and GMI ratio, $\Delta Z/Z$, for as-prepared samples and after heat treatments [5,6].

We used a specially designed micro-strip sample holder described elsewhere [5]. The sample holder was placed inside a sufficiently long solenoid that creates a homogeneous magnetic field, H . The sample impedance, Z , was measured using a vector network analyzer from reflection coefficient S_{11} .

The magneto impedance ratio, $\Delta Z/Z$, has been defined as:

$$\Delta Z/Z = [Z(H) - Z(H_{\max})] \cdot 100/Z(H_{\max}), \quad (1)$$

An axial DC-field with a maximum value H_{\max} up to 8 kA/m was supplied by magnetizing coils.

The frequency range for the diagonal impedance component has been measured from 1 MHz up to 7 GHz.

Hysteresis loops have been determined by the flux-metric method described elsewhere [5,8].

Crystalline structure and phase composition have been checked using a BRUKER (D8 Advance) X-ray diffractometer with $\text{CuK}\alpha$ ($\lambda=1.54 \text{ \AA}$) radiation.

The magnetostriction coefficient has been measured using the small angle magnetization rotation method (SAMR) method described elsewhere [11] and recently modified for the case of thin magnetic wires [12].

3. Experimental results and discussion

3.1. Tailoring of magnetic properties and GMI effect in Co-rich amorphous microwires

As can be seen from Fig. 1 typically as-prepared Co-rich microwires presents typical for Co-rich microwires quasi-linear hysteresis loops and XRD typical for amorphous structure (consisted of a diffuse halo without observation of any crystalline peak). A coercive field of both samples is about 4 A/m that is typical for amorphous Co-based glass-coated microwires with low negative magnetostriction constant. The origin of such magnetic softness is related to the internal stresses arising during preparation of glass-coated microwires[8,14]. These stresses give rise to an easy magnetization direction

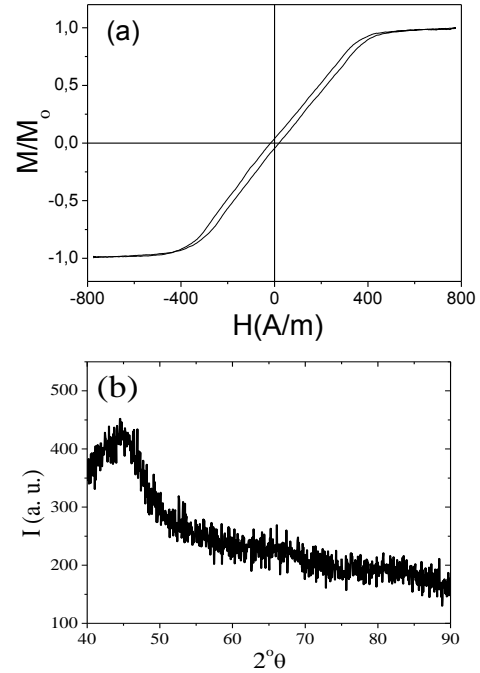


Figure 1: Hysteresis loop (a) and XRD patterns (b) of as-prepared $\text{Co}_{50.69}\text{Fe}_{8.13}\text{Ni}_{17.55}\text{B}_{13.29}\text{Si}_{10.34}$ microwire

perpendicular to the wire axis, leading to an alignment of the magnetic moments in the direction which is perpendicular (circumferential) to the wire axis.

The annealing even for quite short time and at low temperature leads to significant changing of the magnetic properties of both studied Co-rich microwires (Figs 2a-c).

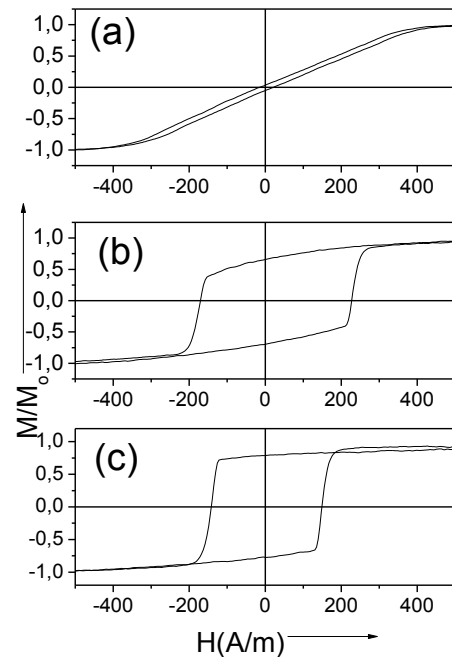


Figure 2: Hysteresis loops of as-prepared (a) and annealed for 5 min at 200°C (b) and 250°C (c) $\text{Co}_{50.69}\text{Fe}_{8.13}\text{Ni}_{17.55}\text{B}_{13.29}\text{Si}_{10.34}$ microwires

Increasing of the annealing temperature the hysteresis loop becomes more rectangular: remanent magnetization rises with increasing of T_{ann} , although coercivity, H_c , remains almost the same for all annealing conditions.

In spite of considerable magnetic hardening (a remarkable increasing of coercivity from 4 to 200 A/m for $Co_{50.69}Fe_{8.13}Ni_{17.55}B_{13.29}Si_{10.34}$ sample), both as-prepared and annealed microwires at different annealing conditions present considerable GMI effect as shown in Fig 3.

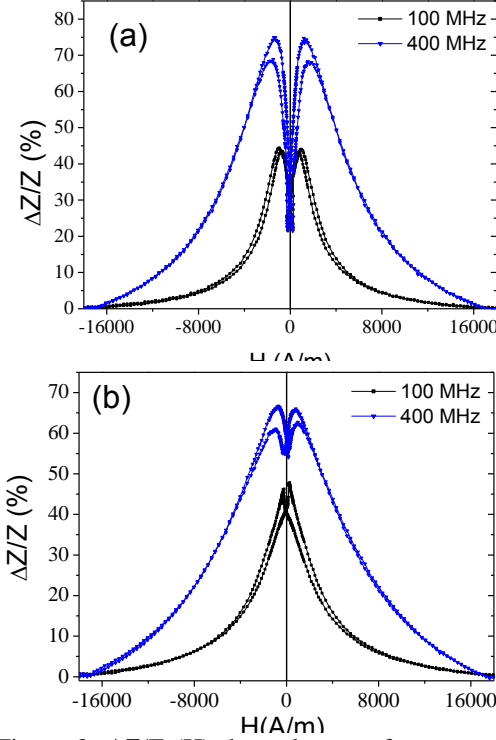


Figure 3: $\Delta Z/Z$ (H) dependences of as-prepared (a) and annealed at $200^\circ C$ for 5 min (b) $Co_{50.69}Fe_{8.13}Ni_{17.55}B_{13.29}Si_{10.34}$ microwires measured at different frequencies

The difference of $\Delta Z/Z$ (H) dependences measured for as-prepared (Fig.3a) and annealed (Fig.3b) samples is the value of the magnetic field, H_m , at which $\Delta Z/Z$ maximum takes place: for annealed samples H_m -values are lower than for as-prepared samples for all measured frequencies. Increasing the frequency, f , the maximum GMI ratio, $\Delta Z/Z_m$, rises (see Fig.3).

Observed changes of the hysteresis loops after annealing must be associated with the stress relaxation. Indeed the magnetostriction constant depends on stresses (both applied and internal) in according the following equation:

$$\lambda_s(\sigma) = \lambda_s(0) - B\sigma \quad (2)$$

where $\lambda_s(\sigma)$ is the magnetostriction constant under stress; $\lambda_s(0)$ is the zero-stress magnetostriction constant; B is a positive coefficient of order 10^{-10} MPa, and σ stresses. Furthermore, as experimentally shown in Fig. 4, the magnetostriction considerably change after annealing to

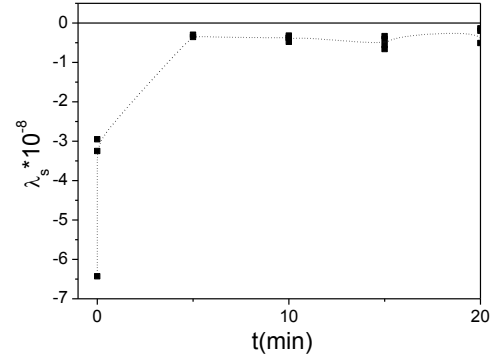


Figure 4: Dependence of the magnetostriction coefficient on annealing time for annealed $Co_{69.2}Fe_{4.1}B_{11.8}Si_{13.8}C_{1.1}$ microwire samples at $T_{ann} = 300^\circ C$

nearly zero for annealed $Co_{69.2}Fe_{4.1}B_{11.8}Si_{13.8}C_{1.1}$ microwire samples after annealing at $t_{ann} \geq 5$ min.

In addition, if the magnetostriction coefficient is low and negative, we must consider two opposite consequences of the internal stresses. The first contribution is an increase of the total magnetoelastic energy given by eq (3):

$$K_{me} = 3/2 \lambda_s \sigma_i, \quad (3)$$

where λ_s is the saturation magnetostriction and σ_i is the internal stress induced by the glass coating layer during the fabrication technique of glass-coated microwires.

The second one must be related to the stress dependence (either applied or internal stresses: $\sigma = \sigma_{applied} + \sigma_i$) on magnetostriction coefficient described by eq. 2, which is quite relevant for the case of low magnetostriction constant, $\lambda_{s,0}$. Accordingly, the magnetostriction constant under stress, $\lambda_{s,\sigma}$, must decrease. Based on the dependencies observed in Figs.2-3, the increase of coercivity and rectangular character of hysteresis loops after annealing must be attributed to the stress relaxation and corresponding magnetostriction changes. We can also assume that the outer domain shell of the annealed Co-rich microwire that exhibits both rectangular hysteresis loop and a GMI effect has high circumferential magnetic permeability.

3.2. Tailoring of GMI effect in nanocrystalline Fe-rich microwires

Usually amorphous Fe-rich microwires present rectangular hysteresis loop as shown in Fig. 5 typical for Fe-rich amorphous microwires.

Typically Fe-rich amorphous microwires present relatively low GMI effect (1-2 order smaller than Co-rich microwire).

The conventional way of formation of the nanocrystalline structure from the amorphous state, is the heat treatment (with appropriate annealing conditions as temperature, annealing time, heating rate, etc.) [14,15]. The evolution of structural and magnetic properties of $Fe_{70.8}Cu_1Nb_{3.1}Si_{14.5}B_{10.6}$ microwire has been studied in at different annealing temperature in the range between $400-650^\circ C$ for 1 hour in order to investigate the devitrification process (Fig. 6).

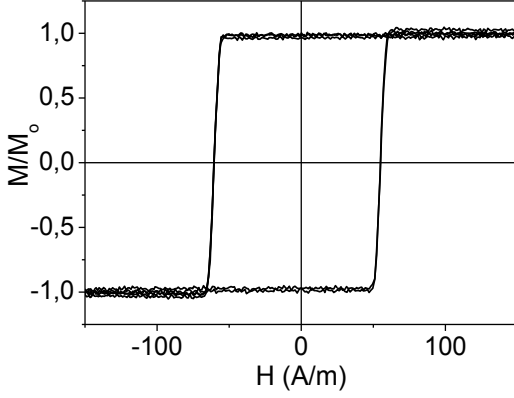


Figure 5: Hysteresis loops of as-prepared $\text{Fe}_{70.8}\text{Cu}_1\text{Nb}_{3.1}\text{Si}_{14.5}\text{B}_{10.6}$ microwires .

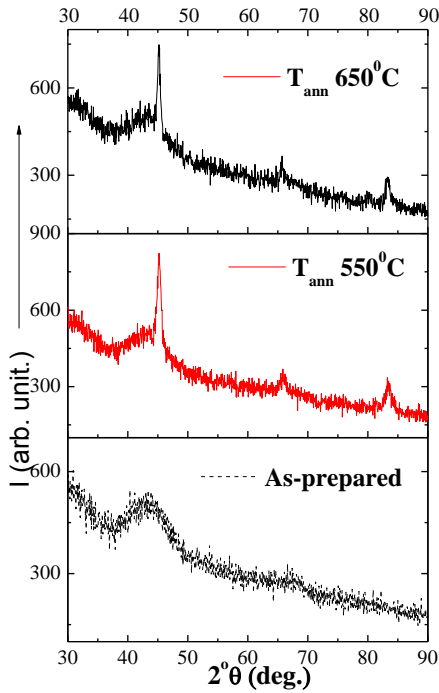


Figure 6: XRD patterns of as-prepared and annealed at different temperature for 1 hour $\text{Fe}_{70.8}\text{Cu}_1\text{Nb}_{3.1}\text{Si}_{14.5}\text{B}_{10.6}$ glass-coated microwires.

Starting from 550°C to 650°C a main crystalline peak is appearing in the range between 42° to 45° which is correspond to the existence of $\alpha\text{-Fe (Si)}$ BCC crystal structure [13,14], as well as another two weak peaks appear in the range between 65° to 85°.

The grain size has been estimated based on Scherrer equation as we previously reported [16]. From this analysis we can underline that the grain size of studied microwires increases from 17 to 22 nm upon increasing the annealing temperature from 550 to 650°C, respectively.

The formation of fine nanograins within the amorphous matrix allows reducing the net magnetostriction, according to this equation:

$$\lambda_{s,eff} = V_{cr} \lambda_{s,cr} + (1 - V_{cr}) \lambda_{s,am} \quad (4)$$

where $\lambda_{s,eff}$ the saturation magnetostriction coefficient and V_{cr} the crystalline volume fraction.

Consequently, the enhanced soft magnetic properties of these kinds of material can be achieved. As can be observed from Fig.7 considerable magnetic softening is observed after samples annealing.

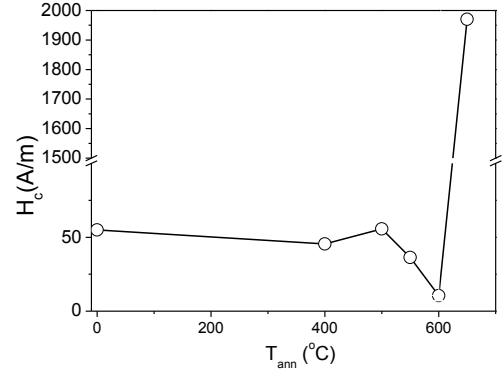


Figure 7: Coercivity dependence on annealing temperature measured in $\text{Fe}_{70.8}\text{Cu}_1\text{Nb}_{3.1}\text{Si}_{14.5}\text{B}_{10.6}$ microwire with $\rho=0.6$

Magnetic softening (optimum softest behavior) with quite low value of coercivity is obtained in the samples treated at $T_{ann} \approx 500\text{--}600^\circ\text{C}$ which is ascribed to the fact that the first crystallization process has been developed, leading to fine nanocrystals $\alpha\text{-Fe (Si)}$ of grain size around 10-20 nm, such it has been widely reported for FINEMET- ribbons (see for example ref. 17). The precipitation of the second phase results in abrupt increase of the coercivity observed for annealing temperature above 600°C .

Consequently together with magnetic magnetic softening we observed great enhancement of the GMI effect (see Fig.8) after devitrification of studied sample: maximum

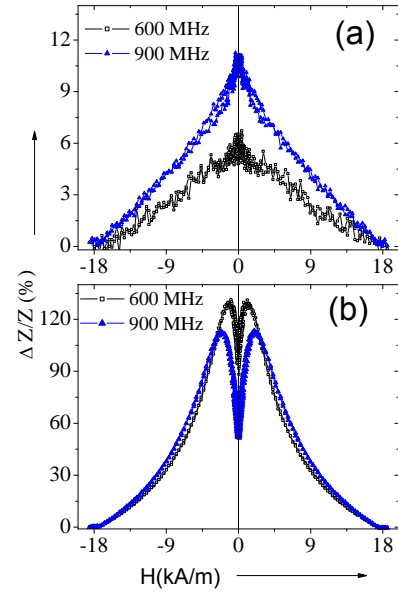


Figure 8: $\Delta Z/Z (H)$ dependences of as-prepared (a) and annealed at $T_{ann} = 550^\circ\text{C}$ (b) $\text{Fe}_{70.8}\text{Cu}_1\text{Nb}_{3.1}\text{Si}_{14.5}\text{B}_{10.6}$ microwires measured at different frequencies

GMI ratio increases more than one order from $\approx 7\%$ up to 130 %. Observed values of GMI effect in less expensive Fe-rich microwires with nanocrystalline structure are of practical interest for GMI related-applications.

4. Conclusions

We showed that the GMI effect of magnetic wires can be tuned by annealing. We observed that annealing of amorphous Co-rich microwire considerably affects its hysteresis loop, GMI effect. The observed dependences of these characteristics are attributed to stress relaxation and changes in the magnetostriction after sample annealing.

Considerable magnetic softening and increasing of the GMI effect is observed in less expensive Fe-rich nanocrystalline FINEMET-type glass-coated microwires after the devitrification process caused by thermal annealing.

Acknowledgements

This work was supported by Spanish MINECO under MAT2013-47231-C2-1-P and the Russian Science Foundation under the 16-19-10490 grant. Technical and human support provided by SGIker (UPV/EHU, MICINN, GV/EJ, ERDF and ESF) is gratefully acknowledged.

References

- [1] D.P. Makhnovskiy, L.V. Panina, C. Garcia, A.P. Zhukov, and J. Gonzalez, Experimental demonstration of tunable scattering spectra at microwave frequencies in composite media containing CoFeCrSiB glass-coated amorphous ferromagnetic wires and comparison with theory, *Phys. Rev. B*, Vol. 74 No. 6: 2006.
- [2] M. Ipatov, V. Zhukova, A. Zhukov and L. V. Panina, Microwave Metamaterials Containing Magnetically Soft Microwires, *Advances in Science and Technology*, 75: 224-229, 2010.
- [3] F.X. Qin, H.X. Peng, M.H. Phan, L.V. Panina, M. Ipatov, A. Zhukov, Effects of wire properties on the field-tunable behaviour of continuous-microwire composites, *Sensors and Actuators A* 178: 118– 125, 2012.
- [4] L.V. Panina and K. Mohri, Magneto-impedance effect in amorphous wires,” *Appl. Phys. Lett.*, 65: 1189-1191, 1994.
- [5] A. Zhukov, A. Talaat, M. Ipatov and V. Zhukova, Tailoring the high-frequency giant magnetoimpedance effect of amorphous Co-rich microwires, *IEEE Magn. Lett.*, 6: 2500104, 2015.
- [6] A. Zhukov, M. Ipatov and V. Zhukova, Advances in Giant Magnetoimpedance of Materials, *Handbook of Magnetic Materials*, ed. K.H.J. Buschow, 24: chapter 2, 139-236, 2015
- [7] D.C. Jiles, Recent advances and future directions in magnetic materials. *Acta Mater.* 51: 5907-5939, 2003
- [8] H. Chiriac, T. A. Ovari, and Gh. Pop, Internal stress distribution in glass-covered amorphous magnetic wires, *Phys. Rev. B* 42: 10105-10113, 1995.
- [9] J. M. Blanco, A. Zhukov and J. Gonzalez, Effect of tensile and torsion on GMI effect in amorphous wire, *J. Magn. Magn. Mat.* 196-197: 377-379, 1999.
- [10] J.M. Blanco, A. Zhukov and J.Gonzalez, Torsional Stress Impedance and Magneto-impedance in $(\text{Co}_{0.95}\text{Fe}_{0.05})_{72.5}\text{Si}_{12.5}\text{B}_{15}$ Amorphous Wire with Helical Induced Anisotropy, *J. Phys. D:Appl. Phys.* 32: 3140-3145, 1999.
- [11] K. Narita, J. Yamasaki and H. Fukunaga, *IEEE Trans.Magn.*, Measurement of Saturation Magnetostriction of a Thin Amorphous ribbon by Means of Small-Angle Magnetization Rotation, 16: 435-439, 1980.
- [12] A. Zhukov, M. Churyukanova, S. Kaloshkin, V. Sudarchikova, S. Gudoshnikov, M. Ipatov, A. Talaat, J.M. Blanco and V. Zhukova, Magnetostriction of Co-Fe-based amorphous soft magnetic microwires, *J. Electr. Mater.* 45: Issue 1, 226-234, 2016
- [13] A. Zhukov, J. M. Blanco, M. Ipatov, A. Chizhik and V. Zhukova, Manipulation of domain wall dynamics in amorphous microwires through the magnetoelastic anisotropy, *Nanoscale Research Letters*, 7: 223, 2012.
- [14] Y. Yoshizawa and K. Yamauchi, Fe-based soft magnetic alloy composed of ultrafinegrain structure, *Materials transaction JIM*, 31: 307-314, 1990.
- [15] A.Zhukov, K.Chichay, A.Talaat, V.Rodionova, J.M.Blanco, M.Ipatov, V. Zhukova, Manipulation of magnetic properties of glass-coated microwires by annealing, *J. Magn. Mater.* 383: 232–236, 2015
- [16] A. Zhukov, A. Talaat, M. Ipatov, J. J. del Val, L. Gonzalez-Legarreta, B. Hernando and V. Zhukova, Effect of nanocrystallization on magnetic properties and GMI effect of Fe-rich microwires, *J. Electr. Mater.* 43, No. 12: 4540-4547, 2014
- [17]] H. Q. Guo, H. Kronmüller, T. Dragon, Z. H. Cheng, and B. G. Shen, Influence of nanocrystallization on the evolution of domain patterns and the magnetoimpedance effect in amorphous $\text{Fe}_{73.5}\text{Cu}_1\text{Nb}_3\text{Si}_{13.5}\text{B}_9$ ribbons, *J. Appl. Phys.*, 89: 514-520, 2001.

Bioeffects of EM fields, Biological Media, Medical electromagnetics

Bio-inspired inversion method for the retrieval of the frequency-dependent permittivities of natural multilayer materials

D. Macías¹, D. C. Skigin^{2,3}, M. E. Inchaussandague^{2,3}, and A. Vial¹

¹ICD, P2MN, LNIO, Université de technologie de Troyes, UMR 6281, CNRS, France

²Grupo de Electromagnetismo Aplicado, Departamento de Física, FCEN, Universidad de Buenos Aires, Argentina

³ IFIBA (CONICET), Pabellón I, Ciudad Universitaria, C1428EHA Buenos Aires, Argentina
demetrio.macias@utt.fr, dcs@df.uba.ar

Abstract— In this contribution we enhance the capabilities of our bio-inspired inversion method to retrieve the dielectric frequency-dependent permittivity of the layers that compose a biological structure. For this, we incorporate a statistical processing stage to reliably establish confidence intervals and uncertainties related to the retrieved parameters. Also, we employ a dispersion model to realistically describe the optical properties of materials involved. Ultimately, we evaluate, through some examples, the robustness of the inversion scheme in the presence of noise.

Over the past decades, a significant amount of theoretical and experimental work has provided a better understanding of the electromagnetic and optical response of natural systems. Consequently, this cumulated knowledge has given rise to a fairly new research field known as Optical Biomimetics, which in turn has led to a wide variety of bio-inspired applications in domains such as photonics [1, 2] or optical document security [3, 4], to name but few examples.

In spite of the advances just mentioned, there are still several open questions. In particular, the precise determination of the optical properties of natural systems, directly from scattering and/or spectral information measured experimentally, has not been extensively studied and remains less well understood. This can be explained in terms of the non-trivial interaction between the material and geometrical characteristics of the natural structure studied, e.g. a butterfly’s wing, a bird’s feather or a jewel beetle’s elytra, and the light that illuminates it. Furthermore, the inherent difficulties in measuring reflectance spectra from natural structures, which in general are not perfectly flat and present a certain amount of absorption, makes it difficult to have a reliable data set serving as benchmark to assess the performance of the inversion schemes proposed in the literature. Some pioneer works on this subject are the contributions of Noyes et al. [5] and Yoshioka and Kinoshita [6]. In the first of these references, the authors proposed an inversion scheme based on the Approximation Theory (**AP**) to find the constant refractive index of the *Chrysochroa raja*’s elytra from several p- and s-polarized reflectance spectra measured at different angles of incidence. In [6], the authors search for the dispersive refractive index of *Chrysochroa fulgidissima*’s elytra by means of an iterative procedure involving Fresnel’s Equations as well as Cauchy’s Equation and a decreasing exponential to respectively characterize the real and imaginary parts of the refractive index. In [7, 8, 9], we successfully retrieved, by means of a hybrid inversion scheme combining **AP** and heuristic optimization techniques, the constant constitutive parameters of the layers that compose the elytra of the *Ceroglossus suturalis* beetle. As did the authors of references [5] and [6], we modeled the elytra as a bi-periodic multilayer structure where each layer was filled with a homogeneous, linear and isotropic material. Lately, in reference [10], we extended the applicability of our hybrid approach to the case of dispersive materials and characterized their dielectric constant by means of Lorentz’ Model.

Notwithstanding the encouraging results reported in [7, 8, 9, 10], further work is still required. In the present contribution, we aim not just to better understand the effect of the parameters to be retrieved on the convergence to a physically meaningful solution, but also at enhancing the capabilities of our hybrid inversion method in order to establish confidence intervals and not just one value of each of the parameters retrieved, as it is usually done in the literature. Nevertheless, preliminary numerical results show that this is not a trivial task, as the choice of the right measure of central tendency, e.g. the mean or the median, may have a significant effect on the final results, specially when dispersion is taken into account. Ultimately, in order to be closer to the

experimental situation, we assess the robustness of the inversion scheme in the presence of noise. Numerical experiments conducted with the Wavelength-by-Wavelength Approach (WWA) and its variant based on Lorentz' Model, respectively introduced in [7, 8] and [10], show that retrieving either the dielectric permittivities or Lorentz' Model-related parameters from a noisy spectrum can be critical and could lead the inversion method towards a non physical solution. The computational tool developed in this contribution should settle the basis for the determination of the optical properties of more complex natural structures as, for example, multilayer geometries with rough interfaces constituted of anisotropic media. It is noteworthy to mention that this kind of structures, that can be found in the elytra of jewel beetle *Cetonia aurata*, are usually studied employing ellipsometric techniques [11]. Thus, the approach proposed here in terms of the solution of an inverse problem should open an alternative way not only to study natural structures such as those described in [11], but also for the design of optimal application-dependent biomimetic optical materials [12].

ACKNOWLEDGMENT

D.S. and M. I. acknowledge support from CONICET (PIP 451). D. M. and A. V. gratefully acknowledge financial support from the LabCom IN-FINE (ProjetANR-14LAB5-0007-01). The authors gratefully acknowledge Dr. M. Kharouf for fruitful discussions concerning the statistical data analysis.

REFERENCES

1. Biró, L. P. and J. P. Vigneron, "Photonic nanoarchitectures in butterflies and beetles: valuable sources for bioinspiration," *Laser Photon Rev.*, Vol. 5, No. 1, 27–51, 2011.
2. Karthaus, O., *Biomimetics in photonics*, CRC Press, Boca Raton, 2013.
3. Duempelmann, L., D. Casari, A. Luu-Dinh, B. Gallinet and L. Novotny, "Color Rendering Plasmonic Aluminum Substrates with Angular Symmetry Breaking," *ACS Nano*, Vol. 9, No. 12, 12383–12391, 2015.
4. Lütolf, F., M. Stalder and O. J. F. Martin, "Metallized Gratings Enable Color Effects and Floating Screen Films by First-Order Diffraction," *Adv. Opt. Mater.*, Vol. 3, No. 12, 1793–1799, 2015.
5. Noyes, J. A., P. Vukusic and I. R. Hooper, "Experimental method for reliably establishing the refractive index of buprestid beetle exocuticle," *Opt. Express*, Vol. 15, No. 7, 4351–4357, 2007.
6. Yoshioka, S. and S. Kinoshita, "Direct determination of the refractive index of natural multilayer systems," *Phys. Rev. E*, Vol. 83, No. 5, 051917(7), 2011.
7. Macías Guzman, D., A. Luna, D. Skigin, A. Vial and M. Inchaussandague, "Retrieval of the relevant parameters of natural multilayer systems," in *Proceedings of AES*, Paris, France, April 2012, 335–340.
8. Macías, D., A. Luna, D. Skigin, M. Inchaussandague, A. Vial, and D. Schinca, "Retrieval of relevant parameters of natural multilayer systems by means of bio-inspired optimization strategies," *Appl. Opt.*, Vol. 52, No. 11, 2511–2520, 2013.
9. Luna, A., D. Macías, D. Skigin, M. Inchaussandague, D. Schinca, M. Gigli and A. Vial, "Characterization of the iridescence-causing multilayer structure of the *Ceroglossus suturalis* beetle using bio-inspired optimization strategies," *Opt. Express*, Vol. 21, No. 16, 19189–19201, 2013.
10. Macías, D., A. Vial, A. Luna, D. C. Skigin and M. E. Inchaussandague, "Characterization of natural photonic structures by means of optimization strategies," in *Proceedings of SPIE*, San Diego, United States, March 2015, 94290X-1-7 (7 pages).
11. Arwin, H., T. Berlind, B. Johs and K. Jarrendahl, "Cuticle structure of the scarab beetle *Cetonia aurata* analyzed by regression analysis of Mueller-matrix ellipsometric data," *Opt. Express*, Vol. 21, No. 19, 22645–22656, 2013.
12. Yu, K., T. Fan, S. Lou and D. Zhang, "Biomimetic optical materials: Integration of nature's design for manipulation of light," *Prog. Mater. Sci.*, Vol. 58, No. 6, 825–873, 2013.

Measurement Techniques

In situ permittivity measurements using stand-alone end effect probe

Francois Demontoux¹, Gilles Ruffié¹, Fabrice Bonnaudin¹

1 Laboratoire de l'Intégration du Matériau au Système, Bordeaux, Bordeaux University France

* Corresponding author: francois.demontoux@u-bordeaux.fr

Abstract-Numerous applications using microwave frequency behavior of materials (remote sensing above land surfaces, non-destructive analysis...) are strongly dependent on the material permittivity. Thus, permittivity is a key parameter to develop algorithms for the retrieval of materials properties from remote sensing data. Permittivity measurements are generally carried out in laboratory because *in-situ* measurements are more difficult to obtain. This study deals with the development at IMS laboratory of an in situ dielectric measurement system based on a stand-alone end effect probe.

1 INTRODUCTION

Microwave remote sensing and non-destructive analysis are a powerful way to provide properties estimation of materials. The remote signatures measured at microwave frequency are strongly dependent on the permittivity of materials. This permittivity depends of numerous parameters such as moisture, texture, temperature, frequency or bulk density for example. Experimental measurements can be done in laboratory over various conditions, such as moisture or range of frequencies. Additionally, dielectric mixing models (Dobson [1], Mironov [2]) allow, over restricted range of conditions, the assessment to material permittivity.

Moreover, in situ measurements are possible. Probes based on permittivity properties of soil for example exist (TDR reflectometry probe, Thetaprobe, capacitive probe). Unfortunately they are not dedicated to the estimation of the permittivity over a large range of frequencies.

This study deals with the development at IMS laboratory of an in situ dielectric measurement system based on a stand-alone end effect probe [3][4].

2 METHOD

A basic end effect probe consists of a coaxial waveguide in contact with a sample. The system can be modeled as a capacitor.

The value of this capacitor can be defined by:

$$C = C_0 \varepsilon^b \quad (1)$$

where C is the equivalent capacitor, C_0 and b are the probe parameters and are defined based on measurements on well-known materials,

ε is the relative complex permittivity of the sample. In this paper we will express it as:

$$\varepsilon = \varepsilon' - j \cdot \varepsilon'' \quad (2)$$

The complex admittance of the circuit is Y and is expressed as:

$$Y = j\omega C_0 \varepsilon^b \quad (3)$$

with $\omega = 2\pi f$

The method consists in the measurement of the reflection coefficient S_{11e} at the surface of the probe in the air (without contact with a material) and S_{11s} at the surface of the probe in contact with a material (which permittivity is ε). From these measurements we can define ρ and φ as follow:

$$S_{11s} = \rho \cdot \exp(j \cdot \varphi) \cdot S_{11e} = \rho \cdot \exp(j \cdot \varphi) \cdot \frac{1 - B1}{1 + B1} = B2 \quad (4)$$

Where $B1 = jC_0 Z_0 \omega$.

The reflection coefficient S11 (magnitude and argument) measurement is performed by using a Vector Network Analyzer ANRITSU 37325A at IMS laboratory or ANRITSU VNA MS46121A for in situ measurements.

From equation 4 we obtained:

$$B2 = \frac{1 - B1 \varepsilon^b}{1 + B1 \varepsilon^b} ; \quad (5)$$

Then from equation 5 we obtained:

$$\varepsilon^b = \left(\frac{1-B^2}{1+B^2} \right) \cdot \frac{1}{B^1} = A \cdot \exp(j \cdot \theta) \quad (6)$$

Where A and θ are respectively the magnitude and the argument of the expression ε^b .

Finally from equation 6 we computed the real and imaginary part of the relative permittivity of the material:

$$\varepsilon = \sqrt[b]{A} \cdot \exp\left(j \cdot \frac{\theta}{b}\right) = \varepsilon' + j \cdot \varepsilon'' \quad (7)$$

This expression 7 is used to compute permittivity for each frequency. Measurements on well-known materials (water and Polytetrafluoroethylene for example) are done to calibrate the parameters C0 and b of each probe. The latest parameters depend on the measurement frequency and to a lesser extent, on the permittivity of the samples. Usually ranges of parameters values are defined for large frequency and permittivity ranges measurements.

The properties of the probe depend on the shape, the size of the probe and the materials used. Good accuracy can be reached and large frequency range can be obtained. Nevertheless this technic has several disadvantages (weak volume of material considered, very good contact between probe and sample required). Two probes have been tested (N and SMA probes named due to the connections used).

N probe measurements give more steady value but the measurement has a limited frequency range [0.5GHz;3.5GHz]. SMA probe has a larger frequency range [0.5GHz; 7GHz]. Unfortunately, variations over SMA probe measurements are observed especially due to the small size of the probe diameter.

We began a study to design a new shape of probe to improve the contact surface and the frequency range. To do that we develop a Finite Element Method model of the probe. The results obtained with numerical computation and experimental measurements are closed.

3 CONCLUSION

Measurements using end effect probe (N, SMA) will be presented. It has been compared with measurement made on the same materials at IMS laboratory using resonant cavity method [6] or waveguide technic [7].

New probe will also be presented and its properties (frequency range, accuracy...) will be discussed.

Studies are done to make it a stand-alone probe for long term in situ record measurements. This permittivity probes will be a powerful equipment to provide new instrument for in situ dielectric measurements. At IMS laboratory, applications of this equipment will be the dielectric constants measurements of soil for SMOS remote sensing mission [5] on Calibration/Validation sites and concrete permittivity estimation for non-destructive analysis on buildings.

REFERENCES

- [1] M. C. Dobson, F. T. Ulaby, M. T. Hallikainen, and M.A. El-Rayes, « Microwave dielectric behavior of wet soil-Part II : Dielectric Mixing Models » IEEE Trans. Geosci. Remote Sens., vol. 23,no.1, pp. 35-46, 1985
- [2] V. L. Mironov et al. "Temperature dependent dielectric material properties of soil" IEEE Trans Geosc Remote sensing vol 49 no 7 pp 2518-2530 Jul 2011
- [3] Stuchly M. A. and Stuchly S. S. « Coaxial line reflection method for measuring dielectric properties of biological substances at radio and mi-crowaves frequencies- A review » IEEE Trans Instrum. Meas. 1980, vol IM-29, pp 176-183
- [4] Mosig J.R., Besson J. C. E., Gex-Fabry M. and Gardiol F.E. « Reflection of an open-ended coaxial line and application to non destructive measurements materials » IEEE Trans Instrum. Meas., 1981, vol IM-30, pp 46-51.
- [5] Kerr, Y., P. Waldteufel, J.-P. Wigneron, et al. 2001. Soil moisture retrieval from space: The Soil Moisture and Ocean Salinity (SMOS) mission. IEEE Trans. on Geoscience and Remote Sens., vol. 39(8), pp. 1729-1735.
- [6] Boudouris, G. (1964). Validité de la méthode de perturbation appliquée aux cavités résonnantes pour la mesure de la perméabilité et de la permittivité des petits échantillons. *Annales des Télécommunications*, 19, 63-80
- [7] F. Demontoux, B. Le Crom, G. Ruffie, Jp. Wigneron, J.P Grant, V. Mironov
Electromagnetic characterization of soil-litter media- Application to the simulation of the microwave emissivity of the ground surface in forests- The European Physical Journal - Applied Physics- Volume 44, Issue 3, December 2008, Pages 303-315

Comparison of Software and Hardware Time Gating Techniques on the Measurements of Low RCS Targets in a Bistatic Configuration.

H. Saleh^{1,2*}, J. -M. Geffrin², and H. Tortel²

¹Centre Commun de Ressources en Microondes CCRM, 5 rue Enrico Fermi, 13013, Marseille France

²Aix-Marseille Université, CNRS, Centrale Marseille, Institut Fresnel UMR 7249, 13013, Marseille, France

*corresponding author: hassan.saleh@fresnel.fr

Abstract- One of the main challenges in Radar Cross Section (RCS) measurements is to isolate the target's response from stray signals. Time gating techniques have often been used in compact range and RCS measurements. Previously, a soft-gating noise reduction technique based on Fast Fourier Transform (FFT) was applied to the measurements in the anechoic chamber of the CCRM. Nowadays, a hard-gating setup has been added to this measurement facility to enhance measurement accuracy for low scattering targets investigation. The setup was used to measure targets with dimensions of the order of the wavelength and the results were compared to soft-gated measurement as well as to numerical simulations. To our knowledge, this is the first time a hardware and software gating comparison has been made with such low scattering targets in a bistatic configuration. The presented hard-gating approach has proved good efficiency to deal with low scattering targets and has shown advantages over soft-gating in term of post processing requirements and measurement time.

By RCS measurements one can inspect scattering characteristics of an object. The anechoic chamber absorption imperfections make some stray signals not completely attenuated. Measurement becomes very vulnerable to noise for low RCS-targets and background suppression is no longer efficient. Being dealing with small size targets ranging from some wavelength (λ) down to $\lambda/4$ [1] as well as with very low refractive permittivity targets down to 1.3, we seek to improve our measurement accuracy by applying specific filtering techniques. Hardware and software gating have been used before in compact range antenna and RCS measurements for accuracy enhancement (see for example [2], [3], and [4]). In this work we apply and compare both techniques for low scattering targets investigation in an azimuthal bistatic configuration.

The target under test is placed in the center of the setup and is illuminated by a fixed position horn antenna, a receiving antenna moves circularly around it over 260 degrees at about 2 meters. The setup has been presented in [1]. The applied hard-gating system is based on two RF switches placed near the antennas. The generated CW signal at a few GHz is chopped by the transmitting switch into short pulses of some nanoseconds. The ideal source pulse width is determined according to the traveling time of the undesired multipath signals, whereas the OFF state between two consecutive pulses is long enough to insure that most of these undesired echoes have been dissipated within the chamber. After a delay corresponding to the scattered field propagation time from the target to the receiving antenna, the receiving switch goes to ON state so that only the target's response is captured. These parameters are chosen in such a way to reject the main spurious echoes: coupling between the antennas, stray scattering by the metallic support of the polystyrene object-holder mast but are also related to the hardware characteristics.

In order to assess the performance of the employed hard-gating setup, RCS measurements of different targets were performed. In “Figure 1” we present the results obtained with PMMA dielectric sphere (diameter: 50.75 mm, permittivity: 2.6) at 16 GHz and with both co-polarization cases. The results are compared to soft-gated measurements and simulations.

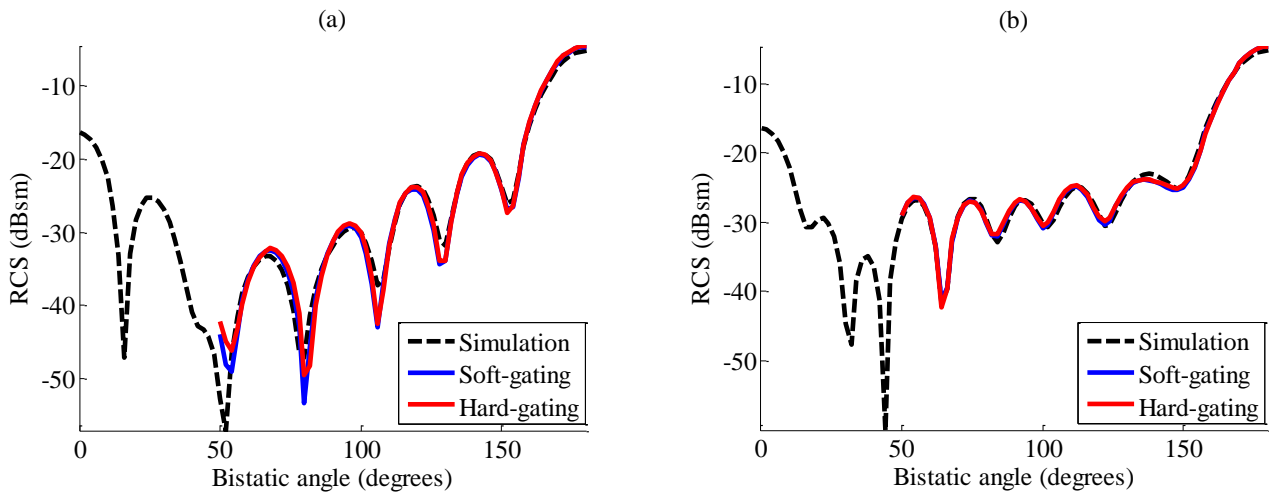


Figure 1: RCS of the PMMA sphere at 16 GHz. (a) VV polarization. (b) HH polarization.

Both hard and soft gating show a good agreement with the simulations. However, one drawback of soft-gating based on FFT is that a large frequency range is required in order to obtain a good time domain sampling. This becomes significantly time consuming with a large number of receiving positions and increases consequently drift errors susceptibility, whereas the presented hard-gating technique has no impact on the measurement time but only on the signal’s power level. In the example 450 frequency steps in soft-gating were reduced to 7 in hard-gating. Furthermore, our new approach allows us to use narrowband antennas instead wideband antennas requirement in soft-gating. We will present the setup and other measurement results but also our advances on the measurement of very low objects (RCS < -50 dBsm) achieved thanks to the used hard-gating system.

REFERENCES

1. Geffrin, J. M. *et al*, “Magnetic and electric coherence in forward- and back- scattered electromagnetic waves by a single dielectric subwavelength sphere,” *Nature Communications*, Vol. 3, 2012, DOI: 10.1038/ncomms2167.
2. Lemanczyk, J., J. Hartmann and D. Fasold, “Evaluation of Hard Gating in the ESA/ESTEC CPTR,” *AMTA*, 2004.
3. Collins, P.J., “Dielectric strings: A low clutter method for bistatic RCS measurements,” *IEEE International Symposium on Antennas and Propagation*, 1639–1642, 2011, DOI: 10.1109/APS.2011.5996617.
4. Escot, D., D. Poyetos, J.A. Aguilar *et al*, “Indoor 3D Full Polarimetric Bistatic Spherical Facility for Electromagnetic Tests,” *Antennas and Propagation Magazines, IEEE*, Vol. 52, No. 4, 112–118, 2010.

Physico-Chemical study of Electrically Degraded Silicone

Nacéra Rouha, Kaissa Djenkel, Kettir Khallil

Laboratoire de Génie Electrique de Bejaia, Faculté de Technologie, Département de Génie Electrique, Université Abderrahmane Mira, Bejaia, Algerie

*corresponding author, E-mail: ceranabougie@gmail.com

Abstract

We investigate the electrical aging phenomenon of Silicone coated insulators. Accelerated testing under alternating 50 Hz homogeneous electrical field, were conducted on both polluted and clean silicone. The permittivity and the loss index are measured before and after aging produced by a series of surfacic breakdown. Then the samples were chemically analyzed using a SEM, an FTIR and an XRD. Phases modification of the insulating material were observed, resulting in the alteration of its dielectric properties.

1. Introduction

Outdoor insulators flashover is one of the challenging problems that affect not only the electrical energy quality, but also the equipments durability of high voltage lines [1, 2]. Again, this fact is aggravated by the insulators contamination when the overhead transmission lines are exposed to natural and industrial pollution [3, 4]. The recourse to hydrophobic materials remains the way to overcome this problem, where silicone coating insulator is used to improve isolator system performance [5]. However, in long-term these materials age under the electric field stress and the silicone coated insulators quality is affected [2]. On this subject, several investigations are conducted to understand these systems degradation mechanisms in order to evaluate their life time and ensure better reliability [6-9]. These studies are also investigating chemical aspects of the material that can reveal its deterioration causes [6, 7, 10-12].

In this paper, we investigate the electrical aging phenomenon of Silicone coated insulators in service. For this purpose, a physico-chemical experimental study on both polluted and unpolluted Silicone Rubber films is undertaken. To characterize the silicone performance, accelerated electrical testing under alternating 50 Hz homogeneous electrical field, were conducted. A series of surfacic breakdown is carried out by considering both polluted and clean silicone surface conditions. Before and after aging, the permittivity and the loss index are measured depending on the frequency f and test voltage V . Then the samples were chemically analyzed using a Scanning Electron Microscopy, an Infrared spectroscopy and an X-

Ray Diffraction in order to follow the degradation at microscopic scale.

The observations of the damaged microstructure morphology allow seeing phase's modification of the insulating material and the effect of the polluting solution conductivity.

2. Experimental Techniques

Paralelepipedic silicone rubber films $100 \times 100 \times 5$ mm³ in dimensions are used to carry out on the accelerated electrical degradation tests. An increasing uniform field under AC - 50 Hz voltage ramp with speed of 2kV/s is applied to the samples up to produce a surface breakdown, and a series of 10 surfacic breakdown is carried out at ambient temperature $\theta = 20$ °C (± 1 °C). To highlight the effect of pollution and its conductivity, we perform these tests both on clean (C) and polluted (P) silicone surfaces, using sodium chloride solution (NaCl) with $\sigma = 5$ mS electrical conductivity.

Also, Electrical measurements of the permittivity ϵ_r and the loss index $\epsilon_r \cdot \tan \delta$ are undertaken before and after the sample's electrical aging. ϵ_r and $\epsilon_r \cdot \tan \delta$ are determined under several applied voltages ($V = 10$ V to 110 V in steps of 10 V) and at increasing frequencies ($f = 100$ Hz to 1100 Hz in increasing steps from 10 to 100 Hz) using the Schering bridge.

The chemical characterization of the material is performed on the basis of three chemical analyzes, namely: The scanning electron microscopy (SEM), the infrared spectroscopy (FTIR) and X- ray diffraction (XRD). Thin fragments are cut from both healthy silicone and degraded area of electrically aged silicone samples. Then, they are observed on scanning electron microscopy, with a magnification of 5000, which allowed seeing the changes occurred in the material structure. The infrared spectroscopy allows for the analysis of chemical functions present in the material. This analysis is performed on translucent pellets provided from virgin (Vg), and electrically aged silicone samples; Aged silicone in both clean (EAC) and polluted (EAP) surface conditions are considered. To recognize if a different crystallization form exists between these three silicone states, the X-ray diffraction is performed on films of 20×10 mm² in dimensions extracted from these three silicone samples (Vg, EAC and EAP).

3. Experimental Results and Discussion

The silicone degrades under the sliding discharge effect. That is reflected by the decrease of its relative permittivity ϵ_r (Fig.1), and the increase of its index loss ($\epsilon_r \text{tg}\delta$) (Fig.2); This effect is accentuated by the increase in the applied voltage frequency, whereas the voltage amplitude has no relevant influence on these two parameters.

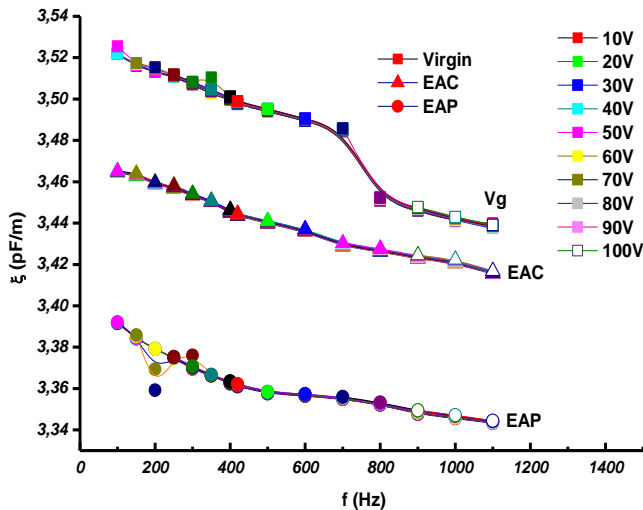


Figure 1: Relative permittivity ϵ_r versus frequency in function of silicone states: virgin, aged in dry (clean) and wet (polluted) conditions

Note that rising silicone's index loss is more intense in the dry ageing case compared to the wet one (fig. 2). Consecutive loss of thermal energy effect would fade by the polluting wet layer, leading to a decrease in dielectric loss, either in the index loss.

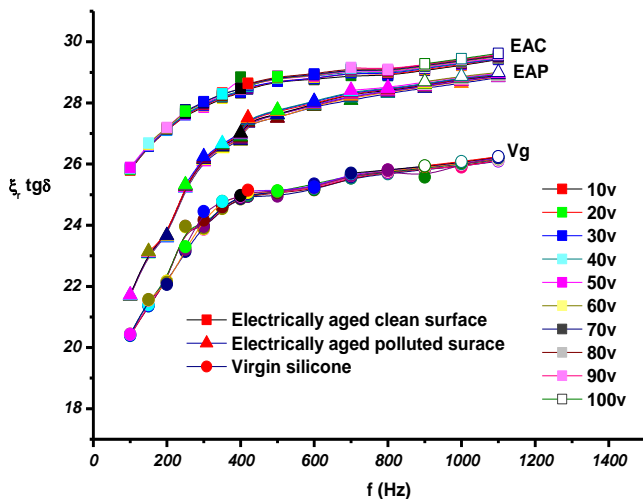


Figure 2: Loss index $\epsilon_r \text{tg}\delta$ versus frequency in function of silicone states: virgin, aged in dry (clean) and wet (polluted) conditions

In addition, the sliding discharge initiated by the electrical field stress causes a significant deterioration of the material

surface, revealed by the SEM observations. The electrical discharge left behind slight grooves distributed all over the silicone sample surface at dry aging, engendering a surface depolishing. The discharge traces, below reproduced in figure 3, follow a sinuous trajectory in weak preferential areas of the material, conforming to tree, in the electrical field direction.

Deep discharge traces of circular shape are showed off in the case of the silicone sample aged under wet pollution. These are a conductive water drop imprint where the discharge is concentrated when the flashover of the sample occurs (Fig .4). The silicone hydrophobicity lets bead the water droplets on the material surface, where concentrates the electrical arcing promoted by the pollution layer salinity. That causes severe deterioration of the material surface. However, the areas surrounding the water droplets remained healthy. The discharge energy, which is proportional to superficial conductivity, causes an increase of the latter due to the carbon deposit resulting from the silicone's carbonization. This vicious process accelerates the material degradation that is greater in the presence of the conductive polluting layer.

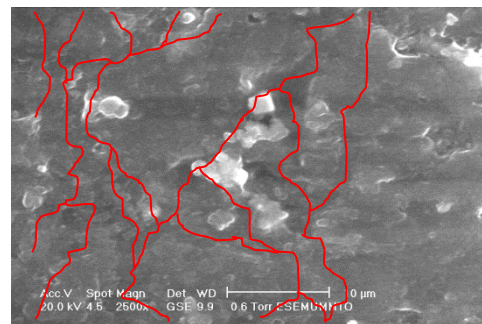


Figure 3 Discharge traces reconstitution on the silicone sample dry-aged surface

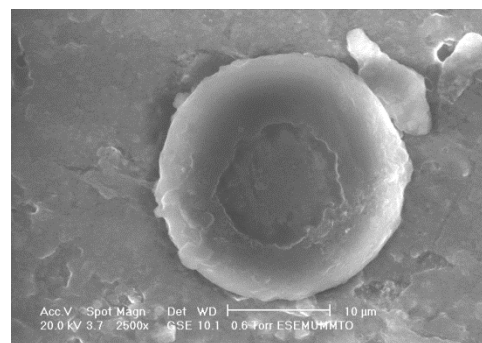


Figure 4: Aged silicone surface under wet pollution

FTIR analysis carried out on blank and electrically aged under pollution and clean silicone surface conditions has identified the existing bonds in the material. The FTIR chemical spectra (fig. 5) show the same pattern for the three analyzed samples. This testifies to the production of a similar oxidation mechanism for the set of samples, to a

higher degree in the case of electrically aged material under wet pollution.

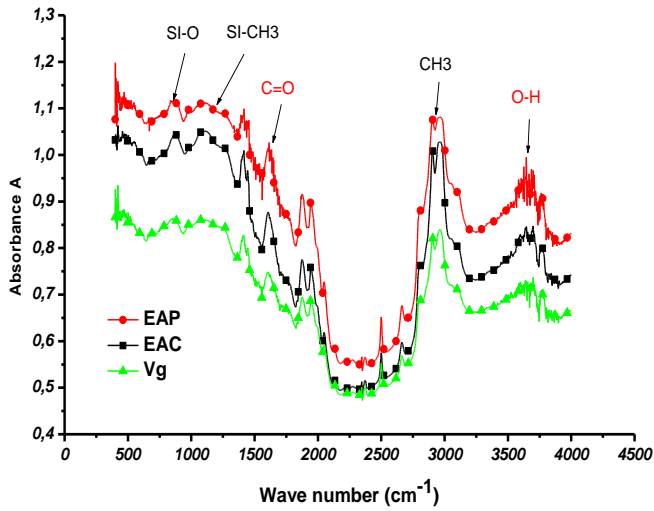


Figure 5: FTIR spectra of silicone states: virgin, aged in dry (clean) and wet (polluted) conditions

However, the XRD analysis revealed that the material has undergone a change in its molecular structure as a result of the alteration due to oxidation. The crystallinities rates χ_c determined for the three considered states of silicone are summarized in table 1 below. The results implied that the silicone crystal structure has been affected by the electrical ageing, thereby increasing its amorphous phase. This assumes that a change is occurred in silicone phases, from crystalline to amorphous ones. This state change of the material is significant in the case of the aged silicone under pollution.

Table 1: Crystallinity degree of silicone analyzed samples

Silicone sample	χ_c (%)
Virgin	65
Aged silicone at dry conditions	61
Aged silicone under wet pollution	57

The intense energy of the sliding discharge causes a severe surface damage of the material when it runs through the preferential electrically weak amorphous zones. The sample surface depolishing involves an electrical proprieties degradation of the material such as permittivity and index loss. This result implies that microstructure modification has occurred under the applied electrical field stress as a consequence of the phase change resulting from a possible molecular chains splitting and to the oxidation mechanism, revealed by the presence of C = O and O-H bonds. Indeed, analyzes showed off that the degradation of silicone dielectric properties is bonded to the amorphous phase strengthening, occurring at the expense of the crystalline phase decrease. The material aging is accelerated by the presence of the wet polluting layer

which increases the discharge energy, promoting thereby the crystallites destruction. However, the moisture mitigates the thermal effect of the discharge and, in corollary, slows down the loss factor increase relatively to silicone aging in dry conditions.

4 Conclusions

Silicone electrical aging is reflected by the alteration of its dielectric properties such as the decrease of its electrical permittivity, thus, capacity, and the increase of its loss factor. This fact is compounded by a conductive pollution deposit which promotes birth arcing at the water droplets concentration points where the produced sliding discharge energy deteriorates locally the material. This degradation is related to an oxidation mechanism, a phase change (crystalline to amorphous) and a surface alteration due to the discharge occurrence as reveled by the observations of the damaged microstructure morphology. Furthermore, the voltage frequency increases the degradation progression.

References

- [1] Z. Guan, X. Wang, X. Bian, L. Wang and Z.Jia, "Analysis of causes of outdoor insulators damages on HV and UHV transmission lines in China", Electrical Insulation Conference (EIC), Philadelphia, USA, June 8-11, 2014.
- [2] R.S. Gorur, E.A. Chemey, R. Hackam, T. orbeck, "The electrical performance of polymeric insulating materials under accelerated aging in a fog chamber", IEEE Transactions on Power Delivery, Volume 3, No. 3, pp 1157-1164, July 1988
- [3] I. Kimoto, T. Fujimurax, "Performance of isolators for direct current transmission line under polluted conditions", IEEE, Trans, On PAS, Vol. Pas-92 N°3, pp 934-949, May June 1973
- [4] A. Mekhaldi, S. Bouazabia, "Conduction phenomena on pollution insulating surface under AC high voltages", 9è Int. Symp. HV Eng. Autriche, 1995
- [5] R. S. Gorur, J. W. Chan, O. G. Amburge, "Surface hydrophobicity of polymers used for outdoor insulation", IEEE Transactions on Power Delivery, Vol. 5, No. 4, pp 1923-1933, November 1990
- [6] Seog-Hyeon Kim, Edward A. Cherney, Reuben Hackam, Kenneth G. Rutherford, "Chemical changes at the surface of rtv silicone rubber coatings on insulators during dry-band arcing ", IEEE Transactions on Dielectrics and Electrical Insulation Vol. 1 No. 1, pp 106-123, February 2004
- [7] P. A. Sorichetti, C. L. Matteo, O. A. Lambri, G. C. Manguzzi, L. M. Salvatierra, O. Herrero, "Structural changes in EPDM subjected to ageing in high voltage transmission lines", IEEE Transactions on Dielectrics and Electrical Insulation Vol. 14, No. 5, pp 1170-1182, October 2007

- [8] Antonios E Vlastos, Elbadri Sherif, "Natural ageing of EPDM composite insulators", , IEEE Transactions on Power Delivery, Vol. 5, No. 1, pp 406-414, January 1990
- [9] R. Raja Prabu, S. Usa, K. Udayakumar, M. Abdullah Khan and S.S.M. Abdul Majeed, "Electrical insulation characteristics of silicone and EPDM polymeric blends. I", IEEE Trans. Electr. Ins., EI Vol. 14, Issue 5, pp 1207 – 1214, October 2007
- [10] P. D. Blackmore, D. Birtwhistle, G. A. Cash, G. A. George, "Condition assessment of epdm composite insulators using FTIR spectroscopy", IEEE Transactions on Dielectrics and Electrical Insulation Vol. 5 No. 1, pp 132-141, February 1998
- [11] R. S. GON, G. G. Karady, A. Jagota, M. Shah, A. M. Yates, "Aging in silicone rubber used for outdoor insulation", IEEE Transactions on Power Delivery, Vol. 7, No. 2, pp 525-538, April 1992
- [12] Antonios E Vlastos, Stanislaw M Gubanski, "Surface structural changes of naturally aged silicone and EPDM composite insulators", IEEE Transactions on Power Delivery Vol. 6, No. 2, pp 888-900, April 1991

Microwave Interferometry Based Open-ended Coaxial Technique

for High Sensitivity Liquid Sensing

Hind Bakli^{1,2*}, Kamel Haddadi², and Tuami Lasri²

¹Department of Sciences and Technologies, Tipaza, Algeria

²Institute of Electronics, Microelectronics and Nanotechnology, University Lille 1, Villeneuve d'Ascq, France

*corresponding authors, E-mail: baklih@yahoo.com, {kamel.haddadi, tuami.lasri}@iemn.univ-lille1.fr

Abstract

This paper describes a modified open-ended coaxial technique for microwave dielectric characterization in liquid media. A calibration model is developed to relate the measured transmission coefficient to the local properties of the sample under test. As a demonstration, the permittivity of different sodium chloride solutions is experimentally determined. Accuracies of 0.17% and 0.19% are obtained respectively for the real and imaginary parts of dielectric permittivity at 5.9 GHz.

1. Introduction

As a versatile tool for measuring the real and imaginary parts of the complex permittivity of dielectric materials, the open-ended coaxial probe has found widespread use in biomedical and food applications [1]. Advantages of the open-ended coaxial such as broadband frequency coverage and no sample preparation make the method a good candidate for liquid and semisolid samples [2]-[3]. However, in contrast with resonant methods, the technique suffers from a lack of sensitivity and accuracy for the determination of slight dielectric contrasts.

In this work, a novel approach based on the combination of the coaxial line method and an interferometric technique is proposed for the electromagnetic characterization of materials. In Section 2, we present the measuring principle based on the association of a coaxial probe and an interferometric set-up. In section 3, instrumentation for the dielectric characterization of liquid based on the interferometric technique is developed. An experimental study related to the detection and evaluation of small concentrations of sodium chloride in aqueous medium shows that the proposed technique is at the state of art in terms of operating frequency range, sensitivity and measurement accuracy. In section 4, a quasi-static approach is used to model the open-ended aperture admittance when a dielectric medium is set to the probe contact. Finally, in section 5, a calibration model is developed to relate the measured transmission coefficient to the local properties of the sample under test. As a demonstration, the permittivity

of different sodium chloride (NaCl) aqueous solutions is experimentally extracted.

2. Interferometric technique

2.1. Problematic of high impedances measurement

This paragraph highlights the problematic of the microwave measurement, based on a conventional vector network analyzer (VNA), of high impedances. The main measurement limitation relies in the impedance mismatch between the intrinsic impedance of the network analyzer close to 50 Ω and the high impedance of the device under test (DUT). The reflection coefficient measured by the VNA is expressed as

$$\Gamma = \frac{Z - Z_0}{Z + Z_0}, \quad (1)$$

Where Z_0 is the 50 Ω reference impedance of the VNA. The situation is illustrated in Fig. 1 which represents the reflection coefficient Γ as a function of a real impedance.

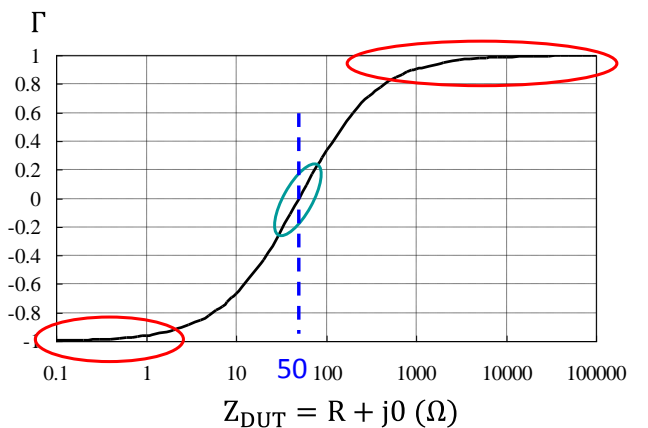


Figure 1: Reflection coefficient Γ as a function of a real impedance Z_{DUT} .

One can note that the measurement sensitivity is maximum for impedances around 50 Ω . But when very high impedances (or very low) are considered, the VNA becomes

practically insensitive to the variations of the reflection coefficient.

Consequently, there is an urgent need to extend the VNA measurement capabilities for impedances greater than the k Ω .

2.2. Principle of the interferometric technique

The proposed interferometric technique consists to cancel the wave reflected by a high impedance device by combining it to a second one called ‘cancellation wave’. The reflected and the cancellation waves have the same magnitude but are phase-shifted by 180°. Consequently, the total reflected signal is theoretically zero. In other words, this technique brings the high impedance to 50 Ω .

Ideally, the cancellation technique should be done under any configurations in terms of operating frequency, impedance, and level of the magnitude of the reflection coefficient. To that end, a measurement set-up is proposed in Fig. 2. This later is built up with a VNA, two power dividers, an impedance tuner (variable attenuator connected to a phase-shifter) and an amplifier.

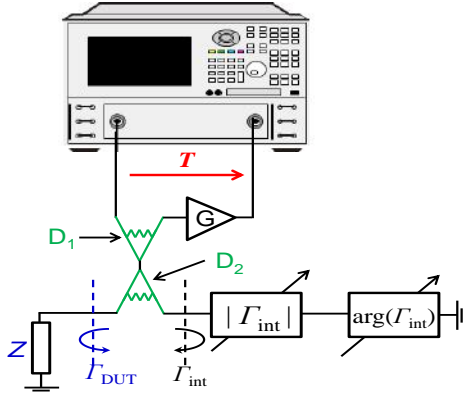


Figure 2: High impedance measurement system configuration based on interferometry.

In this configuration, the microwave signal is delivered from the port 1 of the VNA to feed the input of the first power divider D_1 . At the output of D_1 , the signal is divided between the two ports of the second power divider to supply the device under test (DUT) and the impedance tuner with reflection coefficients respectively Γ_{DUT} and Γ_{INT} . The reflected signals cross again D_1 and D_2 before being amplified (gain G) and then injected on port 2 of the VNA. The measured transmission coefficient T considering ideal components is given by

$$T = \frac{G}{4} (\Gamma_{DUT} + \Gamma_{INT}), \quad (2)$$

The main advantages of this configuration are: (i) the measurement is done in a transmission mode to overcome the main limitation of measurement accuracy encountered when using VNA's in terms of directivity errors, especially for the measurement of small signals. (ii) This architecture provides the possibility to insert an amplifier to further enhance the measurement sensitivity and accuracy.

Before performing a measurement, the interferometric system must be set to a frequency of operation and a given reference device Z_{REF} (reflection coefficient Γ_{REF}) connected to the measurement port (in place of Z_{DUT}). The reflection coefficient Γ_{INT} is then adjusted by the impedance tuner to cancel the reflection coefficient Γ_{REF} at the frequency of interest. Thus, the impedance tuner generates a wave with same magnitude and phase-shifted by 180° in comparison with the wave reflected by the reference impedance. In this condition, the transmission coefficient measured by the network analyzer is therefore zero.

After this step, the device under test is connected to the measurement port. The reflection coefficient of the device is retrieved from the measured transmission coefficient T by inverting the equation (2).

$$\Gamma_{DUT} = \frac{4T}{G} - \Gamma_{REF} \quad (3)$$

The proposed method is suitable for a wide range of applications requiring the detection and measurement of low impedance contrasts. Based on this technique, authors have developed near field microscopy platforms for local dielectric characterization [4]-[7]. In this paper, we investigate the dielectric characterization in a liquid medium using an open-ended coaxial line sensor.

3. Experimental validation

3.1. Theoretical analysis

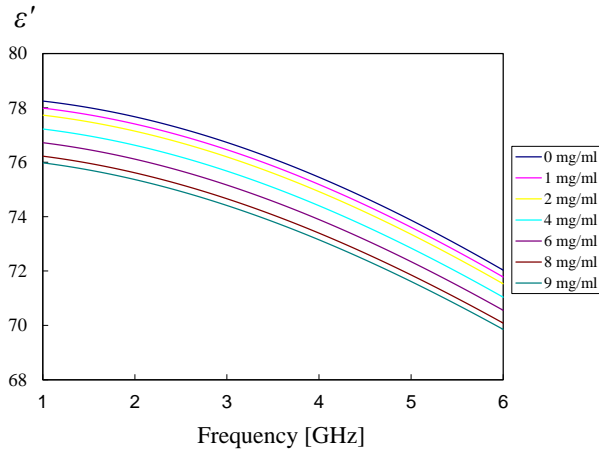
For the demonstration, we have investigated NaCl concentrations in solutions of de-ionized water at different test frequencies. The choice of NaCl solutions is motivated by the fact that it is the most abundant ionic fluid in biological samples. Therefore, sensitive detection of NaCl concentration may become a useful tool for studying the local electrical properties of samples. To remove parasitic capacitances between the probe and the liquid surface and to increase the probe-to-liquid electromagnetic coupling, the probe was immersed in the liquid at a 100 μm -depth. The complex permittivity of the aqueous solutions at 25°C as a function of the NaCl concentration are expressed from the following Cole–Cole model

$$\varepsilon = \varepsilon' - j\varepsilon'' + \frac{\sigma_i}{j\omega\varepsilon_0} = \varepsilon_\infty + \frac{\varepsilon_s - \varepsilon_\infty}{1 - (j\omega\tau)^{1-\alpha}} + \frac{\sigma_i}{j\omega\varepsilon_0} \quad (4)$$

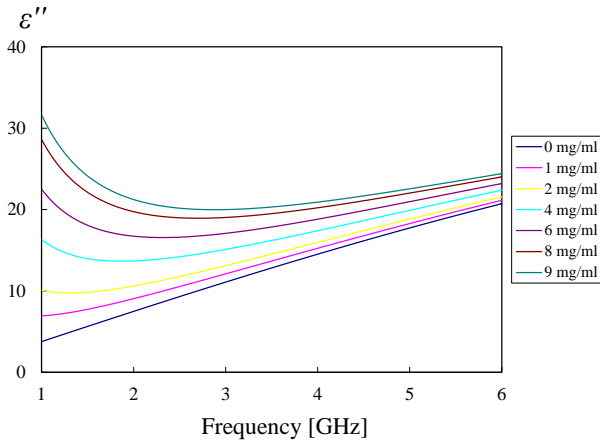
where ε_s and ε_∞ are the limit of the permittivity at low and high frequencies, τ is the relaxation time, σ_i is the ionic conductivity, ε_0 is the permittivity of free space and α is a distribution parameter. The parameters are calculated from empirical relationships derived from the literature [8]. From equation (4), we have determined the real and imaginary part of the complex permittivity for different NaCl solutions for small concentrations (less than 10 mg/ml) in the frequency band 1-6 GHz.

From figure 3 we note, when the NaCl concentration increases, a slight decrease of the value of the dielectric constant ε' in the frequency band considered. The variation of the NaCl in the solutions impacts a lot the dielectric

losses. In particular, a strong increase in the value of the imaginary part ϵ'' of the permittivity is observed for the lowest frequencies. The variation is mainly imputed to the increase of the ionic conductivity that is proportional to the NaCl concentration.



(a)



(b)

Figure 3: Frequency dependence of the complex permittivity for different NaCl solutions. (a) Real part of ϵ as a function of frequency. (b) Imaginary part of ϵ as a function of frequency.

3.2. Experimental validation

The proposed method is based on the test bench given in Fig. 4. The system consists of a network analyzer (Rhode & Schwarz ZVL6), two power dividers (Pasternack PE2028), an impedance tuner built up with a broadband variable attenuator with micrometric adjustments (Radiall R419133) and a high-resolution programmable delay line (Colby Instruments PDL-200A Series), a low noise amplifier and a coaxial probe. The container that holds the liquid sample is set on a xyz stage that offers a positioning accuracy of about ± 100 nm whereas the microwave parts of the microscope remains fixed during measurement. To complete the test bench, a data processing unit is used to control the position of the sample, to tune and record the transmission coefficient T measured by the VNA. The power of the microwave signal is set to -20 dBm and the intermediate

frequency bandwidth (IFBW) of the network analyzer to 10 Hz.

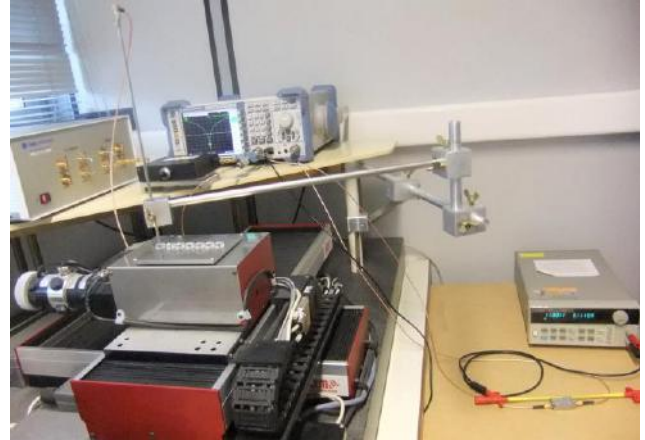
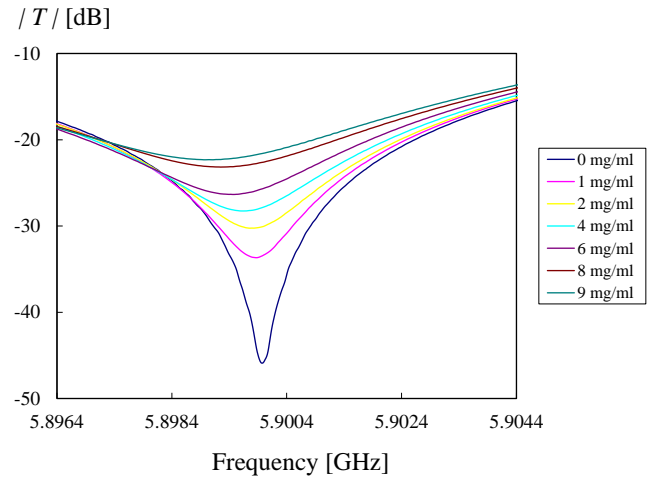


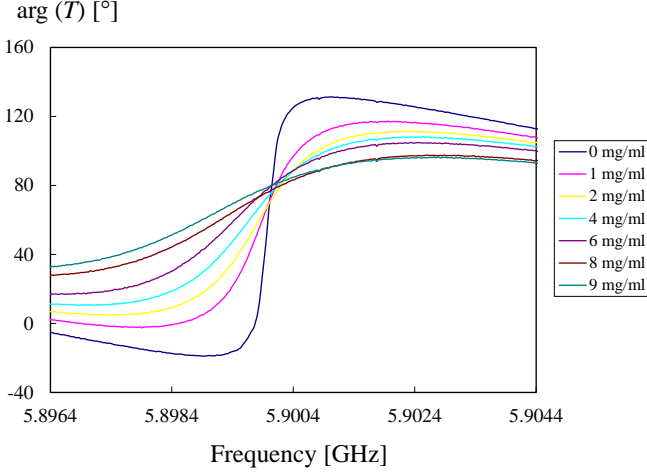
Figure 4: Experimental set-up based on interferometry.

The interferometric method has been tested for different frequencies in the range 2-6 GHz. We present in figure 5, the measured transmission coefficient for the different NaCl concentrations at the test frequency of 5.9 GHz. In this condition, the interferometry procedure is performed for a reference liquid corresponding to de-ionized water at an ambient temperature of 25°C. The quality factor at -3 dB bandwidth is set around 21500.

From this graph, we can note that, when the NaCl concentration increases, the resonant frequency is shifted and the quality factor falls.



(a)



(b)

Figure 5: Measured transmission coefficient T for different NaCl concentrations at the test frequency of 5.9 GHz.

4. Modeling of the open-ended coaxial probe

The open-ended aperture admittance can be expressed as [9]:

$$Y(\varepsilon_r) = j \frac{k^2}{\pi k_c \ln(b/a)} \int_a^b \int_a^b \int_0^\pi \cos\varphi \frac{e^{-jkr}}{r} d\varphi d\rho' d\rho, \quad (5)$$

where $k = \omega\sqrt{\varepsilon_r\varepsilon_0\mu_0}$ is the wave vector in the medium, (ρ, ρ', φ) are the cylindrical coordinates, $r = \sqrt{\rho^2 + \rho'^2 - 2\rho\rho'\cos(\varphi)}$, and a et b are respectively the inner and outer radius of the probe (Table 1). $k_c = \omega\sqrt{\varepsilon_c\varepsilon_0\mu_0}$ is the wave vector in the probe with ε_c set to 1.7.

When considering the quasi-static approach [9]-[10], equation (5) can be reduced to

$$Y(\varepsilon_r) = \frac{j2\omega\varepsilon_r}{(\ln(b/a))^2} \left(I_1 - \frac{k^2 I_3}{2} \right), \quad (6)$$

where

$$I_1 = \int_a^b \int_a^b \int_0^\pi \frac{\cos\varphi}{r} d\varphi d\rho' d\rho, \quad (7)$$

and

$$I_3 = \int_a^b \int_a^b \int_0^\pi r \cos\varphi d\varphi d\rho' d\rho, \quad (8)$$

I_1 and I_3 are independent of the medium characteristics, a quadratic equation in ε_r can be formulated using (6) for a measured admittance $Y(\varepsilon_r)$, which can be solved easily for ε_r .

$$I_3\omega^3\mu_0j\varepsilon_r^2 - 2j\omega I_1\varepsilon_r + Y(\varepsilon_r)(\ln(b/a))^2 = 0. \quad (9)$$

I_1 and I_3 are dependent only on the probe geometry. For the probe used, the calculated values of I_1 and I_3 are given in Table 1.

Table 1: Integrals I_1 and I_3 for the coaxial probe used.

a [mm]	b [mm]	I_1	I_3
0.535	1.458	0.01498	$-1.02994 \cdot 10^{-6}$

5. Calibration model and inverse problem

A traditional one port calibration model is used to make the link between the measured transmission coefficient T and the reflection coefficient at the end of the coaxial probe Γ_t . The resulting model is given by

$$T = E_{11} + \frac{E_{12}E_{21}\Gamma_t}{1 - E_{22}\Gamma_t}, \quad (10)$$

where the complex terms E_{11} , $E_{12}E_{21}$ and E_{22} are calibration coefficients that correspond respectively to the directivity, source match and reflection tracking errors. Three different NaCl solutions are used to determine these calibration coefficients. Thus, by measuring Γ_t , it is possible to determine Y and then retrieve the material permittivity ε_r . To determine the dielectric properties of the different NaCl solutions, the following steps are followed:

1- Estimation of the admittance of the three NaCl solutions (0, 4 and 9 mg/ml) selected for calibration (i.e. Y_{t1} , Y_{t2} , Y_{t3}) by using equation (6).

2- Determination of the reflection coefficients Γ_{t1} , Γ_{t2} and Γ_{t3} of the three known admittances Y_{t1} , Y_{t2} and Y_{t3} ($\Gamma_t = \frac{Y(\varepsilon_r) - Y_0}{Y(\varepsilon_r) + Y_0}$, $Y_0 = 50\Omega$).

3- Solving of the system (10) to find E_{11} , $E_{12}E_{21}$ and E_{22} .

4- Determination of the reflection coefficient Γ_t for the remaining concentrations from the inversion of equation (10) and then calculation of Y .

5- Retrieval of the dielectric properties by the resolution of equation (9).

We present in figure 6 the dielectric constant reported from theory and determined experimentally for the different NaCl aqueous solutions considered. From this graph, we can observe a good agreement between measurement and theory. The average accuracy on the dielectric constant measured is found to be 0.17 %.

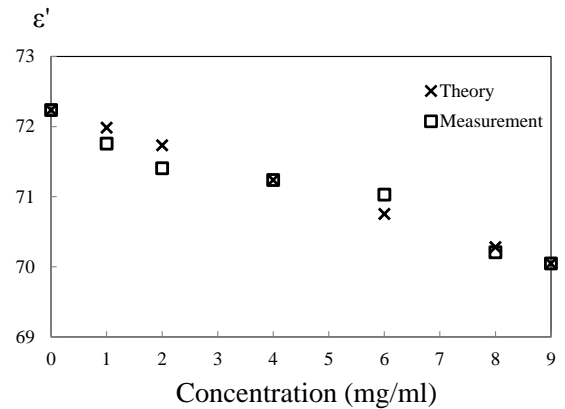


Figure 6: Theoretical and measured values of the dielectric constant ε' for different NaCl aqueous solutions at 5.9 GHz.

In figure 7, the imaginary part of the dielectric permittivity reported from theory and retrieved from the measurement is given for the different NaCl aqueous solutions. From this graph, we can observe also a good agreement between measurement and theory. We can also note that the imaginary part of the dielectric permittivity is measured with an average accuracy of 0.19%.

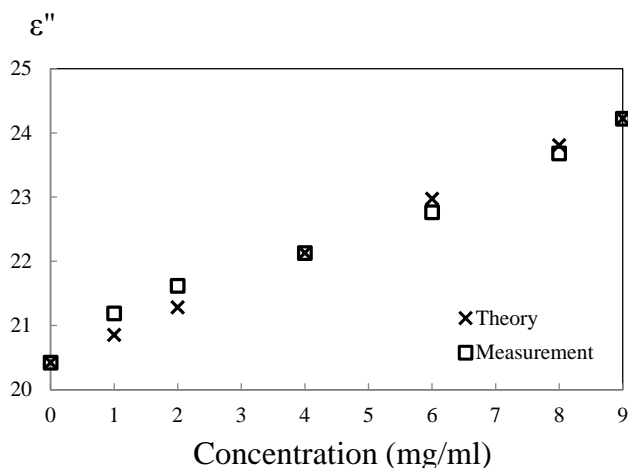


Figure 7: Theoretical and measured values of the imaginary part of the dielectric permittivity ϵ'' for different NaCl aqueous solutions at 5.9 GHz.

6. Conclusion

A microwave interferometry based open-ended coaxial technique was developed for high sensitivity liquid sensing applications. A calibration model was proposed to relate the measured transmission coefficient to the local properties of the liquid. The complex permittivity for different NaCl solutions was experimentally determined using the technique proposed. Average accuracy of 0.17% and 0.19% were obtained respectively for the real and imaginary parts of the permittivity.

References

- [1] T. H. Kim, J. K. Pack, Measurement of electrical characteristics of female breast tissues for the development of the breast cancer detector, *Progress In Electromagnetics Research C* 12: 188–199, 2012.
- [2] D. Popovic, L. McCartney, C. Beasley, M. Lazebnik, M. Okoniewski, S. C. Hagness, J. H. Booske, Precision open-ended coaxial probes for in vivo and ex vivo dielectric spectroscopy of biological tissues at microwave frequencies, *IEEE Trans. Microwave Theory and Techniques* 53: 1713-1722, 2005.
- [3] Agilent Technologies, Inc., Agilent 85070E Dielectric Probe Kit, 200 MHz to 50 GHz, <http://cp.literature.agilent.com/litweb/pdf/5989-0222EN.pdf>
- [4] K. Haddadi, H. Bakli, T. Lasri, Microwave liquid sensing based on interferometry, *IEEE Microw. Wireless Components Letters* 22: 542–544, 2012.
- [5] H. Bakli, K. Haddadi, T. Lasri, Interferometric technique for scanning near-field microwave microscopy applications, *Proc. IEEE Instrum. Meas. Technol. Conference*, Minneapolis, USA, pp. 1694-1698, 2013.
- [6] H. Bakli, K. Haddadi, T. Lasri, Interferometric technique for scanning near-field microwave microscopy applications, *IEEE Trans. Instrumentation Measurement* 63: 1281–1286, 2014.
- [7] H. Bakli, K. Haddadi, T. Lasri, Modeling and calibration in near-field microwave microscopy for dielectric constant and loss tangent measurement, *IEEE Sensors Journal* PP: 1–2, 2016.
- [8] A. Peyman, C. Gabriel, E. H. Grant, Complex permittivity of sodium chloride solutions at microwave frequencies, *Bioelectromagnetics* 28: 264–274, 2007.
- [9] D. K. Misra, Quasi-Static Analysis of Open-Ended Coaxial Lines, *IEEE Trans. Microwave Theory and Techniques* 35: 925–928, 1987.
- [10] B. Filali, F. Boone, J. Rhazi, G. Ballivy, Design and calibration of a large open-ended coaxial probe for the measurement of the dielectric properties of concrete, *IEEE Trans. Microwave Theory and Techniques* 56: 2322–2328, 2008.

General Papers

Sintering temperature and iso-valent dopant effects on microstructural and dielectric properties of lead-free ceramic



Lhoussain Kadira¹, Abdelilah Elmesbahi², and Salaheddine Sayouri³

¹CRMEF, Fès, Morocco

²FST, Tanger, Morocco

³Theoretical and Applied Physics Laboratory, Faculty of Science Dhar - Mahraz, Fès, Morocco

*corresponding author, E-mail: lhoussain-kadira@gmx.fr

Abstract

Ca-doped Lanthanum barium titanate $\text{La}_{0.01}\text{Ba}_{0.99}\text{Ti}_{0.9975}\text{O}_3$ (LBT) ceramics powders were prepared by sol-gel process through Destabilization of Colloidal Solution (DCS) [1]. Sintering of pressed powders was performed at 1150°C, 1250°C and 1300°C for 4 hours. XRD analysis showed a good crystallization of the samples in the pure perovskite structure, and allowed determination of the crystallite size. Microstructure morphology was analyzed using Scanning Electron Microscopy (SEM), and the grain size of the samples was estimated. It was found that lanthanum doping has significant inhibiting effect on densification [2,3], but calcium appears to have a beneficial effect for the improvement of the densification of the material. Dielectric measurements were carried out with an impedance-analyzer in the temperature range from room temperature (RT) to 250°C, and for frequencies ranging from 100Hz to 1MHz. Data obtained from these measurements were fitted to the generalized power law.

1. Introduction

Barium titanate (BT) is the most extensively investigated environmental friendly ferroelectric material, because it is extremely interesting from the point of view of practical applications [4-8]. It is chemically and mechanically very stable and it exhibits ferroelectric properties at and above room temperature (RT) and it can be easily prepared and used in the form of ceramic polycrystalline samples.

Here, we project to study the behavior of the transition temperature following the variation from doping out of Ca^{2+} in the solid solution $\text{La}_{0.01}(\text{Ba}_{1-x}\text{Ca}_x)_{0.99}\text{Ti}_{0.9975}\text{O}_3$ LBCT ($x=0.01, 0.05$ and 0.1) synthesized by sol-gel method. In the present work for $x=0.00, 0.01, 0.05$ & 0.10 , we have used LBT, LBCT0.01, LBCT0.05, LBCT0.1 notations. X-ray Diffraction (XRD), Scanning Electronic Microscopy (SEM) and Impedance-Spectroscopy Analysis (ISA) measurements are used for physical-chemical characterization.

2. Experimental procedures

2.1. Sample preparation

Calcined powders at 900 °C (4h) were cold pressed with 2% polyvinyl alcohol (PVA) as binder under a pressure of 1.14kN/mm² into disks of convenient size (12.5 mm in diameter) and then sintered at a desired temperature (1150, 1250, 1300°C) for 4 hours in air in a microprocessor-controlled furnace.

2.2. Experiment methods

Scanning Electronic Microscopy Analysis was carried out on a JEOL JSM5500 apparatus. Metallization was carried out with carbon by cathodic evaporation by means of a metal sprayer of the type SPI carbon Coater and dielectric measurements were collected by an LCZ3330 impedance analyzer controlled in temperature and computer assisted in both the heating and cooling phases.

3. Results and discussion

3.1. Microstructural results

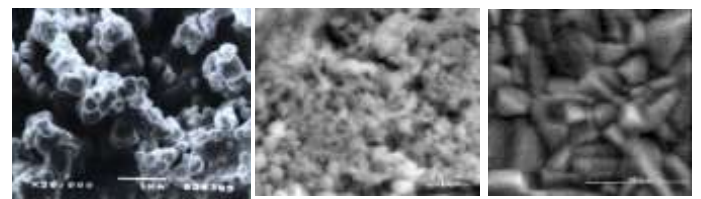


Figure 2: SEM micrographs of LBCT0.1 samples sintered for 4hs at (a) 1150°C (b) 1250°C & (c) 1300°C

Table 2: Grain size of LBCT0.1 vs sintering temperature

Temperature (°C)	Grain size (µm)
1150	0.2
1250	--
1300	2.5

Table 1: Volumetric shrinkage ($\Delta v/v$) of LBCT0.1 vs sintering temperature.

Temperature (°C)	$\frac{\Delta V}{V}$ (%)
1150	8.79
1250	10.16
1300	22.37

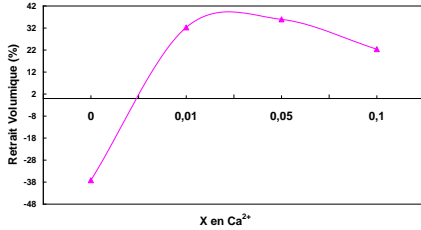


Figure .1 Volumetric shrinkage ($\Delta v/v$) of LBCT sintered at 1300 °C (4h) vs calcium concentration

3.2. Dielectric results

Table .3 Transition temperature for LBCT samples

Ca ²⁺ (%)	T _c (°C)
0	76.8
1	124.6
5	101.6
10	102.4

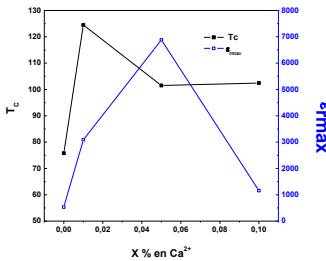


Figure 3: T_c and $\epsilon_{r \max}$ versus calcium concentration

$$\epsilon_r = \frac{C}{T - T_0}, \quad (1) \quad \frac{1}{\epsilon_r} = \frac{1}{\epsilon_{r \max}} \left[1 + \frac{(T - T_m)^\gamma}{2\delta^2} \right], \quad (2)$$

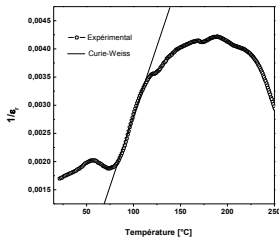


Figure 4: Variation of $1/\epsilon_r$ vs. temperature of LBCT

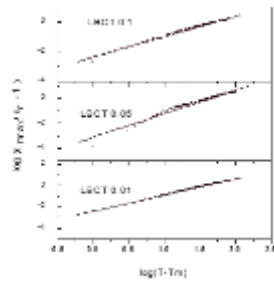


Figure 5: Variation of $\log(\epsilon_{r \max}/\epsilon_r - 1)$ vs. $\log(T - T_{\max})$ of LBCT

Table 4: Critical exponent γ and diffusivity parameter δ of LBCT vs calcium concentration

Ca ²⁺ concentration (x)	γ	δ
0.01	1.52	11.17
0.05	1.88	24.99
0.1	1.37	10.73

4. Conclusions

We demonstrated in this work the study of the influence of calcium doping and sintering temperature on both the dielectric and microstructural properties of LBT. The samples were prepared by the recent sol-gel route. The microstructural characterization of the various concentrations of LBCT by SEM reveals that LBCT0.1, sintered at 1300°C for 4hrs, manifests maximum withdrawal and a better intensification. This sample also shows the best dielectric properties.

The study of the phase transition (ferroelectric-paraelectric) shows that calcium leads particularly to an important increase of the Curie temperature for the range of rates from 0 to 0.05. Therefore, the transition nature passes from classic ferroelectric state, governed by the Curie-Weiss law (equation 1) in the case of BLT, to the diffuse phase transition DPT, governed by the generalized power law (equation 2).

References

- [1] Lh. Kadira, A. Elmesbahi, S. Sayouri, Mr. Zenkouare, A. Kherbeche, Mr. Ech-Chamikh, Mr. Lotfi, *Year. Chim. Chechmate*, 28, p. 75-82, 2003.
- [2] M. -H. Lin, H. -Y. Lu, *Materials Science and Engineering A323*, p. 167, 2002.
- [3] Lh. Kadira, A. Elmesbahi, S. Sayouri, *International Meeting on Materials for Electronic Applications: IMMEA-2015*, Marrakech - Morocco, 2015.
- [4] S. Komarneni & H. Katsuki, *Ceramics International*, 36 [3] 1165, 2010.
- [5] P. Kumar, S. Singh, M. Spah, J.K. Juneja, C. Prakash, K.K. Raina *J. Alloys & Compounds*, 489 [1, 7] 59, 2010.
- [6] S. Marković, Č. Jovalekić, L. Veselinović, S. Mentus, D. Uskoković, *Journal of the European Ceramic Society*, 30 [6] 1427, 2010.
- [7] Fang, D. X. Zhou, S. Gong, *Physica B: Condensed Matter*, 406 [6-7] 1317-1322, 2011.
- [8] H. N. Zadeh, C. Glitzky, W. Oesterle, T. Rabe, *Journal of the European Ceramic Society*, 31 [4] 589, 2011.

Variation of $\log(1/\epsilon_r - 1/\epsilon_{r \max})$ vs. $\log(T - T_{\max})$ of BT samples synthesized by

MSSR route

Exploring the Temporal Aspect of Energy-Tunneling in a Wire-Loaded Microstrip Cavity

Muhammad Arif Shah
FAST-National
Islamabad-44000, Pakistan
arifshah423@gmail.com

Rashad Ramzan
United Arab Emirates University
Al-Ain-15551, UAE
rashad.ramzan@uaeu.ac.ae

Omar Farooq Siddiqui
Taibah University, Madinah
Saudi Arabia
omarsiddiqui2@gmail.com

Abstract- Energy-tunneling is a well-known electromagnetic phenomenon which is observed in narrow channels in waveguide junctions either filled with epsilon-near-zero materials or resonant wires. Energy-tunneling is a frequency-selective phenomenon resulting in very high electromagnetic fields inside the narrow channels and around the resonant wires. This phenomenon can be exploited to design microwave components like filters, multiplexers, and highly sensitive sensors. The frequency domain behavior is well studied, in this paper we will focus on the time domain behavior of wire-based energy tunneling using a Gaussian pulse as it propagates through an energy-tunneling microstrip channel. Simulation shows the temporal dispersion (due to highly selective frequency transmission response) results in considerable slowing of the propagating pulse. Furthermore, a parametric study is conducted to determine the factors influencing the slower propagation of waves resulting in large delays. These large time delays from small physical length of wire can be used to design new type of delay lines, which have multiple application in area of microwave and RFIC design.

I. INTRODUCTION

In recent years, researchers are working on different techniques and technologies to transfer electromagnetic energy through narrow sub-wavelength channels and waveguide configurations [1-2]. The wire-based energy tunneling which is discussed in this paper takes place in the regime of frequencies when the wires become resonant. Such regimes are identified by diminishing group velocities along one of the structure's axes of symmetry and the flatness of the dispersion surfaces [3]. To date, temporal aspect of the wire-based energy tunneling has not been explored. Since the energy tunneling phenomenon is narrowband, a considerable slowing of the underlying electromagnetic wave is anticipated. In this paper, we concentrate on the time domain behavior of the energy tunneling. We first explore the effect of geometrical modifications of the energy tunneling channel on the temporal parameters such as group delay and group velocity in frequency domain. Subsequently, we study the wave propagation of a Gaussian pulse as it passes through the energy tunneling channel. Slowing down of Gaussian pulse in the energy tunneling channel is noted which can be used in potential applications such as digital buffers, synchronization, and other non-linear applications [4].

II. ENERGY TUNNELING WAVEGUIDE TOPOLOGY

In this paper we have used the same experimentally proven model with minor modifications which was presented in [5] for microstrip dielectric sensor based on EM energy tunneling.

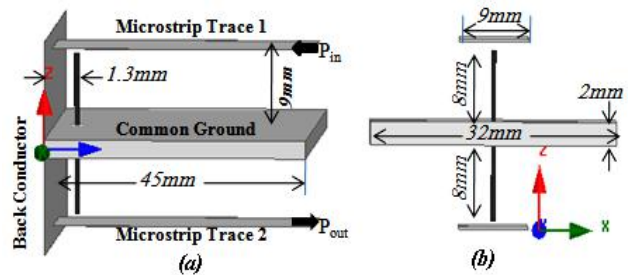


Fig.1. (a) 3D view of energy tunneling model (b) 2D back view of energy tunneling microstrip structure

Physical dimensions of the model are given in Fig. 1 on the basis of different parametric analysis and electromagnetic energy tunnels at 5.6GHz and Rogers RO3006 ($\epsilon_r = 6.15$) is used as a dielectric substrate. All simulation work is carried out using ANSYS HFSS full-wave electromagnetic simulator.

III. FREQUENCY-DOMAIN DISPERSION PLOTS

The electromagnetic energy tunnels from one microstrip to other through the metallic wire and this can be determined through phase and group velocity relationship. In such design, the metallic wire is placed parallel to E-field. At the tunneling frequency which is 5.6GHz in this case, transmission phase is near zero as shown by black line (circular marker) in Fig.2. The second curve of Fig.2 shows transmission phase for a simple microstrip of the same length (90mm) as of the microstrip of energy tunneling system. An increase in phase slope in the vicinity of the resonance is noted for the tunneling microstrip compared to the ordinary microstrip. As shown in the Group delay plot of Fig. 3, this change in slope corresponds to the decrease in the group velocity of electromagnetic wave that propagates in the energy-tunneling microstrip. A difference of almost 1ns is observed between the two cases. Consider the effect of the length of the wire on the energy tunneling group delay is studied and results are depicted in Fig.4. With the increase of wire's length, cause a decrease in the group delay. Although, a seemingly counter intuitive behavior can be explained in terms of the decrease of field concentration over the wire when one of the two parameters is increased. With the decrease in field concentration, the bandwidth of the energy tunneling spectrum increases leading to the smaller phase slopes which correspond to the decrease in the group delay have a similar effect on the group delay the group delay decreases because of the associated wave now travels more distance inside the energy tunneling channel.

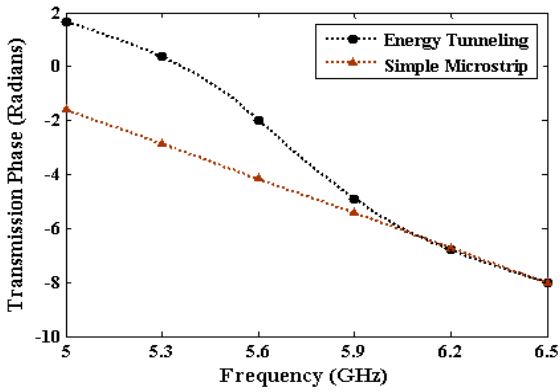


Fig.2. Transmission phase versus frequency plot of energy tunneling microstrip structure

IV. TIME DOMAIN GAUSSIAN PULSE PROPAGATION

Consider a modulated Gaussian pulse passing through a dispersive channel and the propagation behavior of the Gaussian pulse in an electromagnetic energy tunneling channel depicted in Fig 5. For comparison, the propagation of the same Gaussian pulse in simple microstrip of 90mm length is also studied. In frequency domain dispersion plot (Fig. 3), the group delay for energy tunneling channel was almost 1.69ns and group delay for simple microstrip was almost 0.69ns.

The delay of 1.69ns and 0.69ns is observed in time domain when the pulses propagate through energy tunneling channel and microstrip, respectively. However, it important to note that higher delay is accompanied by the reduction in magnitude as plotted in Fig.5. To increase the group delay, radius of the wire is reduced from 0.06mm to 0.03mm and dielectric substrate is changed from Rogers RO3006 ($\epsilon_r = 6.15$) to Arlon AR1000 ($\epsilon_r = 10$) keeping the length of the wire same as in Fig.1. The simulation shows the resulting group delay of 2.2ns.

V. CONCLUSION AND FUTURE DIRECTIONS

Transmission phase and group velocity in energy tunneling channel is simulated. In energy tunneling channel, group velocity is much lower compared to equivalent microstrip due to dispersive nature of the channel. A time domain Gaussian pulse is generated and its propagation behavior is observed in

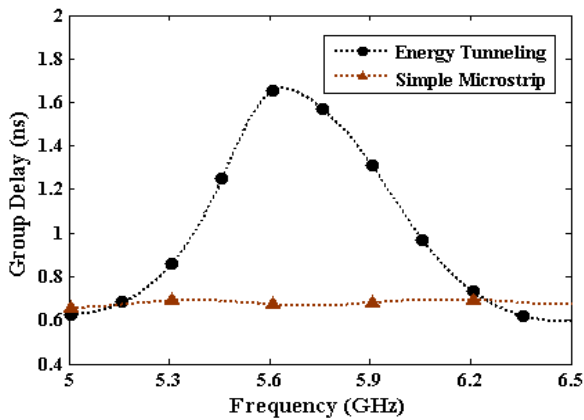


Fig.3. Group delay of energy tunneling channel and microstrip plot versus frequency

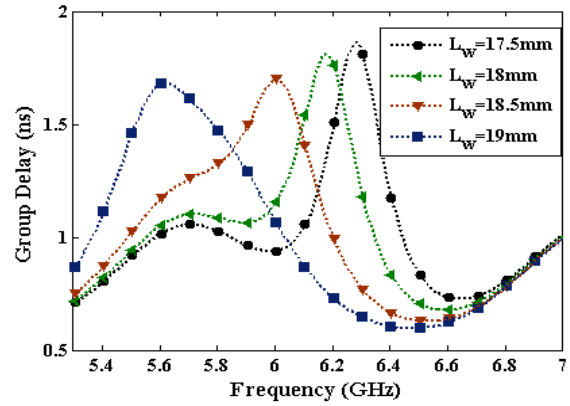


Fig.4. Length of the wire versus group delay of energy tunneling channel

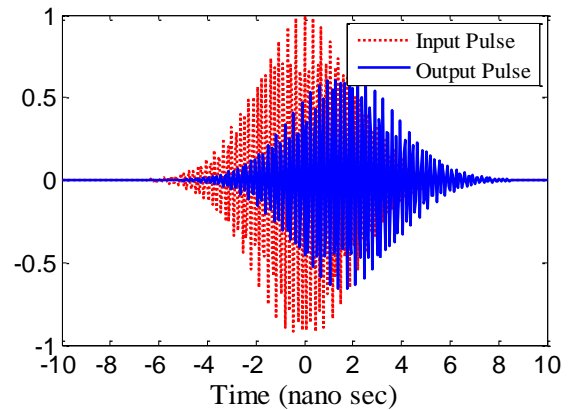


Fig.5. Time domain behavior of the Gaussian pulse in energy tunneling channel

energy tunneling channel and its equivalent microstrip. Group delay values obtained from the time domain output pulse and this type of behaviour in energy tunnelling microstrip structure can be used to design the new class of delay lines for different microwave applications such as buffering, synchronization of digital signals and similar non-linear applications. This is our future area of interest and investigations.

REFERENCES

- [1] M. G. Silveirinha and N. Engheta. "Tunneling of electromagnetic energy through sub-wavelength channels and bends using epsilon-near-zero (ENZ) materials," *Phys. Rev. Lett.*, vol. 97, no. 15, pp.157403–157406, Oct. 2006.
- [2] O.F. Siddiqui and O. Ramahi. "A Novel Dielectric Detection System Based on Wire-Loaded Waveguides", *IEEE Microwave and Wireless Components Letters*, vol. 21, no.2, Feb. 2011.
- [3] J. Witzens, M. Loncar, and A. Scherer A, "Self-collimation in planar photonic crystals", *IEEE Journal of Selected Topics in Quantum Electronics*, vol. 8, no. 6, pp. 1246-1257, November-December 2002.
- [4] R. W. Boyd, D. J. Gauthier, and Al. L. Gaeta, "Applications of Slow Light in Telecommunications", *Optics and Photonics News* Vol. 17, Issue 4, pp. 18-23, 2006.
- [5] R. Ramzan, O. Siddiqui, A. Nauroze and O. Ramahi. "A microstrip probe based on electromagnetic energy tunneling for extremely small and arbitrarily shaped dielectric samples " *IEEE Antennas and Wireless Propagation Letters*, DOI 10. 1109/LAWP, 2015.

Analysis of Electromagnetic Scattering at a Radially Inhomogeneous Dielectric Sphere Using the Hybrid Projection Method

Alina R. Gabdullina¹, Olga N. Smolnikova^{2,3}, and Sergei P. Skobelev^{1,3*}

¹Moscow Institute of Physics and Technology, Dolgoprudny, Moscow Region, Russia

²Moscow Aviation Institute, Moscow, Russia

³Public Joint Stock Company "Radiofizika", Moscow, Russia

*E-mail: s.p.skobelev@mail.ru

Abstract

A modification of the hybrid projection method is proposed for analysis of wave scattering at a radially inhomogeneous dielectric sphere. The approach is based on projection matching of the fields on the boundaries of spherical regions, on projection of the Maxwell equations on the transverse vector functions, and on application of the one-dimensional finite element method to the obtained ordinary differential equations for reduction of the latter to algebraic systems with three-diagonal matrices. The advantages of the approach over some other methods are discussed.

1. Introduction

Analysis of electromagnetic wave scattering at radially inhomogeneous sphere has been of great interest for a long time for the problem has a number of important application in antenna technology, bio-medical modeling, and in modern objects involving metamaterials. Moreover, the indicated sphere is a convenient model for testing new numerical methods arising in the electromagnetic theory for analysis of wave scattering by more complex objects.

The importance of the problem for the modern studies is confirmed by recent publication of two papers [1] and [2] where the authors have made their reviews of the methods available for solution of the problem as well as propose new algorithms based on the method of volume integral equations combined with expansion of the fields over the system of spherical functions [1], and on replacement of the continuous permittivity profile by a step-wise constant profile with subsequent matching of the fields expanded over spherical functions on the boundaries of the homogeneous spherical layers [2].

In the present paper we propose one more approach to solution of the problem. It is based on the hybrid projection method similar to that developed in [3] for analysis of periodic dielectric structures. The approach includes projection matching of the fields on the boundaries of the spherical regions, projection of the Maxwell equations on the transverse vector functions, and application of the one-dimensional finite element method in projection formulation to the obtained ordinary differential equations for reducing the latter to algebraic systems with three-

diagonal matrices. The advantages of the approach over the algorithms described in [1] and [2] will be indicated in the subsequent Sections.

2. Statement of the problem and method of solution

The geometry of the problem under consideration is presented in Fig. 1 where a radially inhomogeneous sphere arranged in the free space consists of a central core of radius a_1 and constant relative permittivity ϵ_1 , as well as of a shell (layer) of outer radius a and relative permittivity $\epsilon(r)$ depending on the radial coordinate. The relative permeability of the core and shell is equal to unity.

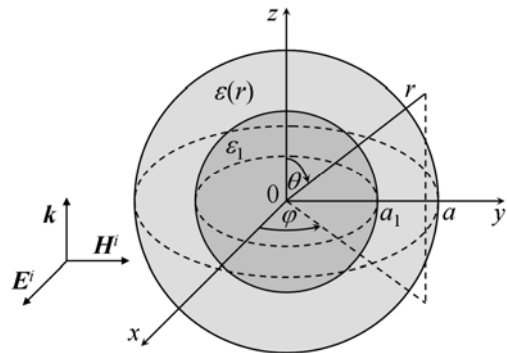


Figure 1: Geometry of the problem.

The sphere is assumed to be illuminated by a plane electromagnetic wave propagating along the z axis and polarized along the x axis as shown in Fig. 1. The electric and magnetic field strengths of the incident wave are determined by formulas $\mathbf{E}^i = \mathbf{e}_x E_0 e^{ikz}$ and $\mathbf{H}^i = \mathbf{e}_y (E_0/\eta) e^{ikz}$, where E_0 is the specified amplitude, η is the wave resistance of the free space, and $k = 2\pi/\lambda$ is the wave number. Dependence of the fields on time assumed to be in the form $e^{-i\omega t}$ here and below is suppressed.

In order to determine the scattered field outside of the sphere and the field inside the sphere, we represent the transverse components of the fields outside ($r \geq a$), in the inhomogeneous layer ($a_1 \leq r \leq a$), and in the core ($r \leq a_1$) as expansions over spherical TE and TM waves

$$\mathbf{E}_{1\tau} = \frac{1}{kr} \sum_{l=1}^{\infty} \{ [A_l \psi_l(kr) + R_{1l} \zeta_l(kr)] \Phi_{1l} - i [A_l \psi'_l(kr) + R_{2l} \zeta'_l(kr)] \Phi_{2l} \}, \quad (1)$$

$$\mathbf{H}_{1\tau} = \frac{1}{\eta kr} \sum_{l=1}^{\infty} \{ -i [A_l \psi'_l(kr) + R_{1l} \zeta'_l(kr)] \Psi_{1l} + [A_l \psi_l(kr) + R_{2l} \zeta_l(kr)] \Psi_{2l} \}, \quad (2)$$

$$\mathbf{E}_{2\tau} = \sum_{l=1}^{\infty} [E_{1l}(r) \Phi_{1l} + E_{2l}(r) \Phi_{2l}], \quad (3)$$

$$\mathbf{H}_{2\tau} = \frac{1}{\eta} \sum_{l=1}^{\infty} [H_{1l}(r) \Psi_{1l} + H_{2l}(r) \Psi_{2l}], \quad (4)$$

$$\mathbf{E}_{3\tau} = \frac{1}{kr} \sum_{l=1}^{\infty} [T_{1l} \psi_l(k_1 r) \Phi_{1l} - i T_{2l} \psi'_l(k_1 r) \Phi_{2l}], \quad (5)$$

$$\mathbf{H}_{3\tau} = \frac{k_1}{\eta k^2 r} \sum_{l=1}^{\infty} [-i T_{1l} \psi'_l(k_1 r) \Psi_{1l} + T_{2l} \psi_l(k_1 r) \Psi_{2l}], \quad (6)$$

where A_l are known coefficients corresponding to the incident wave [4], R_{jl} and T_{jl} are unknown constant coefficients for the TE ($j=1$) and TM ($j=2$) waves, $E_{jl}(r)$ and $H_{jl}(r)$ are unknown variable coefficients, $\psi_l(kr)$ and $\zeta_l(kr)$ are functions of Riccati-Bessel and Riccati-Hankel, $k_1 = k \sqrt{\varepsilon_1}$,

$$\Phi_{1l}(\theta, \varphi) = \sqrt{\frac{2l+1}{2\pi}} \frac{1}{l(l+1)} \left(\mathbf{e}_\theta \frac{P_l^1}{\sin \theta} \cos \varphi - \mathbf{e}_\varphi \frac{dP_l^1}{d\theta} \sin \varphi \right), \quad (7)$$

$$\Phi_{2l}(\theta, \varphi) = \sqrt{\frac{2l+1}{2\pi}} \frac{1}{l(l+1)} \left(\mathbf{e}_\theta \frac{dP_l^1}{d\theta} \cos \varphi - \mathbf{e}_\varphi \frac{P_l^1}{\sin \theta} \sin \varphi \right), \quad (8)$$

are orthonormalized transverse functions, $P_l^1(\cos \theta)$ are associated Legendre functions, $\Psi_{jl} = \mathbf{e}_r \times \Phi_{jl}$, and $\mathbf{e}_r, \mathbf{e}_\theta, \mathbf{e}_\varphi$ are unit vectors over r, θ , and φ , respectively.

The radial components of the fields in the layer are determined via the transverse fields (3) and (4) from the Maxwell equations

$$\nabla \times \mathbf{H} + \frac{ik\varepsilon(r)}{\eta} \mathbf{E} = 0, \quad \nabla \times \mathbf{E} - ik\eta \mathbf{H} = 0. \quad (9)$$

Projection of equations (9) on functions (7) and (8) for each l results in two independent pairs of ordinary differential equations

$$ik \frac{dV_1}{dr} + \left[k^2 \varepsilon(r) - \frac{l(l+1)}{r^2} \right] U_1 = 0, \quad (10)$$

$$\frac{dU_1}{dr} - ikV_1 = 0, \quad (11)$$

$$ik \frac{dU_2}{dr} + \left[k^2 - \frac{l(l+1)}{r^2 \varepsilon(r)} \right] V_2 = 0, \quad (12)$$

$$\frac{dV_2}{dr} - ik\varepsilon(r)U_2 = 0, \quad (13)$$

where $U_j(r) = krE_{jl}(r)$ and $V_j(r) = krH_{jl}(r)$. For solution of the equations obtained above, we represent functions U_1 и V_2 as

$$U_1(r) = \sum_{n=1}^N U_{1n} f_n(r), \quad V_2(r) = \sum_{n=1}^N V_{2n} f_n(r), \quad (14)$$

where U_{1n} and V_{2n} are unknown constant coefficients, $f_n(r)$ are so-called triangular functions [3], and N is the number of the nodes on the interval $[a_1, a]$. Further, projecting equation (10) and (12) on triangle functions $f_n(r)$, like in [3], accounting for (11) and (13), as well as for continuity conditions for fields (1) through (6) at $r=a_1$ and $r=a$, we reduce the problem to the following algebraic systems

$$\begin{aligned} T_{1l} \psi_l(k_1 a_1) - U_{1l} &= 0, \\ -\frac{k_1}{k} T_{1l} \psi'_l(k_1 a_1) \delta_{n1} + \sum_{n=1}^N Z_{n'n}^{(1)} U_{1n} + R_{1l} \zeta'_l(ka) \delta_{nN} &= -A_l \psi'_l(ka) \delta_{nN}, \\ U_{1N} - R_{1l} \zeta_l(ka) &= A_l \psi_l(ka) \end{aligned} \quad (15)$$

for TE waves, and

$$\begin{aligned} \frac{k_1}{k} T_{2l} \psi_l(k_1 a_1) - V_{2l} &= 0, \\ -T_{2l} \psi'_l(k_1 a_1) \delta_{n1} + \sum_{n=1}^N Z_{n'n}^{(2)} V_{2n} + R_{2l} \zeta'_l(ka) \delta_{nN} &= -A_l \psi'_l(ka) \delta_{nN}, \\ V_{2N} - R_{2l} \zeta_l(ka) &= A_l \psi_l(ka) \end{aligned} \quad (16)$$

for TM waves with matrix elements

$$Z_{n'n}^{(1)} = \int_{a_1}^a f_n' f_n' \left[k\varepsilon - \frac{l(l+1)}{kr^2} \right] dr - \frac{1}{k} \int_{a_1}^a f_n' f_n'' dr, \quad (17)$$

$$Z_{n'n}^{(2)} = \int_{a_1}^a f_n' f_n' \left[k - \frac{l(l+1)}{kr^2 \varepsilon} \right] dr - \frac{1}{k} \int_{a_1}^a \frac{1}{\varepsilon} f_n' f_n'' dr, \quad (18)$$

equal to zero for $|n'-n| > 1$.

3. Discussion

The approach proposed above has the following advantages over those in [1] and [2]. Unlike the completely populated matrices in [1], the matrices of (15) and (16) are sparse. Moreover, the dimension of the algebraic system for TM waves (16) is two times smaller than that in [1]. The matrices in [2] are also sparse, however our approach allows reduction of the number of unknowns by the factor of two.

The results of testing of the proposed approach characterizing its effectiveness, as well as the results of numerical study of scattering characteristics for the sphere corresponding to various combinations its parameters will be presented in the final paper.

References

- [1] E. Bilgin, A. Yapar, Electromagnetic scattering by radially inhomogeneous dielectric spheres, *IEEE Trans. Antennas Propagat.*, 63: pp. 2677-2685, June 2015.
- [2] R. A. Shore, Scattering of an electromagnetic linearly polarized plane wave by a multilayered sphere, *IEEE Antennas & Propagat. Mag.*, pp. 69-116, Dec. 2015.
- [3] S. P. Skobelev, *Phased Array Antennas with Optimized Element Patterns*, Norwood: Artech House, 2011.
- [4] J. A. Stratton, *Electromagnetic Theory*, New York: McGraw-Hill, 1941, pp. 563-565.

Automatic finite element Tool for the Error Estimation of the Probe trajectory in Eddy Current NDT of Steam Generator Tubes

Laurent Santandrea

Group of Electrical Engineering-Paris (CNRS), France

*corresponding author: laurent.santandrea@supelec.fr

Abstract-Finite Element Method (FEM) are one of the most popular approach for the simulation of Eddy Current (EC) Non-Destructive Testing problems. Modeling tool can provide information for design and characterization of EC probes. Particularly, they prove useful to evaluate the influence of the probe mispositioning on the measurement. In this work, we propose an automatic finite element tool DOLMEN dedicated to this kind of problem. Simulation of the effect the trajectory of a non axial ferrite core probe during the inspection of a steam generator tube with a diameter variation is presented using the Dolmen code.

Toxic Effects of X-Rays and Frequency Heterodyning

Sara Vesely¹, Sibilla Dolci²

¹ITB-CNR, Milan, Italy

²Via S.Orsola, 11 Milan, Italy

*corresponding author, E-mail: sara.vesely@cnr.it

Abstract

The toxicity of X-rays remained hidden in the short period of time during which this method of investigation established itself both in medicine, where it extended diagnostic capabilities, and in physics, where it unlocked the possibility to extend investigations of the structure of matter from microscopy down to the atomic scale. Enhanced X-ray generation may allow to connect electromagnetic received signals in that frequency range with hazards from X-ray exposure.

1. Introduction

At the beginning, all of the invisible emanations, electrons, X-rays and radioactivity, were likewise associated with fluorescence because they had been discovered by observing the luminescence of materials such as glass, fluoride, barium platinocyanide, and zippeite (potassium uranyl sulfate). They had a great response from the public before the consistency of their discovery was understood. Yet, soon a different degree of hazard was associated with their investigation. Whereas electrons found wide applications in electronics, the harm of radioactivity was recognized at an early stage. In fact, Becquerel reported burns for holding a crystal of radium in his pocket [3], and therefore it is said that he himself or some acquaintance of his immediately suggested to use it for the therapy of tumors. X-rays were put at a level in between: they were promptly related with diagnostic imaging, and only gradually their therapeutic use was assessed.

Since the synchrotron radiation and the free electron laser (FEL) present more progressive X-ray-production techniques than those used up to now [1][2], in this paper we are going to review from this perspective a couple of aspects of the phenomenology, and the way they were initially articulated. We start from Laue's geometric interpretation of X-ray diffraction, and give an outline of how the understanding proceeded hand in hand with the evolution of technical know-how. We concentrate on the effects which are the source of the dynamic theory of diffraction, and on the split of the comprehension of X-ray into a part more related to basic problems in quantum mechanics [4], and one more related to imaging issues [5]. We argue that the technical improvements in the X-ray technology can also allow to go beyond the current diagnostic and therapeutic achievements, and to study more specifically the involved

chemical and biochemical reactions.

2. Revisiting Laue's interpretation

We wish to recall that at the time of the discovery of X-rays, in addition to trying to reproduce the phenomenology under controlled conditions, which is typical of the scientific method, the nature of that emanation was investigated. The almost contemporary discovery of many emanations made it important to distinguish between wave radiations and particle emissions. Therefore the investigation focused on the methods to highlight oscillatory traits or else the possession of a mass. Not much the discovery of the dual nature of light later on as phenomena like will-o'-the-wisps or particles resonance make any distinction among emanations somewhat ephemeral.

2.1. The diffraction interpretation

Perhaps X-rays were comprehended among electromagnetic radiations by Laue, due to Röntgen's experiments, and under the influence of the thesis on the double refraction of light by a three-dimensional anisotropic array of isotropic resonators, that Ewald was writing at the time with Sommerfeld as relator. Laue extrapolated from the latter that, if the X-ray wavelengths are of the order of magnitude of the interatomic distances, a crystal must separate the beam in the way a diffraction grating does.

Before the first diffraction experiment was executed, Röntgen might conceivably have guessed that a crystal would show a shadow resembling that of a radiography of a hand's bones, say. We are not denying that shadows in coherent light quite resemble diffraction patterns. Rather, the problem is, if the observed Laue's patterns of crystals may be interpreted likewise.

Friedrich and Knipping [6] recorded photographs on a film put behind a single crystal of copper sulfate ($CuSO_4$), by shining hard X-rays from a Crookes tube through it. They showed that the recorded pattern consists of spots symmetrically disposed around the undeflected beam. Being driven by an induction coil (generating a maximum potential of about $40kV$), the tube emitted short radiation pulses. Since, in addition, the degree of hardness of the Bremsstrahlung kept increasing in time while the residual gas dropped in the tube, initially Friedrich and Knipping assumed that the beam separated by the crystal was the characteristic (monochromatic) one. On the report of Ewald

[7], their opinion that the diffracted rays consisted of secondary characteristic radiation, sparked in the crystal by the primary incident ray, was retracted right away (p.45), and it was clarified that the measured effect was really due to diffraction of the Bremsstrahlung radiation pulses through the crystal lattice.

Subsequently, it was generally accepted that in Laue's experiments the Crookes tube gave off pulses of sufficiently coherent Bremsstrahlung, and that the observed spots resulted from spectral filtering of wavelengths by diffraction through the crystal sample. Laue's careful calculations on the intensity pattern of a zinc sulfide (ZnS) crystal [8] demonstrated that, if a volume grating transmits diffraction orders higher than zero,¹ only sparse wavelengths determined by integral (Miller) indices are allowed to get through under Fraunhofer diffraction conditions. In detail the resolving power of a linear diffraction grating is far off what was observed, because the diffracted wavelengths were only approximately monochromatic, and their overtones could not be expressed as terms of a harmonic series, but had to be calculated like so

$$h = \sqrt{h_1^2 + h_2^2 + h_3^2}, \quad (1)$$

the integral indices being h_i , ($i = 1, 2, 3$). As a consequence, it proved necessary to develop a geometric model of the diffractogram, the reciprocal space. With the help of it, Laue interpreted Friedrich and Knipping photographs after distinguishing between two types of interaction: the crystal separates a beam into its constituent wavelength components like a three-dimensional transmission grating (A), or it absorbs energy and subsequently releases it as fluorescence (B), and choosing alternative (A). He didn't put forward the alternative (C), that a crystal irradiated with a characteristic line from an X-ray tube behaves like a frequency mixer. We use the word *frequency mixer* to designate a device which modulates an incoming carrier with one or more carriers generated locally at other frequencies.

W.L. and W.H. Bragg maintained that the spatial lattice exerts a selective band pass action on X-radiation, quite similar to that valid for the linear diffraction gratings in the optical range. They updated the geometric condition expressed in eq. (1), specific for three-dimensional diffraction, to the effect that a crystal mirror-reflects X-rays of given wavelength λ when the incidence direction forms a glancing angle $\theta = \arcsin(\lambda/2d)$ with densely packed crystal layers, where d is the layer separation. The reflection off those layers is due to constructive interference. Higher reflections of order n also satisfy the reflection condition, i.e. spots can also occur for wavelengths satisfying

$$n\lambda = 2d \sin \theta, \quad (2)$$

Bragg's law (2) was the simplest in accordance with the data collected in those days. It brought to the construction of the first X-ray spectrometer [9].

¹Under monochromatic light the Talbot self-imaging effect allows the replication of a planar grating structure at multiple distances of the grating period in the Fresnel diffraction zone.

2.1.1. Comparison with light

Although the laws of ray optics were seminal in explaining X-ray diffraction, Bremsstrahlung behaves differently from white light. It does not give rise to interference fringes. It is not likewise refracted by common materials, because the refractive index is $n \leq 1$ for $\lambda < 1nm$, that is the phenomenon of total reflection at the interface between vacuum and sample takes place on the side of the vacuum. In addition it is $n \approx 1$ for $\lambda < 10^{-3}nm$, that is all matter becomes equally transparent in the range of γ -rays. Thus, there exist no lenses which can focus wavelengths shorter than about $1nm$, and an X-ray photograph looks more like a shadow cast on a screen, than like a photographic image in the optical sense.

While studying image formation under a microscope, Abbe related the Fraunhofer diffraction patterns to the images: he demonstrated that a converging lens transforms a diffraction pattern in its focal plane into an image at infinity, and vice versa. If X-rays with $\lambda < 1nm$ are not brought to a focus, the X-ray crystallographic diffraction patterns are so called without possessing the features conforming to the homonymous optical pattern.

To finish the comparison with visible light, it is possible to spectrally decompose coherent white light in two ways:

- using a linear grating. The spectrum obtained is called *diffraction spectrum*;
- by means of a glass or an amorphous quartz prism. The spectrum obtained is called *dispersion spectrum*.

In the first order rainbow obtained by diffraction, the angular inclination as a function of wavelength varies in the opposite direction to that of the refracted light in a glass prism. When light is decomposed in the former way, the orders of diffraction are described by eq. (2), whereas the angular spread of the rainbow is a second order effect with respect to diffraction. When it is decomposed in the latter way, the angular spread of the spectrum constitutes the whole effect, and clearly depends on the material. In glass the dispersion angle of light is normal, i.e. it increases with decreasing wavelength from red to violet. By convention, in linear optical diffraction gratings, the wavelengths are attributed to the colors in the rainbow so as to fit in the gap between the first and the second diffraction order. This suggests that light diffraction is a linear effect, while dispersion is not. Bragg's law (2) states a condition similar to that of Fraunhofer diffraction of a beam at grazing angles in Littrow configuration, that is, assuming that reflection is backwards, and that $n = 1$ means the first diffraction order.

3. The geometry of crystallographers

As a byproduct of Laue's recasting of optical diffraction for X-rays, crystallography became quantitative, and was carried over from mineralogy to chemistry to help characterize chemical compounds besides balance, titration methods, and spectroscopic analysis. Conversely, the development of X-ray techniques was enriched by crystallography.

3.1. Ewald's geometric approach

We already mentioned that the understanding of X-ray diffraction is separated from both, that of radiography, and that of optical images. In fact, the utilization of the X-ray methods to determine the intrinsic structure of crystals is rooted in the crystallographic tradition. In mineralogy, observation of the cleavage properties, and of the development of crystal faces during growth, had led to establish that, not much the exterior shape as the angles formed between surfaces are typical of the crystal structure. A law of rational indices had been formulated, resembling Dalton's law of multiple proportions in chemistry [10]. It states that the quotients of two intercepts of a natural face with the principal axes of a crystal are small ratios. Haüy explained this law supposing that a crystal is built up from a repetition in space of a primitive cell. Later on, his heuristic rule was formalized, and discrete lattice structures were merged with the algebraic approach to symmetry groups [11].

In the course of the quantitative development of crystallographic analysis, sparked by the discovery of X-ray diffraction of crystals, Ewald proposed to associate to the crystal lattice a reciprocal lattice matching Laue's measured diffraction patterns, instead of being consistent with the correlative construction of a honeycomb of polyhedrons [12].² Conceptually, Ewald relates a set of planes of regular spacing d in the real crystal to a point in the reciprocal lattice, whose distance from the origin is $1/d$, and whose radius vector lies along the direction of the normal to the planes.³ For each n , the n^{th} order stack of planes of spacing d/n is represented by a point along the same radius vector, but at n times the distance from the origin (that is, at n/d .) In this way, a pitch d in the direct space corresponds to a pitch $1/d$ in the reciprocal space.⁴ To recover the crystal structure from a Laue's diffraction pattern a sphere, called *sphere of reflection*, is attached to each photographed reflection spot. On this sphere, which should be centered on the common origin of both, the radius vector representing the incoming beam, and that representing the diffracted one, lie their tips. A vector belonging to the reciprocal lattice should close the triangle. It turned out that the purely geometric method was insufficient to resolve crystal structures: besides not allowing to take into account the intensity of the reflections, it didn't explain why crystals which, according to the older crystallography, should belong to the same symmetry group, show different Laue diffractograms.

To take the intensity of the reflections into account, Ewald amended his geometric approach by associating with

²In crystallography, it is assumed that the unit cell (Wigner-Seitz cell) matches the symmetry of the crystal. In geometry polyhedrons are primitive unit cells, while from the outset crystallography needed to define more, such as the face and the body centered cells of holocentric crystals, and in addition hemiedric crystals.

³The reciprocals of the fractional intercepts on the cell axes of a crystal face designate a plane in reciprocal space with Miller indices $(h_1 h_2 h_3)$. For example, if in the (x, y) plane the intercept point on the x axis is (d, ∞) , its fractional intercept is $(d/d, \infty/d) = (1, \infty)$, and its reciprocal designates a line orthogonal to x , with Miller index (10) .

⁴Ewald's reciprocal grating pitch is defined as $|\kappa| = 1/d \approx 1/\lambda$.

each point of the reciprocal lattice a structure factor Φ_{κ} , expressed as a sum $\Phi_{\kappa} = \sum_n \rho_n e^{2\pi\kappa\mathbf{r}}$. Here, ρ_n is a scattering factor, dependent on the electron distribution around individual atoms in the unit cell. Unlike him, Bragg applied from the outset the method of Fourier series to represent physical quantities varying from point to point inside a perfect crystal. In particular, he represented the space lattice structure as a stationary electron density function $\rho(\mathbf{r})$. After having broken up it into densely packed layers, he associated with each stack a set of sinusoidal terms (taken as real part of $e^{-i\kappa\mathbf{r}}$.) Thus, an incident monochromatic X-beam undergoes reflection against the periodic grids estimating $\rho(\mathbf{r})$ in the perfect crystal, and produces the intensities of the observed spots. This method of Fourier analysis was developed further, notwithstanding the difficulty of associating $\rho(\mathbf{r})$ to generic crystal structures with harmonic terms determined by eq. (1).

If crystals possess periodic geometric structures, the Moiré magnifying effect [13] could support Laue's prospect to extend investigations from microscopy down to the atomic scale. Instead of pursuing Ewald's geometric approach further, in this paper we are going to discuss imaging from an information and communications point of view. Integral transform methods started to be applied in the late 1920s to communication systems in relation to signal processing, and the Fourier transform method became slowly established in crystallography, to analyze the reflections of monochromatic X-rays produced by single crystals, when they are rotated about different axes [14].

4. Rise of the telecommunications' approach

With *telecommunications' approach* we designate the trend which consists in carrying out a surveying at a distance and then relying on the acquisition techniques developed in electronics and computer sciences to get a picture. This holistic trend has been catching on in electromagnetism. For example, in medicine imaging technologies have been developed of which the diagnostics can take advantage, and of which radiography was the first example. The advantage consists of the fact that this is a "non-invasive" investigation, that allows to image functioning internal organs without sectioning the patient. However, an imaged organ is totally different from what would be seen while performing an autopsy; moreover the information about it changes with the frequency range, with the acquisition mode and with the image reconstruction technique.

The employed radiant power can have an effect on the images. From the point of view of signal acquisition, a modulation accepted by the passband appears just as linear as the signals that have geometric interpretation. Yet, among the transmitted modulations there can be non-linear ones, which are characteristic of an ongoing process, and thus informative. Since they are non-linear, they express features that would not have a geometric representation by themselves, and don't have any geometric interpretation. As an example, the "therapeutic effect" of X-rays does not depend linearly on their intensity, and is belated compared to

irradiation. To properly use the imaging technologies, it seems to us appropriate to distinguish the linear part in the received signal, which can be geometrically represented, from other modulations.

In the remainder of this section we will analyze the role played by the increasing power of X-ray sources on the changeover from Laue-space's diagram to the Fourier transform representation. This issue is related to alternative (C) (sect. 2.1.1). We will try and show that the introduction of Fourier methods tended to hide the distinction between diffraction and dispersion frequencies (sect. 2.1.2), as well as that between second order approximation and non-linearity.

4.1. Dynamical scattering and Fourier transform

In 1958 Slater summarized the dynamical theory of X-ray diffraction, subsuming crystallography under the general band theory of solids [15]. The key point is to represent the material crystal lattice as a self-consistent potential energy, and to deal with the total wave field inside the crystal, instead of just with X-rays. The construction of the reciprocal lattice boils down to the requirement that the electron function $\Psi(\mathbf{r})$ be of the form

$$\Psi(\mathbf{r}) = \sum_{\mathbf{p}} \Phi(\mathbf{p}) e^{-i(\mathbf{k}_0 + \mathbf{p})\mathbf{r}} \quad (3)$$

The wave function (3) is such that $\Psi^*(\mathbf{r})\Psi(\mathbf{r})$ is the electron density. Here, $\Phi(\mathbf{p})$ has about the same meaning as Φ_{κ} , $\mathbf{p} = 2\pi(h_1\mathbf{b}_1 + h_2\mathbf{b}_2 + h_3\mathbf{b}_3)$ is such that its phase is the same at equivalent points in the crystal, and h_i are Miller indices; $\mathbf{r} = m_1\mathbf{a}_1 + m_2\mathbf{a}_2 + m_3\mathbf{a}_3$, with integer m_i , refers to lattice positions computed from the origin of the unit cell, and the phase exponent $\mathbf{p}\mathbf{r}$ is $m_1h_1 + m_2h_2 + m_3h_3 = 2n\pi$, with n a positive integer. An incident X-beam is represented by a monochromatic plane wave $Ae^{i(\omega_0 t \pm \mathbf{k}_0 \mathbf{r})}$, where $|\mathbf{k}_0| = 2\pi/\lambda$ is its propagation vector, and $\omega_0 = c|\mathbf{k}_0|$ is its angular frequency.

We are interested in coherently scattered X-rays⁵, when \mathbf{k}_0 is in the neighborhood of the angle θ_B satisfying Bragg's reflection condition $\sin(\theta_B) = \frac{1}{2}\lambda/d$ (cf. also eq. (2).) In conformity with the above conventions Bragg's condition, i.e. the condition that the frequency be unaltered after scattering, can be restated as

$$|\mathbf{k}' \pm \mathbf{k}_0| = |\mathbf{k}_0|, \quad (4)$$

A wave vector \mathbf{k}' related to momentum change has been substituted for the pitch of the crystal lattice κ .⁶ Since the modulus of the propagation vector \mathbf{k}_0 is unchanged after scattering, while its direction changes, in the dynamical

⁵When "coherent" is used in this context, it means "capable of producing a Laue diffraction pattern".

⁶We recall that in Bragg's equation, $n\lambda = 2d \sin \theta$, $n = 1$ means reflection of the monochromatic wavelength $n\lambda$, $n = 1$. In the new notation, $|\mathbf{k}'|$ is a vector $|\kappa'|$ of the reciprocal lattice times 2π . Correspondingly, there is just one Fourier component with propagation constant \mathbf{k}' , ($|\mathbf{k}'| = 2\pi/d$). Nowadays diffraction by a sinusoidal grating, characterized by $n = \pm 1$, is called *Bragg diffraction regime*.

cal interpretation Bragg's process corresponds to an *elastic scattering* of the impinging X-beam from the space lattice.

If we take the periodicity of (3) into account, and add a condition $\mathbf{k}' - \mathbf{k}_0 = \mathbf{p}$ with $\mathbf{p} = \pm 1$ to eq. (4), the crystal wave function $\Psi(\mathbf{r})$ is solution to a wave equation, which depends on the potential energy arising from both, nuclei and electron density within the unit cell. In contrast, if we drop the condition $\mathbf{p} = \pm 1$, $\Psi(\mathbf{r})$ becomes a periodic function extended over the whole crystal, and we are allowing the occurrence of multiple scattering. The dispersion curve $\omega = \omega(\mathbf{k}_0)$, obtained by determining the set of values k_0 from the eigenvalue problem, becomes a multi-valued function. To deal with the general case $\mathbf{p} \neq \pm 1$ (and $\neq 0$), Brillouin restricted the solution by limiting to the range $[-\frac{1}{2}k', \frac{1}{2}k']$ where $\omega = \omega(\mathbf{k}_0)$ is continuous.⁷

If thermal agitation of the spatial lattice is taken into account, the electron density fluctuates due to the random displacements of the lattice unit cells with respect to one another. Until \mathbf{k}' belongs to the lowest ω -branch, the dynamical theory continues predicting the same spots as did Bragg-Laue's. But, inasmuch as \mathbf{p} is responsible for the multivaluedness of the dispersion curve, and the vectors \mathbf{k}_0 fill up the whole Brillouin zone, the theory accounts for thermal diffuse scattering. Consequently, thermal energy contributes an atomic scattering factor and a Debye-Waller temperature factor to \mathbf{k}' , which we hence rename \mathbf{k}_1 .

At the next stage of approximation, thermal energy allows to explain the displacement of the recorded spots from the locations predicted on the basis of Bragg's law (2). An acoustic wave of propagation vector $\mathbf{k}_1 + \mathbf{k}_a$ is assigned to each collective elastic vibrational mode of the crystal lattice. Setting $\mathbf{K} \equiv \mathbf{k}_1 + \mathbf{k}_a + \mathbf{p}$, an inelastic scattering condition $|\mathbf{K} \pm \mathbf{k}_0| = |\mathbf{k}_0|$ is satisfied instead of eq. (4), and thermal energy contributes to X-ray diffraction on account of the elastic vibration modes of the lattice, by promoting leaps to the next energy band (Umklapp process).⁸ The energy gap between the bands arises from the fact that in the neighborhood of the frequencies corresponding to the limits of Brillouin's fundamental zone $[-\frac{1}{2}k', \frac{1}{2}k']$, where Bragg's reflection condition is satisfied, there are no real values of ω .

The dynamical theory of X-ray diffraction, which we briefly sketched out, served to face the fact pointed out by Raman in 1940, that besides the reflections accounted for by Laue-Bragg there are extra- and forbidden reflections, and that X-rays do indeed directly interact with thermal vibrations in diamond.⁹

⁷In this approach Brillouin's fundamental zone replaces the reciprocal space. It is the reciprocal of the Wigner-Seitz cell.

⁸The energy band structure of a crystal is the set of the succeeding branches of the dispersion curve $\hbar\omega = E = E(\mathbf{k}_0)$. If a crystal has $3N$ degrees of freedom, it has 3 acoustic branches and $3N - 3$ optical branches.

⁹Actually, the vibration concerned is that at $\lambda \approx 7.5\mu\text{m}$, (1332cm^{-1}). Raman himself didn't attribute it to the lattice, but rather to a Reststrahlen band belonging to an optical branch.

4.1.1. Brillouin scattering of light by sound waves

In 1922 Brillouin had propounded to trace back the observed X-ray spots to diffraction by thermally excited fluctuations. Superposition of the acoustic waves assigned to the elastic normal modes of the lattice, and traveling in all possible directions inside the crystal, would give rise to a volume grating. The ensuing X-ray diffraction theory would be as simple as Bragg's one, apart from being directly linked to heat transfer. In order to explain diffraction by thermal energy, it is supposed that each acoustic vibration yields a mass density gradient which, in turn, determines a maximum variation of the crystal refractive index $\delta\mu_{max}$. Owing to the slowness of sound with respect to the speed of electromagnetic radiation, to a first approximation the pitch depends on an averaged refractive index. Yet, for diamond, which has a very high Debye frequency, namely the maximum frequency of atomic thermal vibrations, the order of magnitude of the diffracted wavelength λ had been readily estimated to be $\lambda \approx 7.5\mu m$, ($1332cm^{-1}$).¹⁰ Apparently, the order of magnitude of the pitch induced by thermal fluctuations is far to low to diffract X-rays.

Although Brillouin's mechanism had been ruled out, the feasibility of observing diffraction patterns generated by means of acoustic waves was deemed worthy of an in-depth examination. In 1932 Debye and Sears resumed his idea [16][17], and showed that light undergoes volume diffraction by ultrasound. If compression waves, generated within the volume of a liquid of density σ ,¹¹ propagate at velocity $c_a = \sqrt{B/\sigma}$ ($B = dp/(dV/V)$ is the bulk modulus, p the pressure), the condition that diffraction leaves the frequency of the impinging radiation unchanged is relaxed, because the moving lattice is described by a function $\Theta e^{-2\pi i(\mathbf{k}'\mathbf{r}-\omega't)}$ with $\omega' \neq 0$. Anyway, acoustically excited vibrations within the liquid were expected to behave like a phase grating, and to give rise to a Bragg diffraction pattern, if only the lattice periodicity is not far off the optical frequency-domain. In Debye Sears' experimental disposition, a piezoelectric quartz was immersed in a trough of rectangular cross-section filled with a liquid, and was excited by means of a radio-frequency oscillator at about $5.7MHz$. Benzene (C_6H_6), carbon tetrachloride (CCl_4), toluene (C_7H_8) and glycerin ($C_3H_8O_3$) were among the chosen liquids.¹² The trough was irradiated with a line of a mercury arc light source laterally, that is, in a direction

¹⁰Since the qualitative behavior of the specific heat of solids is much like that of an oscillator, even in classical thermodynamics the thermal energy of solids is associated with the oscillations of molecules. If the molecules occupy lattice points, the lattice constant sets a lower limit to the wavelength of elastic wave propagation.

¹¹The electrooptical effect should neither involve surface waves, nor vibrations of the enclosure. We presume that, in the linear regime, the pressure difference of the generated elastic waves is even less conspicuous than that measured in quiet air when someone is speaking.

¹²Sound speed in those liquids ranges between about 900 and 1900m/s at room temperature, and ultrasound is only weakly absorbed. As ultrasounds can be transmitted underseas, after WWI, quartz oscillators were secretly being developed for equipping submarines with sonars. The core of a sonar was a thin piezoelectric crystal sandwiched between two metal plates, and mounted in a case suitable for submersion.

normal to the quartz mounting, and the pattern transmitted through the liquid was recorded. Under those conditions Bragg's glancing angle of incidence onto the elastic waves was about 0° , there was a small time-modulation at the ultrasound frequency, and the trough cross-section was perhaps too small. Thus, in spite of the fact that the liquid conceivably formed a three-dimensional wave-lattice, no typical Bragg-Laue pattern could be visualized in the optical frequency range.

Debye and Sears confirmed that the scattering of light depends on the vibration frequency of the piezoelectric quartz, and that if neither the monochromatic light intensity, nor that of ultrasound are too high, the intensity of the diffracted light is proportional to the crystal exciting power. In the meantime (1928) the optical Raman effect had been discovered [18], and analogous experiments were conducted in the X-ray range [19]. Nowadays, it is known that all of the solvents tested in the above experiment possess Raman lines in the range of electro-optical applications. Thus, the increase in peak fluence due to the use of a laser light source must evidence their contribute.

5. The diamond and the carbon backbone

For radio circuits it is expedient to link up amplitude and phase when analyzing the performance of simple filters, such as tuned RCL circuits, whereas in the X-ray domain these two properties are kept distinct. According to the Beer-Lambert law, a sample attenuates impinging X-rays either by absorption or by scattering. Absorption involves energy loss, and is accompanied by emission of photoelectrons, while diffraction does not. Moreover, since the absorption edges are fingerprints of chemical elements, the ionized electrons belong to the atomic core, and hence their extraction corresponds to a considerable amount of energy. In contrast, the scattering mechanism depends on the total electron density distribution, and is chiefly determined by the phase relationships of the diffracted radiations. Nevertheless, this picture is valid to first Born approximation, i.e. until the intensity of the diffracted beams is small with respect to the incident rays.

Toward the end of sect. 4.1.1, we remarked that the dynamical theory of X-ray diffraction conceives of the atomic scattering factor as a complex quantity. Since the energy content of signals is computed from their spectral energy distribution, the Fourier transform is related to energy conservation. The small energy changes (compared with ionization) summoned up by the imaginary component of the atomic scattering factor are accounted for by creation/absorption of phonons. The theory of lattice dynamics developed by Faxén and Waller retains that non-linear permittivity waves linked to the acoustic modes $\mathbf{k}_1 + \mathbf{k}_a$ contribute mostly at the boundary of the Brillouin zone. It states that thermal energy associated with the acoustic branches must elicit stronger effects than energy originated by "hidden" multiple modes of vibration inside the crystal unit cell, and linked up to the optical branches.

5.0.2. Infrared vibrations directly sparked by X-rays

If we take a closer look at the characteristic X-bands, there are indications that fluorescence bands can be very narrow and polarized. Irradiated samples may show long post-radiation emissions at very low intensity. Again, it is reported that characteristic X-beams emitted from secondary radiators can be as directional as laser light. Altogether, these features indicate that, although the X-ray intensity may be densely packed within a narrow range, the overall power exchanged with a sample is low. The fact is, that these features readily give rise to non-linear response by matter.

Even Barkla noticed that outgoing characteristic X-beams can be depolarized, and somewhat softer, i.e. of lower energy, than the incoming ones, so that Stokes fluorescence law applies to them. The experiments pursued on diamond by Raman and coworkers with improved, more powerful Coolidge tubes [20] strengthen Barkla's interpretation, because some samples gave clearly rise to secondary X-spots at positions fairly independent from the scattering angle, and failing to correspond with those calculated from the simple theory of interference of rays developed by Laue and Bragg. Raman himself called the spots *reflections of the second kind*, and remarked that they comply with Rydberg-Ritz combination principle, being more akin to transition lines than to harmonics. He suggested that a characteristic X-ray of frequency ω may be either Stokes ($\Delta\omega = \omega - \omega^*$) or anti-Stokes ($\Delta\omega = \omega + \omega^*$) shifted, depending on a narrow-banded coherent radiation at frequency ω^* .¹³ Since the ω^* of a Stokes-shifted radiation lies in the infrared part of the electromagnetic spectrum, he suggested that X-rays might be used to study this part of the spectrum. Besides these experiments on diamond, other experiments were carried out, for example by Venkateswaran [21], on silicon carbide (*SiC*), sodium nitrate (*NaNO₃*), sodium chloride (*NaCl*), and pentaerythritol (*C₅H₁₂O₄*). The existence of emission bands ω^* with thermal frequencies respectively at 800, 200, 160 and less than 100cm^{-1} was predicted, based on the temperature dependence of the relative intensities of Raman's $\Delta\omega$ with respect to Bragg-Laue's ω . The predicted values were dismissed as inaccurate, though [22]. Raman's own suggestion was discarded on account of the extremely low cross-section for inelastic scattering, which was at the resolution limit. Further, his interpretation, that the narrow line of diamond at 1332cm^{-1} is a Reststrahlen band – a “hidden” mode – didn't seem well-founded. As Faxén and Waller theory doesn't allow attribution of the $\Delta\omega$ -line in terms of lattice vibrations of the ideal carbon structure of diamond, it was rather deemed specific only to some diamonds [23][24]. As a result, the connection between X-ray and infrared range didn't seem to reveal a universal behavior of matter. By now, the X-ray Raman scattering is well established. It gets more remarkable under resonance conditions, and at higher temperatures.

¹³Here, coherent radiation means that its spatial extent is small (Nadelstrahlung).

5.0.3. Raman effect as heterodyning in the X-ray range

We sketch an argument in favor of the compatibility of the Raman effect with the alternative (C) mentioned in sect. 2.1.1. For the diamonds showing the effect, the local oscillator (LO) is sparked off inside the sample at 1332cm^{-1} by the incoming X-ray itself. At low intensities the effect is faint. However, if the primary radiator transmits too much power under resonance coupling, system overload occurs.¹⁴ The bands of secondary radiators broaden (self-absorption), and narrow sidebands (satellites) become observable.

A frequency mixer at $3 \cdot 10^{17}\text{Hz}$ to $3 \cdot 10^{19}\text{Hz}$ can be thought of as a parametric oscillator whose loaded Q varies with the coupling impedance between a crystal and an X-ray source. The technical feasibility of producing parametric radiation (PXR) in the range 0.25nm to 0.05nm implies the control of a process that otherwise occurs in an uncontrolled way. Since the electrical terminology is neutral, it is advisable to create a mental image of X-ray frequency mixing by explaining it with the help of an analogy.

First of all, we outline the quantum mechanical explanation of the Raman effect in terms of the Kramers-Heisenberg dispersion formula. Simplifying matters, the X-beam is considered a time dependent perturbation field acting on energetically characterized oscillator states of the sample, and causing dipole transitions between them. Raman scattering occurs between electron states belonging to the core and roto-vibrational energy levels. Near resonance the scattering (real part) is often described as a two-photon process involving absorption and re-emission of energy from intermediate virtual oscillator states [25]. Next, we explain the Raman effect availing ourselves of an analogy with sound. If two matched tuning forks are mechanically coupled, and one of them is gently excited, the other will be driven to ring in unison, and will give off a clean fundamental tone ω . Increasing the power of the blow, fading away ω^* -tones become clearly audible without any sound box. They are characteristic tones of the stressed material.¹⁵ Since the vibration of the prongs is strain dependent, the supervening load variation elicits slightly mismatched modes from the tuning fork. A modulated sound $\Delta\omega$ becomes audible (with sound box) as a purely acoustic effect of the mismatch.¹⁶ In this picture neither the acoustic wave ω nor the ω^* are able to drive the dependent fork into resonance, but a mechanical coupling of the forks is necessary. In particular, ω^* , which cannot even be transferred by the sound box, should be thought of as a *mechano-acoustic conversion* at resonance rather than a linear transformation of conserved energy. At a difference with sound, observation of the X-ray Raman effect, i.e. of frequency mixing $\Delta\omega$, can imply a LO sparked at ω^* with some efficiency [26]. Moreover, if a LO can be related to

¹⁴We are assuming that detectors behave linearly.

¹⁵The characteristic tones ω^* are not related to normal modes, as those modes may interact with one another.

¹⁶Combination tones can be heard *without having been produced*, because of the non-linear functioning of the ear. If the same picture is adopted for coupled forks, the modulation cannot be conceptualized as a back and forth transfer of extant energy.

a chemico-physical conversion process, the Raman effect may help revealing one step of the multifarious biological conversions occurring under X-ray irradiation.

5.0.4. Altered metabolism and toxic effects

While the radiations diffracted by a ruled grating are related to the grating period and to its irregularities, that is, to its geometrical shape, X-rays may interfere with chemical reactions. Heterodyning frequencies depend on the specific wavelength at which a given sample is irradiated, and can promote accompanying conversion processes contingent on both, the radiation and the material, possibly with a small yield. Taking up diamond again, the modulating carrier is a strong resonance frequency at 1332cm^{-1} . In fact, diamond is a quite good heat conductor, and has a distinct tendency to oxidize if heated. It even may turn blue under γ -irradiation.

Covalently bound carbon forms the backbone of living matter. Hard X-beams are known to be penetrating. However, mixing can excite additional internal modes in the soft X-ray zones and beneath, where materials exhibit very many resonances, and limited penetrating power. If the radiation power is raised, nonlinear effects will be accentuated at once. Chemical and other reactions can as well be associated with their appearance.¹⁷ Since biological samples have metabolic pathways, the effects of irradiation are propagated through a sequence of reactions [27]. For example, a radiation between 100nm and 1nm generated by frequency mixing is germicidal. It also interferes with many biological functions, which have finely tuned chemical reactions [28].

Since chemical reactions depend primarily on the availability of reagents, characterization of the radiation is not enough to understand all the chemical and biochemical effects, which the radiation may give rise to [29].¹⁸ But there are effects associated with the hazard, which can indeed be followed as the composition of the X-beams becomes more definite, powerful, and controllable. Finally, we believe that, studying chemical chain reactions, it could be figured out how to get a specific reaction step by irradiating with a lower frequency. Means could be devised to amplify the yield of a specific product by irradiation at lower frequency.

6. Conclusions

We saw that Laue's interpretation of the patterns observed by Friedrich and Knipping in terms of volume diffraction of waves by crystals was rooted in crystallography, and retained about the same connotation for W.L. and W.H. Bragg. The belief that the inherent constitution of matter can be comprehended through space structures, and that

¹⁷Currently, parasitic reflections and multiple scattering are combined so as to fulfill Laue conditions. If they are heterodyned frequencies, their intensity rises with that of X-rays, and further spurious frequencies appear.

¹⁸To give an example, heating pyrite is not enough to derive iron from it, but it is necessary to understand the effects of the content of carbon oxides and sulfides, and where they are formed while the pyrite is melted.

X-rays afford their visualization in a quite direct and fundamental way, led X-ray analysis to become instrumental in the elucidation of the atomic structure of chemical elements. As of today the X-ray methods developed for crystal structure determinations have been extended to organic compounds. Yet, the approaches to image reconstruction that gained ground in other frequency ranges with the support of electronics and computer science take on a slightly different purpose, i.e. that of ascertaining the external shapes peculiar to the objects.

The improvements in the production and analysis of X-rays could lead to take up again the suggestion by Raman, that these radiations interact selectively with matter, thereby eliciting resonance bands in other frequency ranges (in particular in the infrared). Frequency heterodyning could hint at an ongoing occurrence of chemico-physical conversion processes in matter, possibly with small yield. If the toxic effects of X-rays can be related to small signal modulations, crystallography can be approached from an information and communications point of view, backed by chemical analysis.

References

- [1] R. L. Owen, J. Juanhuix, M. Fuchs, Current advances in synchrotron radiation instrumentation for MX experiments, *Arch. Biochem. Biophys.* XX: 1–11, 2016.
- [2] A. Pálffy, X-ray physics: straight outta Compton, *NATURE PHYSICS* 11: 893–894, 2015.
- [3] H. Becquerel, P. Curie, Action physiologique des rayons du radium, *C. R. T.* 132: 1289–1291, 1901.
- [4] G. Dixit, O. Vendrell, R. Santra, Imaging electronic quantum motion with light, *PNAS* 169(29): 11636–11640, 2012.
- [5] H. Wen, A.A. Gomella, A. Patel, S.K. Lynch, N. M. Morgan, A.A. Anderson, E.E. Bennett, X. Xiao, C. Liu, D.E. Wolfe, Subnanoradian X-ray phase-contrast imaging using a far-field interferometer of nanometric phase gratings, *Nat. Commun.* 4:2659 1–9, 2013.
- [6] Friedrich, W., P. Knipping and M. Laue, Interferenzerscheinungen bei Röntgenstrahlen, *Ann. Phys. (Berlin)*, 346(10): 971–988, 1913.
- [7] P.P. Ewald, *Fifty Years of X-Ray Diffraction*, IUCr, Utrecht, 1962.
- [8] M. Laue, Eine quantitative Prüfung der Theorie für die Interferenzerscheinungen bei Röntgenstrahlungen, *Ann. Phys. (Berlin)* 346(10): 989–1002, 1913.
- [9] W.H. Bragg, W.L. Bragg, *X-Rays and Crystal Structure*, G.Bell and Sons, Ltd, London, 1915.
- [10] A.F. Rogers, The validity of the law of rational indices, and the analogy between the fundamental laws of chemistry and crystallography, *P. Am. Philos. Soc.* 51: 103–117, 1912.

- [11] E. Scholz, *Symmetrie, Gruppe, Dualität*, Birkhäuser Verlag, Basel, 1989.
- [12] A. Andreini, Sulle reti di poliedri regolari e semiregolari e sulle corrispondenti reti correlative, *Mem. Società Italiana delle Scienze Ser.3*, 14: 75–129, 1905.
- [13] H. Kamala, R. Völkel, J. Alda, Properties of Moiré magnifier, *Opt. Eng.* 37(11): 3007–3014, 1998.
- [14] A.J. Gibbs, A.J. Rowe, Reconstruction of images from transforms by an optical method, *Nature* 246: 509–511, 1973.
- [15] J.C. Slater, Interactions of waves in crystals, *Rev. Mod. Phys.* 30(1): 197–222, 1958.
- [16] P. Debye, F.W. Sears, On the scattering of light by supersonic waves, *P.N.A.S.* 18(6): 409–414, 1932.
- [17] E. Gross, Change of wave-length of light due to elastic heat waves at scattering in liquids, *NATURE* 126(3171): 201–202, 1930.
- [18] C.V. Raman, K.S. Krishnan, A new type of secondary radiation, *Nature* 121(3048) 501–502, 1928.
- [19] A. Pimpale, C. Mande, Raman effect in the X-ray region, *Pramana* 23(3): 279–295, 1984.
- [20] C.V. Raman, Dynamic X-ray reflections in crystals, *Curr. Sci.* 17: 65–75, 1948.
- [21] C.S. Venkateswaran, Low-temperature studies of the Raman X-ray reflections in crystals, *P. Indian Acad. Sci. A* 14(4):387–394, 1941
- [22] K. Lonsdale, X-ray study of crystal dynamics: An historical and critical survey of experiment and theory, *Proc. Phys. Soc.* 54: 314–353, 1942.
- [23] G.B.B.M. Sutherland, Some comments on the infrared spectra of diamond, silicon, and germanium, *J. Opt. Soc. Am.* 50(12): 1201–1203, 1960.
- [24] S.A. Solin, A.K. Ramdas, Raman spectrum of diamond, *Phys. Rev. B* 1(4): 1687–1698, 1970.
- [25] Y.B. Barnett, I. Freund, Resonant X-ray Raman scattering, *Phys. Rev. Lett.* 34(6): 372–376, 1975.
- [26] K. Okada, K. Kanda, S. Komatsu, S. Matsumoto, Effect of the excitation wavelength on Raman scattering of microcrystalline diamond prepared in a low pressure inductively coupled plasma, *J. Appl. Phys.* 88(3): 1674–1678, 2000.
- [27] D.S. Grosch, L.E. Hopwood, *Biological Effects of Radiations*, II Ed., Academic Press, New York, 1979.
- [28] S.A. Meo, A.M. Al Drees, S. ZA Zadi, S. Al Damgh, A.S. Al-Tuwaijri, Hazards of X-ray radiation on the quantitative and phagocytic functions of polymorphonuclear neutrophils in X-ray technicians, *J. Occup. Health* 48(2): 88–92, 2006.
- [29] Z. Wang, Y. Zhao, C.-S. Zha, Q. Xue, R.T. Downs, R.-G. Duan, R. Caracas, X. Liao, X-ray induced synthesis of 8H diamond, *Adv. Mater.* 20: 3303–3307, 2008.